Boosting the potential of superoxide dismutase mimics as treatment for inflammatory bowel diseases : from chemical design and production to intestinal delivery in mice

Gabrielle Schanne

Sorbonne Université

Ecole doctorale 406 Chimie Moléculaire Paris Centre

Laboratoire des Biomolécules / Métaux en Biologie

Centre de recherche Saint-Antoine / Microbiote, intestin et inflammation

Boosting the potential of superoxide dismutase mimics as treatment for inflammatory bowel diseases: from chemical design and production to intestinal delivery in mice.

Par Gabrielle Schanne

Thèse de doctorat de Chimie-Biologie

Dirigée par Nicolas Delsuc et Philippe Seksik

Présentée et soutenue publiquement le 16 Décembre 2022

Devant un jury composé de :

Olivier Espeli, Directeur de recherche, Rapporteur

Christelle Hureau, Directrice de recherche, Rapporteur

Fabienne Burlina, Directrice de recherche, Examinateur

Bénédicte Pigneur, Maîtresse de conférences - praticienne hospitalière, Examinateur

Luis Bermudez, Directeur de recherche, Invité

Clotilde Policar, Professeure, Invitée

Philippe Seksik, Professeur des universités - praticien hospitalier, Co-directeur de thèse

Nicolas Delsuc, Chargé de recherche, Directeur de thèse

Mes premiers remerciements vont à Nicolas Delsuc pour son encadrement, sa disponibilité et son aide précieuse essentielle à la réalisation de cette thèse. Je te remercie également pour ta bonne humeur et ta bienveillance qui ont fait de cette thèse trois années très agréables. J'adresse tous mes remerciements à Philippe Seksik qui a co-encadré cette thèse. Merci pour tes conseils mais aussi pour ton optimisme et ta bonne humeur, c'était un plaisir de travailler avec toi. Je souhaiterais ensuite remercier Clotilde Policar pour son encadrement, son soutien et son enthousiasme communicatif. J'ai appris énormément de choses à tes côtés. Merci à vous 3 pour la confiance que vous m'avez accordé pendant ces 3 ans. J'ai eu beaucoup de chance de travailler avec vous. Merci de m'avoir donné l'opportunité de vivre une aventure très riche scientifiquement à travers un sujet très pluridisciplinaire et de nombreuses collaborations.

J'adresse mes remerciements à Christelle Hureau et Olivier Espéli d'avoir accepté d'être rapporteur de ce travail de thèse. Je remercie également Fabienne Burlina et Bénédicte Pigneur d'avoir accepté de faire partie du jury de thèse.

Ce travail de thèse est avant tout le résultat de nombreuses collaborations. Je remercie chaleureusement Luis Bermudez, Philippe Langella, Florian Chain, Anne Aucouturier, Jade Loiseau, Emeric Dupe, Célia Carbonne et tous les membres de l'équipe ProbiHote du laboratoire MICALIS à l'INRAE pour leur accueil chaleureux. Merci de m'avoir initié au développement de bactéries lactiques recombinantes. Merci beaucoup Florian pour les essais souris. J'adresse également tous mes remerciements à Ryszard Lobinski et Hugues Preudhomme de l'IPREM pour leur précieuse collaboration sur la mobilité ionique. Merci à Hélène Bertrand de m'avoir associé à un de ses projets me permettant ainsi de découvrir le domaine de l'imagerie cellulaire.

J'ai rencontré au cours de cette trois années un grand nombre de personne qui ont contribué au bon déroulement de cette thèse. Je tiens à remercier en particulier, Marie-Aude Plamont pour son accueil au LBT, Elodie Quevrain pour m'avoir formé à la culture cellulaire, Bernard Goetz et Patrice Legeay pour les expériences d'ICP-MS, Zoher Gueroui pour l'accés et la formation au microscope de fluorescence, Sylvain Trepout pour l'initiation à la cryofixation, Eric Ait Yahiatène pour l'impression 3D et enfin Sylvain Bohic et Murielle Salomé ainsi que Kadda Medjoubi et Andrea Somogyi, nos local contact à l'ESRF et SOLEIL pour leur aide indispensable.

Je remercie sincèrement tous les autres membres de l'équipe du LBM. Un merci particulier à Martha Zoumpoulaki qui m'a encadrée à mon arrivée en M2 et à Géraldine Gazzah pour son support en synthèse. Merci à tous pour votre soutien et votre motivation qui m'ont permis d'effectuer ce travail dans des conditions idéales. Merci à nos voisins du pôle 1 pour les conseils en synthèse organique et la bonne ambiance générale qui régnait dans notre couloir. Merci à toute mon équipe au CRSA pour votre aide avec les cellules et les bactéries et pour les coups de main au labo. Un grand merci à Sylvie Demignot pour sa gentillesse, ses corrections sur la review et ses réponses à toutes mes questions.

Je remercie Olivier Lequin (directeur du LBM), Laurence Grimaud (directrice du pôle 1 du LBM), Rodolphe Vuillemier (directeur du département de chimie de l'ENS), Bruno Fève (directeur du CRSA) pour l'accueil au sein de leur structure.

Merci à Fabienne Burlina et Marc Fontecave pour nos discussions annuelles très enrichissantes lors des comités de suivi de thèse.

Merci aux stagiaires que j'ai eu l'occasion d'encadrer, Paul Rochette, Yael Lellouche Jakob, Sorine Brisseau et Yaqine Ben Hadj Hammouda.

Enfin, un grand merci général à toutes les personnes que j'ai côtoyées pendant ces trois années, j'ai beaucoup apprécié travailler à vos côtés et j'ai partagé de très bons moments avec vous dans le labo et en dehors !

Résumé 6

Abstract 8

Abbreviations 10

I. General introduction 13

I.1. Reactive oxygen species and oxidative stress 13

I.1.a. Definition of reactive oxygen species 13

I.1.b. Generation of ROS in cells 13

I.1.c. ROS reactivity 15

I.1.d. Functions of ROS 16

I.1.e. Antioxidant defenses: focus on superoxide dismutase and catalase 18

I.1.e.i. Superoxide dismutases (SODs) 19

I.1.e.ii. Catalases enzymes (CATs) 21

I.2. Inflammatory bowel diseases: inflammation and oxidative stress 24

I.2.a. Inflammatory bowel diseases: a global health issue 24

I.2.b. Intestinal inflammation and dysbiosis of the intestinal microbiota in IBDs 24

I.2.c. IBDs and oxidative stress 26

I.2.d. Administration of antioxidant enzymes for IBDs treatment 28

I.2.e. A new therapeutic strategy : administration of low-molecular weight SOD and CAT mimics. 29

I.3. Metal complexes with SOD activity, so-called SOD mimics 29

I.3.a. Important criteria for efficient SOD mimics 29

I.3.a.i. Intrinsic SOD activity 29

I.3.a.ii. Bioavailability 31

I.3.a.iii. Cellular distribution 31

I.3.b. State of the art of metal-based SOD mimics 32

I.3.b.i. Iron-, copper- and nickel-based SOD mimics 32

I.3.b.ii. Manganese-based SOD mimics 33

I.3.c. Metal complexes with CAT-like activity 36

I.3.c.i. Mononuclear Fe- or Mn- CAT mimics 36

I.3.c.ii. Bio-inspired dinuclear Mn(II) CAT mimics 38

I.3.c.iii. Copper-based CAT mimics 39

I.4. Evaluation of the SOD mimics activity 40

I.4.a. Determination of the intrinsic SOD activity 40

I.4.a.i. Indirect assay of SOD activity: the McCord and Fridovich assay 40

I.4.a.ii. Direct assays of SOD activity 42

I.4.a.iii. Critical factors for interpretation 43
I.4.a.iv. Evaluation of intrinsic CAT activity 44
I.4.a.v. In-gel activity assays for the determination of SOD and CAT activity 46
I.4.b. Evaluation of SOD mimics activity *in cellulo: HT29-MD2 cells* 46

I.5. Objectives of the PhD 48

II. Mn(II) complexes SOD mimics based on synthetic open-chain ligands : relationship between inertness, activity in cells and in vivo, intracellular penetration and distribution. 50

II.1. Introduction 50
II.1.a. Mn1, a Mn(II) complex SOD mimic inspired from the MnSOD active site 50
II.1.b. SOD mimics metal complexes: choice of manganese (II) 53
II.1.b.i. Advantages of Mn(II) over other transitions metals 53
II.1.b.ii. Efforts to counterbalance the lability of Mn(II) complexes 55
II.1.c. Detection and quantification of Mn(II) complexes within cells 57
II.1.c.i. Overall cellular uptake of SOD mimics 57
II.1.c.ii. Study of SOD mimics speciation in the cellular environment 59
II.1.c.iii. Subcellular distribution of SOD mimics 61

II.2. Publication: "Inertness of superoxide dismutase mimics Mn(II) complexes based on an open-chain ligand, bioactivity, and detection in intestinal epithelial cells" 63

II.3. Publication : "Deciphering the Metal Speciation in Low-Molecular-Weight Complexes by IMS-MS: Application to the Detection of Manganese Superoxide Dismutase Mimics in Cell Lysates" 92

II.4. Intra-cellular distribution of SOD mimics 109
II.4.a. Nano-scale X-ray fluorescence microscopy approach 109
II.4.b. Design of a multi-modal probe targeting mitochondria for X-ray fluorescence imaging 109
II.4.c. Co-incubation between the SOD mimics and the Re-based XRF probe : nano-XRF imaging. 111
II.4.c.i. Objectives 111
II.4.c.ii. Experimental sections 112
II.4.c.iii. Results and discussion 114
II.4.c.iv. Supplementary figures 118

II.5. Evaluation of Mn1-derived SOD mimics in DNBS-induced murine colitis: chemically modified bacteria as delivery vectors. 121
II.5.a. Use of bacteria so-called chemically modified bacteria (CMB) as delivery vectors. 121
II.5.a.i. Benefits of SOD mimics loading in bacteria. 121
II.5.a.ii. Choice of the strain 122

II.5.b. Experimental section 122
II.5.b.i. Bacteria loading with SOD mimics 122
II.5.b.ii. Induction of DNBS colitis and bacteria administration 123
II.5.b.iii. Evaluation of colitis severity 124
II.5.c. Results and discussion 125
II.5.c.i. Effect of SOD mimics-loaded bacteria on the weight 125
II.5.c.ii. Effect of SOD mimics-loaded bacteria on the macroscopic scores 127
II.5.c.iii. Effect of SOD mimics-loaded bacteria on the MPO activity 128
II.5.c.iv. Effect of SOD mimics-loaded bacteria on the intestinal barrier permeability. 129
II.5.c.v. Effect of SOD mimics-loaded bacteria on SOD2 gene transcription. 129

II.6. Conclusion and perspectives 131

III. Chapter III: Genetically modified lactic acid bacteria for the production and delivery of peptidyl superoxide dismutase and catalase mimics. 133

III.1. Introduction 133

III.1.a. Probiotics as therapy in IBDs 133
III.1.a.i. Probiotics and lactic acid bacteria 133
III.1.a.ii. Mechanisms of actions of probiotics 134
III.1.b. Genetically modified probiotic with additional anti-inflammatory properties 137
III.1.b.i. Cloning expression system 140
III.1.b.ii. Expression of anti-inflammatory agents by recombinant LAB 144
III.1.c. Peptidyl SOD and CAT mimics 153
III.1.c.i. Advantages of SOD and CAT mimics over native enzymes 153
III.1.c.ii. State of the art of peptidyl complexes mimicking SOD and CAT 154

III.2. Draft publication 160

Abstract. 160
III.2.a. Introduction 161
III.2.b. Material and methods 163
III.2.b.i. Bacterial strains and growth conditions 163
III.2.b.ii. Construction of recLAB expressing peptidyl SOD and CAT mimics 164
III.2.b.iii. Effect of metal supplementation on bacterial growth 165
III.2.b.iv. Nisin or stress induction of peptides expression 166
III.2.b.v. Measurement of SOD and CAT activity using in-gel activity assays 166
III.2.b.vi. Anti-inflammatory effects of recombinant strains on LPS-stimulated HT29-MD2 cells 167
III.2.c. Results and discussion 169
III.2.c.i. Design of the constructs 169
III.2.c.ii. Choice of the bacteria strains 170

III.2.c.iii. Construction of the recombinant Lactococcus lactis or Lactobacillus plantarum strains expressing peptidyl ligands of SOD and CAT mimics 171
III.2.c.iv. Supplementation of the bacterial culture medium with copper or manganese salt 172
III.2.c.v. Examination of SOD and CAT mimics production by recombinant strains 173
III.2.c.vi. Evaluation of recombinant LAB activity in LPS-stimulated HT29-MD2 cells 178
III.2.d. Conclusion 190

III.3. Conclusion and perspectives 191
III.3.a. Conclusion 191
III.3.b. Perspectives 191

IV. General conclusion 195

V. Bibliography 197

VI. Annexes 215

VI.1. Chapter II 215
VI.1.a. Supplementary materials of "Inertness of superoxide dismutase mimics Mn(II) complexes based on an open-chain ligand, bioactivity, and detection in intestinal epithelial cells" publication 215
VI.1.a.i. Supplementary information 215
VI.1.a.ii. Supplementary tables 227
VI.1.a.iii. Supplementary figures 228
VI.1.a.iv. References 249
VI.1.b. Supplementary materials of "Deciphering the Metal Speciation in Low-Molecular-Weight Complexes by IMS-MS: Application to the Detection of Manganese Superoxide Dismutase Mimics in Cell Lysates" publication 249
VI.1.b.i. Experimental Procedures 249
VI.1.b.ii. Supplementary Figures 272
VI.1.b.iii. Supplementary References 285
VI.1.b.iv. Author Contributions 285
VI.1.c. Publication and supplementary materials of "Rhenium carbonyl complexes bearing methylated triphenylphosphonium cations as antibody-free mitochondria trackers for X-ray fluorescence imaging". 286

VI.2. Chapter III 336
VI.2.a. Supplementary tables 336
VI.2.b. Supplementary figures 337

Résumé

Les superoxide dismutases (SODs) sont des metalloenzymes qui jouent un rôle important dans les défenses cellulaires anti-oxydantes en régulant la concentration en ion radical superoxide, un dérivé réactif de l'oxygène (DRO). Il a été montré que les SODs, et les défenses anti-oxydantes en général, sont déficientes chez les patients atteints de maladies inflammatoires chroniques de l'intestin (MICI). Il en résulte une augmentation de la concentration en DRO qui semblerait être impliquée dans la pathogénèse des MICI. L'utilisation de complexes métalliques à faible poids moléculaire mimant l'activité SOD pourrait donc constituer une solution prometteuse pour le traitement des MICI. Deux sortes de mimes de SOD ont été étudiées ici : 1) des mimes bio-inspirés de la SOD2 endogène et 2) des complexes peptidiques à base de Cu et Mn.

Dans le premier cas, une stratégie biomimétique a été suivie et a conduit au développement de Mn1, un complexe de Mn reproduisant le site actif de la SOD2 et son activité. Ce composé a une activité anti-inflammatoire sur cellules et sur modèle murin. Cependant, Mn1 est très flexible, ce qui favorise la décoordination du Mn qui peut s'échanger avec d'autres cations. Dans le but de s'affranchir des problèmes d'échanges métalliques et déprotonation, des groupements cyclohexyle (C) et propyl (P) ont été ajoutés. Le groupe cyclohexyle a été introduit de sorte à rigidifier la structure du complexe pour améliorer son inertie. Les complexes Mn1C, Mn1P et Mn1CP obtenus possèdent une activité SOD légèrement améliorée mais surtout une résistance fortement accrue aux échanges métalliques. De plus, ils sont capables d'exercer des effets anti-inflammatoires et anti-oxydants à plus faible dose que Mn1 sur un modèle de cellules intestinales stimulées au LPS. Cela peut être corrélé au moins en partie à leur plus grande inertie dans l'environnement cellulaire. La détection et la quantification des espèces actives sont indispensables pour comprendre et rationaliser les activités observées in cells. Cependant, elles ne sont pas évidentes pour de tels composés labiles qui peuvent souffrir d'échanges métalliques au sein des systèmes analytiques. En lien avec sa meilleure inertie, nous avons pu détecter et quantifier la présence de Mn1CP dans les cellules par spectrométrie de masse (MS). Cette technique ne permettait pas la détection de Mn1 et Mn1P, qui a nécessité le couplage de la spectrométrie de mobilité ionique avec la MS. Par ailleurs, nous avons étudié la localisation intracellulaire de Mn1 et Mn1CP et en particulier

leur capacité à atteindre les mitochondries, principaux foyers cellulaires du stress oxydant, par microscopie de fluorescence aux rayons X. Dans ce but, une sonde à base de Re ciblant les mitochondries a été développée et utilisée. Enfin, le potentiel thérapeutique des mimes a été évalué sur un modèle murin de colite aigüe. Les complexes de Mn ont été vectorisés dans des bactéries lactiques afin de les protéger de l'acidité gastrique lors de leur administration orale. L'administration par gavage de Mn1C a permis de légèrement réduire la sévérité de la colite.

Concernant le second type de mimes de SOD, ils sont constitués de ligands peptidiques qui présentent l'avantage d'être génétiquement encodables. De cette façon, des bactéries lactiques ont été modifiées génétiquement de sorte à exprimer ces peptides qui possèdent une activité SOD après coordination du cuivre ou du manganèse. La construction génétique a été vérifiée à trois niveaux : contrôle de la présence du gène, vérification de l'expression du peptide cloné et de son activité SOD en présence du métal adéquat. De plus, la co-incubation de cellules intestinales avec les bactéries lactiques recombinantes s'est montrée ici encore efficace pour limiter la sécrétion d'interleukin-8, une cytokine pro-inflammatoire, induite par le LPS. Les bactéries servent alors à la fois de vecteur de délivrance protecteur et d'usine de production des mimes de SOD.

Abstract

Superoxide Dismutases (SODs) are metalloenzymes involved in the cellular antioxidant defenses. They regulate the concentration of the superoxide anion, a reactive oxygen species (ROS). It has been shown that SOD and others antioxidant defenses are weakened in patients with chronic inflammatory bowel diseases (IBDs). The resulting increase in ROS amount may contribute to the pathogenesis in IBDs. Low-molecular weight complexes, mimicking SOD activity, may be promising antioxidant metallodrugs for the management of IBDs. Two kinds of SOD mimics were considered here, 1) bio-inspired Mn complexes and 2) peptidyl Cu or Mn complexes.

On the one hand, a biomimetic strategy has led to the development of Mn1, a Mn complex reproducing SOD2 active site and its SOD activity and showing an anti-inflammatory activity in cells and in mice. However, Mn1 being flexible is prone to metal-assisted dissociation in biological environment. Aiming at improving its bioactivity and at preventing any deprotonation issue during the subsequent speciation studies, a cyclohexyl (C) and a propyl (P) groups were included in its structure. More precisely, the cyclohexyl group was introduced to rigidify the ligand and thus to improve the kinetic inertness of the resulting Mn1C and Mn1CP complexes. Mn1P, Mn1C and Mn1CP demonstrated slightly higher intrinsic SOD activity and a slower kinetics of metal exchanges. Very interestingly, they were shown to provide anti-inflammatory and antioxidant effects in intestinal LPS- stressed epithelial cells at lower doses than Mn1. This can be at least partly correlated to their higher inertness in the cellular environment. The understanding of the SOD mimics bioactivities can be boosted by the direct detection and quantification of the active species inside the cells, which is not straightforward due to their propensity to exchange metal ions, in particular in the analytical systems. Because of its higher kinetic inertness, Mn1CP was successfully detected inside cell lysates by classical mass spectrometry (MS), and its intracellular concentration was estimated. On the contrary, the more labile Mn1 and Mn1P complexes were not detected by this technique. Very interestingly, coupling ion mobility and MS allowed us to successfully detect and quantify Mn1P in cells. Besides the cellular uptake, the intracellular location of the SOD mimics is a key factor for bioactivity. The distribution of Mn1 and Mn1CP within cells and in particular their ability to reach the mitochondria, regions rich in ROS, were examined by X-ray

fluorescence microscopy. For this purpose, we developed and used a mitochondria-targeting X-ray probe bearing a Re. Lastly, the bioactivity of Mn1 derivatives was investigated in a murine model of acute colitis. To protect the Mn complexes from decoordination and degradation in the acidic gastric conditions upon oral administration, they were vectorized inside food-grade bacteria. The mice that orally received Mn1C by gavage showed a slightly better recovery than mice from the control group.

On the other hand, SOD mimics based on peptidyl ligands are advantageously genetically encodable. In this way, food-grade lactic acid bacteria were engineered to express and secrete the peptidyl ligand of Mn- or Cu-based SOD mimics. One peptide developed as a Cu-complex catalase mimic was also studied, catalase being an antioxidant protein controlling the hydrogen peroxide concentration, another deleterious ROS. The engineering was checked at three levels: sequencing of the cloned gene, expression of the encoded peptides and SOD activity of the expressed peptides upon metal coordination. Interestingly, the recombinant lactic acid bacteria producing either the Cu or Mn peptidyl SOD mimics were efficient in limiting the secretion of interleukin-8 inflammatory marker in LPS-stimulated intestinal cells. The bacteria hence serve as both protective delivery vectors and production factories of the SOD mimics.

Abbreviations

ACN: Acetonitrile
ATP: Adenosine triphosphate
BAEC : Bovine Aorta Endothelial Cells
BCA: Bicinchoninic Acid
H/BSA: Human/Bovine Serum Albumin
CAMP : Commensal-Associated Molecular Pattern
CAT: Catalase
CCS: Collision cross-section
CD: Crohn Disease
CDTA: CyclohexyleneDiamineTetraacetic Acid
CFU: Colony-forming unit
CMB: Chemically Modified Bacteria
CPP: Cell-Penetrating Peptide
CPS: Counts per second
CRISPR: Clustered Regularly Interspaced Short Palindromic Repeats
Cryo-CLEM: cryogenic Correlative Light and Electron Microscopy
DMEM: Dulbecco's Modified Eagle's Medium
DMF: Dimethylformamide
DMSO: Dimethylsulfoxide
DNA: Deoxyribonucleic Acid
DNBS: Dinitrobenzene sulfonic acid
DSS: Dextran Sulfate Sodium
EDTA: EthyleneDiamineTetraacetic Acid
ELISA: Enzyme-Linked Immunosorbent Assay
EPR: Electron paramagnetic resonance
EXAFS: Extended X-ray Absorption Fine Structure
FBS: Fetal Bovine Serum
FITC: Fluorescein isothiocyanate
GADPH: Glyceraldehyde 3-phosphate dehydrogenase
GALT: Gut-associated lymphoid tissue
GIT: Gastrointestinal tract
GMB: Genetically Modified Bacteria
GM-CSF: Granulocyte Macrophage-Colony Stimulating Factors
GMO: Genetically modified organism
GPx : Glutathion peroxidase
GRAS: Generally Recognized As Safe
GSSG: Glutathione disulfide
HEPES: 2-[4-(2-hydroxyethyl)piperazin-1-yl]ethanesulfonic acid
HPLC: High-Performance Liquid Chromatography
HRP: Horse-radish peroxidase
IBD: Inflammatory Bowel Disease
IC_{50}: Inhibition concentration at 50 %
ICP-AES: Inductively Coupled Plasma Atomic Emission Spectroscopy
ICP-MS: Inductively Coupled Plasma Mass Spectrometry

IECs : Intestinal epithelial cells
IMS-MS: Ion Mobility Spectrometry coupled to Mass Spectrometry
IFN-γ: Interferon-γ
IL-x: Interleukin-x
KGF-2: Keratinocyte Growth Factor 2
L : Lysate
LAB: Lactic Acid Bacteria
LBM: Laboratory of Biomolecules
LBPs: Live Biotherapeutics Products
LDH: Lactate Dehydrogenase
LC-MS/MS: Liquid Chromatography coupled to tandem Mass Spectrometry
LMW: Low molecular weight
LPS: Lipopolysaccharide
MAM: Microbial Anti-inflammatory Molecule
MLCT: Metal-to-ligand charge transfer band
Mn-PAM: Mn-Pentaazamacrocycle
MnP: Mn-Porphyrin
MPP: Mitochondria-Penetrating Peptide
MPO: Myeloperoxidase
MOI: multiplicity of infection
MOPS: 3-(Morpholin-4-yl)propane-1-sulfonic acid
mRNA: messenger Ribonucleic Acid
mTPP: methylated triphenylphosphonium
NADPH: reduced Nicotinamide adenine dinucleotide phosphate
NBT: Nitro Blue Tetrazolium
NF-kB: nuclear factor-kappa B
NHE: Normal Hydrogen Electrode
NICE: Nisin-Inducible Controlled Expression
NLR : Nod-Like Receptor
NO: Nitric oxide
NOXs: NADPH oxidases
OCT: Optimal cutting temperature
OD: Optical Density
OS: Oxidative Stress
PAP: Pancreatitis-Associated Protein
PBS: Phosphate-Buffered Saline
PCR: Polymerase Chain Reaction
PFA: Paraformaldehyde
PMA: phorbol 12-myristate 13-acetate
P/MAMP : Pathogen/Microbe-Associated Molecular Pattern
PPR : Pattern Recognition Receptor
Prx: Peroxyredoxin
qPCR: quantitative Polymerase Chain Reaction
QPS: Qualified Presumption of Safety
recLAB: Recombinant Lactic Acid Bacteria
RNA: Ribonucleic Acid
RNS : Reactive Nitrogen Species

ROS: Reactive Oxygen Species
RPP: Resolution peak to peak
RR: Resonant Raman
RT-PCR: real-time Polymerase Chain Reaction
SCE: Saturated calomel electrode (saturated with KCl)
SICE: Stress-Inducible Controlled Expression
SN : Supernatant
SOD: Superoxide Dismutase
SODm: SOD mimic
SP : Signal Peptide
TBP: TATA-binding protein
TCA: Trichloroacetic acid
TFA: Trifluoroacetic acid
TFF: Trefoil Factor
TGF-β: Transforming Growth Factor β
TIMS: Trapped Ion Mobility Spectrometry
TLR : Toll-Like Receptor
TNBS: Trinitrobenzene sulfonic Acid
TNF-α: Tumor necrosis factor-α
TOF-MS: Time of flight mass spectrometry
TPP: Triphenylphosphonium
TNBS: TrinitroBenzene Sulfonic Acid
UC: Ulcerative Colitis
WB: Western Blot
WHO: World Health Organization
WT: Wild-type
XAS: X-ray Absorption Spectroscopy
XANES: X-ray Absorption Near Edge Structure
XIES: Xylose-Inducible Expression System
XRF: X-Ray Fluorescence
XFM: X-ray Fluorescence Microscopy
XTT: 2,3-Bis-(2-méthoxy-4-Nitro-5-sulfophényl)-2H-tétrazolium-5-carboxanilide

I. General introduction

I.1. Reactive oxygen species and oxidative stress

I.1.a. Definition of reactive oxygen species

Reactive oxygen species (ROS) are defined as byproducts of the dioxygen reduction. Indeed, molecular dioxygen can undergo either a single-step four-electron reduction leading directly to the formation of water or partial and consecutive one-electron reductions, then producing a series of ROS [1]. In more details, the first monoelectronic reduction of dioxygen results in the formation of superoxide radical anion $O_2^{\bullet -}$, abbreviated as superoxide thereafter. Superoxide contains an additional electron in one of the two degenerate orbitals of ground state dioxygen, creating thus a single unpaired electron (S=1/2) and a net negative charge of −1. Superoxide is the first ROS in the cascade of ROS and can act as precursor of other ROS. The further addition of electrons, one after another, generates stepwise hydrogen peroxide (H_2O_2) and hydroxyl radical ($HO^{\bullet}$) (Figure 1). $O_2^{\bullet -}$, H_2O_2 and $HO^{\bullet}$ can then react with other cellular components to form other ROS such as alkoxyl $RO^{\bullet}$, peroxyl radical $ROO^{\bullet}$ or hydroperoxyl radical $HOO^{\bullet}$.

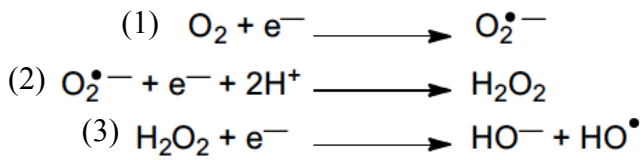

Figure 1: Figure from [1]. Reduction cascade of dioxygen resulting in the sequential formation of (1) superoxide, (2) hydrogen peroxide and (3) hydroxyl radical.

I.1.b. Generation of ROS in cells

ROS are generated by multiple endogenous processes that were summarized by A. Snezhkina *et. al* in Table 1 [2]. However, the mitochondrial respiration [3] and the NADPH oxidase enzymes [4] are considered to be the two major producers of ROS. First, mitochondrial respiration, that is part of all normal aerobic life, plays a key role in oxidative ATP production *via* a reverse process of photosynthesis in which dioxygen is converted into water. However, a decoupling in the four-electron transfer occurring along the electron transport chain is known to affect about 3% of processed dioxygen. This is responsible for the aforementioned

incomplete reduction of dioxygen into superoxide [1,3]. Consequently, high amounts of superoxide are released in the mitochondrial matrix and into the intermembrane mitochondrial space. Note that many others enzymes were shown to induce ROS generation in the mitochondria, including cytochrome P450 enzymes, NADH-cytochrome b5 reductase, various dehydrogenases, monoamine oxidases (MAO) and mitochondrial aconitase [5].

ROS	Generation	Detoxification
Superoxide radical ($O_2^{\bullet-}$)	Mitochondrial respiratory chain Electron transport chain in the peroxisomal membrane NADPH oxidases CYP catalytic cycle Mitochondrial enzymes (glycerol 3-phosphate dehydrogenase, 2-oxoglutarate dehydrogenase, NADH-cytochrome b5 reductase, etc.) Xanthine oxidoreductase	Superoxide dismutases Polyamines Superoxide reductases
Hydrogen peroxide (H_2O_2)	Spontaneous dismutation of superoxide radicals Superoxide dismutases Superoxide reductases Polyamine catabolism Thymidine catabolism NADPH oxidases Monoamine oxidases Lysyl oxidases Dihydroorotate dehydrogenase CYP catalytic cycle Peroxisomal enzymes (acyl-CoA oxidases, d-amino acid oxidase, d-aspartate oxidase, etc.) Microsomal monooxygenase (MMO) system Normal protein folding/unfolded protein response Polyunsaturated fatty acid metabolism	Polyamines Glutathione peroxidases Thioredoxin peroxidases Catalase Peroxiredoxins Glutathione S-transferases Glutaredoxins Thioredoxins Nonenzymatic scavengers* Glycolysis Pentose phosphate pathway
Hydroxyl radical ($^{\bullet}OH$)	Fenton and Haber-Weiss reactions Thymidine catabolism (supposed) Aconitase via Fenton reaction	$^{\bullet}OH$ has a very short half-life and is very rapidly involved in other reactions Polyamines
Singlet oxygen (O_2)	Nonphotosensitized mechanisms of O_2 generation**	O_2 is rapidly implicated in many oxidation reactions Polyamines
Hydroperoxyl radical ($HOO^{\bullet}$)	Protonated form of $O_2^{\bullet-}$	Nonenzymatic scavengers
Peroxyl radical ($ROO^{\bullet}$)	Polyunsaturated fatty acid metabolism	Nonenzymatic scavengers
Alkoxyl radical ($RO^{\bullet}$)	Polyunsaturated fatty acid metabolism	Nonenzymatic scavengers

*Table 1: Table adapted from [2]. List of ROS and major mechanisms of their generation and detoxification. * : described in [6]. ** : reviewed in [7]. CYP = Cytochrome P450*

Secondly, while multiple enzymes produce ROS as secondary effects, nicotinamide adenine dinucleotide phosphate (NADPH) oxidases (NOXs) constitute the rare enzymes for which ROS production is the primary action. NOXs enzymes are located in the plasma membrane and in the phagosomes (created after bacteria phagocytosis) and catalyze the reduction of dioxygen into superoxide and hydrogen peroxide via NADPH oxidation [8]. Lastly, Haber-Weiss chemistry is strongly involved in the production of hydroxyl radical in living cells. As illustrated in Figure 2, reduced metal cations such as iron Fe(II) can induce the reduction of hydrogen peroxide into hydroxide and hydroxyl radical (Fenton reaction) *via* metal oxidation into Fe(III)

[9]. In turn, Fe(III) can be reduced back to Fe(II) by superoxide: this renders the process catalytic (Haber-Weiss reaction) (Figure 2). To limit this phenomenon, cells have developed multiple storage components (ferritin, lipocalin-2, siderophores, etc.) to tightly regulate the cellular ferrous availability.

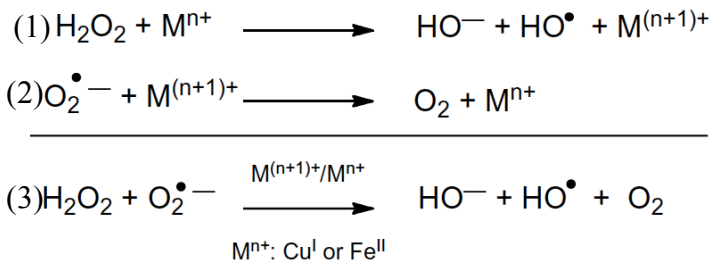

Figure 2: Figure from [1]. (3) Haber Weiss reaction: (1) oxidation of low-oxidation state metal ion by hydrogen peroxide (Fenton reaction) and (2) cycling back to low-oxidation state with superoxide.

In addition to all processes mentioned in Table 1, ionizing radiations such as X-rays or UV also mediate the decomposition of water into hydroxyl radical within biological systems [10].

I.1.c. ROS reactivity

Because of its triplet spin-state, molecular dioxygen reacts very slowly with organic molecules that are in singlet spin state according to the spin conservation rule (Figure 3). In contrast, for radical ROS like $O_2^{\bullet -}$ and $HO^\bullet$ that possess only one unpaired electron (S=1/2), the spin-state kinetic barrier is relieved, which renders them much more reactive [11]. Consequently, the activation of dioxygen into excited singlet oxygen or ROS (doublet in the case of $O_2^{\bullet -}$ and $HO^\bullet$) is required to allow the incorporation of oxygen into organic molecules such as alkanes. In this way, ROS are considered as a way to provide the molecular diversity observed in living organisms that probably accelerated evolution and adaptation to changes in the oxidative environment at the origins of life [1,12].

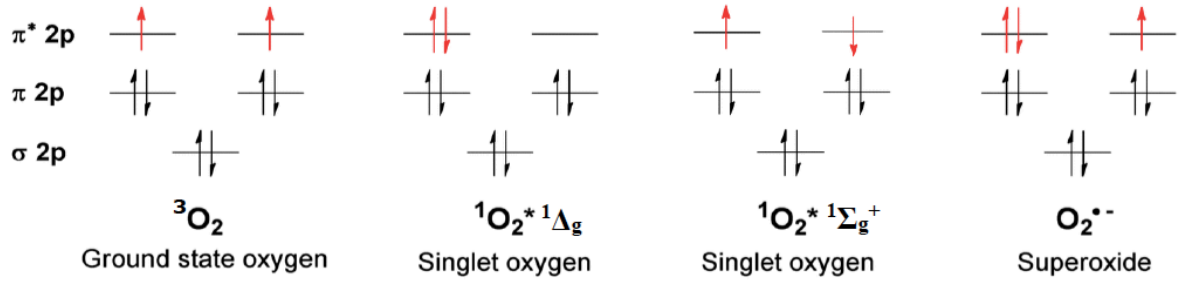

Figure 3: Figure from [13]. Molecular orbital diagrams of the oxygen states in molecular dioxygen, singlet dioxygen and superoxide radical anion.

All ROS possess inherent chemical properties that confer them not only different reactivities but also different biological targets. For instance, the reactivity of aforementioned ROS can be ranked with the following order: $H_2O_2 < O_2^{\bullet-} < HO^{\bullet}$ [14].

On one hand, $HO^{\bullet}$ indiscriminately attacks every bio-molecules around it with a kinetic rate limited by diffusion. $HO^{\bullet}$ consequently has a very short half-life (10^{-9} s) and reacts at its site of formation. Its extreme reactivity is related to its very high one-electron redox potential ($E°(HO^{\bullet}/H_2O) = 2.33$ V/NHE). $HO^{\bullet}$ can engender very important damages through the oxidation of lipids, DNA (attack of the guanine residues mostly) [15] or proteins and is consider as the most dangerous and toxic ROS. On the other hand, H_2O_2 and $O_2^{\bullet-}$ are much less toxic and deleterious than $HO^{\bullet}$. $O_2^{\bullet-}$ possesses a lower but still high one-electron redox potential ($E°(O_2^{\bullet-}/H_2O_2) = 0.93$ V/NHE) compared to hydroxyl radical. Consistently, its half-life is longer (10^{-5} s) which allows superoxide to migrate and reach further targets. However, superoxide is also confined close to its production site since its negative charge prevent any diffusion through membranes. While superoxide oxidizes a smaller range of biomolecules than hydroxyl radical, it is still involved in DNA nicking, in lipid peroxidation and in the inactivation of enzymes containing iron-sulfur clusters [16]. For its part, H_2O_2 is the most stable ROS with a half-life around 10^{-2}-10^{-3} s and has the ability to cross membranes thanks to its neutral charge. H_2O_2 is notably responsible for the oxidation of cysteines (that will be detailed in the next section) but its oxidizing power mostly results from its conversion to hydroxyl radical by the Haber-Weiss reactions.

I.1.d. Functions of ROS

ROS have two faces: they are indeed key actor of both redox biology and oxidative stress. ROS can hence induce opposite effects, depending not only on their concentration but also on their cellular location which itself depends on their site of production and their stability (type of ROS).

On one hand, excessive intracellular levels ROS induce oxidative stress. Oxidative stress indeed refers to an overproduction of ROS that damage lipids, proteins and DNA and subsequently alter cell homeostasis, structures, and functions [6,16]. As a results, high intracellular ROS levels were shown to contribute to the development of various human pathology including cardiovascular, neurodegenerative and metabolic disorders as well as cancer, diabetes and

inflammation [17]. On the other hand, appropriate levels of ROS were shown to dictate redox biology. At controlled concentrations, ROS maintain the redox balance of the cells that is essential for the proper course of physiological processes. In this way, ROS are strongly implicated in the redox signaling of various pathways initiating for instance cellular differentiation, cell adhesion and growth, tissue regeneration and prevention of aging [18]. Moreover, small increases of ROS can be useful when considering that they do not always cause toxicity to the host but rather to invading pathogens. Indeed, macrophages, white blood cells and other immune cells are known to generate oxidative burst to eliminate infectious microorganisms [19].

The redox-dependent oxidation of cysteines within proteins is a relevant example to illustrate that the local concentration in ROS is an important determinant of whether redox biology or oxidative stress occurs. At nanomolar levels, H_2O_2 reversibly oxidized cysteines residues present in the thiolate anion form (Cys-S^-) into the sulfenic form (Cys-SOH) (Figure 4) or disulfide bridges. This first-degree of oxidation can divert transiently the target protein from its original enzymatic function and this way serves as reversible signal transduction mechanism associated to redox biology [20,21]. However, higher levels of ROS may induce higher oxidation states, from sulfenic species (Cys-SOH), into sulfinic (SOH_2) and sulfonic (SO_3H) ones. These modifications are irreversible and consequently lead to permanent protein damages.

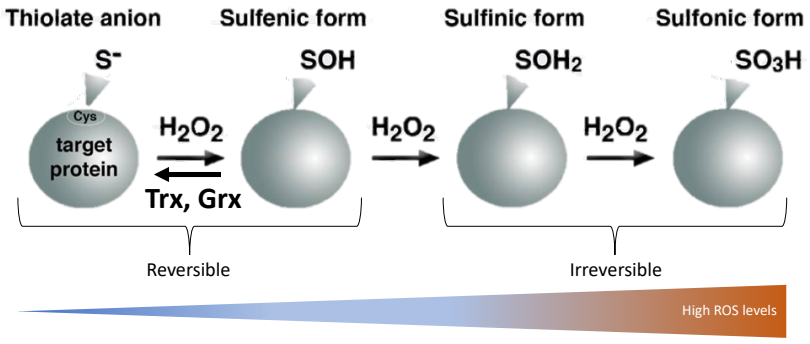

Figure 4: Figure adapted from [18]. Illustration of the reversible and irreversible oxidation of cysteines mediated by hydrogen peroxide. Trx stands for disulfide reductases thioredoxin and Grx for glutaredoxin.

The dual role of ROS in cancer development constitutes another interesting example revealing the two faces of ROS [22,23]. Indeed, ROS participate in the tumor initiation, progression and resistance to therapy through oxidative damages of cellular structures, in particular DNA (somatic mutations, genome instability, activation of oncogenes and inactivation of tumor

suppressor genes). However, in turn, elevated ROS levels can promote tumor cell death. This strategy to take advantage of ROS toxicity against cancer cells has been effectively used for anticancer treatment [24].

I.1.e. Antioxidant defenses: focus on superoxide dismutase and catalase

To fight oxidative stress while ensuring redox homeostasis, the concentration in ROS is tightly regulated by an arsenal of endogenous molecules that react with ROS to form nontoxic or less toxic products. These antioxidant defenses gather redox enzymes and stoichiometric scavenger [25,26]. The formers are specific to one type of ROS; the most important are detailed below and summarized in Figure 5. First, superoxide dismutase enzymes specifically catalyze the dismutation of superoxide into dioxygen and hydrogen peroxide [16]. Alternatively to SODs, a superoxide reductase (SOR) enzyme was shown to reduce superoxide into H_2O_2 without releasing dioxygen in an air-sensitive bacteria [27,28]. In turn, H_2O_2 is mostly converted to water by peroxiredoxin/thioredoxin reductase systems. Under increased amount of H_2O_2, the glutathione peroxidase/ glutathione reductase systems and catalase provide additional support to catabolize H_2O_2 [26,29]. The activity of these enzymes is continuously regulated to finely tune the concentration in each ROS.

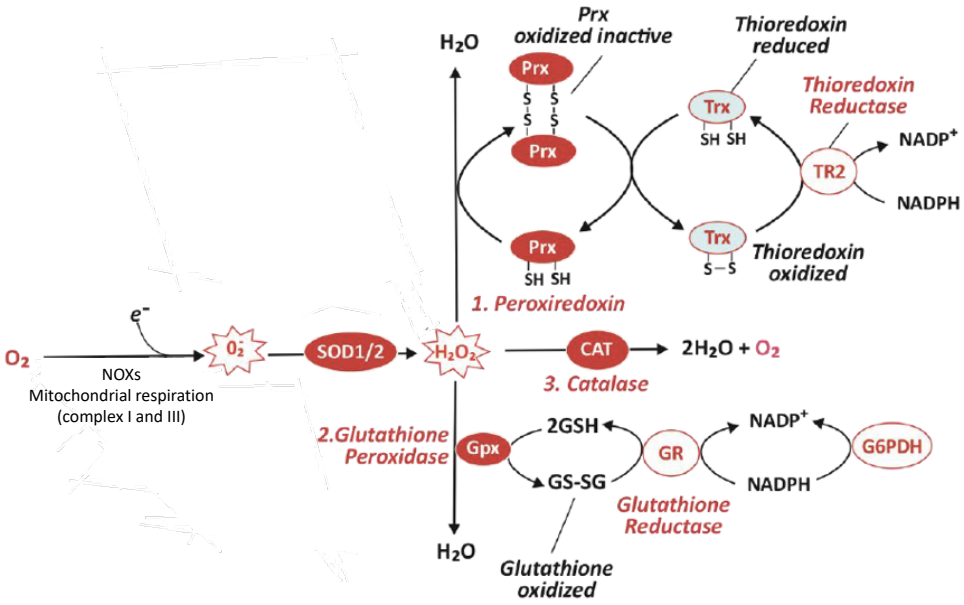

Figure 5: Figure adapted from [13]. Schematic illustrations of the catalytic defenses dedicated to protect the cells from oxidative stress.

In addition to these catalytic defenses, cells are equipped with stochiometric scavengers of ROS. The two most predominant are ascorbic acid and the tripeptide glutathione (GSH) which

are present in cells at millimolar concentrations [29,30]. GSH detoxify ROS through its oxidation into glutathione disulfide (GSSG). GSH can then be regenerated by NADPH-dependent glutathione reductase (Figure 5). Exogenous non-enzymatic ROS neutralizers are also able to complement endogenous defenses, they include vitamin C and E, flavonoids and carotene [26,29,31].

I.1.e.i. Superoxide dismutases (SODs)

SOD enzymes constitute the first line of defense against oxidative stress since superoxide is the primary ROS generated from the cascade of dioxygen monoelectronic reduction (I.1.a). Related to their key protective role, SODs are found in many organisms : almost all aerobic ones and some of the anaerobic [28]. These metalloenzymes catalyzes very efficiently the dismutation of superoxide — oxidation to dioxygen and reduction to hydrogen peroxide — at a rate close to the diffusion limit. To this end, SODs require a metallic center that is successively oxidized and reduced via a ping-pong mechanism as represented in Figure 6.

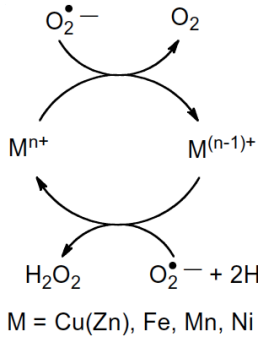

Figure 6: Figure from [1]. Simplified catalytic cycle of metal-containing SOD enzymes.

All SODs, whatever their difference in structure, possess a high catalytic rate ($\approx 10^9$ $M^{-1}.s^{-1}$) that can be correlated to their favorable standard redox potential (≈0.36 V/NHE) [32]. As a matter of fact, whatever the metal involved in the active site of SODs, the redox potentials are all positioned in a narrow potential range around the optimal value, i.e., at the midpoint potential between superoxide oxidation (-0.18 V/NHE) and reduction (0.91 V/NHE pH7) (Figure 7) [33]. Moreover, the presence of positively charges residues arranged as a funnel in SODs structure facilitates the approach of negative-charged superoxide toward the active site and hence contribute to the high catalytic activity. Owing to these advantageous parameters, SODs are very efficient in maintaining low and steady-state level of superoxide inside cells (superoxide

content was measured around 0.2 pM and 30 pM in *E. coli* and mammalian cells respectively) [34,35].

Eukaryotic cells produce three different SODs, numbered from 1 to 3, and differing by the metal involved in their active site (copper-zinc, the zinc playing mainly a structural role, or manganese) and by their cellular location [1,28,36]. SOD1 or Cu/ZnSOD is primarily located in the cytosol but is also found in the nuclear compartments, in the mitochondrial intermembrane space and in peroxisomes. SOD2 or MnSOD is exclusively compartmentalized in the mitochondrial matrix. Lastly, SOD3 or EC-SOD is another Cu/ZnSOD secreted in the extracellular environment and binds to the outer plasma membrane and extracellular matrix [37,38]. Among these 3 SODs, MnSOD was shown to be the most crucial for survival [1], which could be related to its compartmentalization in the mitochondria, the major site of ROS production. Additional SODs were found to be expressed only by prokaryotic cells: an iron SOD (FeSOD), mainly found in the chloroplasts of plant cells, a rarer nickel SOD (NiSOD) primarily present in the cytoplasm [28,32,39–41] and a class of copper-only SODs discovered in *C. Albicans* [42].

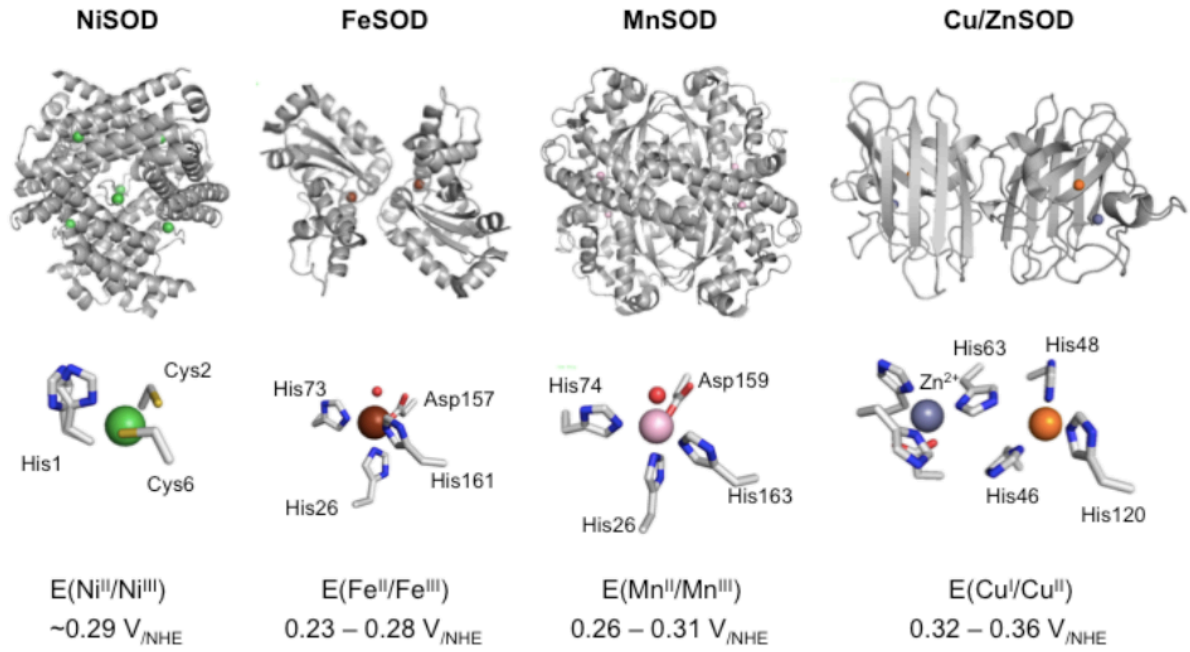

Figure 7: Figure from [43]. X-ray crystal structure of the four type of SODs (NiSOD [44], FeSOD [45], MnSOD [46] and Cu/ZnSOD[47]) and their active site. The standard potentials of the SODs at pH 7 are indicated [1].

The crystallographic structure of each SOD is given in Figure 7. Briefly, the active site of MnSOD is constituted of a Mn(III) cation in a trigonal bipyramidal geometry, the Mn-ion being bound

to two histidines and one aspartate in the equatorial plane and a third histidine and one water molecule in axial positions. Interestingly, FeSOD shows the same first coordination sphere around the iron center. In SOD1, catalysis was shown to occur at the copper center which is surrounded by three histidine in its first coordination sphere. The zinc center was first believed to only serve as a structural scaffold until S. Nedd *et. al* report in 2015 its participation in the catalysis efficacy via the adjustment of Cu site reduction potential and geometry [48].

I.1.e.ii. Catalases enzymes (CATs)

The catalase enzymes (CATs) are present in all aerobic species suggesting they may play an important role as part of the antioxidant defenses. Still, CATs are mostly restricted in the peroxisomes and are active only upon severe oxidative stress conditions, which limit its essentiality under healthy physiological conditions. However, the lack of CATs activity in knock-out mice was shown to increase the risk of oxidative stress-mediated pathology [49].

CATs catalyze the dismutation of H_2O_2 into H_2O and O_2 via a two-step reaction detailed in Figure 8. The detoxification of H_2O_2 by CATs implies a two-electron redox process accompanied with the transfer of two protons [50]. CATs are known to display high catalytic rate with respect to the auto-dismutation of H_2O_2 ($k_{cat} \approx 10^7$ $M^{-1}.s^{-1}$) and high turnover numbers: the Braunschweig Enzyme Database (BRENDA) indicates that one catalase molecule is able to dismute 2.8 millions H_2O_2 per second [51]. Besides their optimal redox properties, the presence of an access channel that favors the approach of the reagents (H_2O_2) and the release of the products (H_2O and O_2) was reported to contribute to the efficacy of the catalysis [52].

$$\mathbf{2\ H_2O_2 \rightarrow O_2 + 2\ H_2O}$$

$$\text{Reduction : } H_2O_2 + 2H^+ + 2e^- = 2H_2O$$

$$\text{Oxydation : } H_2O_2 = 2H^+ + 2e^- + O_2$$

Figure 8: Catalases accelerate the breaking down of two hydrogen peroxide molecules into two water molecules and one of dioxygen.

CATs can be subdivided in two groups: the heme-containing catalases (that comprise the human CAT) and the manganese (non-heme) catalases.

The active site of the heme-containing CATs is composed of an iron center, penta-coordinated by a tyrosine proximal ligand (Tyr358) in addition to the 4 pyrroles of the porphyrin (N-Fe bonds). A distal histidine residue (His75) was also shown to be strongly implicated in the

catalysis mechanism by stabilizing CAT- H_2O_2 adducts via proton exchanges [53,50,54]. A proposed mechanism of the histidine-mediated catalytic cycle is illustrated in Figure 9. In addition to these monofunctional CAT, heme-containing class comprises a less widespread subsection (only found in bacteria, archaebacteria, and fungi) that display both catalase and peroxidase activity.

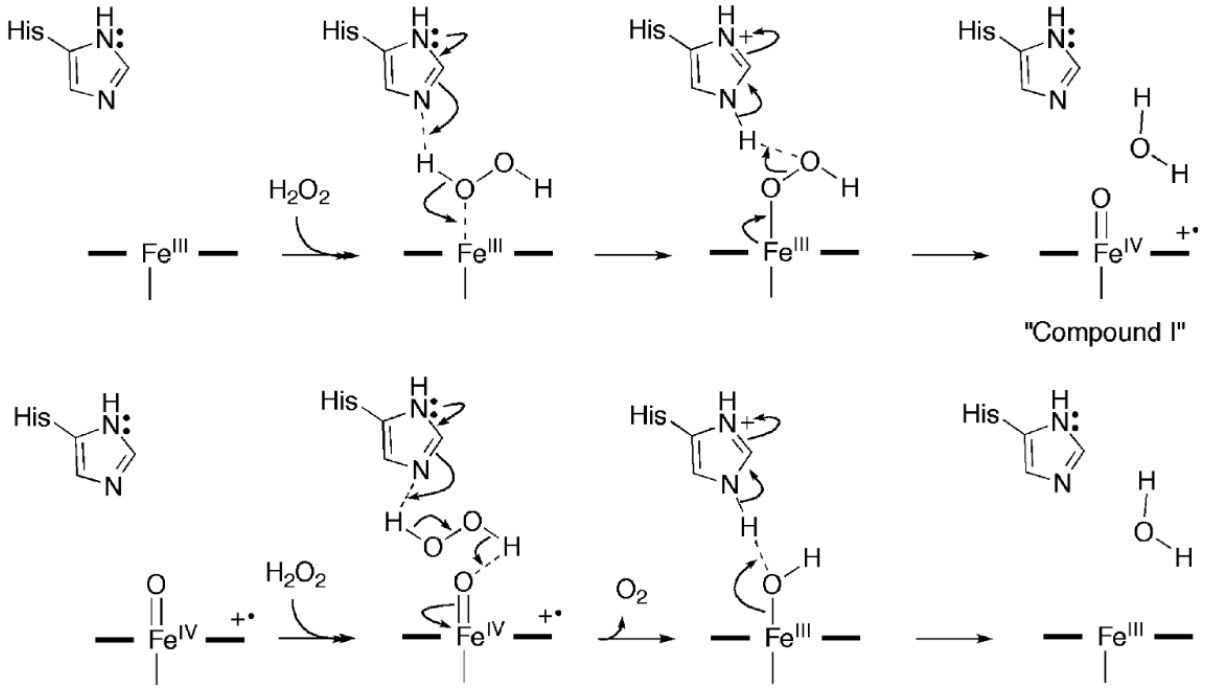

Figure 9: Figure from [55]. Mechanisms of heme-containing CATs for H_2O_2 dismutation [50,54]. Briefly, a first H_2O_2 molecule oxidizes the Fe(III) heme leading to the release of one water molecule and the formation of an unstable oxoferryl porphyrin cation radical [Fe(IV)=O]. Then a second H_2O_2 rapidly reacts with the porphyrin-Fe(IV)=O to reform porphyrin-Fe(III) via the formation of a porphyrin-Fe(III)-OH intermediate and the subsequent generation of one molecule of water and dioxygen.

Lastly, the MnCAT was isolated in various bacteria: mostly lactic acid bacteria. Crystallographic and mechanistic studies revealed that MnCAT possess two manganese centers that both cycle between Mn(II) and Mn(III) [56,57]. The two manganese ions are hexacoordinated with an octahedral geometry (Figure 10). First, they are linked by a μ-oxo bridge, a μ-hydroxo one and another one formed by the carboxylate moiety of the glutamate residue Glu65. Proximal histidines (His69 and His181), monodentate or bidentate glutamate (Glu35 and Glu148) and a water molecule complete their first sphere of coordination.

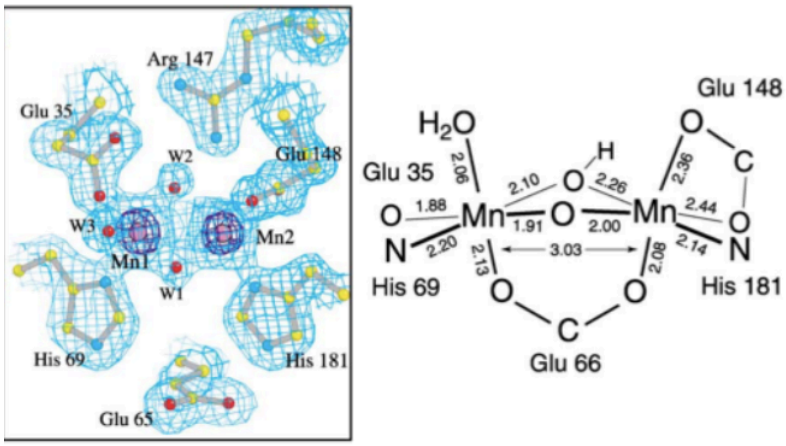

Figure 10: Figure from [57]. Crystallographic structure of MnCAT isolated from L. plantarum. (Left) Electron density map of the dinuclear manganese active site. (Right) Geometric details (bond lengths).

To sum up, Figure 11, published in a review from M. Schieber and N. Chandel, provides an overview of the basic knowledges on ROS : 1) major production by NOXs enzymes and during the mitochondrial respiration, 2) detoxification of ROS by antioxidant enzymes such as SOD, CAT, PRx and GPx, 3) protective functions of ROS in redox biology and 4) deleterious effects of ROS in oxidative stress. Case 4 is observed when the concentration in ROS is not properly regulated either because they are overproduced or because the defenses are weakened. Oxidative stress situations were shown to participate in the physiopathology of various diseases such as inflammatory disorders.

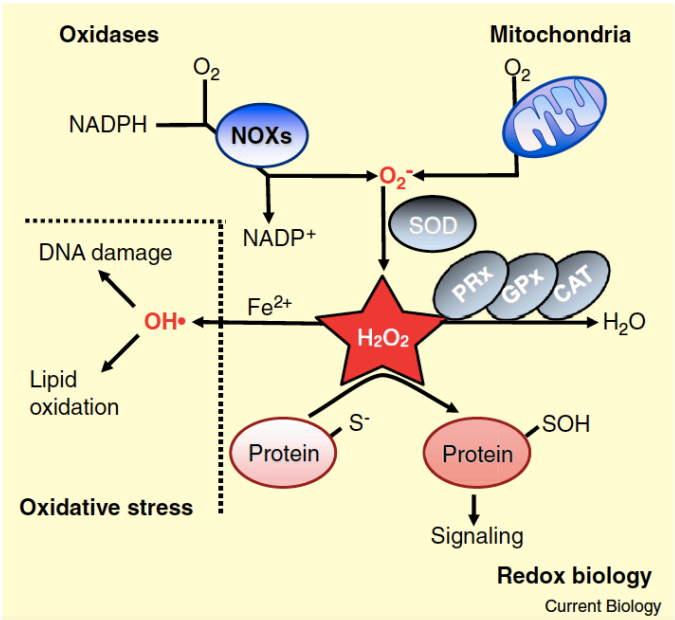

Figure 11: Figure from [22]. Illustrations summarizing the basics of ROS.

I.2. Inflammatory bowel diseases: inflammation and oxidative stress

I.2.a. Inflammatory bowel diseases: a global health issue

Inflammatory Bowel Diseases (IBDs) are chronic disorders characterized by a severe inflammation of some part of the gastro-intestinal tract. They include Crohn's disease (CD) and ulcerative colitis (UC) that differ at least by the location of the inflammation. They both can cause diarrhea, rectal bleeding, anemia, weight loss and abdominal pains [58]. IBDs constitute a global health issue as their incidence is particularly high (and keep increasing) in developed countries reaching in cumulative incidence (over life time) 1 per cent in Europe. [59,60]. The number of IBDs cases in the world is estimated at 6.8 millions people [61]. For now, no curative therapy exists to treat IBDs and patients mostly receive drugs aiming to control inflammation in order to alleviate the symptoms and to prevent the flare-ups. The main treatments include corticosteroids and immunomodulators comprising small molecules and monoclonal antibodies targeting specific inflammatory pathways or cytokines [62]. However, these expensive drugs are not always efficient and can induce loss of response and adverse effects. Eventually, surgery, and particularly intestinal resection, is often advocated to reduce symptoms or following complications [63]. There is therefore an urgent need for novel, safe and efficient therapeutic alternatives to fight IBDs.

I.2.b. Intestinal inflammation and dysbiosis of the intestinal microbiota in IBDs

Aiming the development of therapy to "cure" IBDs, the scientific community has mostly focused on one well-recognized feature of IBDs: the dysbiosis of the intestinal microbiota (Figure 12). Intestinal microbiota is made of a large and complex variety of micro-organisms indigenous or transient. While most of them are commensals, others, named pathobionts (mostly proteobacteria), are pathogenic and can have pro-inflammatory effect when allowed to grow in number. To prevent dysbiosis and maintain the intestinal homeostasis, the gut-associated lymphoid tissue (GALT), must specifically eliminate the pathogenic species while tolerating the symbiotic ones via a dynamic equilibrium between regulatory T cells and activated effector T cells. Moreover, the mucus layer present in the semi-permeable intestinal epithelial barrier protects the intestinal epithelial cells from commensal bacteria and pathobionts [64,65]. If bacteria eventually penetrate into the mucus, intestinal epithelial

Paneth cells are responsible to secrete antimicrobial peptides to eliminate them and regulate the microbial load at the mucosal surface (Figure 12) [66]. In addition, when bacteria translocate from the intestinal lumen to the inner layers of the mucosa, the host immune response is activated and produce pro-inflammatory mediators. Consequently, when IBD dysbiosis is seen, it favors inflammatory responses due to broken homeostasis between regulatory and effector T cells leading to excess production of inflammatory mediators. This causes exacerbated mucosal immune response and results in inflamed tissues, disrupted and dysfunctional intestinal barrier, mucosal inflammation and more generally in IBDs symptoms (Figure 12) [59,67].

IBDs are thus characterized by an impairment of the gut microbiome composition associated to an excessive amount of commensals and pathobionts and reduced amount of symbiotics [68]. In particular, the number of *F. prausnitzii* bacteria, known to display protective effects via the blockage of NF-kB and IL-8 production, is significantly reduced in IBDs patients microbiota [69]. As mentioned above, the gut microbiome alteration, combined with genetic and environmental (diet, stress, drugs) factors, is both the result and the cause of an overreactive immune system.

To revert the IBD dysbiosis, manipulating gut microbiota using for example probiotics or fecal microbiome transplants are currently evaluated in clinical trials through a very attractive approach [70–72].

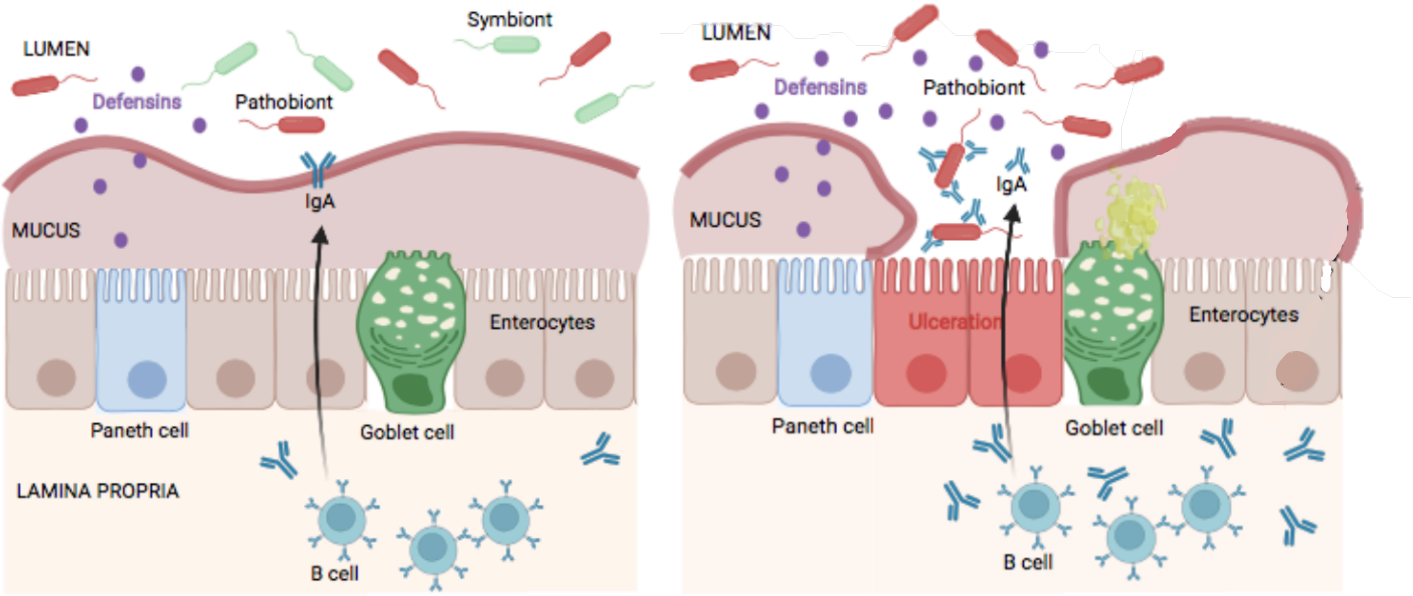

Figure 12: Intestinal inflammation in IBDs (scheme drawn with Biorender). (Left) Intestinal homeostasis is associated to functional epithelial barrier and healthy microbiota. (Right) Intestinal inflammation is accompanied with damages in the mucus layer and dysbiosis of the microbiota.

I.2.c. IBDs and oxidative stress

As a reminder, oxidative stress (OS) is characterized by an excessive amount of reactive oxygen and nitrogen species ROS/RNS in the tissues resulting from an imbalance between prooxidants and antioxidants. ROS were reported to play a key role in regulating the activation of the immune system and mediating inflammation [22]. Indeed, redox homeostasis is efficient in maintaining a healthy immune system. In contrast, decreased level of ROS leads to immuno-suppression while oxidative stress (increased ROS levels) contributes to auto-immunity and subsequently to inflammation [22]. Not surprisingly, many studies evidenced the implication of OS in IBDs. They investigate the molecular basis of OS as pathophysiological component [73–75]. OS was notably associated to several IBD clinical features, including tissue injury and fibrosis, mucosal erosions and the ulcerative colitis–associated colorectal cancer [73]. For these reasons, oxidative stress biomarkers were proposed as a way to diagnose IBDs [76].

The mechanisms underlying oxidative stress and inflammation are intimately intertwined. Oxidative stress is thus considered as both a cause and a consequence of the inflammation, playing a key role in IBDs physiopathology [77]. To go more into details, ROS were suggested to contribute to the pathogenesis of IBDs via different processes. First, their sensing by innate immune receptors from the Toll-like (TLRs) and the NOD-like (NLRs) families is known to induce the activation of signaling pathways triggering the inflammation [77]. Besides, the

activation of TLRs or NLRs receptors was also shown to stimulate the production of ROS by mitochondria and NOXs enzymes, thus amplifying the inflammatory process [22,78]. Secondly, oxidative stress causes impairment in the mucosal barrier permeability allowing bacteria present in the intestinal lumen to cross the mucosal barrier and infiltrate the sterile epithelium. The host responds to this bacterial invasion with the engagement of neutrophils cells that initiate the inflammatory process. This theory, named the "radical induction theory", thus proposes a strong involvement of OS in the inflammatory trigger on the intestinal mucosa [79,80]. Thirdly, it is well-established that ROS can activate the NF-kB inflammatory pathway. The activation mechanisms have long been investigated and publications mentioned mostly the classical IKK-dependent pathway but also other more atypical pathways such as the IkBa Y42 phosphorylation [81]. Lastly, more recent findings identified oxidative-stress related genetic susceptibility loci for IBD, again supporting the implications of OS in IBD pathogenesis [82]. In return, the inflammatory process results in the release of large amounts of ROS by the activated immune cells (macrophages, leukocytes, phagocytes, neutrophils) as part of the host defense mechanism. Moreover, the inflammation mediates the overexpression of other various ROS-producing enzymes such as lipoxygenases (LOX), myeloperoxidase (MPO), and inducible isoforms of nitric oxide (NO) synthase (NOS2) [76]. The subsequent oxidative burden is responsible for major cell injury and participate in maintaining and even exacerbating the ongoing inflammation. To conclude, OS is assumed to be not only one source of the inflammation but also its etiology. This constitutes thus a vicious spiral deeply implied in IBDs physiopathology.

The OS occurring in IBDs patients is detectable at different levels: the direct presence of ROS, the oxidation of biomolecules and the depletion of antioxidant activity. This last point was largely demonstrated in various clinical cases [83–87]. The activity of the main antioxidant enzymes responsible for the catalytic consumption of ROS were assessed in patient samples. The activity of SOD enzymes was in particular significantly reduced in plasma [83,85,87] from IBDs patients compared to healthy subjects. Interestingly, K. Szczeklik *et. al* observed that the SOD activity was returned at normal levels in CD remission group [87]. Furthermore, L. Kruidenier *et al.* reported that the expression and concordantly the activity of the extracellular SOD is diminished in tissues homogenates from IBDs patients compared to the control group [84]. Likewise, the activity of the MnSOD was abnormally reduced in IBD tissues. However,

immunological assessment indicated an increase in MnSOD content suggesting that MnSOD is overexpressed but in an enzymatically inactive form [84]. The activity of other endogenous antioxidant enzymes were also shown to be imbalanced in IBD patients including catalase (CAT) and glutathione peroxidase (GPx) [85]. To sum up, the antioxidant enzymes do not fulfill their mission of counterbalancing the pro-oxidants activity in IBDs cases. In other words, they are not efficient enough in regulating the ROS concentrations and hence maintaining the redox homeostasis. These observations emphasize the potential of antioxidant drugs as promising therapeutic to compensate for these deficiencies in endogenous defenses and hopefully to control the inflammation in IBDs.

I.2.d. Administration of antioxidant enzymes for IBDs treatment

Considering the tight correlation between oxidative stress and inflammation as well as the deficiency in SOD and CAT enzymes in IBDs cases, the administration of SOD and CAT enzymes at therapeutics purposes were explored in both murine colitis model and IBDs clinical cases. A relevant example is that of the Cu/ZnSOD that was efficient in attenuating different markers of inflammation (weight loss, macroscopic/microscopic damage scores..) in mice suffering from TNBS-induced colitis and daily treated with subcutaneous doses of the enzyme [88]. Based on these promising findings, the Cu/ZnSOD was very early (in 1991) examined in Phase II trial for CD treatment by subcutaneous injection [89]. The trial obtained 73% positive results for short term response and 82% positive results for long term evolution. Lecithinized SOD (SOD covalently bound to 4 phosphatidylcholine-derivative molecules named lecithin) also afforded significant amelioration in UC patients [90]. Moreover, a dietary supplementation with SOD purified from Bacillus amyloliquefaciens appears to protect against OS and to improve inflammation in γ-radiation- and DSS-induced colitis mouse model [91]. For its part, catalase was also examined as a potent IBD treatment in murine model [92,93]. In 2016, K.E. Barrett and D.F. McCole highlighted the ability of catalase to slightly improve DSS-induced colitis in mice and more importantly to suppress the DSS-induced decrease in baseline ion transport [92]. More recently, an atypical commensal *E. coli* strain expressing an additional extra-cellular catalase permitted to decrease H_2O_2 levels in DSS-induced murine colitis. This antioxidant activity was correlated with reduced diseases activity scores [92].

I.2.e. A new therapeutic strategy : administration of low-molecular weight SOD and CAT mimics.

Overall, proteins make poor drugs for the following reasons. First, they poorly penetrate inside the cells because of their large molecular radius and inappropriate charge density. Consequently, only little fraction of the administered SOD/CAT proteins will reach the action site where oxidative stress occurs in the cells. The administrated circulating enzymes are rapidly cleared in the kidneys. Secondly, the enzymes possess short half-lives as they are not very stable outside of their native environment. Last but not least, the administration of proteins originating from foreign organisms frequently results in a strong immunogenicity leading to an unwanted immune response against them. To overcome these limitations, the use of synthetic low-molecular weight molecules reproducing the antioxidant activity of the SOD or CAT enzymes was explored. Based on their lower molecular weight and the possibility to tune their charge density, these synthetic SOD or CAT mimics may afford improved pharmacodynamics and pharmacokinetics properties. They are also less subjected to immunogenicity issues. A general description of the existing SOD mimics is provided in the next section.

I.3. Metal complexes with SOD activity, so-called SOD mimics

Multiple redox-active metal-based compounds were described in the literature for their ability to catalyze superoxide dismutation. A number of reviews from Salvemini *et. al* [94], Iranzo *et. al* [95], Miriyala *et. al* [96], Batinic *et. al* [97], Policar *et. al* [1] or Signorella *et. al* [98] provide a comprehensive overview of the state of the art of SOD mimics and report the major knowledges on the understanding of their activity.

I.3.a. Important criteria for efficient SOD mimics

To exert efficient therapeutic effects, SOD mimics need to exhibit several characteristics that are shared by native SODs: high intrinsic SOD activity, high bioavailability and appropriate cellular location. The combination of these parameters, detailed below, constitutes a guideline for the design of SOD mimics.

I.3.a.i. Intrinsic SOD activity

The most valuable characteristic of SOD mimics as drug candidates is undoubtedly their ability to catalyze the dismutation of superoxide: the faster the kinetic of the dismutation, the better the antioxidant benefits. Two major features were delineated to obtain the most kinetically competent SOD mimics: 1) a finely tuned redox potential and 2) favorable electrostatic attraction of superoxide.

- Tuned redox potential

We already mentioned in section I.1.e.i that the optimal redox potential for SOD activity is equal to 0.36 V/NHE, the midpoint potential between superoxide oxidation and reduction. At this potential, the two half-reactions (oxidation to dioxygen and reduction to H_2O_2) occur at the same rate. For the purpose to finely tune the redox potential close to this optima value, the coordination sphere of the metal ion can be adapted. According to its Lewis nature, the ligand can control the redox potential through electronic effects. As an example, the hexaaqua Mn(III)/Mn(II) couple possess a too high redox potential (1.51 V/NHE) to catalyze superoxide dismutation. Consequently, the acceleration of the reaction with superoxide require to reduce the redox potential. To this end, one could for instance stabilize Mn(III) via the coordination of electrons-donating group (N-donors) that will increase the electron density onto the manganese center. In addition, the tuning of redox potential can be achieved by modulating the charge of the ligand and the geometry of the complexes. On one hand, a negatively-charged ligand (resp. positively charged) decreases (resp. increases) the redox potential. On the other hand, the redox potential can be decreased by using a ligand that constrains the complex in an axial-distorted octahedral structure (Jahn-teller effect) [1,99].

- Electrostatic guidance of superoxide

In addition, researchers have focused on mimicking the positively-charged entrance funnel found in native SODs [100], that guides superoxide from the protein exterior toward the active metallic center [101]. In this way, the presence of charges and their topography within Mn-porphyrin was shown to strongly impact the catalytic rate for superoxide dismutation [101,102]. In more details, the distribution of charge at the far periphery of the porphyrin was less efficient in accelerating superoxide dismutation than when distributed over a donut above the manganese center. Otherwise, the group of C. Policar conjugated a SOD mimic to cationic unstructured polyarginine moiety (up to 9 moieties) to favor the approach of

superoxide via electrostatic effect, [103] and they showed that only the three closest charge from the metal center were electrostatically efficient.

I.3.a.ii. Bioavailability

- Stability and inertness

To exhibit beneficial effect *in cells* or *in vivo*, the SOD mimics have to remain intact in the biological conditions. However, the cellular environment is very rich in competitive free metal ions (or loosely bound metal ions) and metal-coordinating bioligands that may react with the SOD mimics and inactivate it (*via* metal or ligand exchanges). For this reason, efforts must be made to design inert and stable SOD mimics.

- Cellular penetration

The ability of SOD mimics to penetrate inside cells is an essential parameter for therapeutic effects. Since this parameter was corelated with amphiphilic properties, some SOD mimics were conjugated to lipophilic alkyl chain to promote their cellular uptake [104]. Alternatively, other SOD mimics were coupled to moieties that are specifically recognized by cells and subsequently internalized (galactose or lactose) [105,106].

I.3.a.iii. Cellular distribution

Lastly, the cellular distribution of SOD mimics is an important determinant of the bioactivity [97]. As a matter of fact, in a study from Munroe *et. al*, the absence of bioactivity observed for yet SOD-active metal complexes was attributed to their mislocation [107]. Indeed, to induce benefits, the SOD mimics need to reach the ROS-enriched cellular regions. Based on the fact that oxidative stress is mostly initiated in mitochondria, some SOD mimics were functionalized with mitochondria-targeting moieties (mostly cationic and hydrophobic) including mitochondria-targeting peptide [106] and triphenylphosphonium moieties [108]. The improvement of the protective effects displayed by the SOD mimics were linked to their increased accumulation at the mitochondria. In addition, Mathieu *et al.* study a SOD mimic conjugated to a multimodal probe based on a $Re(CO)_3$ lipophilic complex [109]. They showed that the resulting conjugate goes to the mitochondria and they linked the amount at the mitochondria with the anti-inflammatory activity.

In the end, another primary requirement, that applied to any drugs, is of course the non-toxicity of the metal complexes.

I.3.b. State of the art of metal-based SOD mimics

This section aims to summarize the major advances in the development of metal complexes mimicking SOD. The SOD mimics described in the literature gather complexes containing iron, copper, nickel or manganese center. However, the manganese-based complexes represent the large majority of designed SOD mimics since manganese is preferred for *in cells* or *in vivo* applications due to its lower toxicity (do not catalyze Fenton reaction) and higher bioavailability (see section II.1.b.i).

I.3.b.i. Iron-, copper- and nickel-based SOD mimics

The first metal complex with SOD activity that has been described in the literature is a Fe(III) porphyrin: Fe^{3+}-tetrakis(4-N-méthylpyridyl)porphyrine, abbreviated $Fe(TMPyP)^{3+}$ (Figure 13 (A)) [110]. $Fe(TMPyP)^{3+}$ is able to catalyze superoxide dismutation with a high catalytic rate (3.10^7 $M^{-1}.s^{-1}$) but is afterwards rapidly degraded by produced H_2O_2 leading to the release of toxic free iron, probably reduced in the intracellular reducing environment into Fe(II), resulting in an increased $HO^{\bullet}$ production (see section I.1.b) [111]. One copper porphyrin (Cu^{2+}-Br_8TM-4-PyP4$^+$) whose structure is given in Figure 13 (B) was also reported to display a significant SOD activity (3.10^6 $M^{-1}.s^{-1}$) and to be more resistant to demetallation than the analog Mn complex [112]. Indeed, while being more toxic when free, the use of copper led to more stable complexes with higher association constant. Otherwise, most of the discovered copper complexes with SOD activity are based on peptidyl ligands inspired from Cu/Zn SOD active site and thus rich in histidines (see section I.1.e.i). One Co(II) complexes has also been described, built on a glycoligand [113]. Lastly, few nickel complexes were designed based on the active site of the native Ni-SOD that contain 2 nitrogen and 2 sulfur donating atoms in its first sphere of coordination (see section I.1.e.i) [114–116].

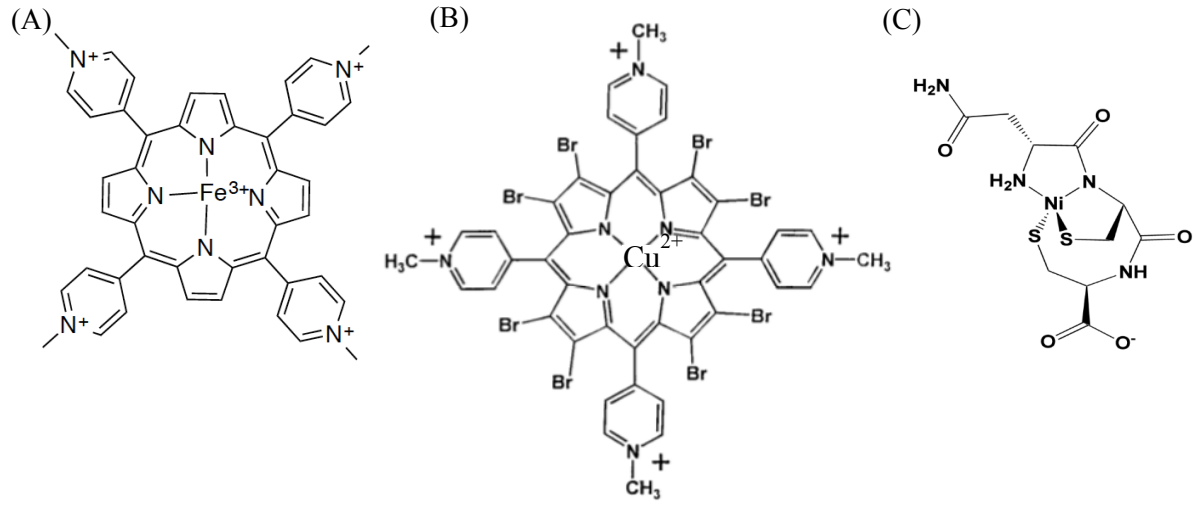

Figure 13:Structure of the (A) iron and (B) copper porphyrin-based SOD mimics mentioned in the text. (A) Fe(TMPyP)$^{3+}$, (B) Cu(Br$_8$TM-4-PyP)$^{4+}$, (C) tri-peptide asparagine-cysteine-cysteine mimicking the coordination sphere in NiSOD [114].

I.3.b.ii. Manganese-based SOD mimics

A large variety of manganese complexes have been described in the literature for their SOD activity [1,94–96,117,118]. Most of them consist of porphyrin, cyclic polyamine or salen-type ligands coordinating a Mn(II) or Mn(III) ion. Others contain a $N_{3/4}O$ ligand bio-inspired from the active site of endogenous MnSOD.

- Porphyrin-based Mn complexes

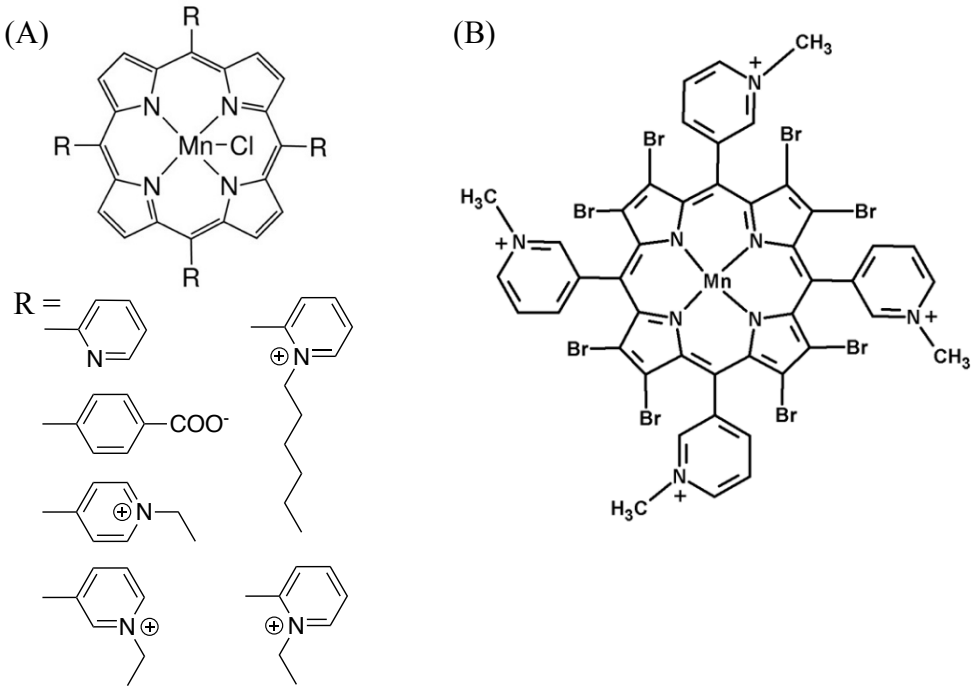

Figure 14: (A) Chemical structure of Mn(III)-porphyrin SOD mimics. Multiple R substituents have been tested [119]. (B) Best reported MnP: Mn(II)-Br$_8$TM-3-PyP^{4+}

The Mn-porphyrins (MnPs) count among the most developed and efficient SOD mimics. Porphyrins are of particular interest for *in vivo* applications because they are non-toxic and form very stable metal complexes. Moreover, they are chemically accessible meaning that the core structure can be quite easily functionalized with a large range of substituents to modulate their redox potential and thus their SOD activity [119]. The catalytic rate for superoxide dismutation of MnPs are usually found around 10^7-10^8 $M^{-1}.s^{-1}$. One MnP in particular, Mn(II)-Br_8TM-3-PyP^{4+} (Figure 14 (B)), stands out with a catalytic rate equal to 7.10^8 $M^{-1}.s^{-1}$, approaching that of the native enzyme [120]. Surprisingly, besides their SOD activity, MnPs were shown to act as pro-oxidant, possibly through the production of H_2O_2 and the oxidation of various cellular components (p65 subunit of NF-κB, complex I and III and IV in the mitochondria…) [121]. Researchers have taken advantages from the prooxidant activity of MnPs to selectively fragilize tumor cells (that are more sensitive to H_2O_2), while protecting normal cells via the anti-superoxide activity [119,122,123]. In this way, two MnPs: MnTE-2-PyP^{5+} (BMX-010) and MnTnBuOE-2-PyP^{5+} (BMX-001) entered clinical trial as anti-cancer drug candidates. MnTE-2-PyP^{5+} is also in phase II clinical trial for atopical dermatitis treatment (= eczema, appears in response to excessive epidermal inflammation). The use of porphyrin-related ligands such as corroles was also investigated as scaffold for the design of manganese SOD mimics [117]. However, this did not lead to as efficient SOD mimics.

- Pentaazamacrocyclic Mn complexes

The Mn(II) pentaazamacrocycles (Mn-PAM), also called cyclic polyamines, constitute another important class of Mn-based SOD mimics. Similarly to MnPs, their catalytic rate ranges around 10^7-10^8 $M^{-1}.s^{-1}$ and reach up to 10^9 $M^{-1}.s^{-1}$ for the most efficient (named GC4419 and represented in Figure 15 (B)) [124]. Complex M4043 (Figure 15 (A)) is probably the most studied MnPAM. Its SOD activity was largely demonstrated outside of any cellular environment (k_{cat}=1.2x10^7 $M^{-1}.s^{-1}$) and i*n cells*. M40403 was notably involved in two clinical trials for cancer and hypotension treatment. Unfortunately, while M40403 was well tolerated in humans, the two clinical trials were suspended or terminated due to lack of therapeutic action. For its part, GC4419 is currently tested in phase II clinical trial for its ability to reduce oral mucositis in patients suffering from head and neck cancer [125].

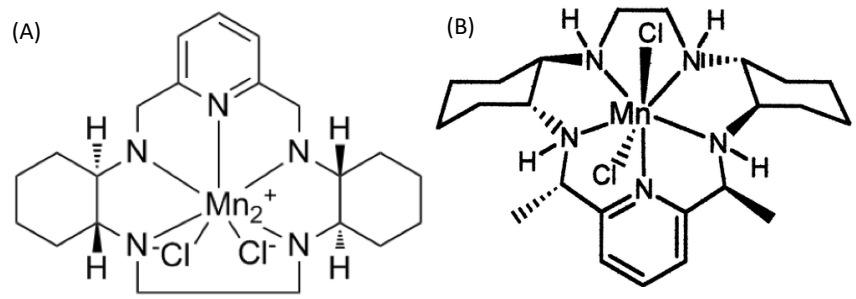

Figure 15: Structure of two Mn-PAM mentioned in the text: (A) M40403 and (B) GC4419.

- Salen- based Mn complexes

Another acknowledged kind of Mn-based SOD mimics consist in Mn complexes with an open-chain tetradentate N_2O_2 ligand named salen. This latter is synthetized from one ethylenediamine moiety and two phenol groups functionalized with aldehyde forming a bis-Schiff base ligand (Figure 16 (A)). Nevertheless, even the two most efficient Mn-salen (EUK-8 and EUK-134, Figure 16) described in the literature possess limited intrinsic SOD activity ($k_{cat} \approx 10^6$-10^7 $M^{-1}.s^{-1}$) and suffer from low stability, linked to the open-chain ligand [126,127].

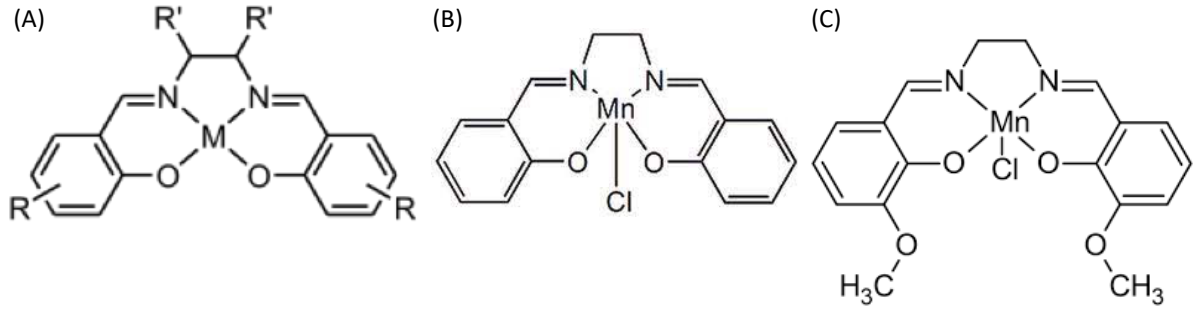

Figure 16: (A) Structural scaffold of salen-type ligands. (B) Structure of EUK-8. (C) Structure of EUK-134.

- Mn-N_3/$_4$O complexes inspired from endogenous MnSOD active site

The group of C. Policar has been focused in designing complexes that reproduce the chemical environment of Mn in native SODs [1,43,128–131]. As a reminder (see section I.1.e.i), the Mn ion in MnSOD is surrounded by three histidines (N-bonding) and one aspartate (O-bonding). Hence, to mimic the Mn sphere of coordination in MnSOD active site, this team synthetized a first series of tripodal nitrogen-centered ligand bearing a carboxylate moiety (Figure 17) [128,129]. They observed that the redox potential of the manganese complexes was higher than the optimal value at 0.36 V/NHE. Efforts have then been made to reduce the redox potential [132]. First, the carboxylate moiety was replaced with a more electron-donating phenol group [131]. Secondly, they incorporated an additional N-bond while taking care to

leave an inner sphere free site, required for the binding of superoxide to the Mn center. As expected (see section I.3.a.i), the decrease in redox potential (to get closer to 0.36 V/NHE) was positively correlated with increased catalytic activity for superoxide dismutation [129].

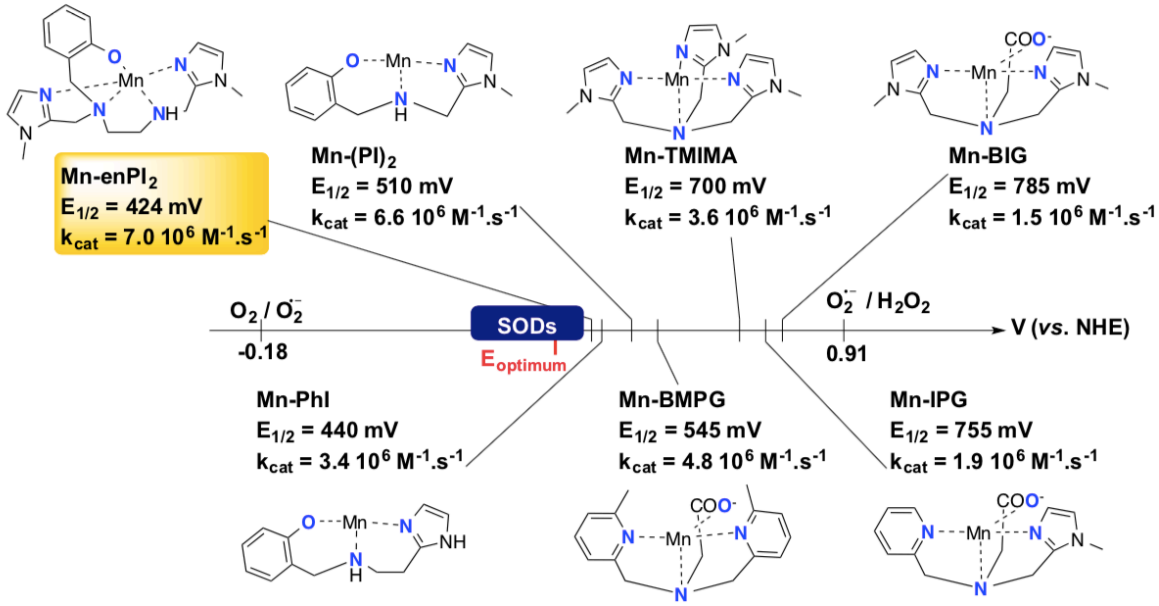

Figure 17: Figure from [43]. Structure and kinetic constant for superoxide dismutation of bio-inspired SOD mimics developed in the group of C. Policar. The mimics are ranked according to their redox potential.

In conclusion, multiple types of metallic complexes with different degrees of SOD activities were explored as antioxidant therapeutics. A last common type, that was not detailed here, gather the peptidyl SOD mimics: the section III.1.c is dedicated to their description.

I.3.c. Metal complexes with CAT-like activity

The dismutation of superoxide results in the release of H_2O_2, another ROS that, while less reactive and toxic, can induce oxidative damages when a threshold is exceeded. For this reason, many work have been focused on the development of catalytic H_2O_2 scavengers in parallel to that of SOD mimics to reduce synergistically oxidative stress [133]. To detoxify H_2O_2, two main strategies were considered: the mimicking of CAT or peroxidase reactivity, which are in fact frequently co-existent in redox-active metal complexes [134]. This section aims to provide a short overview of the small molecular complexes mimicking CAT described in the literature. In addition to their distinct redox potential, the major difference between CAT mimics and SOD mimics is the ability to transfer two electrons to ensure the bi-electronic process of catalase, while SOD activity only requires mono-electronic catalysts.

I.3.c.i. Mononuclear Fe- or Mn- CAT mimics

A large number of reported CAT mimics was initially developed as SOD mimics. Indeed as the redox properties required for both reactivity are close, many SOD mimics were found to additionally possess substantial CAT activity [135,136]. This class of CAT mimics mostly comprises Mn and Fe porphyrins and Mn salens [135]. For instance, the MnPs labelled MnTMPyP, MnTBAP, MnTE-2-PyP^{5+}, MnTDE-2-ImP^{5+} and AEOL 11207 (Figure 18 (A)) were reported to exhibit dual SOD and CAT activity [137–139]. Likewise, numerous manganese salen complexes from the EUK series (EUK-8/113/134/172/178/189 etc.) are able to dismute H_2O_2 at a rate close to that measured for the aforementioned MnPs [127,140]. However, the activity remains much lower than that of the native enzymes (≈0.001-0.05%). Interestingly, EUK derivatives conjugated with cyclopentane-fixed auxiliaries (Figure 18 (B)) [55,141] or with cyclodextrins [142] or bearing electron-withdrawing substituents on the phenyl ring [143,144] (e.g. sulphonato-, halide (Figure 18 (C)) display enhanced CAT activity. In contrast, the famous MnPAM SOD mimics M40403 and M40404 display no detectable CAT-like activity.

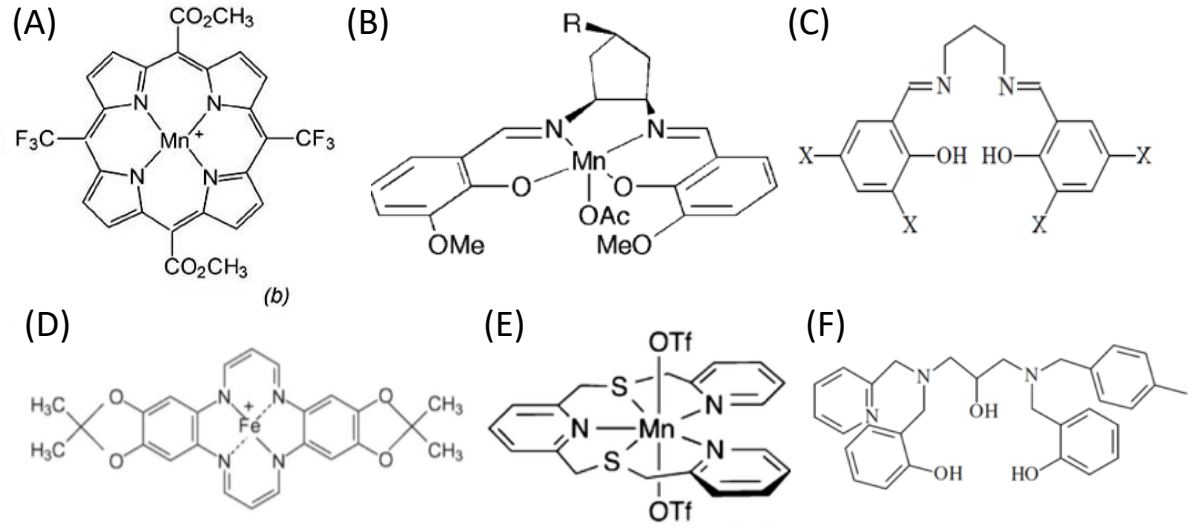

Figure 18: Structure of some complexes/ligands mentioned in the text. (A) AEOL 11207. (B) Mn-salen complex functionalized with acid-base auxiliary. Multiple auxiliary groups R have been tested [55]. (C) Difluoro- and dichloro-substituted Schiff-base ligands (X = F or Cl). The halogenated substituents impact specifically the CAT activity. (D) Fe-tetraaza macrocycle. (E) CAT mimic based on NSNSN motif. (F) Unsymmetrical hexadentate N_3O_3 ligand possessing SOD and CAT activity upon Mn(III) binding.

Furthermore, other types of mononuclear iron and manganese complexes were shown to catalytically scavenge H_2O_2 to oxygen and water [145]. One example was published by W. Sicking *et. al* and revealed the ability of a non-heme tretraaza macrocycles Fe(III) complex (Figure 18 (D)) to catalyze H_2O_2 dismutation [146]. Moreover, the use of linear pentadentate

ligands forming a NSNSN binding motif prove to be efficient for dismuting H_2O_2 with high kinetic rate and turnover efficiency (similar to that of MnPs and EUK Mn salen complexes) upon coordination to Mn(II) (Figure 18 (E)) [147,148]. The resulting Mn(II) complexes are besides relatively stable in aqueous environments, in particular compared to salen-type complexes that are rapidly degraded in water. In addition, the groups of S. Signorella and C. Hureau designed stable mononuclear Mn(III) complexes composed of unsymmetrical N_3O_3 ligands which display both CAT- and SOD-like activity (Figure 18 (F)) [149]. For non-heme mononuclear CAT mimics, a dimerization probably occurs to provide the two required electrons for each of the metal centers.

I.3.c.ii. Bio-inspired dinuclear Mn(II) CAT mimics

Another class of metal complexes with catalase activity are the di-manganese complexes whose structure was bio-inspired from that of the natural enzyme MnCAT described in section I.1.e.ii. The review entitled "Bio-inspired Functional Mimics of the Manganese Catalases" published by S. Signorella and C. Hureau provides a comprehensive overview of this kind of CAT mimics. Some relevant examples will be briefly summarized here. The first example of structural and functional analog of the *L. plantarum* MnCAT active site was reported by Dismukes and coworkers in 1987 (Figure 19 (A)) [150]. Briefly, they designed a septadentate ligand, containing 4 benzimidazole groups linked to a diaminopropanol moiety, that is able to bind two manganese ions. Interestingly, the binuclear Mn(II) complex successfully catalyzes the dismutation of H_2O_2 via a mechanism similar to that of the native enzyme.

Later, the group of Signorella developed multiple synthetic di-manganese MnCAT biomimetic complexes [143,151–153] that were highly efficient to disproportionate H_2O_2 in aqueous solution. The structure-activity relationship study evidenced a correlation between the nature of the bridging and terminal ligands with the redox potential and thus with the catalase activity. In addition, the use of alkoxo- bridging ligand was associated with higher rate constant for H_2O_2 dismutation, independently to the redox potential (Figure 19 (B)). This was explained by their ability to serve as intramolecular bases that favors the proton transfer required for the catalysis. Following this same strategy, numerous phenoxo-, aceto- or carboxylato- bridged di Mn complexes were developed (Figure 19 (C,D)) and showed high catalytic activity for H_2O_2 disproportionation [145].

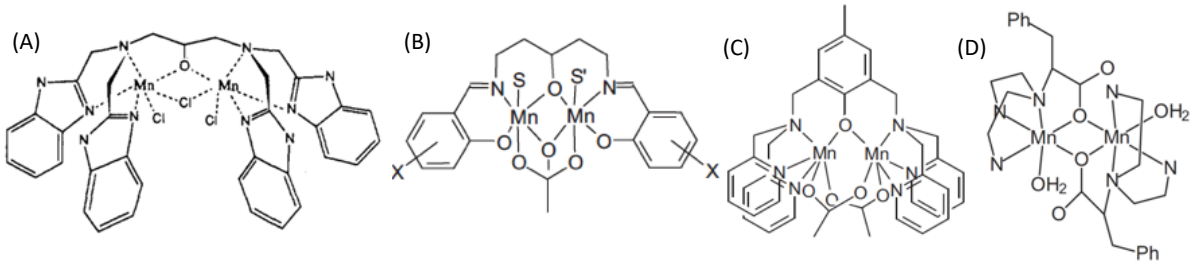

Figure 19: Dinuclear manganese complexes designed as small artificial MnCAT enzymes.(A) First- developed MnCAT analog.(B) Example of alkoxo-bridged MnCAT mimic. (C) Example of phenoxo-bridged MnCAT mimic. (D) Example of carboylato-bridged MnCAT mimic [145]

To conclude on Mn CAT mimics, it has to be highlighted that their catalytic cycle were shown to frequently involve high valent intermediates with the cycling between $Mn(III)_2$ and $Mn(IV)_2$

I.3.c.iii. Copper-based CAT mimics

Alternatively to iron and manganese CAT mimics, few mononuclear and dinuclear copper complexes were developed and explored for their CAT activity. This section presents non-exhaustively some examples of Cu-based CAT mimics described in the literature. In the 1960s, a first demonstration, that mononuclear Cu(II) complexes with various ligands (peptides, nucleotides, RNA, DNA etc.) can displayed CAT activity, was reported by H. Sigel [154]. In particular, a Cu(II) complex composed of a bipyridyl ligand was shown to display catalase and peroxidase activities. Likewise, the coordination of Cu(II) with a ligand composed of a phenanthroline moiety and two N-Benzoylanthranilic acid groups (Figure 20 (A)) was shown to confer it with significant CAT activity [155]. Similarly a tetraazamacrocylic Cu(II) represented in Figure 20 (B) was shown to decompose both $O_2^{\bullet-}$ and H_2O_2 catalytically with high rate[156]. As last example, a four-coordinating N_2O_2 ligand (Figure 20 (C)) was evidenced to act as CAT and SOD mimics upon coordination of one Cu(II) ion. Related to its CAT and SOD activity, the mononuclear Cu(II) complex showed anti-metastatic properties in glioma cells and in 3D multicellular spheroids [157].

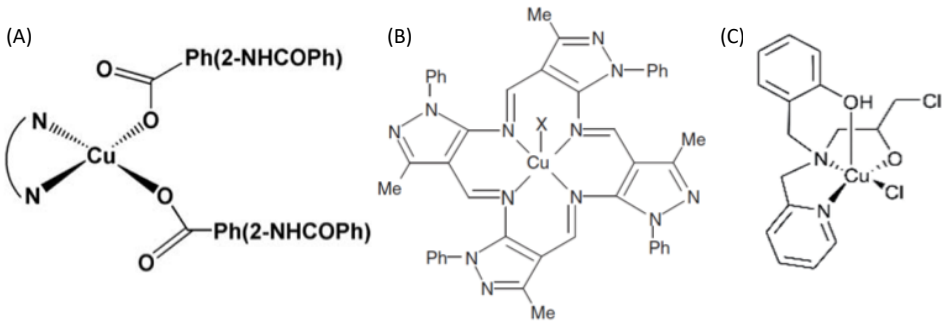

Figure 20: Mononuclear copper(II) CAT mimics mentioned in the text.

The examples of dinuclear copper complexes with CAT activity are rarer. They include macrocyclic dinuclear structures [158,159] or N_3O ligands like that given in Figure 21 [160,161].

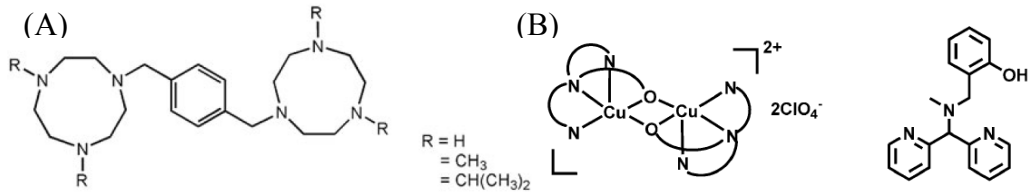

Figure 21: Dinuclear Cu(II) CAT mimics. (A) Polyamine macrocyclic bearing alkyl substituents and bridged by xylylene. (B) N3O3 ligands with dual OSD/CAT activity.

The comparative study of the catalytic rate for H_2O_2 dismutation between the different kinds of CAT mimics is not straightforward because the data published in the literature are not always comparable. Indeed, the CAT mimics were studied in various solvents (H_2O, DMF, MeOH) at different pH but more importantly the values reported by the authors to describe the kinetic of H_2O_2 dismutation are of various natures/types. These kinetic parameters include the initial rate of O_2 production ($M.s^{-1}$), the endpoint (maximal concentration of produced O_2), the first-order kinetic constant (s^{-1}) or the second-order kinetic constant ($M^{-1}.s^{-1}$). In general, the second-order kinetic constant of the described cupper-based CAT mimics is around 1-10 $M^{-1}.s^{-1}$, which represents about 0.0001% to 0.001% that of the native di-manganese catalases (*ca*. 3.1 x 10^6 $M^{-1}.s^{-1}$).

To conclude this part, we must also mention that, similarly to SOD mimics, the presence of at least one labile coordination position on the metal center of the CAT mimic is required for binding H_2O_2 substrate.

I.4. Evaluation of the SOD mimics activity

The following section intends to describe the main tools provided to evaluate the reaction kinetic of superoxide with the SOD mimics *in vitro* and *in cells*. There is some confusions regarding the use of the term *in vitro*; *in vitro* refers here as the intrinsic ability of the complexes to catalyze superoxide dismutation outside of any cellular context, whereas biologist would use it for an activity in cell cultured as opposed to *in vivo*.

I.4.a. Determination of the intrinsic SOD activity

I.4.a.i. Indirect assay of SOD activity: the McCord and Fridovich assay

Among the techniques used to assess SOD activity, most rely on an indirect monitoring of superoxide consumption. In these methods, superoxide is provided in an aqueous buffer at a constant rate. The superoxide concentration reaches this way concentrations close to that observed physiologically under oxidative stress conditions, as a continuous flow. The most known SOD indirect assay is undoubtedly the assay originally developed by McCord and Fridovich in 1969 and largely optimized since then [162].

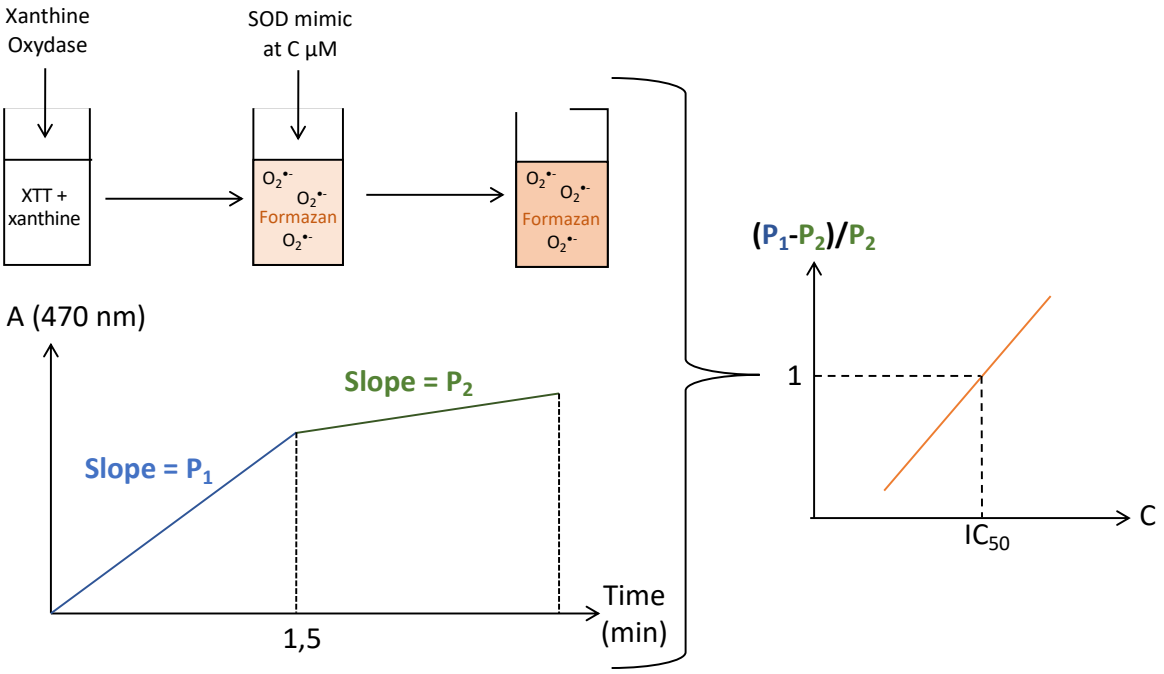

Figure 22: Global strategy of the McCord and Fridovich assay for an indirect measurement of the SOD activity.

Briefly, this assay is based on the oxidation of xanthine into uric acid catalyzed by the xanthine oxidase enzyme which results in a continuous and slow flow of superoxide in water [162,163]. A kinetic competition to react with superoxide then occurred between the putative SOD mimics and a superoxide UV-vis indicator, which changes color upon oxidation with superoxide. The UV-visible monitoring of the superoxide-induced oxidation of the indicator is required because the direct spectrophotometric detection of superoxide is not possible due to its weak absorption coefficient and its low concentration in the assay conditions. A number of superoxide marker have been developed including cytochrome c Fe(III), XTT (2,3-Bis-(2-méthoxy-4-Nitro-5-sulfophényl)-2H-tétrazolium-5-carboxanilide) or NBT (nitro blue tetrazolium) [164]. As illustrated in Figure 22, this assay allows to retrieve the IC_{50} corresponding to the concentration of SOD mimic necessary to slow down the reduction of the redox indicator by 50%. However, this value is dependent on the used superoxide indicator

and its concentration. For comparison with available data published in the literature, one needs to calculate the apparent catalytic rate for superoxide dismutation of the SOD mimic from the following formula : $k_{cat} = k_{XTT}*C_{XTT}/IC_{50}$ [1,129]. In the case of cytochrome c Fe(III), NBT and XTT, the kinetic constants are respectively equals to $k_{cyt\text{-}c}(pH=7.8)=2.6\times10^{5}mol^{-1}.L.s^{-1}$ [165], $k_{NBT}(pH=7.8)=5.9\times10^{4}mol^{-1}.L.s^{-1}$ [166] and k_{XTT} $(pH=7.8)=8.6\times10^{4}mol^{-1}.L.s^{-1}$ [167]. Alternatively to the enzymatic generation of superoxide, L. Costanzo *et. al* obtained a slow flow of superoxide through the photolysis of ketoprofen when irradiated at 313 nm with intensity comparable to sunlight. Then, the SOD mimics likewise compete with cytochrome for the dismutation of superoxide, allowing the determination of the catalytic constant which were found similar to that measured with the classical xanthine/xanthine oxidase assay [168].

The McCord and Fridovich assay was applied to a large number of SOD mimics [169,170,168,171,172]. The main advantages of this assay is its simple setting up as it requires only commercially available reagents and a classical UV-visible spectrophotometer and that it replicates the biologically relevant slow flow of production of superoxide. However, this indirect method is most of the time not sufficient to prove the catalytic action of the SOD mimics rather than a stoichiometric one due to the low concentration of superoxide. To observe several turnovers of SOD mimics reaction with superoxide, higher concentrations of superoxide need to be achieved. In this way, direct assays were established but required non-routine and onerous systems.

I.4.a.ii. Direct assays of SOD activity

To distinguish between a catalyst and a scavenger, the reaction of superoxide dismutation has to be observed with a high turnover number. In this way, systems providing superoxide in large excess compared to the SOD mimics are required. Such high concentrations of superoxide are not physiological but allow ascertaining the catalytic reactivity of some SOD mimics.

First, superoxide can be produced in high amount in anhydrous aprotic medium, where no protons are available for the reduction of superoxide intro hydrogen peroxide, thus restricting the self-dismutation of superoxide [128,129]. Hence, the dissolution of KO_2 or the electrochemical reduction of dissolved dioxygen were shown to be an efficient way to generate superoxide in DMSO, DMF or ACN. The presence of metal complexes with different

hydration levels evidenced their catalytic SOD activity. Moreover, the isolation of intermediates metal-$O_2^{\bullet-}$ adduct under low temperature and their characterization by spectroscopy (UV-visible or EPR) inform on the reaction mechanisms [173]. However, such anhydrous conditions are not reminiscent of that encountered in biological environment. The two following techniques for SOD activity determination are compatible with aqueous solutions: pulse radiolysis and stopped-flow. Pulse radiolysis assay is based on the use of high-energy ionizing radiation to generate rapidly and quantitatively a pulse of highly concentrated superoxide in dioxygen-saturated alkaline or ethanolic aqueous solutions [174–176]. Micromolar concentrations of superoxide were this way reached following short ionizing pulses of high intensity (1.5 µs, 4 MeV). Secondly, the mixing of SOD mimics with a large excess of superoxide was conducted by stopped-flow experiments. Superoxide radical is stabilized at high concentration in an aprotic solvent which is then rapidly diluted in an aqueous solution containing the SOD mimics. The fast mixing of the two reagents allows a kinetic monitoring of the reaction in few microseconds delay [177]. These two methods are said to be direct assays as they directly rely on the spectrophotometric detection of concentrated superoxide around 250 nm. The monitoring of superoxide disappearance in presence of SOD mimic while taking into account the spontaneous dismutation of superoxide enable the calculation of the kinetic constant for superoxide dismutation of the SOD mimics. They were most of the time consistent with that from the McCord and Fridovich assay [103,129,130,178]. When significant differences were observed between the data obtained from direct and indirect assays [179], they were explained by various processes whose intensity is dependent on the assay time scale or on in superoxide concentration. For instance, the re-oxidation of the reduced redox indicator by molecular oxygen is responsible for an under-estimation of SOD mimics activity in indirect assay.

To sum-up, the directs assays provide evidences on the catalytic nature of SOD mimics metal complexes but the indirect ones are established in conditions closer to the physiological situations. The two approaches are thus complementary.

I.4.a.iii. Critical factors for interpretation

The mentioned-above direct and indirect assays for SOD activity were largely applied to a wide range of SOD mimics [1,122].

However, to better interpret the kinetic measurement of superoxide dismutation and in particular to correctly attribute the SOD activity, speciation studies are of main importance. For these reasons, one should notably consider the stability constants and the protonation constants of all the compounds present in the solution to calculate a pertinent catalytic rate [168,180].

Last but not least, one must highlight the strong dependence of the assays on the experimental variables [181]. Indeed, whatever the technique used, a minor change in pH, in buffer nature, concentration or ionic force or in temperature impacts the measured kinetic constants. One must consequently keep a close look on the experimental conditions before comparing data.

I.4.a.iv. Evaluation of intrinsic CAT activity

The last chapter of this manuscript will deal with metal complexes displaying both SOD and CAT activity. This section provides a short overview of the main techniques used to evaluate the CAT activity of CAT mimics.

The easiest and most common way for measuring CAT activity is based on the colorimetric measurement of H_2O_2 disappearance over time . This can be achieved by spectrophotometric assays based on the color change of probes upon reaction with H_2O_2 specifically. They include permanganate, ferrous ions/xylenol orange, ferrous ions/thiocyanate, ammonium molybdate, pyrogallol red, cobalt/bicarbonate ions, etc.

The decrease in the absorbance of the probe or the increase in that of the H_2O_2-oxidized probe are directly related to the amount of residual unreacted H_2O_2 (that were not decomposed by the CAT mimic) and in turn inversely proportional to CAT activity.

These colorimetric assays were optimized over time to exclude the interferences that arise from the presence of other unrelated compounds absorbing at the same wavelength such as amino acids and proteins in serum [185]. Moreover, a strong advantage of this method is its easy implementation on multi-well plates for a rapid screening of many compounds at the same time [183].

Likewise, a chemiluminescence assay for H_2O_2 measurement at sub-micromolar concentrations was also developed by S. Mueller *et. al* as a way to assess catalase activity

[188]. The assay is based on the oxidation of luminol by hypochlorous acid (NaOCl) resulting in a diazaquinone which is specifically converted by H_2O_2 into an excited aminophthalate that emits luminescence signal.

The described-above methods constitute accurate and sensitive methods for evaluating H_2O_2 disappearance. Nevertheless, to prove that the observed anti-H_2O_2 activity occurs through a catalase pathway involving the dismutation of H_2O_2 into water and dioxygen, one can consider measuring the formation of dioxygen. Among the different methods reported for O_2 measurement, one of the most known is probably the Clark oxygen electrode that was initially established by L.C. Clark *et. al* in 1953 to determine oxygen levels in blood [189]. The Clark oxygen electrode was then adapted to the determination catalase-like activity of redox-active therapeutics in classical aqueous buffer [135,190].

The functioning of the Clark electrode relies on the reduction of dissolved dioxygen into water at the cathode electrode (platine) while Ag is oxidized into AgCl at the anode electrode (Figure 23). For the experimental set-up, the electrode is immerged in a solution of H_2O_2 prealably purged with inert gas to remove all dioxygen trace. The CAT mimic is then added in the solution and the formation of dioxygen is monitored by means of the current intensity between the anode and cathode [135].

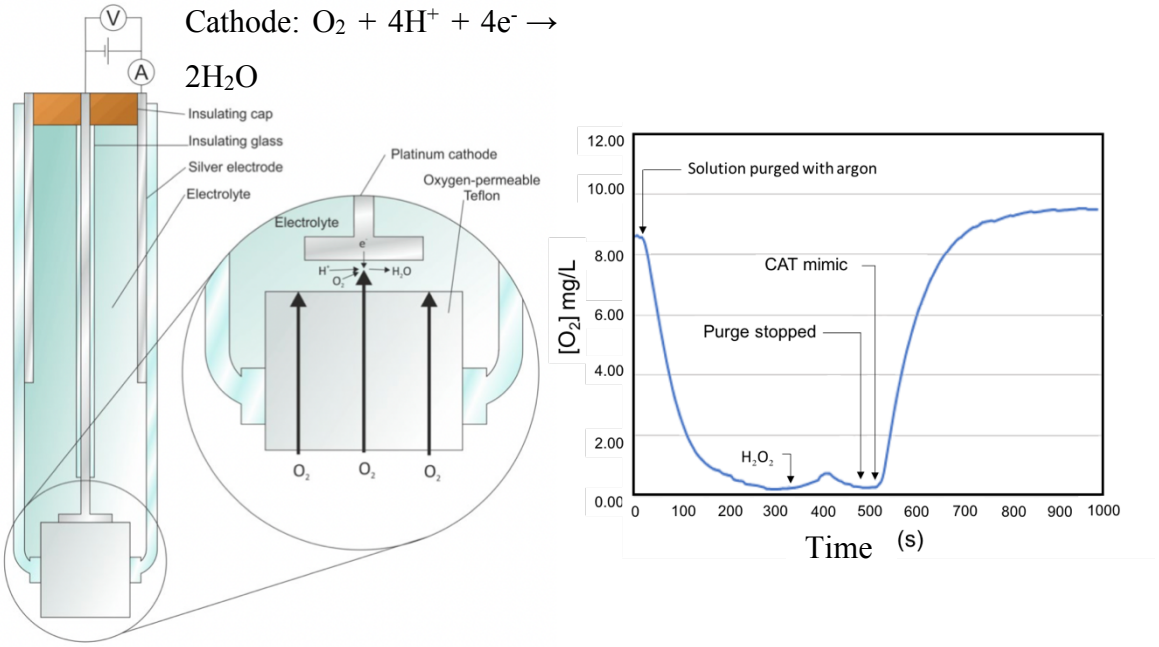

Figure 23: Principle of the Clark dioxygen electrode for measurement of catalase activity. (Left) Schematic representation of a Clark electrode from O. Connell (Wikipedia) and redox reactions occurring at each electrode. (Right) Figure from K. Coulibaly PhD manuscript. Example of dioxygen monitoring data obtained with the Clark electrode when evaluating the catalase activity of a CAT mimic.

From the kinetic of dioxygen formation for different concentration in CAT mimic, the pseudo-first order rate constant for CAT activity as well as the turnover number and frequency can be calculated.

I.4.a.v. In-gel activity assays for the determination of SOD and CAT activity

In addition to the activity assays presented in the last section, activity gels were designed as a preferential mean to detect and quantify SOD or CAT activity in biological samples (cell or tissue homogenates) [191,192]. Indeed, the very crowded biological environment is separated on gel by electrophoresis which allows to distinguish the activity coming from the studied therapeutic to that from unspecific proteins for instance. In contrast, the activity measured in biological samples using the above-mentioned assays could not be rigorously attributed to the target compound. Moreover, the gels assays are known to require less proteins compared to classical assays as they do not require sample dilution steps.

The protocol for SOD and CAT activity gel assay was thoroughly described by C. Weydert and J. Cullen [191]. Briefly, the constituents of the biological samples are let to migrate in gel by electrophoresis under non-denaturating conditions. For SOD activity gel assay, the gel is then incubated in presence of riboflavin, as a source of superoxide in the presence of light, and of NBT (nitro blue tetrazolium), as UV-visible detector. Similarly to the McCord and Fridovich kinetic assay in solution, NBT enters in competition with the SOD mimic to react with superoxide and forms yellow tetrazolium within the gel. For CAT activity gel assay, following separation of native protein, the gel is incubated in presence of H_2O_2, ferric chloride ($FeCl_3$) and potassium ferricyanide (K_3FeCN_6). Again, the ferrous reagents compete with the CAT mimic to react with H_2O_2 and form Prussian blue. In both cases, the presence of a clear achromatic bands are thus indicative of SOD and CAT activity.

These activity assays on gel took however more time than the other activity assays. Indeed they classically last between 24 to 48 hours [191]. Moreover, the acquisition of quantitative results using gel assays is less obvious and requires an external standard (commercial purified enzyme at known catalytic rate). Such in-gel methods are then rather considered as qualitative or semi-quantitative.

I.4.b. Evaluation of SOD mimics activity *in cellulo: HT29-MD2 cells*

Many cellular models have been investigated for the evaluation of SOD mimics bioactivity. I will here focus on the HT29-MD2 cell line on which I have been working. But one will find in Annex a broad-based review of the existing and published cellular model used for SOD mimics screening as well as of the main biological effects induced by SOD mimics observed in these models. Overall, it has to be kept in mind that the bioactivity of the SOD (resp. CAT) mimics observed *in cells* or *in vivo* may not be (at least not totally) related to their SOD (resp. CAT) activity but to other antioxidant (reaction with other ROS) or even pro-oxidant effects (cf. MnPs, see section I.3.b.ii "Porphyrin-based Mn complexes"). For these reasons, these compounds should rather be referred, more broadly, as redox-active therapeutic. This non-specificity of SOD and CAT mimics renders the study of their mechanism of action more tedious but may be to their advantage in pre-clinics and clinics.

HT29-MD2 cell line consists in human colon HT29 cells that were stably transfected to overexpress MD2, a soluble coreceptor of toll-like receptor 4 (TLR-4) [193]. The receptor TLR-4, present at the surface of cell membrane, is responsible for the recognition of lipopolysaccharides (LPS). LPS are bacterial toxins composed by a lipid and a polysaccharide moiety. They are one of the main constituents of Gram negative bacteria external membrane. Upon LPS stimulation of TLR-4 receptors, intestinal cells are known to trigger a strong inflammatory response toward the activation of NFκB pathway particularly [194,195].

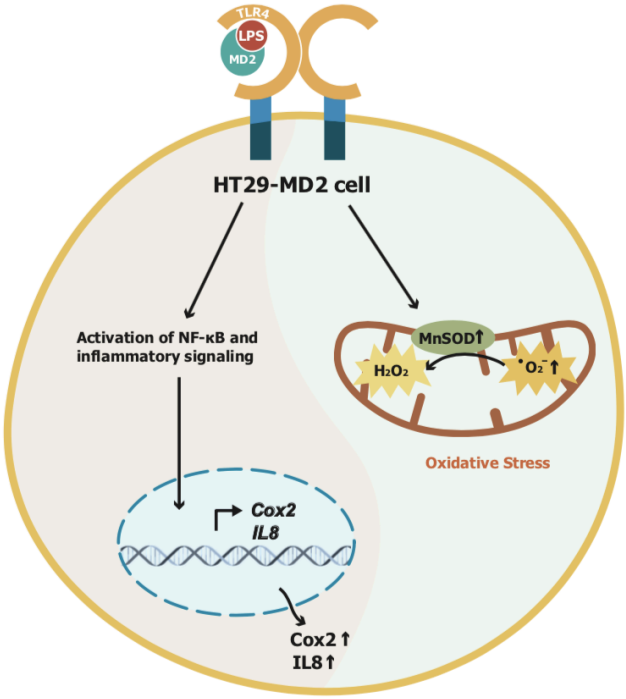

Figure 24: Figure done by M. Zoumpoulaki, a former PhD student in the lab. Schematic illustration of HT29-MD2 cell line.

Unmodified HT29 cells, as intestinal epithelial cells, are not adapted to study intestinal inflammation as they have been conferred a limited response to LPS via a reduced expression of TLR4 and MD2 in order to better tolerate the presence of commensal bacteria. Transfection of HT29 cells with MD2 was shown to increase cell sensitivity and responsiveness to LPS by 100-fold according to measurement of several inflammatory markers (Interleukin-8 IL-8, cyclooxygenase-2 Cox-2) [193,196]. Moreover, the mechanisms of oxidative stress and inflammation (notably NFκB) are known to be tightly intertwined [81,197]. Hence, ROS levels are regulated by the NFκB signaling, which is itself affected (activation or inhibition) by ROS. Consistently, a strong overexpression of MnSOD antioxidant enzyme was observed in HT29-MD2 cells challenged by LPS suggesting the presence of an oxidative stress situation [172,196].

HT29-MD2 cells activated by bacterial LPS were hence used as a cellular model of inflammation mediated by oxidative stress to evaluate both the antioxidant and anti-inflammatory properties of antioxidant therapeutics.

I.5. Objectives of the PhD

My PhD project is articulated along two main projects both addressing the benefits of metallodrugs mimicking the activity of the superoxide dismutase enzymes, that constitute the first line of cellular antioxidant defense, in the context of IBDs.

Concerning the first project, the so-called SOD mimics are metal complexes composed of synthetic ligands containing a diaminoethane scaffold bearing one phenolate and two imidazole moieties. In contrast, in a second part, I have undertaken the study of SOD mimics based on a peptidyl ligand. The manuscript is thus divided in two parts detailing both types.

The first section focuses on Mn(II) complexes derived from Mn1, a SOD mimic widely studied by the C. Policar's team. First, a brief bibliographic review on Mn1, on inertness of metal complexes and on analytical techniques available for SOD mimics detection in cells is reported. Secondly, a novel generation of Mn1-derived SOD mimics were prepared and studied leading to a publication. Briefly, these newly-designed SOD mimics were assessed for their higher resistance to metal exchanges, and thus higher inertness, and their intrinsic SOD activity. Their improved anti-inflammatory and antioxidant bioactivities were evidenced using the above-presented cellular model and correlated to their physico-chemical properties [172]. The most inert Mn1CP derivative was also successfully detected and quantified in cells using mass

spectrometry. Due to their high lability, the detection of the other SOD mimics in their intact form required analytical system in which metal exchanges are limited. Ion-mobility spectrometry coupled to mass spectrometry was in this case highly efficient. To our knowledge, this work constitutes the first example of IMS-MS application for the determination of SOD mimics speciation inside cells. This resulted in a second publication disclosed in a third subsection [198]. Fourthly, we investigated the distribution of Mn1 derivatives within the cells using micro X-ray fluorescence. Lastly, the anti-inflammatory activity of the SOD mimics was evaluated *in vivo* in a murine model of chemically-induced colitis.

The second section presents SOD and CAT mimics made of peptidyl ligands chelating either Cu(II) or Mn(II) ions. Another objective of my PhD was to construct recombinant lactic acid bacteria (recLAB) for the production of the peptidyl ligands constituting these SOD and CAT mimics. Following an elaborate overview on the benefits of probiotics and recombinant probiotics in IBDs, the next part presents the results obtained for this second project. In more details, *L. lactis* MG1363 and NZ9000 and *L. plantarum* NCIMB8826 strains were genetically modified to contain one of the gene coding for the peptidyl ligands of the mentioned-above SOD or CAT mimics. After checking the expression of the peptidyl ligands by the recLAB, the SOD/CAT activity of the expressed peptide upon bacteria supplementation with the appropriate metal (Cu(II) or Mn(II)) was examined. Finally, co-incubation experiments of the recombinant bacteria with LPS-stimulated intestinal epithelial cells were conducted to evaluate the anti-inflammatory properties of the recLAB *in cells*. A *"declaration of invention (DI)"* is in progress with the aim to apply for a patent afterwards.

II. Mn(II) complexes SOD mimics based on synthetic open-chain ligands : relationship between inertness, activity in cells and in vivo, intracellular penetration and distribution.

II.1. Introduction

II.1.a. Mn1, a Mn(II) complex SOD mimic inspired from the MnSOD active site

A general state of the art of existing SOD mimics was described in introductive chapter I. I will here focus on Mn1, a Mn(II) complex bio-inspired from the native MnSOD active site, which was developed and largely characterized by the group of C. Policar.

Mn1 was first synthetized in 2007 and is composed of a pentadentate N_4O ligand, named EnPI2, containing a di-amino ethane moiety bearing two imidazole and one phenolate groups [131]. The structure of Mn1 and the X-ray crystal structure of the di-nuclear Mn(II) complex [Enpi2-Mn(II)-Mn(II)-Enpi2] are given in Figure 25. The cyclic voltammogram of Mn1 revealed that Mn1 possesses a redox potential (0.44V/NHE in PIPES pH 7.5 [131]) close to the targeted redox potential (0.36 V/NHE) compatible with a fast catalysis of superoxide dismutation [1,129,196]. Consistently, Mn1 displays SOD activity with an apparent catalytic rate equal to 7.10^6 $M^{-1}.s^{-1}$ according to McCord and Fridovich assay [131].

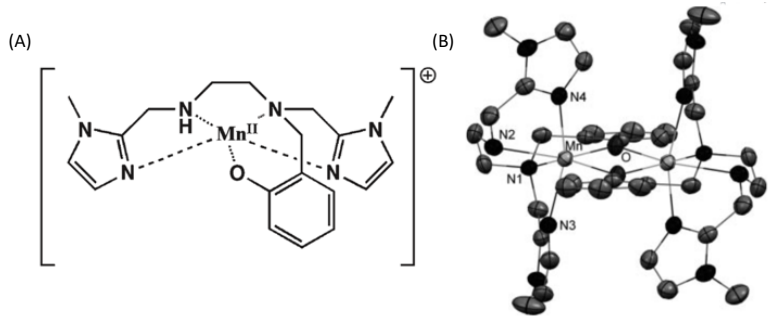

Figure 25: (A) Structure of Mn(II)-EnPI2 complex Mn1. (B) Crystal structure [Enpi2-Mn(II)-Mn(II)-Enpi2] from Cisnetti et. al obtained from X-ray diffraction data [131]. Ellipsoid plot of the centrosymmetric cationic moiety, produced with Mercury 1.4.2. Ellipsoids are drawn at 50 % probability level.

The bioactivity of Mn1 was evaluated in different cell lines (Figure 26). Mn1 was first tested on activated RAW 264.7 macrophages [199]. These immune cells generate strong ROS fluxes upon activation and thus constitute a relevant cellular model. The quantification of

extracellular superoxide in RAW 264.7 supernatants evidenced the anti-superoxide activity of Mn1. Later, the antioxidant and anti-inflammatory effects of Mn1 were evaluated on HT29-MD2 cells [196]. Again, Mn1 had interesting bioactivity as it was able to attenuate the LPS-induced increase in inflammatory marker IL-8 secretion and the overexpression of MnSOD. During my master internship, the kinetics of Mn1 bioactivities on HT29-MD2 cells were investigated (Figure 27). It appeared that Mn1 was able to reduce the monitored effects of LPS (IL-8 secretion and MnSOD overexpression) that appeared after 1-3h of LPS challenge. Interestingly, it seemed that there is a delay between inflammation apparition (observed through iL-8 secretion) and MnSOD overexpression. This delay maybe due to protein expression that requires more time.

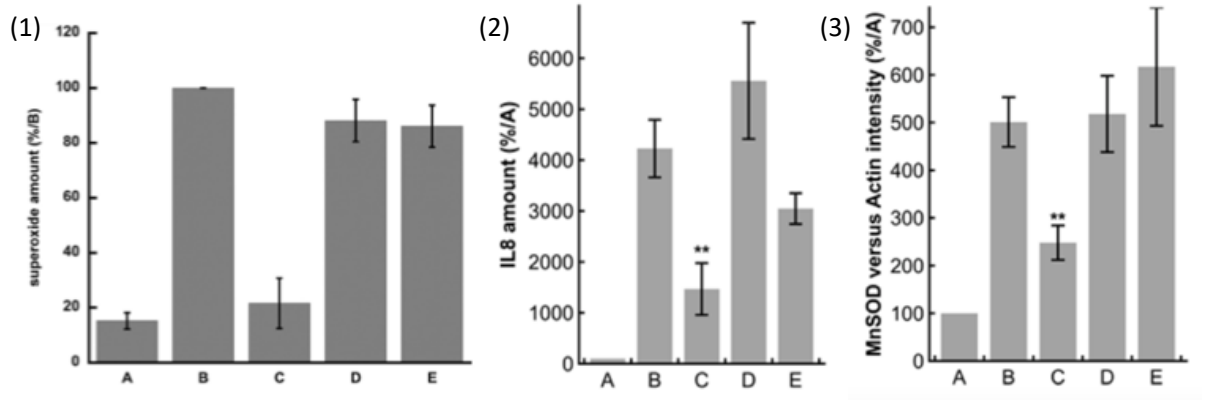

Figure 26: Evaluation of Mn1 bioactivity in (1) Raw 264.7 and (2,3) HT29-MD2 cell lines. (1) Measurement of the superoxide amount in Raw 264.7 supernatants [199]. (2) Quantification of IL-8 levels in HT29-MD2 supernatants [196]. (3) Quantification of MnSOD expression versus actin expression in HT29-MD2 lysates [196]. (1,2,3) The data are plotted as a percentage compared to LPS control. A = control without LPS, B = LPS, C = LPS + Mn1 100µM, D = LPS + $MnCl_2$ 100µM and E = LPS + bovine SOD 100 U/mL. Note that raw 264.7 are activated via the addition of IFN-γ and PMA besides LPS.

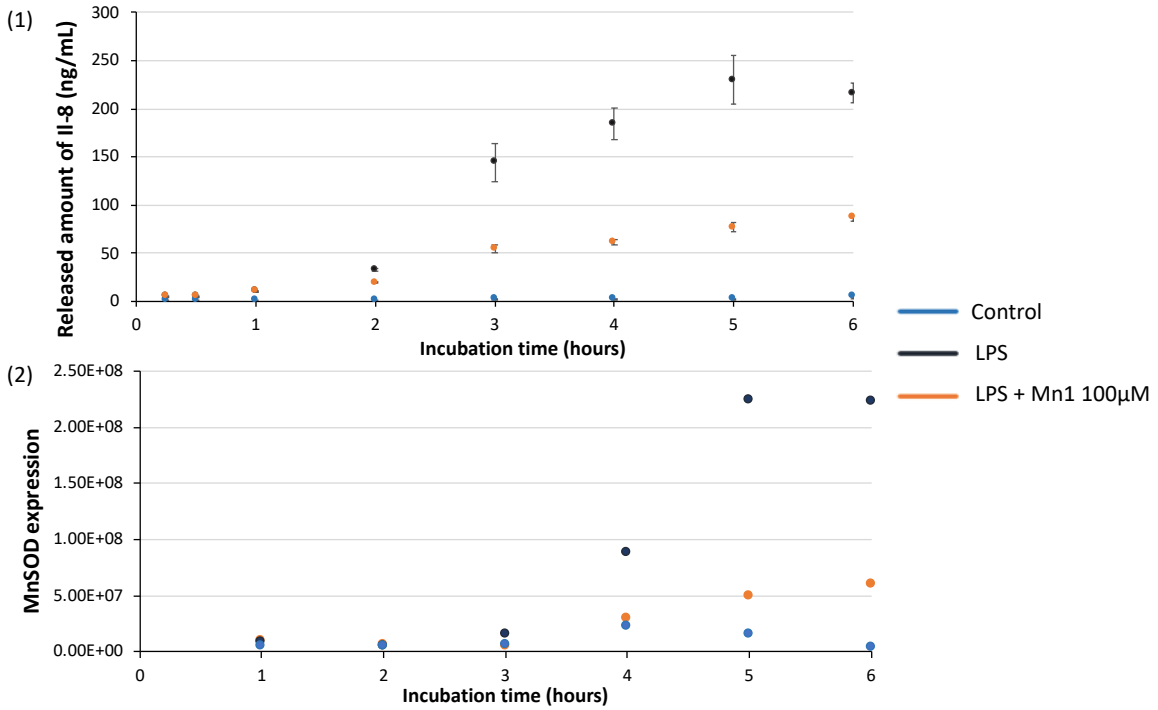

Figure 27: ***Kinetic study of the effect of Mn1 on the secretion of IL-8 and MnSOD expression on LPS-activated HT29-MD2 cells.*** *(1) Amount of IL-8 released in the supernatant as a function of the incubation time, measured by ELISA. (2) Quantification of MnSOD in cell lysates as a function of the incubation time by Western Blot.*

A former PhD student of the laboratory (LBM) studied the cell feedback to LPS and Mn1 at the proteome level to decipher the mechanisms of action of both LPS and Mn1. To this end, she conducted proteomics and redoxomics studies via the OcSILAC (Oxidized Cysteine Stable Isotope Labeling of Amino acids in Cell culture) strategy and identified numbers of proteins either up-regulated or down-regulated and either oxidized or reduced in response to LPS and Mn1 treatment.

To endorse the attribution of the observed bioactivity to Mn1 in HT29-MD2 cells, the intra-cellular penetration of the SOD mimic was checked by EPR and ICP-MS [172,196], and found consistent by the two techniques. The quantification results confirm its accumulation inside the cells with a maximal threshold reached after about 3 hours of incubation. Lastly, high spatially resolved synchrotron-based X-ray fluorescence microscopy experiments revealed a diffuse distribution of Mn1 throughout the cell body [196].

Regarding its promising activity in cells, Mn1 was then administrated by oral gavage in mice subjected to DNS-induced colitis [196]. This murine model of colitis will be detailed later. Mn1 was prepared at relatively high concentration (4 mM) in a basic buffer in order to protect it

from the acidic gastric conditions. Remarkably, mice treating with Mn1 recovered earlier and displayed globally improved health status compared to mice treated with the vehicle (Figure 28). Further *in vivo* assays would require efficient delivery vectors to optimize the activity of Mn1 and reduce the administration doses.

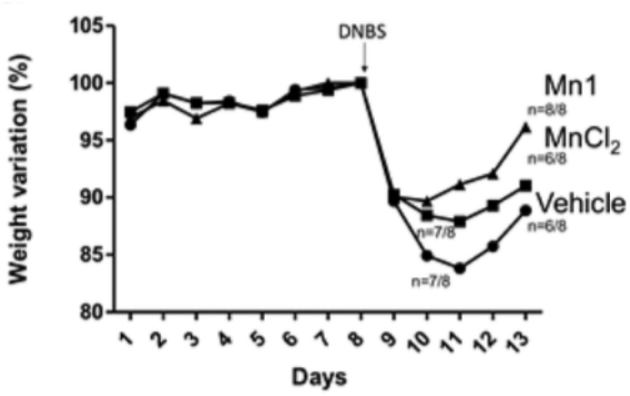

Figure 28: Effect of Mn1 on weight variation in a DNBS-induced murine model of colitis. Mice were treated daily by oral gavage, starting the day of DNBS injection, with 100 µL of vehicle ($NaHCO_3$ 4.2%), $MnCl_2$ (8 mM), or Mn1 (4 mM) in $NaHCO_3$ 4.2% [196].

Finally, some efforts were made to increase its bioactivity by conjugating it with three different peptidyl moieties: two cell-penetrating peptides (CPP) namely a poly-arginine peptide (R9) and a CPP inspired from TAT and penetratin (RW9) and a mitochondria-penetrating peptide (MPP). Note that for both CPP, they may also mimic the positively charged electrostatic funnel encountered in native MnSOD which favors the guidance of negatively-charged superoxide toward the manganese active center [103,200]. Even if the conjugation with these moieties did not allow reaching higher intracellular concentration, in the case of Mn1-R9, a better anti-inflammatory activity than Mn1 ones was observed at a lower incubation concentration (10 µM).

II.1.b. SOD mimics metal complexes: choice of manganese (II)

II.1.b.i. Advantages of Mn(II) over other transitions metals

The general introduction highlighted the efficacy of redox-tuned metal complexes to reproduce the SOD activity. Manganese(II) ion appears to be a valuable metal cation in the design of such SOD mimics for a number of reasons. First, manganese(II) is better tolerated in living systems in comparison to other transitions metal such as Cu(I) and Fe(II). Both of them are indeed able to take part in the Haber-Weiss chemistry, responsible for the formation of

the highly reactive and toxic hydroxyl radical (Figure 29). In more details, the oxidation of the metal cation (Cu(I) or Fe(II)) is able to mono-electronically reduce H_2O_2 into HO^- leading to a $HO^\bullet$ flow (Fenton reaction) and the low oxidation-state metal can be then regenerated by reacting with superoxide or other reductants (Figure 29).

(1) $H_2O_2 + M^{n+} \rightarrow HO^- + HO^\bullet + M^{(n+1)+}$ (Fenton reaction)

(2) $O_2^{\bullet-} + M^{(n+1)+} \rightarrow O_2 + M^{n+}$

$H_2O_2 + O_2^{\bullet-} \rightarrow HO^- + HO^\bullet + O_2$ (Haber Weiss reaction)

Figure 29: Haber Weiss reaction

Secondly, manganese(II) has a high bioavailability compared to the other divalent transition metal cations (Figure 30). This aspect can be related to the low affinity of manganese for bioligands. Indeed, the half-filled electron outer shell precludes any ligand-field stabilization, yielding to Mn(II) complexes that are less stable and more labile than any other divalent transition metal complexes (Figure 30) [201,202]. Moreover, the endogenous content in manganese(II) is very rich in in a large variety of organisms. In particular *L. plantarum [203]*, *D. radiodurans* [204–206]*, C. elegans* [205,207] and *S. cerevisiae* [208] were shown to accumulate large amount of manganese (≈ mM) which was correlated with important protective effects against oxidative stress. The antioxidant effects were associated to non-proteyl complexes (referred to as “manganese-antioxidants”) notably based on lactate and phosphate ligands [209,210]. While its too high redox potential prevents any catalytic activity, the hexaaqua Mn(II) complex was also shown to act as a weak stoichiometric scavenger of superoxide [130,209]. Overall, manganese in its various forms (free cations or coordinated to salts/cellular metabolites, etc.) is widely recognized for its protective effects against oxidative stress [211–213].

In addition, manganese is known to play a vital role in humans as it is involved as co-factor of many enzymes (phosphoenolpyruvate decarboxylase, arginase, glutamine synthetase, MnSOD etc.). Moreover, manganese starvation through calprotectin-induced manganese chelation was described as a defense mechanism used by host against pathogens infections [214]. However, like any compound, manganese becomes toxic when in excessive amount. Fortunately, biological systems have developed effective ways to control the homeostasis of endogenous metal and hence maintain manganese abundance at regulated levels [215].

Eventually, the lower toxicity, the higher bioavailability and the well-demonstrated antioxidant benefits of manganese make its use as redox-active metal center of SOD mimics particularly suitable. For all these reasons, many Mn(II) complexes chelated with various ligands were investigated for their SOD activity but they all suffer from the same limit: the highly labile nature of Mn^{2+} (Figure 30).

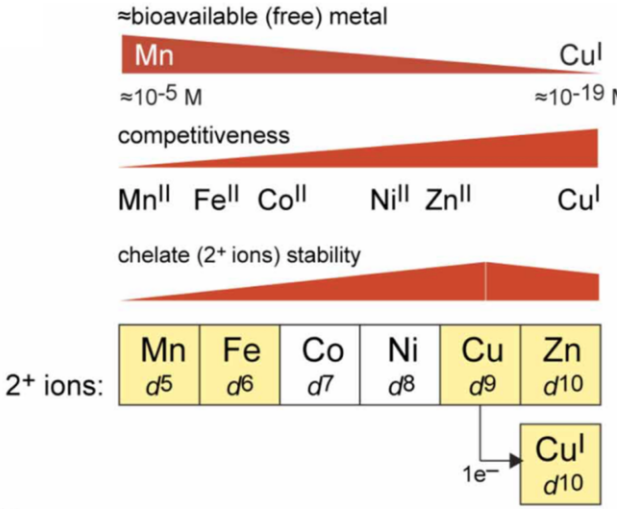

Figure 30: Figure from [215]. Schematic illustration of the bioavailability, the competitiveness for ligand binding and the chelate M^{2+} stability of biologically important first-row transition metals. The trend in metal(II) complex stability is overall inversely related to competitiveness which itself is inversely related to the metal "bioavailability" in the biological environment.

II.1.b.ii. Efforts to counterbalance the lability of Mn(II) complexes

As mentioned earlier, the symmetric d^5 electron configuration system of the Mn^{2+} ion results in a lack of inertness of Mn(II) complexes. Consequently, many Mn(II) complexes such as the SOD mimic mangafodipir $[Mn(DPDP)]^{3-}$ were found to undergo fast dissociation under *in vivo* conditions [96,216]. The dissociation can occur either via spontaneous pathway, proton-assisted pathway or metal-assisted pathway for which a competing ion (such as Mg^{2+}, Ca^{2+}, Zn^{2+} or Cu^{2+}) replaces the manganese center resulting into transmetallation of the complex. As the free ligands or the ligands coordinated to other transition metals do not possess the appropriate redox properties to catalyze SOD, it is mandatory to design stable Mn(II) chelates with enhanced inertness. Regarding these considerations, efforts have been made to rigidify the structure of the ligands in order to promote the inertness of the Mn(II) complex. A first great improvement was achieved by the group of G. Tircso that designed an EDTA-derived ligand based on a trans-1,2-diaminocyclohexane backbone (Figure 31) [217]. The resistance to metal exchange of the corresponding Mn(II) complex, named Mn-CDTA (cyclohexyle

diamine tetraacetate), was more than 100 fold better compared to the corresponding complex possessing an ethylene backbone (EDTA). It was suggested that CDTA ligand provides a compact and pre-organized coordination cavity suitable for manganese encapsulation. This example constitutes one of the first proof that open-chain ligands can form Mn(II) complexes with acceptable lability. Recently, the structure of CDTA was improved by incorporating a pyridyl-N donor group with the aims of further rigidifying the chelate (Figure 7) [218,219]. The resulting [Mn(PyC3A)(H_2O)] open-chain chelate displayed a 2-fold decreased Mn^{2+} dissociation rate in the presence of competing Zn^{2+} ions compared to Mn-CDTA.

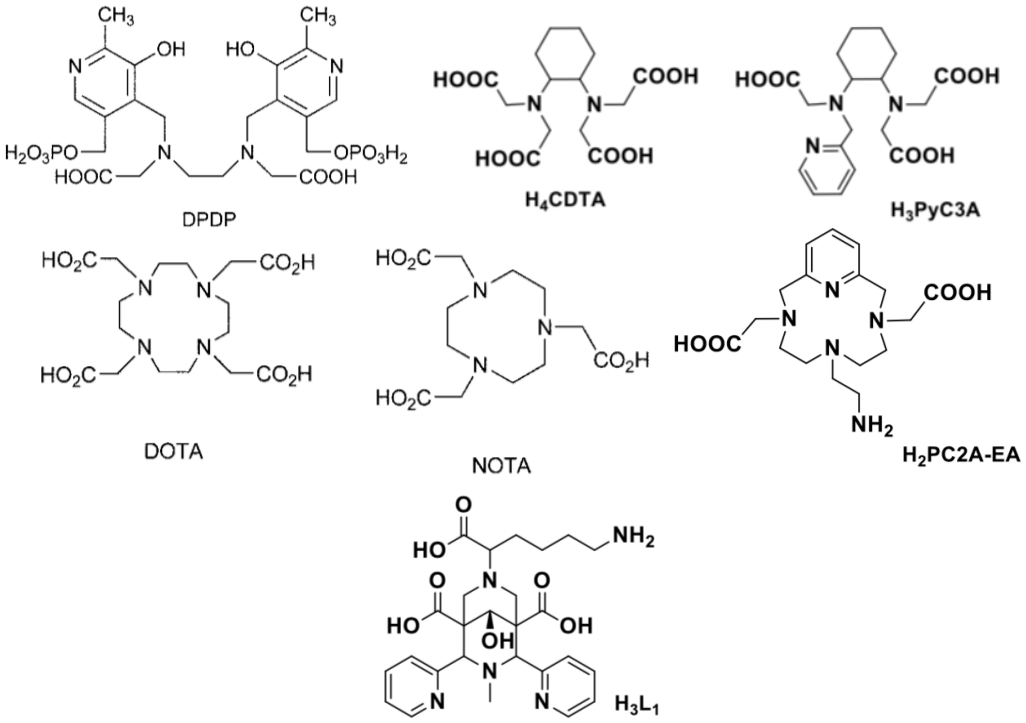

Figure 31: Ligands mentioned in the text.

In contrast, Mn(II) complexes made of macrocyclic ligands were recognized as the most kinetically inert and stable systems. They notably include Mn(II) chelates with the common polydentate macrocyclic NOTA and DOTA ligands (Figure 7) [220]. The dissociation kinetic study of $[Mn(DOTA)]^{2-}$ and $[Mn(NOTA)]^{-}$ revealed unexpectedly high inertness with respect to transmetallation in the presence of a high excess of zinc exchanging ion. This was explained by different reasons: 1) the saturation of the Mn^{2+} coordination with exclusively ligand donor atoms, 2) the remarkably high thermodynamic complexes stability resulting from the macrocyclic ligands and 3) the formation of stable dinuclear Mn^{2+}–L–Zn^{2+} complexes. Following the promising direction of $[Mn(DOTA)]^{2-}$-like and $[Mn(CTDA)]^{2-}$-like structures, a new complex, MnPC2A-EA (Figure 31), based on a pyclen macrocycle containing a pyridine

and bearing an ethylenediamine pendant arm was designed [221]. Interestingly, the dissociation proceeded almost 200 times slower than for [Mn(PyC3A)(H_2O)]. At its publication date in 2020, MnPC2A-EA had the highest resistance to dissociation reported so far for a monohydrated Mn^{2+} complex. However, a bispidine type ligand (L_1 = 2,4-pyridyl-disubstituted bispidol bearing one methylene carboxylic acid) developed by D. Ndiaye *et. al* leading to a Mn(II) complex with higher resistance toward metal exchange has been described very recently [222]. The rigid and preorganized bispidine skeleton endows its Mn^{2+} complex with unprecedented resistance to acid catalyzed dissociation and metal exchanges. In particular, no dissociation of MnL_1 through metal exchange were observed for 140 days when incubated in presence of 50 equivalents of Zn^{2+}. Likewise, the rate constant for proton assisted dissociation was found two orders of magnitude lower than that reported for MnPC2A-EA.

To conclude, the inertness has been largely recognized as a very important feature to be considered for the *in vivo* applications. While manganese complexes do not appear at first sight as ideal candidate due to their general lability, many published data have unambiguously shown that Mn^{2+} complexes with improved inertness can be developed. For now, the most promising structures for Mn(II) complexation consist in bispidine-type and macrocyclic chelators. Nevertheless, some rigidified linear structure including trans-1,2-cyclohexylene backbone and pyridine moiety were also shown to provide slow dissociation . Such ligand skeleton could be adapted to Mn1 in order to improve its kinetic inertness and hopefully its bioactivity.

II.1.c. Detection and quantification of Mn(II) complexes within cells

The biological efficiency of SOD mimics is obviously dependent on their intrinsic SOD activity but other parameters are also of main importance. Among them, cellular uptake, speciation in biological environments and subcellular distribution are key features that have to be characterized to better understand SOD mimic bio-activities.

Several analytical techniques are available to investigate these parameters, especially in the case of metal complexes. They will be briefly detailed in the following section.

II.1.c.i. Overall cellular uptake of SOD mimics

- Metal content measurement

Most of the existing SOD mimics contain a metallic center. The quantification of the associated metal hence permits, in a first approximation, to estimate the amounts of intracellular SOD mimic. Two main techniques for the quantification of metal ions are used: inductive-coupled plasma mass spectrometry (ICP-MS) and electron paramagnetic resonance (EPR) which have both been widely applied to biological samples. EPR detects only paramagnetic metal ions such as Mn(II) (S=5/2) and is less sensitive than ICP-MS.

ICP-MS and EPR were commonly used by the group of C. Policar to quantify SOD mimics penetration inside HT29-MD2 cells [171,172,196,223]. ICP-MS analysis were also conducted by K. Cheng *et al.* to assess the intracellular accumulation of the well-studied MnTM-4-PyP (Mn-porphyrin) SOD mimic in rat cortical neurons [224]. Another example of ICP-MS quantification reported by TP. Ribeiro *et. al* proved that Mn-complexes SOD mimics have the ability to enter inside *S. cerevisiae* [225]. A close alternative to ICP-MS is inductive-coupled plasma atomic emission spectroscopy (ICP-AES). ICP-AES similarly allows the quantification of metals based on the emission of electromagnetic radiation at wavelengths specific to the excited chemical element. ICP-AES has been notably used to evaluate the cell penetration of four Mn(II) complexes SOD mimics in rat aorta smooth muscle cells. Interestingly, the efficacy of cellular uptake was correlated to the lipophilic properties, assumed to favor the transmembrane passage of the complexes [226].

All of ICP-MS and ICP-AES techniques do not allow to detect and quantify the intact SOD-active metal complexes but only provide the total cellular content in metallic elements. Before being analyzed, the cell homogenates are in fact acidified to free the metal of interest from all coordination sites and then afford an accurate quantification of its total amount. The measurement of physiological metal levels in control cells incubated without SOD mimics is thus required to discriminate between the amount of metal coming from the SOD mimics to the endogenous one. Nevertheless, the incubation with SOD mimics may itself alter the homeostasis of the metal ions within the cells and thus could bias the quantification.

Interestingly, EPR can inform on its part about the coordination state of the metal. To illustrate this point, in the 80's, DE. Ash and VL. Schramm successfully distinguished free and bound Mn(II) in rats hepatocytes from EPR signals [227]. Indeed, they noticed that the six sharp lines of hexaaqua Mn(II) EPR signal are typically broadened when bound to small molecules because of the coordination sphere geometry, being distorted from the regular octahedron.

X-ray fluorescence (XRF) is another available technique useful to quantify heavy metallic elements in freeze-dried whole-cell pellets [228].

- Ligand content evaluation

To overcome the drawbacks associated to the quantification of the metallic center, other tools were described in the literature relying on the quantification of the overall complex or to the ligands via either 1) UV-visible absorption or 2) fluorescence spectroscopy.

First, UV-visible spectroscopy is suitable for the quantification of porphyrin-based SOD mimics (MnP). The UV spectra of porphyrins indeed possesses a characteristic band around 400 nm named the Soret band. The measurement of the area under Soret band was then largely used to calculate the levels of porphyrins inside cell lysates [122,171,229,230]. The group of Batinic-Haberle largely followed this approach to quantify the cellular accumulation of various MnP [122,230]. They notably evaluated MnP SOD mimics levels in cytosolic and membrane fraction of SOD deficient *E. coli* and *S. cerevisiae*. Likewise, A. Tovmasyan *et al.* and A. Vincent *et. al* performed UV spectroscopy to assess the cellular uptake of MnPs respectively in 4T1 cells and in HT29-MD2 cells [171,229].

Another strategy to detect SOD mimics in biological samples consists in conjugating the SOD mimics with a fluorescent dye. Hence, spectrofluorimetric measurement of cell lysates confirmed the presence inside human neuroblastoma cells of manganese (II) pentaazamacrocyclic SOD mimics labelled with fluorescent rhodamine B or pyrene tags [228]. Besides allowing an accurate monitoring of the SOD mimic's ligand uptake inside cells, fluorescence microscopy can inform on the subcellular distribution. For this reason, this technique will be detailed later in the corresponding section II.1.c.iii

II.1.c.ii. Study of SOD mimics speciation in the cellular environment

The analytical techniques described above proved to be efficient for the quantification of SOD mimics cellular uptake. However, they do not give further information on their speciation in the cells. Still the investigation of the cellular fate of SOD mimics (stability, oxidation state, etc.) is required for a better understanding of their mechanisms of action.

Liquid chromatography coupled to tandem mass spectrometry (LC-MS/MS) allowed, beyond the intracellular quantification of SOD mimics, the detection of the entire SOD-active metal

complexes (and not just the metal or the ligand) *in cells* and *in vivo* [223]. The MS/MS detection of the intact SOD mimics in cell lysates was successfully used to demonstrate their intracellular stability. In other case, chemical modification of the SOD mimics (degradation, protonation etc.) may be evidenced according to LC-MS/MS. LC-MS/MS methodology was applied to the detection of Mn1 in HT29-MD2 lysates [196]. They observed two peaks corresponding to the free ligand EnPI2 and the expected complex (at m/z 355.2 and 408.2, respectively) and other peaks related to their fragmentation patterns. This specific LC-MS/MS signature of Mn1 and EnPI2 thus revealed the presence of intact Mn1 in cells lysates and its partial decoordination either in the cellular environment or under the LC-MS/MS conditions.

Another possible approach to explore the speciation of MnP SOD mimics in cells relies on resonant Raman (RR) spectroscopy in the 1250-1550 cm^{-1} range. RR spectroscopy informs on both cellular uptake and redox state of the MnP SOD mimics. Indeed the RR bands of porphyrin-based metal complexes are characteristic of the redox state, the spin and the axial coordination of the metal center [231]. In particular the band at 1370 cm^{-1} assigned to Mn(III)-porphyrins is shifted toward lower frequencies (1347 cm^{-1}) for Mn(II)P [232]. The group of R. Radi monitored the intensity of this RR band to investigate the redox state of two MnPs incubated with isolated mitochondria and bovine aorta endothelial cells (BAEC) [16]. They observed that Mn(III)Ps accumulated inside BAEC and were then rapidly and mostly reduced to Mn(II)P by the intracellular components. Interestingly, the addition of SIN-1 (Morpholinosydnonimine), that generates spontaneously nitric oxide and superoxide, in BAEC medium induces the oxidation to Mn(III) of the MnPs. This study supports RR spectroscopy as an efficient and useful way to conduct redox speciation analysis of MnPs in biological systems and hence to rationalize the antioxidant activity of the SOD mimics.

Lastly, C. Weekley *et. al* recently reported the ability of two X-ray absorption spectroscopy (XAS) subsets: X-ray absorption near edge structure (XANES) and Extended X-ray absorption fine structure (EXAFS) to explore MnPAM metabolism in cells [228]. XANES provide information on manganese oxidation state and on the first coordination sphere of Mn while EXAFS completes the analysis by estimating the distance between the Mn center and the atoms of the first and second coordination sphere. Their data revealed inter alia that up to 85% of the original MnPAM SOD mimics remained intact and most of the residues were

metabolized into Mn(II) phosphates. Interestingly the degree of biotransformation into Mn(II)-phosphate did not correlated with the thermodynamic stability of MnPAM

II.1.c.iii. Subcellular distribution of SOD mimics

For an optimal bioactivity, the SOD mimics must reach the regions rich in ROS, namely mitochondria, to exert their anti-superoxide activity more efficiently. The elucidation of SOD mimics distribution inside the cell is of great interest. To this end, researchers have adapted some of the techniques described above to microscopy for cellular imaging.

Hence, as mentioned above, fluorescence microscopy was largely applied to the intracellular imaging of SOD mimics ligand containing fluorescent moiety. For instance, a peptidyl mimic of SOD and glutathione peroxidase was conjugated to both a fluorescent FITC moiety and a cell-penetrating peptide TAT [233]. This allowed to check the SOD mimics penetration inside L02 cells with the aid of the TAT sequence and to map the intracellular localization. Similarly, Y. Fang *et. al* encapsulated a CuZnSOD mimic in mesoporous silica nanoparticles functionalized with FITC to image it in cells [234]. Nevertheless, the conjugations of SOD mimics to fluorescent dye may perturb the redox properties of the complexes and more importantly may alter their cellular penetration and distribution.

In addition, XRF microspectroscopy has been more and more employed to image with high spatial resolution the distribution of the metal of some therapeutic complexes, including SOD mimics [196,228,235]. For instance, JB. Aitken *et. al* employed XRF imaging to localize the MnP MnTnHex-2-PyP^{5+} inside A549 cells (Figure 32 (2)) [236]. For their part, C. Weekley *et. al* used, in the one hand, fluorescent confocal microscopy to image the ligand of the above-mentioned MnPAM SOD mimics coupled to a fluorescent tag inside SH-SY5Y human neuroblastoma and A549 human lung cancer cell lines (Figure 32 (1)) [228]. The maps reveal a preferential localization of the rhodamine or pyrene-conjugated SOD mimic in the cytosol. In the other hand, they have used XRF and XAS techniques to map heavy elements in the cells at the micrometer scale [228]. They were then able to compare the cellular distributions of manganese with that of the fluorescent tags (Figure 32 (1)). For rhodamine conjugates, the localization of Mn did not match with that of the fluorescent tag suggesting either decoordination of the Mn complex or cleavage of the rhodamine. In contrast, a clear

colocalization was noticed between pyrene tag and Mn which indicate that the complex most probably remains intact in the cells.

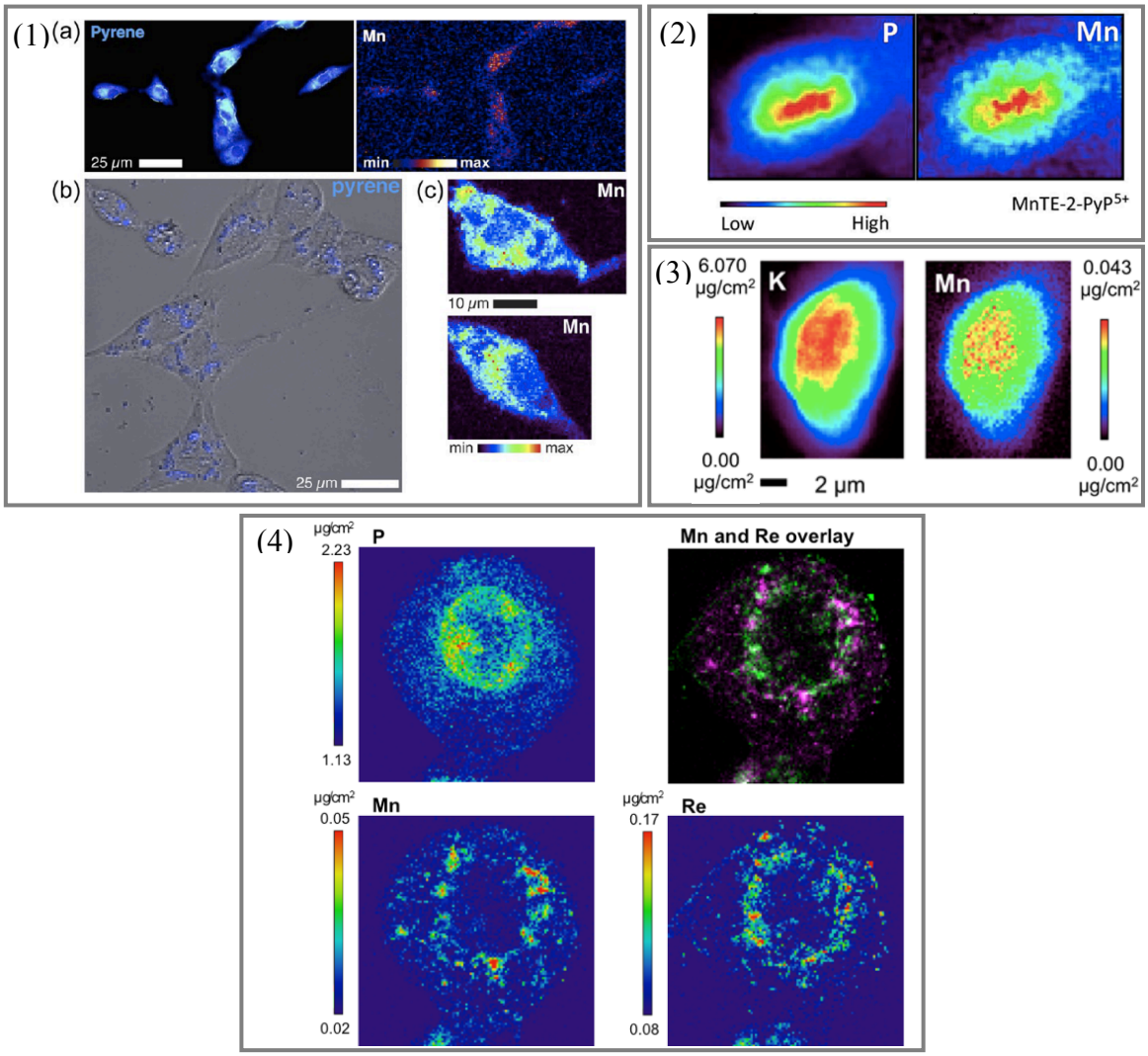

Figure 32: Investigation of SOD mimics intracellular distribution: imaging of SOD mimics inside cells by classical fluorescence and X-ray fluorescence microscopy. (1) Figure from C. Weekley et. al [228]. SH-SY5Y cells were treated for 24h with the pyrene-labelled MnPAM. (a) Distribution of pyrene tag and manganese in fixed SH-SY5Y cells obtained by respectively classical fluorescence and XRF. (b) Confocal fluorescence microscopy image of the pyrene tag (blue) in living cells (bright field). (c) High-resolution XRF maps of manganese in fixed cells. (2) Figure from JB. Aitken et. al [236]. XRF elemental maps of phosphorus (showing the nucleus) and of manganese (showing drug localization) of A549 cells treated with MnP MnTnHex-2-PyP5+. (3) Figure from E. Mathieu et. al [196]. XRF elemental maps of potassium (showing the nucleus) and of manganese (showing drug localization) of HT29-MD2 cells treated with Mn1. (4) Elemental distribution of P, Mn and Re in HT29-MD2 cells incubated with the conjugate Mn1+Re probe at 100μM for 2 hours. Top right image represents the overlay of Mn (magenta) and Re (green) map. The overlap of both elements are displayed in white.

Moreover, XRF Mn map of cells incubated with Mn1 has shown an homogenous distribution of Mn suggesting that this complex does not accumulate in specific organelles (Figure 32 (3)) [196]. More recently, efforts have been devoted to colocalize the ligand and the metal to potentially afford insights in locations where the complexes are intact. Briefly, Policar *et al.*

have conjugated the Mn1 complex with a rhenium-based multimodal probe [223]. The resulting complex was investigated in HT29-MD2 cells and the subcellular distribution of Mn (the redox active site) and Re (linked to the ligand) were determined using XRF microspectroscopy (Figure 32 (4)) [223]. In this situation, a single XRF experiment was required to colocalize the metal (Mn) and the ligand (Re). They have shown that Mn and Re maps partially overlap suggesting that some intact complex remained in cells (Figure 32 (4)). The non-homogenous and punctuated distribution of Mn and Re indicated a different cellular localization than the parent Mn1 complex (that showed a homogenous distribution [237]) highlighting the fact that conjugation of the Re probe had a non-negligible impact on the SOD mimic cellular distribution.

To conclude, classical fluorescence, XRF and XAS are useful techniques to determine SOD mimics intracellular uptake and localization and to relate it to their chemical form and physical properties. The intracellular distribution data can also be confirmed via the quantification of SOD mimics contained in cell fractions specifically enriched with particular organelles such as mitochondria [223].

II.2. Publication: “Inertness of superoxide dismutase mimics Mn(II) complexes based on an open-chain ligand, bioactivity, and detection in intestinal epithelial cells”

Inertness of superoxide dismutase mimics Mn(II) complexes based on an open-chain ligand, bioactivity, and detection in intestinal epithelial cells

Gabrielle Schanne[a],[b], Martha Zoumpoulaki[a], Géraldine Gazzah[a], Amandine Vincent[a], Hugues Preud'homme[c], Ryszard Lobinski[c], Sylvie Demignot[b],[d], Philippe Seksik[b],[e], Nicolas Delsuc[a], Clotilde Policar[a]

[a] Laboratoire des biomolécules, LBM, Département de chimie, Ecole Normale Supérieure, PSL University, Sorbonne Université, CNRS, 75005 Paris, France
[b] Centre de Recherche Saint Antoine, INSERM, UMRS 938, Metabolism-Inflammation Department, 184 rue du Faubourg Saint-Antoine, 75012 Paris, France
[c] IPREM-UMR5254, E2S UPPA, CNRS, Technopôle Helioparc, 2 avenue P. Angot 64053 Pau Cedex 9 (France)
[d] EPHE, PSL University, 75014 Paris, France
[e] Gastroenterology Department, Saint-Antoine Hospital, Sorbonne Université, APHP Paris, France.

I conducted the work presented below and I have contributed to the writing of the following paper (proposal of a draft that was corrected and edited by my supervisors) [172].

The objective of this project was to increase the inertness of Mn1 that is subjected to metal exchanges with the competing free metal ions present in the cellular environment. Mn1 also undergoes fast transmetallation within non-metal-free analytical systems preventing the accurate detection, quantification and speciation study of Mn1 in cells using classical mass spectrometry (MS) techniques coupled to liquid chromatography [198].

We designed here a new generation of SOD mimics derived from Mn1 and modeled by the CDTA ligand described by FK. Kalman *et. al* which is known to enhance the inertness of the Mn(II) chelate [217]. The Mn(II) complexes based on rigidified open-chain EnPI2-derived ligands were as expected more resistant to metal exchanges and displayed higher bioactivity *in cells*. Moreover, we succeed in detecting and quantifying the intracellular presence of the most inert SOD mimic in its intact form using classical MS experiments.

Abstract

Oxidative stress is known to play a major role in the pathogenesis of inflammatory bowel diseases (IBDs) and, in particular, superoxide dismutase (SODs) defenses were shown to be weakened in patients suffering from IBDs. SOD mimics, also called SOD mimetics, as low molecular weight complexes reproducing the activity of SOD, constitute promising antioxidant catalytic metallodrugs in the context of IBDs. A Mn(II) complex SOD mimic (Mn1) based on an open-chain diamino-ethane ligand exerting antioxidant and anti-inflammatory effects on an

intestinal epithelial cellular model was shown to be experience metal exchanges between the manganese center and metal ions present in the biological environment (such as Zn(II)) to some degrees. As the resulting complexes (mainly Zn(II)) were shown to be inactive, improving the kinetic inertness of Mn(II) complexes based on open-chain ligands is key to improve their bioactivity in a cellular context.

We report here the study of three new Mn(II) complexes resulting from Mn1 functionalization with a cyclohexyl and/or a propyl group meant to limit respectively (a) metal exchanges and (b) deprotonation of an amine from the 1,2-diaminoethane central scaffold. The new manganese-based SOD mimics display a higher intrinsic SOD activity, and also improved kinetic inertness in metal ion exchange processes (with Zn(II), Cu(II), Ni(II) and Co(II)). They were shown to provide anti-inflammatory and antioxidant effects in cells at lower doses than Mn1 (down to 10 µM). This improvement was due to their higher inertness against metal-assisted dissociation and not to different cellular overall accumulation. Based on its higher inertness, the SOD mimic containing both the propyl and the cyclohexyl moiety was suitable for intracellular detection and quantification by mass spectrometry, quantification, that was achieved by using a ^{13}C-labelled Co-based analog of the SOD mimics as an external heavy standard.

Introduction

Superoxide dismutases (SODs) are metalloenzymes that catalyze very efficiently the superoxide dismutation at a rate close to the diffusion limit [4]. Superoxide is one of the reactive oxygen species (ROS) and is mainly produced at the mitochondria as byproduct of the respiratory metabolism in living aerobic systems. SODs are responsible for maintaining superoxide at tightly controlled levels and contribute to prevent oxidative stress situations known to be implicated in various diseases [5]. In their active site, all of the SODs contain a metal cation (Cu(Zn), , Cu, Fe, Mn or Ni) that cycles between two redox states to successively reduce superoxide to H_2O_2 and to oxidize it into O_2. Three different kinds of human SODs have been described: two copper/zinc SODs, SOD1 found in the cytosol and in the mitochondrial intermembrane space [6] and SOD3 found in the extracellular environment [7] (within the extracellular matrix and at cell surface), and the manganese SOD (SOD2) localized in the mitochondria matrix [8]. Inflammatory bowel diseases (IBDs) including Crohn's disease and ulcerative colitis are accompanied by an over-expression of the intestinal MnSOD in an

enzymatically inactive form and by an under-expression of the intestinal cytoplasmic Cu/Zn SOD [9]. These deficiencies in the SOD antioxidant system may cause or, at least, exacerbate the oxidative stress observed in IBDs which is known to be closely related to chronic inflammation [10–12]. A SOD-based antioxidant treatment thus appears as a promising therapy for IBDs. MnSODs were shown to efficiently reduce lipid peroxidation and neutrophil recruitments and to attenuate the inflammation in both DSS-induced and TNBS-induced colitis murine models [13]. However, the use of purified enzymes as therapeutics is still limited by their short half-life, the triggered immunogenicity and their low cell-penetration [14]. To overcome these shortcomings, the use of synthetic low-molecular weight SOD mimics, also called SOD mimetics, was examined as therapeutic candidates for IBDs management [14,15].

A large variety of SOD mimics have been reported including iron, copper, zinc and manganese complexes [14–23]. Manganese complexes are favored in comparison with Cu, Fe and Ni complexes since manganese, if released, is better tolerated by cells and does not catalyze the Fenton or Haber-Weiss reactions that lead to the formation of the extremely reactive and toxic $HO^{\bullet}$ radical[24]. Manganese SOD mimics described in the literature include complexes with ligands such as porphyrins [17,25–31], salens [32,33], cyclic polyamine [14,34–40] phthalocyanines [41] or peptidyl ligands [42–44]. We have been developing a 1,2-ethanediamine-centered ligand, called EnPI2 [45], inspired by the MnSOD active site, with a coordination sphere consisting of three imidazole and one phenolate, easily amenable to synthetic modulation [46–49]. Mn(II)-EnPI2, labelled Mn1, is a positively charged complex with a redox potential close to the optimal value for superoxide dismutation [45,47]. Mn1 shows a clear anti-superoxide activity out of any cellular context, as well as antioxidant and anti-inflammatory effects on intestinal epithelial cells and macrophages [47,50,51]. Mn1 also ameliorates DNBS-induced colitis in a murine model according to the weight variation and macroscopic scores [47].

The structure of EnPI2 can be optimized to improve the stability and, especially, the inertness of the derived Mn(II) complex since Mn decoordination in cells was suggested in a previous study [49]. Indeed, given the symmetrical d^5 electronic configuration of the Mn^{2+} ion, the corresponding complexes lack ligand field stabilization energy and are much less stable than other divalent transition metal analogues (Ni^{2+}, Cu^{2+}, Co^{2+}, Zn^{2+}…). Consequently, many manganese complexes, particularly with open-chain ligands such as EnPI2, may suffer from

dissociation [3]. In a recent paper, we have investigated speciation of a complex derived from Mn1 based on a ligand tagged with a Re-probe: the Mn and Re X-fluorescence maps, recorded above the edges of both Re and Mn, were overlapping, but only partly: a few areas showed only Re, revealing indirectly some dissociation have occurred in cells [44]. The dissociation may occur via different pathways, such as spontaneous decoordination, acid-catalyzed or metal-assisted decomplexation involving Mn^{2+} exchange with a competitive metal ion. However, in biological systems, the endogenous ligands competing for Mn(II) binding also have low association constants, rendering the criteria on the association constant paradoxically less drastic for Mn(II) than for other metal cations [18,47].

To date, the cellular accumulation of SOD mimics was usually examined by measuring the increase in the overall intracellular content in manganese using ICP-MS [49,52–54], EPR [47–49], Raman [55], X-ray absorption spectroscopy [39] and X-ray fluorescence imaging [16,39,47–49], or by detecting the cellular uptake using UV quantification of Mn-porphyrin via the Soret band area [19,56] or of fluorescently labelled SOD mimics using laser confocal microscopy [39,43,49,57]. At best, these techniques enable determining the intracellular distribution of the ligand, complexes and/or of Mn. In the latter case, the differential distribution of Mn from that of endogenous Mn provides insight on the Mn-complex distribution [16,39,47–49]. However, for the bio-inspired series developed in our group, even if the MS-MS spectrum of Mn1 was observed in cell lysates [45], no direct information on the speciation and metal exchanges or quantification in cell lysates of the complexes has been reported [18,44,46–50].

As mentioned above, a higher inertness of the manganese complexes would be an important asset for improving the bioactivity of the SOD mimics and make them more suitable for *in vivo* application. Open-chain ligands derived from EDTA containing a cyclohexyl group bearing the diamino moiety in order to rigidify the structure of the ligand, with appended carboxylate (CDTA) or pyridine (PyC3A) (see Figure S1), have been developed by Tóth, Tircso and Caravan (Figure S1) [3,58]. The $[Mn(II)\text{-}(CDTA)]^{2+}$ complex revealed a highly improved resistance to dissociation *via* metal exchanges [3]. This behavior was explained by the formation of a pre-organized and more rigid coordination cavity that encapsulates the manganese ion. Other open-chain ligands for Mn coordination were described but they did not reach as good kinetic inertness as Mn-CDTA [59]. Mn-CDTA complex is hence considered as the gold standard for

rigid and inert Mn^{2+} complex involving an open chain ligand. Only very recently, E. Tóth succeeded in synthetizing a new Mn^{2+} bispidine chelate with unprecedented kinetic inertness [60]. Inspired by these strategies, we have replaced the 1,2-diamino group of EnPI2 by a (±)-trans-1,2-cyclohexyl diamine to rigidify the structure and hopefully increase the resulting SOD mimic inertness. Stability, inertness and more generally bioactivity of the corresponding complexes have been investigated. N-propylated analogs of Mn1 and of its cyclohexyl analogue were also investigated and evaluated in a cellular model consisting of intestinal epithelial cells (HT29-MD2) activated with bacterial lipopolysaccharide (LPS) [61]. We have compared the ability of these Mn1-derived SOD mimics to limit oxidative stress and inflammation when incubated at different doses ranging from 0.1 µm to 100 µM. We propose to use high-definition mass spectrometry to detect unambiguously one of these complexes in cells lysates and to quantify their amount by using a ^{13}C-labelled analog as a reference standard.

Material and methods

- Synthesis of the ligands

See supplementary information

- Titration of the ligands by UV experiments

The concentration of the ligands in solution was determined by a UV-vis titration experiment. Small quantities of $MnCl_2$ were successively added to a solution of ligand estimated at ca. 200 µM (in HEPES 50mM, pH 7.5) and the absorbance of the Mn(II) complexes was monitored at 288 nm (MLCT $O_{phenolate} \rightarrow Mn$) [47]. The concentration of ligand was calculated from the amount of added $MnCl_2$ at the equivalence.

- Preparation of the complexes for experiments other than cellular assays

The manganese complexes Mn1, Mn1P, Mn1C and Mn1CP (Figure 1) were prepared by the addition of 1 equivalent of $MnCl_2$ to a solution of the ligand (pre-titrated as explained above) in HEPES buffer (50 mM, pH 7.5).

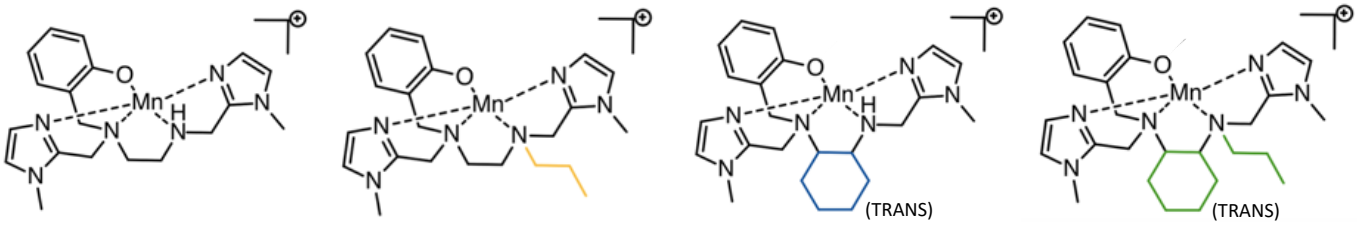

Figure 1: Structures of the manganese (II) complexes mentioned in the text.

- Association constants

The association constants of the manganese complexes were determined by UV-vis titration experiments. The absorbance at 288 nm was monitored while adding successively 0.1 equivalent of manganese to a solution of ligand at 45 µM in HEPES (50 mM pH 7.5). The initial concentration in ligand was chosen lower than $100*K_d$ known for Mn1 (ca. 7.57 10^{-7} M [47]) in order to observe an equilibrium between uncoordinated ligand L, Mn^{2+} and the complex in solution at the 1:1 Mn:L ratio and obtain not only the stoichiometry but also the association constant (C_{ligand} should be smaller than $100*K_d$; see caption of figure S2) [62]. The association constant was then obtained by fitting the theoretical absorbance curve to the experimental one using the MATLAB curve fitting tool (Figure S2). The calculations are detailed in the supplementary information. The association constants of the Zn(II) and Co(II) complexes are too high to be determined using the same protocol, as they would require a too weak concentration to meet the criterium of an equilibrium at the 1:1 ratio, too weak to follow the complexation using UV-vis. Therefore, we performed competition experiments between the Mn(II) and Zn(II) or Co(II) complexes. For Zn(II) complexes, solutions of manganese complexes prepared at 10 µM with 200 equivalents of $MnCl_2$ in HEPES (50 mM pH 7.5) were titrated with $ZnCl_2$ solution (Figure S19). For Co1CP, a solution of Mn1CP prepared at 40 µM with 50 equivalents of Mn (in HEPES 50 mM pH 7.5) were titrated with $CoCl_2$ solution (Figure S28). The association constants of the zinc or cobalt complexes were then similarly obtained by fitting the theoretical absorbance curve to the experimental one using the MATLAB curve fitting tool (Figure S19 and Figure S28). The calculations are detailed in supplementary information.

- Kinetic study of the metal exchanges by UV-spectroscopy

A solution of each of the SOD mimics was prepared at 0.1 mM in TRIS buffer (50 mM, pH 7.5) in a semi-microcuvette (1.5 mL). One equivalent of competitive metal salts ($ZnCl_2$, $CuSO_4$, $NiCl_2.6H_2O$, or $CoCl_2$) was then added in the microcuvette and, after a quick manual stirring,

the absorbance at a specific wavelength was measured for about 10 min. The wavelengths were chosen to have a high difference in absorbance between the manganese complex and the exchanged ion complex (Figure S3, S4, S5 and S6). For Cu^{2+}, Zn^{2+} and Co^{2+}, the experiments were performed at 5°C as the metal exchanges were too fast at 25°C preventing any kinetic study. For Ni^{2+} exchanges study, the temperature was maintained at 25°C.

- Kinetic study of the metal exchanges using a stopped-flow technique

Solutions of SOD mimics and competitive metal ions were prepared respectively at 300 µM and at 4 mM in TRIS buffer (50 mM buffer pH 7.5). The solutions of SOD mimic and competitive metal ion were added in two different syringes (V = 10 mL) of the stopped-flow apparatus and a similar mixing sequence were used for each analysis. A total volume of 226 µL were injected with a flow rate of 13 mL/s: 88 µL of the SOD mimic solution and 138 µL of the competitive metal solution. After mixing in a high-density mixer, the SOD mimic is thus at 120 µM and the competitive metal ions at 2400 µM (20-fold excess). The metal exchanges were monitored at ambient temperature by UV-vis spectroscopy between 200 nm and 400 nm. The pseudo-first order rate were then obtained by fitting the theoretical time-absorbance curve to the experimental one using the Biokine32 software.

- Electrochemistry

Cyclic voltammetry experiments were performed with manganese(II) complexes solutions at 100 µM in HEPES buffer (50 mM, pH 7.5, ionic strength = 12.5 mM). Experiments were carried out under an argon stream at room temperature. The auxiliary electrode was a Pt wire and the working electrode was a glassy carbon or a platinum disk. The reference electrode was a SCE saturated with KCl.

- Intrinsic SOD activity

The catalytic rate (k_{cat}) for superoxide dismutation with the SOD mimics were determined in HEPES buffer (50 mM pH 7.4) using an indirect assay developed by McCord and Fridovich [18,45,63–65]. This assay is based on a competition between the SOD mimic and a redox marker, in our case XTT (2,3-bis-(2-methoxy-4-nitro-5-sulfophenyl)-2H-tetrazolium-5-carboxanilide), to react with superoxide that is continuously produced via an enzymatic xanthine (200 µM) /xanthine oxidase system. In this assay, we used [XTT] = 100 µM. The formation of formazan resulting from XTT oxidation by superoxide was monitored by UV

spectroscopy. The k_{cat} of the SOD mimics were obtained from the IC_{50}, concentration of SOD mimics required to reduce by 50% the formation of formazan and from the known value of k_{cat} of XTT [18,66].

- Cell culture

HT29−MD2 intestinal epithelial cells were used for all experiments. HT29 human colon adenocarcinoma were obtained from the European Collection of Cell Cultures (Wiltshire, UK) and stably transfected to overexpress the protein MD2, a coreceptor of TLR4 necessary to confer sensitivity to LPS [61]. Cells were cultured in DMEM supplemented with 10% heat-inactivated FBS and blasticidin (10 µg/mL) at 37 °C in a 5% CO_2/air atmosphere.

- Cell Activation with LPS and Incubation with the SOD mimics

Cells were seeded in 12-wells plate (for cells assays) or in T75 flasks (for manganese and complexes quantification) at 50 000 cells/cm^2 and cultured until 90% confluence. Cells were co-incubated for 6 hours with LPS at 0.1 µg/mL and with the complexes at concentrations varying between 0.1 µM and 100 µM with a ratio ligand:Mn 1:1.4. An incubation time of 6h was chosen based on previously published results on Mn1 intracellular quantification by EPR and for the detection of the inflammatory markers, IL8 and COX2 [47]. The titration of manganese content over time showed that Mn1 accumulation was stabilized after 3-4 hours. We can thus consider that the maximal accumulation is reached after 6 hours, time at which the inflammation markers were easily quantified after LPS challenge. Supernatants were collected and stored at −20 °C until enzyme-linked immunosorbent assay (ELISA) and lactate dehydrogenase (LDH) assay were performed. For cell assays, the cells were washed with phosphate-buffered saline (PBS), lysed in PBS containing a 1% Triton X-100 and protease inhibitors cocktail, and sonicated. For total Mn and Mn-complexes quantification, the cells were washed with PBS, harvested in NH_4HCO_3 buffer (50 mM, pH 7.4) by scraping and sonicated.

- Cell assays

Cell assays were conducted as previously described by Mathieu *et al*. and Vincent *et al*. [44,47–49,51]. Briefly, the cytotoxicity of the SOD mimics was assessed using the lactate dehydrogenase assay (LDH). The protein concentrations were determined in cell lysates using bicinchoninic acid (BCA) protein assay reagents and bovine serum albumin (BSA) as the

standard. The amount of interleukin-8 (IL-8) secreted in the cell supernatant were measured using a commercially available ELISA kit according to the instructions of the manufacturer (DuoSet). The IL8 levels were normalized by the protein content determined in the corresponding cell lysates. The expression of MnSOD in cell lysates was examined by Western blot. The abundance of MnSOD was normalized to the total amount of protein loaded using the stain free imaging technology (BioRad).

- Quantification of the Mn contents by ICP MS

The total Mn content was quantified in cell lysates by ICP MS. Cell lysates were acidified using 2% HNO_3, to free Mn from all coordination sites, and filtered. A calibration curve was established using a commercial Mn standard. The total Mn amount was normalized by the mass of proteins in the cell lysate.

- Detection and quantification of Mn1CP in cell lysates by mass spectrometry

The cells lysates were ultra-centrifuged at 100,000 rpm for 20 min and then diluted in 20% NH_4CO_3/ 80% ACN. For the quantification, an external standard was added at 0.4 µM in the diluted cell lysates before analysis. The standard consisted of the cobalt(II) complex with EnPI2CP labelled with ^{13}C on the phenol moiety obtained using $CoCl_2$. The samples were then analyzed by TOF MS in direct infusion mode. Sample injection was performed with a 250 µL syringe at 5 µL/min flow rate. Acquisition was performed after 1 min, once the spray was stabilized, over 3-5 min. Between each measurement, the system was washed, successively with isopropanol, water and isopropanol, to avoid contamination of the next sample and capillary blockage. To avoid metal contaminations, ultrapure solvents (acetonitrile, isopropanol, water) and metal-free labware were used. A calibration curve was established by spiking control LPS-stimulated HT29-MD2 lysates with the Co1CP(^{13}C) standard at 0.4 µM and with Mn1CP at concentrations in the range 0.05 µM to 0.8 µM. The ratio between the signal intensity of Mn1CP and that of the standard were plotted as a function of Mn1CP concentration (Figure S29). For the calibration and quantification, the signal intensity of both Mn1CP and the standard were obtained by summing the peak intensities of the noticeable isotopes. This quantification based on the use of a heavy analog of Mn1CP as a standard was validated by the method of standard additions. For the latter, lysates of HT29-MD2 cells, beforehand incubated with Mn1CP at 100 µM for 6 hours, were similarly ultra-centrifuged at 100,000 rpm for 20 minutes, diluted in 20% NH_4CO_3/ 80% ACN and spiked with the standard

Co1CP(^{13}C) at 0.4 µM. Before MS injection, Mn1CP was spiked at known concentration (0 µM, 0.2 µM and 0.4 µM) in the lysate. The ratio of the signal intensity of Mn1CP on that of the standard were plotted as a function of spiked Mn1CP concentration (Figure S31) and the equation of the linear regression gave us the estimated concentration in Mn1CP.

Results and Discussion

- Design and synthesis

Three new ligands derived from the parent EnPI2 were designed (Figure 1). For EnPI2C and EnPI2CP, a cyclohexyl group was added between the two amino groups in order to introduce rigidity into the ligands skeleton and consequently reduce the kinetic lability. As previously shown, the Mn complex $[Mn(CDTA)]^{2+}$ or $[Mn(PyC3A)]^{2+}$ studied respectively by Tircso, Tóth and Gale *et al.* contain a similar diamino cyclohexane motif (Figure S1) and displayed remarkably slow dissociation rate, possibly due to a weaker ability to reach open conformation [3,58,59]. EnPI2-derived ligands were synthetized using a protocol similar to that used for EnPI2, previously reported by Cisnetti *et al.* [45] but with racemic (±)-(trans)-1,2-diaminocyclohexane instead of 1,2-diaminoethane as a reagent. Additionally, the secondary amine in EnPI2 and EnPI2C were propylated to obtain respectively EnPI2P and EnPI2CP. This allows to avoid the formation of a deprotonated form when studied in MS. The propylation was performed *via* a reductive amination using propanaldehyde.

For physico-chemical characterization (not for cellular assays), the Mn^{II} complexes were prepared *in situ* by mixing the pre-titrated ligand (see above) and $MnCl_2$ in a 1:1 ratio in HEPES Buffer (50 mM, pH 7.5), as previously described [47–49]. They were labeled Mn1, Mn1P, Mn1C and Mn1CP depending on the associated ligand (respectively EnPI2, EnPI2P, EnPI2C and EnPI2CP) (Figure 1). Note that for the biological experiments, the SOD mimics were prepared with a ratio 1:1.4 ligand: Mn (see below).

- Physico-chemical properties

Different criteria are required for an efficient SOD mimics [14,47]. They include a high catalytic activity of superoxide dismutation (or intrinsic activity), a good stability in biological environment and the ability to penetrate inside cells to reach the site of action. The potential of the four SOD mimics to fulfill these criteria were evaluated and compared.

L	K_1 (Mn-L) (M^{-1})	k_{cat} (Mn-L) ($10^6\ M^{-1}s^{-1}$)	$E_{cathodic}$ (V/SCE)	E_{anodic} (V/SCE)	E_{anodic}–$E_{cathodic}$ (mV)	$E_{1/2}$ (V/SCE)
EnPI2	$1.22 \pm 0.18 \times 10^6$	3.40 ± 0.10	0.16	0.24	80	0.20
EnPI2P	$1.04 \pm 0.18 \times 10^6$	4.58 ± 0.01	0.17	0.29	120	0.23
EnPI2C	$0.71 \pm 0.11 \times 10^6$	4.38 ± 0.13	0.12	0.21	90	0.17
EnPI2CP	$0.28 \pm 0.03 \times 10^6$	5.41 ± 0.24	0.20	0.28	80	0.24

Table 1: Association constants of the four ligands with manganese(II) (MnCl2), the catalytic rate constant for superoxide dismutation observed with the four Mn-complexes and their redox potentials. The association constants were determined by UV-vis titration experiments in HEPES (50 mM, pH 7.5, 25°C, Cligand = 45 µM, see Figure S2) and are indicated with the 95 % confidence intervals based on asymptomatic standard errors. These values were calculated using the MATLAB curve fitting tool based on a non-linear least-square regression method. The calculation of K1 and the UV-titrations plots are detailed in supplementary information and in Figure S2. The catalytic rate constant for superoxide dismutation of the manganese complexes were measured in HEPES (50 mM at pH 7.4) using the McCord and Fridovich assay (Figure S11). The anodic, cathodic, ΔE and midpoint potentials (E1/2=(Ec+Ea)/2) of the four manganese complexes were extracted from their cyclic voltammogram given in Figure S9.

- SOD mimics stability

- Association constants

The association constant of the four manganese complexes in HEPES (50 mM, pH 7.5) were determined by UV-vis titration experiments, as shown in Figure S2, and results are given in Table 1. The association constant of Mn1 was found to be $(1.215 \pm 0.176) \times 10^6$ (M^{-1}) which is consistent with the previously reported value determined by Isothermal Titration Calorimetry [47] and UV-visible [67]. The inclusion of a cyclohexyl group on the diamino-central scaffold of both EnPI2 and EnPI2P structures was associated to a weak decrease of the ligands' association constant with Mn^{2+}. The decrease can be explained by the stiffed structure of the ligands: the rigidity can induce enthalpically unfavorable constraints leading to a reduction in the association constant, and also a slower complexation. The substitution on the secondary amine by a propyl group resulted also in a slight decrease of the association constant with Mn^{2+}. A similar effect of N-alkylations on association constants was described by Martínez-Camarena *et al.* [68]: the presence of isopropyl substituents on the secondary amines of a tetra-azacyclophanes ligand was shown to produce a decrease in the stability of the corresponding copper complex. Riley *et al.* reported elsewhere that methyl substituents on cyclic polyamine ligands were not affecting clearly the association constant with Mn^{2+} [69], and previous functionalization with peptides showed the same weak effect of tertiarization of the secondary amine in EnPI2 [46]. The lower thermodynamic stability of manganese complexes compared to other divalent transition metal ions can be explained by the lack of

ligand-field stabilization due to the symmetric d^5 electron configuration system of the Mn^{2+} ion (Irving-Williams series) [47]. Biological media abound of coordinating biomolecules. However, considering the association constant for Mn^{2+} we have measured, no ligand exchange with the competitive biomolecules should take place in the cellular environment for any of the studied SOD mimics. Indeed, as mentioned above, the competitive endogenous ligands display low association constant with Mn^{2+}, such as the archetypal bioligand: human serum albumin (K_1 = 8.4 × 10^3 M^{-1}) [70]. This renders the criteria on the association paradoxically less drastic for Mn(II) than for other metal cations [18,47]. The exchangeable pool of metal ions [71] contained in biological media could compete with the manganese(II) ion resulting in metal ion exchange and possibly loss of activity. However, it should be kept in mind that, although metal ions are overall abundant in cells (ca. 70 µM for Cu, 0.001 to 10 µM for Fe, 180 µM for Zn for example) [72], metal ions are tightly controlled, either through coordination with proteic scaffolds (Zn, Cu) [71] or through precipitation (Fe in ferritine). Thus the intracellular exchangeable pools of metal ions are much less concentrated (ca. 10^{-10} M for Cu (Cu(I)), 10^{-11} M for Zn) [71,73]. Mn(II) has been classified as one of the most available metal cation (10^{-5} M for the bio-available Mn(II) [71], as opposite to Zn and Cu, classified as the most competitive [71].

All these features make the requirement for the stability of complexes less drastic for Mn complexes than for any other metal ion [18,47,71]. However, as metal ions exchange their ligand are fast, we decided to explore the kinetic inertness of the SOD mimics that could be a crucial parameter for a better bioactivity.

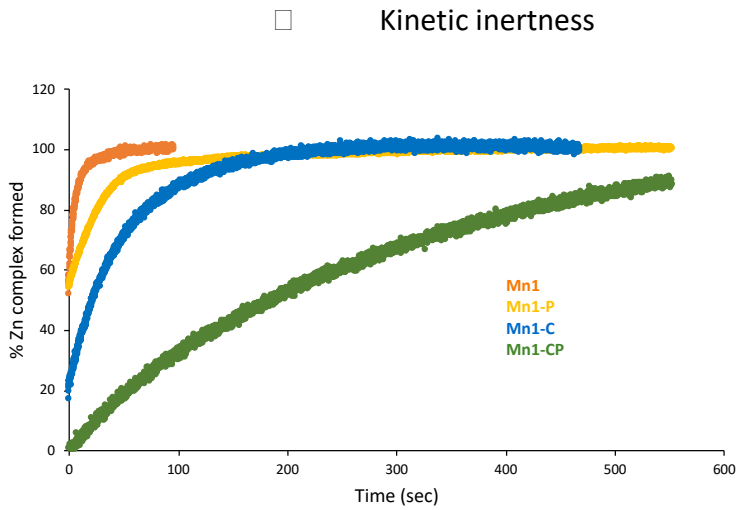

		Zn^{2+}	Cu^{2+}	Ni^{2+}	Co^{2+}
$t_{1/2}$ (s)	Mn1	n.d	4	45	11
	Mn1-P	n.d	17	16	16
	Mn1-C	22	28	120	50
	Mn1-CP	188	139	133	60

*Figure 2: **Kinetics study of the metal exchanges occurring between the manganese center of the SOD mimics and with Zn^{2+}**. The percentage of complexes that underwent metal exchanges was monitored spectrophotometrically by following the absorbance at a wavelength, chosen to have a high difference in absorbance between the manganese complex and the Zn(II) complex. The spectra of the Mn(II) complexes and Zn(II) complexes are given in Figure S3 and were used to choose these monitoring wavelengths. The graph presenting the kinetic of metal exchanges occurring between the Mn(II) center of the SOD mimics and Cu^{2+}, Ni^{2+} and Co^{2+} are given in Figure S7.*

*Table 2: **Half-lives of the metal-assisted dissociation reaction of manganese complexes**. The exchanges were monitored by UV-visible spectrophotometry after addition of one equivalent of salts of the exchanging metal ions ($ZnCl_2$, $CuSO_4$, $NiCl_2.6H_2O$, or $CoCl_2$) in a solution of the manganese complexes at 100 µM (TRIS 50 mM, pH 7.5). For Zn^{2+}, Cu^{2+} and Co^{2+}, the experiments were performed at 5°C as the metal exchanges were too fast at room temperature (25°C) preventing any kinetic study. For Ni^{2+} exchanges study, the temperature was maintained at 25°C. n.d means not determined; as in some cases the exchanges were too fast, even at low temperature, and could not be monitored by UV-vis spectroscopy.*

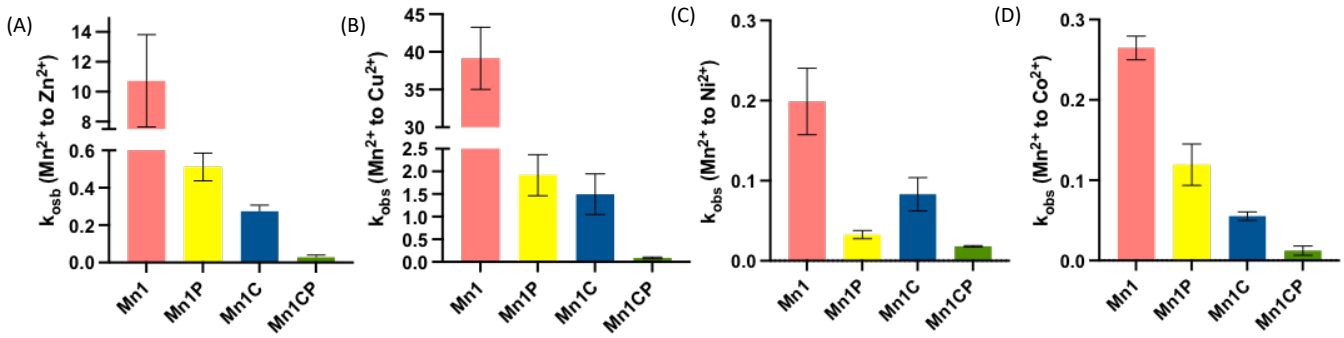

Figure 3: Pseudo-first order rate constants k_{obs} (s^{-1}) characterizing the metal exchanges occurring between the manganese center of the SOD mimics with (A) Zn^{2+}, (B) Cu^{2+}, (C) Ni^{2+} and (D) Co^{2+}. Kinetics of the exchanges were monitored in TRIS (50 mM pH 7.5) using a stopped-flow technique in the presence of 20-fold excess of competitive metal in order to ensure pseudo-first order conditions. The exchanges were observed spectrophotometrically at room temperature and at specific wavelengths chosen to have a high difference in absorbance between the manganese complex and the competitive metal complex. The pseudo-first order rate were then obtained by fitting the theoretical time-absorbance curve to the experimental one using the Biokine32 software. The numerical values of the k_{obs} are given in Table S1. Data represent mean ± SEM for three independent experiments and each independent experiments were performed in duplicates.

The kinetics of the metal exchanges between manganese(II) and four biologically important divalent transition metal ions: Cu^{2+}, Zn^{2+}, Ni^{2+} and Co^{2+}, added at one equivalent in a solution of each SOD mimic were monitored spectrophotometrically (Figure 2 and Figure S7). As predicted by the Irving-Williams series, metal exchanges take place in all cases until formation

of 100% of the more stable competitive metal complex [74,75]. To characterize the kinetic inertness of the Mn complexes, the half-lives ($t_{1/2}$) of the transmetallation 1:1 reaction were determined for each experiment (). As shown in and Figure 2, the exchanges are clearly slowed down for Mn1C and Mn1CP compared to Mn1 and Mn1P. The comparison of the $t_{1/2}$ reveals that the inertness of Mn1CP differs by orders of magnitude in some cases depending on the nature of the competing metal ion. This qualitative approach confirms that EnPI2C and EnPI2CP constitute rigid open-chain ligands that efficiently reduce the kinetic lability of the manganese complexes [3]. In the case of Zn^{2+} or Cu^{2+} ions, the propylated complexes display higher $t_{1/2}$ and so increased kinetic inertness compared to the corresponding non propylated complexes. A similar trend was observed by Riley *et al.* who observed that the number of hydrocarbon substituents on cyclic polyamine ligands generally increases the kinetic inertness of the corresponding manganese complexes to dissociation [69]. However, this effect of the propylation is not seen for Ni^{2+} and Co^{2+} metal exchanges.

To ensure pseudo first order conditions and thus retrieve pseudo-first order rate constants, the competitive metal ions have to be in large excess compared to the SOD mimic. However, in such conditions, the exchanges are too fast to be monitored by classical UV-vis techniques with manual mixing, particularly for Zn^{2+} and Cu^{2+}. Stopped-flow analysis were then conducted to study the kinetics of metal exchanges when competitive metal ions were in 20-fold excess. The obtained pseudo-first order rate constants (k_{obs}) are given in Figure 3 (and Table S1). The new SOD mimics display lower k_{obs} compared to Mn1, confirming that they are more inert. In case of Zn^{2+}, Cu^{2+} and Co^{2+} exchanges, we observe the same ranking of increasing inertness between the SOD mimics, with the following order: Mn1, Mn1P, Mn1C and lastly Mn1CP. These results are consistent with the previous UV-vis experiments. However, we observe a different trend for Ni^{2+} exchanges: Mn1P is surprisingly more inert than Mn1C while Mn1P undergo faster exchange than the others SOD mimics when in presence of only one equivalent of Ni^{2+} according to UV-vis experiments. The stopped-flow experiments confirm the improved resistance to metal exchanges of the new SOD mimics and in particular of Mn1CP that displays the lower k_{obs} for each competitive metal ions exchanges.

- Intrinsic SOD activity

- Electrochemistry

For an efficient intrinsic SOD-like activity, redox potential of the SOD mimics has to be tuned between that of superoxide oxidation ($E°'(O_{2aq}/O_2^{\cdot-})$ = −0.42 V/SCE pH 7, 25°C) and reduction ($E°'(O_2^{\cdot-}/H_2O_2)$ = 0.67 V/SCE pH 7, 25°C) for an efficient catalysis of superoxide dismutation [76]. The electrochemical properties of the four Mn complexes were analyzed by cyclic voltammetry at a glassy carbon electrode in HEPES (50 mM, pH 7.5, ionic strength = 12.5 mM). The Mn^{3+}/Mn^{2+} redox couples displayed reversible waves (see Figure S9) described in Table 1. The values obtained for Mn1 matched those previously reported (0.20 V/SCE) [47] and all of the complexes display a midpoint potential in the range 0.17-0.24 V/SCE, close to the optimal value for superoxide dismutation (0.12 V/SCE) [18]. It has been shown that the closer the Mn^{3+}/Mn^{2+} midpoint redox potential to 0.12 V/SCE, the higher the intrinsic SOD activity (Figure S11) [18,66,77]. The inclusion of a cyclohexyl or a propyl group does not strongly impact the redox properties. We observe that the propylation of the secondary amine resulted in an increase in the midpoint potential. The propylation may induce a change in the complex geometry that disfavors Mn(III) [18]. A similar effect was observed elsewhere upon functionalization of the amine in enPI2 with cell-penetrating peptide (positively-charged peptides) [46,48].

- McCord and Fridovich assay

The catalytic rate constants for superoxide dismutation k_{cat} of the studied SOD mimics were measured under conditions of slow flow of superoxide with the McCord-Fridovich assay in HEPES buffer (50 mM, pH 7.4). This assay is based on the competition between a SOD mimic and a visible probe specific for superoxide, XTT in this study, to react with superoxide [18,49,63,64,78]. This assay is relevant as a characterization of the kinetics under conditions of slow flow of superoxide, close to what is encountered in biological environment [18,79]. In a series of complexes derived from Mn1, the McCord-Fridovich assay was shown to provide kinetic constants consistent to that obtained in a large excess of superoxide with stopped-flow [46,48,49] or pulse radiolysis [65]. In the McCord-Fridovich assay, the IC_{50} is defined as the concentration of SOD mimics that reduces by 50% the reaction rate of the oxidation of XTT indicator (Figure S11). The k_{cat} of the four SOD mimics could be retrieved from their IC_{50} and k_{XTT} (2.9×10^4 $M^{-1}s^{-1}$) with $k_{cat} = k_{XTT}*[XTT]/IC_{50}$ [18,44,66] and are reported in Table 1. The measured catalytic rate constants fall in a range already observed for similar complexes ($\approx 10^7$ $M^{-1}s^{-1}$) [65,66]. We observed that the intrinsic SOD activity increased upon propylation of the

secondary amine of EnPI2 and EnPI2C. This is consistent with results recently published by the group of E. Garcia-Espana. The authors reported an increase in SOD activity upon N-alkylation of tetra-azacyclophanes copper complexes [68]. They ran quantum mechanics/molecular mechanics molecular dynamics simulations to rationalize this effect. Briefly, in absence of the alkyl groups on the secondary amines of the ligand (L), hydrogen bonds can formed between $O_2^{\bullet-}$ and the hydrogen atoms belonging to the secondary amines, which results in an over-stabilization of the catalyst-substrate adduct, $O_2^{\bullet-}$-Cu(II)-L. By increasing the energy barrier, this over-stabilization slows down one half reaction of superoxide dismutation: the reduction of the Cu(II) center to Cu(I) and the leaving of dioxygen. The addition of alkyl group on the secondary amines allows to prevent the formation of these hydrogen bonds and thus increases the catalysts turnover. The intrinsic SOD activity also increased upon inclusion of a cyclohexyl group in EnPI2 structure. Mn1CP containing both the cyclohexyl and the propyl groups displayed the best intrinsic SOD activity. Lastly, we noticed that the k_{cat} results in the EnPI2 series are not consistent with the ranking associated with the electrochemical properties of the complexes. This suggests that other factors such as the kinetic inertness of the mimics or second coordination sphere effects associated with propylation (see above) may prevail over their weak differences in redox potentials [80].

- Studies in LPS-activated HT29-MD2 cells

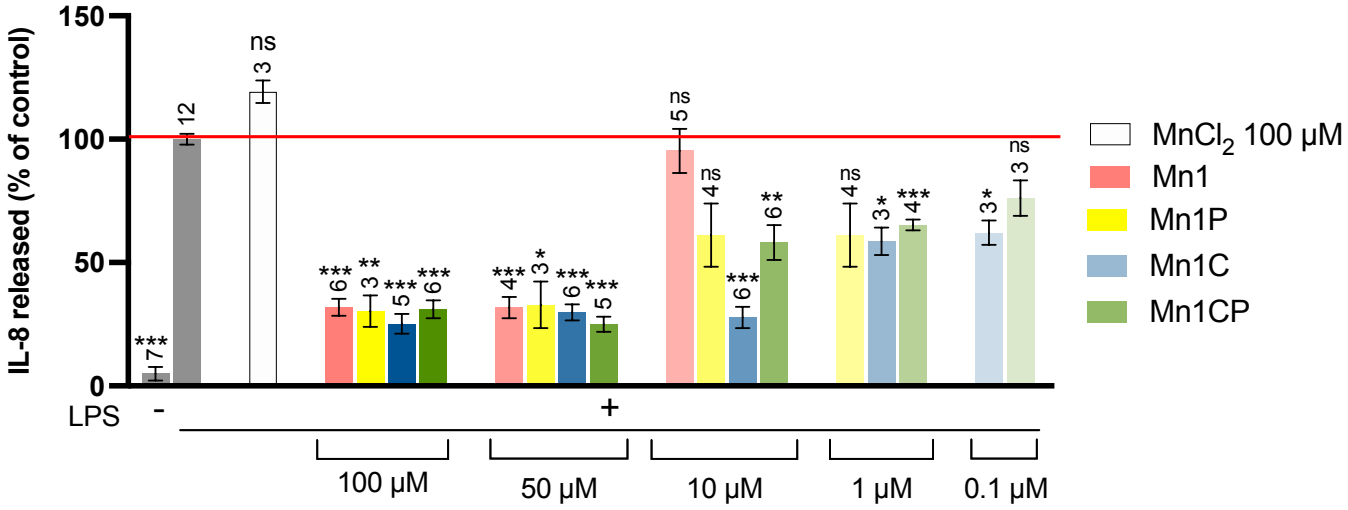

Figure 4: ***Quantification of the inflammatory marker IL-8 in intestinal epithelial cells activated with LPS (0.1 µg/mL).*** *IL-8 secretion was measured by ELISA in supernatant of LPS-activated HT29−MD2 cells incubated for 6 hours with the SOD mimics at different concentrations. The IL-8 amount measured for LPS-activated cells is set at 100 % for each independent experiment. Data represent mean ± SEM for at least three independent experiments: the number of independent experiments is indicated above each column. The p-values were calculated using the student test (bilateral test with equal variances not assumed). The mean ranks of each column were compared to that of the LPS control, each comparison stands alone. (***) p < 0.001, (**) p < 0.01 and (*) p < 0.05 versus LPS control, and ns means non-significant. Without LPS, no significant differences were observed between all of these conditions (see Figure S15). IL-8 secretion in controls LPS + zinc complexes (Zn1, Zn1C, Zn1P and Zn1CP) are shown in Figure S16.*

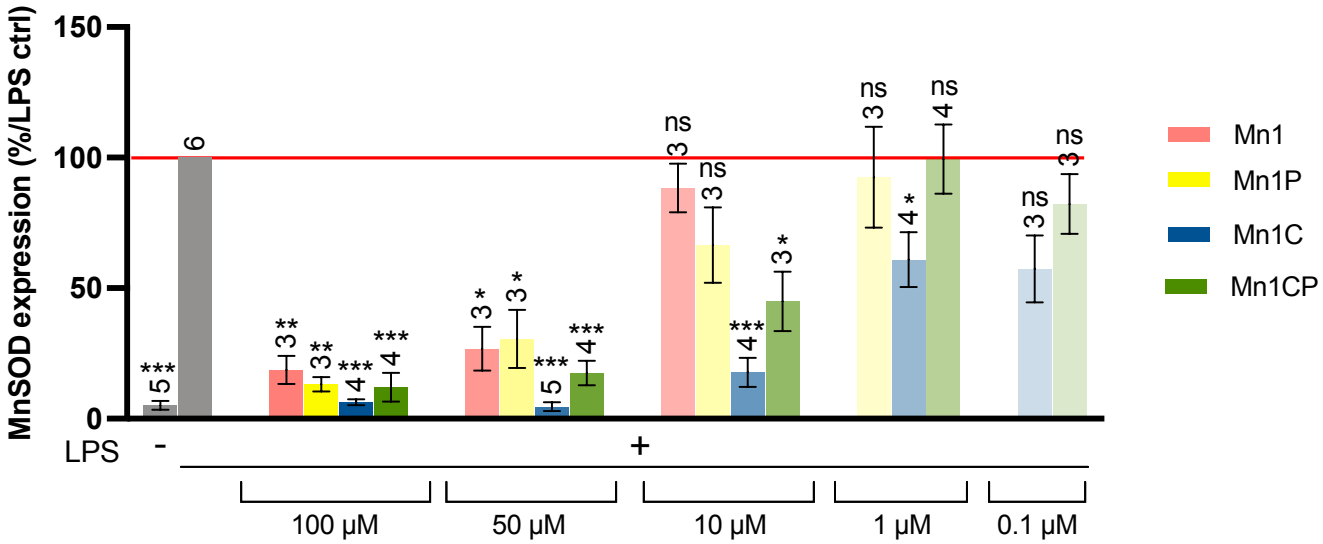

Figure 5: ***Quantification of MnSOD expression in intestinal epithelial cells activated with LPS (0.1 µg/mL).*** *MnSOD expression was measured by Western blot in lysates of LPS-activated HT29−MD2 cells incubated for 6 hours with the SOD mimics at different concentrations. The MnSOD expression intensity measured for activated cells is set at 100 % for each independent experiment. The abundances of MnSOD were normalized to the total amount of protein in each lane. Data represent mean ± SEM for at least three independent experiments: the number of independent experiments is indicated above each column. The p-values were calculated using the student test (bilateral test with equal variances not assumed). The mean rank of each column was compared to that of the LPS control, each comparison stands alone. (***) $p < 0.001$, (**) $p < 0.01$ and (*) $p < 0.05$ versus LPS control, and ns means non-significant. Without LPS, no significant differences were observed between all of these conditions (Figure S15). Control MnCl2 at 100 µM was also assessed and did not display any antioxidant activity as expected (see figure S13). Full blots are shown in Figure S12.*

- Cellular model

The four SOD mimics were assessed on a cellular model of inflammation mediated by oxidative stress. This model consists of intestinal epithelial cells named HT29-MD2, able to activate the inflammatory cascade NFκB after recognition of bacterial lipopolysaccharide (LPS), a component of the bacterial cell-membrane, by the toll-like receptors (TLR-4) present at the cells surface. To increase their sensitivity to LPS, HT29 cells have been stably transfected to over express the MD2 protein, a soluble coreceptor of TLR-4 [61]. This model, in which the LPS-induced inflammatory reaction is associated with oxidative stress [47,61,81] was used to evaluate this bio-activity of various SOD mimics [44,47–49,51].

Prior to the biological evaluation, the cytotoxicity of the four mimics was evaluated by a LDH release assay (Figure S14). No cytotoxicity in HT29−MD2 cells (LDH released extracellularly <10%) was observed for Mn1, Mn1P and Mn1CP at 100 µM when prepared with a 1:1 manganese-to-ligand ratio (6h incubation). The non-coordinated ligands were found to be cytotoxic in the same conditions, as previously published in the case of EnPI2 [47]. The Zn(II)-complexes were not cytotoxic: as redox inactive complexes with the same overall charge as the Mn-SOD mimics, they constitute a relevant inactive control [47,48]. A weak toxicity was

observed in HT29-MD2 cells for Mn1C at 100 µM prepared in the same conditions. This may be due to the slower and incomplete complexation of the cytotoxic EnPI2C ligand to manganese. To avoid that, all Mn complexes were prepared by mixing the ligand and $MnCl_2$ in a 1:1.4 ratio for 2 hours prior to the cell incubation. Using this protocol, we achieved to reduce the extracellular LDH released below 10% even for Mn1C.

The following section summarizes the effect of the four SOD mimics in LPS-activated HT29-MD2 cells. For all experiments, HT29-MD2 cells were incubated with LPS at 0.1 µg/mL to induce inflammation with or without the four SOD mimics at different concentrations for 6 hours. The anti-inflammatory and antioxidant activities of the SOD mimics were evaluated by looking at their ability to limit respectively the secretion of interleukin-8 (IL-8) and to reduce MnSOD overexpression induced by LPS (Figure 4 and Figure 5) [44,47–49,51].

- Anti-inflammatory activity

As previously published, LPS-activation induced a strong increase of IL-8 secretion in HT29-MD2 cell compared to control [44,47,48,61]. When co-incubated in presence of all of the studied SOD mimics at the non-toxic concentrations 50 µM and 100 µM, LPS-induced IL-8 levels were significantly reduced (<35% that of LPS positive control). The decrease of IL-8 secretion in response to LPS was not detected for Mn1 at 10 µM, as previously published [48]. In contrast, Mn1P, Mn1C and Mn1CP assayed at 10 µM were still able to reduce the IL-8 production to 60%, 30% and 50% that of LPS positive control respectively, without reaching statistical significance for Mn1P and significantly for Mn1C and Mn1CP (Figure 4). Therefore, the new SOD mimics, particularly Mn1C, retain significant anti-inflammatory properties at lower doses than Mn1 (even at 1 µM) and are thus efficacious against inflammation at lower incubation concentrations than Mn1. Non-significant effect on IL-8 secretion was observed for the corresponding zinc complexes Zn1, Zn1C, Zn1P and Zn1CP at 10 µM, that constitutes relevant redox-inactive analogs of the manganese SOD mimics (Figure S16) [47,48]. This confirms that these specific bioactivities are associated to the Mn complexes redox properties. Zn1 activity on cells at 100 µM was already controlled earlier [47] and reveals no effect on IL-8 secretion and MnSOD expression. Given the high kinetic rate of metal exchange from Mn1+ Zn(II) to Zn1+Mn(II), Zn1 was the most important Zn-analog to control at 100 µM. Still, all the Zn-analogs were evaluated at 10 µM since at such concentrations about 30 % of the SOD

mimics should be theoretically dissociated (based on the association constants) and subjected to Zn-coordination.

- Antioxidant activity

The effect of the SOD mimics on MnSOD expression was investigated by Western blot analysis (Figure 5). As previously shown by Mathieu *et al.*, the LPS activation of HT29-MD2 cells leads to a significant overexpression of catalytically active MnSOD. This is most probably related to the establishment of an oxidative stress situation associated with the appropriate cellular feedback response to counteract the LPS-induced oxidative stress [44,47,48]. The four studied SOD mimics limit significantly the LPS-induced MnSOD overexpression to 19%, 13%, 6% et 12% that of LPS positive control respectively when incubated at 100 µM. As previously reported, the SOD mimics seem to be able to complement for SOD in cells [44,47,48]. But at 10 µM, the effect of Mn1 on MnSOD overexpression was almost completely suppressed (89% that of LPS positive control). In contrast, at 10 µM, Mn1C and Mn1CP were still able to significantly limit MnSOD upregulation (18% and 45% that of LPS positive control), whereas the activity of Mn1P was less efficient with an over-expression to 66% that of LPS positive control. This remanence of the anti-inflammatory and antioxidant activity of Mn1C and Mn1CP at concentrations lower than those required for Mn1 is consistent with the previous results showing the improved capacity of Mn1C and Mn1CP to fulfill the criteria required to get an efficient SOD mimic. Therefore, just as for IL-8 secretion, Mn1C can reduce MnSOD overexpression at lower doses than Mn1, Mn1P and Mn1CP.

- Intracellular detection and quantification

The detection and the quantification of the SOD mimics in HT29-MD2 lysates is important to support their involvement on the biological effects observed upon LPS stimulation.

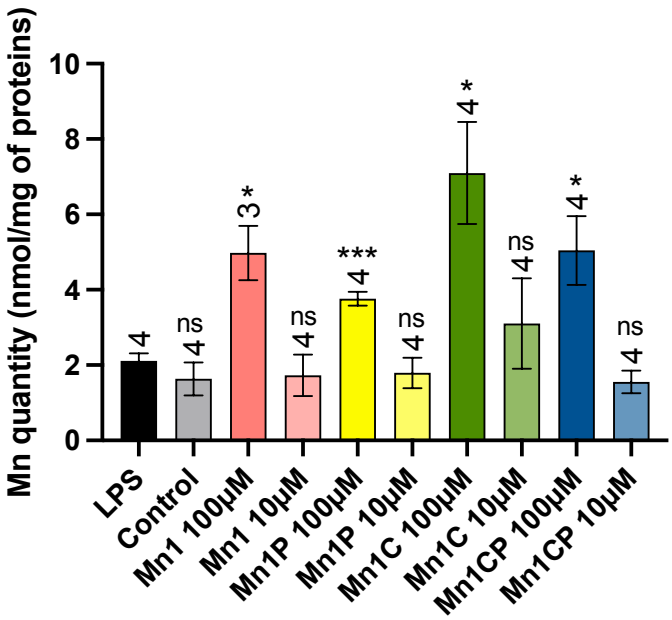

Figure 6: Quantification by ICP MS of total manganese content in LPS-activated HT29-MD2 cells incubated with the four SOD mimics at 10 and 100 µM for 6 hours. Cell lysates were digested in HNO_3 2% to release manganese from all coordination sites. The amount of Mn in cell lysates were normalized by the mass of proteins determined by BCA assay. Data represent mean ± SEM for at least three independent experiments: the number of independent experiments is indicated above each column. The p-values were calculated using the student test (bilateral test with equal variances not assumed). The mean rank of each column was compared to that of the LPS control, each comparison stands alone. (***) $p < 0.001$, (**) $p < 0.01$ and (*) $p < 0.05$ versus LPS control, and ns means non-significant. The p-values and significance results corresponding to the comparison of the SOD mimics with each other are given in Figure S18.

The accumulation of the SOD mimics in HT29-MD2 cells was first checked by measuring the total amount of Mn content in cell lysates by ICP-MS (Figure 6). A significant increase from 2.1 (control LPS cells) to 6.4, 3.8, 7.1 and 5.0 nmol of Mn per mg of proteins was recorded in cells incubated with respectively Mn1, Mn1P, Mn1C and Mn1CP at 100 µM. This shows that the SOD mimics were all able to penetrate and accumulate significantly inside cells. At 100 µM, no significant difference in intracellular manganese amount was observed for any of the 4 SOD mimics. We only noticed that the addition of a propyl group whether in Mn1 or Mn1C structures results to a non-significant but systematic and visible decrease in the amount of Mn in cell lysate. This suggests a lower cell penetration of Mn1P and Mn1CP in comparison to their respective non-propylated analog Mn1 and Mn1C. This may contribute to the slightly improved bioactivity of Mn1C over Mn1CP in HT29-MD2 cells.

We then sought to detect the active species, i.e. intact manganese complexes, and to study their speciation in the cell lysates. To do so, we conducted mass spectrometry experiments on lysates of LPS-activated HT29-MD2 cells incubated with the SOD mimics at 100 µM. In the case of Mn1, Mn1P and Mn1C, the detection was biased either by deprotonation issues (Mn1 and Mn1C) happening in gas phase and/or by rapid metal exchanges with transition metals (Ni,

Zn, Fe) present endogenously or in the different parts of the analytical instrument (Figure S20, S21, S22, S23, S24, S25, S26 and S27). This prevented us either to detect them in the cell lysates or to determine accurately their cellular amount. However, the analysis of pure Mn1CP by mass spectrometry reveals that no metal exchange occurred between the Mn(II) center and the other metal ions present in the analytical system (Figure S26 and S27), making it suitable for unbiased quantification. Indeed, we observe two intense peaks at 504.24 and at 505.25 m/z corresponding to Mn1CP and its first isotope while the peaks corresponding to the complex with other divalent metals cations are not visible except for Zn1CP but with a very weak intensity (20-times lower than that of Mn1CP).

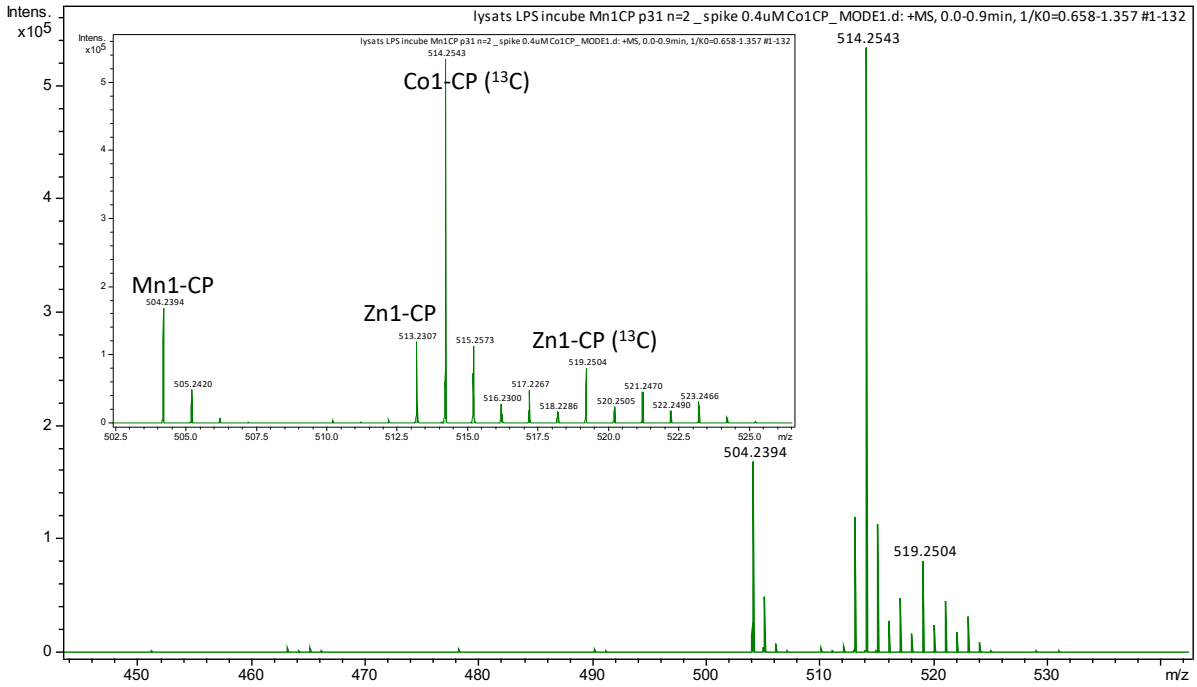

Figure 7: Mass spectrum of a LPS-stimulated HT29-MD2 lysate, previously incubated with the SOD mimic Mn1CP for 6 hours and ultra-centrifuged at 100,000 rpm for 20 minutes. The lysate (10-15 10^6cells in 2 mL NH_4CO_3 50 mM) was diluted in 20% NH_4CO_3/ 80% ACN and spiked with the standard Co1CP (^{13}C) at 0.4 µM. The figure was zoomed onto the m/z region for the studied complexes. The peak corresponding to Mn1CP, Co1CP (^{13}C) and their isotopic pattern are clearly visible and annotated on the spectrum. Other similar mass spectra of cells lysates incubated with Mn1CP are given in Figure S30. Zn1CP(^{13}C) displays peaks with relatively low intensity and was neglected for the quantification.

One example of mass spectrum corresponding to lysates of cells incubated with Mn1CP at 100 µM is given in Figure 7. Three others examples of obtained mass spectra are given in Figure S30. We observed that Mn1CP partially dissociated and exchanged within the cell with Zn(II) to form mainly Zn1CP and, to a very extent, Cu1CP. These exchanges were expected considering the high association constant of the ligand with Zn(II) (Figure S19). As we checked that the Zn(II) complexes do not have any activity in HT29-MD2 cells (Figure S16), this exchange merely led to a decrease in Mn1CP concentration in cells which is the bioactive

molecule. We also checked the SOD activity of Cu-complexes by McCord and Fridovich. Cu1, CuP1, Cu1C and Cu1CP display SOD activity with the following catalytic rates: 0.34×10^6 $M^{-1}s^{-1}$, 0.63×10^6 $M^{-1}s^{-1}$, 0.60×10^6 $M^{-1}s^{-1}$ and 0.17×10^6 $M^{-1}s^{-1}$ (Figure S17). The measured catalytic rates are all slower than that of the copper salt $(CuOAc)_2$ (14.5 $M^{-1}s^{-1}$). Then the measured SOD activity could be due to released copper (Figure S17), to weakly active Cu-complexes or to combination of both. Whatever the explanation, this again supports the conclusion that these exchanges solely result in a decrease of bioactive Mn1CP bioavailability and do not contribute the observed activity in cells.

Mn1CP in lysates of HT29-MD2 cells was quantified by spiking a standard at 0.4 µM before mass spectrometry analysis. The used standard consists of a heavy analog of Mn1CP, namely Co1CP (^{13}C) with a Co(II) ion center instead of Mn(II) and a ligand EnPI2CP bearing a phenol group labelled with ^{13}C. ^{13}C-labelled cobalt heavy complex constitutes a good standard as (a) it is very stable ($K_{1\_Co1CP} = 4.85 \pm 1.15 \times 10^8$ M^{-1}, Figure S28), (b) it undergoes minimal metal exchange with the free divalent metal ions present in the cell lysates and (c) has physicochemical properties close to that of Mn1CP. The peaks corresponding to the standard (514.26 m/z, 515.26 m/z) are also clearly visible in Figure 7. In some cases, the spectra revealed relatively weak peaks corresponding to Zn1CP (^{13}C) and Cu1CP (^{13}C) that were neglected for the quantification. From the ratio of the signal intensity of Mn1CP with that of the standard Co1CP (^{13}C) and, using a calibration curve (Figure S29), the amount of Mn1CP in the cell lysates could be retrieved by taking into account the dilution done for the sample preparation for MS. Eventually, from the concentration of cells in the lysates, the intracellular molar amount of Mn1CP can be retrieved and was determined equal to **$2.8 \pm 0.5 \times 10^{-16}$ mol per cells** (mean $\pm$ SEM). The results of the quantification for the different cellular samples are detailed in Table S2 and were confirmed by the method of standard additions (Figure S31).

Owing the Irving-Williams series, or association constant, one could fear that no Mn(II) complex should be present in cells. However, as mentioned earlier, (*i*) the endogenous ligands that could compete with EnPI2-type ligands also have a weak affinity for Mn(II) (see above the association constant of the archetypal HSA for Mn(II)) and (*ii*) as highlighted by Giedroc *et al.* metal ions such as Zn(II) or Cu(II) are indeed competitive metal ions, showing high association constants for most ligands but their exchangeable pool is also very weak as they are tightly controlled in cells by proteins. In contrast, Mn(II) being a weaker binder is non-competitive

but much more bio-available [71]. This could explain that, despite the lower stability of Mn(II) complexes than Zn(II) or Cu(II) complexes, Mn1CP is clearly present in cells.

The presence of Mn1CP at **$2.8 \pm 0.5 \times 10^{-16}$ mol per cells** supports the accumulation and the persistence of the Mn complex inside the cells as well as its role in the decrease in IL-8 levels and in MnSOD expression observed in LPS-stimulated HT29-MD2.

Conclusion

The 1,2-diaminoethane central scaffold of the parent SOD mimic Mn1 was replaced by a (±)-trans-1,2-cyclohexyl group and substituted with a propyl group on its secondary amine in order to improve its kinetic inertness and to avoid any deprotonation during the speciation studies by mass spectrometry. Characterization of the resulting complexes demonstrated that these Mn1-derived SOD mimics displayed improved features for biological applications. Thanks to its rigidified skeleton, Mn1CP in particular, is more resistant to metal exchanges that may lead to the formation of redox inactive analogues in a biological medium. The modifications of the SOD mimics led to an improvement of the anti-inflammatory and antioxidant activities in a cellular model, consisting of epithelial intestinal cells HT29-MD2 under LPS-mediated inflammation, and relevant to IBD. Indeed, Mn1C displays the best bioactivity, with significant effects when incubated at 10 µM. These improved efficacies could be correlated to the higher bioavailability of the new SOD mimics in the cellular environment. associated to a higher inertness. Note that, at this stage, we cannot exclude the possibility of a different sub-cellular location that could also be responsible for the better activity of Mn1C. This is now under exploration.

The rationalization of the SOD mimics bioactivities can be boosted by the direct detection and quantification of the active species inside the cells. The detection of open-chain manganese complexes in biological environments is not straightforward due to their high lability and thus possible metal exchanges. This is what showed the mass spectrometry experiments described in this work. For the most inert derivative Mn1CP, we investigate further its intracellular accumulation and speciation to quantify it in cells. Mn1CP partially exchanges Mn(II) with endogenous Zn(II) but remained present with an intracellular molar amount of 2.8×10^{-16} mol. The others Mn SOD mimics studied here were subjected to metal exchanges in the mass spectrometer and thus would require other metal-free techniques for unbiased detection.

The approach presented here, combining investigation of metal exchanges, bioactivity and intracellular detection indicates that kinetic inertness is a key property to be considered for biological applications. Overall, the newly-designed more inert SOD mimics display a better ratio activity/concentration, and thus constitute promising catalytic drug candidates for antioxidant and anti-inflammatory treatments in IBD context.

Acknowledgments

We thank ENS-PSL, Sorbonne university and CNRS for recurrent funding, the program *Interface pour le Vivant* (Sorbonne university) for G. Schanne's PhD fellowship, B. Goetz and P. Legeay for help with ICP-MS, L. Brot, E. Quevrain and E. Tauziet for their guidance and help with cell culture and cell assays.

Abbreviations

BCA Bicinchoninic acid
H/BSA Human/Bovine serum albumin
CDTA cyclohexanediamine tetraacetic acid
EDTA Ethylenediamine tetraacetic acid
ELISA Enzyme-linked immunosorbent assay
EPR Electron paramagnetic resonance
HEPES 4-(2-hydroxyethyl)-1-piperazineethanesulfonic acid
HPLC High performance liquid chromatography
HRP Horse-radish peroxidase
IBDs Inflammatory Bowel Diseases
ICP-MS Inductively coupled plasma mass spectrometry
IL-8 Interleukin 8
LDH Lactate dehydrogenase
LPS Lipopolysaccharides
MnSOD Manganese superoxide dismutase
NADH Nicotinamide adenine dinucleotide
NHE Normal hydrogen electrode
PBS Phosphate buffer saline
ROS Reactive oxygen species
SCE Saturated calomel electrode (saturated with KCl)
SODs Superoxide Dismutases
TFA trifluoroacetic acid
TIMS Trapped Ion Mobility Spectrometry
TLR-4 Toll-like receptors
TOF-MS Time of flight mass spectrometry
WB Western Blot
XTT 2,3-bis-(2-methoxy-4-nitro-5-sulfophenyl)-2H-tetrazolium-5-carboxanilide

References

[1] G. Schanne, M. Zoumpoulaki, G. Gazzah, A. Vincent, H. Preud'homme, R. Lobinski, S. Demignot, P. Seksik, N. Delsuc, C. Policar, Inertness of Superoxide Dismutase Mimics Mn(II) Complexes Based on an Open-Chain Ligand, Bioactivity, and Detection in Intestinal Epithelial Cells, Oxidative Medicine and Cellular Longevity. 2022 (2022) 3858122. https://doi.org/10.1155/2022/3858122.

[2] M. Zoumpoulaki, G. Schanne, N. Delsuc, H. Preud'homme, E. Quévrain, N. Eskenazi, G. Gazzah, R. Guillot, P. Seksik, J. Vinh, R. Lobinski, C. Policar, Deciphering the Metal Speciation in Low-Molecular-Weight Complexes by IMS-MS: Application to the Detection of Manganese Superoxide Dismutase Mimics in Cell Lysates, Angew Chem Int Ed. (2022). https://doi.org/10.1002/anie.202203066.

[3] F.K. Kálmán, G. Tircsó, Kinetic Inertness of the Mn^{2+} Complexes Formed with AAZTA and Some Open-Chain EDTA Derivatives, Inorg. Chem. 51 (2012) 10065–10067. https://doi.org/10.1021/ic300832e.

[4] Y. Sheng, I.A. Abreu, D.E. Cabelli, M.J. Maroney, A.-F. Miller, M. Teixeira, J.S. Valentine, Superoxide Dismutases and Superoxide Reductases, Chem. Rev. 114 (2014) 3854–3918. https://doi.org/10.1021/cr4005296.

[5] B. Halliwell, J.M. Gutteridge, Free radicals in biology and medicine, 2007.

[6] J.D. Crapo, T. Oury, C. Rabouille, J.W. Slot, L.Y. Chang, Copper,zinc superoxide dismutase is primarily a cytosolic protein in human cells., Proceedings of the National Academy of Sciences. 89 (1992) 10405–10409. https://doi.org/10.1073/pnas.89.21.10405.

[7] S.L. Marklund, E. Holme, L. Hellner, Superoxide dismutase in extracellular fluids, Clinica Chimica Acta. 126 (1982) 41–51. https://doi.org/10.1016/0009-8981(82)90360-6.

[8] R.A. Weisiger, I. Fridovich, Mitochondrial Superoxide Dismutase, Journal of Biological Chemistry. 248 (1973) 4793–4796. https://doi.org/10.1016/S0021-9258(19)43735-6.

[9] L. Kruidenier, I. Kuiper, W. van Duijn, S.L. Marklund, R.A. van Hogezand, C.B. Lamers, H.W. Verspaget, Differential mucosal expression of three superoxide dismutase isoforms in inflammatory bowel disease, J. Pathol. 201 (2003) 7–16. https://doi.org/10.1002/path.1407.

[10] J.M. McCord, M.A. Edeas, SOD, oxidative stress and human pathologies: a brief history and a future vision, Biomedicine & Pharmacotherapy. 59 (2005) 139–142. https://doi.org/10.1016/j.biopha.2005.03.005.

[11] C. Pereira, D. Grácio, J.P. Teixeira, F. Magro, Oxidative Stress and DNA Damage: Implications in Inflammatory Bowel Disease, Inflammatory Bowel Diseases. (2015) 1. https://doi.org/10.1097/MIB.0000000000000506.

[12] M. Krzystek-Korpacka, R. Kempiński, M.A. Bromke, K. Neubauer, Oxidative Stress Markers in Inflammatory Bowel Diseases: Systematic Review, Diagnostics. 10 (2020) 601. https://doi.org/10.3390/diagnostics10080601.

[13] Y. Naito, H. Takano, T. Yoshikawa, Oxidative Stress-Related Molecules as a Therapeutic Target for Inflammatory and Allergic Diseases, CDTIA. 4 (2005) 511–515. https://doi.org/10.2174/1568010054526269.

[14] D. Salvemini, C. Muscoli, D.P. Riley, S. Cuzzocrea, Superoxide Dismutase Mimetics, Pulmonary Pharmacology & Therapeutics. 15 (2002) 439–447. https://doi.org/10.1006/pupt.2002.0374.

[15] S. Miriyala, I. Spasojevic, A. Tovmasyan, D. Salvemini, Z. Vujaskovic, D. St. Clair, I. Batinic-Haberle, Manganese superoxide dismutase, MnSOD and its mimics, Biochimica et Biophysica Acta (BBA) - Molecular Basis of Disease. 1822 (2012) 794–814. https://doi.org/10.1016/j.bbadis.2011.12.002.

[16] J.B. Aitken, E.L. Shearer, N.M. Giles, B. Lai, S. Vogt, J.S. Reboucas, I. Batinic-Haberle, P.A. Lay, G.I. Giles, Intracellular Targeting and Pharmacological Activity of the Superoxide Dismutase Mimics MnTE-2-PyP^{5+} and MnTnHex-2-PyP^{5+} Regulated by Their Porphyrin Ring Substituents, Inorg. Chem. 52 (2013) 4121–4123. https://doi.org/10.1021/ic300700g.

[17] I. Batinic-Haberle, A. Tovmasyan, I. Spasojevic, An educational overview of the chemistry, biochemistry and therapeutic aspects of Mn porphyrins – From superoxide dismutation to H2O2-driven pathways, Redox Biology. 5 (2015) 43–65. https://doi.org/10.1016/j.redox.2015.01.017.

[18] C. Policar, Mimicking SOD, Why and How: Bio-Inspired Manganese Complexes as SOD Mimic, in: Redox-Active Therapeutics, Springer, 2016: pp. 125–164.

[19] I. Batinic-Haberle, A. Tovmasyan, I. Spasojevic, Mn porphyrin-based redox-active therapeutics, in: Redox-Active Therapeutics, Springer International, 2016: pp. 165–212.

[20] S. Signorella, C. Palopoli, G. Ledesma, Rationally designed mimics of antioxidant manganoenzymes: Role of structural features in the quest for catalysts with catalase and superoxide dismutase activity, Coordination Chemistry Reviews. 365 (2018) 75–102. https://doi.org/10.1016/j.ccr.2018.03.005.

[21] O. Iranzo, Manganese complexes displaying superoxide dismutase activity: A balance between different factors, Bioorganic Chemistry. 39 (2011) 73–87. https://doi.org/10.1016/j.bioorg.2011.02.001.

[22] R. Bonetta, Potential Therapeutic Applications of MnSODs and SOD-Mimetics, Chem. Eur. J. 24 (2018) 5032–5041. https://doi.org/10.1002/chem.201704561.

[23] C. Policar, J. Bouvet, H.C. Bertrand, N. Delsuc, SOD mimics: From the tool box of the chemists to cellular studies, Current Opinion in Chemical Biology. 67 (2022) 102109. https://doi.org/10.1016/j.cbpa.2021.102109.

[24] JG. Charrier, C. Anastasio, Impacts of antioxidants on hydroxyl radical production from individual and mixed transition metals in a surrogate lung fluid, Atmospheric Environment. 45 (2011) 7555–7562. https://doi.org/10.1016/j.atmosenv.2010.12.021.

[25] B.J. Day, I. Batinic-Haberle, J.D. Crapo, Metalloporphyrins are potent inhibitors of lipid peroxidation, Free Radical Biology and Medicine. 26 (1999) 730–736. https://doi.org/10.1016/S0891-5849(98)00261-5.

[26] I. Batinić-Haberle, I. Spasojević, P. Hambright, L. Benov, A.L. Crumbliss, I. Fridovich, Relationship among Redox Potentials, Proton Dissociation Constants of Pyrrolic Nitrogens, and in Vivo and in Vitro Superoxide Dismutating Activities of

Manganese(III) and Iron(III) Water-Soluble Porphyrins, Inorg. Chem. 38 (1999) 4011–4022. https://doi.org/10.1021/ic990118k.
[27] P.J.F. Gauuan, M.P. Trova, L. Gregor-Boros, S.B. Bocckino, J.D. Crapo, B.J. Day, Superoxide dismutase mimetics: synthesis and structure–activity relationship study of MnTBAP analogues, Bioorganic & Medicinal Chemistry. 10 (2002) 3013–3021. https://doi.org/10.1016/S0968-0896(02)00153-0.
[28] I. Batinić-Haberle, I. Spasojević, R.D. Stevens, B. Bondurant, A. Okado-Matsumoto, I. Fridovich, Ž. Vujašković, M.W. Dewhirst, New PEG-ylated Mn(III) porphyrins approaching catalytic activity of SOD enzyme, Dalton Trans. (2006) 617–624. https://doi.org/10.1039/B513761F.
[29] J.S. Rebouças, G. DeFreitas-Silva, I. Spasojević, Y.M. Idemori, L. Benov, I. Batinić-Haberle, Impact of electrostatics in redox modulation of oxidative stress by Mn porphyrins: Protection of SOD-deficient Escherichia coli via alternative mechanism where Mn porphyrin acts as a Mn carrier, Free Radical Biology and Medicine. 45 (2008) 201–210. https://doi.org/10.1016/j.freeradbiomed.2008.04.009.
[30] I. Batinic-Haberle, A. Tovmasyan, I. Spasojevic, Mn Porphyrin-Based Redox-Active Drugs: Differential Effects as Cancer Therapeutics and Protectors of Normal Tissue Against Oxidative Injury, Antioxidants & Redox Signaling. 29 (2018) 1691–1724. https://doi.org/10.1089/ars.2017.7453.
[31] I. Batinic-Haberle, M.E. Tome, Thiol regulation by Mn porphyrins, commonly known as SOD mimics, Redox Biology. 25 (2019) 101139. https://doi.org/10.1016/j.redox.2019.101139.
[32] M. Baudry, S. Etienne, A. Bruce, M. Palucki, E. Jacobsen, B. Malfroy, Salen-manganese complexes are superoxide dismutase- mimics, Biochemical and Biophysical Research Communications. 192 (1993). https://doi.org/10.1006/bbrc.1993.1509.
[33] A. Puglisi, G. Tabbì, G. Vecchio, Bioconjugates of cyclodextrins of manganese salen-type ligand with superoxide dismutase activity, Journal of Inorganic Biochemistry. 98 (2004) 969–976. https://doi.org/10.1016/j.jinorgbio.2004.02.012.
[34] D.P. Riley, R.H. Weiss, Manganese macrocyclic ligand complexes as mimics of superoxide dismutase, J. Am. Chem. Soc. 116 (1994) 387–388. https://doi.org/10.1021/ja00080a051.
[35] A. Dees, A. Zahl, R. Puchta, N.J.R. van Eikema Hommes, F.W. Heinemann, I. Ivanović-Burmazović, Water Exchange on Seven-Coordinate Mn(II) Complexes with Macrocyclic Pentadentate Ligands: Insight in the Mechanism of Mn(II) SOD Mimetics, Inorg. Chem. 46 (2007) 2459–2470. https://doi.org/10.1021/ic061852o.
[36] M.R. Filipović, A.C.W. Koh, S. Arbault, V. Niketić, A. Debus, U. Schleicher, C. Bogdan, M. Guille, F. Lemaître, C. Amatore, I. Ivanović-Burmazović, Striking Inflammation from Both Sides: Manganese(II) Pentaazamacrocyclic SOD Mimics Act Also as Nitric Oxide Dismutases: A Single-Cell Study, Angewandte Chemie International Edition. 49 (2010) 4228–4232. https://doi.org/10.1002/anie.200905936.
[37] F.C. Friedel, D. Lieb, I. Ivanović-Burmazović, Comparative studies on manganese-based SOD mimetics, including the phosphate effect, by using global spectral analysis, Journal of Inorganic Biochemistry. 109 (2012) 26–32. https://doi.org/10.1016/j.jinorgbio.2011.12.008.
[38] D. Lieb, I. Kenkell, J.Lj. Miljković, D. Moldenhauer, N. Weber, M.R. Filipović, F. Gröhn, I. Ivanović-Burmazović, Amphiphilic Pentaazamacrocyclic Manganese Superoxide Dismutase Mimetics, Inorg. Chem. 53 (2014) 1009–1020. https://doi.org/10.1021/ic402469t.
[39] C.M. Weekley, I. Kenkel, R. Lippert, S. Wei, D. Lieb, T. Cranwell, J.L. Wedding, A.S. Zillmann, R. Rohr, M.R. Filipovic, I. Ivanović-Burmazović, H.H. Harris, Cellular Fates of Manganese(II) Pentaazamacrocyclic Superoxide Dismutase (SOD) Mimetics: Fluorescently Labeled MnSOD Mimetics, X-ray Absorption Spectroscopy, and X-ray Fluorescence Microscopy Studies, Inorg. Chem. 56 (2017) 6076–6093. https://doi.org/10.1021/acs.inorgchem.6b03073.
[40] Z. Garda, E. Molnár, N. Hamon, J.L. Barriada, D. Esteban-Gómez, B. Váradi, V. Nagy, K. Pota, F.K. Kálmán, I. Tóth, N. Lihi, C. Platas-Iglesias, É. Tóth, R. Tripier, G. Tircsó, Complexation of Mn(II) by Rigid Pyclen Diacetates: Equilibrium, Kinetic, Relaxometric, Density Functional Theory, and Superoxide Dismutase Activity Studies, Inorg. Chem. 60 (2021) 1133–1148. https://doi.org/10.1021/acs.inorgchem.0c03276.
[41] F. Matemadombo, M. Durmus, V. Escriou, S. Griveau, D. Scherman, F. Bedioui, T. Nyokong, Evaluation of the Performance of Manganese Phthalocyanines as Superoxide Dismutase Mimics, CAC. 5 (2009) 330–338. https://doi.org/10.2174/157341109789077731.
[42] A.E.O. Fisher, D.P. Naughton, Metal ion chelating peptides with superoxide dismutase activity, Biomedicine & Pharmacotherapy. 59 (2005) 158–162. https://doi.org/10.1016/j.biopha.2005.03.008.
[43] Y. Xu, Y. Zhou, R. Yin, C. Wang, H. Chu, J. Wang, A novel 76-mer peptide mimic with the synergism of superoxide dismutase and glutathione peroxidase, In Vitro Cell.Dev.Biol.-Animal. 54 (2018) 335–345. https://doi.org/10.1007/s11626-018-0240-z.
[44] A. Vincent, J.R. Fores, E. Tauziet, E. Quévrain, Á. Dancs, A. Conte-Daban, A.-S. Bernard, P. Pelupessy, K. Coulibaly, P. Seksik, C. Hureau, K. Selmeczi, C. Policar, N. Delsuc, An easy-to-implement combinatorial approach involving an activity-based assay for the discovery of a peptidyl copper complex mimicking superoxide dismutase, Chem. Commun. 56 (2020) 399–402. https://doi.org/10.1039/C9CC07920C.
[45] F. Cisnetti, A.-S. Lefèvre, R. Guillot, F. Lambert, G. Blain, E. Anxolabéhère-Mallart, C. Policar, A New Pentadentate Ligand Forms Both a Di- and a Mononuclear MnII Complex: Electrochemical, Spectroscopic and Superoxide Dismutase Activity Studies, Eur. J. Inorg. Chem. 2007 (2007) 4472–4480. https://doi.org/10.1002/ejic.200601236.
[46] H.Y.V. Ching, I. Kenkel, N. Delsuc, E. Mathieu, I. Ivanović-Burmazović, C. Policar, Bioinspired superoxide-dismutase mimics: The effects of functionalization with cationic polyarginine peptides, Journal of Inorganic Biochemistry. 160 (2016) 172–179. https://doi.org/10.1016/j.jinorgbio.2016.01.025.

[47] E. Mathieu, A.-S. Bernard, N. Delsuc, E. Quévrain, G. Gazzah, B. Lai, F. Chain, P. Langella, M. Bachelet, J. Masliah, P. Seksik, C. Policar, A Cell-Penetrant Manganese Superoxide Dismutase (MnSOD) Mimic Is Able To Complement MnSOD and Exerts an Antiinflammatory Effect on Cellular and Animal Models of Inflammatory Bowel Diseases, Inorg. Chem. 56 (2017) 2545–2555. https://doi.org/10.1021/acs.inorgchem.6b02695.
[48] E. Mathieu, A.-S. Bernard, H.Y.V. Ching, A. Somogyi, K. Medjoubi, J.R. Fores, H.C. Bertrand, A. Vincent, S. Trépout, J.-L. Guerquin-Kern, A. Scheitler, I. Ivanović-Burmazović, P. Seksik, N. Delsuc, C. Policar, Anti-inflammatory activity of superoxide dismutase mimics functionalized with cell-penetrating peptides, Dalton Trans. 49 (2020) 2323–2330. https://doi.org/10.1039/C9DT04619D.
[49] E. Mathieu, A.-S. Bernard, E. Quévrain, M. Zoumpoulaki, S. Iriart, C. Lung-Soong, B. Lai, K. Medjoubi, L. Henry, S. Nagarajan, F. Poyer, A. Scheitler, I. Ivanović-Burmazović, S. Marco, A. Somogyi, P. Seksik, N. Delsuc, C. Policar, Intracellular location matters: rationalization of the anti-inflammatory activity of a manganese(ii) superoxide dismutase mimic complex, Chem. Commun. 56 (2020) 7885–7888. https://doi.org/10.1039/D0CC03398G.
[50] A.-S. Bernard, C. Giroud, H.Y.V. Ching, A. Meunier, V. Ambike, C. Amatore, M.G. Collignon, F. Lemaître, C. Policar, Evaluation of the anti-oxidant properties of a SOD-mimic Mn-complex in activated macrophages, Dalton Trans. 41 (2012) 6399. https://doi.org/10.1039/c2dt12479c.
[51] A. Vincent, M. Thauvin, E. Quévrain, E. Mathieu, S. Layani, P. Seksik, I. Batinic-Haberle, S. Vriz, C. Policar, N. Delsuc, Evaluation of the compounds commonly known as superoxide dismutase and catalase mimics in cellular models, Journal of Inorganic Biochemistry. 219 (2021) 111431. https://doi.org/10.1016/j.jinorgbio.2021.111431.
[52] P. Failli, D. Bani, A. Bencini, M. Cantore, L. Di Cesare Mannelli, C. Ghelardini, C. Giorgi, M. Innocenti, F. Rugi, A. Spepi, R. Udisti, B. Valtancoli, A Novel Manganese Complex Effective as Superoxide Anion Scavenger and Therapeutic Agent against Cell and Tissue Oxidative Injury, J. Med. Chem. 52 (2009) 7273–7283. https://doi.org/10.1021/jm901298x.
[53] K.-Y. Cheng, F. Guo, J.-Q. Lu, Y.-Z. Cao, T.-C. Wang, Q. Yang, Q. Xia, MnTM-4-PyP Modulates Endogenous Antioxidant Responses and Protects Primary Cortical Neurons against Oxidative Stress, CNS Neurosci Ther. 21 (2015) 435–445. https://doi.org/10.1111/cns.12373.
[54] T. de P. Ribeiro, F.L. Fonseca, M.D.C. de Carvalho, R.M. da C. Godinho, F.P. de Almeida, T.D. Saint'Pierre, N.A. Rey, C. Fernandes, A. Horn, M.D. Pereira, Metal-based superoxide dismutase and catalase mimics reduce oxidative stress biomarkers and extend life span of Saccharomyces cerevisiae, Biochemical Journal. 474 (2017) 301–315. https://doi.org/10.1042/BCJ20160480.
[55] S. Carballal, V. Valez, D. Alvarez-Paggi, A. Tovmasyan, I. Batinic-Haberle, G. Ferrer-Sueta, D.H. Murgida, R. Radi, Manganese porphyrin redox state in endothelial cells: Resonance Raman studies and implications for antioxidant protection towards peroxynitrite, Free Radical Biology and Medicine. 126 (2018) 379–392. https://doi.org/10.1016/j.freeradbiomed.2018.08.023.
[56] I. Kos, L. Benov, I. Spasojević, J.S. Rebouças, I. Batinić-Haberle, High Lipophilicity of meta Mn(III) *N* -Alkylpyridylporphyrin-Based Superoxide Dismutase Mimics Compensates for Their Lower Antioxidant Potency and Makes Them as Effective as Ortho Analogues in Protecting Superoxide Dismutase-Deficient *Escherichia coli*, J. Med. Chem. 52 (2009) 7868–7872. https://doi.org/10.1021/jm900576g.
[57] Y.-C. Fang, Y.-P. Chen, C.-T. Chen, T.-S. Lin, C.-Y. Mou, Protection of HeLa cells against ROS stress by CuZnSOD mimic system, J. Mater. Chem. B. 1 (2013) 6042. https://doi.org/10.1039/c3tb21052a.
[58] E.M. Gale, I.P. Atanasova, F. Blasi, I. Ay, P. Caravan, A Manganese Alternative to Gadolinium for MRI Contrast, J. Am. Chem. Soc. 137 (2015) 15548–15557. https://doi.org/10.1021/jacs.5b10748.
[59] S. Laine, C.S. Bonnet, F.K. Kálmán, Z. Garda, A. Pallier, F. Caillé, F. Suzenet, G. Tircsó, É. Tóth, Mn $^{2+}$ complexes of open-chain ligands with a pyridine backbone: less donor atoms lead to higher kinetic inertness, New J. Chem. 42 (2018) 8012–8020. https://doi.org/10.1039/C8NJ00648B.
[60] D. Ndiaye, M. Sy, A. Pallier, S. Même, I. Silva, S. Lacerda, A.M. Nonat, L.J. Charbonnière, É. Tóth, Unprecedented Kinetic Inertness for a Mn $^{2+}$ -Bispidine Chelate: A Novel Structural Entry for Mn $^{2+}$ -Based Imaging Agents, Angew. Chem. Int. Ed. 59 (2020) 11958–11963. https://doi.org/10.1002/anie.202003685.
[61] C. Lenoir, C. Sapin, A.H. Broquet, A.-M. Jouniaux, S. Bardin, I. Gasnereau, G. Thomas, P. Seksik, G. Trugnan, J. Masliah, M. Bachelet, MD-2 controls bacterial lipopolysaccharide hyporesponsiveness in human intestinal epithelial cells, Life Sciences. 82 (2008) 519–528. https://doi.org/10.1016/j.lfs.2007.12.007.
[62] P. Thordarson, Determining association constants from titration experiments in supramolecular chemistry, Chem. Soc. Rev. 40 (2011) 1305–1323. https://doi.org/10.1039/C0CS00062K.
[63] J. McCord, I. Fridovich, Superoxide dismutase. An enzymic function for erythrocuprein (hemocuprein), The Journal of Biological Chemistry. 244 (1969) 6045–6055.
[64] K.M. Faulkner, S.I. Liochev, I. Fridovich, Stable Mn(II1) Porphyrins Mimic Superoxide Dismutasein Vitro and Substitute forIt in Viuo, The Journal of Biological Chemistry. 269 (1994) 23471–23476.
[65] S. Durot, F. Lambert, J.-P. Renault, C. Policar, A Pulse Radiolysis Study of Catalytic Superoxide Radical Dismutation by a Manganese(II) Complex with an N-Tripodal Ligand, Eur. J. Inorg. Chem. 2005 (2005) 2789–2793. https://doi.org/10.1002/ejic.200400834.
[66] S. Durot, C. Policar, F. Cisnetti, F. Lambert, J.-P. Renault, G. Pelosi, G. Blain, H. Korri-Youssoufi, J.-P. Mahy, Series of Mn Complexes Based onN-Centered Ligands and Superoxide - Reactivity in an Anhydrous Medium and SOD-Like Activity in an Aqueous Medium Correlated to MnII/MnIII Redox Potentials, Eur. J. Inorg. Chem. 2005 (2005) 3513–3523. https://doi.org/10.1002/ejic.200400835.

[67] A. Conte-Daban, V. Ambike, R. Guillot, N. Delsuc, C. Policar, C. Hureau, A Metallo Pro-Drug to Target Cu ^{II} in the Context of Alzheimer's Disease, Chem. Eur. J. 24 (2018) 5095–5099. https://doi.org/10.1002/chem.201706049.
[68] Á. Martínez-Camarena, P.A. Sánchez-Murcia, S. Blasco, L. González, E. García-España, Unveiling the reaction mechanism of novel copper *N* -alkylated tetra-azacyclophanes with outstanding superoxide dismutase activity, Chem. Commun. 56 (2020) 7511–7514. https://doi.org/10.1039/D0CC01926G.
[69] D.P. Riley, S.L. Henke, P.J. Lennon, R.H. Weiss, W.L. Neumann, W.J. Rivers, K.W. Aston, K.R. Sample, H. Rahman, C.-S. Ling, J.-J. Shieh, D.H. Busch, Witold Szulbinski, Synthesis, Characterization, and Stability of Manganese(II) C-Substituted 1,4,7,10,13-Pentaazacyclopentadecane Complexes Exhibiting Superoxide Dismutase Activity, Inorg. Chem. 35 (1996) 5213–5231. https://doi.org/10.1021/ic960262v.
[70] L. Hong, T. Chu-Qiao, Z. Hong-Zhi, S. Xing-Can, Z. Yong-Qia, S. Pan-Wen, Binding equilibrium study between Mn(II) and HSA or BSA, Chin. J. Chem. 18 (2010) 35–41. https://doi.org/10.1002/cjoc.20000180107.
[71] J.P. Lisher, D.P. Giedroc, Manganese acquisition and homeostasis at the host-pathogen interface, Front. Cell. Infect. Microbiol. 3 (2013). https://doi.org/10.3389/fcimb.2013.00091.
[72] T.J. Lyons, D.J. Eide, Transport and storage of metal ions in biology, in: Biological Inorganic Chemistry: Structure and Reactivity, 2007: pp. 57–78.
[73] RJP. Williams, The biodistribution of metal ions, in: Concepts and Models in Bioinorganic Chemistry, 2006: pp. 1–23.
[74] H. Irving, P. Williams, Order of stability of metal complexes, Nature. (1948) 746–747.
[75] H. Irving, P. Williams, The stability of transition-metal complexes, J. Chem. Soc. 637 (1953) 3192–3210. https://doi.org/10.1039/jr9530003192.
[76] W.H. Koppenol, D.M. Stanbury, P.L. Bounds, Electrode potentials of partially reduced oxygen species, from dioxygen to water, Free Radical Biology and Medicine. 49 (2010) 317–322. https://doi.org/10.1016/j.freeradbiomed.2010.04.011.
[77] W. Barrette, D. Sawyer, J. Fee, K. Asada, Potentiometric Titrations and Oxidation-Reduction Potentials of Several Iron Superoxide Dismutases, Biochemistry. 22 (1983) 624–627.
[78] R.H. Weiss, A.G. Flickinger, W.J. Rivers, M.M. Hardy, K.W. Aston, U.S. Ryan, D.P. Riley, Evaluation of activity of putative superoxide dismutase mimics. Direct analysis by stopped-flow kinetics., Journal of Biological Chemistry. 268 (1993) 23049–23054. https://doi.org/10.1016/S0021-9258(19)49423-4.
[79] G. Czapski, A. Samuni, S. Goldstein, Superoxide Dismutase Mimics: Antioxidative and Adverse Effects, Methods in Enzymology. 349 (2002) 9.
[80] E. Mathieu, A.E. Tolbert, K.J. Koebke, C. Tard, O. Iranzo, J.E. Penner-Hahn, C. Policar, V. Pecoraro, Rational De Novo Design of a Cu Metalloenzyme for Superoxide Dismutation, Chem. Eur. J. 26 (2020) 249–258. https://doi.org/10.1002/chem.201903808.
[81] G. Gloire, S. Legrand-Poels, J. Piette, NF-κB activation by reactive oxygen species: Fifteen years later, Biochemical Pharmacology. 72 (2006) 1493–1505. https://doi.org/10.1016/j.bcp.2006.04.011.
[82] Z.-M. Yang, L. Lu, Synthesis of deuterated herbicidal ZJ0273, ZJ0702, ZJ0777, and SIOC0163, J Label Compd Radiopharm. (2010) n/a-n/a. https://doi.org/10.1002/jlcr.1749.

II.3. Publication : “Deciphering the Metal Speciation in Low-Molecular-Weight Complexes by IMS-MS: Application to the Detection of Manganese Superoxide Dismutase Mimics in Cell Lysates”

Deciphering the Metal Speciation in Low-Molecular-Weight Complexes by IMS-MS: Application to the Detection of Manganese Superoxide Dismutase Mimics in Cell Lysates

Martha Zoumpoulaki[1,2,3], Gabrielle Schanne[1,3], Nicolas Delsuc[1], Hugues Preud'homme[4], Elodie Quévrain[1,3], Nicolas Eskenazi[2], Géraldine Gazzah[1], Regis Guillot[5], Philippe Seksik[3], Joelle Vinh[2], Ryszard Lobinski[4], Clotilde Policar[1]

[1] Laboratoire des biomolécules (LBM), Département de chimie, École normale supérieure, PSL University, Sorbonne Université, CNRS, 75005 Paris, France
[2] SMBP ESPCI Paris, PSL University, UMR 8249 CNRS
[3] Centre de Recherche de Saint-Antoine, Sorbonne University, INSERM, 75012 Paris (France)
[4] IPREM-UMR5254, E2S UPPA, CNRS, Technopôle Helioparc, 64053 Pau Cedex 9 (France)
[5] Université Paris-Saclay, CNRS, 91405 Orsay (France)

As mentioned in the introduction of chapter II, most of the techniques available for SOD mimics quantification in cells relie on the detection of either the ligand or the metallic center. This study aims to demonstrate the use of ion mobility spectrometry coupled to mass spectrometry (IMS-MS) to track the presence of intact Mn(II) complexes SOD mimics (Mn(II)-ligand) inside cells.

The intracellular detection of Mn1 in its intact form is very challenging for three main reasons: 1) the biological environment is very intricate and overcrowded, 2) Mn1 is subjected to fast metal exchanges within the analytical system, hence preventing any unbiased detection and quantification and 3) the amine moiety of Mn1 may be deprotonated.

We report here the capacity of IMS-MS to provide a metal-free (to some extent) detection system (MS) and an upstream separation system (IMS) ensuring a second dimension for the analyses. This allowed the accurate determination of the intracellular speciation of both Mn1 and its propylated analog labelled Mn1P.

This project was led by a former PhD student of the laboratory of Biomolecules : Martha Zoumpoulaki. I contributed in the synthesis/purification/titration of the heavy analog of Mn1P required for the quantification, in the sample preparation of HT29-MD2 cell lysates prealably incubated with the two SOD mimics and in the IMS-MS analysis of these latter samples at IPREM in Pau. This work was recently published in Angewandte Chemie journal (doi.org/10.1002/anie.202203066). I participated in the paper proofreading.

Abstract

The detection and quantification of exogenous metal complexes are crucial to understanding their activity in intricate biological media. Mn(II) complexes are difficult to detect and quantify because of low association constants and high lability. The superoxide dismutase (SOD) mimic (or mimetic) labelled Mn1 is based on a 1,2-di-aminoethane functionalized with imidazole and phenolate and has good intrinsic anti-superoxide, antioxidant and anti-inflammatory activity in lipopolysaccharide (LPS)-activated intestinal epithelial HT29-MD2 cells, similar to that of its propylated analogue labelled Mn1P. Ion mobility spectrometry-mass spectrometry (IMS-MS) is a powerful technique for separating low molecular weight (LMW) metal complexes and can even separate complexes with the same ligand but bound to different divalent metal cations with similar ionic radii. We demonstrated the intracellular presence of the Mn1 and Mn1P complexes, at least partly intact, in lysates of cells incubated with the complexes and estimated the intracellular Mn1P concentration using a Co-$^{13}C_6$ analogue.

Introduction

The reliable detection and quantification of exogenous metal complexes, such as metallodrugs or metal-based probes in intricate biological media, is essential for a good understanding of their bioactivity and can be particularly challenging. Various imaging techniques [1] based on fluorescence [2–4], vibrational spectroscopies, including μFourier transform infrared spectroscopy (μ-FTIR) [5–12], μRaman [13,14], laser ablation inductively coupled plasma mass spectrometry LA-ICP-MS [15,16] or X-ray fluorescence (XRF) [5,17–29] can be used for the intracellular detection and mapping of metal complexes. Furthermore, mass spectrometry-based techniques [30], such as ICP-MS [30–33], electrospray ionization tandem mass spectrometry (ESI-MS/MS) [34], liquid chromatography-mass spectrometry (LC-MS) [35, 36], as well as electron paramagnetic resonance (EPR) [25,37] or atomic absorption spectrometry (AAS) [35, 38–44], have been used for their detection and quantification in cells or organisms.

Manganese(II) complexes, developed as contrast agents for magnetic resonance imaging (MRI) [45–51], or as catalytic antioxidants mimicking the mitochondrial manganese superoxide dismutase (MnSOD) [52–59], constitute a unique challenge. Biological environments are rich in Lewis bases [60] and contain a variety of divalent metal ions that constitute an exchangeable pool [61]. Due to their d^5 metal ion with no ligand-field-

stabilization energy (LFSE) [25, 62, 63], Mn(II) complexes display association constants in the low range of the Irving and Williams series [64,65]. Their d^5 configuration contributes to a low kinetic barrier to ligand dissociation or association [25, 62, 63], and renders Mn(II) complexes highly labile, with fast exchange of coordinated ligands and metal ions [66,67], except for some ligands specifically designed to achieve impressive inertness [46]. The knowledge of the speciation of a Mn(II) complex or Mn(II) ion in a biological environment is thus crucial.

A metal-free analytical environment is needed to avoid adventitious metal ion exchanges coming from the analytical system. Considering the plethora of species in the LMW range in cells, coupling of MS with a separation system is required. A comprehensive evaluation of high-performance liquid chromatography-mass spectrometry (HPLC-MS) for a large-scale study of metal complexes was reported elsewhere [68]. It has been also applied very recently to a more inert Mn-based complex similar to Mn1 [69]. More labile compounds present additional problems, especially when they interact with the stationary phase and the tubing of the system. These interactions can lead to metal exchange and the decomposition of the target metal complexes.

Ion mobility spectrometry, first developed by Cohen and Karasek in 1970 [70], to detect traces of organic molecules in the gas phase, involves the movement of ions against a gas flow under an applied electric field. The velocity of ions is proportional to their reduced mobility constant K [$cm^2\,V^{-1}\,s^{-1}$], which is associated with their rotationally averaged collision cross-section (CCS) also noted Ω (in $Å^2$). In IMS coupled with mass spectrometry, ion detection is performed using MS [71–73]. IMS-MS is a powerful technique used for structural characterization of biomolecules to probe the folding of proteins upon ligand binding [74], and to study the dynamic of those interactions [75], to characterize supramolecular complexes showing differences in host shape due to guest interaction [76–79]. It can also be used to separate species of very similar mobility with a high resolving power (>100 as defined by Ω/ΔΩ measured at full width at half maximum) [75]. For instance, IMS-MS was used to characterize metal speciation in peptides [80]. Its application to the coordination of LMW ligands is not highly developed, probably because the change in shape upon folding around a metal ion is small, and as far as we know, IMS-MS has never been applied to study metal speciation [81] in LMW complexes in cell lysates.

We are interested in bioinspired metal-based catalytic antioxidants [82–84], namely manganese(II) complexes that mimic SODs, metalloenzymes that catalyze the dismutation of superoxide and constitute the first line of cellular antioxidant defense [52,54]. One of these SOD mimics, Mn1 (Figure 1a), involves an open-chain ligand built on a 1,2- diaminoethane-scaffold, with two imidazole and one phenolate as appended coordinating moieties. Mn1 has good intrinsic anti-superoxide activity, as measured by the k_{cat} outside of a cellular context [25, 54], in line with its redox potential, which is close to the optimal SOD potential $E_{1/2}$ (V/SCE) typically ranging from 0 to 0.2 V/SCE, with an optimal value at 0.12 V/SCE [52,54,82,85], which is the midpoint between $E^{0'}{}_{1/2}(O_{2aq}/O_2^{\bullet-})$=-0.42 V/SCE and $E^{0'}{}_{1/2}(O_2^{\bullet-}/H_2O_2)$=0.66 V/SCE [86]. One of the cellular models we use to evaluate SOD mimics [5,22,25,87,88] consists of intestinal epithelial cells, HT29- MD2, under lipopolysaccharide activation [89, 90]. Mn1 displayed a good antioxidant and anti-inflammatory activity in this model, while its zinc(II) redox-inactive analogue, referred to as Zn1, and $MnCl_2$ showed no effect [5,22,25,87]. The quantification methods previously used (EPR, ICP-MS, XRF) [5, 22, 25] were focused on the metal ion cellular content and its comparison with the endogenous content, assuming that excess of Mn was due to internalized Mn1. This could have some drawbacks as incubation with a non-native coordination complex may itself alter the homeostasis of the metal ions within the cells*. To avoid this possible bias and to also determine the amount of intact metal complex in cells, we wanted to directly track it in cell lysates. We showed previously using LC/MS-MS [25], that Mn1 penetrates the cells but the fact that the m/z peak of $[Mn1]^+$ (408.1465) is very close to that of the m/z peak of $[Fe1\text{-}H]^+$ (408.1355), with overlapping isotopic patterns prevented any reliable quantitative analysis, as previously performed with a more inert analogue [69]. Recently, to investigate the Mn1 subcellular location, a multimodal Re-tris carbonyl probe was conjugated to the ligand. The Mn(II) complex showed the same activity as Mn1 but a different cellular distribution. Tagging the ligand was used as an indirect way to study speciation. Mn and Re were only partially colocalized, suggesting possible dissociation [5].

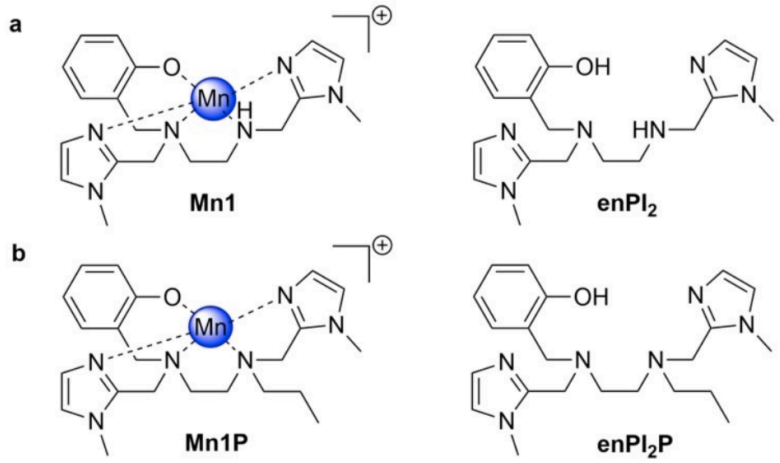

Figure 1: Chemical structure of MnSOD mimics. a) Mn1 and enPI2 ligand. b) Propylated analogue Mn1P and enPI2P ligand. The analogues with Zn(II), not shown in this figure, were labeled Zn1 and Zn1P similar to other metal cations (Co1, Fe1, Cu1, etc.).

This study aims to elucidate the fate of Mn1 and its propylated analogue Mn1P (Figure 1b) in HT29-MD2 cell lysates using MS-based methods. To match the conditions under which we study the anti-inflammatory and antioxidant activity of the SOD mimics [5,22,25] (Figure 2), we co-incubated the SOD mimics with LPS. The fact that Mn of natural abundance is monoisotopic precludes considering mass isotopic distribution to ascertain whether a Mn complex is present. We have explored here IMS-MS to demonstrate unambiguously the intracellular presence of the intact Mn1 and Mn1P complexes (Mn(II)-Ligand) and to estimate the intracellular concentration of Mn1P.

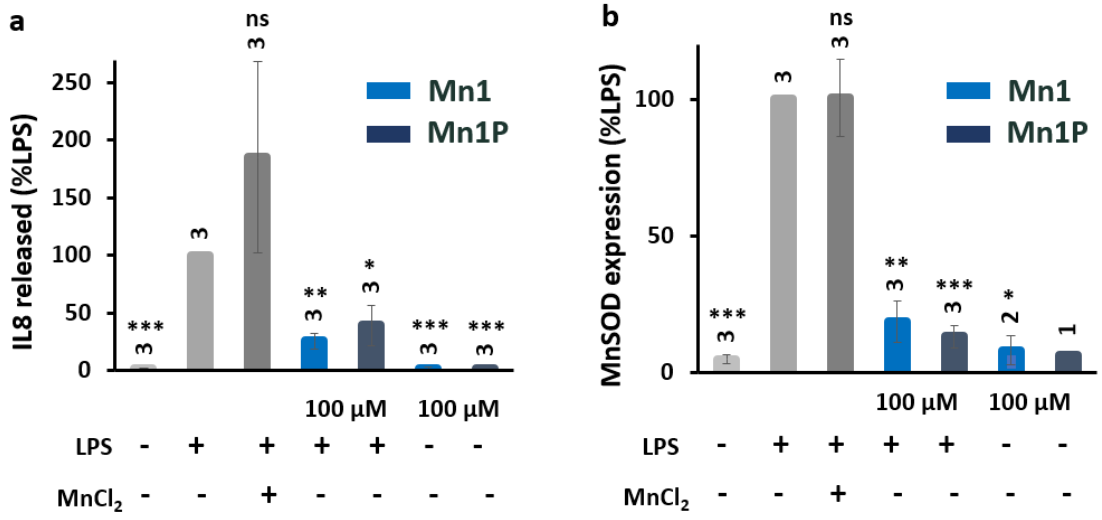

Figure 2: Anti-inflammatory and antioxidant activity of Mn1 and Mn1P. LPS-activated (0.1 µg/mL) cells were incubated in the presence of $MnCl_2$, Mn1, or Mn1P at 100 µM for 6 h. Non-activated cells were incubated with cell media, Mn1 or Mn1P at 100 µM for 6 h. Positive and negative controls consist of LPS-activated and non-activated HT29- MD2 cells (light grey), respectively. a) Quantification of interleukin 8 (IL-8) inflammation chemokine, in supernatants, measured by ELISA. The IL-8 amount was normalized by the total protein amount in each sample and was reported as ng/mg of proteins. Normalized IL-8 amount is presented % vs. the LPS positive control. Results represent mean±SEM for three biological experiments in technical duplicates. b) MnSOD expression in cell lysates measured by Western Blot. MnSOD expression was normalized to the total amount of

protein in each sample. Normalized MnSOD expression intensity is presented % vs. the LPS positive control. Data represent mean± SEM with the number of independent experiments indicated above each column. The p-values were calculated using the Student's t-test. The mean rank of each column was compared to that of the LPS control, each comparison stands alone. (***) p < 0.001, (**) p < 0.01, and (*) p < 0.05 versus LPS control, and ns means nonsignificant.

Results and Discussion

- Physico-Chemical Properties of Mn1 and Mn1P

Anticipating possible issues with deprotonation of the NH group in Mn1 during MS experiments, we decided to derivatize the secondary amine of the 1,2-diaminoethane-scaffold by adding a propyl chain leading to Mn1P. Mn1P was prepared as Mn1 [5,22,25] using a propylated version of the enPI2 ligand as described elsewhere [69]. The functionalization of the nitrogen with a propyl group did not greatly alter the properties of the SOD mimic, as shown in Tables 1 and 2, and Figures 2, S1a–d. Mn1P showed a peak higher than Mn1 when analyzed in 1/1 ratio by ESI-MS, indicating better ionization properties for Mn1P (Figure S1e). The crystallographic structure of Mn1P consists of the dimeric [(enPI$_2$P) Mn Mn (enPI$_2$P)] $(PF_6)_2$, with each Mn(II) ion hexacoordinate with four nitrogen atoms of the anionic form enPI$_2$P$^-$ of the ligand and two bridging oxygen atoms from the phenolate groups (Tables S1 and S2, Figure S2). As for Zn1 [5,22,25], the redox inactive analogue Zn1P did not demonstrate any anti-inflammatory activity in inflamed HT29-MD2 cells (FigureS3). None of the above-mentioned complexes was cytotoxic (Figure S4).

	Mn1	Mn1P
Redox potential $E_{1/2}$ [V/SCE][a]	0.20	0.21
SOD activity[b]	$IC_{50} = 1.26$ µM Log $k_{cat} = 7.31$	$IC_{50} = 1.26$ µM Log $k_{cat} = 7.32$

Table 1: Comparison of Mn1P and Mn1 physicochemical properties (HEPES, 50 mM, pH 7.5). [a] Measured with a 200 µM solution of the complexes in HEPES (50 mM, pH 7.5), with a Pt auxiliary electrode and a glassy carbon disk as working electrode, at scan rates 0.1 or 0.2 V/s. See Supporting Information for additional details. [b] Measured using the Fridovich assay [54,83,91,92] in HEPES (50 mM, pH 7.5), with cytochrome c Fe(III) as UV/Visible marker, [CytcFe(III)] = 100 µM. See Supporting Information for additional details.

Ligand	K_{MnL}	K_{CoL}	K_{ZnL}
L = enPI$_2$	$1.22 \pm 0.18 \times 10^6$	$1.10 \pm 0.62 \times 10^8$	$1.0 \pm 0.2 \times 10^{10}$
L = enPI$_2$P	$1.04 \pm 0.18 \times 10^6$	$2.30 \pm 1.32 \times 10^7$	$6.0 \pm 1.4 \times 10^9$

Table 2: Association constants K_{ML} (equivalent to M^{-1}) of the studied ligands with Mn(II), Co(II), and Zn(II). Measurements were performed in a HEPES 50 mM buffer at pH 7.5 with an ionic strength of 12.5 mM and at 25 °C (see Figure S5 for Co(II) and Supporting Information for experimental details). Association constants of the complexes with Cu(II) and Fe(II), less relevant in this study, are given only in the Supporting Information for information.

- IMS-MS: A Powerful Analytical Technique to Discriminate between LMW Complexes with Similar Divalent Metal Ions

We investigated whether IMS-MS could discriminate between the same LMW ligand bound to various divalent metal cations from the first series of the transition elements or Zn(II), that are folded differently due to small changes in ionic radii [93]. The capacity to distinguish two species with a close CCS, is dependent on the capacity to separate two peaks. If we consider that two peaks of equal intensity are resolved if the valley between them is less than 0.1 of the peak intensity, the minimum difference in mobility allowing the distinction among two species is close to 2 $Å^2$ CCS difference. Table 3 gives the CCS and inverse of the reduced mobility constant K_0 [73] for a series of complexes derived from $enPI_2$ and $enPI_2P$, namely Mn1 and its analogues Zn1, Ni1, Fe1, Co1, Cu1 on the one hand, and Mn1P and its analogues Zn1P, Ni1P, Fe1P, Co1P, Cu1P, on the other hand (see also Figure 3). Mobilograms extracted at a given molecular mass for each complexes analyzed separately, are presented in Figure 4, as an overlay. Figure S6 shows that the various complexes can be identified in an equimolar mixture of complexes. These data show that the discrimination between the complexes is achievable in both series, with CCS ranging from 180.557 to 188.124 $Å^2$ for $enPI_2$ and from 190.825 to 197.485 $Å^2$ for $enPI_2P$.

Name	Species	m/z $[L+M]^+$ exp	m/z $[L+M]^+$ calc	δm [ppm]	$1/K_0$ $[cm^2V^{-1}s^{-1}]$	CCS $[Å^2]$	r_{ion} [Å]
$enPI_2$	$[enPI_2+H]^+$	355.22404	355.2241	0.14	0.8607±0.001	181.109	–
Mn1	$[enPI_2+Mn]^+$	408.14615	408.1465	0.80	0.8983±0.001	188.124	0.75
Mn1-H	$[enPI_2+Mn-H]^+$	407.13839	407.13865	0.65	0.8621±0.001	180.557	–
Fe1-H	$[enPI_2+Fe-H]^+$	408.13570	408.1355	−0.33	0.8926±0.001	186.932	0.78
Co1	$[enPI_2+Co]^+$	412.14131	412.1416	0.77	0.8922±0.001	186.788	0.67
Ni1	$[enPI_2+Ni]^+$	414.14356	411.1438	0.52	0.8895±0.001	186.226	0.63
Cu1	$[enPI_2+Cu]^+$	416.13796	416.1380	0.18	0.8837±0.001	184.944	0.65
Zn1	$[enPI_2+Zn]^+$	417.13732	417.1376	0.62	0.8922±0.001	186.697	0.68
$enPI_2P$	$[enPI_2P+H]^+$	397.27043	397.2710	1.53	0.9104±0.001	190.825	–
Mn1P	$[enPI_2P+Mn]^+$	450.19296	450.1934	1.05	0.9344±0.001	195.096	0.75
Fe1P	$[enPI_2P+H_2O+Fe]^+$	468.19296	468.19306	0.27	0.9469±0.001	197.485	0.78
Co1P	$[enPI_2P+Co]^+$	454.18858	454.1886	0.24	0.9299±0.001	194.107	0.67
Ni1P	$[enPI_2P+Ni]^+$	453.19023	453.1907	1.09	0.9254±0.001	193.170	0.63
Cu1P	$[enPI_2P+Cu]^+$	458.18474	458.1850	0.53	0.9218±0.001	192.360	0.65
Zn1P	$[enPI_2P+Zn]^+$	459.18433	459.1845	0.44	0.9290±0.001	193.840	0.68

Table 3: IMS-MS data of the metallated forms of the $enPI_2$ and $enPI_2P$ ligand (with Mn(II), Fe(II), Co(II), Ni(II), Cu(II), Zn(II), as in the order of the periodic table). MS and IMS parameters determined after injection at neutral pH (20 µM in 20 % NH_4HCO_3 50 mM pH 7.4/80 % acetonitrile or ACN). m/z $[L+M]^+$ exp refers to the experimental m/z value of each species, whereas m/z $[L+M]^+$ calc refers to the corresponding theoretical calculated m/z value. δm describes the precision of the measure (m/z) (in ppm, or [(m/z)measured - (m/z)theoretical]/(m/z)theoretical × 10^6). K_0 is the reduced mobility constant, with $K_0 = K \times (273/T) \times (P/760)$, where K is the mobility coefficient of the ion in $cm^2/V/s$, T is the absolute temperature in Kelvin (fixed at 298 K) and P is the pressure in Torr of the N_2 gas through which ions move (set to get an accurate CCS for a m/z 622 compound). The CCS (or Ω) is related to the ion mobility according to the following equation: $K=3/16*\sqrt{(2\pi/\mu \times k_B \times T)} \times (ze/N \times \Omega)$ where µ is the reduced mass of the ion-gas pair (µ = mM/(m + M), with m and M the ion and gas-particle masses), k_B is the Boltzmann constant, and ze is the analyte charge [95]. r_{ion} is the ionic radius of metal cations in Å. Note that the CCS values measured here are highly reproducible with replicates having <0.3% relative standard deviation (RSD) (< 0.6 % in previous work for traveling wave mobility techniques) [96, 97]. Typically, the RSD values reported in the literature are < 2 % deviation (uniform field mobility techniques)[98] (see Supporting Information for further details).

The observed ion mobilities of the metallated forms correlate well with theoretical ionic radii of the divalent transition metal cations (high spin, pentacoordinate) [Mn(II) > Fe(II) > Co(II) > Zn(II) > Ni(II) > Cu(II)], except Fe1P whose MS peak shows the presence of an additional water molecule (Figure 3, Table 3) [93]. Metal complexes can form hydrogen bonds with water molecules when in solution [94]. The difference between Fe1 and Fe1P may be related to the presence of a more hydrophobic environment for Fe1P (presence of an additional propyl group) which protects Fe1P from the loss of a water molecule. In the case of enPI2 and Cu(II), the correlation with CCS matched better with an ionic radius for a high spin tetra-coordination, maybe suggesting a partial ligand dechelation (Figure 3). Overall, this specificity of CCS with the coordinated metal ions opens up interesting perspectives for the study of speciation in LMW metal complexes and, here, for the characterization of the complexes in cell lysates after cell incubation with Mn1 or Mn1P. Note that the intensity of peaks in the mobilograms does not depend on the ion mobility but on the efficiency of electrospray ionization of a metal complex. No models allowing a correlation of the efficiency of electrospray ionization with the structure of metal complexes are available.

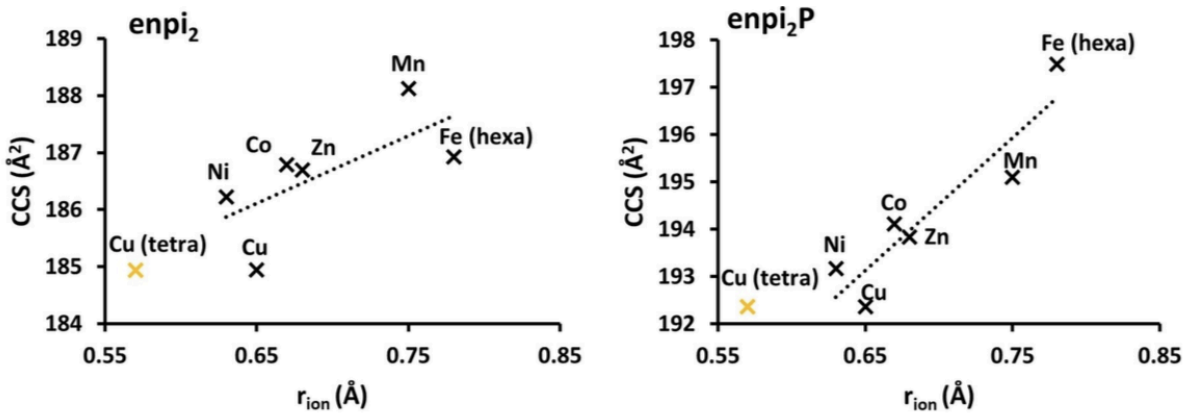

Figure 3: Collision cross-section in Å² plotted against the ionic radius of metal cations in Å. The r_{ion} of any M(II) corresponds to a high spin penta- coordination, except for Fe(II) (high-spin hexa-coordination). The r_{ion} for Cu(II) is also shown (in yellow) for a high-spin tetra-coordination. The r_{ion} values were taken from http://abulafia.mt.ic.ac.uk/shannon/ptable.php.[76]

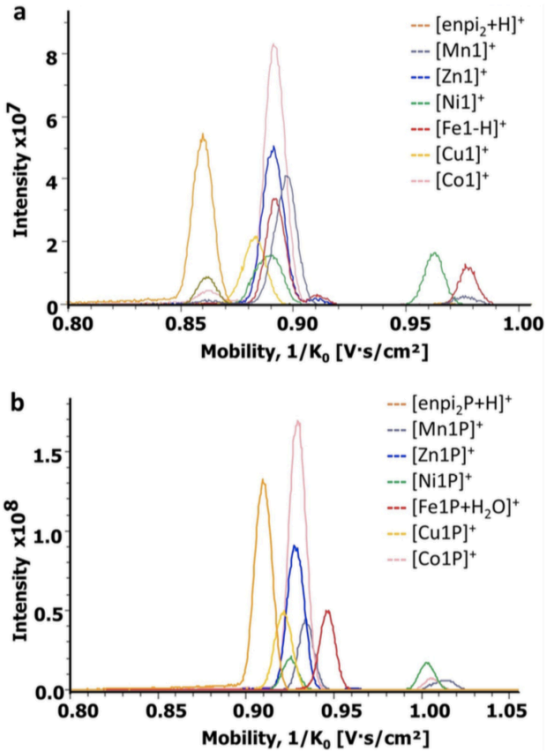

Figure 4: Overlay of extracted ion mobilograms of pure solutions of each complex (20 µM). a) IM of $[enPI_2+H]^+$, $[Mn1]^+$, $[Zn1]^+$, $[Ni1]^+$, $[Fe1\text{-}H]^+$, $[Cu1]^+$, $[Co1]^+$ and b) $[enPI_2P+H]^+$, $[Mn1P]^+$, $[Zn1P]^+$, $[Ni1P]^+$, $[Fe1P+H_2O]^+$, $[Cu1P]^+$, $[Co1P]^+$ were extracted with their corresponding theoretical m/z (see Table S3) with 5 mDa precision. All complexes were analyzed separately at 20 µM in 80 % ACN/20 % NH_4HCO_3 50 mM pH 7.4.

- Towards the use of IMS-MS to detect metal complexes in cells

ESI-MS with a metal-free ionization source allowed the detection of Mn1 (resp. Mn1P) at m/z 408.1465 (resp. m/z 450.1935) (Figure S7a) by direct infusion of pure Mn1 (resp. Mn1P) solutions (50 µM in 20 % NH_4HCO_3 50 mM pH 7.4/ 80 % ACN). Optimal ionization was observed for 80 % ACN (Figure S8). No other metal ions were observed in the pure Mn1 (resp. Mn1P) samples when analyzed by ICP-MS (Figure S9). When cell-lysates of LPS-activated HT29-MD2 cells incubated with Mn1 (100 µM, 6 h) were analyzed using direct infusion in ESI-MS, the peak of Mn1 was not seen amongst other more abundant cellular species (Figure S7b), highlighting the need for a second dimension. Note that using LC-ESI-MS, when we analyzed pure Mn1 in solution, complexes with divalent transition metals other than Mn(II) were observed, showing the release of transition metals ions from the analytical system (Figure S10).

Interestingly, no metal exchange was detectable from a pure solution Mn1 (resp. Mn1P) at 50 µM when analyzed by IMS-MS direct infusion (Figures S11a, 12a). Similarly, when the ligands, $enPI_2$ and $enPI_2P$, were injected, they were not found metallated (Figures S11b, 12b), highlighting the fact that at 50 µM, no contamination from the analytical system was detectable. Nevertheless, when pure solutions of Mn1 or Mn1P were injected at lower

concentrations, some exchange with Zn was observed. When Mn1 was injected at 2 µM, although the Mn analogue was the more abundant species, a peak ratio of $[Zn1]^+/[Mn1]^+$ of 1/3 was observed, and $[Zn1]^+$ contribution was higher than $[Mn1]^+$ when a solution of Mn1 at 0.02 µM was injected (Figure S13a). Similarly, the $[Zn1]^+/[Mn1]^+$ ratio was 1/8 when Mn1P was injected at 2 µM and was 1/3 when injected at 0.02 µM (Figure S14a). Clearly, when comparing Figure S13a and S14a, one can tell that Mn1P experienced less exchange with Zn than Mn1, especially at lower concentrations.

We then explored the effect of the cellular medium. When Mn1 or Mn1P were added to cell lysates at 2 µM, the Zn analogues were the more abundant species both with Mn1 and Mn1P. This showed that the Zn(II) contribution from the cell lysates exceeded the zinc contribution from the IMS-MS system (Figure S13b, S14b), which can then be disregarded. Thus, 2 µM is the threshold for the detection of these Mn-complexes in cell lysates, with minimal interferences from the analytical IMS-MS system.

- Application of IMS-MS to Detect and Quantify SOD Mimics in Cell Lysates Using a Heavy-Ligand ($^{13}C_6$) Co-analogue

IMS-MS was used for Mn complexes detection by IMS-MS direct infusion of HT29-MD2 cell lysates after cell incubation with LPS at 0.1 µg/mL and the compounds at 100 µM for 6 h (see Supporting Information, Figure S15). The complexes were detected in cell lysates in extracted exact mass and exact ion mobilogram of Mn1 or Mn1P (Figure 5a, b, d, e). Thus, combining two orthogonal dimensions (ion mobility and exact mass) is an efficient approach for characterizing metal complexes in intricate biological environments, showing here unambiguously that both Mn1 and Mn1P are present at least partly intact in lysates of cells incubated with the compounds.

In addition to the IMS-MS signature of Mn1 (resp. Mn1P), we extracted peaks corresponding to Zn1 (resp. Zn1P), indicating metal exchanges (Figures 5c–f, S16). In the case of Mn1, we also observed peaks resulting from dehydrogenation (Mn1-H and Fe1-H overlapping with Mn1) (Figure 5c). Interestingly, IMS-MS is powerful enough to distinguish between isobaric Mn1 and Fe1-H. However, the overlapping of the peaks prevented a reliable quantification of low cellular levels of Mn1. Since Mn1P undergoes fewer metal exchange events in cells (Figure S16) and cannot be dehydrogenated (Figure 5f), it was the most suitable candidate to attempt intracellular quantification using an internal standard.

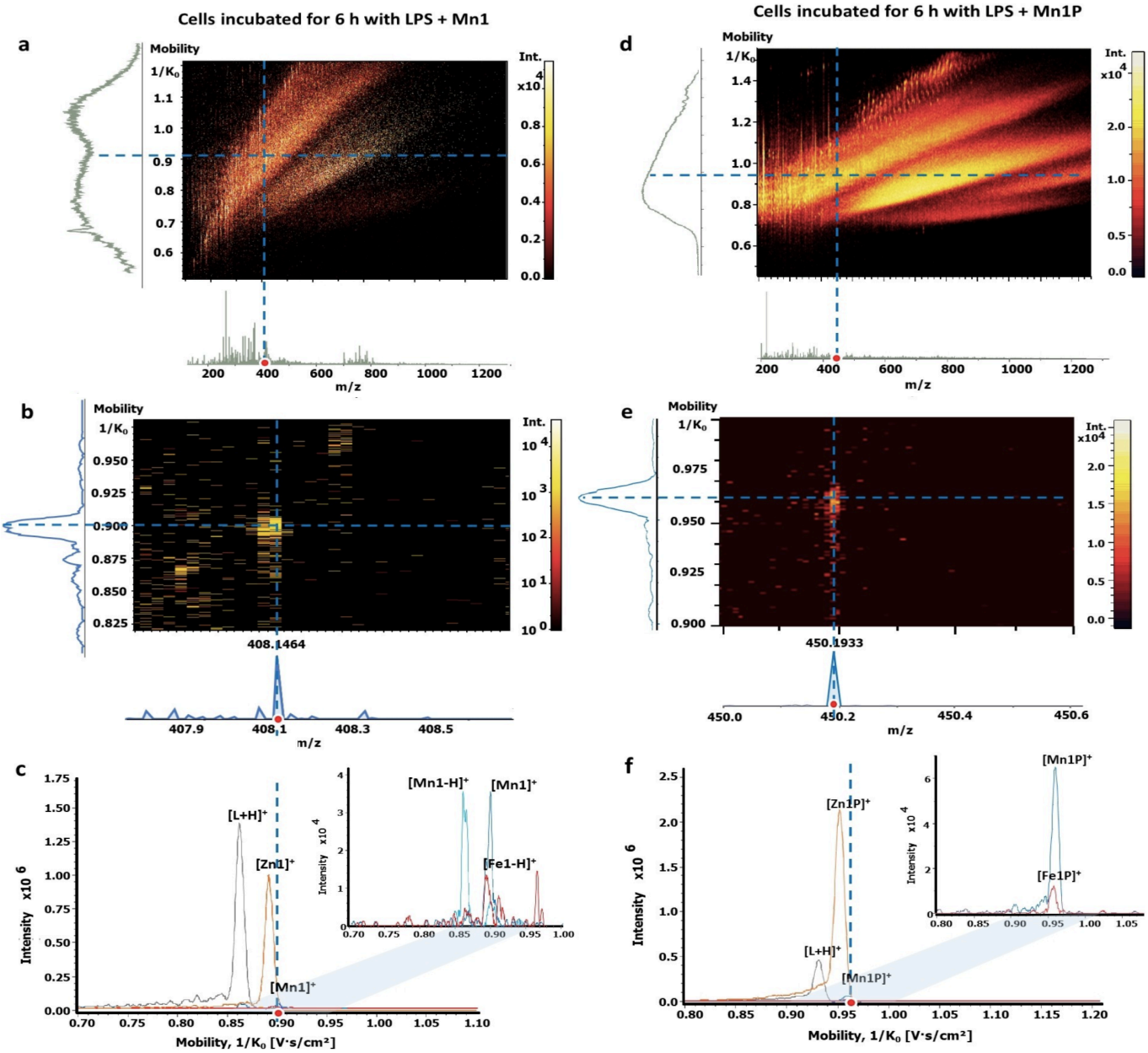

Figure 5: Detection of Mn1 and Mn1P in cell lysates by IMS-MS. Cells were incubated with Mn1 or Mn1P (100 µM) and LPS (0.1 µg/mL) for 6 h and corresponding cell lysates were ionized in 80 % ACN/20 % NH_4HCO_3 50 mM pH 7.4. Full heat maps with corresponding IMS and MS spectra for a) Mn1 and d) Mn1P. Extracted heat maps with corresponding IMS and MS spectra for b) Mn1 and e) Mn1P. The IM of $[Mn1]^+$ was extracted at 408.1465 m/z, 0.909 V.s/cm², and of $[Mn1P]^+$ at 450.1933 m/z, 0.960 V.s/cm² with 5 mDa precision. Corresponding extracted ion mobilograms for c) Mn1 and f) Mn1P. The IM of $[Mn1]^+$, $[Mn1\text{-}H]^+$, $[Fe1\text{-}H]^+$, $[L+H]^+$, $[Zn1]^+$ and $[Mn1P]^+$, $[Fe1P]^+$, $[LP+H]^+$, $[Zn1P]^+$ were extracted with their corresponding theoretical m/z (see Table S3) with 5 mDa precision.

We decided to use Co1$^{13}C_6$P (Figure 6a) as an internal standard because a) Co1$^{13}C_6$P and Mn1P are structurally very similar and possess the same charge, b) Co(II) is not naturally present in cells, c) no metal exchange was observed for Co1$^{13}C_6$P (resp. enPI$_2$$^{13}C_6$P) at 50 µM by IMS-MS (Figure S17) and d) no exchange was observed between Mn1P and Co1$^{13}C_6$P, or between Zn1P and Co1$^{13}C_6$P (1:1 by ESI-MS) even after 24 h (Figure S18). This showed that Co1$^{13}C_6$P was sufficiently stable and inert. Using a heavy analogue of the ligand (enPI$_2$$^{13}C_6$P instead of

enPI$_2$P) has the additional advantage to enable tracking of possible exchange between Mn1P and the standard in cell lysates, and little exchange of Co-Zn was seen in cell lysates. As the intensities are dependent on the ionization properties of Mn1P and Co1P (see Figure 4b), a calibration curve was established in a pure buffer/ionization solution for the quantification of Mn1P (Figure S19). After incubation with Mn1P and LPS, the cell lysates (see Supporting Information) were spiked with Co1$^{13}C_6$P at 0.02 µM. The estimate of the Mn1P concentration in the injected solution of cell lysate (see Supporting Information) was 0.017 to 0.005 µM (corresponding to 0.093±0.028 µM in the cell lysate). The intracellular Mn1P concentration was estimated at 0.013±0.006 fmol/cell (Figures 6b, S19, Table S4). This value corresponds to a minimal quantity of Mn1P found in the cells, as exchange or dissociation may have occurred during the lysis process and sample preparation, associated with the possible release of metal cation, here seemingly mainly Zn(II), from biological coordination and dilution.

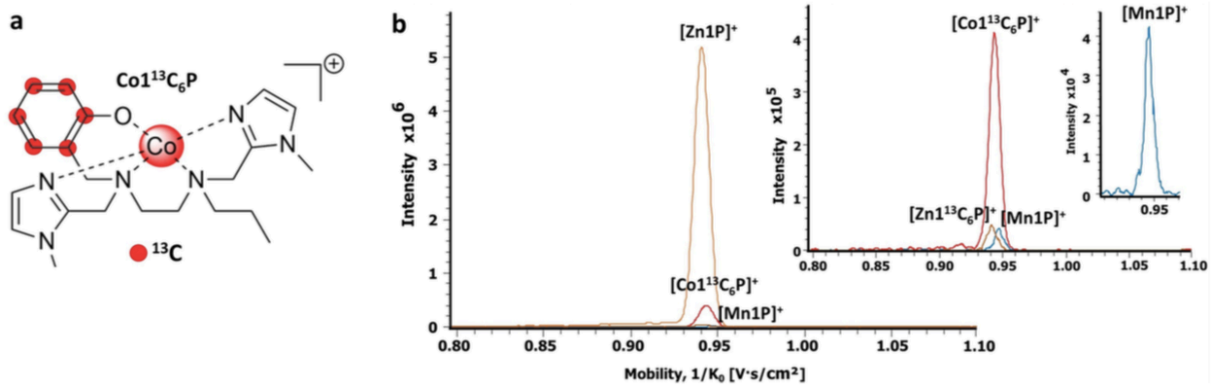

Figure 6: Quantification of Mn1P in cell lysates. a) Chemical structure of $^{13}C_6$-labeled propylated internal standard (Co1$^{13}C_6$P). b) Extracted ion mobilogram of cell lysate from cells incubated with Mn1P (100 µM) and LPS (0.1 µg/mL) for 6 h, spiked with Co1$^{13}C_6$P at 0.02 µM, just before IMS-MS analysis in 80% ACN/20% NH_4HCO_3 50 mM pH 7.4. The IM of [Co1$^{13}C_6$P]$^+$, [Mn1P]$^+$, [Zn1P]$^+$, [Zn1$^{13}C_6$P]$^+$ were extracted with their corresponding theoretical m/z (see Table S3) with 5 mDa precision.

Conclusion

In summary, we have demonstrated that the intracellular detection of the Mn1 and Mn1P SOD mimics can be performed using IMS-MS. This technique allowed efficient discrimination between the various metallic analogues of LMW complexes. This study exemplifies the IMS-MS potential for LMW molecules with the same charge and minor shape changes associated with small ionic radius differences between metal ions: for instance, Fe1 and Mn1 with $\Delta r_{ion}/r_{ion}$ of 4% could be distinguished by IMS-MS. Compared to LC-MS, very little metal release was observed from the IMS-MS analytical system, which allowed the characterization of labile complexes with negligible metal exchange from the analytical system. Therefore, the two-dimensionality of IMS-MS, involving both ion mobility and m/z ratio can be used to track LMW

complexes in an intricate environment such as a cell lysate. This study shows unambiguously that both intact Mn1 and Mn1P are present in cell lysates after cells incubation with the complexes. In the case of Mn1P, we were able to establish a dynamic range to analyze the cell lysates for which the metal exchange was associated, not with the analytical system, but only with the metals pool from the cell lysate. Quantification with a heavy $^{13}C_6$-Co analogue allowed us to estimate the content of Mn1P in cells.

Acknowledgements

ANR (ANR-10-IDEX-0001-02 PSL and ANR-15-CE07- 0027-MAGIC), Fondation pour la Recherche Biomédicale (DEI20151234413), IDEX ENS-PSL (ANR-10-IDEX-0001- 02 PSL) are acknowledged for financial support and M.Z.'s Ph.D. fellowship (ANR-15-CE07-0027-MAGIC). Sorbonne Université and the program IPV (interface pour le vivant) are acknowledged for G.S.'s Ph.D. fellowship, Conseil scientifique régional Ile de France for financial support (Sesame 2010-10022268 & 2018-EX039194). Financial sup- port from the National FT-ICR network (FR 3624 CNRS) is gratefully acknowledged. CNRS and the program MITI (mission pour les initiatives transverses et l'interdisciplinarité) are acknowledged for funding (call Metallomix, project ANACOMDA). We thank ENS-PSL, Sorbonne Université, CNRS for recurrent funding. We thank S. Shakir for help with LC-MS, B. Goetz and P. Legeay for help with ICP-MS, and L. Brot for help with cell culture.

* We thank one of the reviewers for this wise remark, that gives the efforts for detecting whole SOD mimics in cell lysates additional value.

Conflict of Interest

P. Seksik has received personal fees from Takeda, Merck MSD, Biocodex, Ferring, Fresenius Kabi, Astellas, Amgen, Pfizer, Pilege and Abbvie but has no conflict of interest linked to this work.

Data Availability Statement

The data that support the findings of this study are available in the Supporting Information of this article.

References

[1] R. McRae, P. Bagchi, S. Sumalekshmy, C. J. Fahrni, Chem. Rev. 2009, 109, 4780–4827.
[2] S. Banerjee, A. R. Chakravarty, Acc. Chem. Res. 2015, 48, 2075–2083.
[3] T. Zou, C. T. Lum, S. S.-Y. Chui, C.-M. Che, Angew. Chem. Int. Ed. 2013, 52, 2930–2933; Angew. Chem. 2013, 125, 3002–3005.

[4] F. Schmitt, P. Govindaswamy, G. Süss-Fink, W. H. Ang, P. J. Dyson, L. Juillerat-Jeanneret, B. Therrien, J. Med. Chem. 2008, 51, 1811–1816.
[5] E. Mathieu, A.-S. Bernard, E. Quévrain, M. Zoumpoulaki, S. Iriart, C. Lung-Soong, B. Lai, K. Medjoubi, L. Henry, S. Nagarajan, F. Poyer, A. Scheitler, I. Ivanović-Burmazović, S. Marco, A. Somogyi, P. Seksik, N. Delsuc, C. Policar, Chem. Commun. 2020, 56, 7885–7888.
[6] F. Zobi, L. Quaroni, G. Santoro, T. Zlateva, O. Blacque, B. Sarafimov, M. C. Schaub, A. Yu Bogdanova, J. Med. Chem. 2013, 56, 6719–6731.
[7] K. V. Kong, W. Chew, L. H. K. Lim, W. Y. Fan, W. K. Leong, Bioconjugate Chem. 2007, 18, 1370–1374.
[8] S. Clède, N. Cowan, F. Lambert, H. C. Bertrand, R. Rubbiani, M. Patra, J. Hess, C. Sandt, N. Trcera, G. Gasser, J. Keiser, C. Policar, ChemBioChem 2016, 17, 1004–1007.
[9] L. Henry, N. Delsuc, C. Laugel, F. Lambert, C. Sandt, S. Hostachy, A.-S. Bernard, H.C. Bertrand, L. Grimaud, A. Baillet-Guffroy, C. Policar, Bioconjugate Chem. 2018, 29, 987– 991.
[10] S. Clède, N. Delsuc, C. Laugel, F. Lambert, C. Sandt, A. Baillet-Guffroy, C. Policar, Chem. Commun. 2015, 51, 2687– 2689.
[11] S. Clède, F. Lambert, C. Sandt, Z. Gueroui, M. Réfrégiers, M.- A. Plamont, P. Dumas, A. Vessières, C. Policar, Chem. Commun. 2012, 48, 7729.
[12] C. Policar, J. B. Waern, M.-A. Plamont, S. Clède, C. Mayet, R. Prazeres, J.-M. Ortega, A. Vessières, A. Dazzi, Angew. Chem. Int. Ed. 2011, 50, 860–864; Angew. Chem. 2011, 123, 890–894.
[13] P. Hildebrandt, Angew. Chem. Int. Ed. 2010, 49, 4540–4541; Angew. Chem. 2010, 122, 4642–4644.
[14] K. Meister, J. Niesel, U. Schatzschneider, N. Metzler-Nolte, D. A. Schmidt, M. Havenith, Angew. Chem. Int. Ed. 2010, 49, 3310–3312; Angew. Chem. 2010, 122, 3382–3384.
[15] J. S. Becker, J. Mass Spectrom. 2013, 48, 255–268.
[16] L. Mueller, A.J. Herrmann, S. Techritz, U. Panne, N. Jakubowski, Anal. Bioanal. Chem. 2017, 409, 3667–3676.
[17] J. H. Lovett, H. H. Harris, Curr. Opin. Chem. Biol. 2021, 61, 135–142.
[18] E. M. Bolitho, C. Sanchez-Cano, H. Shi, P. D. Quinn, M. Harkiolaki, C. Imberti, P. J. Sadler, J. Am. Chem. Soc. 2021, 143, 20224–20240.
[19] F. Fus, Y. Yang, H. Z. S. Lee, S. Top, M. Carriere, A. Bouron, A. Pacureanu, J. C. da Silva, M. Salmain, A. Vessières, P. Cloetens, G. Jaouen, S. Bohic, Angew. Chem. Int. Ed. 2019, 58, 3461–3465; Angew. Chem. 2019, 131, 3499–3503.
[20] A. Enriquez Garcia, B. Lai, S. G. Gopinathan, H. H. Harris, C. S. Shemanko, F. Jalilehvand, Chem. Commun. 2019, 55, 8223–8226.
[21] J. J. Conesa, A. C. Carrasco, V. Rodríguez-Fanjul, Y. Yang, J. L. Carrascosa, P. Cloetens, E. Pereiro, A. M. Pizarro, Angew. Chem. Int. Ed. 2020, 59, 1270–1278; Angew. Chem. 2020, 132, 1286–1294.
[22] E. Mathieu, A.-S. Bernard, H. Y. V. Ching, A. Somogyi, K. Medjoubi, J. R. Fores, H. C. Bertrand, A. Vincent, S. Trépout, J.-L. Guerquin-Kern, A. Scheitler, I. Ivanović-Burmazović, P. Seksik, N. Delsuc, C. Policar, Dalton Trans. 2020, 49, 2323– 2330.
[23] S. Hostachy, M. Masuda, T. Miki, I. Hamachi, S. Sagan, O. Lequin, K. Medjoubi, A. Somogyi, N. Delsuc, C. Policar, Chem. Sci. 2018, 9, 4483–4487.
[24] S. Hostachy, C. Policar, N. Delsuc, Coord. Chem. Rev. 2017, 351, 172–188.
[25] E. Mathieu, A.-S. Bernard, N. Delsuc, E. Quévrain, G. Gazzah, B. Lai, F. Chain, P. Langella, M. Bachelet, J. Masliah, P. Seksik, C. Policar, Inorg. Chem. 2017, 56, 2545–2555.
[26] C. M. Weekley, I. Kenkel, R. Lippert, S. Wei, D. Lieb, T. Cranwell, J. L. Wedding, A. S. Zillmann, R. Rohr, M. R. Filipovic, I. Ivanović-Burmazović, H. H. Harris, Inorg. Chem. 2017, 56, 6076–6093.
[27] S. Clède, C. Policar, Chem. Eur. J. 2015, 21, 942–958.
[28] J. B. Aitken, E. L. Shearer, N. M. Giles, B. Lai, S. Vogt, J. S. Reboucas, I. Batinic-Haberle, P. A. Lay, G. I. Giles, Inorg. Chem. 2013, 52, 4121–4123.
[29] J. B. Waern, H. H. Harris, B. Lai, Z. Cai, M. M. Harding, C. T.Dillon, J. Biol. Inorg. Chem. 2005, 10, 443–452.
[30] C. Ionescu, P. Grill, H. Witte, C. Boigues, A. Blanchard, B. Löffler, B. Michalke, J. Trace Elem. Med. Biol. 2019, 56, 207–212.
[31] M. R. M. Williams, B. Bertrand, D. L. Hughes, Z. A. E. Waller, C. Schmidt, I. Ott, M. O'Connell, M. Searcey, M. Bochmann, Metallomics 2018, 10, 1655–1666.
[32] S. P. McCormick, M. J. Moore, P. A. Lindahl, Biochemistry, 2015, 54, 3442–3453.
[33] M. Groessl, O. Zava, P. J. Dyson, Metallomics 2011, 3, 591– 599.
[34] M. Tsednee, Y.-C. Huang, Y.-R. Chen, K.-C. Yeh, Sci. Rep. 2016, 6, 1–13.
[35] J. Wojcieszek, P. Kwiatkowski, L. Ruzik, J. Chromatogr. A 2017, 1492, 70–78.
[36] C. Støving Dam, S. Alejo Perez Henarejos, T. Tsolakou, C. Alexander Segato, B. Gammelgaard, G. S. Yellol, J. Ruiz, I. Henry Lambert, S. Stürup, Metallomics 2015, 7, 885–895.
[37] C. J. Murgas, S. P. Green, A. K. Forney, R. M. Korba, S.-S. An, T. Kitten, H. R. Lucas, ACS Infect. Dis. 2020, 6, 1906– 1921.
[38] J. Schur, A. Lüning, A. Klein, R. W. Köster, I. Ott, Inorg. Chim. Acta 2019, 495, 118982.
[39] P. Hikisz, Ł. Szczupak, A. Koceva-Chyła, A. Guśpiel, L. Oehninger, I. Ott, B. Therrien, J. Solecka, K. Kowalski, Molecules 2015, 20, 19699–19718.
[40] T. V. Serebryanskaya, A. S. Lyakhov, L. S. Ivashkevich, J. Schur, C. Frias, A. Prokop, I. Ott, Dalton Trans. 2015, 44, 1161–1169.
[41] F. Liu, F. Pei, A. M. Mariga, L. Gao, G. Chen, L. Zhao, J. Food Drug Anal. 2015, 23, 630–635.
[42] J. Schur, C. M. Manna, A. Deally, R. W. Köster, M. Tacke, E. Y. Tshuva, I. Ott, Chem. Commun. 2013, 49, 4785.

[43] S. I. Kirin, I. Ott, R. Gust, W. Mier, T. Weyhermüller, N. Metzler-Nolte, Angew. Chem. Int. Ed. 2008, 47, 955–959; Angew. Chem. 2008, 120, 969–973.
[44] I. Ott, H. Scheffler, R. Gust, ChemMedChem 2007, 2, 702–707. [45] Z. Garda, E. Molnár, N. Hamon, J. L. Barriada, D. Esteban- Gómez, B. Váradi, V. Nagy, K. Pota, F. K. Kálmán, I. Tóth, N. Lihi, C. Platas-Iglesias, É. Tóth, R. Tripier, G. Tircsó, Inorg. Chem. 2021, 60, 1133–1148.
[46] D. Ndiaye, M. Sy, A. Pallier, S. Même, I. de Silva, S. Lacerda, A. M. Nonat, L. J. Charbonnière, É. Tóth, Angew. Chem. Int. Ed. 2020, 59, 11958–11963; Angew. Chem. 2020, 132, 12056– 12061.
[47] S. Laine, C. S. Bonnet, F. K. Kálmán, Z. Garda, A. Pallier, F. Caillé, F. Suzenet, G. Tircsó, É. Tóth, New J. Chem. 2018, 42, 8012–8020.
[48] M. Yu, M. B. Ward, A. Franke, S. L. Ambrose, Z. L. Whaley, T. M. Bradford, J. D. Gorden, R. J. Beyers, R. C. Cattley, I. Ivanović-Burmazović, D. D. Schwartz, C. R. Goldsmith, Inorg. Chem. 2017, 56, 2812–2826.
[49] E. M. Gale, I. P. Atanasova, F. Blasi, I. Ay, P. Caravan, J. Am. Chem. Soc. 2015, 137, 15548–15557.
[50] E. M. Gale, S. Mukherjee, C. Liu, G. S. Loving, P. Caravan, Inorg. Chem. 2014, 53, 10748–10761.
[51] G. S. Loving, S. Mukherjee, P. Caravan, J. Am. Chem. Soc. 2013, 135, 4620–4623.
[52] C. Policar, J. Bouvet, H. C. Bertrand, N. Delsuc, Curr. Opin. Chem. Biol. 2022, 67, 102109.
[53] R. Bonetta, Chem. Eur. J. 2018, 24, 5032–5041.
[54] C. Policar, in Redox-Active Therapeutics (Eds.: I. Batinic- Haberle, J. Reboucas, I. Spasojević), Springer Science, New-York, 2016, pp. 125–164.
[55] I. Batinic-Haberle, A. Tovmasyan, I. Spasojevic, Redox Biol. 2015, 5, 43–65.
[56] S. Miriyala, I. Spasojevic, A. Tovmasyan, D. Salvemini, Z. Vujaskovic, D. St Clair, I. Batinic-Haberle, Biochim. Biophys. Acta Mol. Basis Dis. 2012, 1822, 794–814.
[57] O. Iranzo, Bioorg. Chem. 2011, 39, 73–87.
[58] I. Batinić-Haberle, J.S. Rebouças, I. Spasojević, Antioxid. Redox Signaling 2010, 13, 877–918.
[59] S. Signorella, C. Palopoli, G. Ledesma, Coord. Chem. Rev. 2018, 365, 75–102.
[60] J. D. Aguirre, V. C. Culotta, J. Biol. Chem. 2012, 287, 13541–13548.
[61] J. P. Lisher, D. P. Giedroc, Front. Cell. Infect. Microbiol. 2013,3, https://doi.org/10.3389/fcimb.2013.00091.
[62] F. Basolo, R. G. Pearson, Mechanisms of Inorganic Reactions a Study of Metal Complexes in Solution, Wiley, New York, 1967.
[63] M. Gerloch, E.C. Constable, Transition Metal Chemistry,VCH, New York, 1994.
[64] H. Irving, R. J. P. Williams, J. Chem. Soc. 1953, 3192–3210.
[65] H. Irving, R. J. P. Williams, Nature 1948, 162, 746–747.
[66] Y. Inada, T. Sugata, K. Ozutsumi, S. Funahashi, Inorg. Chem. 1998, 37, 1886–1891.
[67] S. F. Lincoln, A. E. Merbach in Advances in Inorganic Chemistry (Eds.: A. G. Sykes), Academic Press, San Diego,1995, pp. 1–88.
[68] P. Flis, L. Ouerdane, L. Grillet, C. Curie, S. Mari, R. Lobinski,
[69] G. Schanne, M. Zoumpoulaki, G. Gazzah, A. Vincent, H. Preud'homme, R. Lobinski, S. Demignot, P. Seksik, N. Delsuc, C. Policar, Oxid. Med. Cell. Longev., 2022, 2022, e3858122.
[70] M. J. Cohen, F. W. Karasek, J. Chromatogr. Sci. 1970, 8, 330– 337.
[71] J. C. May, J. A. McLean, Anal. Chem. 2015, 87, 1422–1436.
[72] R. Cumeras, E. Figueras, C. E. Davis, J. I. Baumbach, I. Gràcia, Analyst 2015, 140, 1376–1390.
[73] G. A. Eiceman, Z. Karpas, H. H. Hill, Jr., Ion Mobility Spectrometry, CRC, Boca Raton, 2013.
[74] E. Kalenius, M. Groessl, K. Rissanen, Nat. Chem. Rev. 2019, 3, 4–14.
[75] F. Lanucara, S. W. Holman, C. J. Gray, C. E. Eyers, Nat. Chem. 2014, 6, 281–294.
[76] B. A. Link, A. J. Sindt, L. S. Shimizu, T. D. Do, Phys. Chem. Chem. Phys. 2020, 22, 9290–9300.
[77] A. Kruve, K. Caprice, R. Lavendomme, J. M. Wollschläger, S. Schoder, H. V. Schröder, J. R. Nitschke, F. B. L. Cougnon, C. A. Schalley, Angew. Chem. Int. Ed. 2019, 58, 11324–11328; Angew. Chem. 2019, 131, 11446–11450.
[78] D. Liu, M. Chen, Y. Li, Y. Shen, J. Huang, X. Yang, Z. Jiang, X. Li, G. R. Newkome, P. Wang, Angew. Chem. Int. Ed. 2018, 57, 14116–14120; Angew. Chem. 2018, 130, 14312–14316.
[79] E. R. Brocker, S. E. Anderson, B. H. Northrop, P. J. Stang, M. T. Bowers, J. Am. Chem. Soc. 2010, 132, 13486–13494.
[80] Z. Du, R. E. F. de Paiva, K. Nelson, N. P. Farrell, Angew. Chem. Int. Ed. 2017, 56, 4464–4467; Angew. Chem. 2017, 129, 4535–4538.
[81] D. M. Templeton, F. Ariese, R. Cornelis, L.-G. Danielsson, H. Muntau, H. P. van Leeuwen, R. Lobinski, Pure Appl. Chem. 2000, 72, 1453–1470.
[82] F. Cisnetti, A.-S. Lefèvre, R. Guillot, F. Lambert, G. Blain, E. Anxolabéhère-Mallart, C. Policar, Eur. J. Inorg. Chem. 2007, 4472–4480.
[83] S. Durot, C. Policar, F. Cisnetti, F. Lambert, J.-P. Renault, G. Pelosi, G. Blain, H. Korri-Youssoufi, J.-P. Mahy, Eur. J. Inorg. Chem. 2005, 3513–3523.
[84] C. Policar, S. Durot, F. Lambert, M. Cesario, F. Ramiandrasoa, I. Morgenstern-Badarau, Eur. J. Inorg. Chem. 2001, 1807–1818.
[85] A.-S. Bernard, C. Giroud, H. Y. V. Ching, A. Meunier, V. Ambike, C. Amatore, M. G. Collignon, F. Lemaître, C. Policar, Dalton Trans. 2012, 41, 6399–6403.
[86] W. H. Koppenol, D. M. Stanbury, P. L. Bounds, Free Radical Biol. Med. 2010, 49, 317–322.

[87] A. Vincent, M. Thauvin, E. Quévrain, E. Mathieu, S. Layani, P. Seksik, I. Batinic-Haberle, S. Vriz, C. Policar, N. Delsuc, J. Inorg. Biochem. 2021, 219, 111431.
[88] A. Vincent, J. R. Fores, E. Tauziet, E. Quévrain, Á. Dancs, A. Conte-Daban, A.-S. Bernard, P. Pelupessy, K. Coulibaly, P. Seksik, C. Hureau, K. Selmeczi, C. Policar, N. Delsuc, Chem. Commun. 2020, 56, 399–402.
[89] P. Seksik, H. Sokol, V. Grondin, C. Adrie, H. Duboc, B. Pigneur, G. Thomas, L. Beaugerie, G. Trugnan, J. Masliah, M. Bachelet, Innate Immun. 2010, 16, 381–390.
[90] C. Lenoir, C. Sapin, A. H. Broquet, A.-M. Jouniaux, S. Bardin, I. Gasnereau, G. Thomas, P. Seksik, G. Trugnan, J. Masliah, M. Bachelet, Life Sci. 2008, 82, 519–528.
[91] J. M. McCord, I. Fridovich, J. Biol. Chem. 1969, 244, 6049– 6055.
[92] R. F. Pasternack, B. Halliwell, J. Am. Chem. Soc. 1979, 101, 1026–1031.
[93] R. D. Shannon, Acta Crystallogr. Sect. A 1976, 32, 751–767.
[94] J. M. Andrić, M. Z. Misini-Ignjatović, J. S. Murray, P. Politzer, S. D. Zarić, ChemPhysChem 2016, 17, 2035–2042.
[95] V. Gabelica, E. Marklund, Curr. Opin. Chem. Biol. 2018, 42, 51–59.
[96] K. Michelmann, J. A. Silveira, M. E. Ridgeway, M. A. Park, J. Am. Soc. Mass Spectrom. 2015, 26, 14–24.
[97] M. E. Ridgeway, M. Lubeck, J. Jordens, M. Mann, M. A. Park, Int. J. Mass Spectrom. 2018, 425, 22–35.
[98] J. R. N. Haler, C. Kune, P. Massonnet, C. Comby-Zerbino, J. Jordens, M. Honing, Y. Mengerink, J. Far, E. De Pauw, Anal. Chem. 2017, 89, 12076–12086.

II.4. Intra-cellular distribution of SOD mimics

The variations in bioactivity observed over the four Mn1-derived SOD mimics can be explained by differences in inertness but also possibly by different intra-cellular localizations. As a reminder, the ICP-MS quantification of manganese inside cells allows to rule out the argument of difference in cellular penetration. The intra-cellular distribution of SOD mimics is of main importance for bioactivity [238]. Indeed, for an optimal action, the SOD mimics have to reach regions rich in ROS such as the mitochondria.

II.4.a. Nano-scale X-ray fluorescence microscopy approach

We intend to study the intra-cellular distribution of Mn1 derivatives by mapping the manganese content of HT29-MD2 cells treated with the SOD mimics. To this end, we performed X-ray fluorescence microscopy (XFM) experiments. This analytical technique informs on the quantity and location of heavy elements at the single-cell level with high sensitivity and spatial resolution. In particular, the use of nano-Synchrotron X-Ray Fluorescence allows to map metals in subcellular organelles with resolution up to 40 nm [239]. Such nano-scale imaging equipments are available at the French national synchrotron facility (SOLEIL, Saclay) and European Synchrotron Radiation Facility (ESRF, Grenoble).

Prior to their imaging, cells have to be fixed to preserve their structure. This can be achieved either chemically via the use of agents (PFA or methanol) known to cause covalent cross-links between molecules. Cryofixation is another fixation process in which cells are frozen upon ultra-rapid plunging in a liquid ethane bath. The high cooling rate allow to produce amorphous ice which does not disrupt the subcellular structures compared to crystallized ice. The cryofixation is in most cases privileged as it is more efficient in maintaining the native elements bio-distribution and cellular substructures. Indeed, chemical fixation requires washing after PFA or MeOH treatment that can drastically modify the cellular distribution of diffusible low-molecular weight molecules and ions (that are not fixed).

II.4.b. Design of a multi-modal probe targeting mitochondria for X-ray fluorescence imaging

While the XFM technologies are making great advances, there is an important need for X-ray probes enabling organelle localization when doing XFM imaging [239]. As for classical

fluorescence microscopy, such XRF imaging probes targeting specific organelles are indeed essential to interpret metal distribution and subsequently elucidate their physiological functions.

As part of my PhD project, I was also involved in the characterization of a new Rhenium tri-carbonyl probe bearing methylated triphenylphosphonium (mTPP) cations. Thanks to its rhenium center, the probe was remarkably convenient for XRF imaging of chemically-fixed A549 cells (Figure 33) since Re is in extremely low concentration in biological samples leading to very weak background signal [240]. Moreover, excitation of the metal-to-ligand charge transfer band (MLCT) at ca. 330 nm leads to luminescence emission at ca. 550 nm, providing then an additional modality. Classical fluorescence experiments demonstrate the mitochondrial localization of the probe as its signal was colocalized with that of a commercial mitochondria tracker, Mitotracker Deep Red (Figure 34) in PFA-fixed cells.

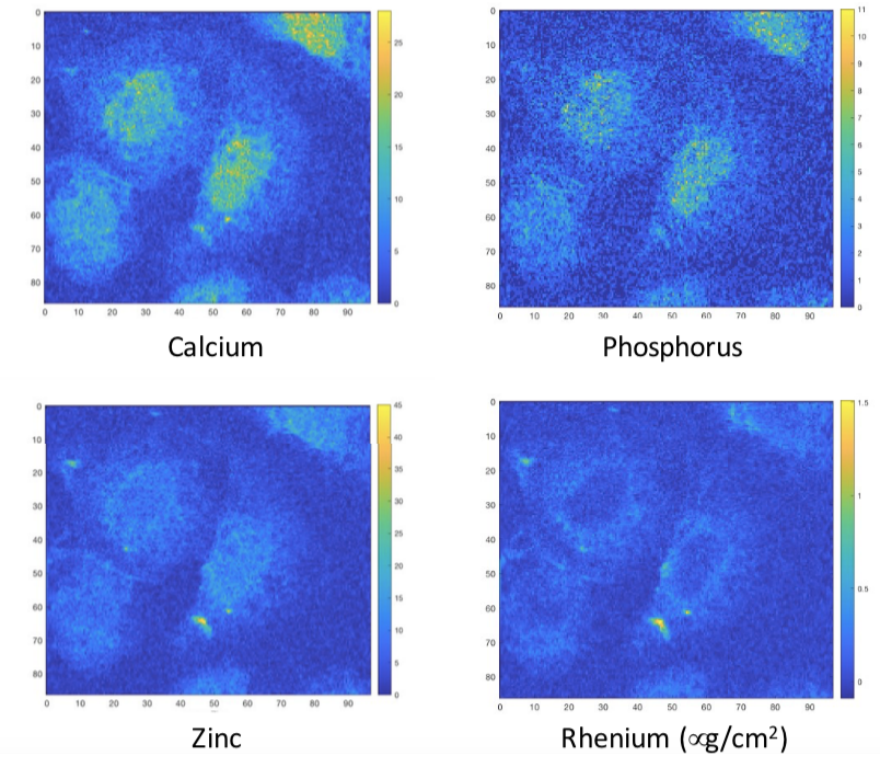

Figure 33: Elemental distributions of Ca, P, Re, and Zn in chemically-fixed A549 cells incubated with the Re-(CO)$_3$-mTPP probe (20 µM, 4 h) (right). The phosphorus (P), and zinc (Zn, K-lines) maps are used to identify the nucleus area. Re was mapped using the Lß lines (~10.15 and 10.28 keV). XFM parameters : excitation at 14 keV; integration time = 300 ms per pixel; pixel size = 500 nm. Scale axis in µm.

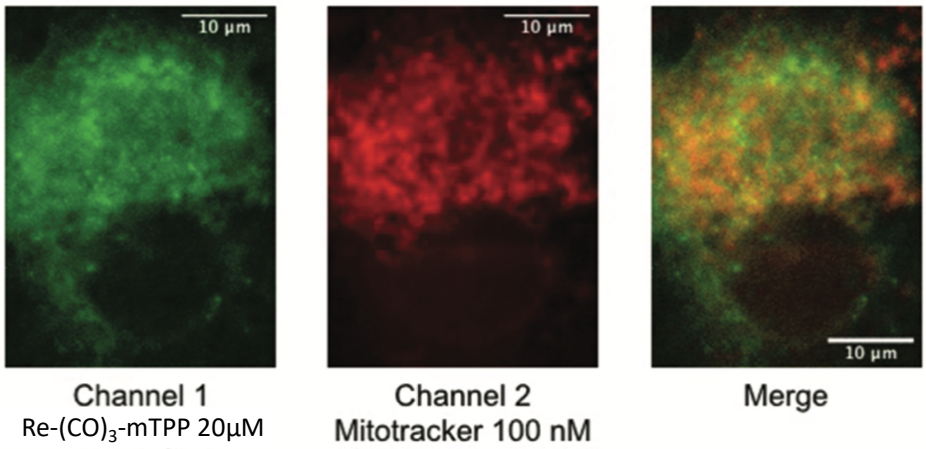

Figure 34: A549 cells incubated with the Re-$(CO)_3$-mTPP probe (20 µM, 4 h) and chemically fixed. Left: fluorescence signal of the conjugate (λ_{exc} 350 nm); middle: fluorescence signal of Mitotracker Deep Red (λ_{exc} 644 nm); right: merge of conjugate (green) and Mitotracker Deep Red (red) with their overlay in yellow.

This work was published in "Inorganic Chemistry Frontiers" journal [241]. I contributed to the photophysical characterization of the studied probes (quantum yield evaluation). I also conducted the cellular imaging experiments by classical and X-ray fluorescence microscopy and processed the obtained images. I have participated in the writing of the manuscript (experimental section, figures and supplementary figures linked to my experiments). The paper and the SI are given in Annex.

Finally, the studied Re-$(CO)_3$-mTPP probe possesses very advantageous multimodal and mitochondria-targeting features. This makes it a valuable alternative to immunolabeling with gold-modified secondary antibodies which may perturb the proteins distributions.

II.4.c. Co-incubation between the SOD mimics and the Re-based XRF probe : nano-XRF imaging.

II.4.c.i. Objectives

In addition to their improved inertness, the better bioactivity of Mn1-C, Mn1-P or Mn1-CP compared to Mn1 could be due to an accumulation of the SOD mimics at the mitochondria. To test this hypothesis, we imaged by nano-XRF microscopy the SOD mimics in HT29-MD2 cells co-incubated with the Re-based XRF mitotracker probe in cryo-fixed samples. A colocalization between the Re signal and that of the Mn would indicate a mitochondrial localization of the SOD mimics. In all cases, the accurate localization of manganese complexes

in cells will answer the question about their cellular distribution and help to understand their beneficial effects in cells.

The Re-based XRF mitotracker probe was not yet validated in cryofixed HT29-MD2 cells but these studies are underway on a classical fluorescence microscope equipped with a special cryogenic stage (cryo-CLEM).

II.4.c.ii. Experimental sections

- Cells preparation

HT29-MD2 cells were grown on Si_3N_4 silicon nitride membranes (purchased from Silson Ltd, membrane size: 1.5 mm x 1.5 mm; membrane thickness: 500 nm) to reach around 50% confluency. The SOD mimics were prepared with a ratio ligand:Mn 1:1.4 for 2 hours in HEPES 100 mM prior to the cell incubation to ensure a complete complexation ligand, known to be cytotoxic ligands. They were then added to the cellular medium (100 µM final concentration) simultaneously with LPS (0.1 µg/mL) and the Re-based mitotracker XRF probe (20 µM). The two Mn- and Re- complexes were allowed to co-incubate with the LPS-stimulated HT29-MD2 cells for 4 hours at 37°C, 5% CO_2.

After incubation, the cells were successively washed with 0.9% NaCl, NaCl 1 M, EDTA 50 mM and again with 0.9% NaCl.

A manual blot of the membranes was then applied to remove the excess aqueous buffer. An insufficient blotting results in a thick ice layer covering the cells after cryofixation, which will partially absorb the X-ray energy and hence decrease the sensitivity. At best, the remaining ice thickness must be around 10-25 µm. Lastly, the cells were cryofixed in liquid ethane and stored immerged in liquid nitrogen until the nano-XRF imaging. For the blotting and cryofixation steps, we followed the detailed protocol published by C. Bissardon *et al*. [242].

- Synchrotron Radiation X-ray Fluorescence (SXRF) Nano-imaging.

The samples were examined on the X-ray beamline ID16a of the European Synchrotron Radiation Facility (ESRF, Grenoble). The incident beam energy was fixed to 17 keV (above the L-edge of Re and K-edge of Mn). During their loading and mapping, the samples were kept frozen thanks to a cryo-transfer system, the cryogenic cooling of the sample stage and the maintenance of a high-vacuum in the sample chamber. The maps were recorded using a

continuous scanning mode with a pixel size of 50 nm and an exposure time per pixel of 50 ms. The imaging of one cell hence required about 2 hours. Coarse scans were beforehand performed with a lower resolution of 400 nm and a longer exposure time of 100 ms to identify interesting cells (rich in K, no metallic hot spot). The fluorescent signal emitted by metallic element was collected in each pixel by two independent X-rays detectors “Arwen” and “Ardesia16”. The registered 2D-images correspond to a projection of the cells in the z-axis normal to the membrane surface. We also conducted 3D XRF nanoimaging by fluotomography. In that case, 2D-images were recorded at 24 different angles with a spatial resolution of 120 nm and an exposure time of 50 ms. The 24 projections were then spatially reconstructed to provide the 3D-distributions of the metallic elements inside the cells. Note that for fluotomography, the choice of the 3D-imaged cell has to be carefully done because one run lasts about 24 hours. In particular, the chosen cell must not be shaded by close neighbor cells because it will be illuminated with low-angled excitation X-rays.

During the synchrotron beamtime, we have imaged 4 LPS-stimulated cells co-incubated with the Re Probe and Mn1 and 6 LPS-stimulated cells co-incubated with the Re Probe and Mn1CP. For these two former conditions, we selected one cell that was imaged in 3D via fluotomography. In order to compare the SOD mimics distribution in a basal context and under oxidative stress, 4 non-activated HT29-MD2 cells co-incubated with the Re-probe and Mn1 were also imaged. As a control, we mapped LPS-stimulated cells incubated with the Re probe only to observe the distribution of endogenous manganese.

- Data processing

The sum XRF spectra were visualized on PyMca software. The wavelengths of the emission lines of interest are given in Table 2. The spectra deconvolution was then performed by PyMca to attribute correctly the overlapping emission lines. This allows to fit unambiguously the full spectra with the contributions of all element and hence to extract their individual distribution map. Following the deconvolution of the XRF signal collected by the two detectors, the weighted sum of each fit was realized, using a MATLAB program developed by the ID16a team, giving then the total weighted distribution maps. Lastly, these arbitrary intensity maps were converted into ng/mm^2 by taking into account the ice thickness and the beforehand calibration of the system with an external standard purchased from Axo. The used standard was not composed of Mn and Re but of Pb, La, PD, Mo, Cu, Fe and Si elements, that are

relevant for the calibration of the fundamental measure parameters. This allows a little bit less precise but sufficient extrapolated quantification in area density of all the elements.

Re	$L_{\alpha,2}$ = 8.59 keV
	$L_{\alpha,1}$ = 8.65 keV
	$L_{\beta,1}$ = 10.01 keV
	$L_{\beta,2}$ = 10.28 keV
	$L_{\gamma,1}$ = 11.69 keV
Mn	$K_{\alpha,2}$ = 5.89 keV
	$K_{\alpha,1}$ = 5.90 keV
	$K_{\beta,1}$ = 6.49 keV

Table 2: Emission line of Re and Mn elements upon X-ray excitation.

The area density maps of elemental K, Mn and Re were processed on Fiji. The intensity scale bar of Mn images was fixed between 0 to 1 ng/mm^2. The colocalization analysis of Mn and Re images were performed using the plugin JacoP implemented on Fiji software.

II.4.c.iii. Results and discussion

- Re elemental distribution

The mapping of Re in HT29-MD2 cells incubated with the Re-$(CO)_3$-mTPP XRF probes are given in Figure 35, Figure S1, Figure S2, Figure S3 and Figure S4. In all cases, a perinuclear accumulation of punctuate appearance consistent with a partial mitochondrial localization was observed. These are encouraging results for the validation of this probe as a mitochondrial marker of cryofixed HT29-MD2 cells for XRF imaging. Sometimes, Re hot spots as in Figure 3 image 4A were observed. These highly concentrated Re spots most probably correspond to Re probe that has precipitated during the incubation.

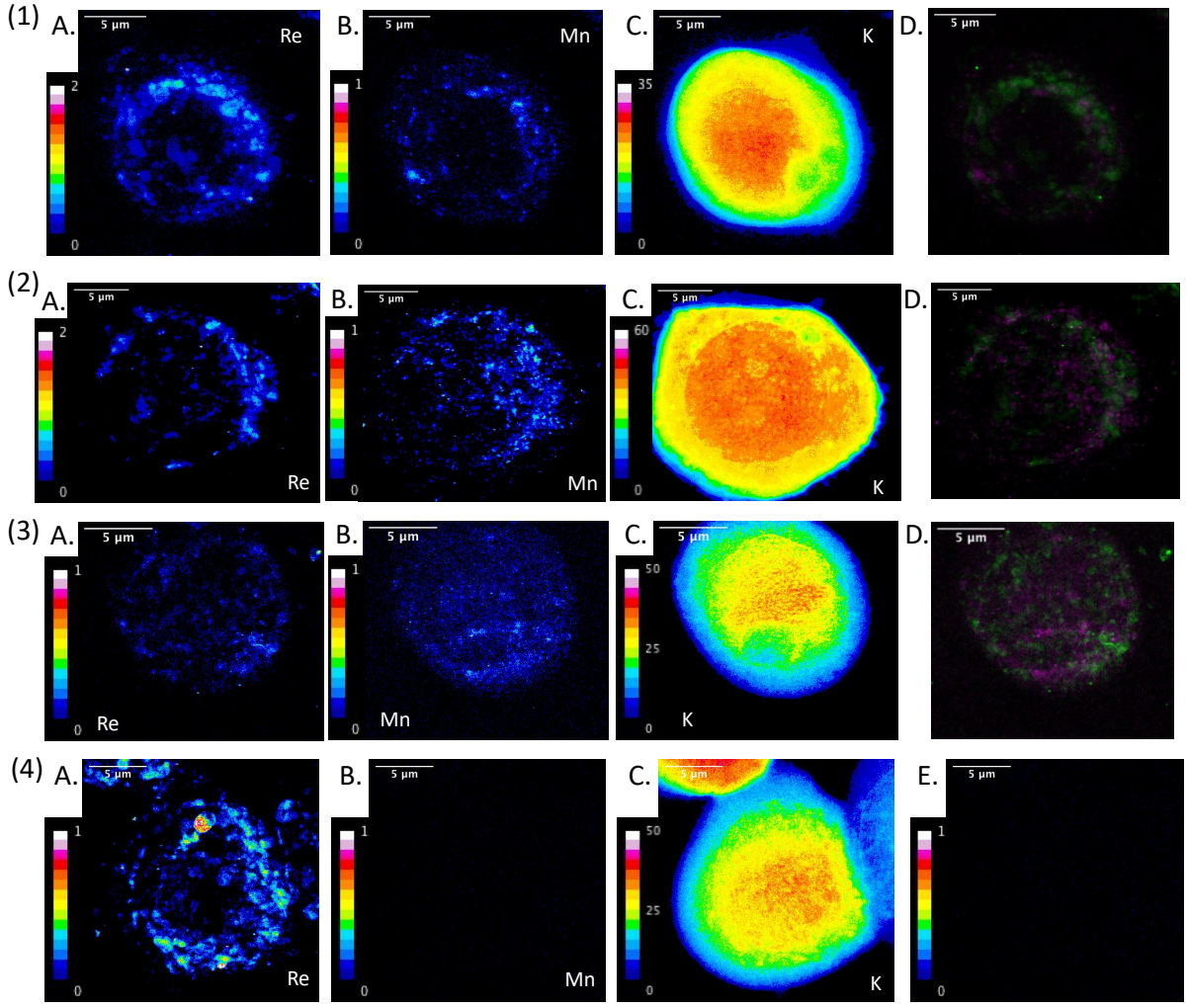

Figure 35: Projected 2D- elemental distributions of A. Re, B. Mn and C. K in HT29-MD2 cells measured by XRF nano-imaging (excitation at 17 keV, pixel size: 50 nm, exposure time: 50 ms). D. corresponds to the merge of Re (green) and Mn (magenta) distributions. The intensity color bar represents the area density (ng/mm^2). The intensity scale bar of Mn images was fixed between 0 to 1 ng/mm^2. K is a highly abundant metal assumed to be homogeneously distributed in cells. Its area density mapping hence informs on the cell depth along z-axis at each pixel. HT29-MD2 were incubated for 4 hours with (1) LPS (0.1 µg/mL) + Mn1 (100 µM) + Re-probe (20 µM) ; (2) LPS (0.1 µg/mL) + Mn1CP (100 µM) + Re-probe (20 µM) ; (3) Mn1 (100 µM) + Re-probe (20 µM) and (4) LPS (0.1µg/mL) + Re-probe (20 µM). The Pearson coefficient for Mn and Re colocalization was found equal to 0.47, 0.64 and 0.32 for (1), (2) and (3), respectively.

- Mn elemental distribution

Figure 35, Figure S1, Figure S2 and Figure S3 also show the intracellular localization of Mn in non-activated or LPS-activated HT29-MD2 cells incubated with Mn1 or Mn1CP. First of all, a relatively intense Mn signal was detected and reached up to 1 ng/mm^2 in the cellular structure. This signal can be attributed to the manganese coming from the SOD mimics since in absence of SOD mimics, the endogenous Mn is hardly detectable (Figure 35: 4B and Figure S4).

For LPS-stimulated cells incubated with Mn1CP, the intracellular distribution of Mn seems more punctuated and localized in the perinuclear region than in LPS-stimulated cells incubated with Mn1 (Figure 35: 1B vs 1A). In order to more quantitatively determine the colocalization of Mn with Re, Pearson coefficients were calculated (Table 3). To note, a coefficient of 1 indicates a perfect co-localization between two signals whereas a coefficient of 0 means that the two signals are not colocalized at all. In average, the Pearson coefficients, between the Re and the Mn maps are higher in the cells incubated with Mn1CP (0.6) than in cells incubated with Mn1 (0.49). This enhanced compartmentalization of Mn1CP compared to Mn1 may have a strong impact on its bioactivity. To finish, surprisingly, the Mn distribution in cells incubated with Mn1 without LPS challenge is even less localized (Figure 35: 3B and Figure S3). This suggests that the LPS- treatment may modify the SOD mimic internalization and compartmentalization. Consistently, E. Mathieu *et. al* have previously demonstrated the homogenous distribution of Mn in non-stimulated HT29-MD2 cells incubated with Mn1 on Nanoscopium beamline (SOLEIL) [237]. Note that they imaged lyophilized cryofixed cells with a lower spatial resolution which may explain why they do not observe any Mn localization at all.

Overall, the colocalization analysis to compare the distribution of Mn with that of Re and the merges of Mn and Re maps orient toward a poor mitochondrial localization of the SOD mimics. Indeed, the Pearson value do not exceed 0.7 and the Re and Mn images scarcely overlap. Still a trend can be observed over the different conditions (Table 3).

HT29-MD2 treatment	Mean Pearson value $\pm$ standard deviation
LPS + Mn1 + Re-based probe	0.49 ± 0.03
LPS + Mn1CP + Re-based probe	0.60 ± 0.09
Mn1 + Re-based probe	0.31 ± 0.17

Table 3: Mean Pearson coefficients calculated via the JacoP module of Fiji to evaluate the colocalization between Re and Mn maps for each cells treatment conditions.

The ranking of increasing Pearson values correlates with the localized character of Mn distribution. Hence, Mn1CP, that displays the most punctuate and localized distribution in LPS-activated cells, present the highest colocalization results with the Re-probe. However, as the Pearson value remains very low, it is tricky to correlate the better bioactivity of Mn1CP with an higher mitochondrial localization.

As all previous maps are 2D projections that may bias the colocalization study, analysis of the 3D- distribution of Mn and Re obtained from fluotomography experiments are or great added value. It will definitely allow us to conclude on the partial co-localization of Mn1 and Mn1CP with the Re-probes in LPS-activated cells.

To sum up, we observed a punctuate distribution of Mn in the cytosol around the nucleus for LPS-stimulated cells incubated with Mn1CP. This supports the localization of Mn and maybe the intact SOD mimic in perinuclear organelles. Since a poor colocalization is observed between Mn and the mitochondria targeting Re-based probe, Mn (and maybe Mn1CP) may be also compartmentalized in organelles other than the mitochondria. This may possibly correspond to the Golgi apparatus, the lysosomes or the endoplasmic reticulum (found in the cytoplasm all around the nucleus). In contrast, in healthy conditions, Mn1 essentially diffuses homogeneously within the cytoplasm. To figure out the precise location of Mn1 and Mn1CP in LPS-stimulated HT29-MD2, experiments involving XRF probes targeting other perinuclear organelles (GA, endoplasmic reticulum and lysosomes) are needed.

II.4.c.iv. Supplementary figures

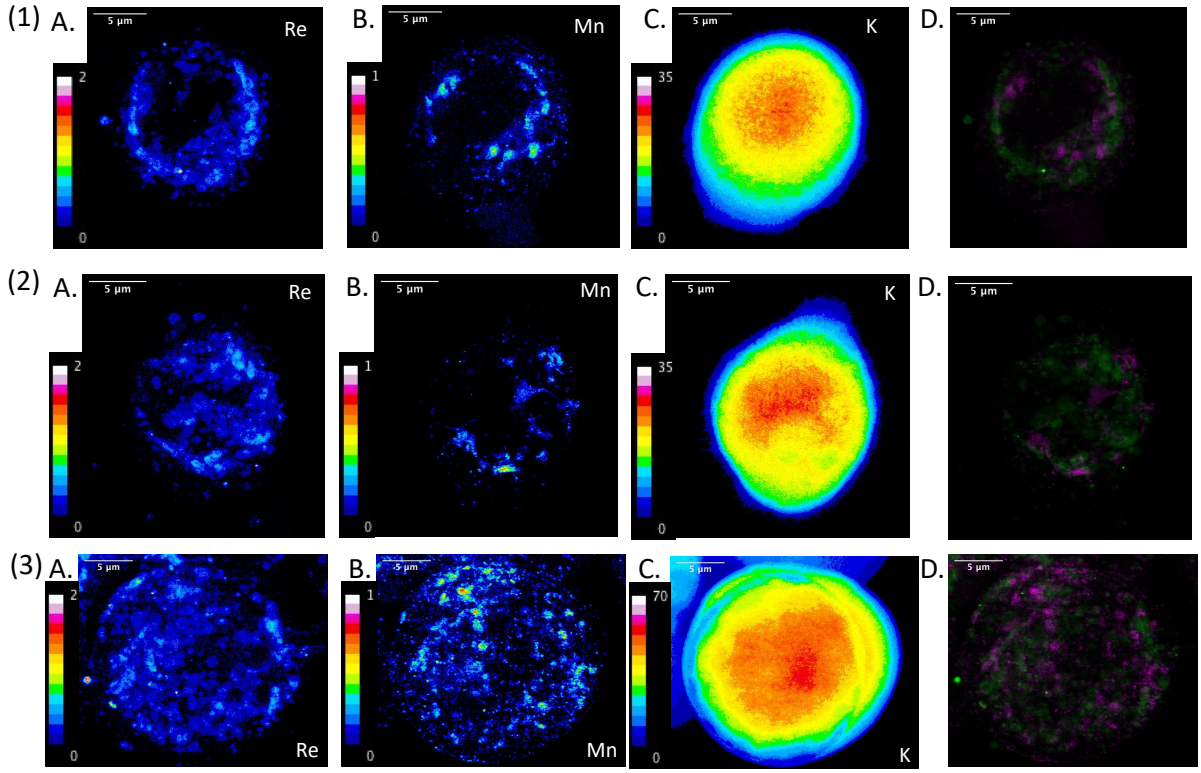

Figure S1: Mn1 distribution in activated cells. Projected 2D- elemental distributions of A. Re, B. Mn and C. K in HT29-MD2 cells incubated for 4 hours with LPS (0.1 µg/mL) + Mn1 (100 µM) + Re-probe (20 µM). The mapping was performed by XRF nano-imaging (excitation at 17 keV, pixel size: 50 nm, exposure time: 50 ms). D. corresponds to the merge of Re (green) and Mn (magenta) distributions. The intensity color bar represents the area density (ng/mm^2). K is a highly abundant metal assumed to be homogeneously distributed in cells. Its area density mapping hence informs on the cell depth along z-axis at each pixel. (1), (2) and (3) are different replicates. The Pearson coefficient for Mn and Re colocalization was found equal to 0.52, 0.45 and 0.50 for respectively (1), (2) and (3).

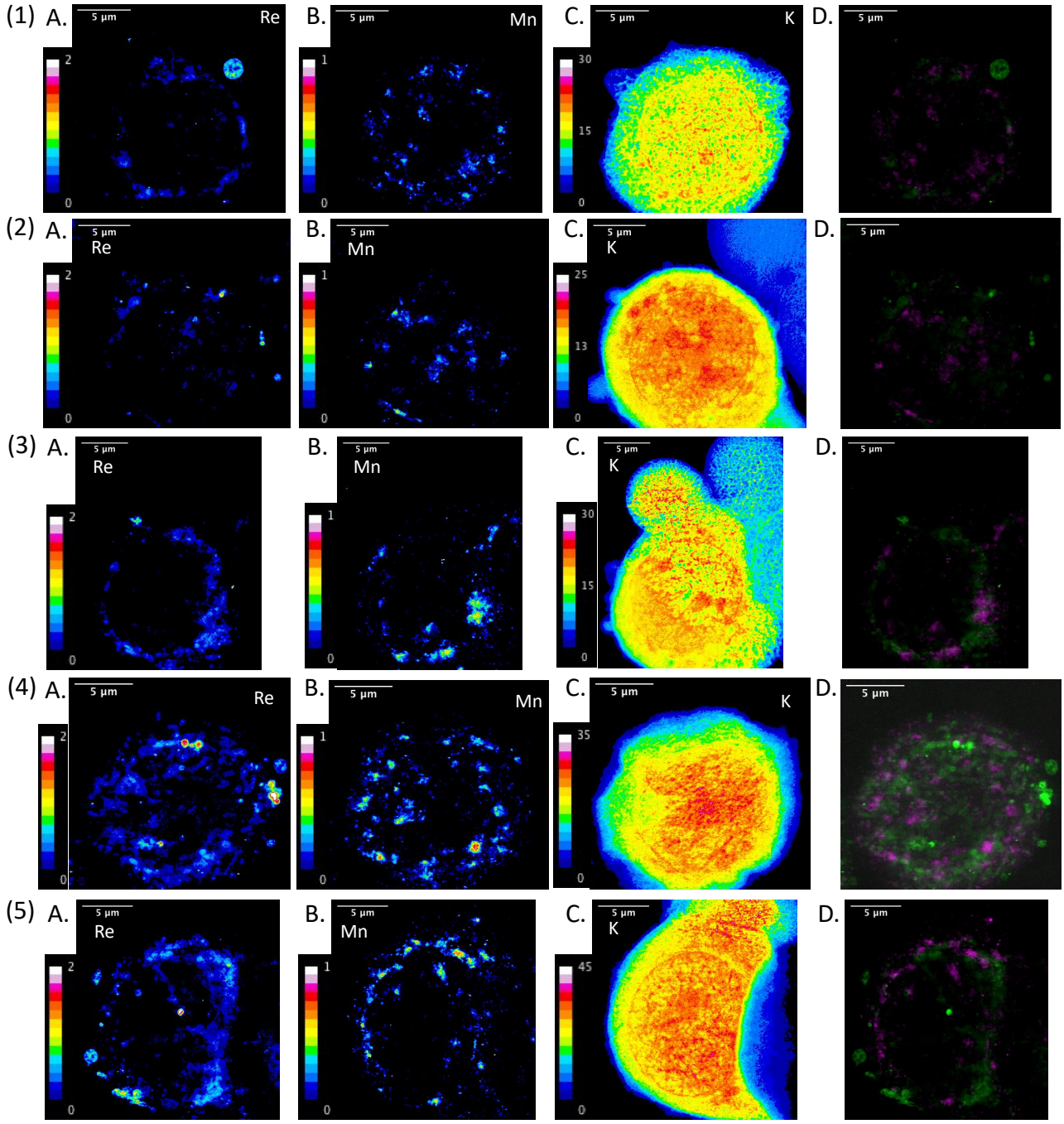

Figure S2: Mn1CP distribution in activated cells. Projected 2D- elemental distributions of A. Re, B. Mn and C. K in HT29-MD2 cells incubated for 4 hours with LPS (0.1 µg/mL) + Mn1CP (100 µM) + Re-probe (20 µM). The mapping was performed by XRF nano-imaging (excitation at 17 keV, pixel size: 50 nm, exposure time: 50 ms). D. corresponds to the merge of Re (green) and Mn (magenta) distributions. The intensity color bar represents the area density (ng/mm^2). K is a highly abundant metal assumed to be homogeneously distributed in cells. Its area density mapping hence informs on the cell depth along z-axis at each pixel. (1), (2), (3), (4) and (5) are different replicates. The Pearson coefficient for Mn and Re colocalization was found equal to 0.69, 0.54, 0.68, 0.57 and 0.45 for respectively (1), (2), (3), (4) and (5).

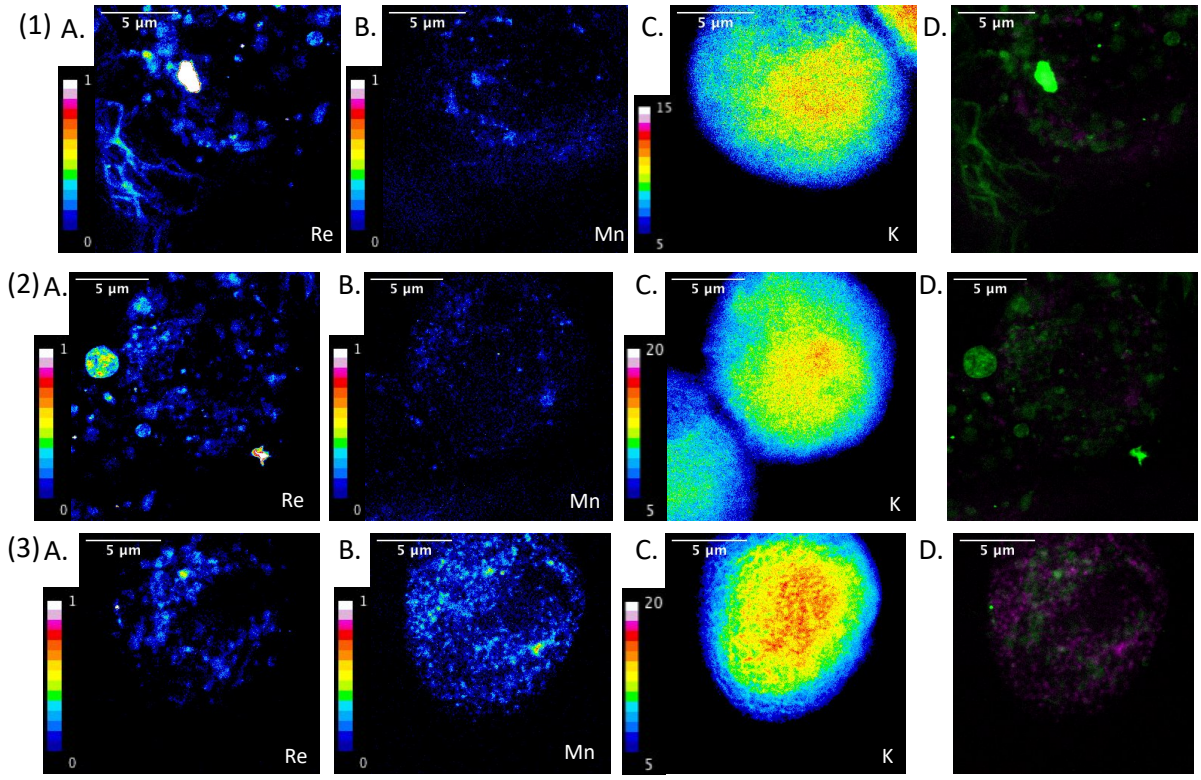

Figure S3: Mn1 distribution in non-activated cells. Projected 2D- elemental distributions of A. Re, B. Mn and C. K in HT29-MD2 cells incubated for 4 hours with Mn1 (100 µM) + Re-probe (20 µM). The mapping was performed by XRF nano-imaging (excitation at 17 keV, pixel size: 50 nm, exposure time: 50 ms). D. corresponds to the merge of Re (green) and Mn (magenta) distributions. The intensity color bar represents the area density (ng/mm^2). K is a highly abundant metal assumed to be homogeneously distributed in cells. Its area density mapping hence informs on the cell depth along z-axis at each pixel. (1), (2) and (3) are different replicates. The Pearson coefficient for Mn and Re colocalization was found equal to 0.18, 0.18 and 0.55 for respectively (1), (2) and (3).

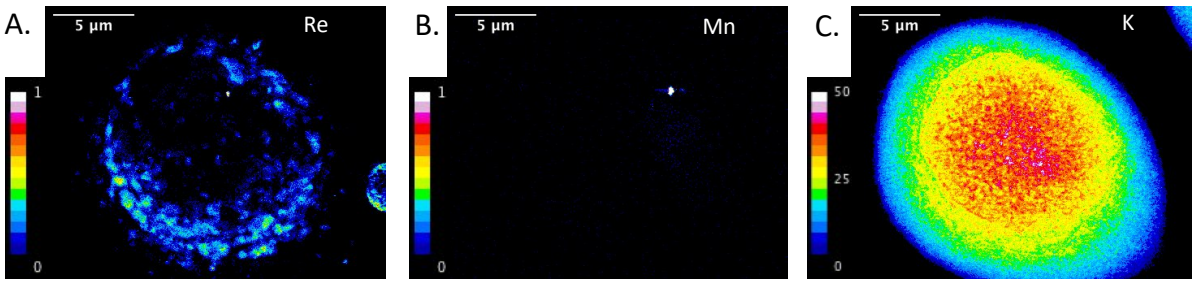

Figure S4: Re probe distribution in activated cells. Projected 2D- elemental distributions of A. Re, B. Mn and C. K in HT29-MD2 cells incubated for 4 hours with LPS (0.1 µg/mL) + Re-probe (20 µM). The mapping was performed by XRF nano-imaging (excitation at 17 keV, pixel size: 50 nm, exposure time: 50 ms). The intensity color bar represents the area density (ng/mm^2). K is a highly abundant metal assumed to be homogeneously distributed in cells. Its area density mapping hence informs on the cell depth along z-axis at each pixel.

II.5. Evaluation of Mn1-derived SOD mimics in DNBS-induced murine colitis: chemically modified bacteria as delivery vectors.

II.5.a. Use of bacteria so-called chemically modified bacteria (CMB) as delivery vectors.

II.5.a.i. Benefits of SOD mimics loading in bacteria.

To maximize the therapeutic action of SOD mimic *in vivo*, we need to ensure the bioavailability and the efficacy of the Mn(II) complexes at their action site in the intestine. In this way, the oral administration of Mn1-derived SOD mimics requires protective delivery vector because unprotected Mn(II) complexes will undergo decomplexation and lose their SOD activity in the acidic conditions of the stomach.

A large range of colonic delivery technologies was developed and was recently detailed in a review from A. Awad *et. al* [243]. These delivery systems incorporate different release mechanism responsive to various stimuli such as pH, time or microbiota [244]. Such stimuli-dependent delivery vectors include carriers made of polymers (polymethacrylate, polylactic co-glycolic acid, cellulose, poly-ethylene glycol) [245–248], starch [249], chitosan [248,250,251], pectin [250,252], mesoporous silica [253] or lipids [254–256].

Herein, an alternative mean for targeted drug delivery to the colon is presented. It is based on the loading of the SOD mimics in food-grade bacteria. This technique consists in co-incubating the SOD mimics with bacteria so as they accumulate it inside, as shown in a previous PhD work (A. Vincent) [257]. Then, the bacteria could be administrated to the IBD patients. This strategy provides several advantages compared to the above-mentioned existing system. First, the choice of autochthonous or food-grade allochthonous bacteria such as lactic acid bacteria (LAB) that possess established safety status (GRAS or QPS: Generally Recognized As Safe and Qualified Presumption of Safety) ensure the absence of induced cytotoxicity to the host. Secondly, LAB are known to adapt to large range of pH and then survive during their passage through the acidic medium of the gastrointestinal tract. Consequently, they constitute an efficient protective vector for the SOD mimics. Thirdly, the bacterial vector can be modified to provide a targeted and efficient release of the encapsulated SOD mimics at the inflammation site. Indeed, the SOD mimics-containing

bacteria will be rendered auxotrophic to alanine and pre-cultured in absence of alanine before their administration. Hence, after crossing the stomach, the bacteria will transiently colonize the intestinal microbiota and more importantly will quickly lyse and liberate the SOD mimics as they were fragilized by the beforehand privation of alanine. Eventually, bacteria so called probiotics with native beneficial properties for the host could be used. This may allow taking advantage synergistically of the probiotics activity of the vector strain and the antioxidant activity of the loaded SOD mimic.

To our knowledge, this study constitutes the first proof of concept for the use of CMB as delivery vector of synthetic drugs.

II.5.a.ii. Choice of the strain

Amandine Vincent, a former PhD student, screened different LAB for their ability to act as protective delivery vector of SOD mimics in a murine model of DNBS-induced colitis.

She selected one strain on the basis of: 1) its neutrality on the DNBS-induced colitis model (neither anti-inflammatory effects nor pro-inflammatory ones), 2) the maximal amount of SOD mimics that can be encapsulated without generating toxicity to the bacteria, 3) the better resistance to freeze-thaw cycles, 4) preliminary results on Mn1-containing strain effects on weight recovery and macroscopic score in DNBS-subjected mice.

The strain MD007 was best fulfilling the criteria and was thus chosen for the following assays. MD007 is a *Lactobacillus plantarum* (NCIMB8826) rendered auxotrophic to alanine. The optimal conditions to encapsulate Mn1 in MD007 were determined by Amandine Vincent and were used in the following.

II.5.b. Experimental section

II.5.b.i. Bacteria loading with SOD mimics

Overnight culture of MD007 in MRS medium supplemented with alanine (MRS-alanine) were diluted to $OD_{600\,nm}$= 0.2 in MRS-alanine and were left to grow until reaching $OD_{600\,nm}$= 0.6. The culture was then centrifugated and the pellet was washed twice and resuspended in MRS without alanine. The bacteria were deprived of alanine for 3 hours to fragilize them for the purpose of accelerating their lysis in mice intestine. Meanwhile, the SOD mimics Mn(II) complexes were prepared by mixing the ligands and $MnCl_2$ in a ratio 1:1.3 in HEPES 0.1 M (pH

7.5) and let 2 hours at ambient temperature to afford a complete complexation of the ligands. After alanine deprivation, the culture was again centrifugated and the pellet was washed twice and resuspended in HEPES 0.1 M. At that time, the culture was split into 5 parts and SOD mimics and $MnCl_2$ were added in four of them to a final concentration of 0.4 mM. The five bacterial suspensions were let to incubate for 2 hours. Lastly, after cultures centrifugation and washing with HEPES 0.1 M, the bacteria were resuspended in HEPES 0.1 M containing 16% glycerol (HEPES-gly) and stored at -80°C in 2 mL aliquots to avoid freeze-thaw cycles.

One of the aliquots was used for Mn quantification by ICP-MS and for the enumeration of viable bacteria through serial dilutions and plating. For ICP-MS analysis, bacteria were acidified in 2% HNO_3, to lyse them and free Mn from all coordination sites, and filtered. A calibration curve was established using a commercial Mn standard.

II.5.b.ii. Induction of DNBS colitis and bacteria administration

The *in vivo* assays were conducted on pathogen-free male C57BL/6 mice in the animal facilities of the National Institute of Agricultural and Environmental Research (INRAE, Jouy-en-Josas). The timeline for colitis induction and mice gavage with CBM is illustrated in Figure 36. Briefly, the assay lasts 5 days and CBM are intragastrically administrated daily to the mice for the first 4 days. On the second day, mice are anesthetized intraperitoneally and colitis is induced by an intra-rectal injection of DNBS through a plastic tube inserted 4 cm into the colon. The fifth and last day mice are sacrificed by cervical dislocation. Mice are weighted every day.

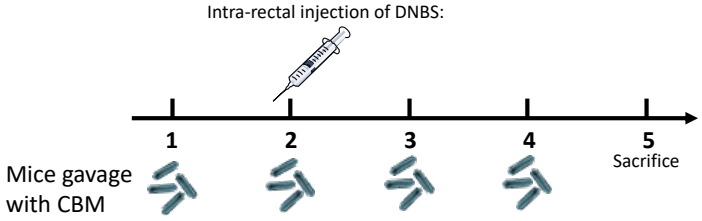

Figure 36: Time line for gavage with CBM and colitis induction in the murine model of DNBS-induced colitis.

The studied groups are as follows: control colitis group (DNBS + HEPES-gly), empty bacteria control group (DNBS + MD007), and 4 CBM groups: DNBS + MD007_$MnCl_2$, DNBS + MD007_Mn1, DNBS + MD007_Mn1C and DNBS + MD007_Mn1CP. Each group was composed of 8 mice. The assay was repeated three times independently meaning that, in total, 48 mice for each condition were used.

The amount of CBM given to the mice was determined in such a way that all mice receive the same amount of total manganese, fixed to 150 nmol per dose. This corresponds to a number of bacteria varying between 5×10^8 to 2×10^9 CFU. The amount of MD007 given to the control DNBS + MB007 group was chosen equal to the maximal amount of viable CBM given to mice from CBM groups. Lastly, the control colitis group receive 200 µL of HEPES-gly.

II.5.b.iii. Evaluation of colitis severity

- Post-sacrifice mice dissection and determination of macroscopic scores

The abdominal cavity of sacrificed mice was opened and the colon was removed, opened longitudinally and washed from feces. A part of fecal material was kept at -80°C for further quantification of anti-inflammatory markers like lipocaline (not done yet). The macroscopic scores were then immediately assessed (by the same experimenter every time: Florian Chain). These scores evaluate the state of the colon by taking into account: colon shrinkage, thickening of colon wall, presence of ulcers, hyperemia, adhesion to other intra-abdominal tissues, consistency of stools (indicator of diarrhea). The colon was then longitudinally separated in two pieces. The left part was swiss-rolled into OCT (Optimal cutting temperature) gel and stored at -80°C. These swiss-rolls could be imaged by X-ray fluorescence microscopy to hopefully detect and localize Mn(II) coming from the SOD mimics in the colon (not done yet). The right part was laterally separated in 4 parts intended to: from distal extremity to proximal one 1) the assay of myeloperoxidase activity, 2) the quantification of SOD2 gene transcription (stored in RNase free buffer for an improved conservation of RNA), 3) the determination of histologic scores (fixed in PFA, scoring not done yet) and 4) a back-up piece. All the colon samples were stored at -80°C.

- Intestinal permeability Assay

Three hours before mice sacrifice, they received by gavage a fluorescent marker: fluorescein (FITC)-labeled dextran. Just before mice sacrifice, blood was collected via the puncture of the retro-orbital vein. The measurement of fluorescence intensity allows to determine FITC dextran concentration in blood sample. The detection of increased levels of FITC dextran in serum evidences its excessive passage from the GIT to the blood and is hence indicative of altered barrier functions.

- Measurement of myeloperoxidase activity

The activity measurement of the myeloperoxidase (MPO) enzyme, that catalyzes the oxidation of proteins by H_2O_2, is relevant to assess colitis severity. Indeed, extracellular MPO activity was shown to be a marker of oxidative stress in inflammatory diseases and intracellular MPO activity a marker of neutrophilic infiltration [258]. The total MPO activity was assayed as previously described [259]. Briefly, H_2O_2 and hexadecyltrimethyl ammonium bromide are added in colon homogenates resulting in the catalytic conversion of H_2O_2 and Cl- into hypobromous acid (BrOH) and water. This reaction was monitored by UV-visible spectroscopy which allows to measure the MPO activity, that can be expressed as units per milligram of wet tissue (1 unit = reaction with 1 mM of H_2O_2 in 1 minute at room temperature).

- Quantification of SOD2 gene transcription

First, the RNA was extracted from colon homogenates by using a Qiagen RNeasy kit. β-mercaptoethanol was used as reducing agent for the irreversible denaturation of RNases enzymes. RT-PCR was then performed to produce the complementary DNA. We followed a classical RT-PCR protocol with oligo $dT_{12\text{-}18}$ and super script II reverse transcriptase enzyme. Eventually, SOD 2 gene was quantified by quantitative PCR on a StepOne Real-time PCR system. We used the following primer pair: ATTAACGCGCAGATCATGCA (forward) and TGTCCCCCACCATTGAACTT (reverse) and set the annealing temperature to 60°C. The SOD2 levels were normalized with that of housekeeping GADPH and TBP genes, which are known to be weakly impacted in inflammatory conditions.

II.5.c. Results and discussion

The results shown and discussed below correspond to a pool of the data obtained from the three assays conducted in March, May and June 2021.

II.5.c.i. Effect of SOD mimics-loaded bacteria on the weight

As expected, the untreated mice subjected to DNBS injection have lost about 16% of their initial weight at day 3 (Figure 37).

The mice feeding with MD007-internalized SOD mimics allow to limit the weight loss of mice with the following ranking of efficacy: Mn1C > Mn1 ≈ Mn1CP. In case of MD007-Mn1 treatement, the average weight loss was about 16% with no weight recovery (Figure 37). In

contrast for MD007-Mn1CP, the weight loss was similar to that of untreated control group (reduction of ≈17%) until day 2 but a weight recovery to almost 87% of initial weight was finally observed at day 3 (Figure 37). Lastly, MD0007-vectorized Mn1C was the most efficient SOD mimic-based treatment to limit weight loss and fasten weight recovery. Indeed, the weight reduction (maximal at day 2) reached only 13% and mice recovered about 90% of their initial weight at day 3 (Figure 37).

However, these therapeutic effects cannot be unambiguously attributed to the vectorized SOD mimics. Indeed, the administration of MD007-internalized $MnCl_2$ to mice also resulted in benefits in term of limited weight loss and maximized weight recovery (≈88% of initial weight) (Figure 37). This is consistent with an epidemiological study, conducted in 2018 on children newly diagnosed with IBD, showing an inverse correlation between nutritional manganese status and IBD [260]. Moreover, M. Daly and coworkers already reported in numerous studies the protective effects of manganese accumulation against oxidative stress and aging in yeast and prokaryotes, particularly in the gamma radiation resistant- *D. radiodurans* strain [206,213,204,261,205]. The protection was inferred to the formation of manganese complexes composed of endogenous metabolites (peptides, nucleosides…) endogenously forming catalytic antioxidants. Likewise, the nutritional supplementation of manganese was shown to efficiently increase mice tolerance to DSS-induced experimental colitis while in contrast Mn deficiency was responsible for exacerbated DSS-induced colitis [262]. In this case, the pharmacological action was linked to the ability of manganese to prevent the DSS-induced impairment of the intestinal barrier functions. Similar mechanisms of action might occur here explaining the protective effects of MD007-internalized $MnCl_2$.

Otherwise, the mice treated with empty MD007 lost very slightly less weight than untreated mice suggesting a small but non-significant probiotic activity of the strain (Figure 37).

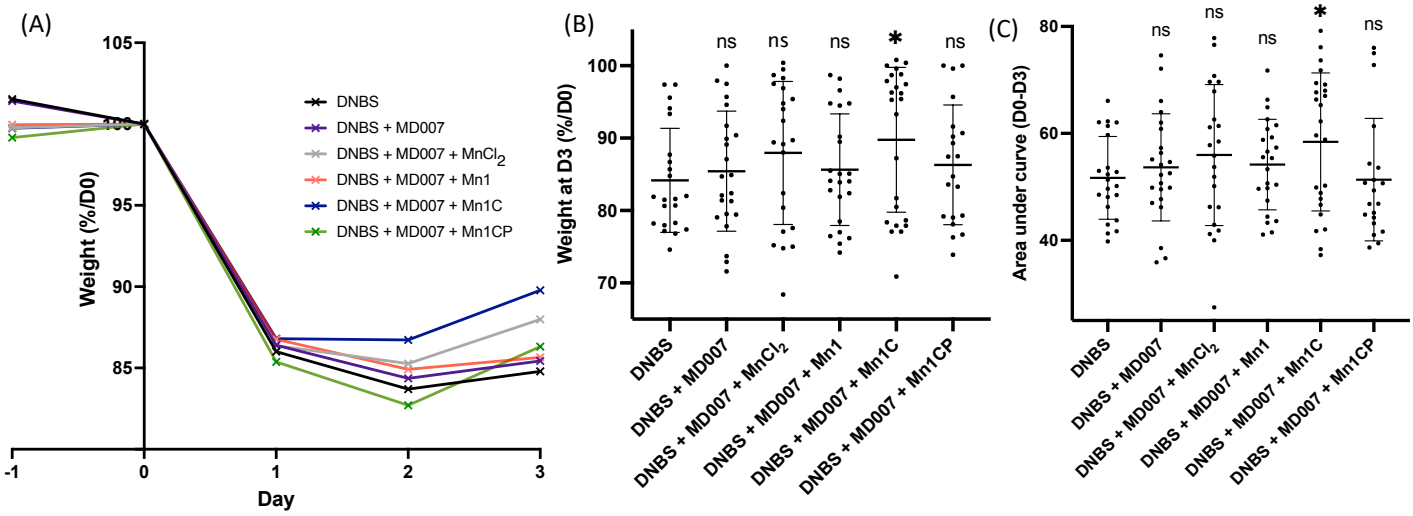

Figure 37: (A)Weight monitoring over time of mice subjected to DNBS injection and treated with SOD mimics-loaded bacteria. The weights are expressed as a percentage of the mice initial weight at day 0. Curves represent the average of approximately 24 mice (three assays with 8 mice but some died or were euthanized before the end of the assay). (B) Mice weight at day 3 (D3) expressed as the percentage of mice weight at day 0 (D0). (C) Area under the curve of weight monitoring between day 0 to 3 (D0-D3). Data represent the mean ± SD for three independent assays (around 24 mice). The p-values were calculated using the non-parametric Mann-Whitney test (one-tailed test) as the gaussian distribution of the data was unvalidated by the Anderson-Darling normality test. The mean ranks of each column were compared to that of the DNBS control; each comparison stands alone. ∗∗∗: $p < 0.001$, ∗∗: $p < 0.01$, and ∗: $p < 0.05$ versus DNBS control, and ns means nonsignificant.

To quantify the effects of each treatment on mice weight and perform statistical analysis, one can for instance focus on the weight at day 3 and/or calculate the area under the weight curve between day 0 to 3 (Figure 37).

The only difference in weight compared to the untreated mice to be significant at day 3 are that with MD007+Mn1C groups. Likewise, only MD007+Mn1C groups show a significative increase in the area under the curves between day 0 to 3 compared to the untreated group.

II.5.c.ii. Effect of SOD mimics-loaded bacteria on the macroscopic scores

Unsurprisingly, the DNBS-injured mice that did not receive any treatement display relatively high macroscopic scores (Figure 38). The other groups fed with loaded or not MD007 show diminished scores (Figure 38). In all cases, these reductions were significant but no difference over the different treatments was noticeable. Hence, the SOD mimics do not provide additional effect compared to that coming from the unmodified MD007 strain, which proves to be not so neutral toward the inflammation.

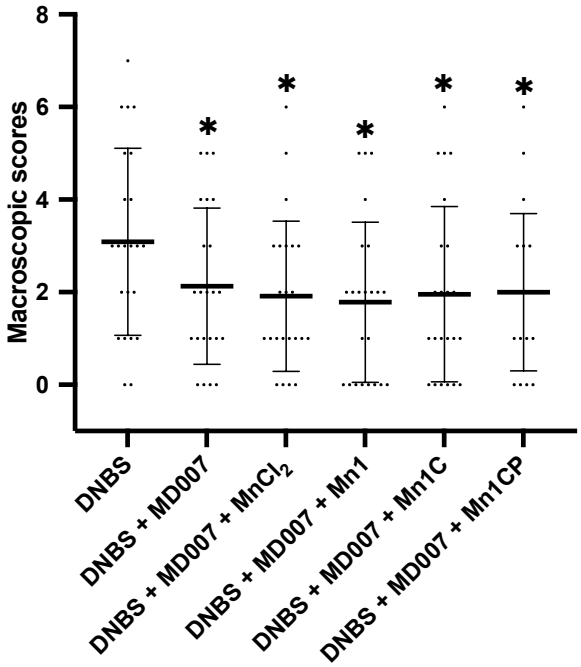

Figure 38:Macroscopic scores of mice subjected to DNBS injection and determined on the sacrifice day. Data represent the mean ± SD for three independent assays (around 24 mice). The p-values were calculated using the non-parametric Mann-Whitney test (one-tailed test) as the gaussian distribution of the data was unvalidated by the Anderson-Darling normality test. The mean ranks of each column were compared to that of the DNBS control; each comparison stands alone. ∗∗∗: p < 0.001, ∗∗: p < 0.01, and ∗: p < 0.05 versus DNBS control, and ns means nonsignificant.

II.5.c.iii. Effect of SOD mimics-loaded bacteria on the MPO activity

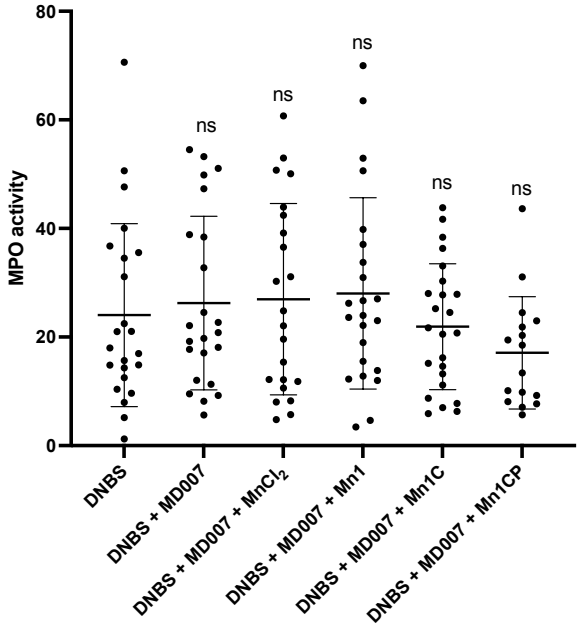

Figure 39: MPO activity measured in colon samples of DNBS-injured mice. Data represent the mean ± SD for three independent assays (around 24 mice). The p-values were calculated using the non-parametric Mann-Whitney test (one-tailed test) as the gaussian distribution of the data was unvalidated by the Anderson-Darling normality test. The mean ranks of each column were compared to that of the DNBS control; each comparison stands alone. ∗∗∗: p < 0.001, ∗∗: p < 0.01, and ∗: p < 0.05 versus DNBS control, and ns means nonsignificant.

The measurement of MPO activity in the colon reveals no significant impact of any treatment on this inflammation marker (Figure 39). Only a very little decrease in MPO activity can be observed in mice that received vectorized Mn1C and especially Mn1CP but not significatively.

II.5.c.iv. Effect of SOD mimics-loaded bacteria on the intestinal barrier permeability.

The DNBS injection is known to provoke an impairment of the intestinal tight junctions resulting in enhanced barrier permeability, which favored passage of FITC-Dextran from the GIT to the blood system. Lower levels of FITC Dextran were quantified in the plasma samples of mice treated with MD007 + Mn1C compared to untreated mice. This demonstrates the efficacy of MD007-vectorized Mn1C to attenuate significatively the DNBS-induced damages on intestinal permeability (Figure 40).

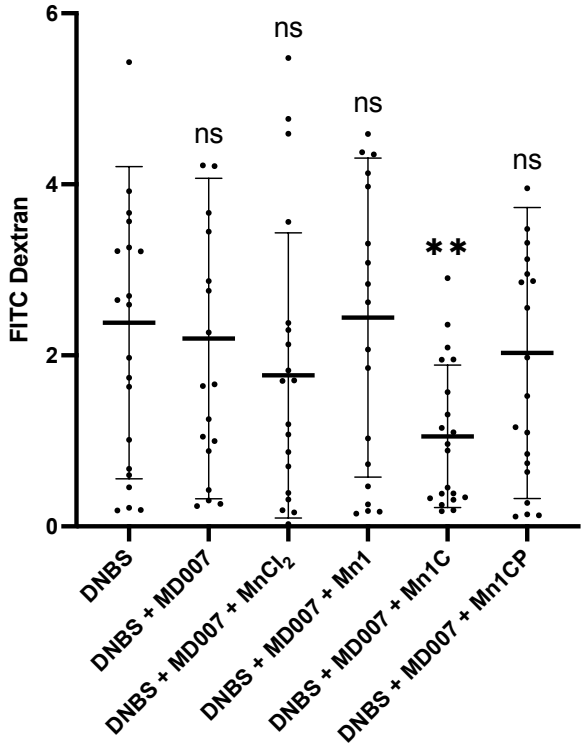

*Figure 40: Quantification of FITC dextran as a marker of the intestinal barrier permeability in mice suffering from DNBS-induced colitis. Data represent the mean ± SD for three independent assays (around 24 mice). The p-values were calculated using the non-parametric Mann-Whitney test (one-tailed test) as the gaussian distribution of the data was unvalidated by the Anderson-Darling normality test. The mean ranks of each column were compared to that of the DNBS control; each comparison stands alone. ***: $p < 0.001$, **: $p < 0.01$, and *: $p < 0.05$ versus DNBS control, and ns means nonsignificant.*

II.5.c.v. Effect of SOD mimics-loaded bacteria on SOD2 gene transcription.

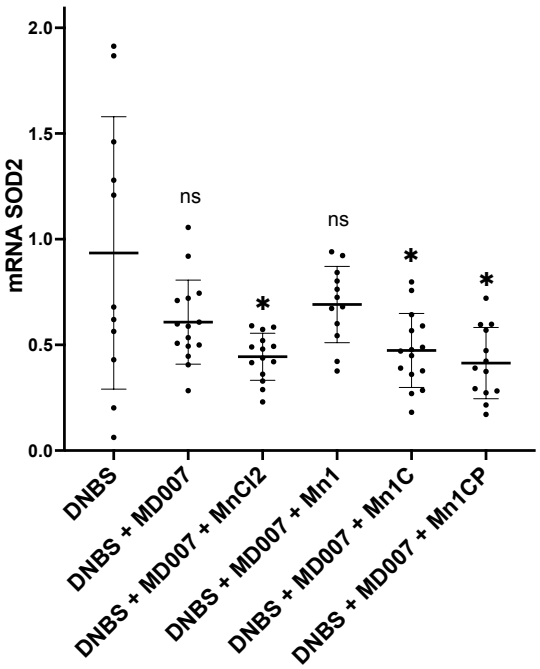

*Figure 41: Levels of mRNA SOD2 in colon samples of mice suffering from DNBS-induced colitis. Data represent the mean ± SD for two independent assays (around 16 mice). The p-values were calculated using the parametric Welch's test (one-tailed test, student test with equal SD not assumed) as the gaussian distribution of the data was validated by the Anderson-Darling normality test. The mean ranks of each column were compared to that of the DNBS control; each comparison stands alone. ***: $p < 0.001$, **: $p < 0.01$, and *: $p < 0.05$ versus DNBS control, and ns means nonsignificant.*

The data presented in this subsection correspond to an average of only two independent assays. The results from the third assay were indeed not included here due to surprisingly high values, which erase the trend visible in the two first assays. The RT-qPCR of mRNA SOD2 thus needs to be repeated for this last assay.

The content in mRNA SOD2 is significantly diminished (divided by 2) upon mice feeding with MD007 loaded with $MnCl_2$, Mn1C and Mn1CP (Figure 41). This suggests that the two SOD mimics are able to complement for the endogenous SOD2 enzyme, thus requiring less SOD2 production by the mice cells. As mentioned above, the activity of $MnCl_2$ could be attributed to the formation of antioxidant Mn-metabolites complexes.

While significant, these decreases remain very low when considering that a 2-times reduction in mRNA amount only represents a difference of one amplification cycle in qPCR. To reinforce these results, we consider to quantify the levels of SOD2 protein in another colon sample by Western Blot. The direct quantification of SOD activity is not suitable in this case since the activity of the native SOD2 could not be distinguished from the intrinsic SOD activity of the administered SOD mimics.

Lastly, to provide a more accurate interpretation of the results, it would have been better to selectively extract the RNA contained in the epithelium of the colon instead of the whole colon.

To conclude this part, MD007-vectorized Mn1C is the only treatment that improves significantly each measured inflammation markers compared to the DNBS group. However, MD007-vectorized Mn1CP and $MnCl_2$ also display visible protective effects on different markers (the effect is even significant for mRNA SOD2). While the activity of MD007-vectorized $MnCl_2$ arises from the antioxidant action of free Mn or Mn- endogenous metabolites complexes, the benefits observed for MD007-vectorized Mn1C/Mn1CP cannot be attributed (at least not totally) to the Mn(II) released from the SOD mimics. Indeed, if the observed activity was exclusively due to released Mn(II), the most labile Mn1 should exert higher therapeutic action than its more inert analog Mn1C and Mn1CP, that are more resistant to metal exchanges and thus less prone to Mn(II) release, which is not observed.

II.6. Conclusion and perspectives

To sum up this chapter, a new generation of SOD mimics inspired from the well-studied Mn1 was shown to display reinforced resistance to metal exchange related to the introduction of a cyclohexyl group on the diaminoethane scaffold of the ligand. The improved inertness of the SOD mimics led not only to improved bioactivity in a cellular model of LPS-induced inflammation but also to the possibility to detect and quantify the intact SOD mimic in cells using classical MS systems.

In parallel, we set up a new protocol based on ion mobility spectrometry coupled to mass spectrometry (IMS-MS) to detect the more labile manganese complex, Mn1, in cells and estimate its intracellular concentration. This approach is very innovative as IMS-MS was so far mostly applied to the speciation study of large proteins. The results obtained here open the way to the use of this analytical technique in a wide range of applications implying low molecular weight metal complexes.

We then investigated the intracellular distribution of the SOD mimics in HT29-MD2 cells by micro-XRF imaging. Upon LPS activation, Mn1 and Mn1CP partially accumulate in mitochondria but mostly elsewhere, probably in other perinuclear organelles. To fully

characterize the cellular fate of the SOD mimics and correlate it with their cellular activity, further speciation study could be completed.

Lastly, the therapeutic potential of Mn1, Mn1C and Mn1CP was assessed *in vivo* in a murine model of DNBS-induced colitis. The three *in vivo* assays discussed in this chapter have given promising results on the ability of MD007-vectorized SOD mimics to rescue DNBS-challenged mice, especially Mn1C. Indeed, Mn1C is the only one to display significant therapeutic effects on all the following features: the weight loss, the macroscopic scores, the intestinal barrier permeability and the transcription of SOD2 gene. To support the efficacy of MD007-vectorized Mn1C in ameliorating DNBS-induced colitis, the measurement of other inflammation markers is under progress. These ongoing analyses include the determination of the microscopic scores, the quantification of several pro-inflammatory cytokines in colon (using a commercial multiplex kit) as well as the quantification of lipocaline, an inflammatory marker, in stool samples. Moreover, the experimental protocol can be optimized in order to 1) better observe and 2) reinforce the effects of MD007-vectorized SOD mimics in DNBS-challenged mice. Concerning 1), the time-line of the assay could be modified. For instance, the sacrifice of the mice could be earlier or postponed to examine whether the SOD mimics effects are more easily detectable at different time points relative to DNBS injection. Secondly, we may quantify daily the levels of various inflammation and oxidative stress markers in mice plasma [76,263] as the blood sampling is a minimally invasive and low-stress method. This will allow to obtain a kinetic monitoring of the SOD mimics effects on DNBS-induced inflammation. As for 2), we consider to deliver a larger quantity of MD007-vectorized SOD mimics to the mice. Yet, the feeding volume is limited to 200 µL for C57BL/6 mice and the bacterial suspension cannot be more concentrated as it may lead to excessively high viscosity. However, we could feed the mice with the MD007-vectorized SOD mimic 2 or 3 times per day. In addition, the preventive administration of MD007-vectorized SOD mimic several days before the DNBS injection (and not the just the day before, as done here) could be interesting when assuming that the lysis of the auxotrophic bacteria may take a while despite their beforehand fragilization through alanine privation. Nevertheless, the lysis of at least a part of the bacteria was confirmed within a few hours following their administration by the means of a dye loaded in the bacteria and detected in stools.

III. Chapter III: Genetically modified lactic acid bacteria for the production and delivery of peptidyl superoxide dismutase and catalase mimics.

III.1. Introduction

III.1.a. Probiotics as therapy in IBDs

III.1.a.i. Probiotics and lactic acid bacteria

The term of probiotics was defined in 2002 by the World Health Organization (WHO) as *"live microorganisms administered in adequate amounts that confer a beneficial effect on the host"* [264]. However, the therapeutic use of host-friendly bacteria was already rationalized since over a century by Elie Metchnikoff [265]. Probiotics gather bacteria and yeasts but the most predominant used species are lactic acid bacteria (LAB) group, including *Lactobacillus*, *Streptococcus* and *Lactococcus* genera [266]. Besides, Gram-negative probiotics also exist. The most studied is *Escherichia coli* Nissle 1917 which was shown to ameliorate inflammatory bowel diseases (IBD), mostly ulcerative colitis, or other intestinal disorders symptoms in clinical trials and *in vivo* assays [267,268]. LAB are a heterogenous group of ubiquitous gram-positive bacteria that are able to metabolize sugars into lactic acid. They mostly comprise allochthonous species, that can be found in different environments such as decomposing fruits and vegetables or other mammals and animals GIT [266]. Due to their ability to produce lactic acid, LAB have been largely used for centuries by man for dairy food production (cheese, yoghurt, sourdough, bread, pickles, etc.) and preservation [269]. Since the introduction of the probiotics concept by Metchnikoff, a rising interest for the therapeutic applications of LAB in IBD prevention and treatment has emerged. Indeed, on the one hand, a vast majority of LAB was shown to exert positive effect on human health. On the other hand, LAB are Generally Recognized As Safe (GRAS) by the U.S. Food and Drug Administration (FDA, USA) and are classified in the list of Qualified Presumption of Safety (QPS) agents according to the European Food Safety Authority (EFSA). This extremely advantageous safety status makes them acceptable for therapeutic use. Moreover, LAB can be delivered orally as they resist the passage through the GIT, which is a highly acidic gastric environment. The oral treatments are

besides recommended by the WHO based on economic, logistical and security reasons (no need for invasive medical device, needle etc.). To avoid any misunderstanding, it is preferable to specify that the probiotics are consumed alive and thus constitute live biotherapeutics products (LBPs).

Many reviews propose an overview of new discovered LAB probiotics [270–273]. Here are some relevant examples of LAB having health-promoting properties for the consumer. *Lactobacillus* are a genus of bacteria frequently described as the most efficient and the best-known probiotics and have been, for these reasons, selected by the World Gastroenterology Organization for the treatment of GIT-related diseases [274]. Two well-studied strains, *Lactobacillus reuteri* ATCCC 55730 and *Lactobacillus casei* BL23, were able to attenuate UC in children [275] and to improve the disease state of murine chemically-induced colitis via the induction of the immune system, respectively [276–278]. More recently, *Lactobacillus bacillus* ZS62, *Lactobacillus rhamnosus* (MTCC-5897), *Lactobacillus acidophilus* XY27 and *Lactobacillus casei* ATTC 393 revealed protective effects on DSS (Dextran Sulfate Sodium)-induced murine colitis [279–282]. Moreover, many preclinical and clinical research have demonstrated that the probiotic mixture VSL#3 containing, among others, 4 *Lactobacillus* strains (*L. acidophilus* BA05, *L. plantarum* BP06, *L. paracasei* BP07 and *L. helveticus* BD08) alleviates the GIT inflammation and provides benefits [283]. Likewise, *Lactobacillus delbrueckii* displayed anti-colitis effects in the DSS-induced colitis murine model [284]. Although *Lactococcus* and *Bifidobacteria* are less common probiotics compared to *Lactobacillus*, several strains such as *Lactococcus lactis* NCDO 2118 and *Bifidobacterium longum* 536 have shown to regulate inflammation in CD and UC patients [285–287]. Note that *Bifidobacteria* (*Bifidobacterium breve* BB02, *Bifidobacterium animalis* BL03 and *Bifidobacterium animalis* BI04) also represent main constituents of the VSL#3 mixture mentioned above.

III.1.a.ii. Mechanisms of actions of probiotics

The probiotic effects of LAB strains involve several mechanisms of action that can be separated in two major aspects both illustrated in Figure 42 [288]:

1) **The restoration of the intestinal microbiota symbiosis (composition and function).** This was illustrated in 2000, when the fecal analysis of irritable bowel syndrome (IBS) patients treated with *Lactobacillus plantarum* DSM 9843 revealed a decrease in the

population of pathogenic enterococci associated with attenuated IBD symptoms [289]. To restore the composition and function of the intestinal microbiota, probiotic LAB particularly function by protecting the host from pathogen invasions. To this end, some LAB can secrete bacteriocins (natural antibiotics) or other antimicrobial substances (Figure 42) [43–45]. Moreover, other LAB activate the secretion of defensins by Paneth cells (specialized secretory intestinal epithelial cells), these defensins exerting microbicidal activity (Figure 42) [290]. For instance, some *Lactobacillus* strains prove to be efficient in restoring the expression of Paneth cell defensins through the stimulation of TLR-MyD88 (myeloid differentiation primary response 88) pathway [291,292]. Likewise, LAB compete with dysbiotic and pathogenic bacteria for nutritional sources and for receptors or adhesion sites in the GIT to exclude them [293,294]. Other studies also suggest that some LAB strains promote an increased production of short chain fatty acids (SCFAs), which plays an important role in resolving inflammation [295]. Lastly, LAB can modulate the intestinal enzymatic activity, for instance they inhibit the deleterious β-glucuronidase activity coming from pathogens and trigger the deconjugation of excessive bile acids via the production of bile salt hydrolases [296,297].

2) **The modulation of the intestinal immunity through improved intestinal barrier function and modified responsiveness of intestinal epithelial cells and immune cells to pathogens.** Firstly, the reinforcement of the intestinal barrier integrity is a well-known probiotic effect of LAB. Indeed, LAB interact with Toll-like receptors like TLR-2, TLR-4, TLR-6, etc., dedicated to the specific recognition of pathogen/commensal-associated molecular pattern (P/CAMPs). The activation of these receptors reinforce the integrity of the intestinal barrier via the enhancement of tight junctions stability that impairs bacterial translocation across the mucosal barrier [298–300]. Moreover, some *Lactobacillus* strains or the mentioned-above VSL#3 mixture contribute to the maintenance of the intestinal mucosal physiology by upregulating the expression by goblet cells of mucin-2/3, the most predominant glycoproteins in the mucus (Figure 42) [301,302]. Mucin-3 overexpression was notably shown to prevent the adhesion of pathogenic *E. coli* [303]. Secondly, probiotics are largely recognized to be able to regulate the host immune system. A proposed mechanism is that the interaction between the host-friendly probiotics and the intestinal dendritic cells leads to an

induced production of regulatory T cells (Tregs). The latter are of main importance for immunological tolerance to the intestinal microbiota since they are the main producers of anti-inflammatory cytokine IL-10 and they prevent effector T cells proliferation [304]. A study published by Santos Rocha *et al.* reports the ability of *L. delbrueckii* strain CNRZ327 to increase Tregs in DSS-induced murine colitis and to counteract inflammation processes in mice [284]. This illustrates the ability of probiotics to prevent auto-immunity, closely related to inflammation. Likewise, D. Groeger *et al.* demonstrate that the administration of *Bifidobacterium infantis* 35624 results in reduced pro-inflammatory biomarkers (plasma levels of TNF-α and IL-6) in UC patients [305]. Moreover, the immunomodulatory effects of probiotics can be correlated to the development of IgA-producing B cells and thereby the stimulation of phagocytic and natural killer cell activity (Figure 42). For instance, mice infected with rotavirus show an increased amount of specific IgA against the rotavirus upon treatment with *B. bifidum*, and B. *infantis* [306]. The probiotics effects also involve the down-regulation of pro-inflammatory cytokines such as TNF-α, IL-8, IL-12 or IFN-γ, frequently accompanied with the suppression of NF-κB involved in the inflammation response [278,307,308].

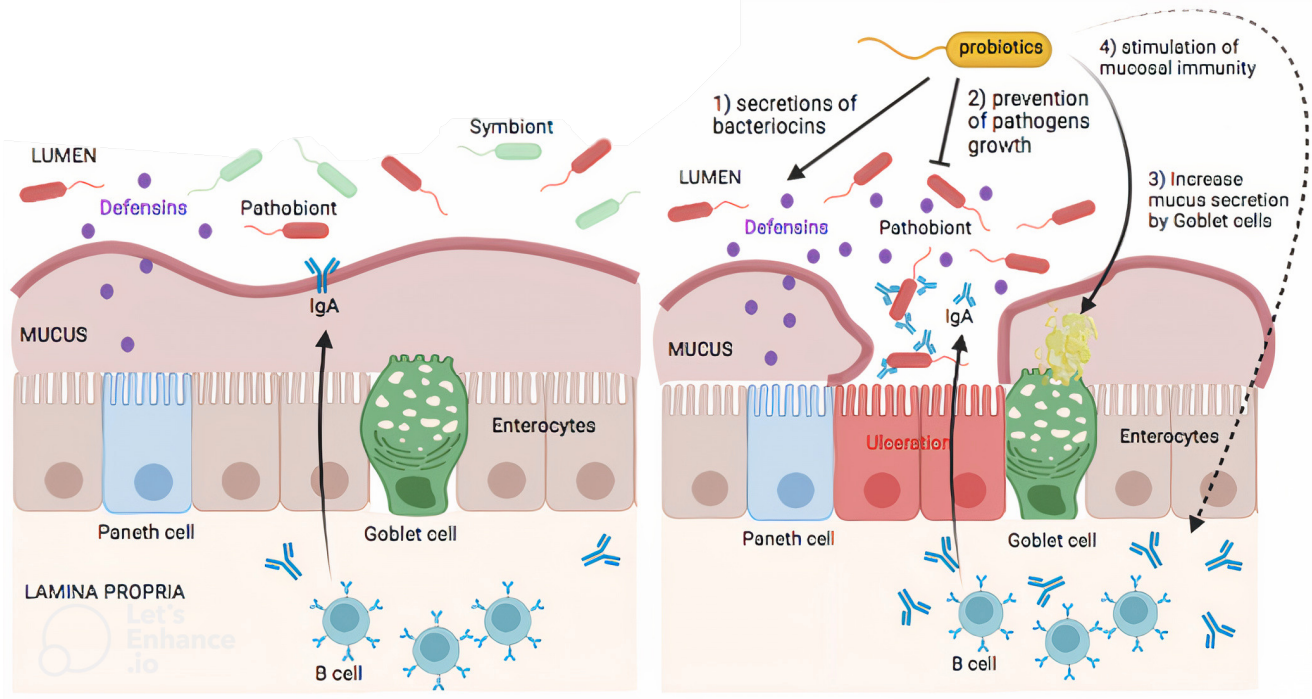

Figure 42: Mechanisms of action of probiotics on intestinal inflammation. Figure inspired from Carvalho et. al [266]. (Left) Intestinal homeostasis is associated to functional epithelial barrier and healthy microbiota. (Right) Intestinal inflammation is accompanied with damages in the mucus layer, dysbiosis of the microbiota and activated immune response. The probiotics alleviate inflammation by remedying these impairments.

In summary, by restoring a healthy commensal microbial ecosystem and by reestablishing regulated mucosal immune functions, some LAB could provide general benefits in IBDs patients (Figure 42). From this starting point and in order to emphasize their effects, with the emergence of new synthetic biology tools, LAB can be genetically engineered to express relevant proteins to treat specific pathological conditions [266,309,288,72,310]. The genetically engineered LAB exert enhanced bioactivity resulting from the synergy between the probiotics effects of the LAB itself and the anti-inflammatory effects of the delivered recombinant protein.

III.1.b. Genetically modified probiotic with additional anti-inflammatory properties

As mentioned above, a probiotic therapeutic strategy can go further with the construction of genetically modified strains producing proteins of health interest to treat intestinal inflammation. Therefore, the genetically engineered probiotic offer personalized treatment with a specific and controlled delivery of one or several therapeutic biomolecules. The research interest on this approach has been accompanied with major advances in synthetic biology. Indeed, since 1960, researchers possess efficient and sophisticated tool to manipulate DNA but meanwhile new more robust technologies have emerged as Golden Gate, Gibson assembly or CRISPR-Cas9 system (Figure 43). The historical technique developed for genetic manipulation is explained in Figure 43 (A). Briefly, the vector plasmid and the target gene are digested with the two same restriction enzymes with the aim to form compatible binding sites. A ligation step then allows to obtain the cloned plasmid which can then be established in bacteria. This strategy is one of the best well-established one and has been largely used for a wide range of applications. Thus, I followed this approach in the framework of my PhD project, presented later in section 0. However, this strategy is time-consuming as it proceeds in multiple (more or less long) steps: digestion, ligation and also intermediate DNA purification and dialysis. Golden Gate assembly is another technique employed by researchers for genetic engineering. The principle is detailed in Figure 43 (B). Briefly, this technique relies on the use of type IIS restriction enzyme which is able to cleave DNA outside of its DNA recognition site sequence. Following IIS digestion, 4 residual single stranded nucleotides remain at the digested extremity. These latter can serve as fusion site between DNA inserts when designed in a way to allow annealing to the end of the next insert or the vector (complementary

sequences). Thus, Golden Gate cloning allows the assembly of several DNA inserts in a defined linear order using a one-pot procedure. Gibson method is another technique to assemble two or more DNA fragments in a single step. As illustrated in Figure 43 (C), this approach is based on the inclusion of homologous overlapping ends at the extremity of the DNA inserts. The annealing of these complementary extremities followed by DNA extension and ligation results in the fully assembled product. The absence in the needing for restriction enzyme digestion drastically accelerates the cloning that can be achieved in few hours. Last but not least, CRISPR-cas9 system (Clustered Regularly Interspaced Short Palindromic Repeats), developed in 2012 by J. Doudna and E. Charpentier (which recently received a Nobel prize for their work), is a genome editing tool that can be applied to eukaryotes, contrarily to the three methods described before [311]. This system is composed of 2 components: an RNA moiety that recognizes the target DNA sequence to cleave thanks to its bases complementary and thus guiding the second component, cas9 enzyme, at the right point of the genome (Figure 43 (D)). Cas9 is a molecular scissors that can then cut double stranded DNA (Figure 43 (D)). CRISPR - cas9 constitutes a simple, versatile, fast and accurate tool that may revolutionize genetic therapy (capacity to delete pathological mutations…).

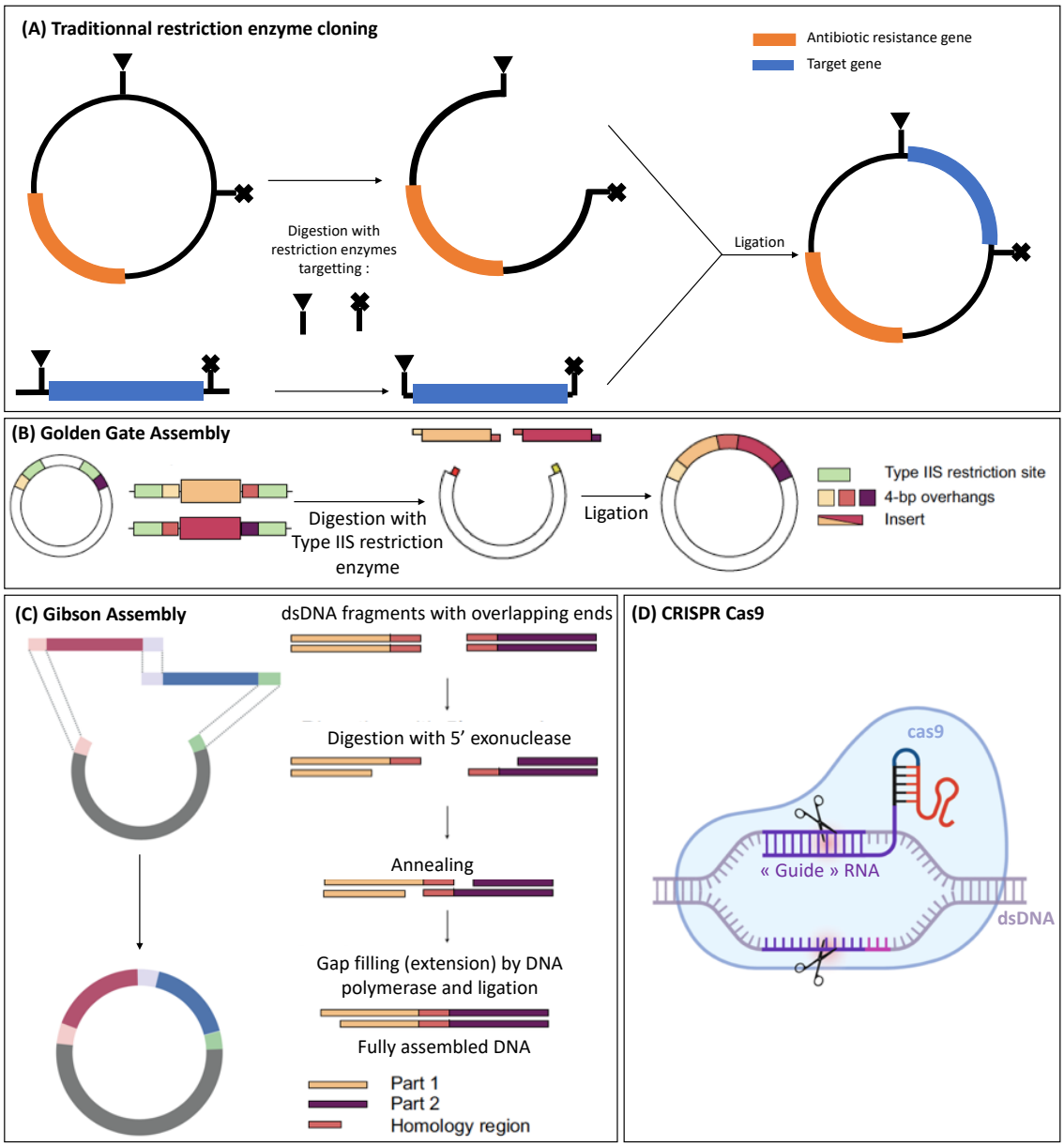

Figure 43: Principles of the main biotechnological tools employed for genetic engineering. (B,C) Figures adapted from [312]. (D) Biorender template.

These knowledges has accelerated the construction of new recombinant strains with boosted bioactivity and, in particular, of LAB (mainly *L. lactis*, considered as the model LAB as they were extensively characterized and thus well-suited for genetic manipulation). The constructed recombinant strains have shown promising results in pre-clinical and even clinical trials for the treatment of many human diseases such as cancer and especially GIT inflammation. Several reviews already offer high-quality and thorough summaries of recombinant LAB tested in IBDs context but the following part aims to give a short updated overview [72,266,288,309,310,313].

III.1.b.i. Cloning expression system

This first section intends to summarize the different expression systems available for the production of heterologous proteins by LAB and all others bacterial strains (Figure 44). The proteins can be expressed either constitutively with the use of native promoters or in a tightly controlled manner. In this last case, the cloning plasmid carries the target gene under the transcriptional control of an inducible promoter. Inducible systems present several advantages over constitutive ones. First, they do not lead to overproduction of the recombinant therapeutic substances, which can become deleterious at excessive concentrations. Secondly, the constant expression of the recombinant proteins costs a lot of energy for the bacteria which are fragilized. Consequently, inducible systems are preferred as they allow a controlled delivery of the therapeutic proteins and they generate less undesirable adverse effects.

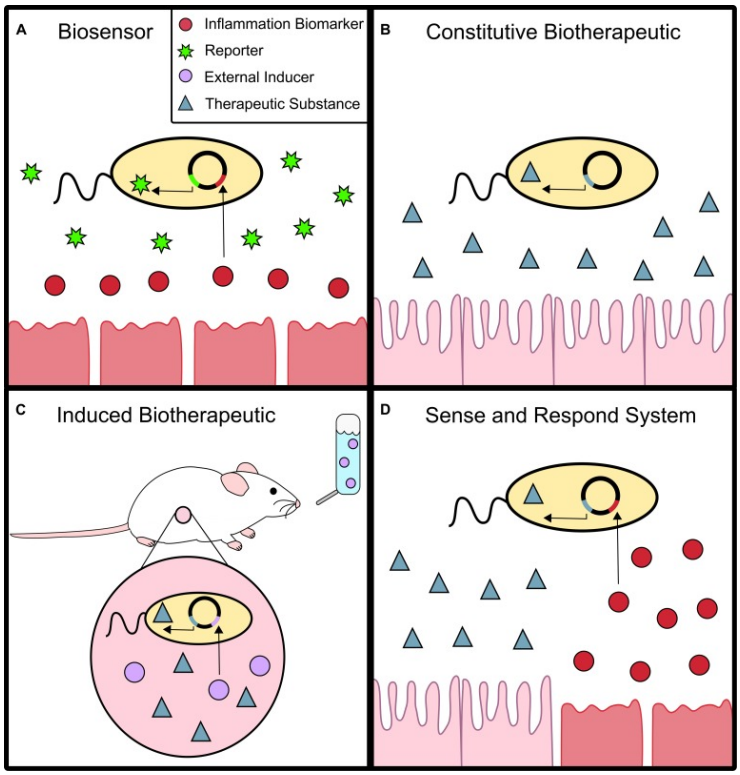

Figure 44: Summary of the different expression systems available for probiotic engineering. Figure from M. Barra et. al. [72] (A) Diagnosis tools : promoter sensitive to inflammatory biomarker leading to the expression of an easily detectable reporter molecule such as green fluorescent protein. (B) Constitutive biotherapeutics, mostly based on native promoter. (C) Induced biotherapeutics, mostly based on promoter activatable by external chemical substances. (D) Sense and respond system: the expression of the therapeutic protein is induced by the sensing of inflammatory biomarker.

Most of the inducible expression systems are based on promoters which are activated under the presence of a specific chemical compound. According to Carvalho *et. al*, the first systems

tried for probiotic engineering were composed of the lac promoter whose induction is dependent of the presence of lactose [314]. Another expression system developed by Miyoshi *et. al* for *L. lactis* is composed of the xylose permease gene promoter. In this case, the transcription of the fused gene is induced by xylose while repressed by fructose or mannose [315]. It allows to turn on or off as desired the recombinant protein expression via a chemical control. This system, named XIES (xylose-inducible expression system) was notably used to control the expression of IL-10 cytokine in recombinant *L. lactis* by adjusting the amount of xylose inducer [316]. Likewise, another inducible system successfully used by the group of Z. Hamady is the xylan-inducible expression system present in *Bacteroides ovatus* [317,318]. The quantity of xylan integrated into the food or the water given to mice treated with modified bacteria was shown to impact the expression of the recombinant protein. Another example of inducible system applied to engineered probiotics relies on an arabinose-induced promoter. In order to induce the protein expression, the water given to the mice can be infused with arabinose.

Many heterologous proteins have been also expressed under the control of the nisin promoter (PnisA). The corresponding system, named Nisin-Controlled Gene Expression system (NICE), were initially implemented in MG1363 bacteria that were subjected to the chromosomal insertion of nisR and nisK genes [319,320]. These latter are involved in the nisin-dependent activation of PnisA. As illustrated in Figure 45, nisR and nisK proteins constitutes a two-component regulatory system: nisK proteins recognizes nisin, signals its identification to nisR which then induces PnisA. The NICE system is considered has one of the most powerful genetic tools for gene cloning and has allowed the controlled expression of various heterologous proteins.

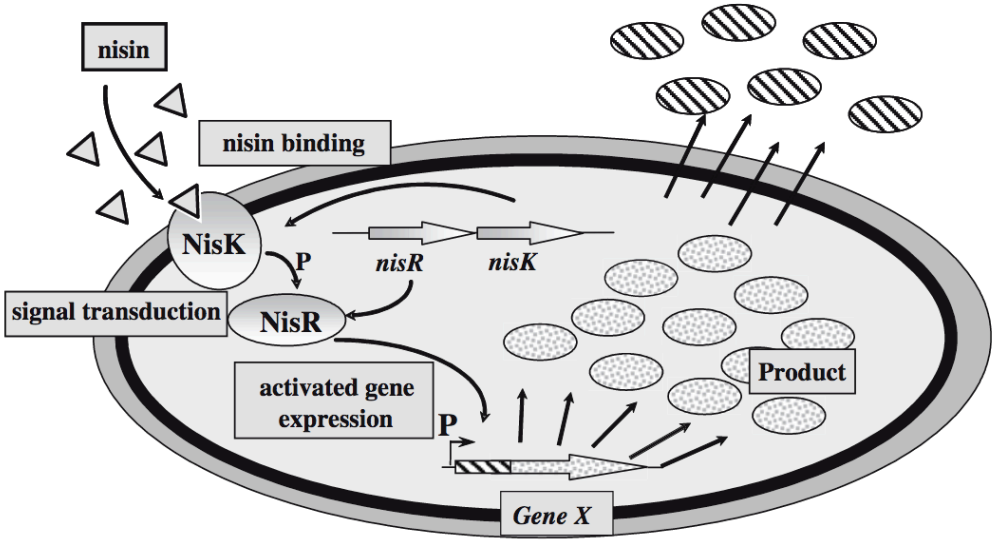

Figure 45: Principle of Nisin-controlled gene expression (NICE) system. Figure from I. Mierau et. al [320]. NisK is a nisin sensor histidine kinase; NisR, a transcriptional activator regulating P_{nisA} promoter; and Gene X, the target gene cloned behind the nisA promoter.

While all these inducible systems allow a regulated and efficient production of the protein of interest, they require the addition of external substrates. Researchers then looked for new inducible systems overcoming this drawback. To this end, they developed new expressions systems containing promoters sensitive to environmental signals such as to particular physiologic state, diseases biomarkers, pH change etc. The resulting probiotics are then able to detect specific biomarkers and to respond by generating the therapeutic proteins. Among these sense-and-respond systems, the most known is probably the stress-inducible controlled expression system (SICE). B. Benbouziane et *al.* had the smart idea to clone the promoter of the groESL operon into a plasmid vector [321]. groESL is a chaperone complex overexpressed during heat-shock conditions and playing a key role in the refolding of denatured proteins. The groESL promoter was shown to respond to different stresses such as heat-shock, low pH, UV-radiation and salt or bile acids addition. As patients suffering from IBDs especially exhibit physiological stresses [322], the SICE system may constitute an interesting strategy for IBDs treatment. Indeed, it allows the localized *in situ* production of the therapeutic protein of interest at the target inflammation site, which should result in greater pharmacological action. Moreover, it does not require the pre-induction of the engineered bacteria with external agents before administration. However, note that upon administration into the host, the recombinant bacteria will encounter other stresses along the GIT like acid stress during passage through the stomach and bile stress in the duodenum. Consequently, the SICE system

do not achieve a delivery completely specific to the gut inflammation. More recently, R. McKay engineered *E. coli* to detect nitric oxide (NO), accumulate at sites rich in NO and secrete the therapeutic protein [323]. Briefly, they designed a complex genetic circuit illustrated in Figure 46 in which the NO-sensitive promoter of Hmp protein, responsible for NO removal to nitrate, controls the expression of a motility regulator protein CheZ. Hence, upon NO activation, the expression of CheZ induces the migration of the engineered strain near the activator sources and so toward NO higher concentrations. NO was chosen as the attractor because it constitutes a relevant biomarker of IBDs. It is, in fact, found in higher amount in the intestinal fluids of IBDs cases compared to healthy patients and it is notably located where the inflammation is prevalent [324–326]. The Hmp promoter simultaneously regulates the expression of T7 polymerase, which activates the T7 promoter that controls the transcription of the gene coding for the biotherapeutic. To sum up this case, the genetic engineering allowed the sensing of an IBDs biomarker and the subsequent pseudotaxis and release of the target therapeutic proteins. Another strategy used in sense-and-respond genetic engineering include the use of tetrathionate biosensor system [327]. Indeed, tetrathionate is known to participate in the generation of gut inflammation.

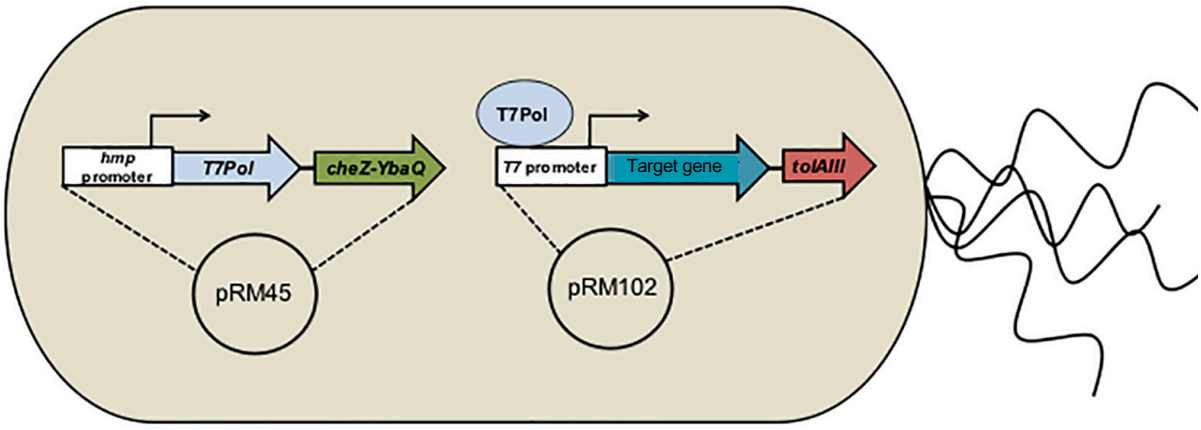

Figure 46: Dual expression plasmid system allowing both pseudotactic motility circuit and the expression of the therapeutic proteins in response to nitric oxide- sensing. Figure from R. McKay et. al [323].

In summary, advances in synthetic biology led to new expression systems that provide ever more specific, efficient and regulated live biotherapeutics. In particular, the combination of biosensor system with the production of therapeutic protein reinforced the potential of engineered bacteria for both IBDs diagnostic and treatment *in vivo*. For further improvement, new biomarkers indicative of intestinal inflammation need to be discovered. These

biomarkers have to ***i)*** be tightly specific to IBDs, ***ii)*** possess promoters responding to their presence to elicit the transcription of the gene coding for the recombinant proteins and ***iii)*** be localized at the precise site where the drug delivery is desired for an improved bio-activity.

Otherwise, the expressed heterologous proteins can be delivered into three different cellular compartments, whatever expression system is used. First, the recombinant protein can be retained inside the bacterium cytoplasm. This cellular location is preferred when the expressed protein has to be protected from the harsh extra bacterial conditions that may degrade it (such as the very acidic gastric environment). However, the bacteria lysis is necessary to release the active protein so as it can reach its site of action. Secondly, the expressed protein can be exported out of the bacterium. In this case, the recombinant protein is in direct interaction with the external inflammatory environment. The extracellular release is achieved by the fusion with a hydrophobic and negatively charged signal peptide favorizing its translocation across the bacterial membrane. A third possible location is attached to the bacteria surface which profits from both advantages of the two previous. To this end, the target therapeutic is conjugated to a cell wall anchor (CWA) that can bind covalently to the peptidoglycan present in the bacteria membrane.

To conclude with this section, genetically modified probiotics offer a combination of delivery technique and therapeutic action. One major drawback of this strategy is the presence of an antibiotic resistance gene in the expression vector. All the above-mentioned expression systems require such a gene to select bacteria expressing the desired biotherapeutics. Indeed, these resistance gene may later be transferred to harmful pathogen on the human GIT. There is then a real need for biological confinement tools or for the replacement of this antibiotic-based selection via the development of plasmid backbones devoid of antibiotic resistance marker for instance.

III.1.b.ii. Expression of anti-inflammatory agents by recombinant LAB

Today, probiotics have been engineered to produce different proteins in order to provide beneficial effects on gut inflammation through different mechanisms. They include the expression of antimicrobial peptides, anti-inflammatory cytokines, trefoil factors and inhibitors of pro-inflammatory cytokines, among others.

The following section focuses on these various types of anti-inflammatory drugs expressed by engineered probiotics. The Table 4 lists all the strains mentioned in this part and classified by the role of the recombinant proteins.

	Recombinant protein	Engineered strain	Expression system	Cellular location	Protective effect	Reference
Antimicrobial peptides	Human α-defensin 5 (HD5) or β-defensin 2 (HBD2)	*E. coli Nissle* 1917	Bacteriophage T7 promoter	Extra bacterial (human α-defensin 5 (HD5) secretion signal)	Antimicrobial activity against *E. coli* and *Salmonella enterica*	[328]
	Mouse cathelin-related antimicrobial peptide (mCRAMP)	*L. lactis* NZ3900	NICE	Cytoplasm	DSS-induced murine colitis	[329]
	Pancreatitis-associated protein I (PAP)	*L. lactis* NZ9000	NICE	Extra bacterial (mouse IgK secretion signal)	5-FU-induced murine mucositis	[330]
Anti-inflammatory cytokines	IL-10	*L. lactis* MG1363	Bacteriophage T7 promoter	Extra bacterial (Usp45 secretion signal)	IL-10-deficient mice and DSS-induced murine colitis	[331,332]
		L. lactis MG1363	ThyA native promoter from L. lactis	Extra bacterial (Usp45 secretion signal)	Phase I clinical trial: CD patients	[333]
		L. lactis MG1363	SICE	Extra bacterial (Exp4 secretion signal)	TNBS-induced murine colitis	[321]
		L. lactis NCDO2118	XIES	Cytoplasm or extra bacterial (Usp45 secretion signal)	TNBS-induced murine colitis	[316]
	IL-27	*L. lactis* MG1363	Constitutive *L. lactis* promoter P1	Extra bacterial (Usp45 secretion signal)	T-cell transfer-induced entero colitis in Rag-/- mice	[334]
	IL-35	*E. coli* BL21	Bacteriophage T7 promoter	Cytoplasm	DSS-induced murine colitis	[335]
	KGF-2	*B.ovatus*	Xylan-induced system	Extra bacterial (*B. fragilis* enterotoxin secretion signal)	DSS-induced murine colitis	[318]
	TGF-β	*B.ovatus*	Xylan-induced system	Extra bacterial (*B. fragilis* enterotoxin secretion signal)	DSS-induced murine colitis	[336]
	TGF-β	*L. lactis* NZ9000	NICE	Extra bacterial (Usp45 secretion signal)	DSS-induced murine colitis	[337]
	GM-CSF	*E. coli* K-12 W3110	NO-induced pseudotaxis and expression.	Extra-bacterial (fusion with pore-forming protein TolAIII)		[323]
Trefoil Factors	TFF1/TFF2/TFF3 separately	*L. lactis* MG1363	Constitutive *L. lactis* promoter P1	Extra bacterial (Usp45 secretion signal)	DSS-induced murine colitis and IL-10-deficient mice	[338]

	TFF3 + TGF-β	*L. lactis* PSM565	pH-regulated promoter (P170)	Extra bacterial (SP310mut2 secretion signal)	Wound healing *in vitro*	[339]
	TFFs fused to CsgA fibrous matrix	*E. coli Nissle* 1917	Arabinose-induced system	Extra bacterial (N22 secretion signal)	DSS-induced murine colitis	[340]
Inhibitors of pro-inflammatory cytokines	Anti-TNF-α affibodies	*L. lactis*		Bacteria surface-displayed : Usp45 secretion signal + AcmA membrane-binding protein	DSS-induced murine colitis	[341]
	Anti-murine TNF-α nanobodies	*L. lactis* MG1363	Constitutive *L. lactis* promoter P1	Extra bacterial (Usp45 secretion signal)	IL-10-deficient mice and DSS-induced murine colitis	[342]
	IL-1 receptor antagonist	*L. lactis* NZ9000	NICE	Extra bacterial (Usp45 secretion signal)	DSS-induced murine colitis	[343]
Anti-proteases enzyme	Elafin	*L. lactis* NZ9000	NICE	Extra bacterial (Usp45 secretion signal)	DSS-induced murine colitis and T-cells transfer-induced colitis in immuno-defficient mice	[344]
Antioxidant enzymes	Human 15-lipoxygenase-1	*L. lactis* NCDO 2118	XIES	Cytoplasm	DSS-induced murine colitis	[345]
	Microbial Anti-inflammatory Molecule (MAM)	*L. lactis* MG1363	Cytomegalovirus (CMV) eukaryotic promoter	Cytoplasm	DNBS-induced murine colitis	[346]
	Heme oxygenase-1	*L. lactis* NZ9000	NICE	Extra bacterial (Usp45 secretion signal)	DSS-induced murine colitis	[347]
	L. lactis MG1363 MnSOD (sodA)	L. lactis NZ9800 and L. latarum NCIMB8826 Int-1	NICE	Cytoplasm	TNBS-induced murine colitis	[348]
	S. thermophilus MnSOD	*Lactobacillus gasseri*	LacZ promoter	cytoplasm	IL-10-deficient mice	[349]
	L. plantarum MnCAT	*L. casei BL23*	Native promoter	cytoplasm	DSS-induced murine colitis	[277]
	L. lactis MG1363 MnSOD (sodA)	*L. lactis* MG1363 and *Lb. casei* BL23	Native promoter	cytoplasm	DSS-induced murine colitis	[350]
	L. plantarum MnCAT and *L. lactis* MG1363 MnSOD (sodA)	*L. casei* BL23	Native promoters	cytoplasm	TNBS-induced murine colitis	[351]
	L. plantarum MnCAT and *L. lactis* MG1363 MnSOD (sodA)	*S. thermophilus* CRL 807	Native promoters	cytoplasm	TNBS-induced murine colitis	[352]
	Human MnSOD (SOD2)	*Bifidobacterium longum HB25*	Hup native promoter from *B. longum*	Extra bacterial (amyB secretion signal)	DSS-induced murine colitis	[353]

Table 4: LAB genetically engineered to express anti-inflammatory therapeutics for GIT inflammation models.

- Antimicrobial peptides

Antimicrobial peptides produced by recombinant bacteria appear to be promising therapeutic candidates to inhibit pathogen proliferation in the gut microbiota and subsequently suppressing microbiota-driven inflammatory events. As a reminder (III.1.a.ii), bacteriocin production is indeed a mechanism used by commensal and probiotic bacteria for competitive exclusion of pathogens. These anti-microbial substances include defensins, cathelicidins and histatins. In 2012, Seo *et. al* reported a genetically engineering strain of *E.coli,* Nissle 1917, to express human α-defensin 5 (HD5) or β-defensin 2 (HBD2) [328]. The purified recombinant defensins showed antimicrobial activity against pathogenic *E. coli* and *Salmonella enterica serovar*. The same year, a modified *L. lactis* strain expressing cathelicidin conferred anti-microbial activity associated to anti-inflammatory activity in DSS-induced murine colitis [329]. Another extensively studied antimicrobial peptide is the C-type lectin Reg3A. Reg3A, also denominated PAP for pancreatitis-associated protein, exerts bactericidal activity against Gram-positive bacteria and in that way have protective effect on GIT inflammation. A striking study published in 2017 shows the efficacy of a PAP-expressing *L. lactis* strain to limit the growth of pathogenic commensal *E. faecalis* in a 5-FU-induced mucositis murine model [330]. In addition to the antimicrobial activity, decreased histological damages and more globally improved mucositis symptoms were recorded.

- Anti-inflammatory cytokines

Most commonly, the application of engineered probiotics on IBDs treatment implies the recombinant production of anti-inflammatory cytokines. These latter are known to play essential roles in the regulation of the inflammation processes, notably through effector T-cells inhibition. For this reason, the administration of purified doses of anti-inflammatory cytokines have been already explored for IBDs therapies but as discussed earlier, genetically engineered probiotics are better candidates for a more localized and specific delivery.

The most studied therapeutic cytokine is interleukin-10 (IL-10) [354]. This may be explained by the growing acknowledgment that IL-10 protects against inflammation by restricting excessive immune response of both innate and adaptive immune cells. Indeed, IL-10 mutations are associated with an increased risks of inflammatory disorders. The first descriptions of genetic engineering for IL-10 expression appeared in 2000. The group of E. Remaut demonstrated the ability of a IL-10 secreting *L. lactis* strain to partially relieve

inflammation in a DSS-induced colitis model and to prevent any IBD onset in IL-10 knockout mice [331,332]. Based on these encouraging pre-clinical results, a recombinant IL-10 producing *L. lactis* strain was evaluated in a phase I clinical trial involving CD patients [333]. Before administrating live genetically modified organisms (GMO) to patients, researchers developed a containment strategy consisting of integrating IL-10 gene as a replacement of thymidylate synthase gene [355]. Consequently, the survival of genetically modified *L. lactis* is dependent on the presence of thymine or thymidine, compounds only available in the body. This clinical trial was a success on two points. First the IL-10-secreting strain was clinically well-tolerated as it did not induce any systemic side effects. Secondly, the containment strategy was efficient in preventing any spreading of the transgene in the external environment lacking of thymine and thymidine. Unfortunately, a phase II clinical trial conducted by Actogenix in 2009 revealed that the engineered IL-10-expressing *L. lactis*, while safe, had no significant impact on wound healing compared to placebo. Since then, few novel preclinical studies of Il-L-10 secreting *L. lactis* were published. They include studies reporting the use of the XIES and SICE systems to produce IL-10 in a regulated manner and evidencing again the efficacy of constructed LAB to alleviate DNBS-induced murine colitis (improvement in weight loss and decrease in macroscopic and histologic scores) [316,321].

More recently, other immunosuppressive-recognized cytokines were expressed by engineered probiotics. In particular, the interleukin-27 (IL-27) whose levels are dysregulated in IBDs patients was expressed in *L. lactis* MG1363 [334]. The engineered *L. lactis* was able to successfully protect mice from T-cell transfer-induced murine colitis. Furthermore, this treatment was more effective both either systemic intraperitoneal injection of IL-27 and IL-10-secreting counterpart *L. lactis*. One hypothesis is that the recombinant IL-27 delivery induced a higher IL-10 endogenous production than could be achieved with recombinant IL-10-secreting bacteria themselves. Indeed, a greater increase in IL-10 amount was measured in the intestinal epithelium of mice treated with IL-27-producing *L. lactis*. Also, a non-pathogenic *E. coli* strain was engineered to express the interleukin-35 (IL-35) cytokine [335]. IL-35 plays a pivotal role on inflammation regulation by promoting the infiltration of Treg cells and the secretion of IL-10. The IL-35- producing *E. coli* strain proved to be effective in reducing disease activity scores and pathology features.

Some growth factors constitute a promising class of anti-inflammatory cytokines for IBDs treatment. They gather, among others, the keratinocyte growth factor 2 (KGF-2), the transforming growth factor β (TGF-β) and granulocyte macrophage-colony stimulating factors (GM-CSF). The genes of the two first were cloned in *B. ovatus* and the resulting engineered strains were able to slow down the pathologic inflammatory process and to accelerate the healing of disrupted epithelium in DSS-induced colitis mice [318,336]. Similarly, a *L. lactis* engineered to express TGF-β also provides significant benefits on the same DSS model [337]. Concerning GM-CFS, its gene was encoded in a dual-plasmid system affording an induced expression in presence of nitric oxide [323].

- Trefoil factors

Trefoil factors (TFFs) are peptides (7-12 kDa) produced by the mucin-secreting epithelial cells (Goblet cells, Figure 42). While their functions are not well elucidated, TFF1, TFF2 and TFF3 are assumed to protect and restore the mucosal barrier functions in case of injury. Three engineered *L. lactis strain were constructed to express and* secrete each individual TFF [338] and were separately administrated to *mice suffering from* DSS-induced colitis. In all three cases, the production of TFFs conferred them *enhanced protective and reparative properties on the intestinal epithelium.* Interestingly, these therapeutic effect on GIT mucosa was considerably boosted compared to the oral or rectal administration of purified TFFs. Otherwise, the co-expression of TFF-3 and TGF-β by L. *lactis* improved the closure of a scratch-created wound in IPEC-J2 cells layers [339]. A more recent publication also reports the secretion and the assembly of an extracellular matrix containing all three TFFs by engineered *E. coli* Nissle 1917 [340]. All three TFFs were fused to the self-assembling monomer unit of the fibrous matrix: CsgA. Again, the intragastric administration of the modified strain *was very efficient in preventing and ameliorating colitis* of DSS-induced colitis.

- Inhibitors of pro-inflammatory cytokines

A common treatment prescribed for severe IBDs involves monoclonal antibodies neutralizing pro-inflammatory cytokines such as TNF-α. To avoid the side effects related to their systemic administration, *L. lactis* were genetically modified to produce such anti-TNF-α antibodies or alternative inhibitors of pro-inflammatory cytokines signaling. Research studies mainly focused on TNF-α as its involvement in IBDs is largely recognized and it is considered as one of the most important inflammation mediators. The secretion of TNF-α-binding affibodies by

a modified *L. lactis* strain resulted in decreasing TNF-α levels in the stools of mice suffering from DSS-induced colitis [341]. Interestingly, this was associated to a general improvement of the colitis which may be correlated to the blockage of TNF-α activity. Furthermore, another study from K. Vandenbroucke *et. al* showed the capacity of anti-TNF-α nanobodies-secreting *L. Lactis* to reduce the inflammation in the same murine model of DSS-induced colitis and in IL-10 knockout mice [342]. The nanobodies are derived from heavy chain fragments of antibodies and are preferred to these latter for their increased stability. Otherwise, some studies also intend the suppression of pro-inflammatory IL-1 signaling to alleviate the inflammation in IBDs. For this, the endogenous IL-1 receptor antagonist (IL-1ra) was suggested to be an interesting target. The oral administration of a recombinant *L. lactis* hypersecreting IL-1ra was shown to block IL-1 signaling and thus to improve DSS-induce colitis symptoms [343].

- Others protective proteins

Various others proteins were expressed by bacteria based on their putative ability to reduce intestinal inflammation. They include:

- Human 15-lipoxygenase-1, an oxidative enzyme that catalyzes the formation of anti-inflammatory mediators [345]
- The Microbial Anti-inflammatory Molecule (MAM) peptide produced by commensal *F. prau* and recognized for its anti-inflammatory properties on the intestinal epithelium [346].
- Heme oxygenase-1, responsible for heme degradation and ensuing production of anti-inflammatory catabolites [347].
- Elafin: an anti-protease enzymes (serine protease inhibitors) able to reduce the excessive proteolytic activity observed in IBDs [344].

The characteristics of the constructed recombinant bacteria and their protective effects *in vivo* are described in Table 4.

- Antioxidant SOD and CAT enzymes

The sections I.2.c, I.2.d and I.2.e in the chapter I emphasize the tight correlation between oxidative stress and inflammation and the potential of CAT and SOD antioxidant as therapeutic targets for IBDs.

Based on these observations, the idea to construct recombinant bacteria expressing SOD and CAT enzymes has naturally emerged. The SOD or CAT enzymes so far used for research and clinical trials was most frequently purified from bovine. The use of such purified bovine enzymes is limited by its high cost, its intramuscular administration, its immunogenicity and its eventual toxicity. This latter may be due to the presence of animal-originated impurities and to the risk of dealing with diseases-affected bovines. For instance, the bovine SOD orgotein, marketed for the treatment of inflammatory diseases, has caused anaphylactic shocks related to contaminants-induced hypersensitivity reactions. Consequently, orgotein was withdrawn from European countries [356]. The use of engineered bacteria expressing SOD or CAT advantageously not requires samples of animal origin and subsequent intricate purification of the enzymes. More generally, the use of live recombinant bacteria as producer of the drug is more favorable than the systemic administration of the purified drug. They indeed provide two main advantages. First, the recombinant bacteria can be orally delivered since the bacteria act as protective delivery vectors in the acidic gastric conditions. Secondly, after reaching the intestine, the bacteria will continuously produce the antioxidant enzyme at the inflammation site (*ie. in situ*). This could reduce the doses administrated. However, the choice of bacteria should be made consciously and, in particular, oriented towards GRAS and QPS bacteria. Note that the advantages discussed here apply to all the genetically engineered probiotics mentioned in the previous sections and not only to those that follow.

Several studies have shown the evaluation of the anti-inflammatory and antioxidant effects of SOD- or CAT-producing bacteria. The following section summarizes some relevant examples. In 2006, a first example of oral treatment with live recombinant LAB producing SOD was published by W. *Han et al.* [348]. The authors gave sodA (MnSOD)-producing *L. lactis* and *L. plantarum* strains to rats suffering from TNBS-induced colitis. They observed a faster recovery of forced-fed rats with SOD-producing *L. plantarum* while the wild-type strain had no effects. One year after, I.M. Caroll published similar results on IL-10 knockout mice treated with *L. gasseri* strain engineered to express the MnSOD from *Streptococcus thermophilus* [349]. Again, the recombinant strain was able to effectively reduce the severity of the colitis but not the native strain. In 2010, L. Watterlot *et al.* designed two *L. casei* BL23 expressing either the *L. plantarum* nonheme manganese catalase (MnKat) or the *L. lactis* MG1363 sodA and evaluated their effect in murine DSS colitis through gavage [277,350]. Unfortunately, the

MnKat-producing strain did not exert more pronounced effect on gut inflammation than the control wild-type strain [277]. In contrast the SOD-producing strain was able to significantly attenuate the colitis [350]. The absence of added protective effects for the MnKat-expressing strain is consistent with the results obtained some time before by T. Rochat *et al.* where the heterologous production of nonheme MnKat by *L. casei* BL23 did not improve its anti-inflammatory and antioxidant bioactivity [277]. Another example by the group of JG. Leblanc implies engineered *L. casei BL23* strains producing sodA or MnKat but evaluated this time on the TNBS-induced murine model [351]. Based on weight loss recovery and damage scores, the mice that received the recombinant strain displayed significantly diminished colitis symptoms in comparison to the wild-type group. JG. Leblanc's group also reported the combination of the antioxidant activity coming from recombinant sodA or MnKat enzymes with the intrinsic immunomodulatory activity of *S. thermophilus* CRL 807 strain. The engineered and the native activity of the bacteria act synergistically to alleviate efficiently the inflammation in a TNBS colitis model [357]. Lastly, a *Bifidobacterium longum* strain expressing human MnSOD_Pep1 fusion protein was recently constructed and examined [353]. The recombinant MnSOD was conjugated to the penetratin Pep-1 with the intent to favor its cell penetration in epithelial cells. The co-incubation between MnSOD_Pep1 bacteria and LPS-induced inflammatory cell model revealed enhanced anti-inflammatory activity of the constructed MnSOD_Pep1-expressing strain. In addition, the supplementation of the engineered *Bifidobacterium* to mice successfully ameliorated DSS-induced colitis.

To conclude, recombinant LAB have been largely used to produce and deliver bioactive proteins that address different root causes of IBDs. Their evaluation on murine colitis model revealed their ability to alleviate colitis as shown by reduced activity scores, faster weight recovery and decreased inflammation markers. The global strategy described above was nicely illustrated in Figure 47 extracted from S. Shigemori *et. al* [309].

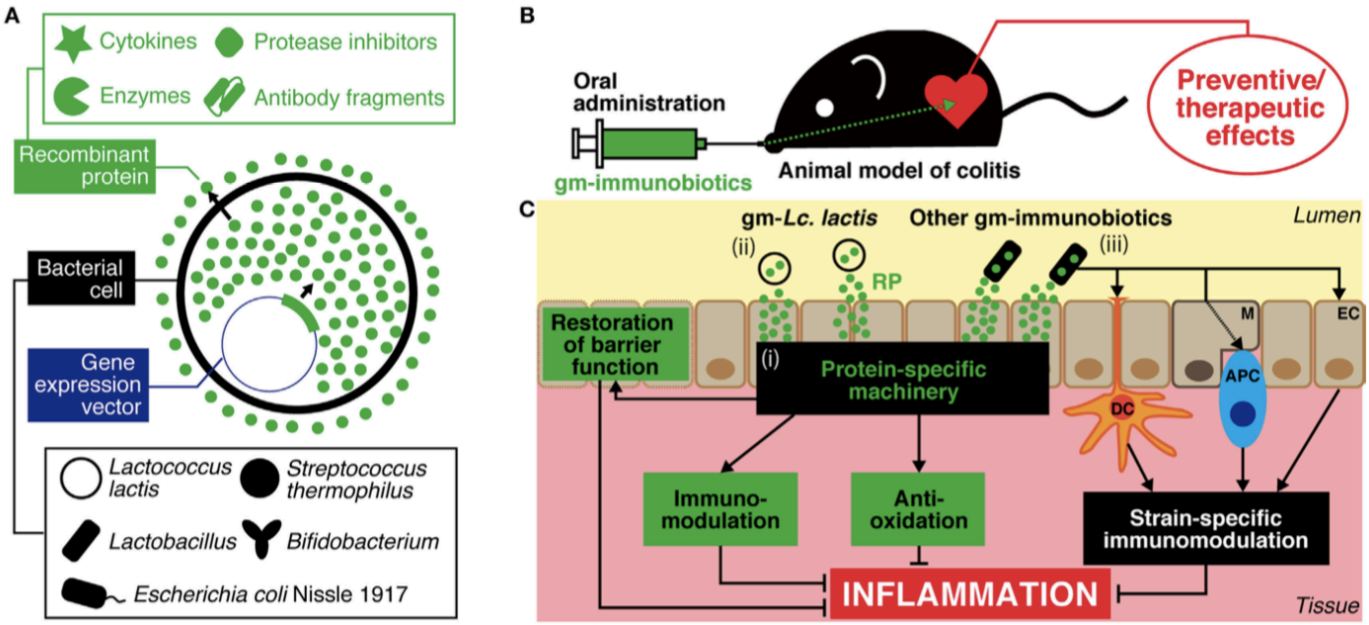

Figure 47: Illustration of the strategy relying on genetically modified probiotics for the expression of recombinant therapeutics proteins. Figure from [309]. (A) The genes encoding for bioactive proteins (cytokines, protease inhibitors, etc.) can be ligated in expression vector and integrated into probiotics. (B) The engineered bacteria can then be orally administrated and modulate the inflammation in animal model of colitis (C) Summary of the different pathways implicated in the preventive and therapeutic effects exerted by recombinant bacteria in vivo.

III.1.c. Peptidyl SOD and CAT mimics

III.1.c.i. Advantages of SOD and CAT mimics over native enzymes

Although successful in several studies, the use of engineered bacteria expressing endogenous antioxidant SOD or CAT enzymes has different drawbacks [12]. Overall, endogenous proteins represent poor drugs because they penetrate slowly inside cells owing to their large molecular radius and inappropriate charge density. Consequently, only a small fraction of the expressed SOD/CAT proteins will reach the action site where oxidative stress occurs in the cells. To overcome these limitations, the use of low-molecular weight synthetic molecules reproducing the antioxidant activity of the SOD or CAT enzymes was explored. Based on their lower molecular radius and the possibility to tune their charge density, these synthetic SOD or CAT mimics can afford improved pharmacodynamics and pharmacokinetics properties. They are also less subjected to hypersensitivity reactions related to immunogenicity (stimulation of the immune system in response to the presence of a foreign substance).

Therefore, it would be very promising to engineer LAB able to produce antioxidant enzyme mimics. In this context, peptidyl metal complexes are of great interest since the peptides are

genetically encodable et LAB can be supplemented in metals at non-toxic doses. The investigation of this strategy constitutes one of the main aims of my PhD project

III.1.c.ii. State of the art of peptidyl complexes mimicking SOD and CAT

A general introduction will provide an overview of existing SOD and CAT mimics and the evaluation of their bioactivity. The following section will give an overview of peptidyl SOD and CAT mimics described so far in the literature.

A variety of peptidyl copper complexes have been reported as catalytic or stoichiometric scavengers of superoxide. Most of them were inspired from the active site of endogenous Cu/ZnSOD. In particular, Cu/ZnSOD isolated from Gram-negative bacteria was shown to possess histidine-rich N-terminal domains containing high affinity copper(II) binding site. These regions are believed to act as the SOD active center upon Cu(II) coordination. In agreement, Cu(II)-coordinated peptidyl fragments composed by the first few amino acids of Cu/ZnSOD N-terminus were able to catalyze superoxide disproportionation [358,359]. Likewise, while with the resolution of the Cu/ZnSOD 3D structure, researchers attempted to design peptides reproducing its Cu(II) binding site [360]. Again, the peptidyl analogs of Cu/ZnSOD active center bind copper efficiently and display intrinsic SOD activity. The speciation, coordination sphere, thermodynamic stability and redox properties of these multi-histidine complexes have been thoroughly characterized. This allows to correlate the Cu(II) affinity and SOD activity with the number of histidines and the distance between them [361,362]. The nature of the amino acids between histidine residues were also shown to impact the SOD activity. For instance, the presence of imidazole donor amino acids decreased the reduction potential value of the Cu(II) complexes. The tuning of these parameters then allow to discover new peptides with reinforced SOD activity [361].

Thus, various small peptides containing 2-4 histidines were synthetized and assessed for their SOD activity. Because, they are bio-inspired from the endogenous SOD active site or by metal-binding proteins, they are commonly named analogs. Some relevant peptides are listed in Table 5.

Peptide (P)	Added metal (M) M:P	Production	Buffer	pH	IC_{50} µM (NBT)	k_{cat}	Reference
Endogenous Cu/Zn SOD	X	Purified from bovine	Phosphate buffer (50mM)	6.8 7.4	0.003 0.0044		[361]
HPO_4	Cu(II)	Synthetic	Phosphate buffer (50mM)	7.4	0.35		[361,362]
cyclo-(His-His)	Cu(II), 1:2	Synthetic	Phosphate buffer (5mM)	7	0.5		[168]
Ac-HVH-NH_2	Cu(II), 1:1	Synthetic	Tris–HCl buffer (20 mM)	7.4	0.2		[180]
Ac-HisValGlyAsp-NH_2	Cu(II), 1:1	Synthetic	Tris–HCl buffer (20 mM)	7.4	0.16		[180]
HADHDHKK-NH_2	Cu(II), 1:1	Synthetic	Phosphate buffer (50mM)	7	0.11		[358]
Ac-HHGH-OH	Cu(II), 1:1	Synthetic	Phosphate buffer (50mM)	7.5	0.15		[363]
Ac-HGDHLHNHDTK-NH_2	Cu(II), 1:1	Synthetic	Phosphate buffer (50mM)	7	0.19		[359]
Ac-S2H3-NH_2	Cu(II), 1:1	Synthetic	Phosphate buffer (50mM)	7.4	0.15		[362]
Ac-HSaHSaHSaH-NH_2	Cu(II), 1:1	Synthetic	Phosphate buffer (50mM)	7.4	0.044		[362]
Ac-HGGH-NH_2	Cu(II), 1:1	Synthetic	Phosphate buffer (50mM)	7.4	0.38		[361]
Ac-HAAHGH-NH_2	Cu(II), 1:1	Synthetic	Phosphate buffer (50mM)	7.4	0.048		[361]
Ac-HAAHVH-NH_2	Cu(II), 1:1	Synthetic	Phosphate buffer (50mM)	7.4	0.077		[361]
Ac-HGGGHGH-NH_2	Cu(II), 1:1	Synthetic	Phosphate buffer (50mM)	7.4	0.082		[361]
Ac-PDHKHHLH-NH_2	Cu(II), 1:1 Cu(II), 1:5	Synthetic	HEPES 50mM	7.4	0.12 0.06 (with XTT!)		[192]
Ac-TYVVHAGSRIYHVHGGH-NH_2	Cu(II), 1:1	Synthetic	PBS 50mM	7		157 U/mg	[364,365]

Table 5: List of multi histidine peptides inspired from the Cu/Zn SOD active site discussed in the main text.

In addition to peptidyl copper SOD mimics, two peptidyl nickel complexes bio-inspired from the square planar Ni(II) center of the native Ni-SOD were reported by the groups of P. Delangle and C. Duboc [366,367]. The first one, described in 2019, is based on an ATCUN-like binding motif displaying a square-planar N_3S coordination. The second one, described in 2021, is composed of a sulfur-rich pseudopeptide ligand, where three cysteines are grafted on a nitrilotriacetic acid scaffold, providing thus a S_3O first coordination sphere for Ni(II). Both

demonstrate similar catalytic SOD activity in water with a catalytic rate around 10^5-10^6 $M^{-1}.s^{-1}$, which is in the same order of magnitude, or a bit lower, than that previously measured for cupper-based peptidyl SOD mimics.

Besides analog peptides, other longer peptides named heterologous peptides were designed by molecular modeling. On the basis of the native SODs 3D-structures, the search for homologous sequence alignment in the active center can be computationally performed. Then, sequences with high homology can be chosen as scaffolds. Finally, structural predictions tools allow to optimize the scaffold by identifying the positions of key residues for SOD activity. The composition and position of the catalytic site around the scaffold can hence be corrected to obtain more efficient catalysts.

As an example, Singh *et. al* used and modified a 63-residues peptidyl scaffold forming a heme-binding four-helix bundle and initially designed by Gibney *et al.* [368,369]. Among others, the substitution of a leucine for histidine allowed the formation of a Mn (II) binding site. The resulting redesigned peptide displayed not neglected SOD activity (IC_{50}=8µM, phosphate buffer 50mM, pH 7.4) [368]. Another SOD mimics based on heterologous peptides was reported by Yan *et. al* [370]. They conducted homology modelling of human SOD1, SOD3 and bovine erythrocyte SOD and selected a 65-residues sequence. Next, they integrated the active site of glutathione peroxidase enzyme (GPx) as replacement of residues showing low homology and they re-designed the general structure to optimize the dual-activity center. Again, the heterologous peptide had efficient SOD and GPx activity upon copper and zinc coordination. Recently, a cell-penetrating peptide was introduced in the structure of this latter to enhance its intracellular penetration and improve its antioxidant activity in cells [233]. The structures of the mentioned heterologous peptides are given in Table 6. It should be noted that the size of these peptides is larger (> 60 amino-acids) than that of the analogous peptides discussed above. These longer peptides are preferred to small peptides because they can achieve higher catalytic efficiency thanks to more stable secondary structures and the potential presence of multiple catalytic sites. However, their intermediate size may avert shortcomings of large molecular weight native enzymes (as a reminder: weak cellular penetration).

This expansion in peptides size is hardly compatible with the classical technic for peptides synthesis. Consequently, these long peptides were produced biochemically. Briefly, the gene encoding for the peptides were cloned into expression vector and transformed in bacteria strains, *Escherichia coli* in the cited cases. The expressed heterologous peptides were then purified by anion-exchange chromatography or reverse-phase preparative HPLC.

Peptide	Metal	Activity	Production	Reference
NH_2-M-L-K-K-L-R-E-E-A-L-K-L-L-E-E-F-K-K-L-L-E-E-H-L-K-W-H-E-G-G-G-G-G-G-G-G-E-L-L-K-D-H-E-E-L-L-K-K-F-E-E-L-L-K-L-A-E-E-R-L-K-K-L-COOH	Mn(II)	SOD	*E. coli* BL21	[368]
NH_2-H-Q-H-Q-F-G-D-L-S-Q-G-A-E-S-T-G-P-H-Y-N-P-L-A-V-P-H-P-Q-H-P-G-D-W-G-N-F-A-V-R-D-G-S-L-**W-P-F-L-R-H-N-V-Y-G-R-P-R-A-C**-V-V-H-A-G-E-D-COOH	Cu(II) Zn(II)	SOD: 1254 U/mg **GPx** : 112 U/mg	*E. coli* BL21	[370]
NH_2-Y-G-R-K-K-R-R-Q-R-R-R-H-Q-H-Q-F-G-D-L-S-Q-G-A-E-S-T-G-P-H-Y-N-P-L-A-V-P-H-P-Q-H-P-G-D-W-G-N-F-A-V-R-D-G-S-L-**W-P-F-L-R-H-N-V-Y-G-R-P-R-A-C**-V-V-H-A-G-E-D-COOH	Cu (II) Zn (II)	SOD: 1218 U/mg **GPx :** 109 U/mg	*E. coli* DH5α	[233]

Table 6: List of the heterologous peptides exhibiting SOD activity upon metal coordination and discussed in the main text.

In conclusion, molecular model building and dynamics simulation are efficient methods for the establishment of novel *de novo* SOD and CAT mimics.

Finally, a new approach for the identification of new metal-binding peptides with SOD or CAT activity has been recently described. Briefly, two large libraries of peptidyl Cu- or Mn-complexes were generated by applying a combinatorial approach. For Cu- complexes library, variability was introduced at fixed positions in a sequence containing efficient Cu^{2+} binding motifs Ac-PX_1X_2KHX_3LH-OH [192,371]. For the Mn-complexes library, the following sequence was used: Ac-WAG$X_1X_2X_3X_4X_5$AK-OH and the positions $X_{1\text{-}5}$ were randomized with non-coordinating amino-acids and with D, E, H amino acids since the DEH motif is known to coordinate Mn^{2+} according to Peana *et al.* [372]. The resulting combinatorial libraries of metal complexes were screened for their SOD or CAT activity using in-gel activity assays [191]. This allowed the isolation of the PDHKHHLH-Cu and PHYKHRLH-Cu_2 complexes, with SOD and CAT activity, respectively, and the WAGDEYEDAK-Mn complex with SOD activity. To our knowledge, the PHYKHRLH-Cu_2 complex constitutes the first peptidyl CAT mimic described in the literature by K. Coulibaly *et al.* [371]. Interestingly, when the complexes were studied in details, it appeared that the SOD mimic PDHKHHLH-Cu complex has a stoichiometry of 1 peptide for 1 copper whereas the CAT mimic PHYKHRLH-Cu_2 complex exhibited a stoichiometry of 1 peptide for 2 coppers. This is fully consistent with their respective catalytical activity, since SOD dismutation involves a single electron transfer whereas H_2O_2 dismutation is a bi-electronic transfer (each copper affords one electron). Concatenation of

two WAGDEYEDAK peptides separated with a folded PG linker (KAEDYEDPGDEYDEAK-Mn) was shown to increase the SOD activity of the resulting complex. The catalytic SOD activity of the Cu(II)-PDHKHHLH complex was found in the same range than the other multi-histidine Cu(II) complexes mentioned above.

The bioactivity of the two copper complexes were evaluated in three different cells lines (Figure 48). The SOD mimic PDHKHHLH-Cu showed anti-superoxide properties in murine macrophage cell line Raw 264.7 and anti-inflammatory properties in LPS-stimulated HT29-MD2 intestinal epithelial cells. Likewise, the CAT mimic PHYKHRLH-Cu_2 was able to decrease hydrogen peroxide levels in HeLa HyPer cells. All these data strongly support the antioxidant properties of the peptidyl Cu(II) complexes in a cellular context.

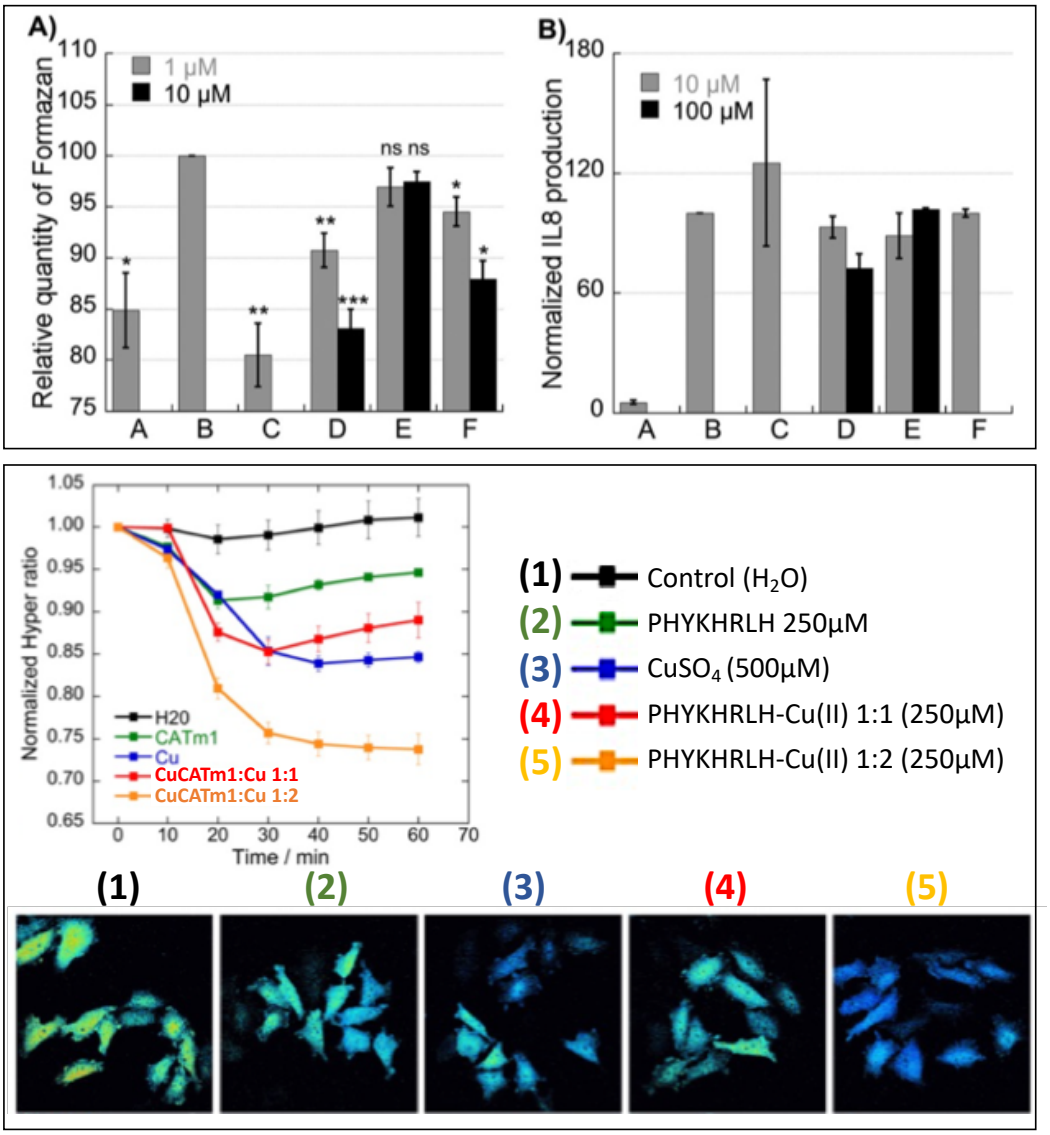

Figure 48: ***In cells bioactivity evaluation of the peptidic Cu-complexes developed by a combinatorial approach.*** *(Top) Figure from [192]. Activity of the SOD mimic PDHKHHLH-Cu(II) on two cellular models of oxidative stress: A) measurement of extracellular superoxide using XTT as UV-visible marker in RAW 264.7 macrophages and B) measurement of extracellular interleukin-8 pro-inflammatory cytokine in LPS-stimulated HT29-MD2 intestinal cells. Different treatments were assessed: A= non-activated cells, B= activated cells, C= native CuZnSOD (100 U/mL), D= PDHKHHLH-Cu(II) 1:1, E= PDHKHHLH, F= $CuSO_4$. In both graphs, the values were set at 100% for activated cells control. (Bottom) Figure from [371]. The levels of H_2O_2 in HeLa HyPer cells were monitored by fluorescence under different conditions: H_2O (control cells),* ***PHYKHRLH*** *(250 µM), $CuSO_4$ (500 µM),* ***PHYKHRLH-Cu(II) 1:1*** *(250 µM) and* ***PHYKHRLH-Cu(II)*** *1:2 (250 µM). Briefly, HeLa HyPer cells express HyPer a genetically ratiometric fluorescent sensor of H_2O_2 based on a circularly permuted yellow fluorescent protein. In presence of H_2O_2, the conformation of HyPer is modified leading to a change in its spectral properties and particularly in the ratio I(491/530)/ I(405/530). The plotted graphs represent the average ratio I(491/530)/ I(405/530) indicative of H_2O_2 levels. The given images were taken by fluorescent microscopy 60 min following cells treatment.*

III.2. Draft publication

Genetically modified lactic acid bacteria for the production and delivery of peptidyl complexes mimicking superoxide dismutase and catalase

Gabrielle Schanne[a],[b],[c], Sorine Brisseau[b],[c], Yaël Lellouche Jakob[b], Paul Rochette[a],[c], Jade Loiseau[c], Anne Aucouturier[c], Philippe Langella[c], Luis Bermudez[c], Philippe Seksik[b], Clotilde Policar[a], Nicolas Delsuc[a]

[a] Laboratoire des biomolécules, LBM, Département de chimie, Ecole Normale Supérieure, PSL University, Sorbonne Université, CNRS, 75005 Paris, France
[b] Centre de Recherche Saint Antoine, INSERM, UMRS 938, Metabolism-Inflammation Department, 184 rue du Faubourg Saint-Antoine, 75012 Paris, France
[c] Commensal and Probiotics-Host Interactions Laboratory, Micalis Institute, INRA, AgroParisTech, Université Paris-Saclay, F-78350, Jouy-en-Josas, France

The work presented below has been conducted in collaboration with the laboratory MICALIS at INRAE institute. I have written the following draft paper that was edited and improved by my supervisors.

This draft does not constitute a final version for the purpose of submission. This version was completed with many details to make it readable for people from all scientific backgrounds and to present the totality of the work that I have conducted on this project.

Abstract. Lactic acid bacteria (LAB) have long been proposed as attractive candidates for the treatment of inflammatory bowel diseases (IBDs) given their intrinsic probiotic characteristics. Together with advances in genetics and bioengineering, LAB have been modified to express therapeutic proteins targeting several causes of inflammation in order to boost their bioactivity. In particular, to suppress inflammation-related oxidative stress, some strains have been genetically engineered to generate antioxidant superoxide dismutase (SOD) and catalase (CAT) enzymes. Although displaying promising anti-inflammatory effects *in vivo*, these recombinant strains suffer from the drawbacks associated to the involvement of native enzymes: low cell penetration into intestinal epithelial cells (IECs), high immunogenicity and short half-life. In this work, we generate novel recombinant LAB (recLAB) producing low-molecular weight peptides reported to exert SOD and CAT activity upon metal coordination. These peptidyl metal complexes mimicking SOD and CAT activities are not limited by the drawbacks mentioned above and have been concordantly shown to display improved beneficial effects in cells compared to native enzymes in previous studies. The anti-superoxide

and anti-hydrogen peroxide activities of recLAB lysates was examined by an activity assay on gel. Live recLAB were also co-incubated with IECs and were able to attenuate the secretion of inflammatory cytokine IL-8 to a greater extent than the wild-type strains. These anti-inflammatory effects can be attributed to SOD and CAT mimics produced by LAB. The strategy employed here hence combines the advantages of using recLAB as producers and delivery vectors of therapeutic molecules with that of using SOD and CAT mimics over native enzymes.

III.2.a. Introduction

Inflammatory bowel diseases (IBDs) constitute a major global health problem affecting 1/100 of the European population [60]. Current therapies prescribed to IBDs patients are not curative, but comprise anti-inflammatory drugs to control inflammation and thereby alleviate symptoms [62]. It has been shown that the inflammation state is tightly correlated to an oxidative stress situation [373]. This could be noticeable through the excessive amount of reactive oxygen species (ROS) and the impairment of several antioxidant enzymes, such as superoxide dismutase (SOD) and catalase (CAT), in IBDs tissues [85]. Based on these findings, SOD and CAT enzymes purified from bovine were largely considered as an alternative treatment for IBDs [88,92]. To overcome the controversy over animal-based drugs, food-grade bacteria have been genetically modified to produce native SOD and CAT. Remarkably, both recombinant enzymes purified from bacteria lysates and direct administration of live genetically modified bacteria were effective in decreasing inflammation *in vivo* [350,351]. Alternatively, low-molecular weight complexes mimicking SOD and CAT are also good candidates. They present the advantage over native enzymes of penetrating better inside cells due to their smaller size and to do not induce immunogenicity. These mimics are mostly porphyrins and salen complexes, but also include complexes with corroles, cyclic polyamine and peptidyl ligands [1,94,95,122,135,171]. Among them, some have been tested in *in vivo* IBDs models. In particular, the well-studied polyamine cyclic M40403 SOD mimic was administrated as an intraperitoneal bolus to rats suffering from TNBS-induced acute colitis and was able to efficiently reduce the severity of the experimental colitis [374]. However, when oral administration, which is a low invasive method, is intended, the delivery of the such molecules to the site of inflammation (*i.e.* the small bowel and especially the colon), becomes a real challenge. Indeed, low-molecular weight complexes mimicking SOD and CAT, being

coordination complexes are fragile, in particular in acidic medium that can be found in stomach. Therefore, few strategies have been developed to optimize the oral delivery of metallic SOD mimics. For instance, our group have succeeded in alleviating the symptoms of murine colitis by force-feeding mice with a bio-inspired SOD mimic prepared in a basic buffer ($NaHCO_3$ 4.2%) [196]. It was suggested that the basic buffer partially protect the SOD mimics from the acidic gastric conditions. Nevertheless, high doses were needed to observe beneficial effects. In another example reported by Q. Zhang *et. al*, the authors encapsulated a SOD mimic called TEMPOL in a nanomatrix that serves not only as protective vector but that also acts as H_2O_2 scavenger [375]. The vectorized SOD mimics was orally given to mice suffering from TBNS- or DSS-induced colitis and showed an effective accumulation in the inflamed colon and the suppression of several colitis symptoms.

In this context, peptidyl metal complexes mimicking SOD and CAT are very promising candidates, as they provide the advantages of low molecular weight complexes while being genetically encodable and thus producible by food-grade bacteria.

In previous studies, our group identified three peptidyl Cu- or Mn- complexes exhibiting SOD or CAT activity: PDHKHHLH-Cu(II) and KAEDYEDPGDEYDEAK-Mn(II) complexes displaying a SOD-like activity [192,257] and PHYKHRLH-Cu(II) displaying CAT-like activity [371]. They were discovered via an activity-based screening of a combinatorial library of peptidyl complexes [192,371]. Interestingly, when the complexes were studied in details, it appeared that the SOD mimic PDHKHHLH-Cu complex has a stoichiometry of 1 peptide for 1 copper whereas the CAT mimic PHYKHRLH-Cu complex exhibited a stoichiometry of 1 peptide for 2 coppers. This is fully consistent with their respective catalytical activities, since SOD dismutation involves a single electron transfer whereas H_2O_2 dismutation is a bi-electronic transfer (each copper provides one electron).

The SOD or CAT catalytic activity of these copper complexes was confirmed by the McCord and Fridovich assay [162,163] and dioxygen evolution monitoring using a Clark-type electrode, respectively. These assays provided the catalytic rates of the complexes for superoxide or hydrogen peroxide dismutation, summarized in Table 7. The bioactivities of the copper complexes were also evaluated in cells. For the copper SOD mimic, its anti-superoxide activity was assessed in murine macrophages cell line Raw 264.7 and its anti-inflammatory activity

was observed in LPS-stimulated HT29-MD2 intestinal epithelial cells. For the copper catalase mimic, its incubation on HeLa HyPer cells, expressing a ratiometric fluorescent sensor of H_2O_2 showed unambiguously a decreased level of H_2O_2 concentration.

SOD mimic	(a) PDHKHHLH:Cu(II) 1:1	$2.4 \times 10^7\ M^{-1}.s^{-1}$	
	(a) PDHKHHLH:Cu(II) 5:1	$4.8 \times 10^7\ M^{-1}.s^{-1}$	
	(b) KAEDYEDPGDEYDEAK:Mn(II) 1:1	$6.8 \times 10^5\ M^{-1}.s^{-1}$	
CAT mimic	(c) PHYKHRLH:Cu(II) 1:2		$1.2 \times 10^{-1}\ s^{-1}$

Table 7: catalytic rate for superoxide (left) and hydrogen peroxide (right) dismutation of the peptidyl metal complexes used in this work. Experimental conditions : (a,b) XTT marker, HEPES 50 mM, pH 7.4, (c) MOPS (3-(Morpholin-4-yl)propane-1-sulfonic acid) buffer 50 mM, pH 7.5.

These peptidyl complexes are thus very promising candidates that could be expressed in food-grade bacteria. In this perspective, bacterial strains have been engineered to produce peptidyl SOD and CAT mimics. Briefly, the gene encoding for the peptidyl ligand of the SOD- or CAT-active complexes was inserted into a plasmid vector and electroporated into LAB. The resulting clones were then successfully confirmed at three levels: 1) DNA cloning and identity of the insert by sequencing, 2) protein expression by western blot and 3) protein antioxidant activity by in-gel activity assay. Finally, their potential benefits were investigated in the lipopolysaccharide (LPS)-responsive IECs line: HT29-MD2. Interestingly, recombinant bacteria were able to limit LPS-induced secretion of IL-8 chemokine by HT29-MD2 to a greater extent than wild-type strains.

III.2.b. Material and methods

III.2.b.i. Bacterial strains and growth conditions

The bacterial strains and plasmids used in this study are listed in Table 8:

	Name	Characteristics
Bacteria strains	MG1363	*Lactococcus lactis* subsp. *cremoris* wild-type strain [376]
	NZ9000	Integration of nisR-K into the pepN gene of MG1363 strain using plasmid pNZ9573 [320,377]
	NCIMB8826	*Lactobacillus plantarum*, wild-type strain
	MG1363 control	MG1363 strain containing pSICE-empty plasmid (no Nuc gene)
	MG1363 sodA	L. lactis MG1363 containing pILKSsodA: overexpression of endogenous sodA, Ery resistance. [350]

Plasmids	pSICE:Nuc	GroESL promoter: Stress-Inducible Controlled Expression system, SP_Exp4 (signal peptide of Exp4 protein):Nuc gene, Cm resistance [321]
	pNICE:Nuc	nisA promoter: Nisin-Inducible Controlled Expression system, SP_Usp45 (signal peptide of Usp45 protein):NucB gene, Cm resistance [378]

Table 8: Characteristics of the bacteria strains and plasmids used in this study.

L. lactis strains were cultured in M17 medium (Difco) supplemented with 0.5% glucose media at 30°C without agitation. *L. plantarum* strains were cultured in MRS medium (Difco) at 37°C without agitation.

III.2.b.ii. Construction of recLAB expressing peptidyl SOD and CAT mimics

The nucleic acid sequences encoding for the three target peptides described in detail below (Table 10) were designed and are presented in supplementary information (Table S1). Particular concern was given to avoid repetitions and hairpin structures, based on the redundancy of genetic code so as to avoid homologous recombination and to ensure good quality sequencing. The DNA sequences encoding for the signal peptides (SPs) are not included, since these sequences are already introduced by the plasmid vectors (pSICE:Nuc and pNICE:Nuc). The sequences were synthetized by Genecust and inserted into pUC57 plasmid. The sequences were amplified by high-fidelity Phusion PCR using the following primers designed on the basis of pUC57 sequence, 5'-GACGTTGTAAAACGACGGCC-3' for the coding strand and 5'-CACAGGAAACAGCTATGACCATG-3' for the complementary strand. The amplified sequences containing SOD-Cu, CAT-Cu and SOD-Mn genes were then purified, digested with *Nsi*I and *Eco*RI restriction enzymes and ligated into *Nsi*I/*Eco*RI-digested plasmid vectors (pSICE or pNICE). The constructions were then electroporated (2.5 kV) into competent MG1363, NZ9000 and/or NCIMB8826 strains. Table 9 summarizes the recombinant strains constructed in this study. Note that SOD-Mn gene was established in a *L. plantarum* strain which is known to be endogenously rich in manganese in order to increase the probability of producing the SOD-active manganese peptidyl complex.

Name	Strain	Plasmid
MG1363 pSICE:SP_SOD-Cu	*L. lactis* MG1363	pSICE:SP_SOD-Cu
MG1363 pSICE:SP_CAT-Cu	*L. lactis* MG1363	pSICE:SP_CAT-Cu
NZ9000 pNICE:SP_SOD-Cu	*L. lactis* NZ9000	pNICE:SP_SOD-Cu
NZ9000 pNICE:SP_CAT-Cu	*L. lactis* NZ9000	pNICE:SP_CAT-Cu
NCIMB8826 pSICE:SP_SOD-Mn	*L. plantarum* NCIMB8826	pSICE:SP_SOD-Mn

Table 9: List of the recLAB constructed in this work.

Transformants were selected for their resistance to chloramphenicol (10µg/mL) and for the absence of Nuc phenotype according to Nuc activity assay [379]. This double selection confirmed that the transformants were successfully transformed with the recombinant plasmids. The presence of the genes coding for SP_SOD-Cu, SP_CAT-Cu and SP_SOD-Mn in some selected clones were confirmed by sequencing (Eurofins) of extracted plasmids or of Dream Taq colony PCR fragments. The PCR fragments containing the complete SP_SOD/CAT-Cu/Mn genes and the promoters were amplified with the following couple of primers: for pNICE clones, 5'-CTAACCTGCCCCGTTAGTTG-3' (forward primer) and 5'-GATTGCCGAAAATATGCACTC-3' (reverse primer) and for pSICE clones, 5'-CCGACTGTACTTTTTACAGTCGGT-3' (forward primer) and 5'-CAAGCTTATCGATACCGTCGACC-3' (reverse primer).

III.2.b.iii. Effect of metal supplementation on bacterial growth

Overnight cultures of MG1363 pSICE:SP_SOD-Cu/SP_CAT-Cu and NZ9000 pNICE:SP_SOD-Cu/SP_CAT-Cu strains were diluted to a 0.1 OD_{600nm} and incubated at 30°C without agitation until an optical density (OD_{600nm}) = 0.6 was reached, corresponding to the beginning of the exponential phase. Then different concentration of copper acetate monohydrate ($Cu(II)(OAc)_2.H_2O$) ranging from 0.2 to 0.5 mM were added into cultures and the growth was monitored for 2 hours. Similarly, overnight cultures of NCIMB8826 pSICE:SP_SOD-Mn strain were diluted to a 0.3 OD_{600nm} and incubated at 37°C without agitation until an OD_{600nm}: 0.8 was reached, corresponding to the beginning of the exponential phase. Then different concentrations of manganese chloride ($MnCl_2$) ranging from 0 mM to 100 mM were added into cultures and the growth was monitored for 2 hours.

For all strains, the OD_{600nm} was measured at 0h, 1h and 2h giving information on total cells contents, live or dead. At the same time, viable cells were enumerated by plating serial dilutions of each culture and by subsequent counting of the number of colonies forming units (CFU).

III.2.b.iv. Nisin or stress induction of peptides expression

Exponential growth cultures of recombinant strains MG1363 pSICE:SP_SOD-Cu/SP_CAT-Cu and NCIMB8826 pSICE:SP_SOD-Mn or NZ9000 pNICE:SP_SOD-Cu/SP_CAT-Cu were treated for 2 hours with NaCl 3% or nisin (10 ng/mL) respectively to induce the expression of the recombinant peptides. Simultaneously to the salt stress- or nisin- induction, metal salt (Cu(II) or Mn(II)) was added at different concentrations varying between 0 to 0.5mM for Cu(II) and 0 to 100mM for Mn(II) in the cultures. The concentrations were appropriately chosen based on previously preliminary results (III.2.b.iii) which provided the maximal amount of metal that can be supplemented without causing a decrease in the bacterial population. Two hours after nisin or stress induction and metal supplementation, the cultures were centrifuged at 3000 rpm for 15 minutes and the supernatants were separated from the bacterial pellets.

Bacterial pellets were resuspended in HEPES buffer (50 mM, pH 7.5) supplemented with anti-proteases and proteins were extracted by mechanical disruption in a Fast Prep apparatus.

Supernatants were processed using two different methods. In a first method, the proteins were extracted in denaturing conditions by TCA precipitation and resuspended in NaOH 50 mM. In a second method, supernatants were filtered through 0.2 µm filters to remove the largest molecules and then centrifuged for 2 hours in Amicon centrifugal concentrators with a molecular cut-off of 3 KDa. This allows removal of small contaminants, salts, buffer and to concentrate the expressed target peptides by 10- to 20-fold in a non-denaturing way.

To check the expression and the secretion of the target peptide, bacterial lysates and supernatant extracts were analyzed by Western Blot using an anti-Flag TAG antibody.

III.2.b.v. Measurement of SOD and CAT activity using in-gel activity assays

SOD and CAT activity in bacteria lysates was measured as described by C. Weydert *et al*. [191]. Briefly the proteins contents of bacteria lysates were separated by non-denaturing PAGE (10%). For SOD activity assay, the gels were incubated in presence of nitroblue tetrazolium

(NBT, 2.43 mM), N,N,N',N'-Tetramethylethylenediamine (TEMED, 28 mM) and riboflavine (28 µM). Upon UV exposure, this latter produces superoxide, which reduces NBT into stable purple formazan. SOD activity prevents the reduction of NBT resulting in an uncolored area in the gel. For CAT activity assay, the gels were subjected to H_2O_2 0.075% and an equimolar solution of $FeCl_3$ and $K_3Fe(CN)_6$ (2%) was then added on top of the gel. $FeCl_3$ and $K_3Fe(CN)_6$ react with hydrogen peroxide to form a stable blue product $KFe^{III}(Fe^{II}(CN)_6)$, called prussian blue. CAT activity consumes H_2O_2 and prevents the formation of this compound resulting again in a clear area in the gel. In both cases, achromatic bands are indicative of an antioxidant activity of the peptidyl complexes. The gels were imaged on a flatbed scanner with light from top and bottom. The intensity of the achromatic bands is directly related to the enzymatic activity and was measured using Fiji processing. Enzymatic activity was normalized by the protein concentration determined by BCA assay. The use of commercial SOD and CAT enzymes purified from bovine were used as standard and loaded at 1U in the gels. The comparison of the band intensity with that of the standard permitted to quantify the enzymatic activity in the bacteria lysates.

III.2.b.vi. Anti-inflammatory effects of recombinant strains on LPS-stimulated HT29-MD2 cells

The biological activity of the recombinant strain producing peptidyl ligand of SOD and CAT mimics was evaluated on HT29-MD2 intestinal epithelial cells. Recombinant bacteria and LPS-activated HT29-MD2 cells were co-incubated for 5.5 h and the anti-inflammatory effect of the bacteria were evaluated by measuring the secreted amount of IL-8 in cells supernatants by ELISA.

- Cell culture

HT29 human colon adenocarcinomas were obtained from the European Collection of Cell Cultures (Wiltshire, UK) and stably transfected to overexpress the protein MD2, a coreceptor of TLR4 necessary to confer sensitivity to LPS. Cells were maintained in DMEM complemented with 10% heat-inactivated FBS and blasticidin (10µg/mL) at 37°C in a 5% CO_2/air atmosphere.

- Recombinant bacteria preparation for co-incubation with HT29-MD2

As described in section III.2.b.iv, 24 hours before cells-bacteria co-incubation, overnight cultures of recombinant bacteria were diluted and cultured to early exponential phase. Then

the expression of the peptides was nisin-induced for NZ9000 strains and temperature-switch for recombinant MG1363 and NCIMB88266 strains (temperature fixed to 37°C and 42°C, respectively). Note that we did not use salt-stress for induction, because no biological activity was observed when the pSICE-containing strains were cultured with NaCl 3%. Lastly, the appropriate metal was added in the culture media and the bacteria were grown overnight. The next day, bacterial cultures were centrifuged and the pellets, previously washed with PBS, were resuspended in DMEM supplemented with 5% FBS. Based on OD_{600nm} measurements, the bacterial suspensions were diluted to obtain suspension with an OD_{600nm}= 1.

- ICP-MS quantification of metal content in bacterial suspension given to HT29-MD2 cells.

The total metal content (manganese or copper) present in these bacterial suspensions (OD_{600nm}=1) were quantified by ICP-MS. Briefly, the bacterial suspensions were diluted in 2% HNO_3, to lyse the bacteria and free Mn/Cu from all coordination sites. To achieve complete bacterial lysis, the 2% HNO_3 solutions were left for 1 hour at ambient temperature and then filtered. A calibration curve was established using a commercial multi-element standard and the total metal amount was normalized by the bacterial suspension OD_{600nm}.

- Cell Activation with LPS and Incubation with the recombinant bacteria.

Cells were seeded in 24-well plates at 40 000 cells/cm^2 and cultured until 90% confluence (1 x 10^6 cells per well). 24 hours prior to the addition of recombinant bacteria, the percentage of heat-inactivated FBS was reduced from 10% to 5% to acclimate cells to such conditions. For the co-incubation cell-bacteria, the use of 5% FBS-containing media is required to prevent an excessive growth of the bacteria. Cells were co-incubated with the bacteria at multiplicity of infection (MOI) equal to 5 for MG1363 and NZ9000 strains and MOI = 125 for NCIMB8826 strains. To reach this MOI, 5 µL (resp. 25µL) of MG1363/NZ9000 (resp. NCIMB8826) bacterial suspensions at OD_{600nm} = 1, containing respectively 5 x 10^6 CFU (resp. 1.25 x 10^8 CFU) were added in each well. Simultaneously, LPS was added at 0.1 µg/mL to induce the NF-κB inflammation pathway. LPS, HT29-MD2 cells and bacteria were co-incubated for 5h30, time at which the secretion of the inflammatory marker, IL-8, by cells is known to reach a threshold.

LPS-stimulated HT29-MD2 cells were also co-incubated for 5h30 in presence of recombinant bacteria lysates. Different amounts of proteins were deposited varying between 20 µg and 50 µg and classical maintenance conditions with 10% of FBS were conserved for cell culture.

Cells supernatants were collected and transferred in 96-deep-well plates and stored at 5°C for IL-8 quantification by ELISA and for lactate dehydrogenase (LDH) assay (Roche commercial kit). The cell layers were washed with phosphate-buffered saline (PBS), harvested in PBS containing a 1% Triton X-100 and protease inhibitor cocktail by scraping and then sonicated.

- Cell assays

The cytotoxicity of the recombinant bacteria and their lysates was assessed by the LDH assay. The protein concentrations in cell lysates were determined using bicinchoninic acid (BCA) protein assay reagents and bovine serum albumin (BSA) as the standard. The amount of interleukin-8 (IL-8) secreted in the cell supernatant was measured using a commercially available ELISA kit (DuoSet). The supernatants were previously centrifugated at 10 000 g for 15 minutes in order to remove the bacteria and debris. The IL8 amounts were normalized by the protein content measured in the corresponding cell lysates.

III.2.c. Results and discussion

III.2.c.i. Design of the constructs

The objective of this study is to engineer LAB able to produce peptidyl metal complexes mimicking the SOD and CAT. To increase the SOD and CAT activity of the metal-coordinated expressed peptides, three repetitions of the peptidyl ligands were concatenated and separated by flexible glycine-serine linkers . A signal peptide (SP) was also introduced in the sequence of the peptides in order to allows their exportation (*i.e.* secretion) outside the bacteria. Two different SPs were used according to the plasmid vector. In case of pNICE, the SP of Usp45 “MKKKIISAILMSTVILSAAAPLSGVYAS”, which is the major MG1363 secreted protein, was used to direct the secretion of the heterologous peptides in recombinant NZ9000. This SP was first reported by Van Asseldonk *et. al* in 1990 and largely applied since then to LAB [380]. In case of pSICE, another signal peptide “MKKINLALLTLATLMGVSSTAVVFADD” issued from *L. lactis* Exp4 protein and described later by I. Poquet *et. al* in 1998 was used [381]. In brief, the authors screened the protein export in *L. lactis* by constructing a genomic library of *L. lactis* for the expression of nuclease fusion proteins. As nuclease activity requires an extracellular location and can be easily visualized for a large number of colonies, this strategy allowed to identify efficiently the exported proteins. Among the twenty nuclease-active phenotypes detected, five of them contained, fused to the

nuclease, polypeptides named Exp for extracellular proteins (numbered from 1 to 5). Based on their amino acids sequence, the authors proposed five export signal sequences. In all cases, the SPs of Exp1-5 and Usp45 are composed of positively charged amino acids at the N-terminal, a central hydrophobic core and a C-terminal cleavage site.

Lastly, a Flag TAG was included to allow the detection and the purification of the expressed peptides (Western Blot, immunoprecipitation…). The complete structure of the target peptides that will be expressed are listed in These peptidyl complexes are thus very promising candidates that could be expressed in food-grade bacteria. In this perspective, bacterial strains have been engineered to produce .

SP_SOD-Cu	SignalPeptideGGGGSGGGGSGGGGSPDHKHHLHGGGGSGGGGSGGGGSPDHKHHLHGGGGSGGGGSGGGGSPDHKHHLHDYKDDDDK
SP_CAT-Cu	SignalPeptideGGGGSGGGGSGGGGSPHYKHRLHGGGGSGGGGSGGGGSPHYKHRLHGGGGSGGGGSGGGGSPHYKHRLHGGGGSGGGGSGGGGSPHYKHRLHDYKDDDDK
SP_SOD-Mn	SignalPeptideGGGGSGGGGSGGGGSKAEDYEDPGDEYDEAKGGGGSGGGGSGGGGSKAEDYEDPGDEYDEAKGGGGSGGGGSGGGGSKAEDYEDPGDEYDEAKDYKDDDDK

Table 10: Complete sequence of the recombinant peptides expressed by the recLAB constructed in this study. The structures of the SPs are given in Table S2. The peptides with SOD-activity upon copper or manganese complexation are in green and blue respectively. The peptides with CAT-activity upon copper complexation are in orange. They are separated by flexible linker made of glycine and serine (in black). The purple part corresponds to the FLAG-tag.

III.2.c.ii. Choice of the bacteria strains

The genes coding for these target peptides were cloned into different plasmids for heterologous expression in LAB. For this, LAB owing to their very favorable safety profile were selected. They are indeed Generally Recognized As Safe (GRAS) by the U.S. Food and Drug Administration (FDA) and are classified in the list of Qualified Presumption of Safety. Two different genera of LAB were used, the *Lactococcus* genus and the *Lactobacillus* genus. The *Lactococcus spp.* constitute the model LAB for heterologous protein production. They have the advantage to secrete relatively few proteins and to persist only short times in the gastrointestinal tract (GIT). The rapid lysis of *Lactococcus spp*. Could be of interest when assuming that only a small portion of expressed recombinant peptides will be effectively secreted outside the bacteria. The lysis would then allow to free in the intestine all the remaining peptides retained in the bacteria interior. Among the *Lactococcus spp.,* the *L. lactis*

species is extensively used as its small-size genome is completely sequenced and it is plasmid-free. In addition, it does not produce endotoxins such as lipopolysaccharides (LPS) and extracellular protease. For these reasons, two *L. lactis* strains MG1363 and NZ9000 (differing by the possible choices for inducible promoters) were engineered to express the SP_SOD-Cu and SP_CAT-Cu peptides.

In contrast, the gene coding for SSOD-Mn was cloned into a *Lactobacillus plantarum* species, named NCIMB8826. Indeed, this species is known to be endogenously rich in manganese (about 30mM) [203] which may favor the formation of the SOD-active manganese complex following SP_SOD-Mn peptide expression. Note that *Lactobacillus spp.* are usually less attractive as production and delivery vector because they possess higher probiotics activity that are hardly discriminated from the heterologous protein beneficial properties. Moreover, *Lactobacillus* genus is much more diverse in term of biochemistry, ecology and immunology which render its characterization more complex. *Lactobacillus spp* also have longer persistence in the GIT but even if they transiently colonize the host, they are not retained in the long term [382].

III.2.c.iii. Construction of the recombinant Lactococcus lactis or Lactobacillus plantarum strains expressing peptidyl ligands of SOD and CAT mimics

In order to deliver SOD and CAT mimics to inflamed IBD cells and tissues, we engineered three strains of food-grade LAB: *L. lactis* MG1363, *L. lactis* NZ9000 and *L. plantarum* NCIMB8826, able to produce the peptidyl ligands of the mimics. The genes encoding for the peptides SOD-Cu and CAT-Cu were cloned into pSICE and pNICE plasmids and then established in MG1363 and NZ9000 strains, respectively. Concerning recombinant *L. lactis* NZ9000 pNICE:SP_SOD-Cu/CAT-Cu strains, in which transcription of the gene of interest is under the control of the NisA promoter, the addition of nisin is required to induce peptide expression. Although the induction of NisA promoter by nisin is particularly efficient and strong, the induction could not be achieved *in vivo* in the long term (only few hours) as nisin is a non-endogenous chemical compound. Otherwise, nisin could be administered exogenously to mice, but then the bioactivity of the recombinant strains could not be distinguished from that of the nisin. Due to the presence of the GroESL promoter in pSICE plasmid, the expression of SP_SOD-Cu or SP_CAT-Cu peptides by recombinant MG1363 pSICE:SP_SOD-Cu/CAT-Cu strains can be induced by stress conditions such as increased temperature (37°C), decreased pH, bile acids

or NaCl additions. This promoter is thus of great interest since the stress conditions can be found *in vivo* especially in inflammatory situations. The expression of the peptidyl ligand of SOD and CAT mimics may thus be endogenously induced when bacteria reach the site of inflammation in IBDs situations.

Similarly, the gene encoding SOD-Mn peptide was ligated in pSICE plasmid and established in a *L. plantarum* strain known to be naturally rich in manganese. pSICE plasmid is indeed functional in *L. plantarum.* To isolate the clones, the targeted genes were amplified by colony PCR and the PCR product was examined by sequencing. In this way, the cloning of the genes encoding for the peptidic ligands was confirmed for each strain constructed (data not shown).

III.2.c.iv. Supplementation of the bacterial culture medium with copper or manganese salt

As mentioned in the introduction, the peptidic ligand expressed by the engineered strains is SOD- or CAT-active only upon coordination of Cu^{2+} or Mn^{2+}. For this reason, the bacteria were incubated with the required metal salt at concentrations up to 0.5 mM for Cu^{2+} and 100 mM for Mn^{2+}. The maximum acceptable metal concentration that do not totally prevent bacterial growth were determined from the growth curves given in Figure 49. The OD monitoring is indicated in Figure S3-1.

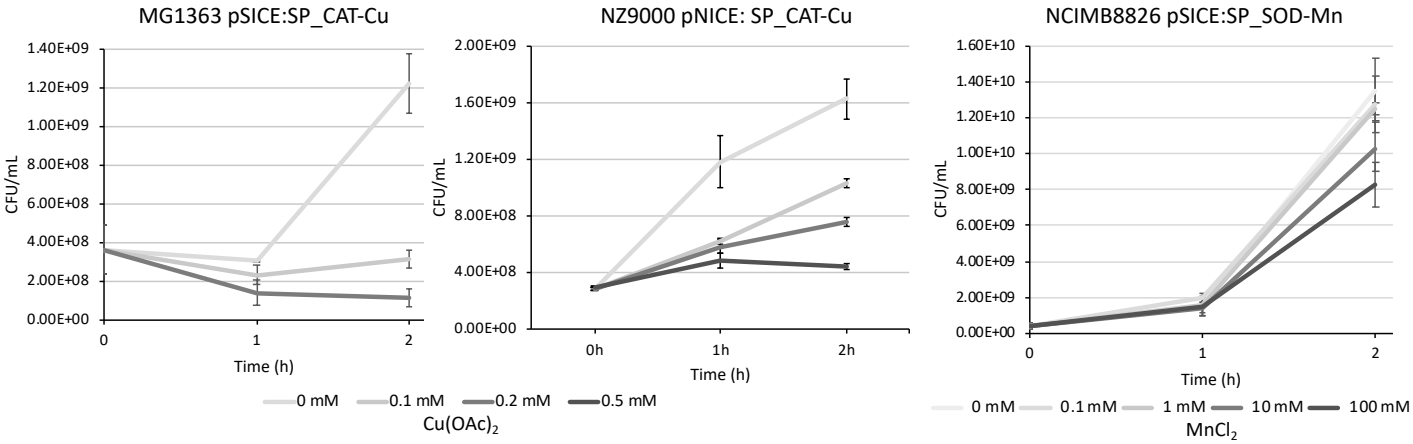

Figure 49: Enumeration of viable cells in culture of MG1363 pSICE:SP_CAT-Cu, NZ9000 pNICE:SP_CAT-Cu and NCIMB8826 pSICE:SP_SOD-Mn incubated with different concentration of metal salts ($Cu(OAc)_2$ for MG1363 and NZ9000 strains and $MnCl_2$ for NCIMB8826 strain) by plating serial dilutions of each cultures and counting the number of colony forming units. Experiments were performed after incubation for 0, 1 and 2 h. Error bars correspond to the standard deviation.

In both cases, the presence of copper salt strongly impaired the growth of recombinant MG1363 and NZ9000 strains. When incubated with Cu^{2+} at 0.2 mM, the number of viable

MG1363 pSICE:SP_CAT-Cu no longer increased but remained stable overtime. The NZ9000 pNICE:SP_CAT-Cu strain was more resistance to Cu^{2+} supplementation as the number of viable strains continues to increase when Cu^{2+} was added at 0.2 mM and remained stable up to 0.5 mM of Cu^{2+}. Manganese had much less adverse effects on recombinant *L. plantarum* strain growth. Indeed, no effect of Mn^{2+} was observed below 1 mM and the growth was scarcely slowed down in presence of Mn^{2+} at 10 mM and 100 mM. Higher concentrations were not tested due to solubility issues of the Mn salt.

The higher deleterious effect of copper over Mn on bacterial growth was expected and consistent with that described in the literature [215]. Indeed, copper has been described as a highly cytotoxic metal notably used by host for protecting against invading pathogens [383]. Due to its strong competitiveness, excessive amount of bioavailable copper can lead to mismetallation of metalloenzymes containing more weakly bound native metals and loss of function [215]. Copper is also known to catalyze the Fenton reaction producing the highly reactive and cytotoxic hydroxyl radical [1]. In contrast, Mn is much more bioavailable and is known to play a key role in bacteria and cell resistance to oxidative stress [211]. Indeed, Mn can not only serve as a cofactor for ROS-detoxifying enzymes such as SOD and CAT but also promote the formation of non-proteinaceous catalytic antioxidant compounds [205,261,384].

Based on these results, a maximum Cu^{2+} concentration of 0.2 mM and of 0.5 mM was determined for recombinant MG1363 and NZ9000 strains, respectively,. Different Mn^{2+} concentrations ranging between 0.1 mM and 100 mM were chosen for further study of NCIMB8826 pSICE:SP_SOD-Mn strain.

III.2.c.v. Examination of SOD and CAT mimics production by recombinant strains

- Western blot confirmation of peptide expression

The ability of the constructed recombinant strains to express the peptidyl ligands forming SOD and CAT mimics was confirmed by Western blot assays (Figure 50). The expressed peptides contain a Flag-TAG moiety recognized by commercially available Flag TAG-specific antibody. For MG1363 pSICE:SP_SOD-Cu/CAT-Cu and NZ9000 pNICE:SP_SOD-Cu/CAT-Cu lysates, Western blot results revealed a single band slightly larger (15 kDa), matching approximatively with the expected size for SP_SOD-Cu and SP_CAT-Cu peptides (~10kDa). Expression of

SP_CAT-Cu peptides was not affected by the presence of Cu^{2+} at the tested concentrations (up to 0.5 mM). Similarly, Western Blot analyses confirmed that MG1363 pSICE:SP_SOD-Cu was still able to express SP_SOD-Cu upon incubation with Cu^{2+} at 0.2 mM. In contrast, the level of SP_SOD-Cu expression by NZ9000 pNICE:SP_SOD-Cu was strongly dependent on the concentration of incubated copper: at a Cu^{2+} incubation concentration of 0.2 mM, SP_SOD-Cu expression was hardly detectable, but it was clearly observed when Cu^{2+} was added at 0.1 mM.

In NCIMB8826 pSICE:SP_SOD-Mn lysates, a band around 25 kDa was observed, which also approximatively matches with the expected size of SP_SOD-Mn peptide (15kDa). Note that the peptide size measured by comparison with the protein ladder in Western blot is only an inaccurate estimate. Indeed, migration is highly dependent on the nature of the amino acids (charge) and the quality of the denaturation step. An excessive amount of supplemented Mn seems to impair the bacterial translation machinery, since no more band appear at 25 kDa when the bacteria were incubated with $MnCl_2$ at 100 mM.

In all cases, no bands were detected in the WT strains lysates, confirming that the observed ones are specific to the recombinant strains and supporting the expression of the peptides SP_CAT-Cu, SP_SOD-Cu and SP_SOD-Mn.

These results demonstrate that bacteria can be supplemented with Cu^{2+} or Mn^{2+} upon incubation with $Cu(OAc)_2$ and $MnCl_2$ at 0.2 mM and 1 mM, respectively, without impairing the expression of the corresponding peptidyl ligand.

We also investigated the presence of the peptides expressed in the external culture medium (*i.e.* supernatant fraction). A first attempt was to isolate and concentrate the proteins from this fraction by TCA precipitation. The Western blot analysis of these samples shows no band of the expected size, suggesting that the expressed peptides are not secreted outside of the bacteria or in an amount undetectable with this procedure for peptide concentration and detection. As a second attempt, we concentrated the external culture medium using centricon filters. This latter allows to selectively recover components larger than 3kDa (retained above the filter) while removing a large part of the buffer (water, salts…). This technique overcomes the solubility issues following TCA precipitation. In addition, it eliminates the risk that the target peptides do not precipitate completely or that, once precipitated, they do not pellet

completely despite long and rapid centrifugation, since they are too light. However, it is less efficient than TCA precipitation to concentrate the total protein content. Again, no band was observed in Western Blot assays. Finally, despite using several different methods to concentrate the supernatant, no detectable quantity of expressed peptides could be observed. A final attempt was to purify the peptides using an anti-Flag TAG antibody conjugated to magnetic beads, which can be retained and separated from the rest using a magnet. Analysis of the eluted peptides by mass spectrometry and Western Blot are ongoing.

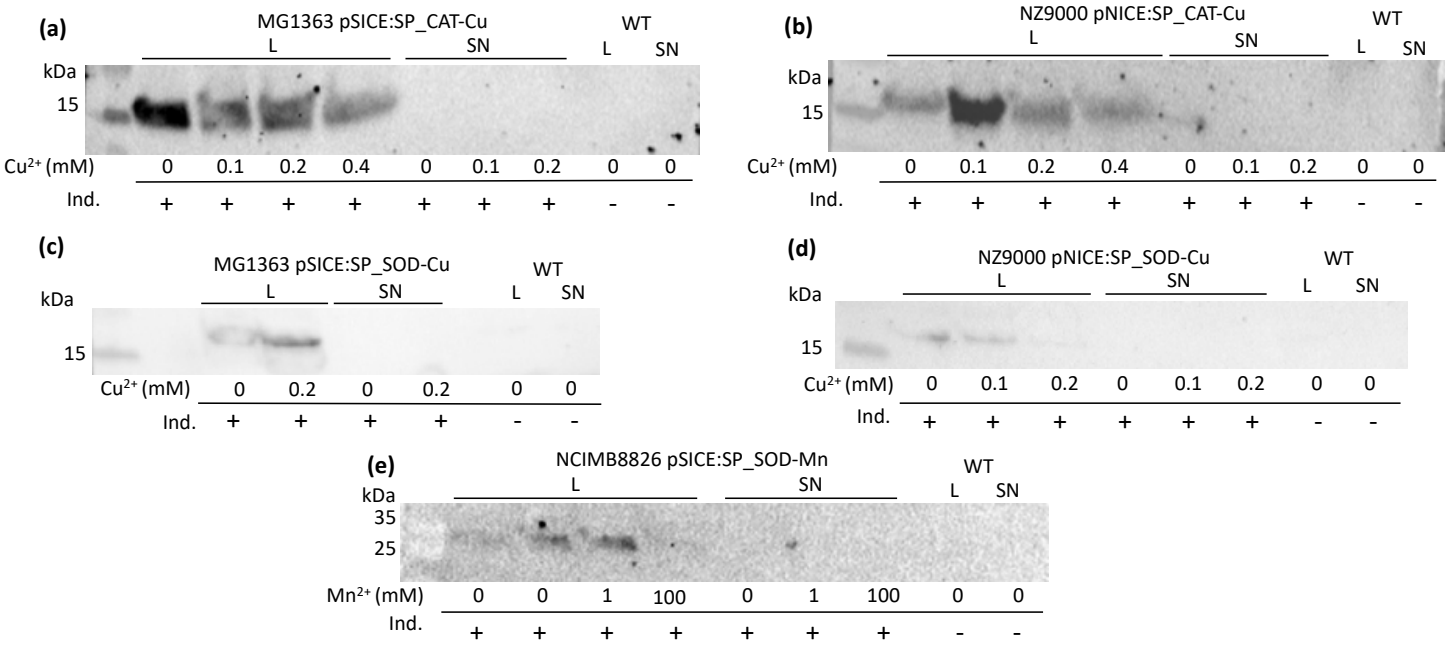

Figure 50: Western Blot analysis to investigate the production and secretion of the peptidyl ligand (SP_SOD-Cu, SP_CAT-Cu and SP_SOD-Mn) by the recombinant bacteria a) MG1363 pSICE:SP_CAT-Cu, b) NZ9000 pNICE:SP_CAT-Cu, c) MG1363 pSICE:SP_SOD-Cu, d) NZ9000 pNICE:SP_SOD-Cu and e) NCIMB8826 pSICE:SP_SOD-Mn. The expression of the peptides was induced using the appropriate inductor that is NaCl 3% for MG1363 and NCIMB8826 strains and nisin at 10 ng/µL for NZ9000 strains. The recombinant bacteria were incubated with various concentrations of the metal required for SOD/CAT activity (Cu^{2+} or Mn^{2+}). After 2 hours of metal incubation and induction, the bacterial cultures were centrifuged, the pellet and the supernatant were then separated. The pellets were homogenized giving bacteria lysates (L) and the proteins from supernatant (SN) were extracted by TCA precipitation. The presence of the expressed peptides in L and SN samples was checked by Western Blot using anti-FLAG tag primary antibody. Full Western blot gels are given in Figure S3-2.

- SOD and CAT activity assays on gel

The next step was to ensure that the expected bioactive complexes were assembled in the bacteria after peptide expression. For this, enzymatic assays on gel were performed as described by C. Weydert *et al.* [191]. Briefly, the SOD activity gel assay is based on a competition between a colorimetric marker (NBT) of superoxide and SOD-active peptides to react with superoxide radical produced by riboflavin upon UV exposure. In this assay, the presence of an achromatic band reveals SOD activity while purple areas resulting from the

reduction by superoxide of the yellow tetrazolium NBT to purple precipitate indicates that no SOD mimic is present (Figure S3-3).

As expected, a single clear band corresponding to endogenous Mn SOD appears in lysates from both recombinant and WT MG1363 and NZ9000 strains (Figure S3-4). Processing of the clear bands obtained by scanner revealed a higher intensity of the bands for recombinant MG1363 pSICE:SP_SOD-Cu and NZ9000 pNICE:SP_SOD-Cu lysates compared to WT. This may be due to the contribution of the SOD-active recombinant peptidyl copper complex. Indeed, the peptidyl ligand SP_SOD-Cu is expected to migrate around 15-20 kDa according to western blot experiments and is thus very similar in size to endogenous SOD (22 kDa). Therefore, they cannot be dissociated under non-denaturing electrophoresis. The bands intensity was normalized by the amount of proteins deposited in the gel and is plotted as a percentage of the control band intensity: salt-induced MG1363 control strain and WT NZ9000 strain (Figure 51).

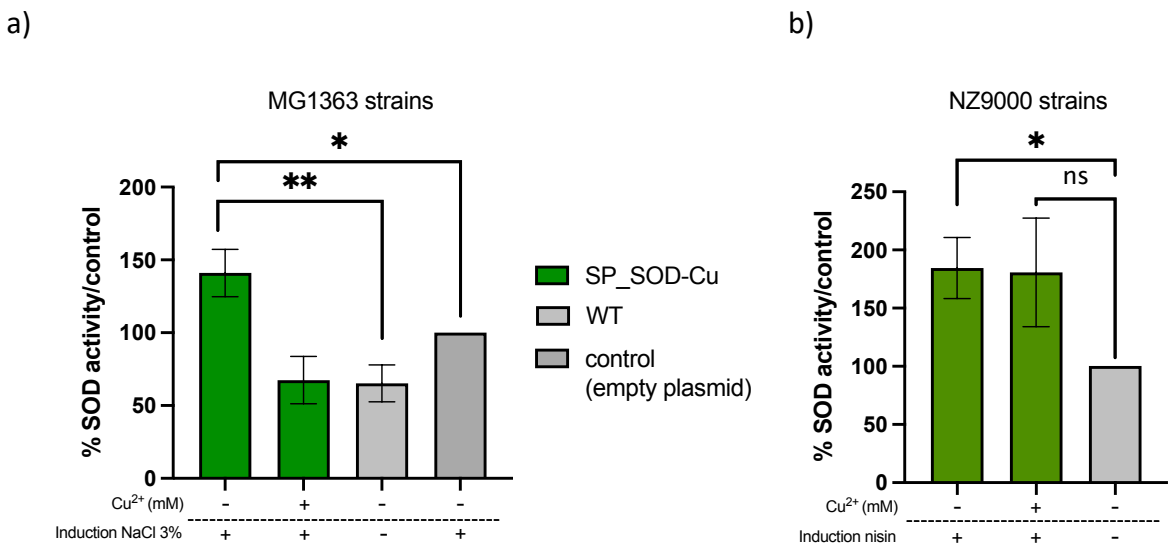

*Figure 51: Evaluation of the SOD activity in bacteria lysates of recombinant SP_SOD-Cu and WT MG1363 (a) and NZ9000 strains (b). The protocol published by C. Weydert and J. Cullen was used to assess the SOD activity in non-denaturing gel [191]. The SOD activity measured for MG1363 control lysates (a) and NZ9000 WT lysates (b) is set at 100% for each independent experiment. The SOD activity was normalized to the total amount of proteins in each lane. Data represent the mean ± SEM for at least three independent experiments. The p values were calculated using the Student t-test (bilateral test with equal variances not assumed): ***: p<0.001, **: p<0.01, *: p<0.05 and ns means non-significant.*

A significant 2.5-fold and 1.5-fold increase in SOD activity was observed in salt-induced MG1363 pSICE:SP_SOD-Cu lysates compared to MG1363 WT lysates and control salt-induced MG1363 lysates, respectively. This improved SOD activity is indeed related to the expression

of SP_SOD-Cu peptide that can coordinate endogenous Cu leading to an active SOD mimic. Surprisingly, copper supplementation at 0.2 mM reduced the SOD activity of MG1363 pSICE:SP_SOD-Cu lysate to the MG1363 WT level. In this later experiment, copper addition at 0.2 mM can reduce SP_SOD-Cu peptide expression by altering the bacterial translation machinery. Indeed, the expression of SP_SOD-Cu by MG1363 pSICE:SP_SOD-Cu strain incubated with copper at 0.2 mM was confirmed by western blot, but this does not provide quantitative information on peptide expression efficiency. Furthermore, the addition of copper in an excessive amount can lead to the formation of multi-Cu-coordinated SP_SOD-Cu complexes and aggregates with multiple that do not display SOD activity anymore. Finally, copper supplementation can also lead to mismetallation of the endogenous SOD enzyme resulting in an inactive protein and thus reducing the observed SOD activity.

The use of a commercial bovine SOD at 1636 U/mg as a standard allowed to calculate the SOD activity of salt-induced MG1363 pSICE:SP_SOD-Cu, MG1363 WT and salt-induced MG1363 control lysates, which were found to be equal to 54 U/mg, 25 U/mg and 39 U/mg, respectively.

For NZ9000 strains, the SOD activity increased 1.8-fold for recombinant SP_SOD-Cu strain compared to the WT strain. In this case, copper supplementation has no effect on measured SOD activity suggesting that endogenous bioavailable copper is sufficient to form the Cu-coordinated SOD-active complex. Again, comparison of band intensities with that of the commercial SOD gave an average SOD activity of 81 U/mg and 49 U/mg for salt-induced NZ9000 pNICE:SP_SOD-Cu and NZ9000 WT lysates, respectively.

The expression of SP_SOD-Cu was already confirmed by Western blot but, altogether, these activity assays show that the recombinant bacteria exhibit improved SOD activity which may be a result of the formation of the active Cu-complex.

The SOD assay on gel was similarly performed on lysates of recombinant NCIMB8826 strains, but no clear band was observed even when Mn^{2+} was added to lysates samples. This result is consistent with the fact that the Mn-coordinated peptide, KAEDYEDPGDEYDEAK-Mn, displays 350-fold lower SOD activity compared to the Cu-coordinated one PDHKHHLH-Cu (Table 7). Moreover, the native strain NCIMB8826 does not possess endogenous SOD. The sensitivity of this assay may not be enough in this case.

Catalase assay on gel was also conducted on lysates from recombinant strains expressing SP_CAT-Cu. This assay consists in pre-incubating the protein gel in a H_2O_2 solution and then adding $K_4Fe(CN)_6$ and $FeCl_3$ solutions that will react simultaneously with H_2O_2 to form Prussian blue. The areas without H_2O_2 remain clear, indicating catalase activity [110]. With the two recombinant strains, no noticeable clear band was observed, indicating either that the active complexes were not formed or a lack of sensitivity of the assay. Again, the lack of sensitivity of the CAT in-gel assay might be expected when considering the low catalytic rate of the CAT-active Cu-complex PHYKHRLH-Cu. Note that the in gel activity of the commercial CAT standard was detectable from 1U of enzyme loaded in the gel (Figure S3-3) but the k_{cat} of the recombinant catalase is 6 orders of magnitude higher than the CAT mimic k_{cat}.

III.2.c.vi. Evaluation of recombinant LAB activity in LPS-stimulated HT29-MD2 cells

The anti-inflammatory bioactivity of the constructed recombinant LAB was then assessed in a cellular model of LPS-induced inflammation. This model, named HT29-MD2, consists of HT29 intestinal epithelial cells stably transfected to overexpress the MD2 protein [193]. HT29-MD2 cells possess an increased sensitivity to bacterial LPS because MD2 is a co-receptor of the Toll-like receptor TLR-4, whose recognition of LPS triggers the NFκB inflammatory pathway. The activated inflammatory response is strongly associated with oxidative stress, which makes the model particularly relevant for evaluating the bioactivity of potentially antioxidant recombinant LAB [196,81].

Overnight cultures of the recombinant strains incubated with the adequate metal and upon induction conditions were supplemented to the cells at fixed MOI. The amount of metal administered to the cells was also measured by ICP-MS.

- Quantification of metal administration to cells

The total amount of copper in recombinant and WT MG1363 and NZ9000 cultures was quantified (Figure 52, Figure 53). An increase in the amount of copper is noticeable in cultures supplemented with copper salt at 0.1 or 0.2 mM, confirming Cu^{2+} internalization and its intra-bacterial retention during PBS washes. A visible but not significant change is visible between the recombinant and the WT strains, indicating that the genetic modification and the peptides expression induction does not drastically impact the Cu^{2+} penetration and retention. Likewise,

some differences in copper content between MG1363 and NZ9000 cultures with similar metal supplementation conditions appear while not significant. Indeed, a lower copper amount was measured in both WT and recombinant NZ9000 cultures compared to MG1363. This suggests that the assimilation of exogenous copper is strain-dependent. In addition, we observed that NZ9000 bacteria grow slightly faster than the MG1363 ones (Figure 49), meaning that the amount of exogenous copper given per bacteria may be lower in NZ9000 cases.

In the co-culture assay, 5 µL of bacterial suspension will be deposited at OD_{600}=1, corresponding to an estimated copper amount of 25 pmol and 37 pmol for MG1363 WT and MG1363 pSICE:SP_SOD-Cu strains, respectively (bacteria incubated with Cu^{2+} at 0.2 mM). For NZ9000 strains, this will correspond to an estimated copper amount of 15 pmol and 20 pmol for NZ9000 WT and NZ9000 pNICE:SP_SOD-Cu strains, respectively (bacteria incubated with Cu^{2+} at 0.2 mM). Note that these calculated amounts take into account both exogenous and endogenous copper and likewise both coordinated and free (bioavailable) copper.

For conditions without copper supplementation, the amount of endogenous copper contained in the bacterial suspensions co-incubated with the cells varied between 0.8 and 1.2 pmol.

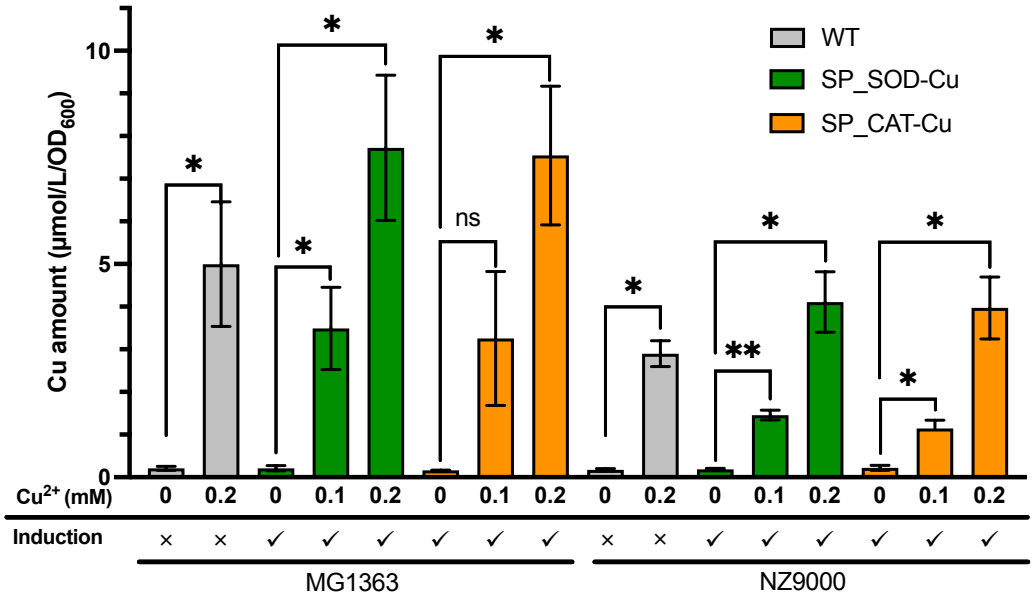

*Figure 52 : Quantification by ICP MS of total copper content in recombinant and WT NZ9000 and MG1363 strains cultured overnight with Cu^{2+} at 0, 0.1 and 0.2 mM. The bacterial suspensions were digested in HNO_3 2% to lyse the bacteria and to release copper from all coordination sites. The amount of Cu in bacterial culture was normalized by the OD at 600 nm. Data represent the mean ± SEM for three independent experiments. The p values were calculated using the Student t-test (with equal variances not assumed and each comparison stands alone) and the relevant significant comparison are indicated on the graph. ***: p < 0.001, **: p < 0.01, and *: p < 0.05, and ns means non-significant.*

The total content of Mn was also quantified in NCIMB8826 cultures co-incubated with LPS-activated HT29-MD2 cells (Figure 53). Consistently with what has been described in the literature, NCIMB8826 WT and SP_SOD-Mn strains were found relatively rich in endogenous manganese. We noticed that the amount of Mn is slightly diminished in recombinant SP_SOD-Mn strains cultured at 42°C compared to the native one cultured at 37°C. This decrease was not observable when both strains were cultured at 42°C (data not shown). This suggests that the decrease in Mn is rather due to the change in temperature, which may alter Mn homeostasis, more than to the genetic engineering for SP_SOD-Mn expression. Moreover, supplementation of the bacteria with Mn results in a very poor increase in Mn content when the bacteria were incubated with $MnCl_2$ at 1 mM and a significant increase when the bacteria were incubated with $MnCl_2$ at 5 mM. From these data, the total quantity of manganese given to cells treated with NCIMB8826 pSICE:SP_SOD-Mn strain previously incubated with no $MnCl_2$, $MnCl_2$ at 1 mM and $MnCl_2$ at 5 mM was estimated to 7.2 pmol, 7.9 pmol and 11.1 pmol, respectively. The estimated values are 11.0 pmol, 11.6 pmol and 17.9 pmol for NCIMB8826 WT strain previously incubated with no $MnCl_2$, $MnCl_2$ at 1 mM and $MnCl_2$ at 5 mM, respectively.

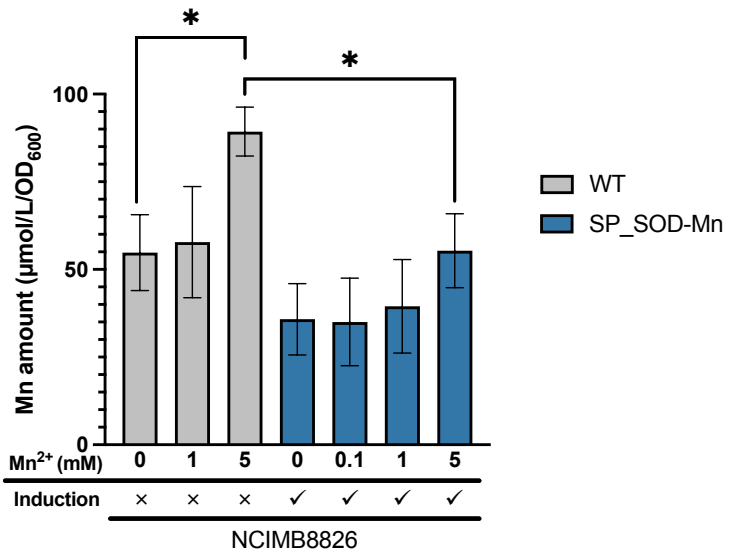

*Figure 53: Quantification by ICP MS of total manganese content in recombinant and WT NCIMB8826 strains cultured overnight with Mn^{2+} at 0, 0.1, 1 and 5 mM. The bacterial suspensions were digested in HNO_3 2% to lyse the bacteria and to release manganese from all coordination sites. The amount of Mn in bacterial culture was normalized by the OD at 600 nm. Data represent the mean ± SEM for three independent experiments. The p values were calculated using the Student t-test (with equal variances not assumed and each comparison stands alone) and the relevant significant comparison are indicated on the graph. ***: $p < 0.001$, **: $p < 0.01$, and *: $p < 0.05$, and ns means non-significant.*

 Quantification of the anti-inflammatory effects of recLAB lysates

Since recombinant antioxidant peptides are not or poorly secreted by bacteria according to our Western Blot analysis, we first administered bacterial lysates to the cells before administrating the live bacteria. The volume of bacterial lysates added to the cells was calculated to deliver 20 µg of proteins for MG1363 and NZ9000 strains and 50 µg of proteins for NCIMB8826 strains. Such quantities of proteins were chosen because no cytotoxicity was detected in the LDH assay under these conditions (Figure 54). The addition of a higher amount resulted in either not improved bioactivity or in LDH assay- detected cytotoxicity (data not shown).

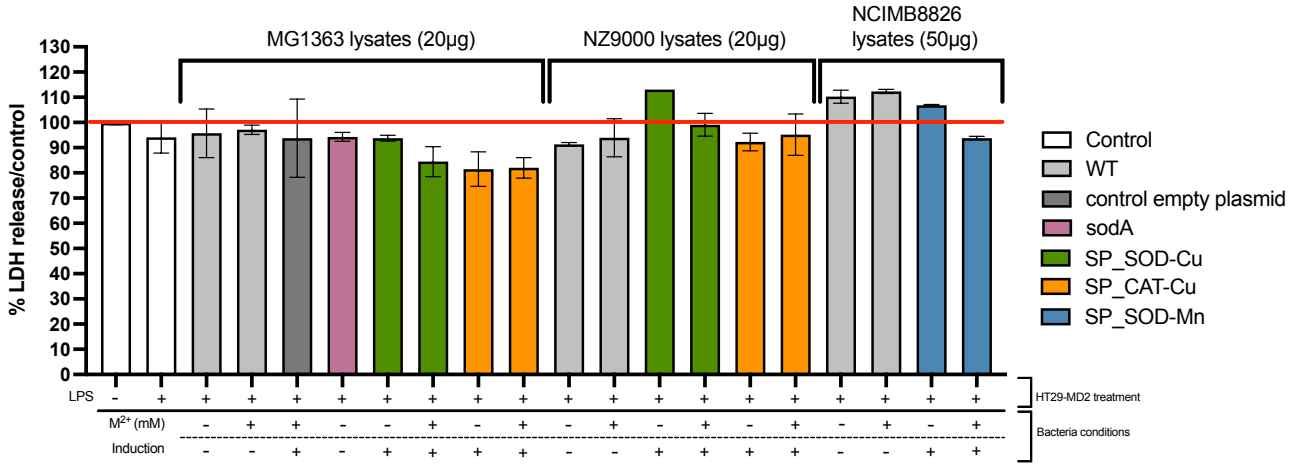

Figure 54: LDH cytotoxicity assay of LAB lysates on HT29-MD2 cells. Following the 5h30 of LAB incubation with HT29-MD2 cells, the amount of lactate dehydrogenase (LDH) released extracellularly was measured in centrifugated cells supernatants. LDH is located in the cytosol in normal state so its presence in the extracellular media is indicative of cell membrane damage. The measure of LDH activity in supernatant is based on the ability of LDH to catalyze the reduction of pyruvate while generating NADH, which can react with water soluble tetrazolium to produce a yellow color. An increase in the OD at 450nm is thus observed in case of cytotoxicity. This plot represents the % of LDH released compared to control cells. In all cases, this percentage was below 110% which were chosen as the limit of noncytotoxicity. We can conclude that the LAB lysates do not induce meaningful cytotoxicity under the tested conditions.

After 5h30 of co-incubation between LAB lysates and LPS-stimulated HT29-MD2 cells, the amount of the inflammatory marker interleukin-8 secreted by the cells was determined. As expected, in all cases IL-8 secretion was highly increased in LPS-stimulated cells compared to control cells, which illustrates the induction of the inflammatory response. The lysates of MG1363 pSICE:SP_SOD-Cu and pSICE:SP_CAT-Cu strains, previously incubated with Cu^{2+} at 0.2 mM, significantly reduced the amount of IL-8 secreted by LPS-activated HT29-MD2 cells compared to LPS control cells (Figure 55). This decrease was also significant when compared to cells treated with MG1363 WT and MG1363 control strains. These results support the role of copper-coordinated SP_SOD-Cu and SP_CAT-Cu peptides on the anti-inflammatory activity.

Surprisingly, under these conditions, the addition of copper to bacterial cultures before lysis seems to weakly strengthen the positive effect on inflammation. It probably favors the coordination of expressed SP_SOD-Cu and SP_CAT-Cu peptides to form the active complexes. Such effect of copper supplementation was not observed in activity assays on gel. For MG1363 sodA lysates, a weak decrease of 15% in secreted IL-8 was measured, which is more than 2-fold lower than the decrease measured with the Cu^{2+}- supplemented MG1363 pSICE:SP_SOD-Cu and pSICE:SP_CAT-Cu strains. This may result from a lower intracellular penetration of recombinant sodA due to its higher molecular weight compared to SP_SOD-Cu and SP_CAT-Cu. Likewise, E. Mathieu *et. al* treated LPS-activated cells with commercial purified bovine SOD at 100 U/mL and visualized a 25% decrease in IL-8 secretion while a synthetic SOD mimics reduced it by 65% [196]. These findings demonstrate the potential of SOD/CAT mimics-producing over endogenous SOD- producing recombinant LAB as an anti-oxidant and anti-inflammatory treatment.

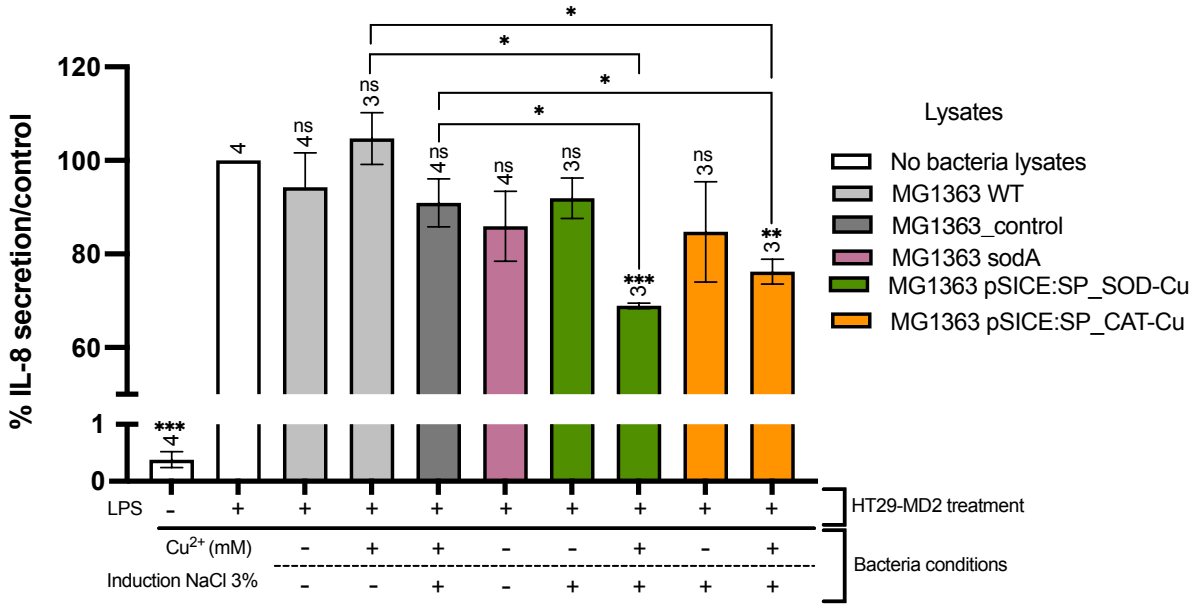

*Figure 55 : Quantification of the inflammatory marker IL-8 secreted by HT29-MD2 cells stimulated with LPS (0.1 µg/mL) and treated with the lysates of recombinant and WT MG1363 strains. 20µg of bacteria lysates were added in the cell culture media and co-incubated for 5h30 with LPS. The amount of IL-8 was measured by ELISA in centrifugated cells supernatants and was set at 100% for LPS-activated cells without treatment. Data represent the mean ± SEM for at least three independent experiments: the number of independent experiments is indicated above each column. The p values were calculated using the Student t-test (bilateral test with equal variances not assumed). ***: p<0.001, **: p<0.01, and *: p<0.05 versus LPS control, and ns means non-significant. The mean ranks of each column were compared to that of the LPS control and the obtained statistical results are annotated above each column. The other relevant significant comparisons are plotted in the graph using square brackets. We checked that the lysates do not induce any IL-8 secretion by HT29-MD2 cells in absence of LPS (Figure S3-5).*

For NZ9000 bacterial lysates, a significant effect on IL-8 secretion was observed for NZ9000 pNICE:SP_SOD-Cu pre-incubated with Cu^{2+} at 0.2 mM and NZ9000 pNICE:SP_CAT-Cu without Cu^{2+} supplementation compared to LPS control (Figure 56). Note that the other two conditions tested for recombinant NZ9000 lysates were not significant due to higher variability of the measurements, but a decrease in the same order of magnitude (by 20%) was observed. Lysates from the WT NZ9000 strain did not prevent the LPS-induced increase in IL-8 secretion, which corroborates again the anti-inflammatory properties of peptidyl SOD/CAT mimics produced by engineered LAB.

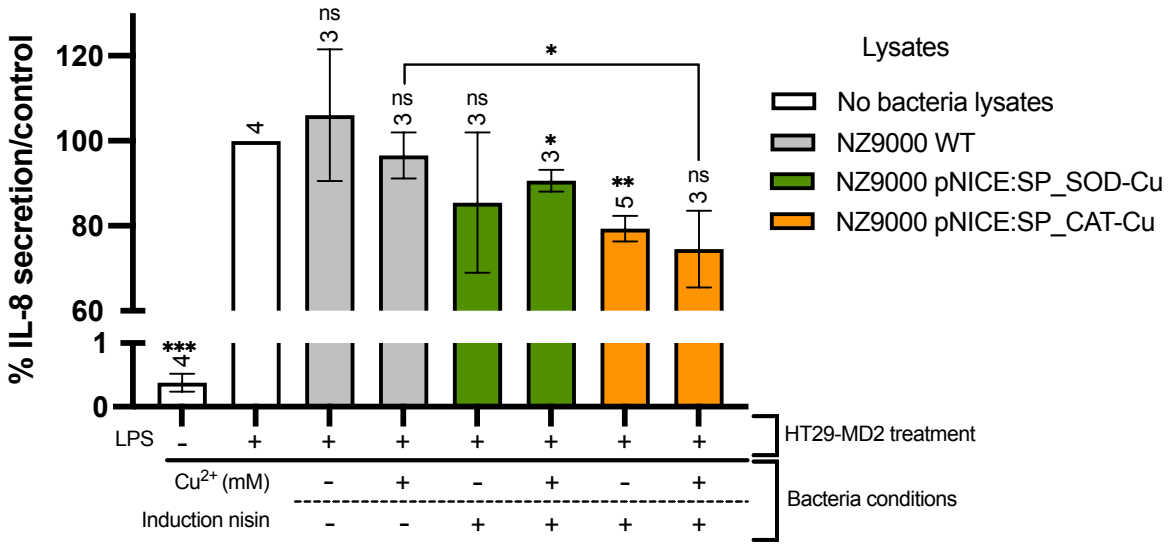

*Figure 56: Quantification of the inflammatory marker IL-8 secreted by HT29-MD2 cells stimulated with LPS (0.1 µg/mL) and treated with the lysates of recombinant and WT NZ9000 strains. 20 µg of bacteria lysates were added in the cell culture media and co-incubated for 5h30 with LPS. The amount of IL-8 was measured by ELISA in centrifugated cells supernatants and was set at 100% for LPS-activated cells without treatment. Data represent the mean ± SEM for at least three independent experiments: the number of independent experiments is indicated above each column. The p values were calculated using the Student t-test (bilateral test with equal variances not assumed). ***: p<0.001, **: p<0.01, and *: p<0.05 versus LPS control, and ns means non-significant. The mean ranks of each column were compared to that of the LPS control and the obtained statistical results are annotated above each column. The other relevant significant comparisons are plotted in the graph using square brackets. We checked that the lysates do not induce any IL-8 secretion by HT29-MD2 cells in absence of LPS (Figure S3-5).*

Finally, the activity of NCIMB8826 LAB lysates was investigated on this cellular model (Figure 57). Once more, lysate from the engineered strain allows significant alleviation of inflammation monitored by IL-8 secretion. However, this result is more difficult to interpret because the Mn-supplemented WT strain also displays significant anti-inflammatory activity that could be related to its probiotic activity. However, administration of NCIMB8826 pSICE:SP_SOD-Mn bacterial lysates previously incubated with Mn^{2+} at 1 mM leads to a

significantly higher decrease in IL-8 secretion than for the corresponding WT condition. This is consistent with what was observed with MG 1363 lysates.

In conclusion, lysates from recombinant bacteria displayed promising anti-inflammatory effects in the LPS-stressed HT29-MD2 cellular model. However, in order to achieve even greater effects, live bacteria were directly co-incubated with LPS-challenged cells. Indeed, the amount of therapeutic recombinant peptides contained in bacterial lysates and administered to the cells is limited, whereas recombinant peptides will be continuously produced using live bacteria.

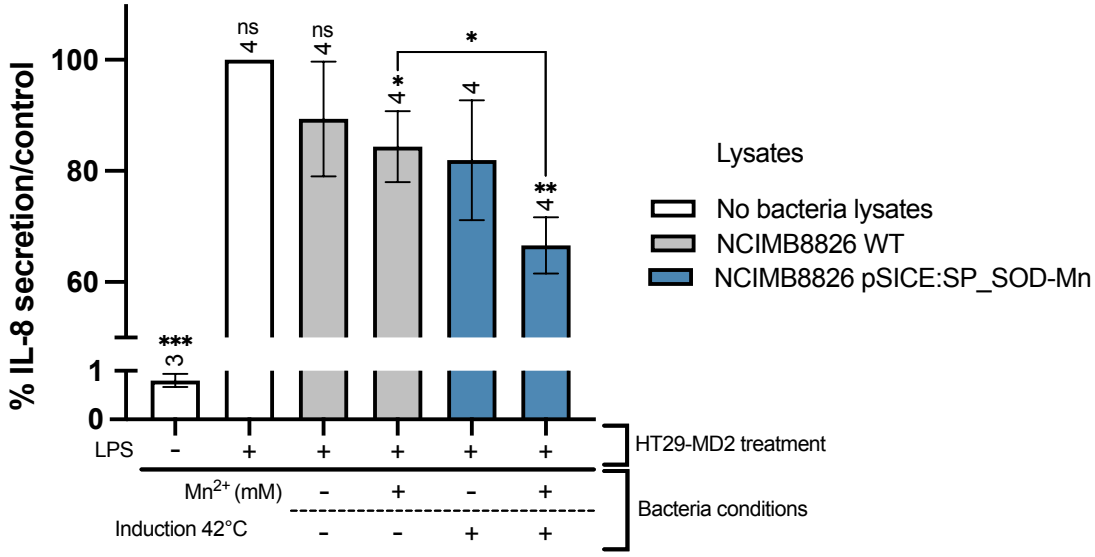

*Figure 57: Quantification of the inflammatory marker IL-8 secreted by HT29-MD2 cells stimulated with LPS (0.1 µg/mL) and treated with the lysates of recombinant and WT NCIMB8826 strains. 50 µg of bacteria lysates were added in the cell culture media and co-incubated for 5h30 with LPS. The amount of IL-8 was measured by ELISA in centrifugated cells supernatants and was set at 100% for LPS-activated cells without treatment. Data represent the mean ± SEM for at least three independent experiments: the number of independent experiments is indicated above each column. The p values were calculated using the Student t-test (bilateral test with equal variances not assumed). ***: p<0.001, **: p<0.01, and *: p<0.05 versus LPS control, and ns means non-significant. The mean ranks of each column were compared to that of the LPS control and the obtained statistical results are annotated above each column. The other relevant significant comparisons are plotted in the graph using square brackets. We checked that the lysates do not induce any IL-8 secretion by HT29-MD2 cells in absence of LPS (Figure S3-5).*

- Quantification of the anti-inflammatory effects of live recLAB

Prior to the biological evaluation, the cytotoxicity induced by the studied LAB in HT29-MD2 cells was analyzed via the quantification of cells membrane damage using the LDH release assay (Figure 58). No cytotoxicity was found in HT29-MD2 cells when LAB were prepared following the described conditions and added at MOI fixed to 5 for MG1363/NZ9000 strains

and 125 for NCIMB8826 strains. Indeed, the percentage of LDH released by the cells did not exceed 110% that of control cells.

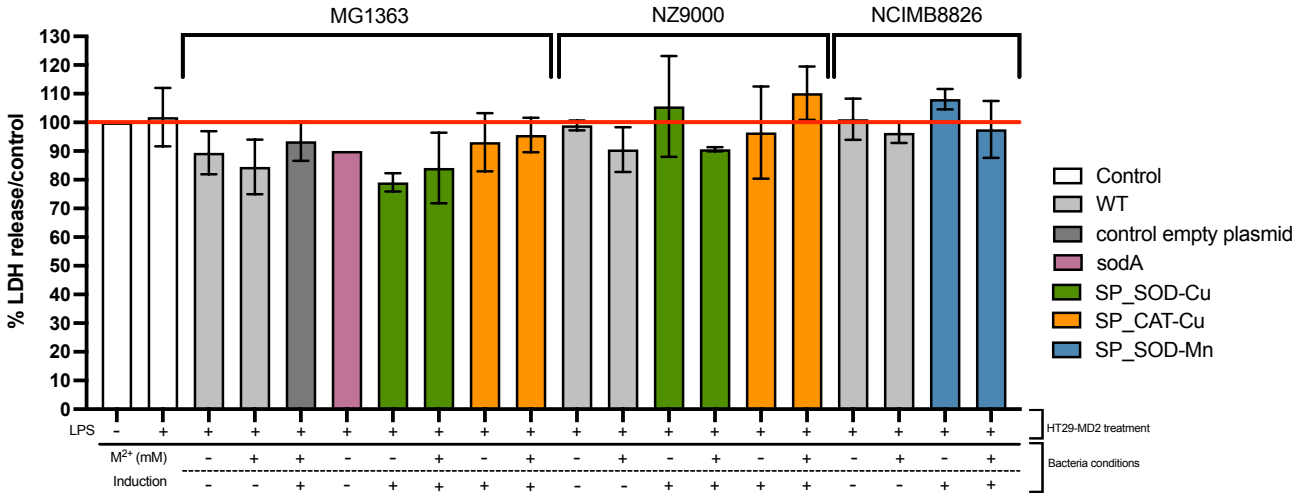

Figure 58: LDH cytotoxicity assay of live LAB on HT29-MD2 cells. Following the 5h30 of LAB incubation with HT29-MD2 cells, the amount of lactate dehydrogenase (LDH) released extracellularly was measured in centrifugated cells supernatants. LDH is located in the cytosol in normal state so its presence in the extracellular media is indicative of cell membrane damage. The measure of LDH activity in supernatant is based on the ability of LDH to catalyze the reduction of pyruvate while generating NADH, which can react with water soluble tetrazolium to produce a yellow color. An increase in the OD at 450 nm is thus observed in case of cytotoxicity. This plot represents the % of LDH released compared to control cells. In all cases, this percentage was below 110% which were chosen as the limit of non-cytotoxicity. We can conclude that the LAB do not induce meaningful cytotoxicity under the tested conditions.

Figure 59, Figure 60 and Figure 61 show the results obtained for HT29-MD2 cells treated with WT and recombinant MG1363, NZ9000 and NCIMB8826 strains. Interestingly, MG1363 pSICE:SP_SOD-Cu and MG1363 pSICE:SP_CAT-Cu strains were able to limit IL-8 secretion to about 60% of that of the LPS control (Figure 59). The decrease in IL-8 secretion is strongly reinforced compared to that obtained with the corresponding lysates. Again, this effect can be attributed to the antioxidant activity of the expressed SP_SOD-Cu and SP_CAT-Cu peptides since oxidative stress is known to be tightly related to inflammation. However, in contrast to what was observed in LAB lysates, prior addition of Cu^{2+} in bacterial cultures does not improve the decrease in Il-8 secretion. This is here consistent with the gel activity assays which similarly show no impact of copper supplementation on anti-superoxide activity. The WT strain has no effect on IL-8 secretion with or without pre-incubation with Cu^{2+}. This in turn confirms the role of recombinant SP_SOD-Cu and SP_CAT-Cu peptides in the observed anti-inflammatory activity. Otherwise, recombinant LAB expressing endogenous sodA was not able to attenuate to the same extent the LPS-induced increase in IL-8 secretion. The amount of IL-8 secreted

was lowered to 80% of that of the LPS control, but this decrease was not significant. Again, this may be due to the low penetration of sodA in epithelial cells.

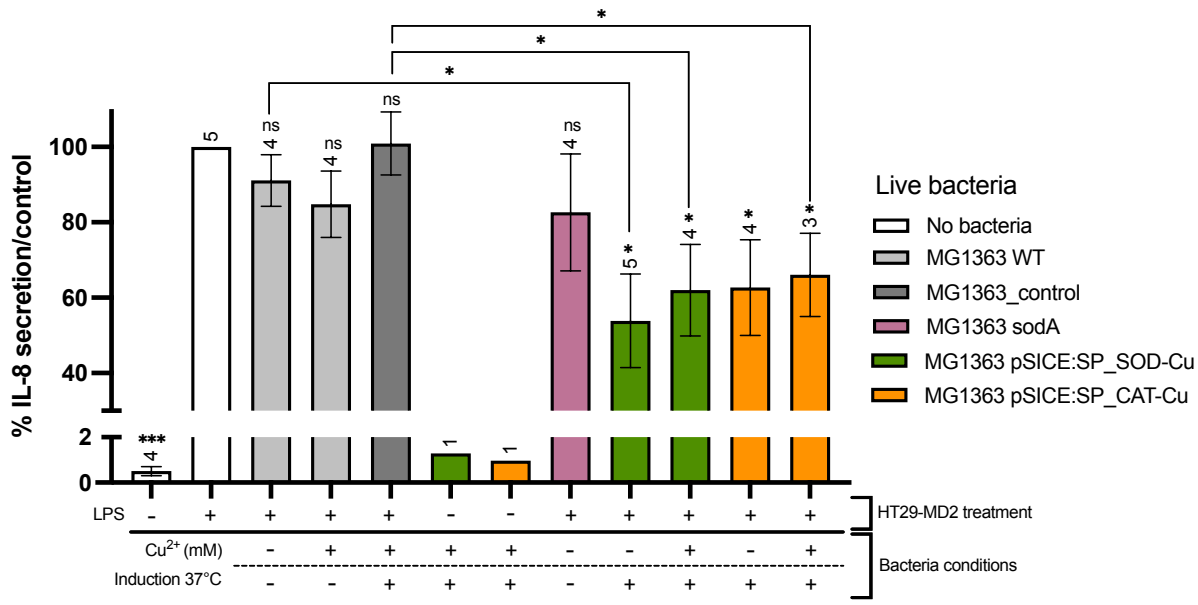

*Figure 59: Quantification of the inflammatory marker IL-8 secreted by HT29-MD2 cells stimulated with LPS (0.1 µg/mL) and co-incubated for 5h30 with recombinant and WT MG1363 strains. 5 µL of bacterial suspensions at OD_{600}=1 was deposited in each cells well corresponding to approximately $5x10^6$ bacteria and thus to a MOI of 5. The supplemented bacteria were previously cultured overnight at different conditions varying by the Cu^{2+} incubation concentration and the temperature. The amount of IL-8 was measured by ELISA in centrifugated cells supernatants and was set at 100% for LPS-activated cells without treatment. Data represent the mean ± SEM for at least three independent experiments except for control without LPS: the number of independent experiments is indicated above each column. The p values were calculated using the Student t-test (bilateral test with equal variances not assumed). ***: p<0.001, **: p<0.01, and *: p<0.05 versus LPS control, and ns means non-significant. The mean ranks of each column were compared to that of the LPS control and the obtained statistical results are annotated above each column. The other relevant significant comparisons are plotted in the graph using square brackets. We also checked that the recombinant LAB do not induce any IL-8 secretion by HT29-MD2 cells in absence of LPS (Figure S3-5).*

The treatment of HT29-MD2 cells with engineered NZ9000 LAB also revealed interesting results (Figure 60). NZ9000 pNICE:SP_SOD-Cu and pNICE:SP_CAT-Cu partially counteracted the LPS-induced increase in IL-8 secretion regardless of the bacterial supplementation with Cu^{2+}. In contrast, the quantity of IL-8 secreted was not reduced when cells were co-incubated with the WT strain. Similarly to recombinant MG1363 LAB, the anti-inflammatory activity of recombinant NZ9000 LAB can be correlated to their genetic engineering associated with the continuous expression of anti-oxidant SP_SOD-Cu and SP_CAT-Cu. However, we observed that recombinant NZ9000 LAB prevent less effectively IL-8 secretion compared to recombinant MG1363. Indeed, the amount of IL-8 was reduced by approximately 20% for cells treated with recombinant NZ9000, while this decrease reached 40% with recombinant MG1363 treatment. This difference in anti-inflammatory activity could be linked to the difference in the promoters

upstream SP_SOD-Cu- and SP_CAT-Cu-encoding genes. Indeed, engineered MG1363 LAB possess a pGroESL promoter that activates the expression of SP_SOD-Cu and SP_CAT-Cu under stress conditions such as change in temperature. The optimal growth temperature for *L. lactis* MG1363 and NZ9000 strains is 30°C. During bacteria co-incubation with LPS-stimulated cells, the temperature is set at 37°C, meaning that pGroESL is continuously activated and generates an extended induction of SP_SOD-Cu and SP_CAT-Cu expression by recombinant MG1363. In contrast, for engineered NZ9000 LAB, peptide expression is induced by the presence of nisin. As LAB are cultured under inducing conditions the day before the co-incubation, the nisA promoter should remain active for few hours. However, due to the absence of nisin in cell media culture this activation may be less intense and not perpetuated for the entire duration of the co-incubation. In summary, the induction of SP_SOD-Cu and SP_CAT-Cu expression during cellular assays might be greater for MG1363 strains, which could explain their enhanced anti-inflammatory activity over NZ9000 strains.

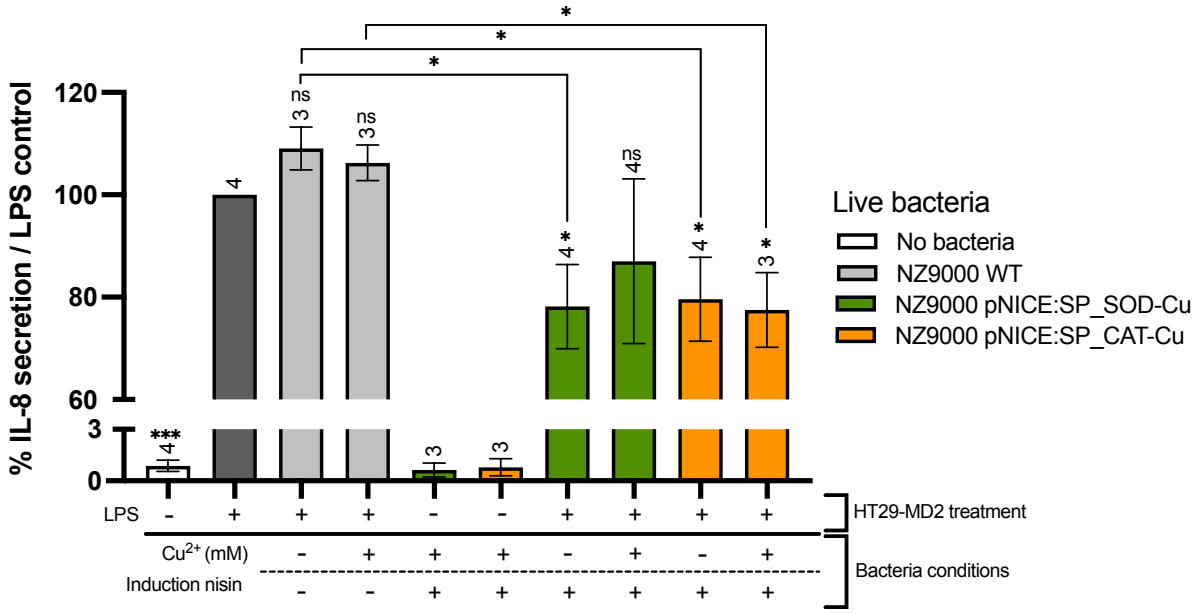

*Figure 60: Quantification of the inflammatory marker IL-8 secreted by HT29-MD2 cells stimulated with LPS (0.1 µg/mL) and co-incubated for 5h30 with recombinant and WT NZ9000 strains. 5 µL of bacterial suspensions at OD_{600}=1 was deposited in each cells well corresponding to approximately $5x10^6$ bacteria and thus to a MOI of 5. The supplemented bacteria were cultured overnight at different conditions varying by the Cu^{2+} incubation concentration and the presence of nisin. The amount of IL-8 was measured by ELISA in centrifugated cells supernatants and was set at 100% for LPS-activated cells without treatment. Data represent the mean ± SEM for at least three independent experiments except for control without LPS: the number of independent experiments is indicated above each column. The p values were calculated using the Student t-test (bilateral test with equal variances not assumed). ***: p<0.001, **: p<0.01, and *: p<0.05 versus LPS control, and ns means non-significant. The mean ranks of each column were compared to that of the LPS control and the obtained statistical results are annotated above each column. The other relevant significant comparisons are plotted in the graph using square brackets. We also checked that the recombinant LAB do not induce any IL-8 secretion by HT29-MD2 cells in absence of LPS (Figure S3-5).*

Lastly, the activity of NCIMB8826 WT strain on LPS-generated inflammation was confirmed when the WT bacteria were administered to HT29-MD2 cells culture (Figure 61). *L. plantarum* strains are largely known for their probiotics effects [385], so it is not surprising that they can impact the inflammatory responses and notably IL-8 secretion in LPS-stressed HT29-MD2 cells. The apparent IL-8 decrease by 30 % compared to LPS control observed in NCIMB8826 pSICE:SP_SOD-Mn strain cannot be attributed, at least not entirely, to the genetically engineered expression of potent antioxidant SP_SOD-Mn. Still, a clear but not significant IL-8 secretion decrease for cells co-incubated with recombinant NCIMB8826 strains pre-cultured without Mn compared to the WT strain. This highlights the heterologous production and anti-inflammatory capacity of Mn-coordinated SP_SOD-Mn complex. Finally, we observed a small and not significant decrease of IL-8 secretion when NCIMB8826 strains were previously subjected to Mn supplementation at 1 mM. Note that the impact of NCIMB8826 pSICE:SP_ SOD-Mn pre-supplementation with Mn on IL-8 decrease was much greater for cell treatment with bacterial lysates. This cannot be associated with increased formation of the SOD-active Mn SP_SOD-Mn complex since this effect is also visible for the WT strain. However, Mn^{2+} can coordinate with various ligands, including endogenous peptides, to form complexes acting as SOD mimics. In particular, the strain *Deinococcus radiodurans,* which exhibits extreme resistance to ionizing radiation, is known to accumulate large amounts of several low-molecular weight Mn(II) complexes forming by proteins-derived peptides. The latter are supposed to protect the cells from oxidative damage [204,372]. The formation of such antioxidant Mn^{2+}-metabolites complexes in NCIMB8826 strains may contribute to the decrease of the inflammation in HT29-MD2 cells.

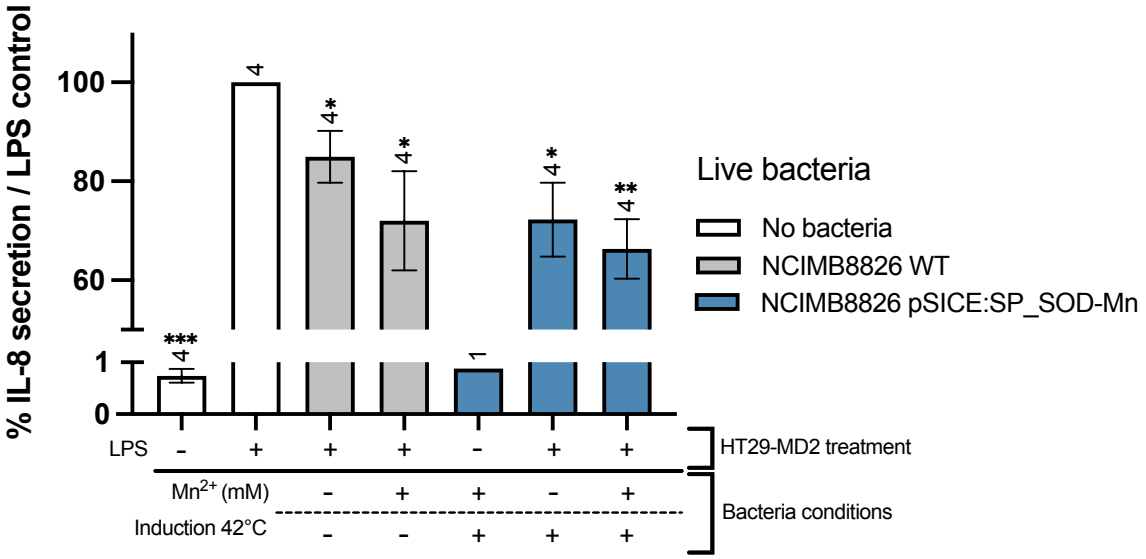

*Figure 61: Quantification of the inflammatory marker IL-8 secreted by HT29-MD2 cells stimulated with LPS (0.1 µg/mL) and co-incubated for 5h30 with recombinant and WT NCIMB8826 strains. 25 µL of bacterial suspensions at OD_{600}=1 was deposited in each cells well corresponding to approximately 1.25x10^8 bacteria and thus to a MOI of 125. The supplemented bacteria were cultured overnight at different conditions varying by the Mn^{2+} incubation concentration and the temperature. The amount of IL-8 was measured by ELISA in centrifugated cells supernatants and was set at 100% for LPS-activated cells without treatment. Data represent the mean ± SEM for at least three independent experiments except for control without LPS: the number of independent experiments is indicated above each column. The p values were calculated using the Student t-test (bilateral test with equal variances not assumed). ***:p<0.001, **:p<0.01, and *:p<0.05 versus LPS control, and ns means non-significant. The mean ranks of each column were compared to that of the LPS control and the obtained statistical results are annotated above each column. No other relevant comparison was found significant. We also checked that the recombinant LAB does not induce any IL-8 secretion by HT29-MD2 cells in absence of LPS (Figure S3-5).*

In conclusion, live recombinant bacteria exhibit a convincing bioactivity in HT29-MD2 cells. The anti-inflammatory effects are strongly improved when live bacteria are administered instead of lysates. The increased efficiency of live recombinant bacteria in alleviating inflammation also suggests that, even if not detectable by western blot analysis, a portion of the expressed peptides are excreted by bacteria and reach the inflamed cells. In order to accelerate the delivery of recombinant SOD or CAT mimics, genetically modified strains auxotrophic for alanine could be envisaged. Before being co-incubated with cells or administrated to mice, the auxotroph recombinant strains can be pre-cultured in the absence of alanine, which will weaken them and favor their subsequent lysis in the cell culture media or in the murine GIT. This may result in delivery of the expressed therapeutic peptides to the site of inflammation after lysis.

III.2.d. Conclusion

This study constitutes the first demonstration of the use of recombinant LAB strains expressing SOD and CAT mimics as LBPs. Their evaluation in LPS-stimulated HT29-MD2 highlighted their ability to significantly attenuate IL-8 secretion. As WT strains did not displays such anti-inflammatory properties, the observed effects could be directly attributed to the expression of SOD and CAT mimics. Further improvements of the *in vitro* and *in vivo* bioactivity of the recombinant LAB may require the development of new metal-coordinated peptides with higher intrinsic SOD and CAT activity. These findings support the potential value of LAB as live delivery vector and therapeutics supplier to attenuate the symptoms of chronic inflammatory diseases such as IBDs.

III.3. Conclusion and perspectives

III.3.a. Conclusion

In summary, this study describes an efficient method for the *in situ* synthesis and delivery of SOD and CAT mimic by safe food-grade LAB. Consistent with their antioxidant properties, the engineered LAB proved to be efficient in attenuating inflammation in LPS-stimulated intestinal cells. These results pave the way towards the use of engineered LAB expressing enzyme mimics as LBPs for GIT inflammatory diseases. They indeed constitute a cost-effective and long-term alternative to current therapies based on systemic administration of unstable anti-inflammatory drugs that require high doses and consequently associated with side effects. Regarding these encouraging results, we have started the filling of a *"declaration of invention (DI)"* with the aim to apply for a patent afterwards.

However, some safety concerns still need to be resolved before considering their use in humans as an alternative treatment for IBDs. On the one hand, LAB are ideal candidates for this strategy related to **1)** their non-pathogenicity, **2)** their inability to colonize the GIT in the long-term, and **3)** their deficiency for conjugative transposition (gene transfer) avoiding antibiotic resistance transmission. On the other hand, researchers still need ensure that no dissemination of the recombinant LAB can happen in the natural ecosystem. A *L. lactis* strain secreting human IL-10 was approved for phase I clinical trial by regulatory agencies, such as the Genetically Modified Organisms (GMOs) European Commission, because a biological containment strategy was developed. This strain was previously made thymidine- or thymine-dependent to prevent its survival in the environment without continuous supplementation of either compound. This example proves the feasibly of using genetically modified LAB for clinical applications. Lastly, public opinion may not be favorable to the use of genetically modified probiotics, although no finding demonstrates any risk for the health and the environment. To reverse this skepticism, scientists need to provide clear and accessible studies evidencing their safety and report on the benefits they conferred over others treatments. Work along these lines is undergoing through the ANR MOBIDIC, funded in 2021.

III.3.b. Perspectives

Several improvements can be made to enhance the therapeutic benefits of recombinant LAB producing SOD- and CAT- mimics:

1) We designed a new target peptide containing PHYKHRLH and PDHKHHLH sequences that possess, respectively, CAT and SOD activity upon copper coordination. The complete sequence of the target peptide is given in Table 11. The gene encoding for this new target peptide will be inserted into pSICE expression vector and established into *L. lactis* MG1363 strain. Such recombinant LAB combining SOD and CAT activity should display enhanced antioxidant activity. Indeed, the H_2O_2 resulting from $O_2^{\bullet -}$ dismutation can be directly removed by the CAT mimic avoiding its conversion into very toxic $HO^{\bullet}$. The synergy between SOD and CAT enzymes has besides been described for a long time [386,387].
2) A key factor for bioactivity is the intra-cellular penetration of the therapeutics compounds. In order to increase the cellular internalization of the expressed SOD- or CAT- active peptides, the incorporation of a cell-penetrating peptide (CPP) into the structure of the recombinant peptides may be an interesting alternative. In this context, the TAT sequence (YGRKKRRQRRR) which was the first identified and most studied CPP [388] is a good candidate [388,389]. Cellular uptake of TAT-conjugated peptides occurs mainly via endocytosis and not by direct translocation [390,391]. Consequently, internalized TAT-proteins conjugates are often trapped in endosomes and cannot reach their site of action. One solution offered by P. Lönn *et al.* is to add an endosomal escape domain (EED) to the TAT CPP (Figure 62) [392]. The addition of such EED composed mainly of hydrophobic amino acids was efficient in accelerating the endosomal escape into the cytoplasm of GFPβ1-TAT-EED conjugates.

   Two novel peptides including the initial SP_SOD-Cu or SP_CAT-Cu peptides, the TAT CPP and the EED have been designed (Table 11).

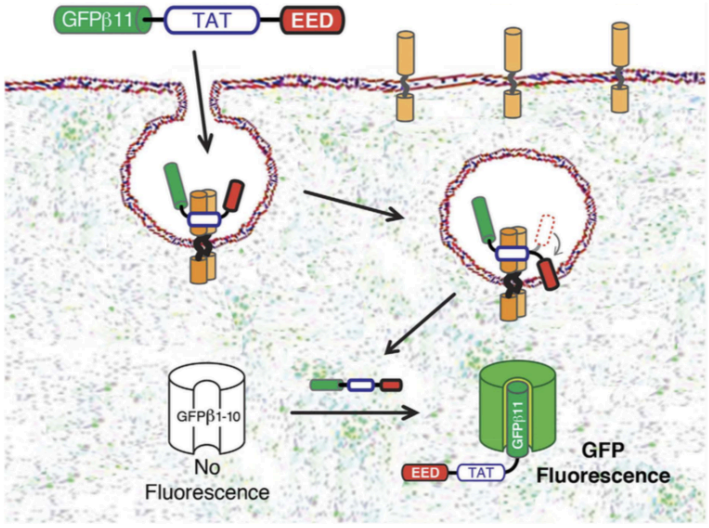

Figure 62: Enhancement of the endosomal escape into cytoplasm of GPFβ1/TAT peptide thanks to its coupling to an EED sequence. When concentrated in the endosome, the hydrophobic EED sequence destabilized the lipid bilayer membrane and thus favored the endosomal escape of the endocytosed peptides. GPFβ1 can then interact with GFPβ1-10 protein and can induce fluorescence. Figure from [392].

SP_SOD-Cu_CAT-Cu_TAG	MKKINLALLTLATLMGVSSTAVVFADDASGGGGSGGGGSGGGGSPHYKHRLHGGGGSGGGGSGGGGS PHYKHRLHGGGGSGGGGSGGGGSPDHKHHLHGGGGSGGGGSGGGGSPDHKHHLHDYKDDDDK
SP_SOD-Cu_TAT-EED_TAG	MKKINLALLTLATLMGVSSTAVVFADDASGGGGSGGGGSGGGGSPDHKHHLHGGGGSGGGGSGGGGS PDHKHHLHGGGGSGGGGSGGGGSPDHKHHLHGGGGSGGGGSGGGGSYGRKKRRQRRRGGSGGSGFWFGDYKDDDDK
SP_CAT-Cu_TAT-EED_TAG	MKKINLALLTLATLMGVSSTAVVFADDASGGGGSGGGGSGGGGSPHYKHRLHGGGGSGGGGSGGGGS PHYKHRLHGGGGSGGGGSGGGGSPHYKHRLHGGGGSGGGGSGGGGSYGRKKRRQRRRGGSGGSGFWFGDYKDDDDK

Table 11 : Design of the new peptides to be expressed by recombinant M1363 via the pSICE expression system. The signal peptide of Exp4 is in red. The peptides with SOD-activity and CAT-activity upon copper complexation are in green and in orange respectively. They are separated by flexible linker made of glycine and serine (in black). The TAT sequence and the endosomal escape domain are in blue. The purple part corresponds to the FLAG-tag.

3) In addition, as mentioned in the discussion, we will establish pSICE:SP_SOD-Cu and pSICE:SP_CAT-Cu plasmids in a *L. lactis* MG1363 strain rendered auxotroph to alanine [393]. The beforehand culture of the recombinant strains in absence of alanine will fragilize them, resulting in their rapid lysis in the intestine and in the delivery of the expressed and non-secreted SP_SOD-Cu and SP_CAT-Cu peptides. In addition, it will allow preventing the dissemination of the recombinant bacteria in the external environment that is free from alanine.
4) Lastly, we consider to replace the glycine/serine linkers with protease cleavable sequences to generate shorter CAT and SOD mimics. Indeed, we have no evidence that concatenation of the three SOD/CAT mimics does not affect their activity via a change in the redox properties or in the conformation.

5) Other perspectives include the evaluation of the antioxidant effects of engineered LAB on RAW 264.7. RAW 264.7 constitute a relevant cellular model since macrophages secrete large amount of ROS that can be consumed by the SOD or CAT mimics- producing LAB.
6) We also plan to administer the most promising recombinant LAB, probably MG1363 pSICE:SP_SOD-Cu, to mice suffering from DNBS-induced colitis.

IV. General conclusion

In conclusion, this work aimed at exploring the potential of antioxidant SOD and CAT mimics for the treatment of inflammatory disorders such as IBDs. SOD and CAT mimics are low-molecular weight metal complexes that reproduce the ROS-scavenging activity of the native SOD and CAT enzymes, respectively. As part of my PhD, I have been studying two different kinds of SOD mimics, which differ by the nature of their ligand and the strategy followed to design them.

The first one consists in manganese complexes bio-inspired from the active site of the endogenous SOD2 (MnSOD) enzyme. A new generation of SOD mimics derived from the well-studied Mn1 complex whose ligand is composed of a diamino-ethane scaffold bearing two imidazole and one phenol moieties has been developed. While appropriate redox properties and intrinsic catalytic SOD activity are primordial for efficient SOD mimics, the bio-availability is another factor of main importance. This feature is dependent: on one hand, on the ability of the complexes to penetrate inside the cells and on the other hand, on their stability and inertness in the cellular environment. Due to its high flexibility, Mn1 is very labile and does not satisfy properly this last requirement. To rigidify its structure and provide a more compact coordination site for Mn(II), a cyclohexyl group was inserted on the diaminoethane scaffold. This way, the newly-designed Mn1 derivatives displayed greatly improved resistance to metal exchange between the Mn(II) center and competitive free metal ions found in the cells like Cu(II) and Zn(II). In addition, they prove to exert anti-inflammatory and antioxidant effects at lower doses than Mn1 in HT29-MD2 cells. Since, no significant change were noticed in term of cellular uptake and stability over Mn1 and its derivatives, the enhanced bioactivity was attributed at least partly to the increased inertness of the complexes. The inertness of the metal complexes is also very useful for their speciation study because it makes the requirement for metal-free analytical system much less strict. Therefore, we succeed in detecting and quantifying the most inert Mn1 derivative in cells by classical MS technique. To better understand the SOD mimics mechanism of action, we also investigated their intracellular distribution by X-rays fluorescence nanoimaging. Lastly, these SOD mimics were assessed in a murine model of acute colitis. The mimics were loaded in lactic acid bacteria, acting as protective delivery vector, to prevent their degradation in the acidic gastric

environment. The oral administration of one of the vectorized SOD mimic provides slight but significant beneficial effects on the colitis. However, the therapeutic activity of the SOD mimic cannot be significantly distinguished from that of the empty bacteria.

The second type of SOD mimics described in this manuscript are Cu or Mn peptidyl complexes. The ligands are octapeptides whose sequence was identified via a powerful screening of a combinatorial library [192,257,371,394]. We succeed in taking advantage from their encodable nature by engineering food-grade lactic acid bacteria generally recognized as safe to express a long peptide comprising three concatenation of the SOD or CAT mimics peptidyl ligands as well as an excretion sequence and a tag. We achieved to demonstrate the valuable contribution of two of the genetic cloning on the intra-bacterial SOD activity. Moreover, all of the recombinant bacteria producing the SOD mimics- or CAT mimics- were able to significantly attenuate the LPS-induced secretion of IL-8 by HT29-MD2. These results support the therapeutic potential of LAB that generate exogenous redox active metal complexes for the treatment of inflammatory disorders. As a perspective, the cloned plasmids may be established in LAB already possessing great natural probiotics activity, to promote these recombinant LAB as improved probiotics.

V. Bibliography

[1] C. Policar, Mimicking SOD, Why and How: Bio-Inspired Manganese Complexes as SOD Mimic, in: Redox-Active Therapeutics, Springer, 2016: pp. 125–164.

[2] A.V. Snezhkina, A.V. Kudryavtseva, O.L. Kardymon, M.V. Savvateeva, N.V. Melnikova, G.S. Krasnov, A.A. Dmitriev, ROS Generation and Antioxidant Defense Systems in Normal and Malignant Cells, Oxidative Medicine and Cellular Longevity. 2019 (2019) 1–17. https://doi.org/10.1155/2019/6175804.

[3] M.D. Brand, The sites and topology of mitochondrial superoxide production, Experimental Gerontology. 45 (2010) 466–472. https://doi.org/10.1016/j.exger.2010.01.003.

[4] J.D. Lambeth, NOX enzymes and the biology of reactive oxygen, Nat Rev Immunol. 4 (2004) 181–189. https://doi.org/10.1038/nri1312.

[5] M.P. Murphy, How mitochondria produce reactive oxygen species, Biochemical Journal. 417 (2009) 1–13. https://doi.org/10.1042/BJ20081386.

[6] E. Birben, U.M. Sahiner, C. Sackesen, S. Erzurum, O. Kalayci, Oxidative Stress and Antioxidant Defense, World Allergy Organization Journal. 5 (2012) 9–19. https://doi.org/10.1097/WOX.0b013e3182439613.

[7] A.N. Onyango, Endogenous Generation of Singlet Oxygen and Ozone in Human and Animal Tissues: Mechanisms, Biological Significance, and Influence of Dietary Components, Oxidative Medicine and Cellular Longevity. 2016 (2016) 1–22. https://doi.org/10.1155/2016/2398573.

[8] F. Magnani, A. Mattevi, Structure and mechanisms of ROS generation by NADPH oxidases, Current Opinion in Structural Biology. 59 (2019) 91–97. https://doi.org/10.1016/j.sbi.2019.03.001.

[9] J.P. Kehrer, The Haber–Weiss reaction and mechanisms of toxicity, Toxicology. 149 (2000) 43–50. https://doi.org/10.1016/S0300-483X(00)00231-6.

[10] C. Von Sonntag, The Chemical Basis of Radiation Biology, Taylor and Francis, 1987.

[11] J.S. Valentine, Dioxygen reactivity and toxicity, in: Biological Inorganic Chemistry, Structure and Reactivity, Mill Valley: University Science Books, 2007: pp. 319–31.

[12] J.M. McCord, M.A. Edeas, SOD, oxidative stress and human pathologies: a brief history and a future vision, Biomedicine & Pharmacotherapy. 59 (2005) 139–142. https://doi.org/10.1016/j.biopha.2005.03.005.

[13] M. Zoumpoulaki, MnSOD Mimics: Analytical mass spectrometry-based techniques to quantify their amount and biological effect in inflamed intestinal epithelial cells, Thesis in chemistry, Sorbonne university, 2021.

[14] C.P. Rubio, J.J. Cerón, Spectrophotometric assays for evaluation of Reactive Oxygen Species (ROS) in serum: general concepts and applications in dogs and humans, BMC Vet Res. 17 (2021) 226. https://doi.org/10.1186/s12917-021-02924-8.

[15] J. Cadet, T. Delatour, T. Douki, D. Gasparutto, J.-P. Pouget, J.-L. Ravanat, S. Sauvaigo, Hydroxyl radicals and DNA base damage, Mutation Research/Fundamental and Molecular Mechanisms of Mutagenesis. 424 (1999) 9–21. https://doi.org/10.1016/S0027-5107(99)00004-4.

[16] I. Fridovich, Superoxide Anion Radical ($O^{\cdot}_2$), Superoxide Dismutases, and Related Matters, Journal of Biological Chemistry. 272 (1997) 18515–18517. https://doi.org/10.1074/jbc.272.30.18515.

[17] C.E. Cross, Oxygen Radicals and Human Disease, Ann Intern Med. 107 (1987) 526. https://doi.org/10.7326/0003-4819-107-4-526.

[18] T. Finkel, Signal transduction by reactive oxygen species, Journal of Cell Biology. 194 (2011) 7–15. https://doi.org/10.1083/jcb.201102095.

[19] A. Panday, M.K. Sahoo, D. Osorio, S. Batra, NADPH oxidases: an overview from structure to innate immunity-associated pathologies, Cell Mol Immunol. 12 (2015) 5–23. https://doi.org/10.1038/cmi.2014.89.

[20] S.G. Rhee, H_2O_2, a Necessary Evil for Cell Signaling, Science. 312 (2006) 1882–1883. https://doi.org/10.1126/science.1130481.

[21] C.C. Winterbourn, M.B. Hampton, Thiol chemistry and specificity in redox signaling, Free Radical Biology and Medicine. 45 (2008) 549–561. https://doi.org/10.1016/j.freeradbiomed.2008.05.004.

[22] M. Schieber, N.S. Chandel, ROS Function in Redox Signaling and Oxidative Stress, Current Biology. 24 (2014) R453–R462. https://doi.org/10.1016/j.cub.2014.03.034.

[23] D. Hanahan, R.A. Weinberg, Hallmarks of Cancer: The Next Generation, Cell. 144 (2011) 646–674. https://doi.org/10.1016/j.cell.2011.02.013.

[24] R.A. Cairns, I.S. Harris, T.W. Mak, Regulation of cancer cell metabolism, Nat Rev Cancer. 11 (2011) 85–95. https://doi.org/10.1038/nrc2981.

[25] C.C. Winterbourn, Reconciling the chemistry and biology of reactive oxygen species, Nat Chem Biol. 4 (2008) 278–286. https://doi.org/10.1038/nchembio.85.

[26] C. Espinosa-Diez, V. Miguel, D. Mennerich, T. Kietzmann, P. Sánchez-Pérez, S. Cadenas, S. Lamas, Antioxidant responses and cellular adjustments to oxidative stress, Redox Biology. 6 (2015) 183–197.

https://doi.org/10.1016/j.redox.2015.07.008.

[27] V. Nivière, M. Fontecave, Discovery of superoxide reductase: an historical perspective, J Biol Inorg Chem. 9 (2004) 119–123. https://doi.org/10.1007/s00775-003-0519-7.

[28] Y. Sheng, I.A. Abreu, D.E. Cabelli, M.J. Maroney, A.-F. Miller, M. Teixeira, J.S. Valentine, Superoxide Dismutases and Superoxide Reductases, Chem. Rev. 114 (2014) 3854–3918. https://doi.org/10.1021/cr4005296.

[29] M. Valko, D. Leibfritz, J. Moncol, M.T.D. Cronin, M. Mazur, J. Telser, Free radicals and antioxidants in normal physiological functions and human disease, The International Journal of Biochemistry & Cell Biology. 39 (2007) 44–84. https://doi.org/10.1016/j.biocel.2006.07.001.

[30] A. Meister, Glutathione metabolism and its selective modification., Journal of Biological Chemistry. 263 (1988) 17205–17208. https://doi.org/10.1016/S0021-9258(19)77815-6.

[31] J. Bouayed, T. Bohn, Exogenous Antioxidants—Double-Edged Swords in Cellular Redox State: Health Beneficial Effects at Physiologic Doses versus Deleterious Effects at High Doses, Oxidative Medicine and Cellular Longevity. 3 (2010) 228–237. https://doi.org/10.4161/oxim.3.4.12858.

[32] I.A. Abreu, D.E. Cabelli, Superoxide dismutases—a review of the metal-associated mechanistic variations, Biochimica et Biophysica Acta (BBA) - Proteins and Proteomics. 1804 (2010) 263–274. https://doi.org/10.1016/j.bbapap.2009.11.005.

[33] W.H. Koppenol, D.M. Stanbury, P.L. Bounds, Electrode potentials of partially reduced oxygen species, from dioxygen to water, Free Radical Biology and Medicine. 49 (2010) 317–322. https://doi.org/10.1016/j.freeradbiomed.2010.04.011.

[34] J.A. Imlay, I. Fridovich, Assay of metabolic superoxide production in Escherichia coli., Journal of Biological Chemistry. 266 (1991) 6957–6965. https://doi.org/10.1016/S0021-9258(20)89596-9.

[35] P.R. Gardner, I. Raineri, L.B. Epstein, C.W. White, Superoxide Radical and Iron Modulate Aconitase Activity in Mammalian Cells, Journal of Biological Chemistry. 270 (1995) 13399–13405. https://doi.org/10.1074/jbc.270.22.13399.

[36] B. Halliwell, J.M. Gutteridge, Free radicals in biology and medicine, 2007.

[37] J. Sandström, K. Karlsson, T. Edlund, S.L. Marklund, Heparin-affinity patterns and composition of extracellular superoxide dismutase in human plasma and tissues, Biochemical Journal. 294 (1993) 853–857. https://doi.org/10.1042/bj2940853.

[38] C.L. Fattman, L.M. Schaefer, T.D. Oury, Extracellular superoxide dismutase in biology and medicine, Free Radical Biology and Medicine. 35 (2003) 236–256. https://doi.org/10.1016/S0891-5849(03)00275-2.

[39] C. Bowler, W. Van Camp, M. Van Montagu, D. Inzé, K. Asada, Superoxide Dismutase in Plants, Critical Reviews in Plant Sciences. 13 (1994) 199–218. https://doi.org/10.1080/07352689409701914.

[40] F.J. Yost, I. Fridovich, An Iron-containing Superoxide Dismutase from Escherichia coli, Journal of Biological Chemistry. 248 (1973) 4905–4908. https://doi.org/10.1016/S0021-9258(19)43649-1.

[41] H.-D. Youn, E.-J. Kim, J.-H. Roe, Y.C. Hah, S.-O. Kang, A novel nickel-containing superoxide dismutase from *Streptomyces* spp, Biochemical Journal. 318 (1996) 889–896. https://doi.org/10.1042/bj3180889.

[42] J.E. Gleason, A. Galaleldeen, R.L. Peterson, A.B. Taylor, S.P. Holloway, J. Waninger-Saroni, B.P. Cormack, D.E. Cabelli, P.J. Hart, V.C. Culotta, Candida albicans SOD5 represents the prototype of an unprecedented class of Cu-only superoxide dismutases required for pathogen defense, Proceedings of the National Academy of Sciences. 111 (2014) 5866–5871. https://doi.org/10.1073/pnas.1400137111.

[43] E. Mathieu, Anti-oxidant MnII-complexes: design and study in a cellular model of inflammatory diseases. Investigation of subcellular location, Thèse de doctorat en Chimie, Sorbonne university, 2017.

[44] D.P. Barondeau, C.J. Kassmann, C.K. Bruns, J.A. Tainer, E.D. Getzoff, Nickel Superoxide Dismutase Structure and Mechanism, Biochemistry. 43 (2004) 8038–8047. https://doi.org/10.1021/bi0496081.

[45] A. Merlino, I.R. Krauss, I. Castellano, E.D. Vendittis, B. Rossi, M. Conte, A. Vergara, F. Sica, Structure and flexibility in cold-adapted iron superoxide dismutases: The case of the enzyme isolated from Pseudoalteromonas haloplanktis, Journal of Structural Biology. 172 (2010) 343–352. https://doi.org/10.1016/j.jsb.2010.08.008.

[46] A.S. Hearn, L. Fan, J.R. Lepock, J.P. Luba, W.B. Greenleaf, D.E. Cabelli, J.A. Tainer, H.S. Nick, D.N. Silverman, Amino Acid Substitution at the Dimeric Interface of Human Manganese Superoxide Dismutase, Journal of Biological Chemistry. 279 (2004) 5861–5866. https://doi.org/10.1074/jbc.M311310200.

[47] M. DiDonato, L. Craig, M.E. Huff, M.M. Thayer, R.M.F. Cardoso, C.J. Kassmann, T.P. Lo, C.K. Bruns, E.T. Powers, J.W. Kelly, E.D. Getzoff, J.A. Tainer, ALS Mutants of Human Superoxide Dismutase Form Fibrous Aggregates Via Framework Destabilization, Journal of Molecular Biology. 332 (2003) 601–615. https://doi.org/10.1016/S0022-2836(03)00889-1.

[48] S. Nedd, R.L. Redler, E.A. Proctor, N.V. Dokholyan, A.N. Alexandrova, Cu,Zn-Superoxide Dismutase without Zn Is Folded but Catalytically Inactive, Journal of Molecular Biology. 426 (2014) 4112–4124. https://doi.org/10.1016/j.jmb.2014.07.016.

[49] A. Nandi, L.-J. Yan, C.K. Jana, N. Das, Role of Catalase in Oxidative Stress- and Age-Associated Degenerative Diseases, Oxidative Medicine and Cellular Longevity. 2019 (2019) 1–19. https://doi.org/10.1155/2019/9613090.

[50] M. Alfonso-Prieto, X. Biarnés, P. Vidossich, C. Rovira, The Molecular Mechanism of the Catalase Reaction, J. Am.

Chem. Soc. 131 (2009) 11751–11761. https://doi.org/10.1021/ja9018572.

[51] I. Schomburg, L. Jeske, M. Ulbrich, S. Placzek, A. Chang, D. Schomburg, The BRENDA enzyme information system–From a database to an expert system, Journal of Biotechnology. 261 (2017) 194–206. https://doi.org/10.1016/j.jbiotec.2017.04.020.

[52] C. Jakopitsch, E. Droghetti, F. Schmuckenschlager, P.G. Furtmüller, G. Smulevich, C. Obinger, Role of the Main Access Channel of Catalase-Peroxidase in Catalysis, Journal of Biological Chemistry. 280 (2005) 42411–42422. https://doi.org/10.1074/jbc.M508009200.

[53] C.D. Putnam, A.S. Arvai, Y. Bourne, J.A. Tainer, Active and inhibited human catalase structures: ligand and NADPH binding and catalytic mechanism 1 1Edited by R. Huber, Journal of Molecular Biology. 296 (2000) 295–309. https://doi.org/10.1006/jmbi.1999.3458.

[54] M. Alfonso-Prieto, P. Vidossich, C. Rovira, The reaction mechanisms of heme catalases: An atomistic view by ab initio molecular dynamics, Archives of Biochemistry and Biophysics. 525 (2012) 121–130. https://doi.org/10.1016/j.abb.2012.04.004.

[55] Y. Noritake, N. Umezawa, N. Kato, T. Higuchi, Manganese Salen Complexes with Acid–Base Catalytic Auxiliary: Functional Mimetics of Catalase, Inorg. Chem. 52 (2013) 3653–3662. https://doi.org/10.1021/ic302101c.

[56] J.W. Whittaker, Non-heme manganese catalase – The 'other' catalase, Archives of Biochemistry and Biophysics. 525 (2012) 111–120. https://doi.org/10.1016/j.abb.2011.12.008.

[57] V.V. Barynin, M.M. Whittaker, S.V. Antonyuk, V.S. Lamzin, P.M. Harrison, P.J. Artymiuk, J.W. Whittaker, Crystal Structure of Manganese Catalase from Lactobacillus plantarum, Structure. 9 (2001) 725–738. https://doi.org/10.1016/S0969-2126(01)00628-1.

[58] A.B. Pithadia, S. Jain, Treatment of inflammatory bowel disease (IBD), Pharmacological Reports. 63 (2011) 629–642. https://doi.org/10.1016/S1734-1140(11)70575-8.

[59] D.C. Baumgart, S.R. Carding, Inflammatory bowel disease: cause and immunobiology, The Lancet. 369 (2007) 1627–1640. https://doi.org/10.1016/S0140-6736(07)60750-8.

[60] J. Burisch, P. Munkholm, Inflammatory bowel disease epidemiology:, Current Opinion in Gastroenterology. 29 (2013) 357–362. https://doi.org/10.1097/MOG.0b013e32836229fb.

[61] V. Jairath, B.G. Feagan, Global burden of inflammatory bowel disease, The Lancet Gastroenterology & Hepatology. 5 (2020) 2–3. https://doi.org/10.1016/S2468-1253(19)30358-9.

[62] S. Paramsothy, A.K. Rosenstein, S. Mehandru, J.-F. Colombel, The current state of the art for biological therapies and new small molecules in inflammatory bowel disease, Mucosal Immunol. 11 (2018) 1558–1570. https://doi.org/10.1038/s41385-018-0050-3.

[63] R. Caprilli, E. Angelucci, V. Clemente, Recent advances in the management of Crohn's disease, Digestive and Liver Disease. 40 (2008) 709–716. https://doi.org/10.1016/j.dld.2008.02.042.

[64] E. Martini, S.M. Krug, B. Siegmund, M.F. Neurath, C. Becker, Mend Your Fences: The Epithelial Barrier and its Relationship With Mucosal Immunity in Inflammatory Bowel Disease, Cellular and Molecular Gastroenterology and Hepatology. 4 (2017) 33–46. https://doi.org/10.1016/j.jcmgh.2017.03.007.

[65] L.W. Peterson, D. Artis, Intestinal epithelial cells: regulators of barrier function and immune homeostasis, Nat Rev Immunol. 14 (2014) 141–153. https://doi.org/10.1038/nri3608.

[66] N.H. Salzman, M.A. Underwood, C.L. Bevins, Paneth cells, defensins, and the commensal microbiota: A hypothesis on intimate interplay at the intestinal mucosa, Seminars in Immunology. 19 (2007) 70–83. https://doi.org/10.1016/j.smim.2007.04.002.

[67] W. Strober, I. Fuss, P. Mannon, The fundamental basis of inflammatory bowel disease, J. Clin. Invest. 117 (2007) 514–521. https://doi.org/10.1172/JCI30587.

[68] C. Chang, H. Lin, Dysbiosis in gastrointestinal disorders, Best Practice & Research Clinical Gastroenterology. 30 (2016) 3–15. https://doi.org/10.1016/j.bpg.2016.02.001.

[69] H. Sokol, B. Pigneur, L. Watterlot, O. Lakhdari, L.G. Bermúdez-Humarán, J.-J. Gratadoux, S. Blugeon, C. Bridonneau, J.-P. Furet, G. Corthier, C. Grangette, N. Vasquez, P. Pochart, G. Trugnan, G. Thomas, H.M. Blottière, J. Doré, P. Marteau, P. Seksik, P. Langella, *Faecalibacterium prausnitzii* is an anti-inflammatory commensal bacterium identified by gut microbiota analysis of Crohn disease patients, Proc. Natl. Acad. Sci. U.S.A. 105 (2008) 16731–16736. https://doi.org/10.1073/pnas.0804812105.

[70] Saint-Antoine IBD Network, H. Sokol, C. Landman, P. Seksik, L. Berard, M. Montil, I. Nion-Larmurier, A. Bourrier, G. Le Gall, V. Lalande, A. De Rougemont, J. Kirchgesner, A. Daguenel, M. Cachanado, A. Rousseau, É. Drouet, M. Rosenzwajg, H. Hagege, X. Dray, D. Klatzman, P. Marteau, L. Beaugerie, T. Simon, Fecal microbiota transplantation to maintain remission in Crohn's disease: a pilot randomized controlled study, Microbiome. 8 (2020) 12. https://doi.org/10.1186/s40168-020-0792-5.

[71] A.R. Weingarden, B.P. Vaughn, Intestinal microbiota, fecal microbiota transplantation, and inflammatory bowel disease, Gut Microbes. 8 (2017) 238–252. https://doi.org/10.1080/19490976.2017.1290757.

[72] M. Barra, T. Danino, D. Garrido, Engineered Probiotics for Detection and Treatment of Inflammatory Intestinal Diseases, Front. Bioeng. Biotechnol. 8 (2020) 265. https://doi.org/10.3389/fbioe.2020.00265.

[73] H. Zhu, Y.R. Li, Oxidative stress and redox signaling mechanisms of inflammatory bowel disease: updated

experimental and clinical evidence, Exp Biol Med (Maywood). 237 (2012) 474–480. https://doi.org/10.1258/ebm.2011.011358.

[74] A.R. Bourgonje, M. Feelisch, K.N. Faber, A. Pasch, G. Dijkstra, H. van Goor, Oxidative Stress and Redox-Modulating Therapeutics in Inflammatory Bowel Disease, Trends in Molecular Medicine. 26 (2020) 1034–1046. https://doi.org/10.1016/j.molmed.2020.06.006.

[75] L. Kruidenier, H.W. Verspaget, Review article: oxidative stress as a pathogenic factor in inflammatory bowel disease — radicals or ridiculous?, Aliment Pharmacol Ther. (2002) 19.

[76] M. Krzystek-Korpacka, R. Kempiński, M.A. Bromke, K. Neubauer, Oxidative Stress Markers in Inflammatory Bowel Diseases: Systematic Review, Diagnostics. 10 (2020) 601. https://doi.org/10.3390/diagnostics10080601.

[77] J. Lugrin, N. Rosenblatt-Velin, R. Parapanov, L. Liaudet, The role of oxidative stress during inflammatory processes, Biological Chemistry. 395 (2014) 203–230. https://doi.org/10.1515/hsz-2013-0241.

[78] N.S. Chandel, W.C. Trzyna, D.S. McClintock, P.T. Schumacker, Role of Oxidants in NF-κB Activation and TNF-α Gene Transcription Induced by Hypoxia and Endotoxin, J Immunol. 165 (2000) 1013–1021. https://doi.org/10.4049/jimmunol.165.2.1013.

[79] J. Pravda, Radical induction theory of ulcerative colitis, WJG. 11 (2005) 2371. https://doi.org/10.3748/wjg.v11.i16.2371.

[80] C.A.R. Martinez, M.L. Ribeiro, A. Gambero, D.D. da C. Miranda, J.A. Pereira, S.R. Nadal, The importance of oxygen free radicals in the etiopathogenesis of diversion colitis in rats, Acta Cir. Bras. 25 (2010) 387–395. https://doi.org/10.1590/S0102-86502010000500002.

[81] G. Gloire, S. Legrand-Poels, J. Piette, NF-κB activation by reactive oxygen species: Fifteen years later, Biochemical Pharmacology. 72 (2006) 1493–1505. https://doi.org/10.1016/j.bcp.2006.04.011.

[82] T. Tian, Z. Wang, J. Zhang, Pathomechanisms of Oxidative Stress in Inflammatory Bowel Disease and Potential Antioxidant Therapies, Oxidative Medicine and Cellular Longevity. 2017 (2017) 1–18. https://doi.org/10.1155/2017/4535194.

[83] M.A. Alzoghaibi, I.A. Al-Mofleh, A.M. Al-Jebreen, Antioxidant activities for superoxide dismutase in patients with Crohn's disease, J Basic Clin Physiol Pharmacol. 25 (2014) 59–62. https://doi.org/10.1515/jbcpp-2013-0042.

[84] L. Kruidenier, I. Kuiper, W. van Duijn, S.L. Marklund, R.A. van Hogezand, C.B. Lamers, H.W. Verspaget, Differential mucosal expression of three superoxide dismutase isoforms in inflammatory bowel disease, J. Pathol. 201 (2003) 7–16. https://doi.org/10.1002/path.1407.

[85] M. Mrowicka, J. Mrowicki, M. Mik, Ł. Dziki, A. Dziki, I. Majsterek, Assessment of DNA damage profile and oxidative /antioxidative biomarker level in patients with inflammatory bowel disease, Pol Przegl Chir. 92 (2020) 8–15. https://doi.org/10.5604/01.3001.0014.1548.

[86] A. D'Odorico, S. Bortolan, R. Cardin, Reduced Plasma Antioxidant Concentrations and Increased Oxidative DNA Damage in Inflammatory Bowel Disease, Scandinavian Journal of Gastroenterology. 36 (2001) 1289–1294. https://doi.org/10.1080/003655201317097146.

[87] K. Szczeklik, W. Krzysciak, R. Domagala-Rodacka, P. Mach, D. Darczuk, D. Cibor, J. Pytko-Polonczyk, T. Rodacki, D. Owczarek, Alterations in glutathione peroxidase and superoxide dismutase activities in plasma and saliva in relation to disease activity in patients with Crohn's disease, J. Physiol. Pharmacol. 67 (2016) 709–715.

[88] J. Seguí, M. Gironella, M. Sans, S. Granell, F. Gil, M. Gimeno, P. Coronel, J.M. Piqué, J. Panés, Superoxide dismutase ameliorates TNBS-induced colitis by reducing oxidative stress, adhesion molecule expression, and leukocyte recruitment into the inflamed intestine, Journal of Leukocyte Biology. 76 (2004) 537–544. https://doi.org/10.1189/jlb.0304196.

[89] J. Emerit, S. Pelletier, J. Likforman, C. Pasquier, A. Thuillier, Phase II trial of copper zinc superoxide dismutase (CuZn SOD) in the treatment of Crohn's disease, Free Radic Res Commun. 12-13 Pt 2 (1991) 563–569. https://doi.org/10.3109/10715769109145831.

[90] Y. Suzuki, T. Matsumoto, S. Okamoto, T. Hibi, A lecithinized superoxide dismutase (PC-SOD) improves ulcerative colitis, Colorectal Dis. 10 (2008) 931–934. https://doi.org/10.1111/j.1463-1318.2008.01487.x.

[91] J.-E. Kang, H.-D. Kim, S.-Y. Park, J.-G. Pan, J.H. Kim, D.-Y. Yum, Dietary Supplementation With a Bacillus Superoxide Dismutase Protects Against γ-Radiation-induced Oxidative Stress and Ameliorates Dextran Sulphate Sodium-induced Ulcerative Colitis in Mice, J Crohns Colitis. 12 (2018) 860–869. https://doi.org/10.1093/ecco-jcc/jjy034.

[92] K.E. Barrett, D.F. McCole, Hydrogen peroxide scavenger, catalase, alleviates ion transport dysfunction in murine colitis, Clin Exp Pharmacol Physiol. 43 (2016) 1097–1106. https://doi.org/10.1111/1440-1681.12646.

[93] D.H. Kim, J. Park, S. Kim, M.Y. Yoon, H.W. Ma, I.S. Park, M. Son, J.H. Kim, T.I. Kim, W.H. Kim, S.S. Yoon, S.W. Kim, J.H. Cheon, An Escherichia coli strain with extra catalase activity protects against murine colitis by scavenging hydrogen peroxide and regulating regulatory t cell/interleukin-17 pathways, Free Radical Biology and Medicine. 174 (2021) 110–120. https://doi.org/10.1016/j.freeradbiomed.2021.08.002.

[94] D. Salvemini, C. Muscoli, D.P. Riley, S. Cuzzocrea, Superoxide Dismutase Mimetics, Pulmonary Pharmacology & Therapeutics. 15 (2002) 439–447. https://doi.org/10.1006/pupt.2002.0374.

[95] O. Iranzo, Manganese complexes displaying superoxide dismutase activity: A balance between different factors, Bioorganic Chemistry. 39 (2011) 73–87. https://doi.org/10.1016/j.bioorg.2011.02.001.

[96] S. Miriyala, I. Spasojevic, A. Tovmasyan, D. Salvemini, Z. Vujaskovic, D. St. Clair, I. Batinic-Haberle, Manganese superoxide dismutase, MnSOD and its mimics, Biochimica et Biophysica Acta (BBA) - Molecular Basis of Disease. 1822

(2012) 794–814. https://doi.org/10.1016/j.bbadis.2011.12.002.

[97] I. Batinic-Haberle, A. Tovmasyan, E.R.H. Roberts, Z. Vujaskovic, K.W. Leong, I. Spasojevic, SOD Therapeutics: Latest Insights into Their Structure-Activity Relationships and Impact on the Cellular Redox-Based Signaling Pathways, Antioxidants & Redox Signaling. 20 (2014) 2372–2415. https://doi.org/10.1089/ars.2012.5147.

[98] S. Signorella, C. Palopoli, G. Ledesma, Rationally designed mimics of antioxidant manganoenzymes: Role of structural features in the quest for catalysts with catalase and superoxide dismutase activity, Coordination Chemistry Reviews. 365 (2018) 75–102. https://doi.org/10.1016/j.ccr.2018.03.005.

[99] M.G.B. Drew, C.J. Harding, V. McKee, G.G. Morgan, J. Nelson, Geometric control of manganese redox state, J. Chem. Soc., Chem. Commun. (1995) 1035. https://doi.org/10.1039/c39950001035.

[100] E.D. Getzoff, J.A. Tainer, P.K. Weiner, P.A. Kollman, J.S. Richardson, D.C. Richardson, Electrostatic recognition between superoxide and copper, zinc superoxide dismutase, Nature. 306 (1983) 287–290. https://doi.org/10.1038/306287a0.

[101] I. Spasojević, I. Batinić-Haberle, J.S. Rebouças, Y.M. Idemori, I. Fridovich, Electrostatic Contribution in the Catalysis of O 2 · _ Dismutation by Superoxide Dismutase Mimics, Journal of Biological Chemistry. 278 (2003) 6831–6837. https://doi.org/10.1074/jbc.M211346200.

[102] J.S. Rebouças, I. Spasojević, D.H. Tjahjono, A. Richaud, F. Méndez, L. Benov, I. Batinić-Haberle, Redox modulation of oxidative stress by Mn porphyrin-based therapeutics: The effect of charge distribution, Dalton Trans. (2008) 1233. https://doi.org/10.1039/b716517j.

[103] H.Y.V. Ching, I. Kenkel, N. Delsuc, E. Mathieu, I. Ivanović-Burmazović, C. Policar, Bioinspired superoxide-dismutase mimics: The effects of functionalization with cationic polyarginine peptides, Journal of Inorganic Biochemistry. 160 (2016) 172–179. https://doi.org/10.1016/j.jinorgbio.2016.01.025.

[104] D. Lieb, I. Kenkell, J.Lj. Miljković, D. Moldenhauer, N. Weber, M.R. Filipović, F. Gröhn, I. Ivanović-Burmazović, Amphiphilic Pentaazamacrocyclic Manganese Superoxide Dismutase Mimetics, Inorg. Chem. 53 (2014) 1009–1020. https://doi.org/10.1021/ic402469t.

[105] R. D'Agata, G. Grasso, G. Iacono, G. Spoto, G. Vecchio, Lectin recognition of a new SOD mimic bioconjugate studied with surface plasmon resonance imaging, Org. Biomol. Chem. 4 (2006) 610. https://doi.org/10.1039/b517074e.

[106] S. Asayama, K. Mizushima, S. Nagaoka, H. Kawakami, Design of Metalloporphyrin−Carbohydrate Conjugates for a New Superoxide Dismutase Mimic with Cellular Recognition, Bioconjugate Chem. 15 (2004) 1360–1363. https://doi.org/10.1021/bc049865i.

[107] W. Munroe, C. Kingsley, A. Durazo, E. Butler Gralla, J.A. Imlay, C. Srinivasan, J. Selverstone Valentine, Only one of a wide assortment of manganese-containing SOD mimicking compounds rescues the slow aerobic growth phenotypes of both Escherichia coli and Saccharomyces cerevisiae strains lacking superoxide dismutase enzymes, Journal of Inorganic Biochemistry. 101 (2007) 1875–1882. https://doi.org/10.1016/j.jinorgbio.2007.07.008.

[108] G.F. Kelso, A. Maroz, H.M. Cochemé, A. Logan, T.A. Prime, A.V. Peskin, C.C. Winterbourn, A.M. James, M.F. Ross, S. Brooker, C.M. Porteous, R.F. Anderson, M.P. Murphy, R.A.J. Smith, A Mitochondria-Targeted Macrocyclic Mn(II) Superoxide Dismutase Mimetic, Chemistry & Biology. 19 (2012) 1237–1246. https://doi.org/10.1016/j.chembiol.2012.08.005.

[109] M. Zoumpoulaki, G. Schanne, N. Delsuc, H. Preud'homme, E. Quévrain, N. Eskenazi, G. Gazzah, R. Guillot, P. Seksik, J. Vinh, R. Lobinski, C. Policar, Deciphering the Metal Speciation in Low-Molecular-Weight Complexes by IMS-MS: Application to the Detection of Manganese Superoxide Dismutase Mimics in Cell Lysates, Angew Chem Int Ed. (2022). https://doi.org/10.1002/anie.202203066.

[110] R.F. Pasternack, B. Halliwell, Superoxide dismutase activities of an iron porphyrin and other iron complexes, J. Am. Chem. Soc. 101 (1979) 1026–1031. https://doi.org/10.1021/ja00498a038.

[111] M.F. Nepomuceno, M. Tabak, A.E. Vercesi, Opposite Effects of Mn(III) and Fe(III) Forms of meso-Tetrakis(4-N-methyl pyridiniumyl) Porphyrins on Isolated Rat Liver Mitochondria, Journal of Bioenergetics and Biomembranes. 34 (2002) 41–47. https://doi.org/10.1023/A:1013818719932.

[112] I. Batinić-Haberle, S.I. Liochev, I. Spasojević, I. Fridovich, A Potent Superoxide Dismutase Mimic: Manganese β-Octabromo-meso-tetrakis-(N-methylpyridinium- 4-yl) Porphyrin, Archives of Biochemistry and Biophysics. 343 (1997) 225–233. https://doi.org/10.1006/abbi.1997.0157.

[113] F. Bellot, R. Hardré, G. Pelosi, M. Thérisod, C. Policar, Superoxide dismutase-like activity of cobalt(ii) complexes based on a sugar platform, Chem. Commun. (2005) 5414. https://doi.org/10.1039/b508893c.

[114] M.E. Krause, A.M. Glass, T.A. Jackson, J.S. Laurence, Novel Tripeptide Model of Nickel Superoxide Dismutase, Inorg. Chem. 49 (2010) 362–364. https://doi.org/10.1021/ic901828m.

[115] E.P. Broering, P.T. Truong, E.M. Gale, T.C. Harrop, Synthetic Analogues of Nickel Superoxide Dismutase: A New Role for Nickel in Biology, Biochemistry. 52 (2013) 4–18. https://doi.org/10.1021/bi3014533.

[116] J. Shearer, L.M. Long, A Nickel Superoxide Dismutase Maquette That Reproduces the Spectroscopic and Functional Properties of the Metalloenzyme, Inorg. Chem. 45 (2006) 2358–2360. https://doi.org/10.1021/ic0514344.

[117] I. Batinić-Haberle, J.S. Rebouças, I. Spasojević, Superoxide Dismutase Mimics: Chemistry, Pharmacology, and Therapeutic Potential, Antioxidants & Redox Signaling. 13 (2010) 877–918. https://doi.org/10.1089/ars.2009.2876.

[118] C. Policar, J. Bouvet, H.C. Bertrand, N. Delsuc, SOD mimics: From the tool box of the chemists to cellular studies, Current Opinion in Chemical Biology. 67 (2022) 102109. https://doi.org/10.1016/j.cbpa.2021.102109.

[119] I. Batinic-Haberle, A. Tovmasyan, I. Spasojevic, An educational overview of the chemistry, biochemistry and

therapeutic aspects of Mn porphyrins – From superoxide dismutation to H2O2-driven pathways, Redox Biology. 5 (2015) 43–65. https://doi.org/10.1016/j.redox.2015.01.017.

[120] G. DeFreitas-Silva, J.S. Rebouças, I. Spasojević, L. Benov, Y.M. Idemori, I. Batinić-Haberle, SOD-like activity of Mn(II) β-octabromo-meso-tetrakis(N-methylpyridinium-3-yl)porphyrin equals that of the enzyme itself, Archives of Biochemistry and Biophysics. 477 (2008) 105–112. https://doi.org/10.1016/j.abb.2008.04.032.

[121] M.C. Jaramillo, M.M. Briehl, J.D. Crapo, I. Batinic-Haberle, M.E. Tome, Manganese Porphyrin, MnTE-2-PyP5+, Acts as a Pro-Oxidant to Potentiate Glucocorticoid-Induced Apoptosis in Lymphoma Cells, Free Radical Biology and Medicine. 52 (2012) 1272–1284. https://doi.org/10.1016/j.freeradbiomed.2012.02.001.

[122] I. Batinic-Haberle, A. Tovmasyan, I. Spasojevic, Mn porphyrin-based redox-active therapeutics, in: Redox-Active Therapeutics, Springer International, 2016: pp. 165–212.

[123] I. Batinic-Haberle, A. Tovmasyan, I. Spasojevic, Mn Porphyrin-Based Redox-Active Drugs: Differential Effects as Cancer Therapeutics and Protectors of Normal Tissue Against Oxidative Injury, Antioxidants & Redox Signaling. 29 (2018) 1691–1724. https://doi.org/10.1089/ars.2017.7453.

[124] K. Aston, N. Rath, A. Naik, U. Slomczynska, O.F. Schall, D.P. Riley, Computer-Aided Design (CAD) of Mn(II) Complexes: Superoxide Dismutase Mimetics with Catalytic Activity Exceeding the Native Enzyme, Inorg. Chem. 40 (2001) 1779–1789. https://doi.org/10.1021/ic000958v.

[125] I. Anderson, C. Adinolfi, S.R. Doctrow, K. Huffman, K. Joy, B. Malfroy, P. Soden, H. Rupniak, J. Barnes, Oxidative signalling and inflammatory pathways in Alzheimer's disease., Biochem Soc Symp. 67 (2001) 141–149.

[126] M. Baudry, S. Etienne, A. Bruce, M. Palucki, E. Jacobsen, B. Malfroy, Salen-manganese complexes are superoxide dismutase- mimics, Biochemical and Biophysical Research Communications. 192 (1993). https://doi.org/10.1006/bbrc.1993.1509.

[127] S.R. Doctrow, K. Huffman, C.B. Marcus, G. Tocco, E. Malfroy, C.A. Adinolfi, H. Kruk, K. Baker, N. Lazarowych, J. Mascarenhas, B. Malfroy, Salen−Manganese Complexes as Catalytic Scavengers of Hydrogen Peroxide and Cytoprotective Agents: Structure−Activity Relationship Studies, J. Med. Chem. 45 (2002) 4549–4558. https://doi.org/10.1021/jm020207y.

[128] C. Policar, S. Durot, F. Lambert, M. Cesario, F. Ramiandrasoa, I. Morgenstern-Badarau, New MnII Complexes with an N/O Coordination Sphere from TripodalN-Centered Ligands − Characterization from Solid State to Solution and Reaction with Superoxide in Non-Aqueous and Aqueous Media, Eur. J. Inorg. Chem. 2001 (2001) 1807–1818. https://doi.org/10.1002/1099-0682(200107)2001:7<1807::AID-EJIC1807>3.0.CO;2-Y.

[129] S. Durot, C. Policar, F. Cisnetti, F. Lambert, J.-P. Renault, G. Pelosi, G. Blain, H. Korri-Youssoufi, J.-P. Mahy, Series of Mn Complexes Based onN-Centered Ligands and Superoxide - Reactivity in an Anhydrous Medium and SOD-Like Activity in an Aqueous Medium Correlated to MnII/MnIII Redox Potentials, Eur. J. Inorg. Chem. 2005 (2005) 3513–3523. https://doi.org/10.1002/ejic.200400835.

[130] S. Durot, F. Lambert, J.-P. Renault, C. Policar, A Pulse Radiolysis Study of Catalytic Superoxide Radical Dismutation by a Manganese(II) Complex with an N-Tripodal Ligand, Eur. J. Inorg. Chem. 2005 (2005) 2789–2793. https://doi.org/10.1002/ejic.200400834.

[131] F. Cisnetti, A.-S. Lefèvre, R. Guillot, F. Lambert, G. Blain, E. Anxolabéhère-Mallart, C. Policar, A New Pentadentate Ligand Forms Both a Di- and a Mononuclear MnII Complex: Electrochemical, Spectroscopic and Superoxide Dismutase Activity Studies, Eur. J. Inorg. Chem. 2007 (2007) 4472–4480. https://doi.org/10.1002/ejic.200601236.

[132] F. Cisnetti, G. Pelosi, C. Policar, Synthesis and superoxide dismutase-like activity of new manganese(III) complexes based on tridentate N2O ligands derived from histamine, Inorganica Chimica Acta. 360 (2007) 557–562. https://doi.org/10.1016/j.ica.2006.07.112.

[133] S. Melov, J. Ravenscroft, S. Malik, M.S. Gill, D.W. Walker, P.E. Clayton, D.C. Wallace, B. Malfroy, S.R. Doctrow, G.J. Lithgow, Extension of Life-Span with Superoxide Dismutase/Catalase Mimetics, Science. 289 (2000) 1567–1569. https://doi.org/10.1126/science.289.5484.1567.

[134] B.J. Day, Catalase and glutathione peroxidase mimics, Biochemical Pharmacology. 77 (2009) 285–296. https://doi.org/10.1016/j.bcp.2008.09.029.

[135] A. Tovmasyan, C.G.C. Maia, T. Weitner, S. Carballal, R.S. Sampaio, D. Lieb, R. Ghazaryan, I. Ivanovic-Burmazovic, G. Ferrer-Sueta, R. Radi, J.S. Reboucas, I. Spasojevic, L. Benov, I. Batinic-Haberle, A comprehensive evaluation of catalase-like activity of different classes of redox-active therapeutics, Free Radical Biology and Medicine. 86 (2015) 308–321. https://doi.org/10.1016/j.freeradbiomed.2015.05.018.

[136] A.E.O. Fisher, S.C. Maxwell, D.P. Naughton, Catalase and superoxide dismutase mimics for the treatment of inflammatory diseases, Inorganic Chemistry Communications. 6 (2003) 1205–1208. https://doi.org/10.1016/S1387-7003(03)00223-5.

[137] B.J. Day, I. Fridovich, J.D. Crapo, Manganic Porphyrins Possess Catalase Activity and Protect Endothelial Cells against Hydrogen Peroxide-Mediated Injury, Archives of Biochemistry and Biophysics. 347 (1997) 256–262. https://doi.org/10.1006/abbi.1997.0341.

[138] R. Kachadourian, C.A. Johnson, E. Min, I. Spasojevic, B.J. Day, Flavin-dependent antioxidant properties of a new series of meso-N,N′-dialkyl-imidazolium substituted manganese(III) porphyrins, Biochemical Pharmacology. 67 (2004) 77–85. https://doi.org/10.1016/j.bcp.2003.08.036.

[139] P.R. Castello, D.A. Drechsel, B.J. Day, M. Patel, Inhibition of Mitochondrial Hydrogen Peroxide Production by Lipophilic Metalloporphyrins, J Pharmacol Exp Ther. 324 (2008) 970–976. https://doi.org/10.1124/jpet.107.132134.

[140] S.R. Doctrow, K. Huffman, C.B. Marcus, W. Musleh, A. Bruce, M. Baudry, B. Malfroy, Salen- Manganese Complexes: Combined Superoxide Dismutase/Catalase Mimics with Broad Pharmacological Efficacy, in: Advances in Pharmacology, Elsevier, 1996: pp. 247–269. https://doi.org/10.1016/S1054-3589(08)60987-4.

[141] Y. Watanabe, A. Namba, N. Umezawa, M. Kawahata, K. Yamaguchi, T. Higuchi, Enhanced catalase-like activity of manganese salen complexes in water: effect of a three-dimensionally fixed auxiliary, Chem. Commun. (2006) 4958. https://doi.org/10.1039/b608846e.

[142] V. Lanza, G. Vecchio, New conjugates of superoxide dismutase/catalase mimetics with cyclodestrins, Journal of Inorganic Biochemistry. 103 (2009) 381–388. https://doi.org/10.1016/j.jinorgbio.2008.11.017.

[143] D. Moreno, C. Palopoli, V. Daier, S. Shova, L. Vendier, M.G. Sierra, J.-P. Tuchagues, S. Signorella, Synthesis, structure and catalase-like activity of dimanganese(iii) complexes of 1,5-bis(X-salicylidenamino)pentan-3-ol (X = 3- and 5-methyl). Influence of phenyl-ring substituents on catalytic activity, Dalton Trans. (2006) 5156. https://doi.org/10.1039/b609366c.

[144] C. Palopoli, G. Gómez, A. Foi, F. Doctorovich, S. Mallet-Ladeira, C. Hureau, S. Signorella, Dimerization, redox properties and antioxidant activity of two manganese(III) complexes of difluoro- and dichloro-substituted Schiff-base ligands, Journal of Inorganic Biochemistry. 167 (2017) 49–59. https://doi.org/10.1016/j.jinorgbio.2016.11.019.

[145] S. Signorella, C. Hureau, Bioinspired functional mimics of the manganese catalases, Coordination Chemistry Reviews. 256 (2012) 1229–1245. https://doi.org/10.1016/j.ccr.2012.02.003.

[146] W. Sicking, H.-G. Korth, G. Jansen, H. de Groot, R. Sustmann, Hydrogen Peroxide Decomposition by a Non-Heme Iron(III) Catalase Mimic: A DFT Study, Chem. Eur. J. 13 (2007) 4230–4245. https://doi.org/10.1002/chem.200601209.

[147] M. Grau, F. Rigodanza, A.J.P. White, A. Sorarù, M. Carraro, M. Bonchio, G.J.P. Britovsek, Ligand tuning of single-site manganese-based catalytic antioxidants with dual superoxide dismutase and catalase activity, Chem. Commun. 50 (2014) 4607–4609. https://doi.org/10.1039/C4CC00758A.

[148] M.L. Merlini, G.J.P. Britovsek, M. Swart, P. Belanzoni, Understanding the Catalase-Like Activity of a Bioinspired Manganese(II) Complex with a Pentadentate NSNSN Ligand Framework. A Computational Insight into the Mechanism, ACS Catal. 8 (2018) 2944–2958. https://doi.org/10.1021/acscatal.7b03559.

[149] G.N. Ledesma, H. Eury, E. Anxolabéhère-Mallart, C. Hureau, S.R. Signorella, A new mononuclear manganese(III) complex of an unsymmetrical hexadentate N3O3 ligand exhibiting superoxide dismutase and catalase-like activity: synthesis, characterization, properties and kinetics studies, Journal of Inorganic Biochemistry. 146 (2015) 69–76. https://doi.org/10.1016/j.jinorgbio.2015.02.012.

[150] P. Mathur, M. Crowder, G.C. Dismukes, Dimanganese Complexes of a Septadentate Ligand. Functional Analogues of the Manganese Pseudocatalase, J. Am. Chem. Soc. 109 (1987) 5227–5233. https://doi.org/10.1021/ja00251a030.

[151] V. Daier, H. Biava, C. Palopoli, S. Shova, J.-P. Tuchagues, S. Signorella, Synthesis, characterisation and catalase-like activity of dimanganese(III) complexes of 1,5-bis(5-X-salicylidenamino)pentan-3-ol (X=nitro and chloro), Journal of Inorganic Biochemistry. 98 (2004) 1806–1817. https://doi.org/10.1016/j.jinorgbio.2004.08.007.

[152] C. Palopoli, M. González-Sierra, G. Robles, F. Dahan, J.-P. Tuchagues, S. Signorella, Synthesis and characterisation of dimanganese(iii) complexes of 1,5-bis(X-salicylidenamino)pentan-3-ol (X = 3- or 5-methoxy) and their catalytic activity towards hydrogen peroxide disproportionation, J. Chem. Soc., Dalton Trans. (2002) 3813. https://doi.org/10.1039/b204566d.

[153] C. Palopoli, N. Bruzzo, C. Hureau, S. Ladeira, D. Murgida, S. Signorella, Synthesis, Characterization, and Catalase Activity of a Water-Soluble diMn ^{III} Complex of a Sulphonato-Substituted Schiff Base Ligand: An Efficient Catalyst for H_2O_2 Disproportionation, Inorg. Chem. 50 (2011) 8973–8983. https://doi.org/10.1021/ic2011452.

[154] H. Sigel, Catalase and Peroxidase Activity of Cu2+ Complexes, Angew. Chem. Int. Ed. Engl. 8 (1969) 167–177. https://doi.org/10.1002/anie.196901671.

[155] J. Kaizer, T. Csay, G. Speier, M. Réglier, M. Giorgi, Synthesis, structure and catalase-like activity of Cu(N-baa)2(phen) (phen=1,10-phenanthroline, N-baaH=N-benzoylanthranilic acid), Inorganic Chemistry Communications. 9 (2006) 1037–1039. https://doi.org/10.1016/j.inoche.2006.06.005.

[156] A.E.-M.M. Ramadan, Syntheses and characterization of new tetraazamacrocyclic copper(II) complexes as a dual functional mimic enzyme (catalase and superoxide dismutase), Journal of Coordination Chemistry. 65 (2012) 1417–1433. https://doi.org/10.1080/00958972.2012.673719.

[157] J.F. Guerreiro, M.A.G.B. Gomes, F. Pagliari, J. Jansen, M.G. Marafioti, C. Nistico, R. Hanley, R.O. Costa, S.S. Ferreira, F. Mendes, C. Fernandes, A. Horn, L. Tirinato, J. Seco, Iron and copper complexes with antioxidant activity as inhibitors of the metastatic potential of glioma cells, RSC Adv. 10 (2020) 12699–12710. https://doi.org/10.1039/D0RA00166J.

[158] J. Gao, A.E. Martell, J.H. Reibenspies, Novel dicopper(II) catalase-like model complexes: synthesis, crystal structure, properties and kinetic studies, Inorganica Chimica Acta. 346 (2003) 32–42. https://doi.org/10.1016/S0020-1693(02)01393-2.

[159] Q. Tang, J.-Q. Wu, H.-Y. Li, Y.-F. Feng, Z. Zhang, Y.-N. Liang, Dinuclear Cu(II) complexes based on *p* -xylylene-bridged bis(1,4,7-triazacyclononane) ligands: Synthesis, characterization, DNA cleavage abilities and evaluation of superoxide dismutase- and catalase-like activities: Dinuclear Cu(II) complexes showing dual SOD/catalase activity, Appl Organometal Chem. 32 (2018) e4297. https://doi.org/10.1002/aoc.4297.

[160] S. Caglar, E. Adıgüzel, B. Caglar, T. Saykal, E. Sahin, O. Büyükgüngör, Synthesis, crystal structure, spectroscopic, thermal, catechol oxidase and catalase-like studies: New copper(II) complexes of 2-benzoylbenzoate and 2-pyridilpropanol ligands, Inorganica Chimica Acta. 397 (2013) 101–109. https://doi.org/10.1016/j.ica.2012.11.028.

[161] A. Squarcina, A. Santoro, N. Hickey, R. De Zorzi, M. Carraro, S. Geremia, M. Bortolus, M. Di Valentin, M. Bonchio, Neutralization of Reactive Oxygen Species at Dinuclear Cu(II)-Cores: Tuning the Antioxidant Manifold in Water by Ligand Design, ACS Catal. 10 (2020) 7295–7306. https://doi.org/10.1021/acscatal.0c01955.

[162] J. McCord, I. Fridovich, Superoxide dismutase. An enzymic function for erythrocuprein (hemocuprein), The Journal of Biological Chemistry. 244 (1969) 6045–6055.

[163] I. Fridovich, Quantitative Aspects of the Production of Superoxide A nion Radical by Milk Xanthine Oxidase, 245 (1970) 6.

[164] A. Okado-Matsumoto, I. Fridovich, Assay of Superoxide Dismutase: Cautions Relevant to the Use of Cytochrome c, a Sulfonated Tetrazolium, and Cyanide, Analytical Biochemistry. 298 (2001) 337–342. https://doi.org/10.1006/abio.2001.5385.

[165] J. Butler, W.H. Koppenol, E. Margoliash, Kinetics and mechanism of the reduction of ferricytochrome c by the superoxide anion., Journal of Biological Chemistry. 257 (1982) 10747–10750. https://doi.org/10.1016/S0021-9258(18)33886-9.

[166] Z.-R. Liao, X.-F. Zheng, B.-S. Luo, L.-R. Shen, D.-F. Li, H.-L. Liu, W. Zhao, Synthesis, characterization and SOD-like activities of manganese-containing complexes with N,N,N′,N′-tetrakis(2′-benzimidazolyl methyl)-1,2-ethanediamine (EDTB), Polyhedron. 20 (2001) 2813–2821. https://doi.org/10.1016/S0277-5387(01)00891-9.

[167] M.W. Sutherland, B.A. Learmonth, The Tetrazolium Dyes MTS and XTT Provide New Quantitative Assays for Superoxide and Superoxide Dismutase, Free Radical Research. 27 (1997) 283–289. https://doi.org/10.3109/10715769709065766.

[168] L.L. Costanzo, G.D. Guidi, S. Giuftida, G. Vecchio, Determination of Superoxide Dismutase- Like Activity of Copper(U) Complexes. Relevance of the Speciation for the Correct Interpretation of In Vitro 0, Scavenger Activity, Joumal of Inorganic Biochemistry. 50 (1993) 273–281.

[169] H. Ukeda, S. Maeda, T. Ishii, M. Sawamura, Spectrophotometric Assay for Superoxide Dismutase Based on Tetrazolium Salt 3′-{1-[(Phenylamino)-carbonyl]-3,4-tetrazolium}-bis(4-methoxy-6-nitro)benzenesulfonic Acid Hydrate Reduction by Xanthine–Xanthine Oxidase, Analytical Biochemistry. 251 (1997) 206–209. https://doi.org/10.1006/abio.1997.2273.

[170] R. Filograna, V.K. Godena, A. Sanchez-Martinez, E. Ferrari, L. Casella, M. Beltramini, L. Bubacco, A.J. Whitworth, M. Bisaglia, Superoxide Dismutase (SOD)-mimetic M40403 Is Protective in Cell and Fly Models of Paraquat Toxicity, Journal of Biological Chemistry. 291 (2016) 9257–9267. https://doi.org/10.1074/jbc.M115.708057.

[171] A. Vincent, M. Thauvin, E. Quévrain, E. Mathieu, S. Layani, P. Seksik, I. Batinic-Haberle, S. Vriz, C. Policar, N. Delsuc, Evaluation of the compounds commonly known as superoxide dismutase and catalase mimics in cellular models, Journal of Inorganic Biochemistry. 219 (2021) 111431. https://doi.org/10.1016/j.jinorgbio.2021.111431.

[172] G. Schanne, M. Zoumpoulaki, G. Gazzah, A. Vincent, H. Preud'homme, R. Lobinski, S. Demignot, P. Seksik, N. Delsuc, C. Policar, Inertness of Superoxide Dismutase Mimics Mn(II) Complexes Based on an Open-Chain Ligand, Bioactivity, and Detection in Intestinal Epithelial Cells, Oxidative Medicine and Cellular Longevity. 2022 (2022) 3858122. https://doi.org/10.1155/2022/3858122.

[173] S. Groni, G. Blain, R. Guillot, C. Policar, E. Anxolabéhère-Mallart, Reactivity of Mn^{II} with Superoxide. Evidence for a $[Mn^{III}OO]^{+}$ Unit by Low-Temperature Spectroscopies, Inorg. Chem. 46 (2007) 1951–1953. https://doi.org/10.1021/ic062063+.

[174] G. Rotilio, R.C. Bray, E.M. Fielden, A pulse radiolysis study of superoxide dismutase, Biochimica et Biophysica Acta (BBA) - Enzymology. 268 (1972) 605–609. https://doi.org/10.1016/0005-2744(72)90359-2.

[175] B.H.J. Bielski, R.L. Arudi, Preparation and stabilization of aqueous/ethanolic superoxide solutions, Analytical Biochemistry. 133 (1983) 170–178. https://doi.org/10.1016/0003-2697(83)90239-7.

[176] S. Durot, F. Lambert, J.-P. Renault, C. Policar, A Pulse Radiolysis Study of Catalytic Superoxide Radical Dismutation by a Manganese(II) Complex with an N-Tripodal Ligand, Eur. J. Inorg. Chem. 2005 (2005) 2789–2793. https://doi.org/10.1002/ejic.200400834.

[177] D.P. Riley, W.J. Rivers, R.H. Weiss, Stopped-flow kinetic analysis for monitoring superoxide decay in aqueous systems, Analytical Biochemistry. 196 (1991) 344–349. https://doi.org/10.1016/0003-2697(91)90476-A.

[178] F.C. Friedel, D. Lieb, I. Ivanović-Burmazović, Comparative studies on manganese-based SOD mimetics, including the phosphate effect, by using global spectral analysis, Journal of Inorganic Biochemistry. 109 (2012) 26–32. https://doi.org/10.1016/j.jinorgbio.2011.12.008.

[179] S. Goldstein, C. Michel, W. Bors, M. Saran, G. Czapski, A critical reevaluation of some assay methods for superoxide dismutase activity, Free Radical Biology and Medicine. 4 (1988) 295–303. https://doi.org/10.1016/0891-5849(88)90050-0.

[180] B. Bóka, A. Myari, I. Sóvágó, N. Hadjiliadis, Copper(II) and zinc(II) complexes of the peptides Ac-HisValHis-NH 2 and Ac-HisValGlyAsp-NH 2 related to the active site of the enzyme CuZnSOD, Journal of Inorganic Biochemistry. 98 (2004) 113–122. https://doi.org/10.1016/j.jinorgbio.2003.09.012.

[181] W.F. Beyer, I. Fridovich, Assaying for superoxide dismutase activity: Some large consequences of minor changes in conditions, Analytical Biochemistry. 161 (1987) 559–566. https://doi.org/10.1016/0003-2697(87)90489-1.

[182] R.F. Beers, I.W. Sizer, A SPECTROPHOTOMETRIC METHOD FOR MEASURING THE BREAKDOWN OF HYDROGEN PEROXIDE BY CATALASE, Journal of Biological Chemistry. 195 (1952) 133–140.

https://doi.org/10.1016/S0021-9258(19)50881-X.

[183] G. Cohen, M. Kim, V. Ogwu, A modified catalase assay suitable for a plate reader and for the analysis of brain cell cultures, Journal of Neuroscience Methods. 67 (1996) 53–56. https://doi.org/10.1016/0165-0270(96)00011-8.

[184] C. Gay, J. Collins, J.M. Gebicki, Hydroperoxide Assay with the Ferric–Xylenol Orange Complex, Analytical Biochemistry. 273 (1999) 149–155. https://doi.org/10.1006/abio.1999.4208.

[185] M.H. Hadwan, H.N. Abed, Data supporting the spectrophotometric method for the estimation of catalase activity, Data in Brief. 6 (2016) 194–199. https://doi.org/10.1016/j.dib.2015.12.012.

[186] M.H. Hadwan, Simple spectrophotometric assay for measuring catalase activity in biological tissues, BMC Biochem. 19 (2018) 7. https://doi.org/10.1186/s12858-018-0097-5.

[187] A.A. Farman, M.H. Hadwan, Simple kinetic method for assessing catalase activity in biological samples, MethodsX. 8 (2021) 101434. https://doi.org/10.1016/j.mex.2021.101434.

[188] S. Mueller, H.-D. Riedel, W. Stremmel, Determination of Catalase Activity at Physiological Hydrogen Peroxide Concentrations, Analytical Biochemistry. 245 (1997) 55–60. https://doi.org/10.1006/abio.1996.9939.

[189] L.C. Clark, R. Wolf, D. Granger, Z. Taylor, *Continuous Recording of Blood Oxygen Tensions by Polarography*, Journal of Applied Physiology. 6 (1953) 189–193. https://doi.org/10.1152/jappl.1953.6.3.189.

[190] M. Rørth, P.K. Jensen, Determination of catalase activity by means of the Clark oxygen electrode, Biochimica et Biophysica Acta (BBA) - Enzymology. 139 (1967) 171–173. https://doi.org/10.1016/0005-2744(67)90124-6.

[191] C.J. Weydert, J.J. Cullen, Measurement of superoxide dismutase, catalase and glutathione peroxidase in cultured cells and tissue, Nat Protoc. 5 (2010) 51–66. https://doi.org/10.1038/nprot.2009.197.

[192] A. Vincent, J.R. Fores, E. Tauziet, E. Quévrain, Á. Dancs, A. Conte-Daban, A.-S. Bernard, P. Pelupessy, K. Coulibaly, P. Seksik, C. Hureau, K. Selmeczi, C. Policar, N. Delsuc, An easy-to-implement combinatorial approach involving an activity-based assay for the discovery of a peptidyl copper complex mimicking superoxide dismutase, Chem. Commun. 56 (2020) 399–402. https://doi.org/10.1039/C9CC07920C.

[193] C. Lenoir, C. Sapin, A.H. Broquet, A.-M. Jouniaux, S. Bardin, I. Gasnereau, G. Thomas, P. Seksik, G. Trugnan, J. Masliah, M. Bachelet, MD-2 controls bacterial lipopolysaccharide hyporesponsiveness in human intestinal epithelial cells, Life Sciences. 82 (2008) 519–528. https://doi.org/10.1016/j.lfs.2007.12.007.

[194] T. Kawai, S. Akira, Signaling to NF-κB by Toll-like receptors, Trends in Molecular Medicine. 13 (2007) 460–469. https://doi.org/10.1016/j.molmed.2007.09.002.

[195] T. Liu, L. Zhang, D. Joo, S.-C. Sun, NF-κB signaling in inflammation, Sig Transduct Target Ther. 2 (2017) 17023. https://doi.org/10.1038/sigtrans.2017.23.

[196] E. Mathieu, A.-S. Bernard, N. Delsuc, E. Quévrain, G. Gazzah, B. Lai, F. Chain, P. Langella, M. Bachelet, J. Masliah, P. Seksik, C. Policar, A Cell-Penetrant Manganese Superoxide Dismutase (MnSOD) Mimic Is Able To Complement MnSOD and Exerts an Antiinflammatory Effect on Cellular and Animal Models of Inflammatory Bowel Diseases, Inorg. Chem. 56 (2017) 2545–2555. https://doi.org/10.1021/acs.inorgchem.6b02695.

[197] M.J. Morgan, Z. Liu, Crosstalk of reactive oxygen species and NF-κB signaling, Cell Res. 21 (2011) 103–115. https://doi.org/10.1038/cr.2010.178.

[198] M. Zoumpoulaki, G. Schanne, N. Delsuc, H. Preud'homme, E. Quévrain, N. Eskenazi, G. Gazzah, R. Guillot, P. Seksik, J. Vinh, R. Lobinski, C. Policar, Deciphering the Metal Speciation in Low-Molecular-Weight Complexes by IMS-MS: Application to the Detection of Manganese Superoxide Dismutase Mimics in Cell Lysates, Angew Chem Int Ed. (2022). https://doi.org/10.1002/anie.202203066.

[199] A.-S. Bernard, C. Giroud, H.Y.V. Ching, A. Meunier, V. Ambike, C. Amatore, M.G. Collignon, F. Lemaître, C. Policar, Evaluation of the anti-oxidant properties of a SOD-mimic Mn-complex in activated macrophages, Dalton Trans. 41 (2012) 6399. https://doi.org/10.1039/c2dt12479c.

[200] E. Mathieu, A.-S. Bernard, H.Y.V. Ching, A. Somogyi, K. Medjoubi, J.R. Fores, H.C. Bertrand, A. Vincent, S. Trépout, J.-L. Guerquin-Kern, A. Scheitler, I. Ivanović-Burmazović, P. Seksik, N. Delsuc, C. Policar, Anti-inflammatory activity of superoxide dismutase mimics functionalized with cell-penetrating peptides, Dalton Trans. 49 (2020) 2323–2330. https://doi.org/10.1039/C9DT04619D.

[201] H. Irving, P. Williams, Order of stability of metal complexes, Nature. (1948) 746–747.

[202] H. Irving, P. Williams, The stability of transition-metal complexes, J. Chem. Soc. 637 (1953) 3192–3210. https://doi.org/10.1039/jr9530003192.

[203] F.S. Archibald, I. Fridovich, Manganese and Defenses against Oxygen Toxicity in *Lactobacillus plantarum*, J Bacteriol. 145 (1981) 442–451. https://doi.org/10.1128/jb.145.1.442-451.1981.

[204] M.J. Daly, E.K. Gaidamakova, V.Y. Matrosova, J.G. Kiang, R. Fukumoto, D.-Y. Lee, N.B. Wehr, G.A. Viteri, B.S. Berlett, R.L. Levine, Small-Molecule Antioxidant Proteome-Shields in Deinococcus radiodurans, PLoS ONE. 5 (2010) e12570. https://doi.org/10.1371/journal.pone.0012570.

[205] E.K. Gaidamakova, A. Sharma, V.Y. Matrosova, O. Grichenko, R.P. Volpe, R. Tkavc, I.H. Conze, P. Klimenkova, I. Balygina, W.H. Horne, C. Gostinčar, X. Chen, K.S. Makarova, I. Shuryak, C. Srinivasan, B. Jackson-Thompson, B.M. Hoffman, M.J. Daly, Small-Molecule Mn Antioxidants in Caenorhabditis elegans and Deinococcus radiodurans Supplant MnSOD Enzymes during Aging and Irradiation, MBio. 13 (2022) e03394-21. https://doi.org/10.1128/mbio.03394-21.

[206] M.J. Daly, E.K. Gaidamakova, V.Y. Matrosova, A. Vasilenko, M. Zhai, A. Venkateswaran, M. Hess, M.V. Omelchenko, H.M. Kostandarithes, K.S. Makarova, L.P. Wackett, J.K. Fredrickson, D. Ghosal, Accumulation of Mn(II) in *Deinococcus radiodurans* Facilitates Gamma-Radiation Resistance, Science. 306 (2004) 1025–1028. https://doi.org/10.1126/science.1103185.

[207] Y.-T. Lin, H. Hoang, S.I. Hsieh, N. Rangel, A.L. Foster, J.N. Sampayo, G.J. Lithgow, C. Srinivasan, Manganous ion supplementation accelerates wild type development, enhances stress resistance, and rescues the life span of a short–lived Caenorhabditis elegans mutant, Free Radical Biology and Medicine. 40 (2006) 1185–1193. https://doi.org/10.1016/j.freeradbiomed.2005.11.007.

[208] R.J. Sanchez, C. Srinivasan, W.H. Munroe, M.A. Wallace, J. Martins, T.Y. Kao, K. Le, E.B. Gralla, J.S. Valentine, Exogenous manganous ion at millimolar levels rescues all known dioxygen-sensitive phenotypes of yeast lacking CuZnSOD, J Biol Inorg Chem. 10 (2005) 913–923. https://doi.org/10.1007/s00775-005-0044-y.

[209] F.S. Archibald, I. Fridovich, The scavenging of superoxide radical by manganous complexes: In vitro, Archives of Biochemistry and Biophysics. 214 (1982) 452–463. https://doi.org/10.1016/0003-9861(82)90049-2.

[210] K. Barnese, E.B. Gralla, D.E. Cabelli, J. Selverstone Valentine, Manganous Phosphate Acts as a Superoxide Dismutase, J. Am. Chem. Soc. 130 (2008) 4604–4606. https://doi.org/10.1021/ja710162n.

[211] J.D. Aguirre, V.C. Culotta, Battles with Iron: Manganese in Oxidative Stress Protection, Journal of Biological Chemistry. 287 (2012) 13541–13548. https://doi.org/10.1074/jbc.R111.312181.

[212] J.-M. Latour, Manganese, the stress reliever, Metallomics. 7 (2015) 25–28. https://doi.org/10.1039/C4MT00180J.

[213] M.J. Daly, A new perspective on radiation resistance based on Deinococcus radiodurans, Nat Rev Microbiol. 7 (2009) 237–245. https://doi.org/10.1038/nrmicro2073.

[214] M. Lipcsey, K. Hanslin, J. Stålberg, D. Smekal, A. Larsson, The time course of calprotectin liberation from human neutrophil granulocytes after *Escherichia coli* and endotoxin challenge, Innate Immun. 25 (2019) 369–373. https://doi.org/10.1177/1753425919848476.

[215] J.P. Lisher, D.P. Giedroc, Manganese acquisition and homeostasis at the host-pathogen interface, Front. Cell. Infect. Microbiol. 3 (2013). https://doi.org/10.3389/fcimb.2013.00091.

[216] B. Gallez, G. Bacic, H.M. Swartz, Evidence for the dissociation of the hepatobiliary MRI contrast agent Mn-DPDP, Magn. Reson. Med. 35 (1996) 14–19. https://doi.org/10.1002/mrm.1910350104.

[217] F.K. Kálmán, G. Tircsó, Kinetic Inertness of the Mn^{2+} Complexes Formed with AAZTA and Some Open-Chain EDTA Derivatives, Inorg. Chem. 51 (2012) 10065–10067. https://doi.org/10.1021/ic300832e.

[218] E.M. Gale, I.P. Atanasova, F. Blasi, I. Ay, P. Caravan, A Manganese Alternative to Gadolinium for MRI Contrast, J. Am. Chem. Soc. 137 (2015) 15548–15557. https://doi.org/10.1021/jacs.5b10748.

[219] S. Laine, C.S. Bonnet, F.K. Kálmán, Z. Garda, A. Pallier, F. Caillé, F. Suzenet, G. Tircsó, É. Tóth, Mn^{2+} complexes of open-chain ligands with a pyridine backbone: less donor atoms lead to higher kinetic inertness, New J. Chem. 42 (2018) 8012–8020. https://doi.org/10.1039/C8NJ00648B.

[220] B. Drahoš, V. Kubíček, C.S. Bonnet, P. Hermann, I. Lukeš, É. Tóth, Dissociation kinetics of Mn2+ complexes of NOTA and DOTA, Dalton Trans. 40 (2011) 1945. https://doi.org/10.1039/c0dt01328e.

[221] R. Botár, E. Molnár, G. Trencsényi, J. Kiss, F.K. Kálmán, G. Tircsó, Stable and Inert Mn(II)-Based and pH-Responsive Contrast Agents, J. Am. Chem. Soc. 142 (2020) 1662–1666. https://doi.org/10.1021/jacs.9b09407.

[222] D. Ndiaye, M. Sy, A. Pallier, S. Même, I. Silva, S. Lacerda, A.M. Nonat, L.J. Charbonnière, É. Tóth, Unprecedented Kinetic Inertness for a Mn^{2+} -Bispidine Chelate: A Novel Structural Entry for Mn^{2+} -Based Imaging Agents, Angew. Chem. Int. Ed. 59 (2020) 11958–11963. https://doi.org/10.1002/anie.202003685.

[223] E. Mathieu, A.-S. Bernard, E. Quévrain, M. Zoumpoulaki, S. Iriart, C. Lung-Soong, B. Lai, K. Medjoubi, L. Henry, S. Nagarajan, F. Poyer, A. Scheitler, I. Ivanović-Burmazović, S. Marco, A. Somogyi, P. Seksik, N. Delsuc, C. Policar, Intracellular location matters: rationalization of the anti-inflammatory activity of a manganese(II) superoxide dismutase mimic complex, Chem. Commun. 56 (2020) 7885–7888. https://doi.org/10.1039/D0CC03398G.

[224] K.-Y. Cheng, F. Guo, J.-Q. Lu, Y.-Z. Cao, T.-C. Wang, Q. Yang, Q. Xia, MnTM-4-PyP Modulates Endogenous Antioxidant Responses and Protects Primary Cortical Neurons against Oxidative Stress, CNS Neurosci Ther. 21 (2015) 435–445. https://doi.org/10.1111/cns.12373.

[225] T. de P. Ribeiro, F.L. Fonseca, M.D.C. de Carvalho, R.M. da C. Godinho, F.P. de Almeida, T.D. Saint'Pierre, N.A. Rey, C. Fernandes, A. Horn, M.D. Pereira, Metal-based superoxide dismutase and catalase mimics reduce oxidative stress biomarkers and extend life span of Saccharomyces cerevisiae, Biochemical Journal. 474 (2017) 301–315. https://doi.org/10.1042/BCJ20160480.

[226] P. Failli, D. Bani, A. Bencini, M. Cantore, L. Di Cesare Mannelli, C. Ghelardini, C. Giorgi, M. Innocenti, F. Rugi, A. Spepi, R. Udisti, B. Valtancoli, A Novel Manganese Complex Effective as Superoxide Anion Scavenger and Therapeutic Agent against Cell and Tissue Oxidative Injury, J. Med. Chem. 52 (2009) 7273–7283. https://doi.org/10.1021/jm901298x.

[227] D.E. Ash, V.L. Schramm, Determination of free and bound manganese(II) in hepatocytes from fed and fasted rats., Journal of Biological Chemistry. 257 (1982) 9261–9264. https://doi.org/10.1016/S0021-9258(18)34061-4.

[228] C.M. Weekley, I. Kenkel, R. Lippert, S. Wei, D. Lieb, T. Cranwell, J.L. Wedding, A.S. Zillmann, R. Rohr, M.R. Filipovic, I. Ivanović-Burmazović, H.H. Harris, Cellular Fates of Manganese(II) Pentaazamacrocyclic Superoxide Dismutase (SOD) Mimetics: Fluorescently Labeled MnSOD Mimetics, X-ray Absorption Spectroscopy, and X-ray Fluorescence

Microscopy Studies, Inorg. Chem. 56 (2017) 6076–6093. https://doi.org/10.1021/acs.inorgchem.6b03073.

[229] A. Tovmasyan, J.C. Bueno-Janice, M.C. Jaramillo, R.S. Sampaio, J.S. Reboucas, N. Kyui, L. Benov, B. Deng, T.-T. Huang, M.E. Tome, I. Spasojevic, I. Batinic-Haberle, Radiation-Mediated Tumor Growth Inhibition Is Significantly Enhanced with Redox-Active Compounds That Cycle with Ascorbate, Antioxidants & Redox Signaling. 29 (2018) 1196–1214. https://doi.org/10.1089/ars.2017.7218.

[230] I. Kos, L. Benov, I. Spasojević, J.S. Rebouças, I. Batinić-Haberle, High Lipophilicity of meta Mn(III) *N* -Alkylpyridylporphyrin-Based Superoxide Dismutase Mimics Compensates for Their Lower Antioxidant Potency and Makes Them as Effective as Ortho Analogues in Protecting Superoxide Dismutase-Deficient *Escherichia coli*, J. Med. Chem. 52 (2009) 7868–7872. https://doi.org/10.1021/jm900576g.

[231] N. Blom, J. Odo, K. Nakamoto, D.P. Strommen, Resonance Raman studies of metal tetrakis(4-N-methylpyridyl)porphine: band assignments, structure-sensitive bands, and species equilibria, J. Phys. Chem. 90 (1986) 2847–2852. https://doi.org/10.1021/j100404a015.

[232] S. Carballal, V. Valez, D. Alvarez-Paggi, A. Tovmasyan, I. Batinic-Haberle, G. Ferrer-Sueta, D.H. Murgida, R. Radi, Manganese porphyrin redox state in endothelial cells: Resonance Raman studies and implications for antioxidant protection towards peroxynitrite, Free Radical Biology and Medicine. 126 (2018) 379–392. https://doi.org/10.1016/j.freeradbiomed.2018.08.023.

[233] Y. Xu, Y. Zhou, R. Yin, C. Wang, H. Chu, J. Wang, A novel 76-mer peptide mimic with the synergism of superoxide dismutase and glutathione peroxidase, In Vitro Cell.Dev.Biol.-Animal. 54 (2018) 335–345. https://doi.org/10.1007/s11626-018-0240-z.

[234] Y.-C. Fang, Y.-P. Chen, C.-T. Chen, T.-S. Lin, C.-Y. Mou, Protection of HeLa cells against ROS stress by CuZnSOD mimic system, J. Mater. Chem. B. 1 (2013) 6042. https://doi.org/10.1039/c3tb21052a.

[235] S.S. Giles, I. Batinić-Haberle, J.R. Perfect, G.M. Cox, Cryptococcus neoformans Mitochondrial Superoxide Dismutase: an Essential Link between Antioxidant Function and High-Temperature Growth, Eukaryotic Cell. 4 (2005) 46–54. https://doi.org/10.1128/EC.4.1.46-54.2005.

[236] J.B. Aitken, E.L. Shearer, N.M. Giles, B. Lai, S. Vogt, J.S. Reboucas, I. Batinic-Haberle, P.A. Lay, G.I. Giles, Intracellular Targeting and Pharmacological Activity of the Superoxide Dismutase Mimics MnTE-2-PyP $^{5+}$ and MnTnHex-2-PyP $^{5+}$ Regulated by Their Porphyrin Ring Substituents, Inorg. Chem. 52 (2013) 4121–4123. https://doi.org/10.1021/ic300700g.

[237] E. Mathieu, A.-S. Bernard, N. Delsuc, E. Quévrain, G. Gazzah, B. Lai, F. Chain, P. Langella, M. Bachelet, J. Masliah, P. Seksik, C. Policar, A Cell-Penetrant Manganese Superoxide Dismutase (MnSOD) Mimic Is Able To Complement MnSOD and Exerts an Antiinflammatory Effect on Cellular and Animal Models of Inflammatory Bowel Diseases, Inorg. Chem. 56 (2017) 2545–2555. https://doi.org/10.1021/acs.inorgchem.6b02695.

[238] E. Mathieu, A.-S. Bernard, E. Quévrain, M. Zoumpoulaki, S. Iriart, C. Lung-Soong, B. Lai, K. Medjoubi, L. Henry, S. Nagarajan, F. Poyer, A. Scheitler, I. Ivanović-Burmazović, S. Marco, A. Somogyi, P. Seksik, N. Delsuc, C. Policar, Intracellular location matters: rationalization of the anti-inflammatory activity of a manganese(ii) superoxide dismutase mimic complex, Chem. Commun. 56 (2020) 7885–7888. https://doi.org/10.1039/D0CC03398G.

[239] D.J. Hare, E.J. New, M.D. de Jonge, G. McColl, Imaging metals in biology: balancing sensitivity, selectivity and spatial resolution, Chem. Soc. Rev. 44 (2015) 5941–5958. https://doi.org/10.1039/C5CS00055F.

[240] I. Rodushkin, E. Engstr□m, A. Stenberg, D.C. Baxter, Determination of low-abundance elements at ultra-trace levels in urine and serum by inductively coupled plasma?sector field mass spectrometry, Anal Bioanal Chem. 380 (2004) 247–257. https://doi.org/10.1007/s00216-004-2742-7.

[241] G. Schanne, L. Henry, H.C. Ong, A. Somogyi, K. Medjoubi, N. Delsuc, C. Policar, F. García, H.C. Bertrand, Rhenium carbonyl complexes bearing methylated triphenylphosphonium cations as antibody-free mitochondria trackers for X-ray fluorescence imaging, Inorg. Chem. Front. 8 (2021) 3905–3915. https://doi.org/10.1039/D1QI00542A.

[242] C. Bissardon, S. Reymond, M. Salomé, L. André, S. Bayat, P. Cloetens, S. Bohic, Cell Culture on Silicon Nitride Membranes and Cryopreparation for Synchrotron X-ray Fluorescence Nano-analysis, JoVE. (2019) 60461. https://doi.org/10.3791/60461.

[243] A. Awad, C.M. Madla, L.E. McCoubrey, F. Ferraro, F.K.H. Gavins, A. Buanz, S. Gaisford, M. Orlu, F. Siepmann, J. Siepmann, A.W. Basit, Clinical translation of advanced colonic drug delivery technologies, Advanced Drug Delivery Reviews. 181 (2022) 114076. https://doi.org/10.1016/j.addr.2021.114076.

[244] W. Fan, S. Zhang, Y. Wu, T. Lu, J. Liu, X. Cao, S. Liu, L. Yan, X. Shi, G. Liu, C. Huang, S. Song, Genistein-Derived ROS-Responsive Nanoparticles Relieve Colitis by Regulating Mucosal Homeostasis, ACS Appl. Mater. Interfaces. 13 (2021) 40249–40266. https://doi.org/10.1021/acsami.1c09215.

[245] Y. Turanlı, F. Acartürk, Preparation and characterization of colon-targeted pH/Time-dependent nanoparticles using anionic and cationic polymethacrylate polymers, Eur J Pharm Sci. 171 (2022) 106122. https://doi.org/10.1016/j.ejps.2022.106122.

[246] M. Zeeshan, A. Atiq, Q.U. Ain, J. Ali, S. Khan, H. Ali, Evaluating the mucoprotective effects of glycyrrhizic acid-loaded polymeric nanoparticles in a murine model of 5-fluorouracil-induced intestinal mucositis via suppression of inflammatory mediators and oxidative stress, Inflammopharmacology. 29 (2021) 1539–1553. https://doi.org/10.1007/s10787-021-00866-z.

[247] J. Xu, Y. Lin, P.N. Zawaneh, I. Nestorov, C.-Y. Leung, P. Boulas, Prediction of in vivo performance of oral extended

release formulations prior to clinical evaluation: A case study for enteric coated polymeric beads formulation, Eur J Pharm Biopharm. 158 (2021) 222–232. https://doi.org/10.1016/j.ejpb.2020.11.023.

[248] Y. Zhu, Z. Gu, Y. Liao, S. Li, Y. Xue, M.A. Firempong, Y. Xu, J. Yu, H.D. Smyth, X. Xu, Improved intestinal absorption and oral bioavailability of astaxanthin using poly (ethylene glycol)-graft-chitosan nanoparticles: preparation, in vitro evaluation, and pharmacokinetics in rats, J Sci Food Agric. 102 (2022) 1002–1011. https://doi.org/10.1002/jsfa.11435.

[249] B. Zhao, J. Du, Y. Zhang, Z. Gu, Z. Li, L. Cheng, C. Li, Y. Hong, Polysaccharide-coated porous starch-based oral carrier for paclitaxel: Adsorption and sustained release in colon, Carbohydr Polym. 291 (2022) 119571. https://doi.org/10.1016/j.carbpol.2022.119571.

[250] R. Deshmukh, Bridging the Gap of Drug Delivery in Colon Cancer: The Role of Chitosan and Pectin Based Nanocarriers System, Curr Drug Deliv. 17 (2020) 911–924. https://doi.org/10.2174/1567201817666200717090623.

[251] A. Almeida, V. Linares, G. Mora-Castaño, M. Casas, I. Caraballo, B. Sarmento, 3D printed systems for colon-specific delivery of camptothecin-loaded chitosan micelles, Eur J Pharm Biopharm. 167 (2021) 48–56. https://doi.org/10.1016/j.ejpb.2021.07.005.

[252] C.Y. Karakas, H.R. Ordu, F. Bozkurt, A. Karadag, Electrosprayed chitosan-coated alginate-pectin beads as potential system for colon-targeted delivery of ellagic acid, J Sci Food Agric. 102 (2022) 965–975. https://doi.org/10.1002/jsfa.11430.

[253] Y. Zhang, M. Xiong, X. Ni, J. Wang, H. Rong, Y. Su, S. Yu, I.S. Mohammad, S.S.Y. Leung, H. Hu, Virus-Mimicking Mesoporous Silica Nanoparticles with an Electrically Neutral and Hydrophilic Surface to Improve the Oral Absorption of Insulin by Breaking Through Dual Barriers of the Mucus Layer and the Intestinal Epithelium, ACS Appl Mater Interfaces. 13 (2021) 18077–18088. https://doi.org/10.1021/acsami.1c00580.

[254] S.-Q. Chen, Y.-Q. Song, C. Wang, S. Tao, F.-Y. Yu, H.-Y. Lou, F.-Q. Hu, H. Yuan, Chitosan-modified lipid nanodrug delivery system for the targeted and responsive treatment of ulcerative colitis, Carbohydr Polym. 230 (2020) 115613. https://doi.org/10.1016/j.carbpol.2019.115613.

[255] C. Dumont, A. Beloqui, C. Miolane, S. Bourgeois, V. Préat, H. Fessi, V. Jannin, Solid lipid nanocarriers diffuse effectively through mucus and enter intestinal cells - but where is my peptide?, Int J Pharm. 586 (2020) 119581. https://doi.org/10.1016/j.ijpharm.2020.119581.

[256] S. Haddadzadegan, F. Dorkoosh, A. Bernkop-Schnürch, Oral delivery of therapeutic peptides and proteins: Technology landscape of lipid-based nanocarriers, Adv Drug Deliv Rev. 182 (2022) 114097. https://doi.org/10.1016/j.addr.2021.114097.

[257] A. Vincent, Étude de complexes mimes de superoxyde dismutases : de la conception de nouveaux composés par chimie combinatoire jusqu'à l'exploration des voies d'administration sur modèle murin, Thèse de doctorat en Chimie bio-inorganique, Paris Sciences et Lettres, 2019.

[258] B. Pulli, M. Ali, R. Forghani, S. Schob, K.L.C. Hsieh, G. Wojtkiewicz, J.J. Linnoila, J.W. Chen, Measuring Myeloperoxidase Activity in Biological Samples, PLoS ONE. 8 (2013) e67976. https://doi.org/10.1371/journal.pone.0067976.

[259] G. Pápai, E. Torres-Maravilla, F. Chain, É. Varga-Visi, O. Antal, Z. Naár, L.G. Bermúdez-Humarán, P. Langella, R. Martín, The Administration Matrix Modifies the Beneficial Properties of a Probiotic Mix of Bifidobacterium animalis subsp. lactis BB-12 and Lactobacillus acidophilus LA-5, Probiotics & Antimicro. Prot. 13 (2021) 484–494. https://doi.org/10.1007/s12602-020-09702-2.

[260] J.M. Cho, H.R. Yang, Hair Mineral and Trace Element Contents as Reliable Markers of Nutritional Status Compared to Serum Levels of These Elements in Children Newly Diagnosed with Inflammatory Bowel Disease, Biol Trace Elem Res. 185 (2018) 20–29. https://doi.org/10.1007/s12011-017-1225-6.

[261] V.C. Culotta, M.J. Daly, Manganese Complexes: Diverse Metabolic Routes to Oxidative Stress Resistance in Prokaryotes and Yeast, Antioxidants & Redox Signaling. 19 (2013) 933–944. https://doi.org/10.1089/ars.2012.5093.

[262] E. Choi, L. Aring, N.K. Das, S. Solanki, N. Inohara, S. Iwase, L.C. Samuelson, Y.M. Shah, Y.A. Seo, Impact of dietary manganese on experimental colitis in mice, FASEB j. 34 (2020) 2929–2943. https://doi.org/10.1096/fj.201902396R.

[263] P. Chen, G. Zhou, J. Lin, L. Li, Z. Zeng, M. Chen, S. Zhang, Serum Biomarkers for Inflammatory Bowel Disease, Front. Med. 7 (2020) 123. https://doi.org/10.3389/fmed.2020.00123.

[264] C. Hill, F. Guarner, G. Reid, G.R. Gibson, D.J. Merenstein, B. Pot, L. Morelli, R.B. Canani, H.J. Flint, S. Salminen, P.C. Calder, M.E. Sanders, The International Scientific Association for Probiotics and Prebiotics consensus statement on the scope and appropriate use of the term probiotic, Nat Rev Gastroenterol Hepatol. 11 (2014) 506–514. https://doi.org/10.1038/nrgastro.2014.66.

[265] E. Metchnikoff, The prolongation of life: Optimistic studies., London, n.d.

[266] R.D.D.O. Carvalho, F.L.R. do Carmo, A. de Oliveira Junior, P. Langella, J.-M. Chatel, L.G. Bermúdez-Humarán, V. Azevedo, M.S. de Azevedo, Use of Wild Type or Recombinant Lactic Acid Bacteria as an Alternative Treatment for Gastrointestinal Inflammatory Diseases: A Focus on Inflammatory Bowel Diseases and Mucositis, Front. Microbiol. 8 (2017) 800. https://doi.org/10.3389/fmicb.2017.00800.

[267] U. Sonnenborn, J. Schulze, The non-pathogenic *Escherichia coli* strain Nissle 1917 – features of a versatile probiotic, Microbial Ecology in Health and Disease. 21 (2009) 122–158. https://doi.org/10.3109/08910600903444267.

[268] E.L.S. Souza, C.L.V. Campos, D.C. Reis, G.D. Cassali, S.V. Generoso, V.N. Cardoso, V. Azevedo, J.D. Medeiros, G.R. Fernandes, J.R. Nicoli, F.S. Martins, Beneficial effects resulting from oral administration of Escherichia coli Nissle 1917 on a chronic colitis model, Benef Microbes. 11 (2020) 779–790. https://doi.org/10.3920/BM2020.0045.

[269] F.J. Carr, D. Chill, N. Maida, The Lactic Acid Bacteria: A Literature Survey, Critical Reviews in Microbiology. 28 (2002) 281–370. https://doi.org/10.1080/1040-840291046759.

[270] E.J. Quinto, P. Jiménez, I. Caro, J. Tejero, J. Mateo, T. Girbés, Probiotic Lactic Acid Bacteria: A Review, (n.d.) 12.

[271] A.C. Ouwehand, S. Salminen, E. Isolauri, Probiotics: an overview of beneficial effects, Antonie van Leeuwenhoek. 82 (2002) 279–289. https://doi.org/10.1023/A:1020620607611.

[272] A. Ljungh, T. Wadström, Lactic acid bacteria as probiotics, Curr Issues Intest Microbiol. 7 (2006) 73–89.

[273] A. Lorentz, L. Müller, Probiotics in the Treatment of Inflammatory Bowel Disease in Adulthood: A Systematic Review, J Gastrointestin Liver Dis. 31 (2022) 74–84. https://doi.org/10.15403/jgld-3936.

[274] F. Guarner, A.G. Khan, J. Garisch, R. Eliakim, A. Gangl, A. Thomson, J. Krabshuis, T. Lemair, P. Kaufmann, J.A. de Paula, R. Fedorak, F. Shanahan, M.E. Sanders, H. Szajewska, B.S. Ramakrishna, T. Karakan, N. Kim, Review TeamInvited outside experts, World Gastroenterology Organisation Global Guidelines: Probiotics and Prebiotics October 2011, Journal of Clinical Gastroenterology. 46 (2012). https://journals.lww.com/jcge/Fulltext/2012/07000/World_Gastroenterology_Organisation_Global.9.aspx.

[275] S. Oliva, G. Di Nardo, F. Ferrari, S. Mallardo, P. Rossi, G. Patrizi, S. Cucchiara, L. Stronati, Randomised clinical trial: the effectiveness of Lactobacillus reuteri ATCC 55730 rectal enema in children with active distal ulcerative colitis: Randomised clinical trial: rectal Lactobacillus reuteri in ulcerative colitis, Alimentary Pharmacology & Therapeutics. 35 (2012) 327–334. https://doi.org/10.1111/j.1365-2036.2011.04939.x.

[276] B. Foligne, Correlation between in vitro and in vivo immunomodulatory properties of lactic acid bacteria, WJG. 13 (2007) 236. https://doi.org/10.3748/wjg.v13.i2.236.

[277] T. Rochat, L. Bermúdez-Humarán, J.-J. Gratadoux, C. Fourage, C. Hoebler, G. Corthier, P. Langella, Anti-inflammatory effects of Lactobacillus casei BL23 producing or not a manganese-dependant catalase on DSS-induced colitis in mice, Microb Cell Fact. 6 (2007) 22. https://doi.org/10.1186/1475-2859-6-22.

[278] W. Ruan, M. Engevik, A. Chang-Graham, J. Hyser, J. Versalovic, 7 LACTOBACILLUS REUTERI SUPPRESSES PRO-INFLAMMATORY DRIVEN REACTIVE OXYGEN SPECIES IN VITRO IN HUMAN INTESTINAL EPITHELIAL CELLS AND IN VIVO IN A TNBS COLITIS MOUSE MODEL, Gastroenterology. 158 (2020) S67. https://doi.org/10.1053/j.gastro.2019.11.171.

[279] Y. Pan, Y. Ning, J. Hu, Z. Wang, X. Chen, X. Zhao, The Preventive Effect of Lactobacillus plantarum ZS62 on DSS-Induced IBD by Regulating Oxidative Stress and the Immune Response, Oxid Med Cell Longev. 2021 (2021) 9416794. https://doi.org/10.1155/2021/9416794.

[280] X. Dou, L. Qiao, J. Chang, S. Yan, X. Song, Y. Chen, Q. Xu, C. Xu, Lactobacillus casei ATCC 393 and it's metabolites alleviate dextran sulphate sodium-induced ulcerative colitis in mice through the NLRP3-(Caspase-1)/IL-1β pathway, Food Funct. 12 (2021) 12022–12035. https://doi.org/10.1039/d1fo02405a.

[281] T. Hu, H. Wang, C. Xiang, J. Mu, X. Zhao, Preventive Effect of Lactobacillus acidophilus XY27 on DSS-Induced Ulcerative Colitis in Mice, Drug Des Devel Ther. 14 (2020) 5645–5657. https://doi.org/10.2147/DDDT.S284422.

[282] H. Kaur, T. Gupta, S. Kapila, R. Kapila, Protective effects of potential probiotic Lactobacillus rhamnosus (MTCC-5897) fermented whey on reinforcement of intestinal epithelial barrier function in a colitis-induced murine model, Food Funct. 12 (2021) 6102–6116. https://doi.org/10.1039/d0fo02641g.

[283] F.-S. Cheng, D. Pan, B. Chang, M. Jiang, L.-X. Sang, Probiotic mixture VSL#3: An overview of basic and clinical studies in chronic diseases, WJCC. 8 (2020) 1361–1384. https://doi.org/10.12998/wjcc.v8.i8.1361.

[284] C. Santos Rocha, A.C. Gomes-Santos, T. Garcias Moreira, M. de Azevedo, T. Diniz Luerce, M. Mariadassou, A.P. Longaray Delamare, P. Langella, E. Maguin, V. Azevedo, A.M. Caetano de Faria, A. Miyoshi, M. van de Guchte, Local and Systemic Immune Mechanisms Underlying the Anti-Colitis Effects of the Dairy Bacterium Lactobacillus delbrueckii, PLoS ONE. 9 (2014) e85923. https://doi.org/10.1371/journal.pone.0085923.

[285] T.D. Luerce, A.C. Gomes-Santos, C.S. Rocha, T.G. Moreira, D.N. Cruz, L. Lemos, A.L. Sousa, V.B. Pereira, M. de Azevedo, K. Moraes, D.C. Cara, J.G. LeBlanc, V. Azevedo, A.M.C. Faria, A. Miyoshi, Anti-inflammatory effects of Lactococcus lactis NCDO 2118 during the remission period of chemically induced colitis, (2014) 11.

[286] H. Tamaki, H. Nakase, S. Inoue, C. Kawanami, T. Itani, M. Ohana, T. Kusaka, S. Uose, H. Hisatsune, M. Tojo, T. Noda, S. Arasawa, M. Izuta, A. Kubo, C. Ogawa, T. Matsunaka, M. Shibatouge, Efficacy of probiotic treatment with *Bifidobacterium longum 536* for induction of remission in active ulcerative colitis: A randomized, double-blinded, placebo-controlled multicenter trial, Digestive Endoscopy. 28 (2016) 67–74. https://doi.org/10.1111/den.12553.

[287] S. Yao, Z. Zhao, W. Wang, X. Liu, Bifidobacterium Longum: Protection against Inflammatory Bowel Disease, J Immunol Res. 2021 (2021) 8030297. https://doi.org/10.1155/2021/8030297.

[288] J. Mishra, M. Stubbs, L. Kuang, N. Vara, P. Kumar, N. Kumar, Inflammatory Bowel Disease Therapeutics: A Focus on Probiotic Engineering, Mediators of Inflammation. 2022 (2022) 1–15. https://doi.org/10.1155/2022/9621668.

[289] S. Nobaek, M.-L. Johansson, G. Molin, S. Ahrné, B. Jeppsson, Alteration of Intestinal Microflora Is Associated With Reduction in Abdominal Bloating and Pain in Patients With Irritable Bowel Syndrome, American Journal of Gastroenterology. 95 (2000) 1231–1238. https://doi.org/10.1111/j.1572-0241.2000.02015.x.

[290] M. Schlee, J. Harder, B. Köten, E.F. Stange, J. Wehkamp, K. Fellermann, Probiotic lactobacilli and VSL#3 induce enterocyte β-defensin 2, Clinical and Experimental Immunology. 151 (2008) 528–535. https://doi.org/10.1111/j.1365-2249.2007.03587.x.

[291] A. Menendez, B.P. Willing, M. Montero, M. Wlodarska, C.C. So, G. Bhinder, B.A. Vallance, B.B. Finlay, Bacterial Stimulation of the TLR-MyD88 Pathway Modulates the Homeostatic Expression of Ileal Paneth Cell α-Defensins, J Innate Immun. 5 (2013) 39–49. https://doi.org/10.1159/000341630.

[292] H.-L. Yang, Y.-Z. Sun, X. Hu, J. Ye, K.-L. Lu, L.-H. Hu, J.-J. Zhang, Bacillus pumilus SE5 originated PG and LTA tuned the intestinal TLRs/MyD88 signaling and microbiota in grouper (Epinephelus coioides), Fish & Shellfish Immunology. 88 (2019) 266–271. https://doi.org/10.1016/j.fsi.2019.03.005.

[293] M.C. Collado, J. Meriluoto, S. Salminen, Role of commercial probiotic strains against human pathogen adhesion to intestinal mucus, Lett Appl Microbiol. 45 (2007) 454–460. https://doi.org/10.1111/j.1472-765X.2007.02212.x.

[294] M. Bermudez-Brito, J. Plaza-Díaz, S. Muñoz-Quezada, C. Gómez-Llorente, A. Gil, Probiotic Mechanisms of Action, Ann Nutr Metab. 61 (2012) 160–174. https://doi.org/10.1159/000342079.

[295] N. Zheng, Y. Gao, W. Zhu, D. Meng, W.A. Walker, Short chain fatty acids produced by colonizing intestinal commensal bacterial interaction with expressed breast milk are anti-inflammatory in human immature enterocytes, PLoS ONE. 15 (2020) e0229283. https://doi.org/10.1371/journal.pone.0229283.

[296] N. Kulkarni, B.S. Reddy, Inhibitory Effect of Bifidobacterium Iongum Cultures on the Azoxymethane-Induced Aberrant Crypt Foci Formation and Fecal Bacterial -Glucuronidase, Experimental Biology and Medicine. 207 (1994) 278–283. https://doi.org/10.3181/00379727-207-43817.

[297] N. Pavlović, K. Stankov, M. Mikov, Probiotics—Interactions with Bile Acids and Impact on Cholesterol Metabolism, Appl Biochem Biotechnol. 168 (2012) 1880–1895. https://doi.org/10.1007/s12010-012-9904-4.

[298] P. Gionchetti, F. Rizzello, U. Helwig, A. Venturi, K.M. Lammers, P. Brigidi, B. Vitali, G. Poggioli, M. Miglioli, M. Campieri, Prophylaxis of pouchitis onset with probiotic therapy: a double-blind, placebo-controlled trial, Gastroenterology. 124 (2003) 1202–1209. https://doi.org/10.1016/S0016-5085(03)00171-9.

[299] J.B. Ewaschuk, H. Diaz, L. Meddings, B. Diederichs, A. Dmytrash, J. Backer, M. Looijer-van Langen, K.L. Madsen, Secreted bioactive factors from *Bifidobacterium infantis* enhance epithelial cell barrier function, American Journal of Physiology-Gastrointestinal and Liver Physiology. 295 (2008) G1025–G1034. https://doi.org/10.1152/ajpgi.90227.2008.

[300] J. Karczewski, F.J. Troost, I. Konings, J. Dekker, M. Kleerebezem, R.-J.M. Brummer, J.M. Wells, Regulation of human epithelial tight junction proteins by Lactobacillus plantarum in vivo and protective effects on the epithelial barrier, American Journal of Physiology-Gastrointestinal and Liver Physiology. 298 (2010) G851–G859. https://doi.org/10.1152/ajpgi.00327.2009.

[301] M. A., D. Teitelbaum, D. R., Y. F., H. C., C. A., Probiotics up-regulate MUC-2 mucin gene expression in a Caco-2 cell-culture model, Pediatric Surgery International. 18 (2002) 586–590. https://doi.org/10.1007/s00383-002-0855-7.

[302] E. Gaudier, C. Michel, J.-P. Segain, C. Cherbut, C. Hoebler, The VSL# 3 Probiotic Mixture Modifies Microflora but Does Not Heal Chronic Dextran-Sodium Sulfate–Induced Colitis or Reinforce the Mucus Barrier in Mice, The Journal of Nutrition. 135 (2005) 2753–2761. https://doi.org/10.1093/jn/135.12.2753.

[303] D.R. Mack, Extracellular MUC3 mucin secretion follows adherence of Lactobacillus strains to intestinal epithelial cells in vitro, Gut. 52 (2003) 827–833. https://doi.org/10.1136/gut.52.6.827.

[304] S.C. Ng, A.L. Hart, M.A. Kamm, A.J. Stagg, S.C. Knight, Mechanisms of action of probiotics: Recent advances:, Inflammatory Bowel Diseases. 15 (2009) 300–310. https://doi.org/10.1002/ibd.20602.

[305] D. Groeger, L. O'Mahony, E.F. Murphy, J.F. Bourke, T.G. Dinan, B. Kiely, F. Shanahan, E.M.M. Quigley, Bifidobacterium infantis 35624 modulates host inflammatory processes beyond the gut, Gut Microbes. 4 (2013) 325–339. https://doi.org/10.4161/gmic.25487.

[306] H. Qiao, L.C. Duffy, E. Griffiths, D. Dryja, A. Leavens, J. Rossman, G. Rich, M. Riepenhoff-Talty, M. Locniskar, Immune Responses in Rhesus Rotavirus-Challenged Balb/c Mice Treated with Bifidobacteria and Prebiotic Supplements, Pediatr Res. 51 (2002) 750–755. https://doi.org/10.1203/00006450-200206000-00015.

[307] K. Shida, J. Kiyoshima-Shibata, R. Kaji, M. Nagaoka, M. Nanno, Peptidoglycan from lactobacilli inhibits interleukin-12 production by macrophages induced by *Lactobacillus casei* through Toll-like receptor 2-dependent and independent mechanisms, Immunology. 128 (2009) e858–e869. https://doi.org/10.1111/j.1365-2567.2009.03095.x.

[308] L.M. Agraib, M.I. Yamani, Y.M. Rayyan, A.T. Abu-Sneineh, T.A. Tamimi, R.F. Tayyem, The probiotic supplementation role in improving the immune system among people with ulcerative colitis: a narrative review, Drug Metabolism and Personalized Therapy. 37 (2022) 7–19. https://doi.org/10.1515/dmpt-2021-0150.

[309] S. Shigemori, T. Shimosato, Applications of Genetically Modified Immunobiotics with High Immunoregulatory Capacity for Treatment of Inflammatory Bowel Diseases, Front. Immunol. 8 (2017). https://doi.org/10.3389/fimmu.2017.00022.

[310] J.G. LeBlanc, C. Aubry, N.G. Cortes-Perez, A. de Moreno de LeBlanc, N. Vergnolle, P. Langella, V. Azevedo, J.-M. Chatel, A. Miyoshi, L.G. Bermúdez-Humarán, Mucosal targeting of therapeutic molecules using genetically modified lactic acid bacteria: an update, FEMS Microbiol Lett. 344 (2013) 1–9. https://doi.org/10.1111/1574-6968.12159.

[311] M. Jinek, K. Chylinski, I. Fonfara, M. Hauer, J.A. Doudna, E. Charpentier, A Programmable Dual-RNA–Guided DNA Endonuclease in Adaptive Bacterial Immunity, Science. 337 (2012) 816–821. https://doi.org/10.1126/science.1225829.

[312] R. Di Blasi, A. Zouein, T. Ellis, F. Ceroni, Genetic Toolkits to Design and Build Mammalian Synthetic Systems, Trends in Biotechnology. 39 (2021) 1004–1018. https://doi.org/10.1016/j.tibtech.2020.12.007.

[313] L.G. Bermúdez-Humarán, C. Aubry, J.-P. Motta, C. Deraison, L. Steidler, N. Vergnolle, J.-M. Chatel, P. Langella,

Engineering lactococci and lactobacilli for human health, Current Opinion in Microbiology. 16 (2013) 278–283. https://doi.org/10.1016/j.mib.2013.06.002.

[314] A.B. Pardee, F. Jacob, J. Monod, [The role of the inducible alleles and the constrtutive alleles in the synthesis of beta-galactosidase in zygotes of Escherichia coli], C R Hebd Seances Acad Sci. 246 (1958) 3125–3128.

[315] A. Miyoshi, E. Jamet, J. Commissaire, P. Renault, P. Langella, V. Azevedo, A xylose-inducible expression system for *Lactococcus lactis*, FEMS Microbiology Letters. 239 (2004) 205–212. https://doi.org/10.1016/j.femsle.2004.08.018.

[316] S. del Carmen, A. de Moreno de LeBlanc, G. Perdigon, V. Bastos Pereira, A. Miyoshi, V. Azevedo, J.G. LeBlanc, Evaluation of the Anti-Inflammatory Effect of Milk Fermented by a Strain of IL-10-Producing Lactococcus lactis Using a Murine Model of Crohn's Disease, J Mol Microbiol Biotechnol. 21 (2011) 138–146. https://doi.org/10.1159/000333830.

[317] Z. Hamady, Novel xylan-controlled delivery of therapeutic proteins to inflamed colon by the human anaerobic commensal bacterium, Annals. 95 (2013) 235–240. https://doi.org/10.1308/003588413X13511609958217.

[318] Z.Z.R. Hamady, N. Scott, M.D. Farrar, J.P.A. Lodge, K.T. Holland, T. Whitehead, S.R. Carding, Xylan-regulated delivery of human keratinocyte growth factor-2 to the inflamed colon by the human anaerobic commensal bacterium Bacteroides ovatus, Gut. 59 (2010) 461–469. https://doi.org/10.1136/gut.2008.176131.

[319] O.P. Kuipers, M.M. Beerthuyzen, R.J. Siezen, W.M. Vos, Characterization of the nisin gene cluster nisABTCIPR of Lactococcus lactis. Requirement of expression of the nisA and nisIgenes for development of immunity, Eur J Biochem. 216 (1993) 281–291. https://doi.org/10.1111/j.1432-1033.1993.tb18143.x.

[320] I. Mierau, M. Kleerebezem, 10 years of the nisin-controlled gene expression system (NICE) in Lactococcus lactis, Appl Microbiol Biotechnol. 68 (2005) 705–717. https://doi.org/10.1007/s00253-005-0107-6.

[321] B. Benbouziane, P. Ribelles, C. Aubry, R. Martin, P. Kharrat, A. Riazi, P. Langella, L.G. Bermúdez-Humarán, Development of a Stress-Inducible Controlled Expression (SICE) system in Lactococcus lactis for the production and delivery of therapeutic molecules at mucosal surfaces, Journal of Biotechnology. 168 (2013) 120–129. https://doi.org/10.1016/j.jbiotec.2013.04.019.

[322] J.E. Mawdsley, Psychological stress in IBD: new insights into pathogenic and therapeutic implications, Gut. 54 (2005) 1481–1491. https://doi.org/10.1136/gut.2005.064261.

[323] R. McKay, M. Ghodasra, J. Schardt, D. Quan, A.E. Pottash, W. Shang, S.M. Jay, G.F. Payne, M.W. Chang, J.C. March, W.E. Bentley, A platform of genetically engineered bacteria as vehicles for localized delivery of therapeutics: Toward applications for Crohn's disease, Bioengineering & Translational Medicine. 3 (2018) 209–221. https://doi.org/10.1002/btm2.10113.

[324] I. Singer, D. Kawka, S. Scott, J. Weidner, R. Mumford, T. Riehl, W. Stenson, Expression of inducible nitric oxide synthase and nitrotyrosine in colonic epithelium in inflammatory bowel disease, Gastroenterology. 111 (1996) 871–885. https://doi.org/10.1016/S0016-5085(96)70055-0.

[325] R.K. Cross, K.T. Wilson, Nitric Oxide in Inflammatory Bowel Disease:, Inflammatory Bowel Diseases. 9 (2003) 179–189. https://doi.org/10.1097/00054725-200305000-00006.

[326] C.I. Reinders, M. Herulf, T. Ljung, J. Hollenberg, E. Weitzberg, J.O. Lundberg, P.M. Hellström, Rectal Mucosal Nitric Oxide in Differentiation of Inflammatory Bowel Disease and Irritable Bowel Syndrome, Clinical Gastroenterology and Hepatology. 3 (2005) 777–783. https://doi.org/10.1016/S1542-3565(05)00182-5.

[327] D.T. Riglar, T.W. Giessen, M. Baym, S.J. Kerns, M.J. Niederhuber, R.T. Bronson, J.W. Kotula, G.K. Gerber, J.C. Way, P.A. Silver, Engineered bacteria can function in the mammalian gut long-term as live diagnostics of inflammation, Nat Biotechnol. 35 (2017) 653–658. https://doi.org/10.1038/nbt.3879.

[328] E. Seo, S. Weibel, J. Wehkamp, T.A. Oelschlaeger, Construction of recombinant E. coli Nissle 1917 (EcN) strains for the expression and secretion of defensins, International Journal of Medical Microbiology. 302 (2012) 276–287. https://doi.org/10.1016/j.ijmm.2012.05.002.

[329] C.C.M. Wong, L. Zhang, Z.J. Li, W.K.K. Wu, S.X. Ren, Y.C. Chen, T.B. Ng, C.H. Cho, Protective effects of cathelicidin-encoding Lactococcus lactis in murine ulcerative colitis: mCRAMP in ulcerative colitis, Journal of Gastroenterology and Hepatology. 27 (2012) 1205–1212. https://doi.org/10.1111/j.1440-1746.2012.07158.x.

[330] R.D. Carvalho, N. Breyner, Z. Menezes-Garcia, N.M. Rodrigues, L. Lemos, T.U. Maioli, D. da Gloria Souza, D. Carmona, A.M.C. de Faria, P. Langella, J.-M. Chatel, L.G. Bermúdez-Humarán, H.C.P. Figueiredo, V. Azevedo, M.S. de Azevedo, Secretion of biologically active pancreatitis-associated protein I (PAP) by genetically modified dairy Lactococcus lactis NZ9000 in the prevention of intestinal mucositis, Microb Cell Fact. 16 (2017) 27. https://doi.org/10.1186/s12934-017-0624-x.

[331] L. Schotte, L. Steidler, J. Vandekerckhove, E. Remaut, Secretion of biologically active murine interleukin-10 by Lactococcus lactis, Enzyme and Microbial Technology. 27 (2000) 761–765. https://doi.org/10.1016/S0141-0229(00)00297-0.

[332] L. Steidler, W. Hans, L. Schotte, S. Neirynck, F. Obermeier, W. Falk, W. Fiers, E. Remaut, Treatment of Murine Colitis by *Lactococcus lactis* Secreting Interleukin-10, Science. 289 (2000) 1352–1355. https://doi.org/10.1126/science.289.5483.1352.

[333] H. Braat, P. Rottiers, D.W. Hommes, N. Huyghebaert, E. Remaut, J. Remon, S.J.H. van Deventer, S. Neirynck, M.P. Peppelenbosch, L. Steidler, A Phase I Trial With Transgenic Bacteria Expressing Interleukin-10 in Crohn's Disease, Clinical Gastroenterology and Hepatology. 4 (2006) 754–759. https://doi.org/10.1016/j.cgh.2006.03.028.

[334] M.L. Hanson, J.A. Hixon, W. Li, B.K. Felber, M.R. Anver, C.A. Stewart, B.M. Janelsins, S.K. Datta, W. Shen, M.H.

McLean, S.K. Durum, Oral Delivery of IL-27 Recombinant Bacteria Attenuates Immune Colitis in Mice, Gastroenterology. 146 (2014) 210-221.e13. https://doi.org/10.1053/j.gastro.2013.09.060.

[335] B. Zhang, Y. Liu, X. Lan, X. Xu, X. Zhang, X. Li, Y. Zhao, G. Li, C. Du, S. Lu, H. Wang, Oral Escherichia coli expressing IL-35 meliorates experimental colitis in mice, J Transl Med. 16 (2018) 71. https://doi.org/10.1186/s12967-018-1441-7.

[336] Z.Z.R. Hamady, N. Scott, M.D. Farrar, M. Wadhwa, P. Dilger, T.R. Whitehead, R. Thorpe, K.T. Holland, P.J.A. Lodge, S.R. Carding, Treatment of colitis with a commensal gut bacterium engineered to secrete human tgf-β1 under the control of dietary xylan:, Inflammatory Bowel Diseases. 17 (2011) 1925–1935. https://doi.org/10.1002/ibd.21565.

[337] L.G. Bermúdez-Humarán, J.-P. Motta, C. Aubry, P. Kharrat, L. Rous-Martin, J.-M. Sallenave, C. Deraison, N. Vergnolle, P. Langella, Serine protease inhibitors protect better than IL-10 and TGF-β anti-inflammatory cytokines against mouse colitis when delivered by recombinant lactococci, Microb Cell Fact. 14 (2015) 26. https://doi.org/10.1186/s12934-015-0198-4.

[338] K. Vandenbroucke, W. Hans, J. Van Huysse, S. Neirynck, P. Demetter, E. Remaut, P. Rottiers, L. Steidler, Active delivery of trefoil factors by genetically modified Lactococcus lactis prevents and heals acute colitis in mice, Gastroenterology. 127 (2004) 502–513. https://doi.org/10.1053/j.gastro.2004.05.020.

[339] E. Huynh, J. Li, Generation of Lactococcus lactis capable of coexpressing epidermal growth factor and trefoil factor to enhance in vitro wound healing, Appl Microbiol Biotechnol. 99 (2015) 4667–4677. https://doi.org/10.1007/s00253-015-6542-0.

[340] P. Praveschotinunt, A.M. Duraj-Thatte, I. Gelfat, F. Bahl, D.B. Chou, N.S. Joshi, Engineered E. coli Nissle 1917 for the delivery of matrix-tethered therapeutic domains to the gut, Nat Commun. 10 (2019) 5580. https://doi.org/10.1038/s41467-019-13336-6.

[341] B. Strukelj, M. Perse, M. Ravnikar, M. Lunder, A. Cerar, A. Berlec, Improvement in treatment of experimental colitis in mice by using recombinant Lactococcus lactis with surface-displayed affibody against TNFα (THER4P.889), J. Immunol. 192 (2014) 137.1.

[342] K. Vandenbroucke, H. de Haard, E. Beirnaert, T. Dreier, M. Lauwereys, L. Huyck, J. Van Huysse, P. Demetter, L. Steidler, E. Remaut, C. Cuvelier, P. Rottiers, Orally administered L. lactis secreting an anti-TNF Nanobody demonstrate efficacy in chronic colitis, Mucosal Immunol. 3 (2010) 49–56. https://doi.org/10.1038/mi.2009.116.

[343] F. Namai, S. Shigemori, T. Ogita, T. Sato, T. Shimosato, Microbial therapeutics for acute colitis based on genetically modified Lactococcus lactis hypersecreting IL-1Ra in mice, Exp Mol Med. 52 (2020) 1627–1636. https://doi.org/10.1038/s12276-020-00507-5.

[344] J.-P. Motta, L.G. Bermúdez-Humarán, C. Deraison, L. Martin, C. Rolland, P. Rousset, J. Boue, G. Dietrich, K. Chapman, P. Kharrat, J.-P. Vinel, L. Alric, E. Mas, J.-M. Sallenave, P. Langella, N. Vergnolle, Food-Grade Bacteria Expressing Elafin Protect Against Inflammation and Restore Colon Homeostasis, Sci. Transl. Med. 4 (2012). https://doi.org/10.1126/scitranslmed.3004212.

[345] R. Carvalho, Oral administration of Lactococcus lactis expressing recombinant 15-lipoxygenase-1 (15 LOX-1) modulates chemically induced colitis in mice, MRAJ. 4 (2016). https://doi.org/10.18103/mra.v4i7.612.

[346] E. Quévrain, M.A. Maubert, C. Michon, F. Chain, R. Marquant, J. Tailhades, S. Miquel, L. Carlier, L.G. Bermúdez-Humarán, B. Pigneur, O. Lequin, P. Kharrat, G. Thomas, D. Rainteau, C. Aubry, N. Breyner, C. Afonso, S. Lavielle, J.-P. Grill, G. Chassaing, J.M. Chatel, G. Trugnan, R. Xavier, P. Langella, H. Sokol, P. Seksik, Identification of an anti-inflammatory protein from *Faecalibacterium prausnitzii* , a commensal bacterium deficient in Crohn's disease, Gut. 65 (2016) 415–425. https://doi.org/10.1136/gutjnl-2014-307649.

[347] S. Shigemori, T. Watanabe, K. Kudoh, M. Ihara, S. Nigar, Y. Yamamoto, Y. Suda, T. Sato, H. Kitazawa, T. Shimosato, Oral delivery of Lactococcus lactis that secretes bioactive heme oxygenase-1 alleviates development of acute colitis in mice, Microb Cell Fact. 14 (2015) 189. https://doi.org/10.1186/s12934-015-0378-2.

[348] W. Han, A. Mercenier, A. Ait-Belgnaoui, S. Pavan, F. Lamine, I.I. van Swam, M. Kleerebezem, C. Salvador-Cartier, M. Hisbergues, L. Bueno, V. Theodorou, J. Fioramonti, Improvement of an experimental colitis in rats by lactic acid bacteria producing superoxide dismutase:, Inflammatory Bowel Diseases. 12 (2006) 1044–1052. https://doi.org/10.1097/01.mib.0000235101.09231.9e.

[349] I.M. Carroll, J.M. Andrus, J.M. Bruno-Bárcena, T.R. Klaenhammer, H.M. Hassan, D.S. Threadgill, Anti-inflammatory properties of *Lactobacillus gasseri* expressing manganese superoxide dismutase using the interleukin 10-deficient mouse model of colitis, American Journal of Physiology-Gastrointestinal and Liver Physiology. 293 (2007) G729–G738. https://doi.org/10.1152/ajpgi.00132.2007.

[350] L. Watterlot, T. Rochat, H. Sokol, C. Cherbuy, I. Bouloufa, F. Lefèvre, J.-J. Gratadoux, E. Honvo-Hueto, S. Chilmonczyk, S. Blugeon, Intragastric administration of a superoxide dismutase-producing recombinant Lactobacillus casei BL23 strain attenuates DSS colitis in mice, International Journal of Food Microbiology. 144 (2010) 35–41. https://doi.org/10.1016/j.ijfoodmicro.2010.03.037.

[351] J.G. LeBlanc, S. del Carmen, A. Miyoshi, V. Azevedo, F. Sesma, P. Langella, L.G. Bermúdez-Humarán, L. Watterlot, G. Perdigon, A. de Moreno de LeBlanc, Use of superoxide dismutase and catalase producing lactic acid bacteria in TNBS induced Crohn's disease in mice, J. Biotechnol. 151 (2011) 287–293. https://doi.org/10.1016/j.jbiotec.2010.11.008.

[352] S. del Carmen, A. de Moreno de LeBlanc, R. Martin, F. Chain, P. Langella, L.G. Bermúdez-Humarán, J.G. LeBlanc, Genetically Engineered Immunomodulatory Streptococcus thermophilus Strains Producing Antioxidant Enzymes Exhibit

Enhanced Anti-Inflammatory Activities, Appl Environ Microbiol. 80 (2014) 869–877. https://doi.org/10.1128/AEM.03296-13.

[353] M. Liu, S. Li, Q. Zhang, Z. Xu, J. Wang, H. Sun, Oral engineered Bifidobacterium longum expressing rhMnSOD to suppress experimental colitis, Int. Immunopharmacol. 57 (2018) 25–32. https://doi.org/10.1016/j.intimp.2018.02.004.

[354] X. Wang, K. Wong, W. Ouyang, S. Rutz, Targeting IL-10 Family Cytokines for the Treatment of Human Diseases, Cold Spring Harb Perspect Biol. 11 (2019) a028548. https://doi.org/10.1101/cshperspect.a028548.

[355] L. Steidler, S. Neirynck, N. Huyghebaert, V. Snoeck, A. Vermeire, B. Goddeeris, E. Cox, J.P. Remon, E. Remaut, Biological containment of genetically modified Lactococcus lactis for intestinal delivery of human interleukin 10, Nat Biotechnol. 21 (2003) 785–789. https://doi.org/10.1038/nbt840.

[356] V. de Benito, M. de Barrio, M.P. de López-Sáez, E. Ordoqui, A. Prieto-García, T. Sainza, M.L. Baeza, Anaphylactic shock caused by impurities in orgotein preparations, Allergologia et Immunopathologia. 29 (2001) 272–275. https://doi.org/10.1016/S0301-0546(01)79069-6.

[357] S. del Carmen, A. de Moreno de LeBlanc, R. Martin, F. Chain, P. Langella, L.G. Bermúdez-Humarán, J.G. LeBlanc, Genetically Engineered Immunomodulatory Streptococcus thermophilus Strains Producing Antioxidant Enzymes Exhibit Enhanced Anti-Inflammatory Activities, Appl Environ Microbiol. 80 (2014) 869–877. https://doi.org/10.1128/AEM.03296-13.

[358] D. Árus, A. Jancsó, D. Szunyogh, F. Matyuska, N.V. Nagy, E. Hoffmann, T. Körtvélyesi, T. Gajda, On the possible roles of N-terminal His-rich domains of Cu,Zn SODs of some Gram-negative bacteria, Journal of Inorganic Biochemistry. 106 (2012) 10–18. https://doi.org/10.1016/j.jinorgbio.2011.09.029.

[359] Z. Paksi, A. Jancsó, F. Pacello, N. Nagy, A. Battistoni, T. Gajda, Copper and zinc binding properties of the N-terminal histidine-rich sequence of Haemophilus ducreyi Cu,Zn superoxide dismutase, Journal of Inorganic Biochemistry. 102 (2008) 1700–1710. https://doi.org/10.1016/j.jinorgbio.2008.04.007.

[360] B. Bóka, A. Myari, I. Sóvágó, N. Hadjiliadis, Copper(II) and zinc(II) complexes of the peptides Ac-HisValHis-NH 2 and Ac-HisValGlyAsp-NH 2 related to the active site of the enzyme CuZnSOD, Journal of Inorganic Biochemistry. 98 (2004) 113–122. https://doi.org/10.1016/j.jinorgbio.2003.09.012.

[361] G. Csire, S. Timári, J. Asztalos, J.M. Király, M. Kiss, K. Várnagy, Coordination, redox properties and SOD activity of Cu(II) complexes of multihistidine peptides, Journal of Inorganic Biochemistry. 177 (2017) 198–210. https://doi.org/10.1016/j.jinorgbio.2017.08.033.

[362] S. Timári, R. Cerea, K. Várnagy, Characterization of CuZnSOD model complexes from a redox point of view: Redox properties of copper(II) complexes of imidazole containing ligands, Journal of Inorganic Biochemistry. 105 (2011) 1009–1017. https://doi.org/10.1016/j.jinorgbio.2011.04.007.

[363] A. Jancsó, Z. Paksi, N. Jakab, B. Gyurcsik, A. Rockenbauer, T. Gajda, Solution chemical properties and catecholase-like activity of the copper(ii)–Ac-His-His-Gly-His-OH system, a relevant functional model for copper containing oxidases, Dalton Trans. (2005) 3187. https://doi.org/10.1039/b507655b.

[364] G.-M. Luo, H.-P. Chen, Y.-H. Cheng, A New Metal-Peptide Complex Displays the Activity of Superoxide Dismutase, Ann NY Acad Sci. 542 (1988) 79–82. https://doi.org/10.1111/j.1749-6632.1988.tb25810.x.

[365] X. Zou, Y. Ji, G. Gao, X. Zhu, S. Lv, F. Yan, S. Han, X. Chen, C. Gao, J. Liu, G. Luo, A Novel Selenium and Copper-containing Peptide with Both Superoxide Dismutase and Glutathione Peroxidase Activities, Journal of Microbiology and Biotechnology. 20 (2010) 88–93. https://doi.org/10.4014/jmb.0907.07014.

[366] J. Domergue, J. Pécaut, O. Proux, C. Lebrun, C. Gateau, A. Le Goff, P. Maldivi, C. Duboc, P. Delangle, Mononuclear Ni(II) Complexes with a S3O Coordination Sphere Based on a Tripodal Cysteine-Rich Ligand: pH Tuning of the Superoxide Dismutase Activity, Inorg. Chem. 58 (2019) 12775–12785. https://doi.org/10.1021/acs.inorgchem.9b01686.

[367] J. Domergue, P. Guinard, M. Douillard, J. Pécaut, O. Proux, C. Lebrun, A. Le Goff, P. Maldivi, P. Delangle, C. Duboc, A Bioinspired Ni ^{II} Superoxide Dismutase Catalyst Designed on an ATCUN-like Binding Motif, Inorg. Chem. 60 (2021) 12772–12780. https://doi.org/10.1021/acs.inorgchem.1c00899.

[368] U.P. Singh, R.K. Singh, Y. Isogai, Y. Shiro, Design and Synthesis of De Novo Peptide for Manganese Binding, Int J Pept Res Ther. 12 (2006) 379–385. https://doi.org/10.1007/s10989-006-9042-3.

[369] B.R. Gibney, F. Rabanal, K.S. Reddy, P.L. Dutton, Effect of Four Helix Bundle Topology on Heme Binding and Redox Properties, Biochemistry. 37 (1998) 4635–4643. https://doi.org/10.1021/bi971856s.

[370] F. Yan, G. Yan, S. Lv, N. Shen, Y. Mu, T. Chen, P. Gong, Y. Xu, L. Lv, J. Liu, J. Shen, G. Luo, A novel 65-mer peptide imitates the synergism of superoxide dismutase and glutathione peroxidase, The International Journal of Biochemistry & Cell Biology. 43 (2011) 1802–1811. https://doi.org/10.1016/j.biocel.2011.08.019.

[371] K. Coulibaly, M. Thauvin, A. Melenbacher, C. Testard, E. Trigoni, A. Vincent, M.J. Stillman, S. Vriz, C. Policar, N. Delsuc, A di-Copper Peptidyl Complex Mimics the Activity of Catalase, a Key Antioxidant Metalloenzyme, Inorg. Chem. 60 (2021) 9309–9319. https://doi.org/10.1021/acs.inorgchem.0c03718.

[372] M. Peana, S. Medici, H.A. Pangburn, T.J. Lamkin, M. Ostrowska, E. Gumienna-Kontecka, M.A. Zoroddu, Manganese binding to antioxidant peptides involved in extreme radiation resistance in Deinococcus radiodurans, Journal of Inorganic Biochemistry. 164 (2016) 49–58. https://doi.org/10.1016/j.jinorgbio.2016.08.012.

[373] M. Mittal, M.R. Siddiqui, K. Tran, S.P. Reddy, A.B. Malik, Reactive Oxygen Species in Inflammation and Tissue Injury, Antioxidants & Redox Signaling. 20 (2014) 1126–1167. https://doi.org/10.1089/ars.2012.5149.

[374] S. Cuzzocrea, E. Mazzon, L. Dugo, A.P. Caputi, D.P. Riley, D. Salvemini, Protective effects of M40403, a superoxide dismutase mimetic, in a rodent model of colitis, European Journal of Pharmacology. 432 (2001) 79–89. https://doi.org/10.1016/S0014-2999(01)01427-3.

[375] Q. Zhang, H. Tao, Y. Lin, Y. Hu, H. An, D. Zhang, S. Feng, H. Hu, R. Wang, X. Li, J. Zhang, A superoxide dismutase/catalase mimetic nanomedicine for targeted therapy of inflammatory bowel disease, Biomaterials. 105 (2016) 206–221. https://doi.org/10.1016/j.biomaterials.2016.08.010.

[376] M.J. Gasson, Plasmid complements of Streptococcus lactis NCDO 712 and other lactic streptococci after protoplast-induced curing, J Bacteriol. 154 (1983) 1–9. https://doi.org/10.1128/jb.154.1.1-9.1983.

[377] O.P. Kuipers, P.G.G.A. de Ruyter, M. Kleerebezem, W.M. de Vos, Quorum sensing-controlled gene expression in lactic acid bacteria, Journal of Biotechnology. 64 (1998) 15–21. https://doi.org/10.1016/S0168-1656(98)00100-X.

[378] L.G. BermÃºdez-HumarÃ¡n, P. Langella, J. Commissaire, S. Gilbert, Y. Loir, R. L'Haridon, G. Corthier, Controlled intra- or extracellular production of staphylococcal nuclease and ovine omega interferon in *Lactococcus lactis*, FEMS Microbiology Letters. 224 (2003) 307–313. https://doi.org/10.1016/S0378-1097(03)00475-0.

[379] Y.L. Loir, A. Gruss, S.D. Ehrlich, P. Langella, Direct Screening of Recombinants in Gram-Positive Bacteria Using the Secreted Staphylococcal Nuclease as a Reporter, 176 (1994) 5.

[380] M. van Asseldonk, G. Rutten, M. Oteman, R.J. Siezen, W.M. de Vos, G. Simons, Cloning of usp45, a gene encoding a secreted protein from Lactococcus lactis subsp. lactis MG1363, Gene. 95 (1990) 155–160. https://doi.org/10.1016/0378-1119(90)90428-T.

[381] I. Poquet, S.D. Ehrlich, A. Gruss, An Export-Specific Reporter Designed for Gram-Positive Bacteria: Application to Lactococcus lactis, J. BACTERIOL. 180 (1998) 9.

[382] M. Derrien, J.E.T. van Hylckama Vlieg, Fate, activity, and impact of ingested bacteria within the human gut microbiota, Trends in Microbiology. 23 (2015) 354–366. https://doi.org/10.1016/j.tim.2015.03.002.

[383] C. White, J. Lee, T. Kambe, K. Fritsche, M.J. Petris, A Role for the ATP7A Copper-transporting ATPase in Macrophage Bactericidal Activity, Journal of Biological Chemistry. 284 (2009) 33949–33956. https://doi.org/10.1074/jbc.M109.070201.

[384] K. Barnese, E.B. Gralla, J.S. Valentine, D.E. Cabelli, Biologically relevant mechanism for catalytic superoxide removal by simple manganese compounds, Proc. Natl. Acad. Sci. U.S.A. 109 (2012) 6892–6897. https://doi.org/10.1073/pnas.1203051109.

[385] H.A. Seddik, F. Bendali, F. Gancel, I. Fliss, G. Spano, D. Drider, Lactobacillus plantarum and Its Probiotic and Food Potentialities, Probiotics & Antimicro. Prot. 9 (2017) 111–122. https://doi.org/10.1007/s12602-017-9264-z.

[386] G.D. Mao, P.D. Thomas, G.D. Lopaschuk, M.J. Poznansky, Superoxide dismutase (SOD)-catalase conjugates. Role of hydrogen peroxide and the Fenton reaction in SOD toxicity., Journal of Biological Chemistry. 268 (1993) 416–420. https://doi.org/10.1016/S0021-9258(18)54167-3.

[387] R.S. Sohal, A. Agarwal, S. Agarwal, W.C. Orr, Simultaneous Overexpression of Copper- and Zinc-containing Superoxide Dismutase and Catalase Retards Age-related Oxidative Damage and Increases Metabolic Potential in Drosophila melanogaster, Journal of Biological Chemistry. 270 (1995) 15671–15674. https://doi.org/10.1074/jbc.270.26.15671.

[388] A.D. Frankel, C.O. Pabo, Cellular uptake of the tat protein from human immunodeficiency virus, Cell. 55 (1988) 1189–1193. https://doi.org/10.1016/0092-8674(88)90263-2.

[389] M. Green, P.M. Loewenstein, Autonomous functional domains of chemically synthesized human immunodeficiency virus tat trans-activator protein, Cell. 55 (1988) 1179–1188. https://doi.org/10.1016/0092-8674(88)90262-0.

[390] F. Duchardt, M. Fotin-Mleczek, H. Schwarz, R. Fischer, R. Brock, A Comprehensive Model for the Cellular Uptake of Cationic Cell-penetrating Peptides, Traffic. 8 (2007) 848–866. https://doi.org/10.1111/j.1600-0854.2007.00572.x.

[391] E. Koren, V.P. Torchilin, Cell-penetrating peptides: breaking through to the other side, Trends in Molecular Medicine. 18 (2012) 385–393. https://doi.org/10.1016/j.molmed.2012.04.012.

[392] P. Lönn, A.D. Kacsinta, X.-S. Cui, A.S. Hamil, M. Kaulich, K. Gogoi, S.F. Dowdy, Enhancing Endosomal Escape for Intracellular Delivery of Macromolecular Biologic Therapeutics, Sci Rep. 6 (2016) 32301. https://doi.org/10.1038/srep32301.

[393] A. Steen, E. Palumbo, M. Deghorain, P.S. Cocconcelli, J. Delcour, O.P. Kuipers, J. Kok, G. Buist, P. Hols, Autolysis of *Lactococcus lactis* Is Increased upon D-Alanine Depletion of Peptidoglycan and Lipoteichoic Acids, J Bacteriol. 187 (2005) 114–124. https://doi.org/10.1128/JB.187.1.114-124.2005.

[394] M. Nitz, K.J. Franz, R.L. Maglathlin, B. Imperiali, A Powerful Combinatorial Screen to Identify High-Affinity Terbium(III)-Binding Peptides, ChemBioChem. 4 (2003) 272–276. https://doi.org/10.1002/cbic.200390047.

VI. Annexes

VI.1. Chapter II

VI.1.a. Supplementary materials of "Inertness of superoxide dismutase mimics Mn(II) complexes based on an open-chain ligand, bioactivity, and detection in intestinal epithelial cells" publication

VI.1.a.i. Supplementary information

- Material and reagents

Chemicals and solvents were purchased from commercial sources (Sigma-Aldrich, Alfa-Aesa, Strem, Acros, Iris) and were used as received without further purification.

For ICP-MS, nitric acid (HNO3) 65% Suprapur was purchased from Merck (#1.00441.1000). Manganese Standard for ICP (1003 mg/L ± 4 mg/L, TraceCERT #74128) were from Sigma Aldrich.

For MS detection of Mn1-CP inside cells, ultrapure ULC/MS – CC/SFC grade solvents were purchased from Biosolve: 2-propanol (#162641), Acetonitrile (#12041), Water (#232141). Syringes for IMS-MS direct infusion were purchased from Agilent: Manual syringe, removable needle 22/51/LC, PTFE-tip plunger 500 µL (#5190-1526), 250 µL (#5190-1520), 100 µL (#5190-1512). PFA (metal-free) labware were purchased from AHF ANALYSENTECHNIK: Narrow Neck Bottle 100 mL (T81-100), Micro Spatulas made of CTFE (T29-578), Measuring Cylinder 50 mL (T89-050).

LPS (Escherichia coli O55:B5), NADH, pyruvic acid, BSA, Tween 20 and Triton 100X were purchased from Sigma Aldrich (Saint-Quentin Fallavier, France). IL8 detection ELISA kit (Duoset) was provided by R&D Systems (Minneapolis, Minnesota, USA). Horseradish peroxidase-conjugated antibodies were from Jackson ImmunoResearch (Ely, UK). BCA was from Uptima-Interchim (Montluçon, France). Detection ECL system, protein gels (Mini Protean TGX Stain free Precast Gel) and nitrocellulose membranes were from Biorad. Blasticidin were purchased from Invivogen (Toulouse, France). Rabbit polyclonal anti-human SOD 2 antibodies were from Invitrogen (Thermo Fisher Scientific, Waltham, Massachussetts, USA). Fetal bovine serum was from GE Healthcare Life Sciences (South Logan, Utah, USA). Dulbecco's modified

Eagle medium (DMEM), HEPES buffer solution (1 M), 0.05% trypsin-EDTA and Dulbecco's Phosphate Buffered Saline (10X, DPBS) was from Gibco (Thermo Fisher Scientific, Waltham, Massachussetts, USA). The protease inhibitor cocktail was from Roche Diagnostics (reference: 11836145001, Sigma-Aldrich, Meylan, France). The mass and IMS calibration of the timsTOF was done with continuous infusion of ESI-Low Concentration Tuning Mix from Agilent (Santa Clara, USA).

- Instrumentation

UV-vis spectra were recorded on a Cary 300 spectrophotometer (Agilent technologies, Santa Clara, CA, USA) using a double-beam mode with media as the reference. Plastic UV-cuvettes, semi-micro (1.5 mL) were purchased from BRAND (12.5 x 12.5 x 45 mm, #7591 50). UV−visible spectra (for all biological experiments) were recorded on a SpectraMax M5 Series Multi-Mode Microplate Reader from Molecular Devices (CRSA, Sorbonne University Medicine campus, with the courtesy of Dr. Philippe Seksik). Analytical HPLC was performed on an Agilent 1200 series equipped with a quaternary pump using a Proto 200 C18 from Higgins Analytical Inc (particles size 3 µm, 100×4.6 mm column). Preparative HLC was performed on an Agilent 1260 Infinity using a Nucleodur C18 HTech column from Macherey-Nagel Inc. (particles size 5 µm, 250×16 mm column). ICP-MS analyses were performed on an Agilent 7700 X. ^{55}Mn were selected as isotopes to avoid isobaric interferences. ESI-MS experiments (HRMS) were carried out using a LTQ-Orbitrap XL from Thermo Scientific (Thermo Fisher Scientific, Courtaboeuf, France) and operated in positive ionization mode, with a spray voltage at 3.6 kV. Applied voltages were 20 and 70 V for the ion transfer capillary and the tube lens, respectively. The ion transfer capillary was held at 275°C. Detection was achieved in the Orbitrap with a resolution set to 100,000 (at m/z 400) and a m/z range between 190-1500 in profile mode. Spectrum was analyzed using the acquisition software XCalibur 2.1 (Thermo Fisher Scientific, Courtaboeuf, France). The automatic gain control (AGC) allowed accumulation of up to 2.10^5 ions for FTMS scans, Maximum injection time was set to 300 ms and 1 µscan was acquired. 10 µL was injected using a Thermo Finnigan Surveyor HPLC system (Thermo Fisher Scientific, Courtaboeuf, France) with a continuous infusion of methanol at 100 µL.min^{-1}. ^{1}H and ^{13}C NMR spectra were recorded on a Bruker DRX300 Ultrashield model spectrometer with a proton and carbon frequency of 300 MHz and 75 MHz respectively. Spectra have been analyzed using the software MestReNova 7.1. The chemical shifts (δ/ppm) were calibrated relative to residual

solvent signals. The following abbreviations are used: singlet (s), doublet (d), triplet (t) and multiplet (m). MS characterization of ligands were conducted with classic electrospray (ESI) 4 kV source (Thermo Fisher Scientific) in positive mode coupled to a Qq Orbitrap mass spectrometer; Q Exactive Hybrid Quadrupole-Orbitrap from Thermo Fisher Scientific (SMBP, ESPCI, with the courtesy of Dr. Joelle Vinh). Direct infusion was performed at 5 µL/min. The ligands (EnPI2P, EnPI2C, EnPI2CP) were analyzed at 100 µM in 85% ACN/ammonium formate 50 mM at pH 6.5. For cyclic voltammetry, a MetrOhm potentiostat (AUTOLAB model) was used. The auxiliary electrode was a Pt wire and the working electrode was a glassy carbon disk (3 mm diameter) carefully polished before each voltammogram with a 1 µm diamond paste, washed with water and finally air dried. The reference electrode was a SCE saturated with KCl. For Mn1CP detection and quantification in cell lysates, the TOF-MS part of the timsTOF provided by Bruker Daltonics (Champ sur Marne, France) were used (IPREM-UMR5254, Pau France). The experiment operated in positive ionization mode and tims detect mode (IMS resolution 120), with a capillary voltage at 4.5 kV. The dry gas transfer capillary was held at 230°C. Detection was achieved in the timsTOF with a resolution set to 70,000 (at m/z 1221) and a m/z range between 200-1250 in profile focused mode. Spectrum was analyzed using the acquisition software DataAnalysis (Bruker Daltonics, Champ sur Marne, France). The acquisition frequency was set to 2 Hz. The sample was first injected during 1 minute for stabilization and 1 additional minute for acquisition, using the embedded infusion pump system from the timsTOF with a continuous infusion flow of 180 µL/min. Stopped-flow experiments were performed on a SFM-3000/S stopped-flow mixer equipped with a HDS mixer and kelraz o-ring, all provided by BioLogic (Seyssinet-Pariset, France). The stopped-flow mixer was connected to a control unit MPS-70/3 (Biologic), a deuterium/tungsten light source 30W (BioLogic) and a MMS-UV/vis-ASPEN- high speed diode array spectrometer. The stopped-flow experiments were controlled using the software Biokine32 (BioLogic).

- Synthesis of EnPI2

EnPI2 was synthesized according to a previously reported procedure [1].

- Synthesis of EnPI2P

Propionaldehyde (960 µL, 13.31 mmol, 1.5 equiv.) was added to a solution of EnPI2 (3.15 g, 8.87 mmol) in absolute ethanol (30 mL). After stirring the reaction mixture for 2 h at room temperature under argon, $NaBH_3CN$ (0.558 g, 8.87 mmol, 1 equiv.) was added and pH was

adjusted to 5 using NaOH 1 M or HCl 1 M. The reaction mixture was stirred two additional hours at room temperature. A 1 M NaOH solution was then added until pH 7 and EtOH was evaporated. The product was resuspended in H_2O (20 mL) and dichloromethane (DCM) (20 mL) and pH was adjusted to 9. The aqueous phase was extracted twice with DCM (2 × 20 mL) and the organic phase was dried over anhydrous sodium sulfate. DCM was eventually evaporated to give crude product. The product was purified by preparative HPLC using an ACN/H_2O (with 0.1 % TFA) gradient going from 10/90 to 40/60 in 30 min. After solvent evaporation, a yellow oil was obtained with a yield of 31%.

^{1}H NMR (EnPI2P) (300 MHz, CD_3OD): δ = 7.7 (m, 2 H, H_{Ar}), 7.5 (s,2 H, H_{Ar}), 7.3 (m, 1 H, H_{Ar}), 7.2 (t, J=6Hz, 1H, H_{Ar}), 6.9 (m, 2 H, H_{Ar}), 4.9 (s, 2 H, N-C**H$_2$**-C_{Im}), 4.5 (s, 2 H, N-C**H$_2$**-C_{Im}), 4.1 (s, 5 H, NC**H$_3$** + N-C**H$_2$**-C_{Ph}), 3.8 (s, 3 H, NC**H$_3$**), 3.6 (t, J=6 Hz, 2 H, N-C**H$_2$**-C**H$_2$**-N), 3.4 (t, J=6 Hz, 2 H, N-C**H$_2$**-CH_2-N), 3.1 (m, 2 H, N-CH_2-C**H$_2$**-CH_3), 1.8 (m, 2 H, N-C**H$_2$**-C**H$_2$**-CH_3), 1.0 (t, J=7.5Hz, 3 H, N-CH_2-CH_2-C**H$_3$**).

^{13}C NMR (EnPI2P) (75 MHz, CD_3OD): δ = 156.8 (C_{Ph}-OH), 146.0 ($C_{quat,Im}$), 144.8 ($C_{quat,Im}$), 132.3 (C_{Ph}-H), 130.5 (C_{Ph}-H), 125.2 (C_{Im}H), 124.9 (C_{Im}H), 123.4 ($C_{quat,Ph}$), 121.5 (C_{Ph}-H), 120.6 (C_{Im}H), 119.6 (C_{Im}H), 116.2 (C_{Ph}-H), 57.5 (N-**C**H_2-CH_2-CH_3), 55.4 (C_{Ph}-**C**H_2), 52.8 (N-**C**H_2-**C**H_2-N), 52.6 (N-**C**H_2-**C**H_2-N), 49.6 (N-**C**H_2-C_{Im}), 49.1 (N-**C**H_2-C_{Im}), 34.6 (N-**C**H_3), 34.5 (N-**C**H_3), 19.8 (N-CH_2-**C**H_2-CH_3) and 11.5 (N-**C**H_2-CH_2-**C**H_3) ppm.

HRMS (ESI) m/z: $[M+H]^+$ calcuId for $C_{22}H_{32}N_6OH$ 397.2710. Found 397.2712; (Error: 0.4 ppm).

Single isotopic mass : 397.3 m/z.

- Synthesis of EnPI2C

EnPI2C was synthesized according to a previously reported procedure [2] using the racemic (±)-(trans)-1,2-diamino cyclohexane instead of 1,2-diaminoethane as reagent.

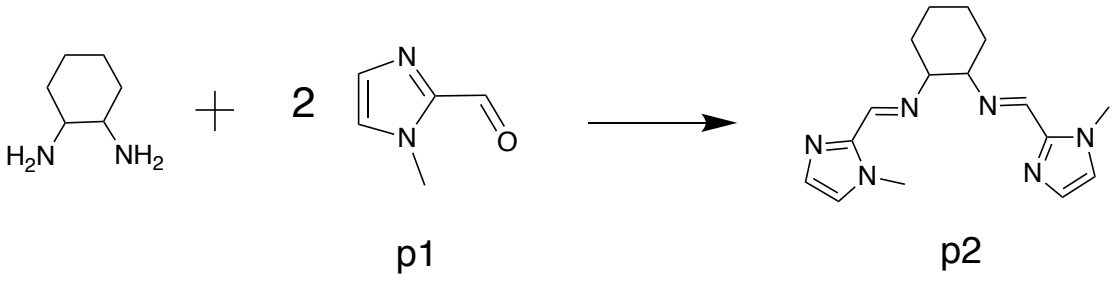

p1 p2

P1 (0.5 g, 4.54 mmol, 2 equiv.) was dissolved in ACN (0.5 mL). (±)-(trans)-1,2-diamino cyclohexane (273 µL, 2.27 mmol, 2 equiv.) was then added and the reaction mixture was stirred under argon until precipitation ended. The precipitate was then filtered off and washed with petrol ether to afford a yellow solid with a yield of 92%.

^{1}H NMR (P2) (300 MHz, $CDCl_3$): δ = 8.2 (s, 2 H, N=CH-Im), 7.0 (d, J=3 Hz, 2 H, CH_{Im}), 6.9 (d, J=3 Hz, 2 H, CH_{Im}), 3.9 (s, 6 H, NCH_3), 3.3 (bm, 2 H, CH_{cyclo}), 1.8 (m, 6 H, CH_{cyclo}), 1.5 (m, 2 H, CH_{cyclo}).

^{13}C NMR (P2) (75 MHz, $CDCl_3$): δ = 152.2 (N=**C**H-Im, 2 C), 143.2 (C_{quatIm}, 2 C), 128.9 (C_{Im}H, 2 C), 124.9 (C_{Im}H, 2 C), 74.8 (N-CH_{cyclo}, 2 C), 42.9 (**C**$H_{2,cyclo}$, 2 C), 35.4 (N-**C**H_3, 2 C), 32.9 (**C**$H_{2,cyclo}$, 2 C), 24.3 (**C**$H_{2,cyclo}$, 2 C).

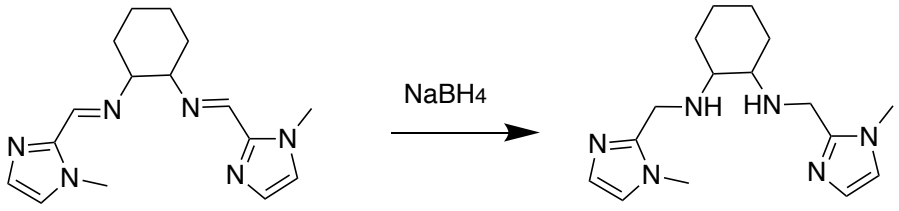

p2 p3

P2 (0.621 g, 2.08 mmol) was dissolved in absolute ethanol (10 mL) and $NaBH_4$ (0.236 g, 6.25 mmol, 3 equiv.) was added. After two hours of stirring at room temperature under argon, HCl 1 M was added to the reaction to pH 7. Water (10 mL) and DCM (20 mL) were added and p5 was extracted in the DCM fraction. The extraction was repeated twice. P3 was then dried over Na_2SO_4, filtered off and DCM was evaporated to afford a yellow solid with a yield of 90%.

^{1}H NMR (P3) (300 MHz, $CDCl_3$): δ = 6.8 (d, J=3 Hz, 2 H, N-CH=CH), 6.7 (d, J=3 Hz, 2H, N-CH=CH), 3.9-3.6 (bm, 4 H, N-CH_2-Imi), 3.6 (s, 6 H, N-CH_3), 2.2-2.1 (bm, 4 H, CH_{cyclo}), 1.7 (m, 2 H, CH_{cyclo}), 1.2-1.0 (bm, 4 H, CH_{cyclo})

^{13}C NMR (P3) ($CDCl_3$, 75 MHz): δ = 146.7 ($C_{quat,Im}$, 2 C), 126.7 (C_{Im}H, 2 C), 121.1 (C_{Im}H, 2 C), 61.0 (N-CH_{cyclo}, 2 C), 42.9 (N-CH_2-Im, 2 C), 32.8 (N-**C**H_3, 2 C), 31.2 (**C**$H_{2,cyclo}$, 2 C), 24.2 (**C**$H_{2,cyclo}$, 2 C)

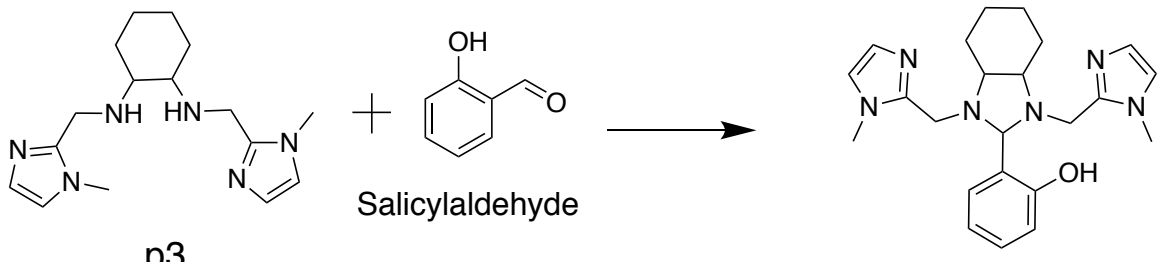

p3 p4

P3 (0.64 g, 2.12 mmol) was dissolved in absolute ethanol (10 mL). Salicylaldehyde (223 µL, 2.12 mmol, 1 equiv.) was added and the reaction mixture was stirred for 48 hours under argon at room temperature. The reaction mixture was then dried over anhydrous sodium sulfate (Na_2SO_4) and filtered off under vacuum. Ethanol was removed by rotary evaporation under vacuum to afford P4 with a quantitative yield.

^{1}H NMR (P4) (300 MHz, $CDCl_3$): δ = 7.1-6.4 (bm, 8 H, H_{Ar}), 3.8 (m, 2 H, N-CH_2-Ph), 3.6-3.5 (m, 2 H, N-CH_2-Im), 3.4 (s, 3 H, N-CH_3), 3.2 (s, 3 H, N-CH_3), 2.8 (m, 1 H, N-CH-CH-N), 2.5 (m, 1 H, N-CH-CH-N), 1.7-1.5 (bm, 3 H, CH_{cyclo}), 1.3-0.8 (bm, 5 H, CH_{cyclo})

^{13}C NMR (P4) ($CDCl_3$, 75 MHz): δ = 157.5 (C_{Ph}-OH), 145.4-143.3 ($C_{quat,Im}$, 2 C), 130.7-129.6 (C_{Ph}-H, 2 C), 127.0-126.4 (C_{Im}H, 2 C), 122.0 ($C_{quat,Ph}$), 121.5-121.1 (C_{Im}H, 2 C),119.0-116.4 (bm, C_{Ph}-H, 2 C), 86.7 (N-CH-N), 68.2-67.8 (N-CH-CH-N, CH_{cyclo}, 2 C) , 47.6-45.7 (N-CH_2-Im, 2 C), 32.8-32.5 (N-CH_3, 2 C), 29.2 (CH_{cyclo}, 2 C), 24,2 (CH_{cyclo}, 2 C)

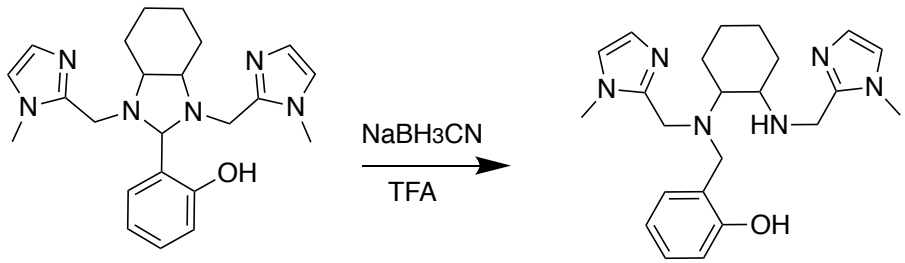

p4 EnPI2C

P4 (0.906 g, 2.22 mmol) was dissolved in of absolute ethanol (20 mL). Sodium cyanoborohydride $NaBH_3CN$ (0.139 g, 2.22 mmol, 1 equiv.) and trifluoroacetic acid TFA (171 µL, 2.22 mmol, 1 equiv.) were added and the reaction mixture was stirred for 2 hours at room temperature. A color change from yellow to colorless was observed. The pH was then adjusted to 8-8.4 by adding NaOH 1 M to neutralize the TFA. After removing the ethanol by rotary evaporation, DCM (20 mL) and water (20 mL) were added. The aqueous layers were then extracted with DCM (3 x 20 mL). The extraction was monitored by measuring the absorbance at 254 nm (one droplet was deposited on a silica gel TLC plate). The combined organic layers were dried over anhydrous sodium sulfate and filtered off. DCM was removed by rotary evaporation and the product was purified by preparative HPLC using a ACN/H_2O (with 0.1 % TFA) gradient going from 10/90 to 30/70 in 30 minutes. After solvent evaporation, we afford a yellow powder (1.36 g, 3.33 mmol) with a yield of 36%.

^{1}H NMR (EnPI2C) (300 MHz, CD_3OD): δ = 7.7 (m, 2 H, H_{Ar}), 7.2 (m, 3 H, H_{Ar}), 7.1 (m, 1 H, H_{Ar}), 6.82 (m, 2 H, H_{Ar}), 4.2 (m, 2 H, N-C**H$_2$**-Im), 4.1 (m, 5 H, NC**H$_3$** + N-C**H$_2$**-Im), 3.9 (m, 2 H, N-C**H$_2$**-Ph), 3.61 (s, 3 H, N-C**H$_3$**), 3.5 (m, 1 H, N-C**H**$_{cylo}$-C**H**$_{cyclo}$-N), 3.2 (m, 1 H, N-C**H**$_{cylo}$-C**H**$_{cyclo}$-N), 2.4 (m, 1 H, C**H**$_{2,cyclo}$), 2.2 (m, 1 H, C**H**$_{2,cyclo}$), 1.9 (m, 2 H, C**H**$_{2,cyclo}$), 1.7-1.4 (bm, 4 H, C**H**$_{2,cyclo}$).

^{13}C NMR (EnPI2C) (75 MHz, D_2O): δ = 153.9 (C_{Ph}-OH), 143.4 ($C_{quat,Im}$), 136.5 ($C_{quat,Im}$), 131.3 (C_{Ph}-H), 130.1 (C_{Ph}-H), 125.6 (C_{Im}H), 123.4 (C_{Im}H), 122.5 (C_{quatPh}), 121.0 (C_{Ph}-H), 120.6 (C_{Im}H), 118.2 (C_{Im}H), 115.8 (C_{Ph}-H), 65.1-60.5 (N-**C**H$_{cylo}$-**C**H$_{cyclo}$-N), 49.8 (N-**C**H$_2$-Ph), 46.3 (N-**C**H$_2$-Im), 36.7 (N-**C**H$_2$-Im), 35.1 (N-**C**H$_3$, 1 C), 33.8 (N-**C**H$_3$, 1 C), 27.1-24.5-23.7-22.7 (**C**H$_{2,cyclo}$, 4 C)

HRMS (ESI) m/z: [M+H]+ Calcd for $C_{23}H_{32}N_6OH$ 409.2710. Found 409.2712; (Error: 0.4 ppm).

Single isotopic mass : 409.3 m/z.

- Synthesis of EnpI2CP

The propylation of EnPI2C to obtain EnPI2CP is performed similarly to the propylation of EnPI2 to obtain EnPI2P (see above).

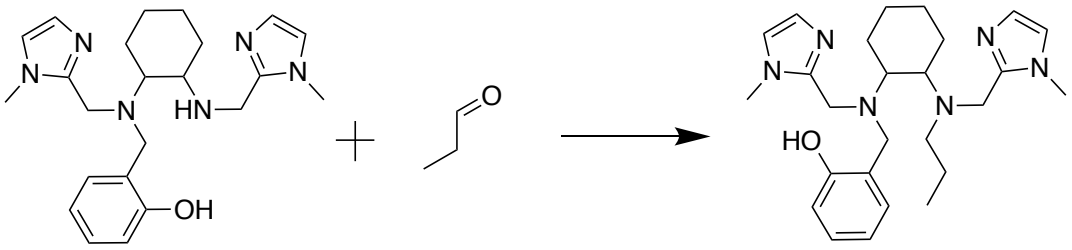

EnPI2C EnPI2CP

Propionaldehyde (1160 µL, 16.12 mmol, 2.5 equiv.) was added to a solution of EnPI2C (2.635 g, 6.45 mmol) in absolute ethanol (50 mL). After stirring the reaction mixture for 2 h at room temperature under argon atmosphere, $NaBH_3CN$ (0.405 g, 6.45 mmol, 1 equiv.) and TFA (476 µL, 6.45 mmol, 1 equiv.) were added and the pH were adjusted to 5 with NaOH 1 M. The reaction mixture was stirred two additional hours at room temperature. NaOH 1 M was then added to pH 7 and EtOH was evaporated. The product was resuspended in H_2O (20 mL) and dichloromethane (DCM) (20 mL) and pH was re-adjusted to 9 with NaOH 1 M. The aqueous phase was extracted twice with DCM (2 × 20 mL) and the organic phase was dried over anhydrous sodium sulfate. After DCM evaporation, the product was purified by preparative HPLC with ACN/H_2O with 0.1 % TFA going from 15/85 to 30/70 in 30 minutes. After solvent evaporation, a yellow oil was obtained with a yield of 27 %.

^{1}H NMR (EnPI2CP) (300 MHz, CD_3OD): δ = 7.40 (m, 1 H, H_{Ar}), 7.32 (m, 2 H, H_{Ar}), 7.18 (m, 1 H, H_{Ar}), 7.01 (m, 2 H, H_{Ar}), 6.65- 6.75 (bm, 2 H, H_{Ar}), 4.80 (bm, 2 H, N-C**H$_2$**-Ph), 4.42 (m, 2 H, N-C**H$_2$**-Im), 4.22 (m, 2 H, N-C**H$_2$**-Im), 3.87 (s, 3 H, N-C**H$_3$**), 3.67 (s, 3 H, N-C**H$_3$**), 3.48 (m, 2 H, N-CH-CH-N), 1.4-2.4 (bm, 12 H, N-C**H$_2$**-C**H$_2$**-CH3 et N-C**H$_{2,cyclo}$**), 0.95 (m, 3 H, N-CH_2-CH_2-C**H$_3$**).

^{13}C NMR (EnIP2CP) (75 MHz, CD_3OD): δ = 163.3 (C_{Ph}-OH), 155.7 ($C_{quat,Im}$), 146.1 ($C_{quat,Im}$), 139.5 (C_{Ph}-H), 131.9 (C_{Ph}-H), 128.8 (C_{Im}H), 125.6 (C_{Im}H), 123.2 (C_{quatPh}), 121.6 (C_{Ph}-H), 119.8 (C_{Im}H), 115.9 (C_{Im}H), 112.0 (C_{Ph}-H), 65.5-63,13 (N-**C**H-**C**H-N, 2C), 55.1 (N-**C**H_2-CH_2-CH_3), 51.4 (N-**C**H_2-Ph), 50.6 (N-**C**H_2-Im), 45.0 (N-**C**H_2-Im), 35.3 (N-**C**H_3, 2C), 31.9-25,3 (**C**$H_{2,cyclo}$, 4 C), 11.92 (N-CH_2-CH_2-**C**H_3)

HRMS (ESI) m/z: $[M+H]^+$ Calcd for $C_{26}H_{38}N_6OH$ 451.3180. Found 451.318; (Error: 0.0 ppm).

Single isotopic mass : 451.3 m/z.

- Synthesis of EnpI2CP labelled with ^{13}C

EnpI2CP labelled with ^{13}C was synthetized following the same procedure than that used for EnPI2CP except the use of ^{13}C labelled salicylaldehyde as reagent. ^{13}C-labelled salicylaldehyde was synthetized by the oxidation of commercial ^{13}C-labelled phenol by paraformaldehyde using the protocol described by Yang *et al*. [3].

A mixture of ($^{13}C_6$) phenol (0.543 g, 5.429 mmol), anhydrous magnesium dichloride (1.312 g, 8.119 mmol), anhydrous triethylamine (2.8 mL) and anhydrous acetonitrile (4.9 mL) was stirred under argon at room temperature for 30 min. Paraformaldehyde (1.315 g, 43.9 mmol) was added to the mixture. The resulting mixture was refluxed for 4 h and then cooled to room temperature. A color change from white to orange was observed. To the mixture was added 10% hydrochloric acid (6.5 mL) to neutralize triethylamine and to reach pH 5. The obtained compound was extracted with diethyl ether (3 × 20 mL). The combined organic layers were washed with distilled water (10 mL) and saturated brine (10 mL), dried over anhydrous Na_2SO_4 and filtered off. The solvent was removed by rotary evaporation to produce a brown oil with a yield of 70%.

NMR ^{1}H (^{13}C-salicylaldehyde) ($CDCl_3$, 300 MHz): δ = 11.0 (m, 1H, C_{Ar}-CH=O), 9.9 (m, 1H, C_{Ar}-OH), 6.5-8 (bm, 4H, H_{Ar}). NMR ^{13}C (^{13}C-salicylaldehyde) ($CDCl_3$, 75 MHz): 161 (m, 1 H, C_{Ar}), 137 (m, 1 H, C_{Ar}), 134 (m, 1 H, C_{Ar}), 121-117 (m, 3 H, C_{Ar})

The synthesis of ^{13}C-EnPI2CP was performed as for its light analogue, with no intermediate purification. The crude intermediates showed similar NMR-spectra to those obtained for the synthesis of the light analogue of EnPI2CP. The crude final product was purified by preparative HPLC with ACN/H_2O with 0.1 % TFA going from 15/85 to 30/70 in 30 minutes. As solubility problems were encountered for the purification, only the water-soluble fraction was purified. After solvent evaporation and lyophilization, we obtained the pure heavy ligand as a white solid with a yield of 15%.

NMR ^{1}H (^{13}C-EnPI2CP) (CD_3OD, 300 MHz): δ = 7.4 (m, 2H, H_{Ar}), 7.31(m, 2H, H_{Ar}), 6.98 (m, 2H, H_{Ar}), 6.73 (m, 1H, H_{Ar}), 6.42 (m, 1H, H_{Ar}), 4.45 (m, 2 H, N-C**H$_2$**-C_{imi}), 4.25 (m, 2 H, N-C**H$_2$**-C_{imi}), 3.87 (s, 3 H, NC**H$_3$**), 3.67 (s, 3 H, NC**H$_3$**), 3.49 (m, 2 H, N-C**H$_2$**-C_{phenol}), 3.2 (m, 2 H, N-C**H$_2$**-CH_2-CH_3), 2.33 (m, 2 H, N-CH_2-C**H$_2$**-CH_3), 2.02 (m,2 H, C_{cyclo}-**H**), 1.81 (m, 4 H, C_{cyclo}-**H**), 1.50 (m, 2 H, C_{cyclo}-**H**), 0.94 (m, 3 H, N-CH_2-CH_2-C**H$_3$**). NMR ^{13}C (^{13}C-EnPI2CP) (CD_3OD, 75 MHz): 156 (m, 1 C_{Ar}), 131 (m, 2 C_{Ar}), 121 (m, 2 C_{Ar}), 116 (m, 1 C_{Ar})

HRMS (ESI) m/z: $[M+H]^+$ Calcd for $C_{20}{}^{13}C_6H_{38}N_6OH$ 457.3381. Found 457.3381; (Error: 0.0 ppm).

The ligands were purified by HPLC and lyophilized. They were dissolved in milliQ water (around 10 mg/mL). An aliquot of the resulting solution was diluted in HEPES buffer (50 mM, pH 7.5) and its concentration was determined by UV-visible titration by successive addition of $MnCl_2$ (10 mM), by following the absorbance at 280 nm. The titration was performed three times. The stock solutions of ligand were diluted to a concentration of 10 mM. Aliquots were prepared and frozen (-20 °C) until used.

Stock solutions of Mn^{2+} (Zn^{2+})-complexes at 10 mM were prepared before each experiment by addition of 1 eq. of anhydrous $MnCl_2$ ($ZnCl_2$, $CuSO_4$, $NiCl_2.6H_2O$, or $CoCl_2$) in HEPES buffer (50 mM) to a solution of ligand.

- K_1 calculation of MnL complexes from UV titration experiments

The protocol is given in the material and method section. The calculation of the theoretical absorbance used to fit the experimental data for K_1 determination is detailed below.

Table summarizing the extent of the reaction:

	Mn^{2+} +	L =	MnL
	$\mathbf{C_{Mn}}$	$\mathbf{C_L}$	$\mathbf{C_{MnL}}$
Initial state	n × $\boldsymbol{C_0}$	$\boldsymbol{C_0}$	0
Equilibrium state (intermediate or for n<1)	$\mathbf{n \times C_0 - C_0 \times e = (n - e) \times C_0}$	$\mathbf{C_0 - C_0 \times e = (1 - e) \times C_0}$	$\mathbf{C_0} \times$ e
Equilibrium state (final or for n>>1)	n × $\boldsymbol{C_0 - C_0}$	0	$\boldsymbol{C_0}$

$C_L =$ Concentration in ligand (L)

$C_{MnL} =$ Concentration in complex MnL

$C_{Mn} =$ Concentration in Mn(II)

$e =$ extent of the reaction of Mn with L to form MnL after the addition of $\mathrm{n} \times \mathrm{C}_0$ Mn

$K_{1,MnL} =$ Association constant of ligand L with Mn

C_0 = initial ligand concentration

n = number of molar equivalent of Mn (compared to initial L) added in the solution

$K_{1,MnL} = \frac{C_{MnL}}{C_L \times C_{Mn}}$

$$\frac{1}{K_{1,MnL}} = \frac{(n-e) \times C_0(1-e)}{e}$$

$$\frac{e}{K_1} = (n-e) \times (C_0 - C_0 e) = nC_0 - e(C_0 + nC_0) + C_0 e^2$$

$$n - e\left(1 + n + \frac{1}{C_0 K_1}\right) + e^2 = 0$$

$$\Delta = \left(1 + n + \frac{1}{C_0 K_1}\right)^2 - 4 \times n$$

$\Delta > 0$ for C_0 = 40 µM, $K_1 \approx 10^5 - 10^6$ and n between 0 and 3.

Solution of the quadratic equation physically relevant ($\mathrm{e} \leq \mathrm{n}$):

$$e = \frac{\left(1 + n + \frac{1}{C_0 K_1}\right) - \sqrt{\left(1 + n + \frac{1}{C_0 K_1}\right)^2 - 4n}}{2}$$

$$A_{th} = \varepsilon_L C_L l + \varepsilon_{MnL} C_{MnL} l$$

$A_{th} =$ Theoretical absorbance at a fixed wavelength

$\varepsilon_{MnL} =$ molar attenuation coefficient of MnL complex at the same fixed wavelength

$\varepsilon_L =$ molar attenuation coefficient of L at the same fixed wavelength

$l =$ width of the spectrophotometer cuvette.

$$A_0 = \varepsilon_L C_0 l$$

$$A_f = \varepsilon_{MnL} C_0 l$$

$A_0 =$ Theoretical initial absorbance of the free ligand solution, no manganese added

$A_f =$ Theoretical final absorbance of the MnL solution (all ligands are bound to Mn)

$$A_{th} = A_0 \times (1 - e) + A_f \times e = A_0 - e(A_0 - A_f)$$

$$A_{th} = A_0 \times \left(1 - \frac{\left(1 + n + \frac{1}{C_0 K_1}\right) - \sqrt{\left(1 + n + \frac{1}{C_0 K_1}\right)^2 - 4n}}{2}\right) + A_f \times \frac{\left(1 + n + \frac{1}{C_0 K_1}\right) - \sqrt{\left(1 + n + \frac{1}{C_0 K_1}\right)^2 - 4n}}{2}$$

- K_1 calculation of ZnL/Co1CP complexes: competition with the formation of MnL

The association constants of the studied ligands with Zn are very high, so classical UV-vis titration experiments are not sufficient for a precise determination of these values. For this reason, we conducted competitions experiments between the formation of ZnL and MnL for which K_1 is known. The protocol is detailed in the material and method section of the main article.

Table summarizing the extent of the reaction.

	$\mathbf{C_{Mn}}$	$\mathbf{C_L}$	$\mathbf{C_{MnL}}$	$\mathbf{C_{Zn}}$	$\mathbf{C_{ZnL}}$
Initial state	C2	C1	0	$\boldsymbol{C_1 \times n_{eq}}$	0
Equilibrium state (intermediate or for n<1)	$\boldsymbol{C_2 - C_1 \times e}$	$\boldsymbol{C_1 \times (1 - e - e')}$	$\boldsymbol{C_1 \times e}$	$\boldsymbol{C_1 \times (n_{eq} - e')}$	$\boldsymbol{C_1 \times e'}$
Equilibrium state (final or for n>>1)	C2	0	0	$\boldsymbol{(n_{eq} - 1) \times C_1}$	C1

$$\frac{K_{1,ZnL}}{K_{1,MnL}} = \frac{e' \times C_1 \times (C_2 - C_1 \times e)}{e \times C_1 \times C_1 \times (n_{eq} - e')} = \frac{e' \times (C_2 - C_1 \times e)}{e \times C_1 \times (n_{eq} - e')}$$

$C_X =$ Concentration in X

e = extent of the reaction of Mn with L to form MnL

e' = extent of the reaction of Zn with L to form ZnL

$K_{1,ZnL}$ = Association constant of ligand L with Zn

$K_{1,MnL}$ = Association constant of ligand L with Mn

C_1 = initial ligand concentration

C_2 = initial Mn concentration = $200 \times C_1$

N_{eq} = number of molar equivalent of Zn (compared to initial L) added in the solution

Assumption: no free ligand in solution (high $K_{1,ZnL}$ and $C_1 \ll C_2$):

$$e = 1 - e'$$

$$\frac{K_{1,ZnL}}{K_{1,MnL}} = \frac{e' \times C_1 \times (C_2 - C_1 \times e)}{e \times C_1 \times C_1 \times (n_{eq} - e')} = \frac{e' \times C_1 \times (C_2 - C_1 \times (1 - e'))}{(1 - e') \times C_1 \times C_1 \times (n_{eq} - e')}$$

$$= \frac{e' \times (C_2 - C_1 \times (1 - e'))}{(1 - e') \times C_1 \times (n_{eq} - e')}$$

$$= \frac{e' \times C_2 - e' \times C_1 + C_1 \times e'^2}{-(e' \times C_1 \times n_{eq}) + (e'^2 \times C_1) + (C_1 \times n_{eq}) - (C_1 \times e')}$$

$$(-(e' \times n_{eq}) + e'^2 + n_{eq} - e') \times \frac{K_{1,ZnL}}{K_{1,MnL}} = e' \times \frac{C_2}{C_1} - e' + e'^2$$

$$e'^2 \times \left(1 - \frac{K_{1,ZnL}}{K_{1,MnL}}\right) + e' \times \left(\frac{C_2}{C_1} - 1 + \frac{K_{1,ZnL}}{K_{1,MnL}}(n_{eq} + 1)\right) - n_{eq} \times \frac{K_{1,ZnL}}{K_{1,MnL}} = 0$$

Solution of the quadratic equation:

$$e' = \frac{-\frac{C_2}{C_1} + 1 - \frac{K_{1,ZnL}}{K_{1,MnL}}(n_{eq} + 1) + \sqrt{\left(\frac{C_2}{C_1} - 1 + \frac{K_{1,ZnL}}{K_{1,MnL}}(n_{eq} + 1)\right)^2 + 4 \times \left(1 - \frac{K_{1,ZnL}}{K_{1,MnL}}\right) \times n_{eq} \times \frac{K_{1,ZnL}}{K_{1,MnL}}}}{2 \times \left(1 - \frac{K_{1,ZnL}}{K_{1,MnL}}\right)}$$

$$A_{th} = \varepsilon_{MnL} C_{MnL} l + \varepsilon_{ZnL} C_{ZnL} l$$

A_{th} = Theoretical absorbance at a fixed wavelength

ε_{MnL} = molar attenuation coefficient of MnL complex at the same fixed wavelength

ε_{ZnL} = molar attenuation coefficient of ZnL complex at the same fixed wavelength

C_{ZnL} = Concentration in ZnL

C_{MnL} = Concentration in MnL

l = width of the spectrophotometer cuvette.

$$A_0 = \varepsilon_{MnL} C_1 l$$

$$A_f = \varepsilon_{ZnL} C_1 l$$

A_0 = Theoretical initial absorbance of the MnL solution

A_f = Theoretical final absorbance of the ZnL solution

$$A_{th} = C_{MnL} \times \frac{A_0}{C_1} + C_{ZnL} \times \frac{A_f}{C_1}$$

$$A_{th} = (1 - e') \times A_0 + e' \times A_f = A_0 - e' \times (A_0 - A_f)$$

With e' detailed above

VI.1.a.ii. Supplementary tables

(a)

	Zn^{2+}	Cu^{2+}	Ni^{2+}	Co^{2+}
Mn1	10.728 ± 2.671	39.150 ± 3.566	0.199 ± 0.036	0.265 ± 0.013
Mn1P	0.511 ± 0.064	1.916 ± 0.393	0.033 ± 0.004	0.119 ± 0.022
Mn1C	0.274 ± 0.028	1.496 ± 0.390	0.083 ± 0.018	0.055 ± 0.005
Mn1CP	0.028 ± 0.011	0.087 ± 0.018	0.018 ± 0.001	0.012 ± 0.005

(b)

	Zn^{2+}	Cu^{2+}	Ni^{2+}	Co^{2+}
Mn1	0.06	0.02	3.48	2.62
Mn1P	1.36	0.36	21.00	5.82
Mn1C	2.53	0.46	8.35	12.60
Mn1CP	24.76	7.97	38.51	57.76

Table S1: (a) Pseudo-first order rate constants kobs (s-1) and (b) half-lives (s) characterizing the metal exchanges occurring between the Mn^{2+} center of the SOD mimics with Zn^{2+}, Cu^{2+}, Ni^{2+} and Co^{2+}. Kinetics of the exchanges were monitored in TRIS (50 mM pH 7.5) using a stopped-flow technique in the presence of 20-fold excess of competitive metal in order to ensure pseudo-first order conditions. The exchanges were observed spectrophotometrically at room temperature and at specific wavelengths chosen to have a high difference in absorbance between the manganese complex and the competitive metal complex. The pseudo-first order rate were then obtained by fitting the theoretical time-absorbance curve to the experimental one using the Biokine32 software. Data represent mean ± SEM for three independent experiments and each independent experiments were performed in duplicates.

	[Mn1CP] in lysates (µM)	Cell concentration in lysates (cells/mL)	n_{Mn1CP} in cells (mol)
Subculture 1	1.38	7115000	$1.9.10^{-16}$
Subculture 2	1.66	5537500	$3.1.10^{-16}$
Subculture 3	2.03	5866500	$3.5.10^{-16}$

Table S2: Quantification of Mn1CP in the lysates of HT29-MD2 cells, stimulated with LPS and incubated with the complex at 100 µM for 6 hours. The quantification was achieved by mass spectrometry by means of a heavy analog of Mn1CP used as a standard. A calibration curve was previously established using this standard (see Figure S33). The molar amount of Mn1CP in each cell was then retrieved by taking into account the dilution executed during the cells' lysis. The quantification was repeated for 3 independent subcultures with different cells passage numbers. For subculture 1 and 2, the quantification was repeated respectively for 3 and 2 analytical replicates.

VI.1.a.iii. Supplementary figures

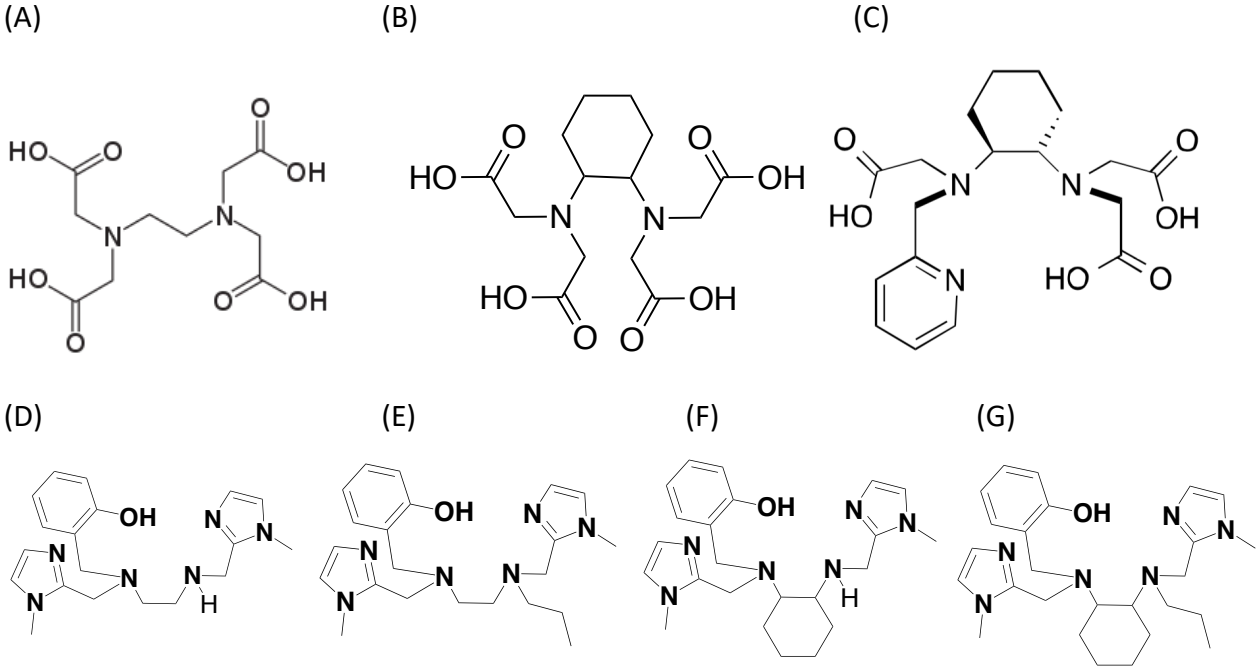

Figure S5: (A) Structure of EDTA (ethylenediamine tetraacetic acid), (B) Structure of CDTA (cyclohexanediamine tetraacetic acid), (C) Structure of PyC3A, (D) Structure of EnPI2, (E) Structure of EnPI2P, (F) Structure of EnPI2C and (G) Structure of EnPI2CP.

$\mathbf{K_{1\_Mn1} = 1.22 \pm 0.18 \times 10^6\ M^{-1}}$ $\mathbf{K_{1_{Mn1}P} = 1.035 \pm 1.795 \times 10^5\ M^{-1}}$

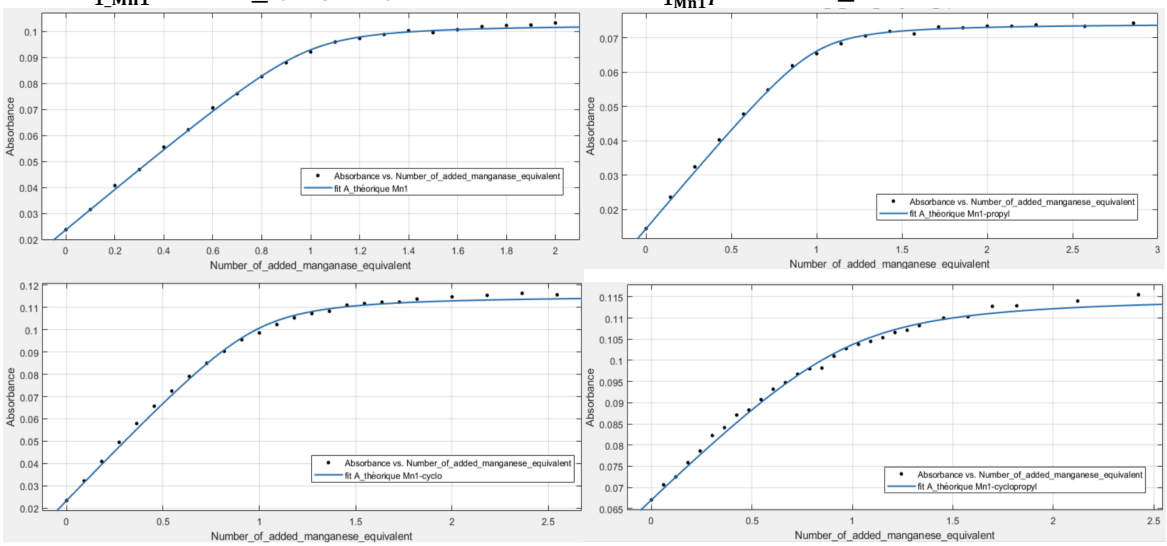

$\mathbf{K_{1_{Mn1}C} = 0.7093 \pm 1.141 \times 10^5\ M^{-1}}$ $\mathbf{K_{1_{Mn1}CP} = 0.2838 \pm 0.329 \times 10^5\ M^{-1}}$

Figure S6: Determination of the association constants K1 of the studied SOD mimics from UV-titration experiments. The absorbance of the manganese complexes (288 nm corresponding to the MLCT $O_{phenolate}$ →Mn) have been monitored while adding successively 0.1 equivalent of manganese (concentration in the cuvette equals to 4.5 µM for 0.1 eq) to a solution of ligand at 45 µM in HEPES (50 mM pH 7.6). The initial concentration in ligand was chosen in order to observe an equilibrium in solution at the 1:1 Mn:L ratio and obtain not only the stoichiometry of the reaction Mn(II) + LH —> L(Mn(II)) + H+ but also an accurate determination of the association constant. In this purpose, $C_{ligand} \times K_1$ has to be smaller than 100 (see Figure 5 (b) from P. Thordarson et. al [4] showing simulated binding isotherms for different $C_{ligand} \times K_1$ ratio's from 1–10000) [4], which is the case here. Note that when C_{ligand} = 100 K_d, the complexation equilibrium is shifted towards the complex at 90 % [4]. The absorbance was plotted as a function of the number of added manganese(II) equivalents. The association constants of the manganese complexes were then obtained by fitting the theoretical absorbance curve to the experimental one using the MATLAB curve fitting tool and based on a non-linear regression method. Blue dots correspond to the experimental data and the continuous blue line corresponds to the fit. The calculated K_1 and the associated Sum of Squares Errors (SSE) are mentioned on each plot.

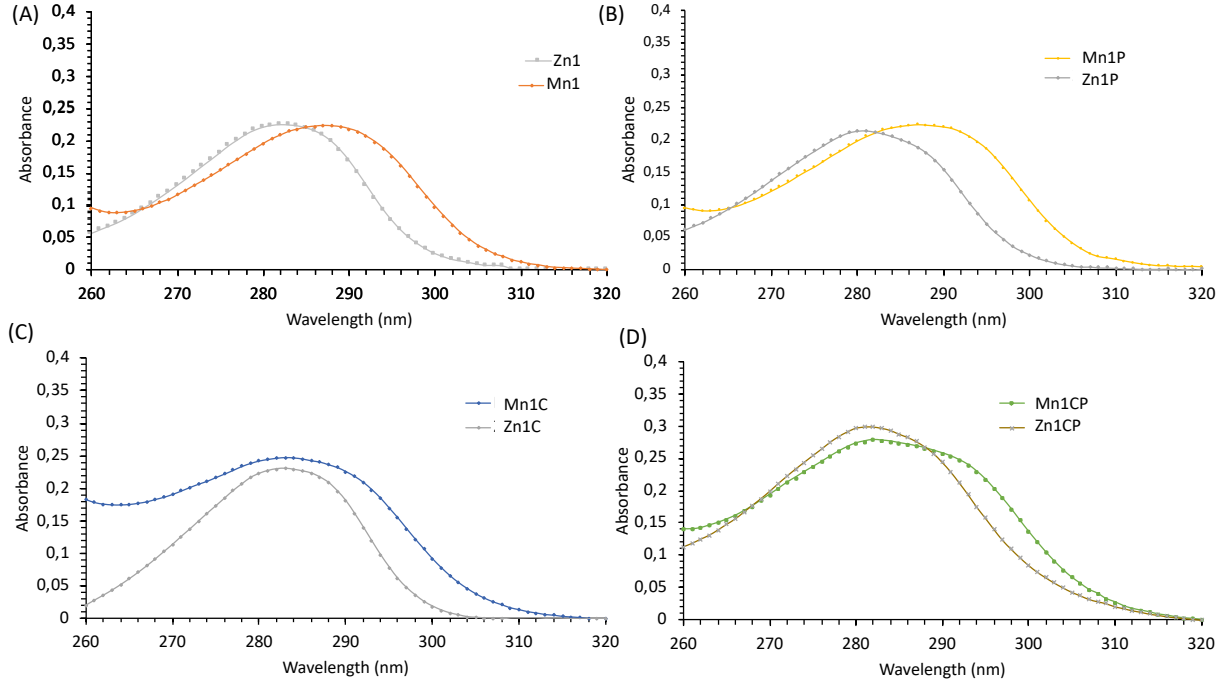

Figure S7: UV-visible spectra of (A) Mn1 and the Zn(II) complex Zn-EnPI2 labelled Zn1, (B) Mn1P and the Zn(II) complex Zn-EnPI2P labelled Zn1P, (C) Mn1C and the Zn(II) complex Zn-EnPI2C labelled Zn1C and (D) Mn1CP and the Zn(II) complex Zn-EnPI2CP labelled Zn1CP. The solutions of complexes were prepared at 100 µM in HEPES 50 mM pH 7.6, by addition of 1:1 ligand: + $MnCl_2$ or $ZnCl_2$.

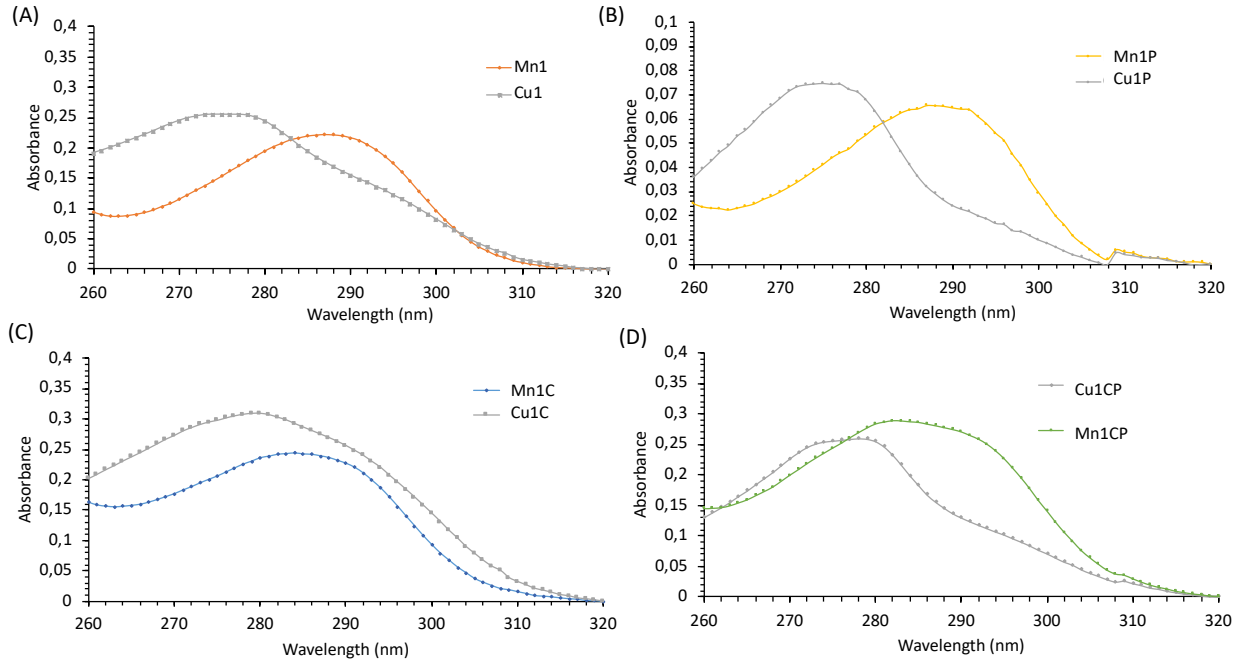

Figure S8: UV-visible spectra of (A) Mn1 and the Cu(II) complex Cu-EnPI2 labelled Cu1, (B) Mn1P and the Cu(II) complex Cu-EnPI2P labelled Cu1P, (C) Mn1C and the Cu(II) complex Cu-EnPI2C labelled Cu1C and (D) Mn1CP and the Cu(II) complex Cu-EnPI2CP labelled Cu1CP. The solutions of complexes were prepared at 100 µM in HEPES 50 mM pH 7.6 by addition of 1:1 ligand: + $MnCl_2$ or $CuSO_4$.

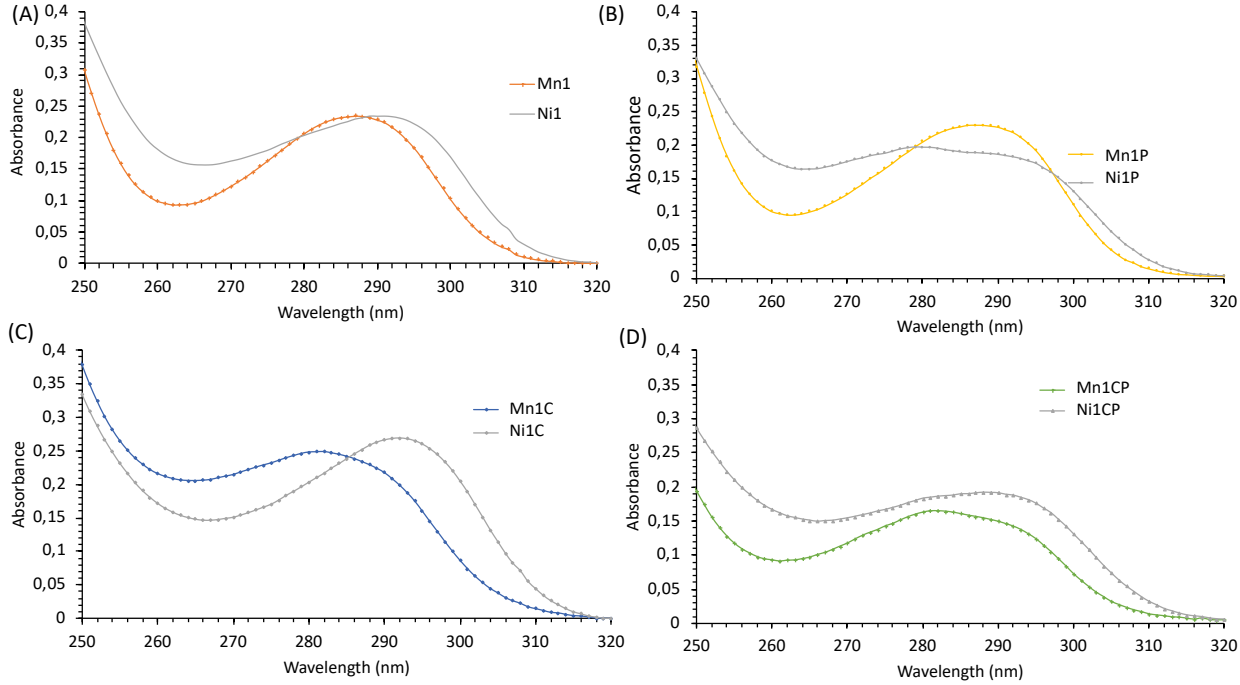

Figure S9: UV-visible spectra of (A) Mn1 and the Ni(II) complex Ni-EnPI2 labelled Ni1, (B) Mn1P and the Ni(II) complex Ni-EnPI2P labelled Ni1P, (C) Mn1C and the Ni(II) complex Ni-EnPI2C labelled Ni1C and (D) Mn1CP and the Ni(II) complex Ni-EnPI2CP labelled Ni1CP. The solutions of complexes were prepared at 100 µM in HEPES 50 mM pH 7.6 by addition of 1:1 ligand: + $MnCl_2$ or $NiCl_2$.

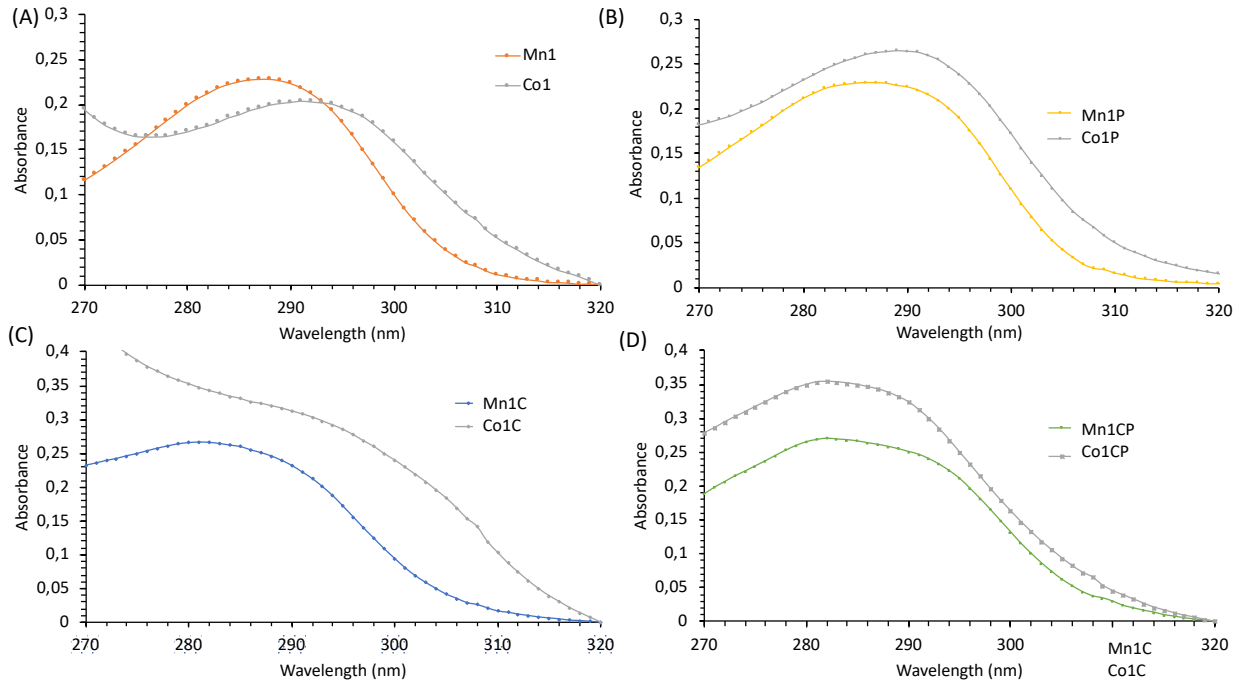

Figure S10: UV-visible spectra of (A) Mn1 and the Co(II) complex Co-EnPI2 labelled Co1, (B) Mn1P and the Co(II) complex Co-EnPI2P labelled Co1P, (C) Mn1C and the Co(II) complex Co-EnPI2C labelled Co1C and (D) Mn1CP and the Co(II) complex Co-EnPI2CP labelled Co1CP. The solutions of complexes were prepared at 100 µM in HEPES 50 mM pH 7.6 by addition of 1:1 ligand: + $MnCl_2$ or $CoCl_2$.

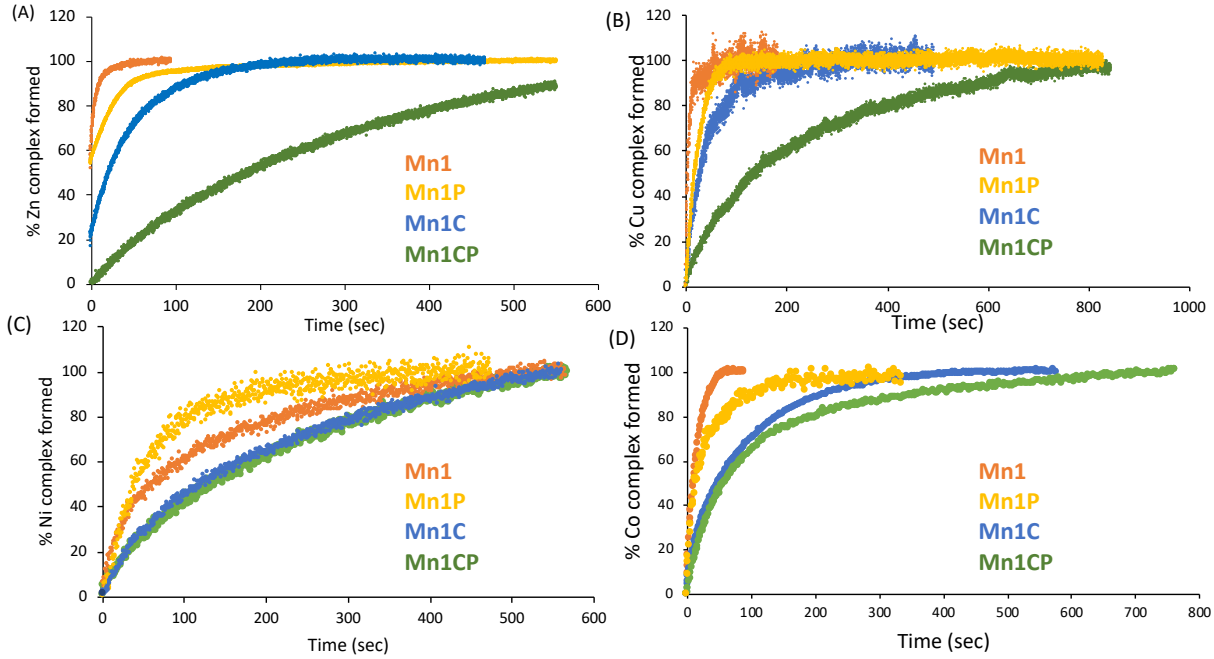

Figure S11: UV-vis kinetics study of the metal exchanges occurring between the manganese center of the SOD mimics and respectively (A) Zn^{2+} ions, (B) Cu^{2+} ions, (C) Ni^{2+} ions and (D) Co^{2+} ions present at one equivalent in solution (addition of $ZnCl_2$, $CuSO_4$, $NiCl_2.6H_2O$, or $CoCl_2$). The percentage of complexes that underwent metal exchanges was monitored spectrophotometrically by following the absorbance at a wavelength, chosen to have a noticeable difference in absorbance between the manganese complex and the exchanging ion complex: 300 nm for Zn^{2+} exchanges, 265 nm for Cu^{2+} exchanges, 300 nm for Co^{2+} exchanges (except 280 nm for Co1CP), 265 nm for Ni^{2+} exchanges. The spectra of the Mn(II) complexes and the exchanging ions complexes are given in Figure S3, S4, S5 et S6 and were used to choose these monitoring wavelengths. A solution of the SOD mimic was prepared at 0.1 mM in TRIS buffer (50 mM buffer pH 7.5) in a semi-microcuvette (1.5 mL). One equivalent of competitive metal was then added in the microcuvette and after a quick stirring, the absorbance was measured for around 10 minutes. For (A), (B) and (D), the experiments were performed at 5°C as the metal exchanges were too fast at 25°C preventing any kinetic study. For Ni^{2+} exchanges study, the temperature was maintained at 25°C.

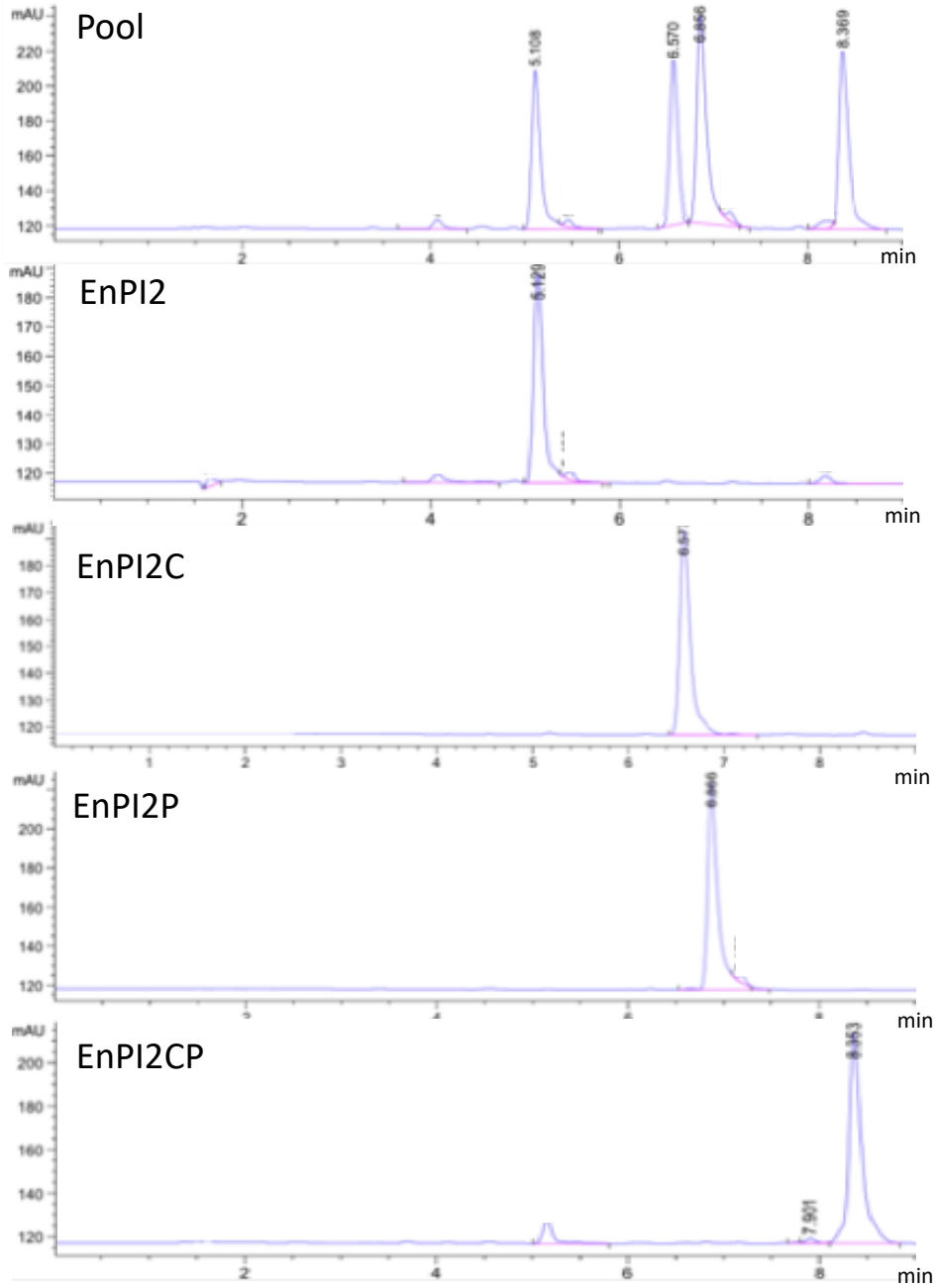

Figure S12: HPLC analysis of the four EnPI2-derivated ligands on a C_{18} column using a gradient of ACN in H_2O from 5 % to 50 % in water over 10 minutes. Both solvents contained TFA (0.1 %). Pool: the four ligands were pooled at 1 mM and injected altogether in the chromatographic system. They were also injected separately at 1 mM to assign the peaks previously visualized in the pooled sample.

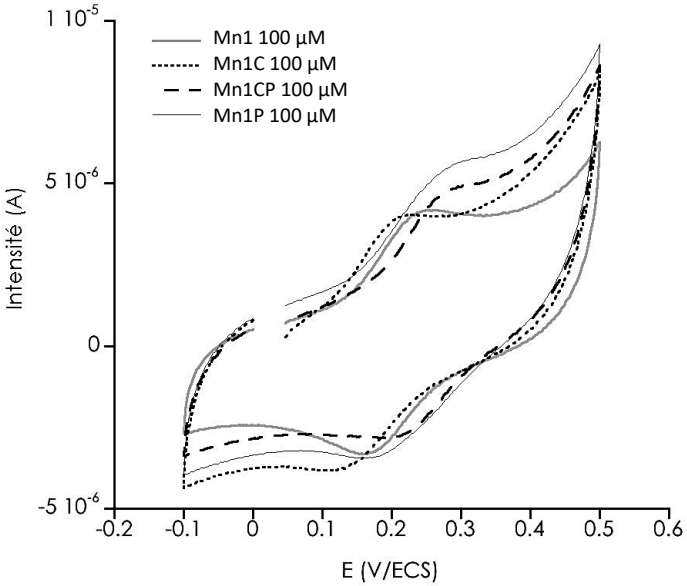

Figure S13: Cyclic voltammograms of the SOD mimics at 100 µM in HEPES (50 mM, pH 7.5, ionic strength = 12.5 mM) at a glassy carbon working electrode (3 mm diameter) with a scan rate of 500 mV/sec. Experiments are carried out under an argon stream at room temperature. The electrochemical apparatus contained a platinum wire counter electrode and an aqueous calomel electrode saturated with KCl (SCE) as the reference electrode (0.241 V + SCE = normal hydrogen electrode).

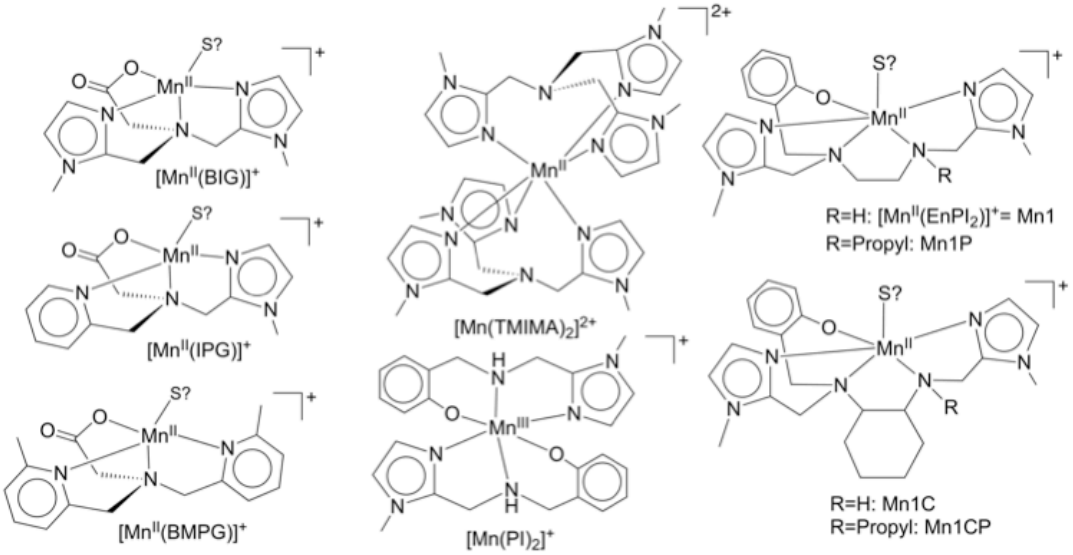

Figure S14: Mn(II)-complexes bio-inspired from SOD. See also [5].

(A)

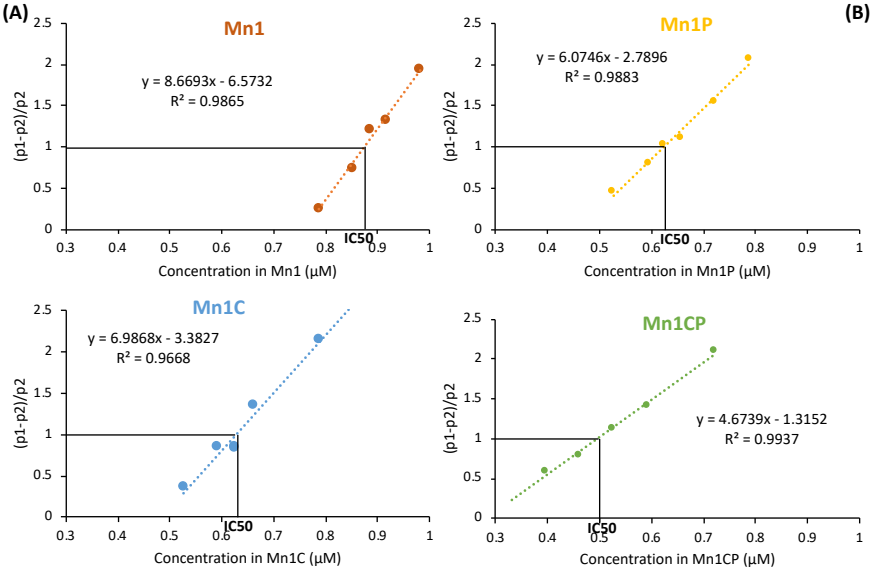

(B)

	IC_{50} (µM)	k_{cat} (10^6 $M^{-1}s^{-1}$)
Mn1	0.854 ± 0.025	3.40 ± 0.10
Mn1P	0.633 ± 0.001	4.58 ± 0.01
Mn1C	0.662 ± 0.019	4.38 ± 0.13
Mn1CP	0.537 ± 0.024	5.41 ± 0.24

Figure S15: McCord and Fridovich assays of SOD mimics performed at pH 7.4 in HEPES 50 mM with the use of XTT as redox competitive indicator. [XTT]= 100 µM. The XTT absorbance at 470 nm is measured over time in absence and in presence of SOD mimics. The slope of the absorbance increase is measured in absence (p1) and in presence (p2) of the SOD mimic.
(A) The ratio (p1-p2)/p2 is plotted as a function of the SOD mimics concentration (dots). The IC_{50} can be extrapolated from the linear regression of this curve (line) by determining the concentration for which (p1-p2)/p2 is equal to 1 ($p1 = 2 * p2$).
(B) Table classifying the SOD mimics IC_{50} and their catalytic constants for superoxide dismutation. IC_{50} is the concentration in SOD mimic at which the reaction rate of the XTT indicator is reduced of 50 % that without any SOD mimic. k_{cat} values were calculated from that of XTT (equal to $2.9.10^4$ $M^{-1}s^{-1}$) and from the SOD mimics IC_{50}: $k_{cat} = k_{XTT}*[XTT]/IC_{50}$ [5,6]. The lower the IC_{50} for the SOD mimics, the higher is the catalytic rate constant for superoxide dismutation. The experiments were repeated twice and the results given here represent the mean ± the standard deviation.

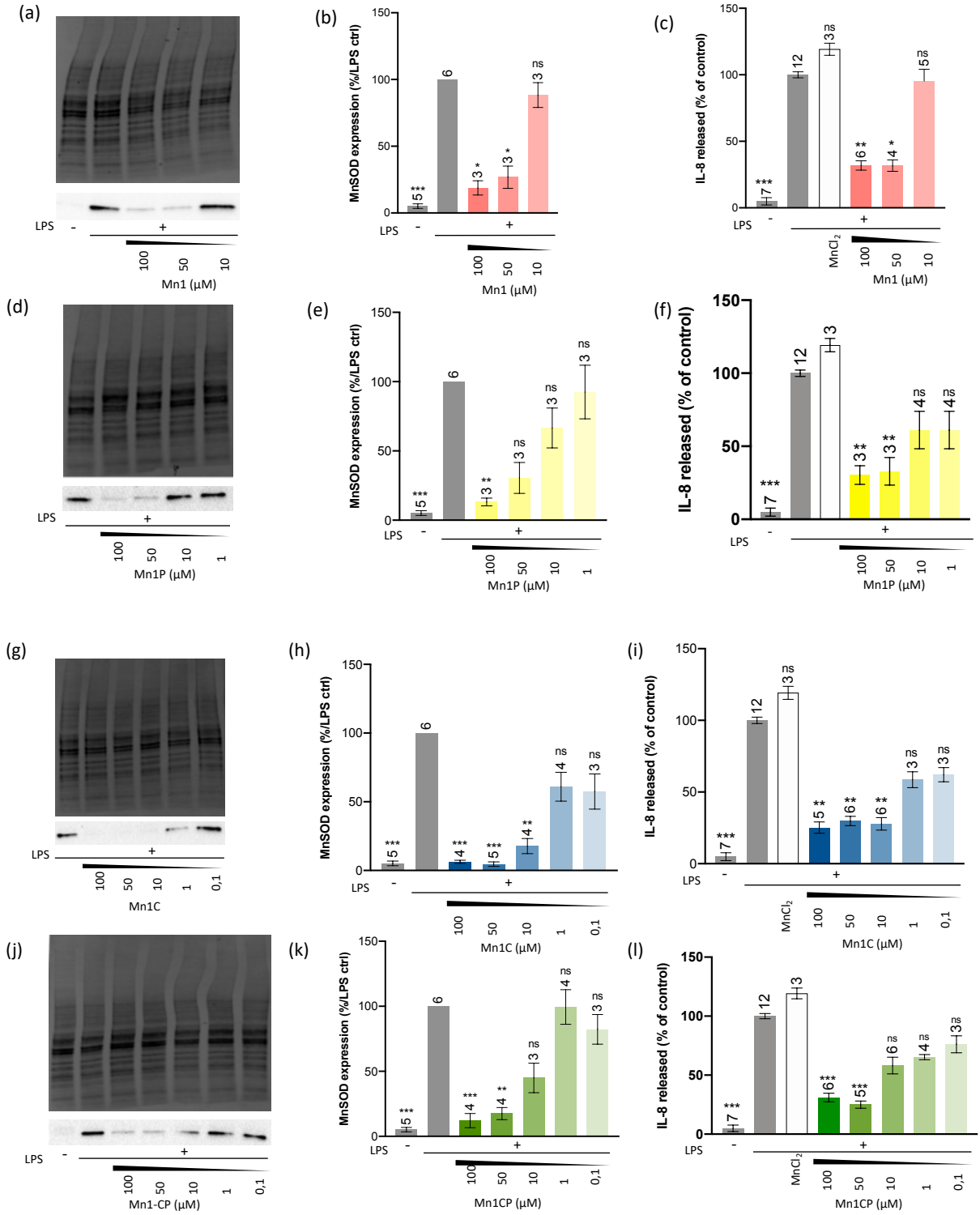

Figure S16: Evaluation of the antioxidant and anti-inflammatory activity of Mn1, Mn1C, Mn1P and Mn1CP in intestinal epithelial cells HT29-MD2 activated with LPS (0.1 µg/mL)
(a,d,g,j) Bottom: representative Western blots of MnSOD expression in HT29–MD2 cells incubated for 6 hours with (a) Mn1, (b) Mn1C, (c) Mn1P and (d) Mn1CP at different concentrations, without (-) and with (+) LPS. Top: stain-free blot imaging showing the total proteins for the same samples.
(b,e,h,k) Quantification of MnSOD expression. MnSOD expression was measured by Western blot in lysates of LPS-activated HT29–MD2 cells incubated for 6 hours with (b) Mn1, (e) Mn1P, (h) Mn1C and (k). Mn1CP at different concentrations. The MnSOD expression intensity measured for activated cells was set at 100 %. The abundances of MnSOD were normalized to the total amount of protein in each lane (top panels a,d,g,j).

(c,f,i,l) Quantification of the inflammatory marker IL-8. IL-8 secretion was measured by ELISA in supernatant of HT29–MD2 cells incubated for 6 hours with (c) Mn1, (f) Mn1P, (i) Mn1C and (l) Mn1CP at different concentrations, without (-) and with (+) LPS and compared to $MnCl_2$ (100 µM)
MnSOD expression and IL-8 secretion data represent mean ± SEM for at least three independent experiments: the number of independent experiments is indicated above each column. The p-values were calculated using the student test (bilateral test with equal variances not assumed). The mean rank of each column was compared to that of the LPS control, each comparison stands alone. (***) $p < 0.001$, (**) $p < 0.01$ and (*) $p < 0.05$ versus LPS control, and ns means non-significant. Without LPS, no significant differences were observed between all of these conditions (see Figure S15).

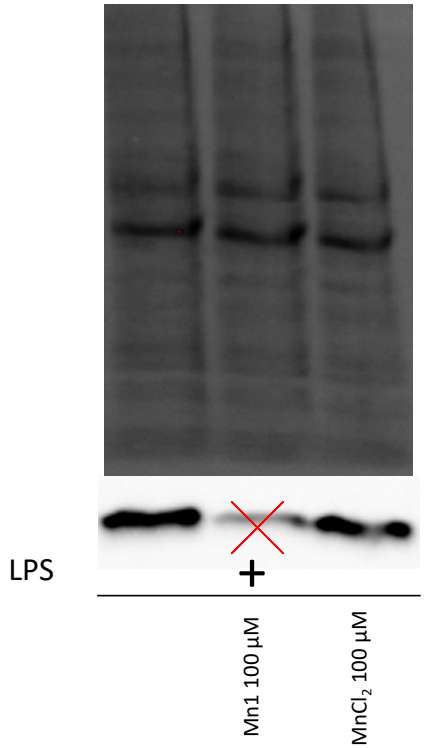

Figure S17: Evaluation of the antioxidant activity of $MnCl_2$ incubated at 100 µM in intestinal epithelial cells HT29-MD2 activated with LPS (0.1 µg/mL). Bottom: representative Western blot of MnSOD expression in HT29–MD2 cells incubated for 6 hours with $MnCl_2$ at 100 µM with (+) LPS. Top: stain-free blot imaging showing the total proteins for the same samples. Red cross: lane of the gel that is not commented here.
By setting the MnSOD expression intensity measured for LPS control at 100 %, the intensity for $MnCl_2$ 100 µM is equal to 98% that of the LPS control. $MnCl_2$ do not have any effect on the LPS-induced overexpression of MnSOD when incubated at 100 µM. This confirms the requirement of the manganese (II) complexation. The ligands allow to tune the redox potential of Mn(III)/Mn(II) in the appropriate range to obtain SOD activity. The abundance of MnSOD were normalized to the total amount of protein in each lane.

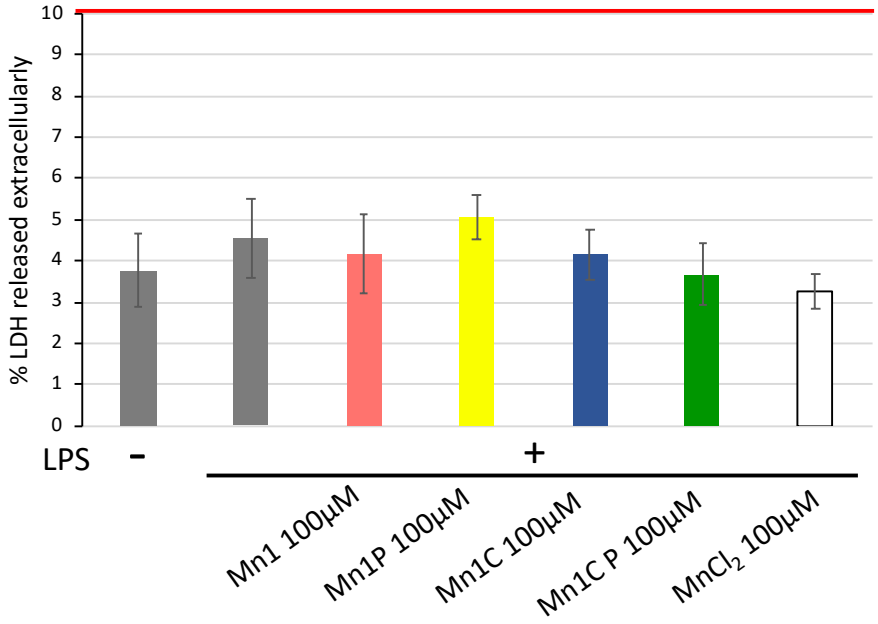

Figure S18: Evaluation of the cytotoxicity induced by the SOD mimics using the LDH assay. LPS-activated HT29-MD2 cells were incubated with the SOD mimics at 100 µM for 6 hours and the cytotoxicity of the compounds was tested by following the release of the cytosolic lactate dehydrogenase (LDH) into the supernatant, indicative of cell membrane damages. LDH activity can be measured based on LDH ability to catalyze the reduction of pyruvate into lactate in presence of NADH absorbing at 340 nm, which is oxidized to form NAD^+. The decrease in absorbance at 340nm due to NADH consumption can be assimilated to LDH activity and eventually the percentage of LDH release can be obtained by dividing the LDH activity in supernatant by the sum of activity in supernatants and cell lysates. Data represent the % of LDH released extracellularly (mean of at least 2 independent experiments). The percentage of LDH released in supernatants were always below 10% (which were chosen as the limit of noncytotoxicity) and in average below 5% for all SOD mimics. We can conclude that none of the SOD mimics induce meaningful cytotoxicity at 100 µM in HT29-MD2 cells when prepared with a 1.4:1 manganese-to-ligand ratio 2 hours before adding to the culture medium.

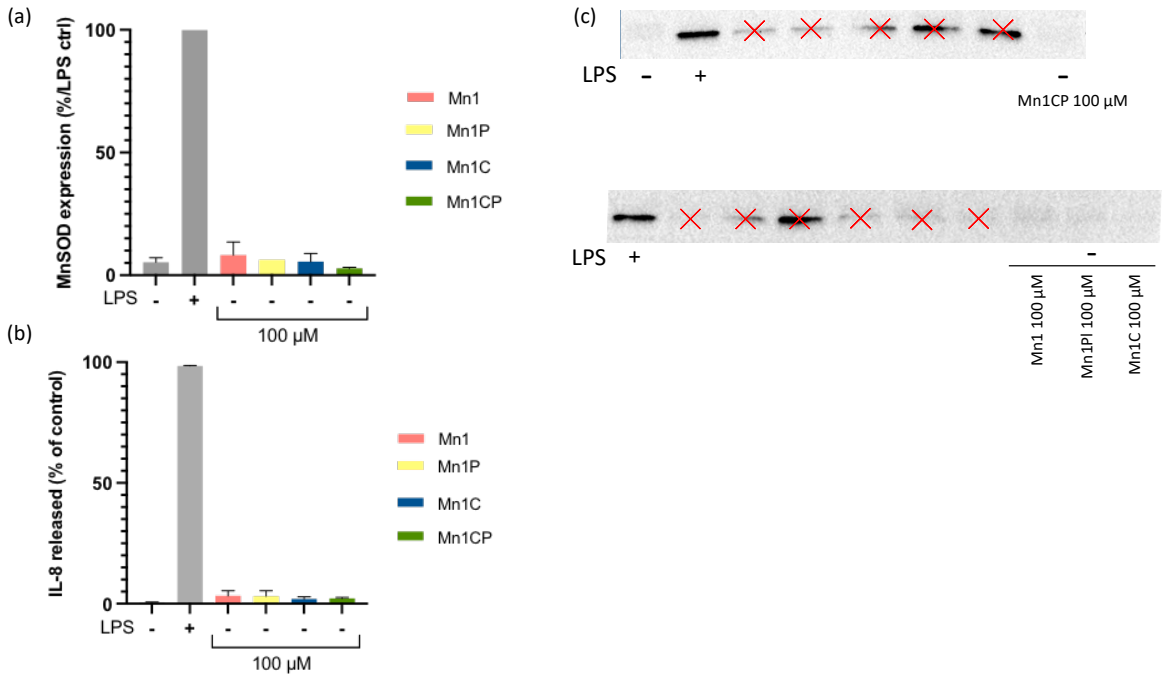

Figure S19: Quantification of IL-8 secretion and of MnSOD expression in controls without LPS. MnSOD expression was measured by Western blot in lysates of non-activated HT29−MD2 cells incubated with the four SOD mimics for 6 hours. The MnSOD expression intensity measured for activated cells is set at 100 %. The abundance of MnSOD were normalized to the total amount of protein in each lane. IL-8 secretion was measured by ELISA in supernatant of non-activated HT29−MD2 cells incubated for 6 hours with the four SOD mimics at 100 µM. The IL-8 amount measured for activated cells is set at 100 %.
(a) and (b) Data represent mean ± SEM for at least two independent experiments (except only one independent experiment for (a)-Mn1P). (c) Representative western blot analysis of MnSOD expression in controls without LPS. Red crosses: lane of the gel that are not commented here

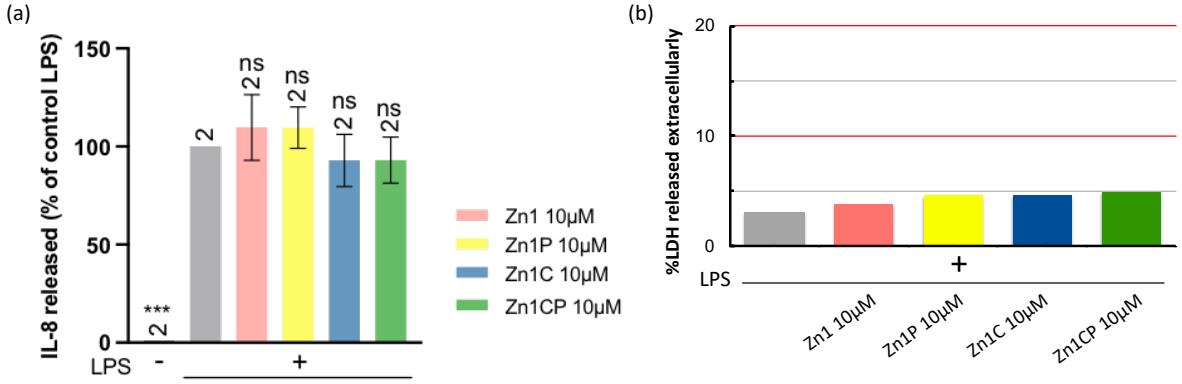

Figure S20: Evaluation of the anti-inflammatory activity and of the cytotoxicity of the four zinc complexes in intestinal epithelial cells activated with LPS (0.1 µg/mL)

- *(a) Quantification of the inflammatory marker IL-8 by ELISA in supernatant of LPS-activated HT29−MD2 cells incubated for 6 hours with the Zn(II) complexes at 10 µM. The IL-8 amount measured for activated cells is set at 100 %. Data represent mean ± SEM: the number of independent experiments is indicated above each column. Each independent experiments was performed in duplicates. The p-values were calculated using the student test (bilateral test with equal variances not assumed). The mean rank of each column was compared to that of the LPS control, each comparison stands alone. (***) $p < 0.001$, (**) $p < 0.002$ and (*) $p < 0.033$ versus LPS control, and ns means non-significant.*
- *(b) The cytotoxicity of the Zn(II) complexes at 10 µM in LPS-activated HT29-MD2 cells was tested by using the LDH assay. Data represent the % of LDH released extracellularly (mean of 2 independent experiments). The percentage of LDH released in supernatants were always below 10 % and in average below 5% for all zinc complexes mimics, showing that they do not induce meaningful cytotoxicity.*

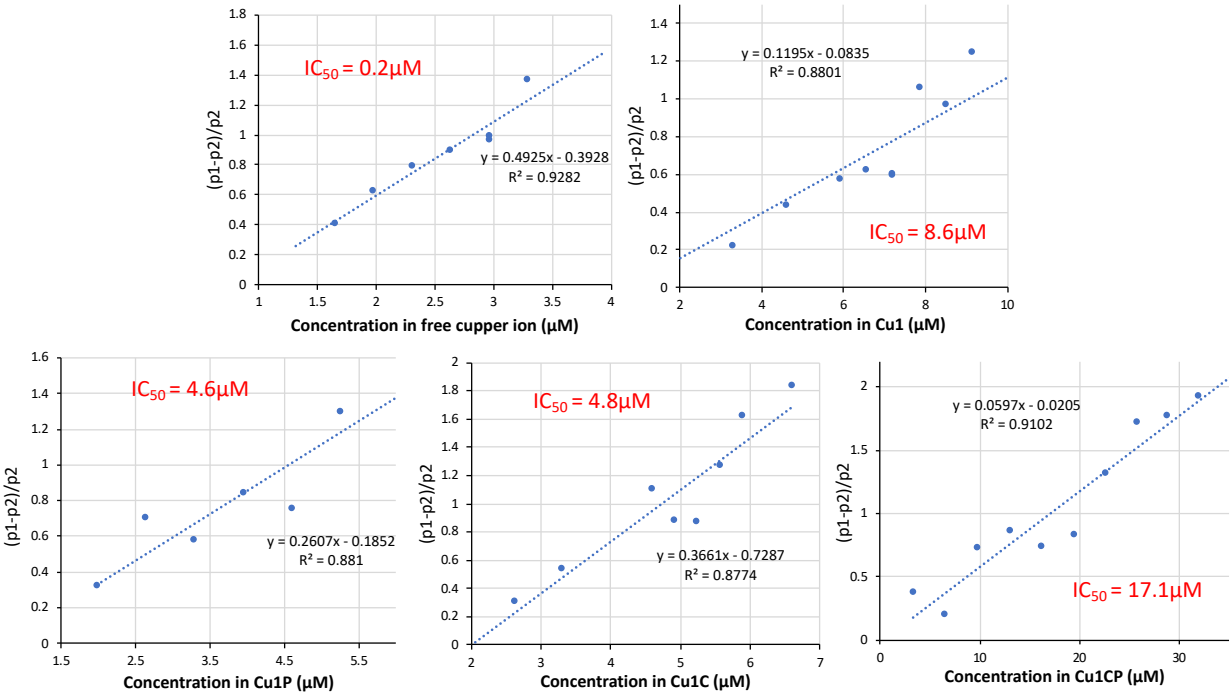

Figure S21: McCord and Fridovich assays of Cu-complexes and free Cu2+ performed at pH 7.4 in HEPES 50 mM with the use of XTT as redox competitive indicator. [XTT]= 100 µM. The XTT absorbance at 470 nm is measured over time in absence and in presence of Cu-complexes. The slope of the absorbance increase is measured in absence (p1) and in presence (p2) of the Cu-complexes. The ratio (p1-p2)/p2 is plotted as a function of the Cu-complex concentration (dots). The IC_{50} can be extrapolated from the linear regression of this curve (line) by determining the concentration for which (p1-p2)/p2 is equal to 1 ($p1 = 2 * p2$). Calculated IC_{50} are given in red on each graph.

	LPS	Control	Mn1 100µM	Mn1 10µM	Mn1P 100µM	Mn1P 10µM	Mn1C 100µM	Mn1C 10µM	Mn1CP 100µM	Mn1CP 10µM
LPS	x	ns	*	ns	***	ns	*	ns	*	ns
Control		x								
Mn1 100µM			x	*	ns		ns		ns	
Mn1 10µM				x		ns		ns		ns
Mn1P 100µM					x	*	ns		ns	
Mn1P 10µM						x		ns		ns
Mn1C 100µM							x	ns	ns	
Mn1C 10µM								x		ns
Mn1CP 100µM									x	*
Mn1CP 10µM										x

	LPS	Control	Mn1 100µM	Mn1 10µM	Mn1P 100µM	Mn1P 10µM	Mn1C 100µM	Mn1C 10µM	Mn1CP 100µM	Mn1CP 10µM
LPS	x	0,3736	0,049	0,5477	0,0009	0,5084	0,0333	0,4747	0,0457	1778
Control		x								
Mn1 100µM			x	0,022	0,229		0,232		0,96	
Mn1 10µM				x		0,929		0,3549		0,7942
Mn1P 100µM					x	0,0102	0,0893		0,2553	
Mn1P 10µM						x		0,3647		0,6548
Mn1C 100µM							x	0,0699	0,2612	
Mn1C 10µM								x		0,2913
Mn1CP 100µM									x	0,0259
Mn1CP 10µM										x

Figure S22: Statistical results of manganese quantification by ICP-MS in LPS-activated HT29-MD2 cells incubated with the 4 studied SOD mimics at 10µM and 100µM for 6 hours. A two-by-two comparison was achieved by using a student test (bilateral test with equal variances not assumed). The calculated p-values are given in the right table. Asterisk annotations for significance are given in the left table with the following threshold level (***) $p < 0.001$, (**) $p < 0.01$ and (*) $p < 0.05$.

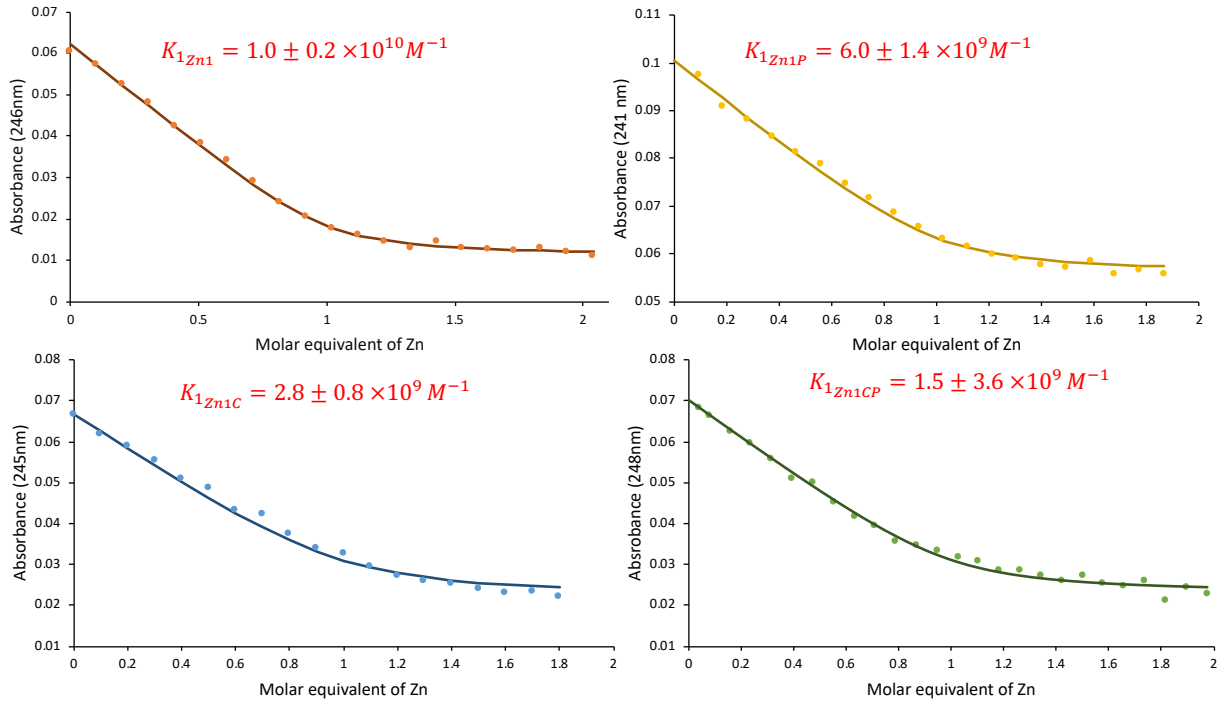

Figure S23: Determination of the association constants K_1 of the studied ligands with Zn(II) from competition experiments in HEPES 50 mM pH 7.5. The direct measure of K_1 for Zn(II) complexes was not possible because the K_1 values are too high which would impose to use a very low concentration for the titration at which the absorbance is too small to be precisely measured by a classical spectrophotometer. The absorbance of the Zn(II) complex have been monitored while adding successively 0.1 equivalent of Zn(II) ($ZnCl_2$) to a solution of manganese complex at 10 µM.

The initial concentration in manganese complex is very low in order to observe an equilibrium in solution and obtain not only the stoichiometry but also the association constant. The initial solution was prepared by adding 200 equivalents of manganese (2 mM) to a solution of ligand at 10 µM. The addition of a large excess of manganese is necessary to 1) make the assumption that the concentration of ligand is null (see calculation of $K_{1,ZnL}$ in supplementary information), 2) to shift the equilibrium to the formation of the Mn(II) complex and disfavored the Zn(II) complex that is very thermodynamically favored.

The absorbance is plotted as a function of the number of added Zn(II) equivalents. The association constant of the zinc complexes were then obtained by fitting the theoretical absorbance curve to the experimental one using the MATLAB curve fitting tool based on a non-linear least-square regression method (see calculation of $K_{1,ZnL}$ in supplementary information). Dots correspond to the experimental data and the continuous line correspond to the fit. The calculated K_1 and the associated Sum of Squares Errors (SSE) are mentioned on each plot.

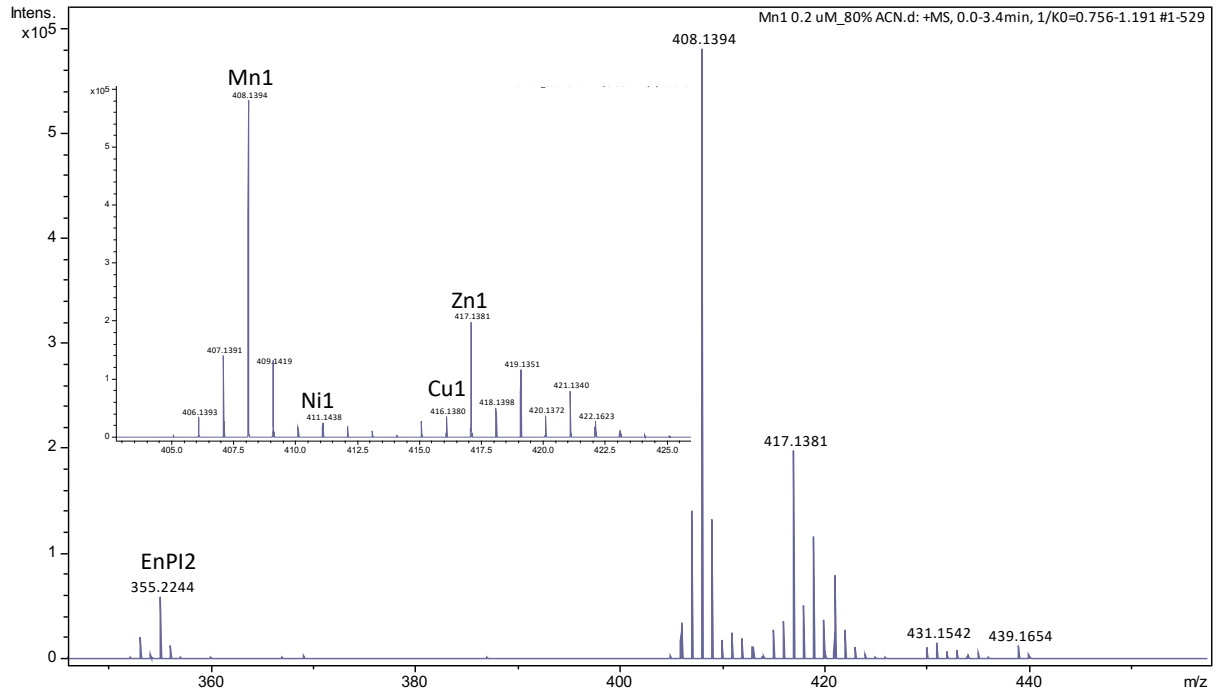

Figure S24: Mass spectrum of Mn1 diluted at 0.2 µM in 20% NH_4CO_3/ 80% ACN. The figure was zoomed onto the m/z region containing the studied complex.

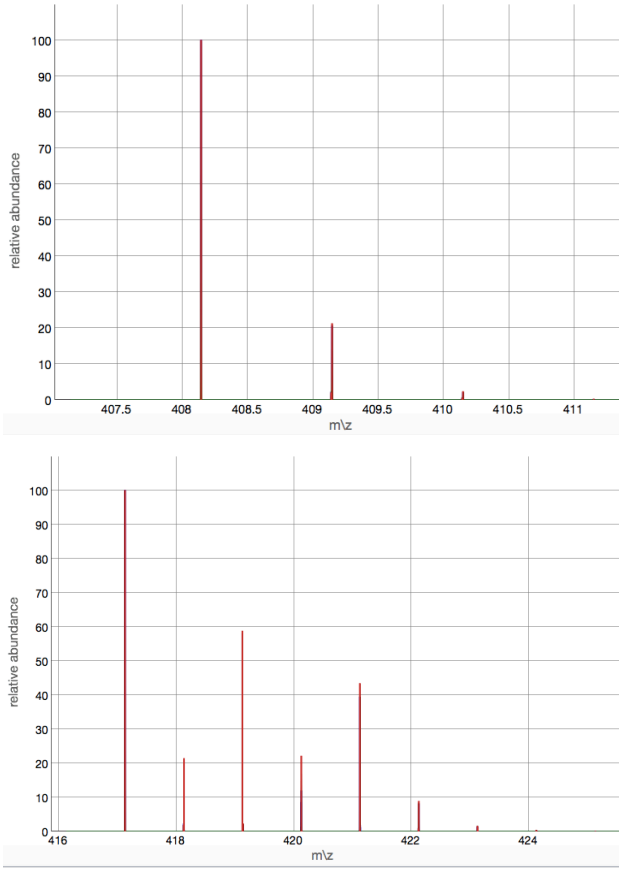

Figure S25: Predicted isotopic patterns of Mn1 (left) and Zn1 (right).

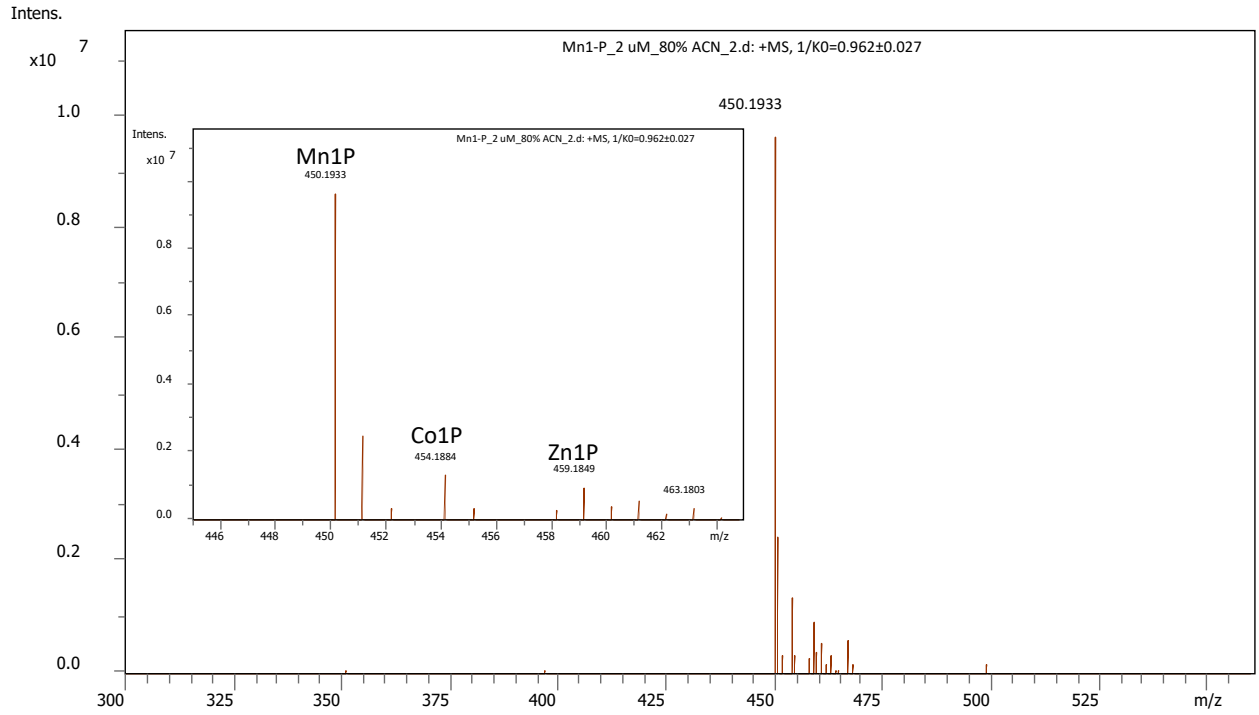

Figure S26: Mass spectrum of Mn1P diluted at 2 µM in 20% NH_4CO_3/ 80% ACN. The figure was zoomed onto the m/z region containing the studied complex.

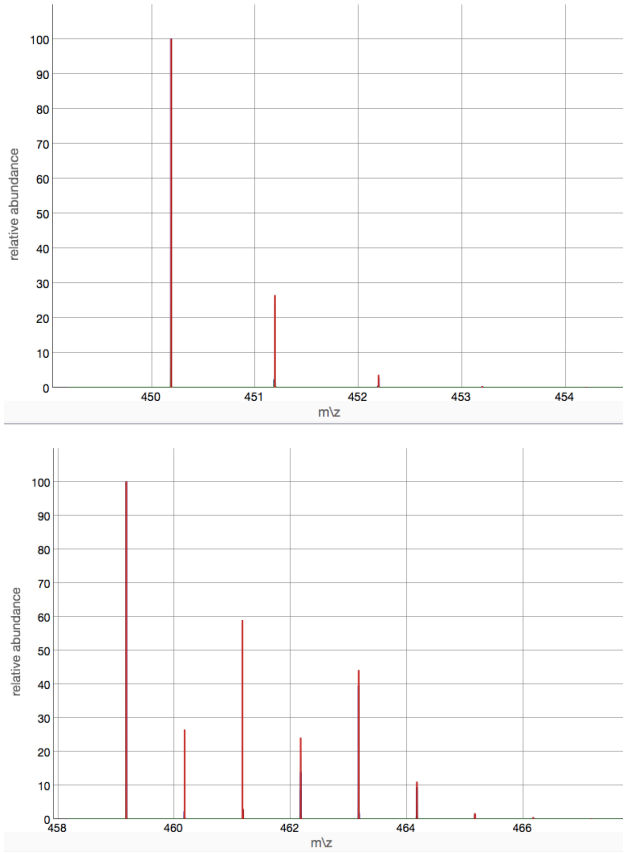

Figure S27: Predicted isotopic patterns of Mn1P (left) and Zn1P (right).

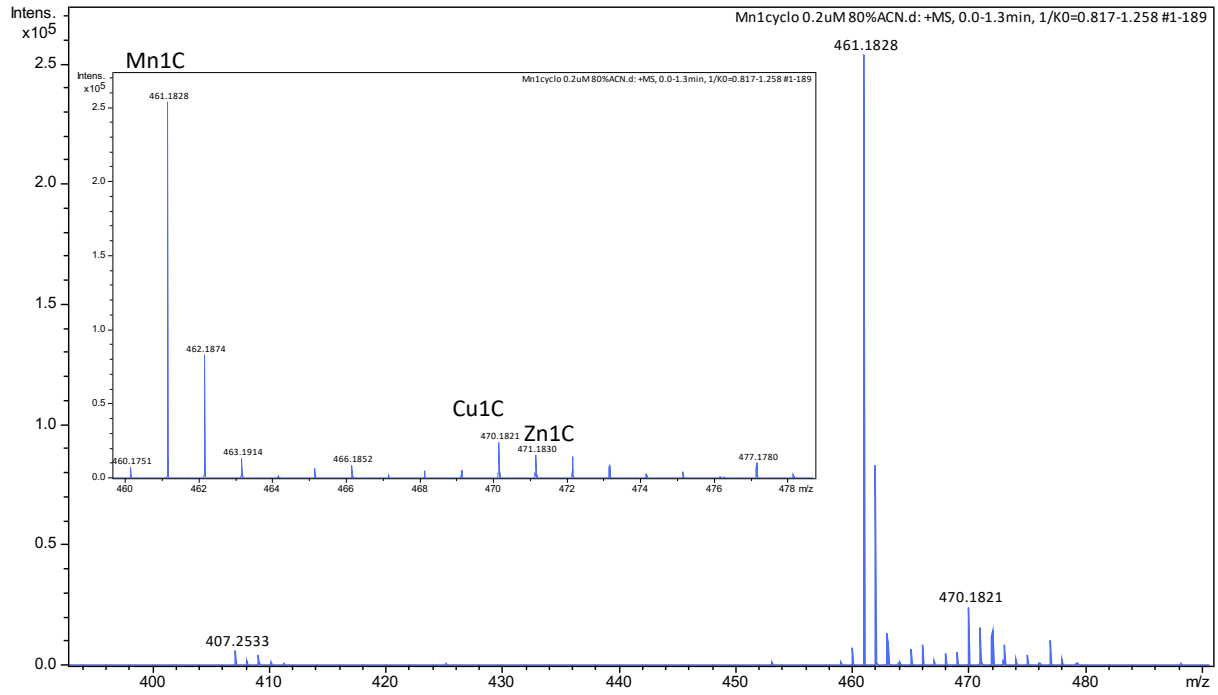

Figure S28: Mass spectrum of Mn1C diluted at 0.2 µM in 20% NH_4CO_3/ 80% ACN. The figure was zoomed onto the m/z region containing the studied complex.

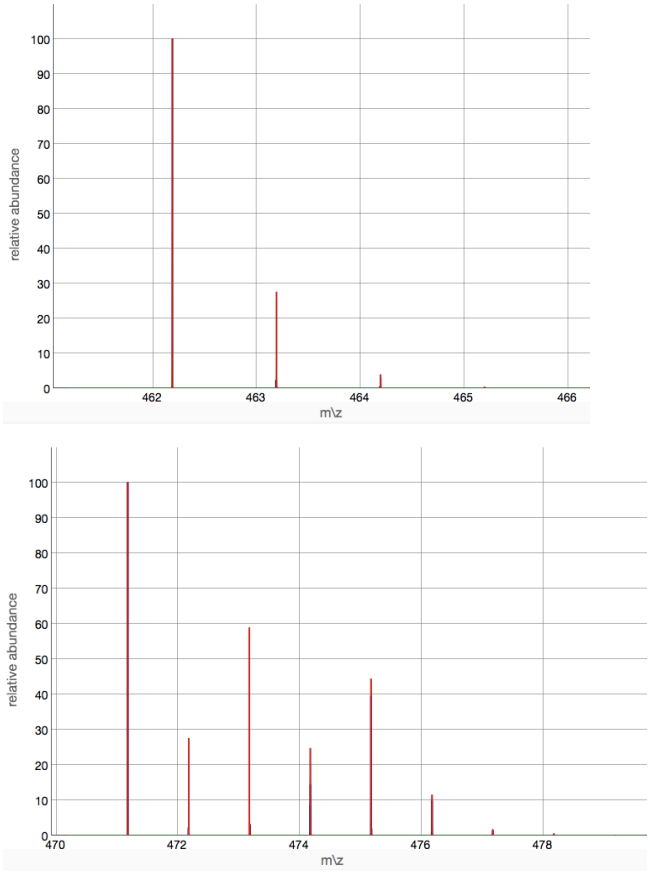

Figure S29: Predicted isotopic patterns of Mn1C (left) and Zn1C (right).

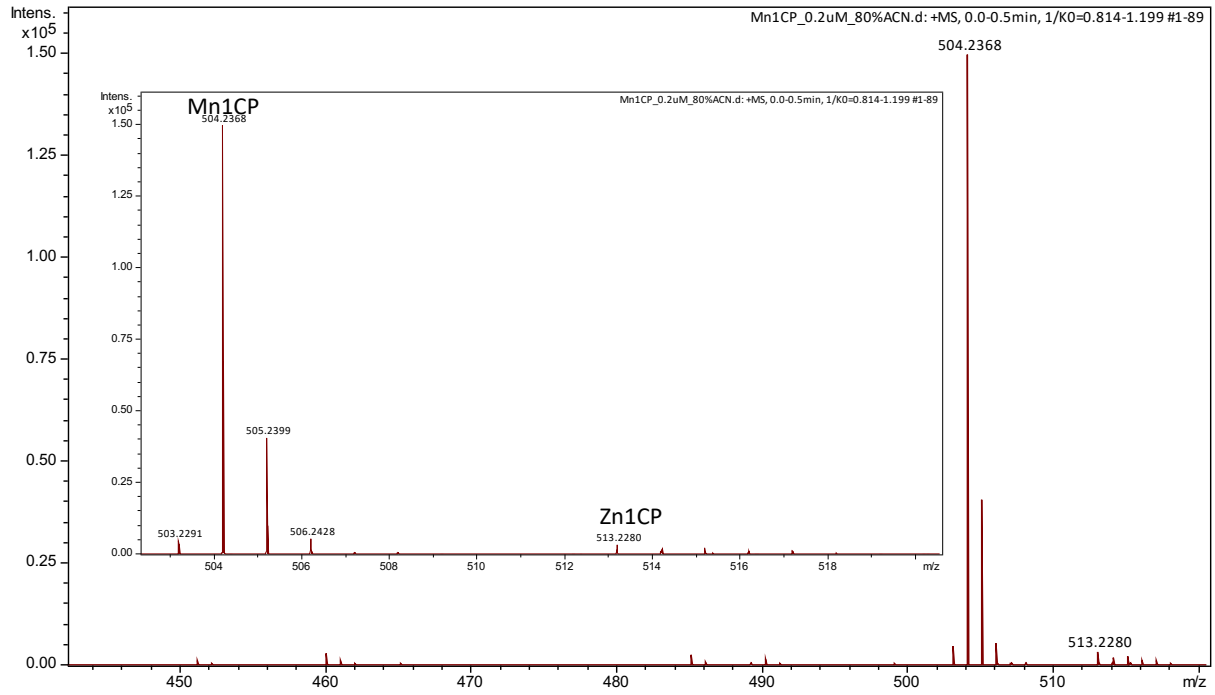

Figure S30: Mass spectrum of Mn1CP diluted at 0.2 µM in 20% NH_4CO_3/ 80% ACN. The figure was zoomed onto the m/z region containing the studied complex.

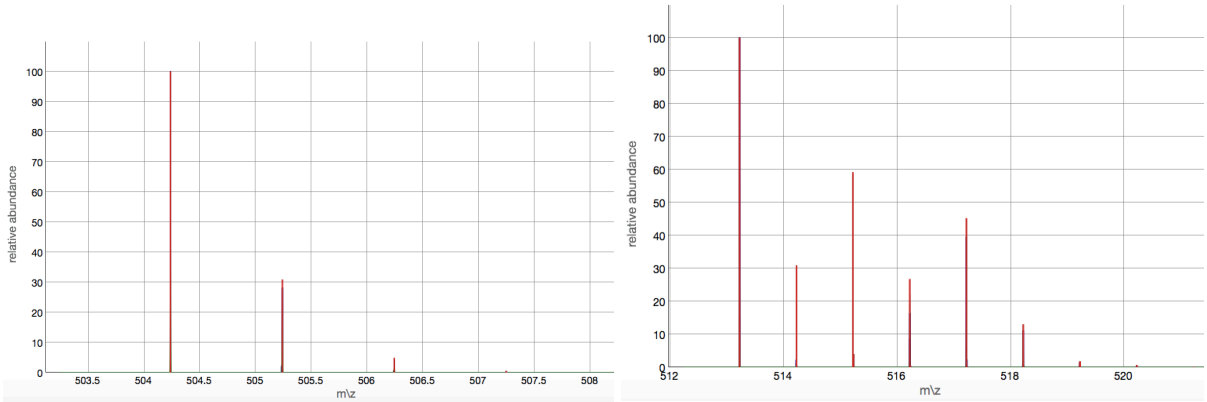

Figure S31: Predicted isotopic patterns of Mn1CP (left) and Zn1CP (right).

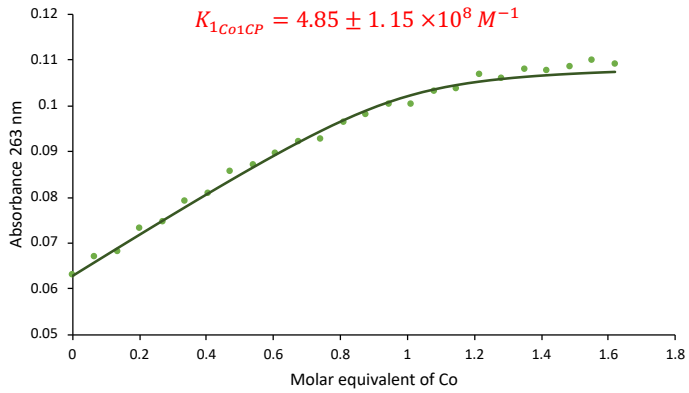

Figure S32: Determination of the association constants K_1 of EnpI2CP ligand with Co(II) from competition experiments with Mn1CP in HEPES (50 mM pH 7.5). The direct measure of K_1 for Co(II) complexes is not possible because the K_1 value is too high which would impose to use a very low concentration for the titration, at which the absorbance would be too small to be precisely measured by a classical spectrophotometer. The absorbance of the Co(II) complex have been monitored while adding successively 0.1 equivalent of Co(II) ($CoCl_2$) to a solution of manganese complex at 40 µM.
The initial concentration in manganese complex is very low in order to observe an equilibrium in solution and obtain not only the stoichiometry but also the association constant. The initial solution was prepared by adding 50 equivalents of manganese (2 mM) to a solution of ligand at 40 µM. The addition of a large excess of manganese is necessary to 1) make the assumption that the concentration of ligand is null, 2) to hinder the formation of the cobalt complexes that is very thermodynamically favored.
The absorbance is plotted as a function of the number of added Co(II) equivalents. The association constant of the Co(II) complexes were then obtained by fitting the theoretical absorbance curve to the experimental one using the MATLAB curve fitting tool based on a non-linear least-square regression method. Dots correspond to the experimental data and the continuous line correspond to the fit. The calculated K_1 and the associated Sum of Squares Errors (SSE) are mentioned on the plot.

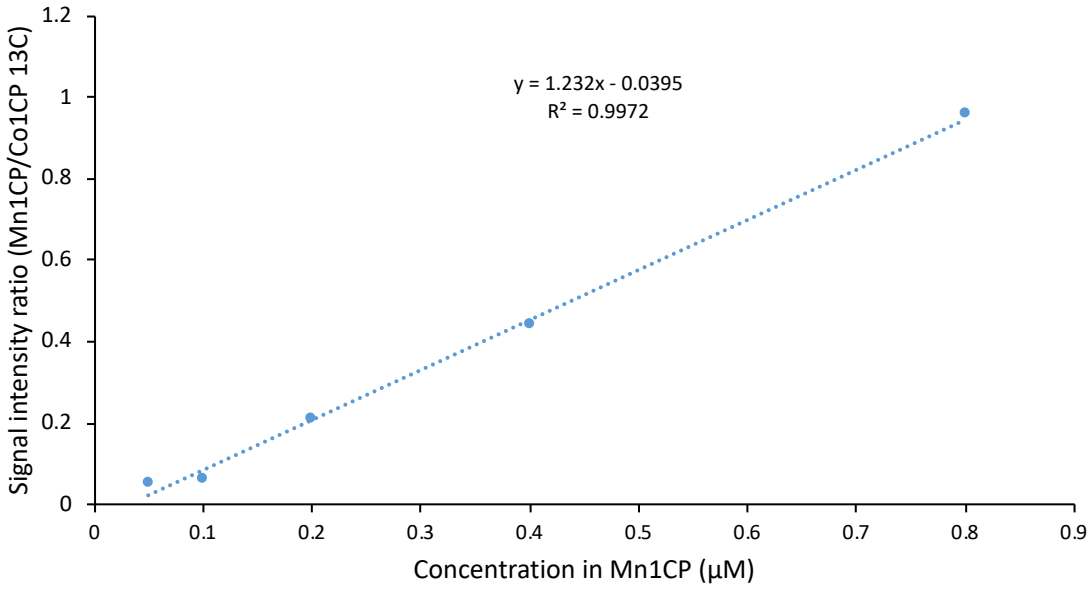

Figure S33: Calibration curves for Mn1CP quantification obtained in cell lysates diluted in 20% NH_4CO_3/ 80% ACN. The calibration curve was obtained by spiking LPS-stimulated HT29-MD2 lysates with the standard at 0.4 µM and with Mn1CP at concentrations varying between 0.05 µM to 0.8 µM. The ratio of the signal intensity of Mn1CP on that of the standard were plotted as a function of Mn1CP concentration. The signal intensity of both Mn1CP and the standard were obtained by summing the peak intensity of the complexes and their first isotopes.

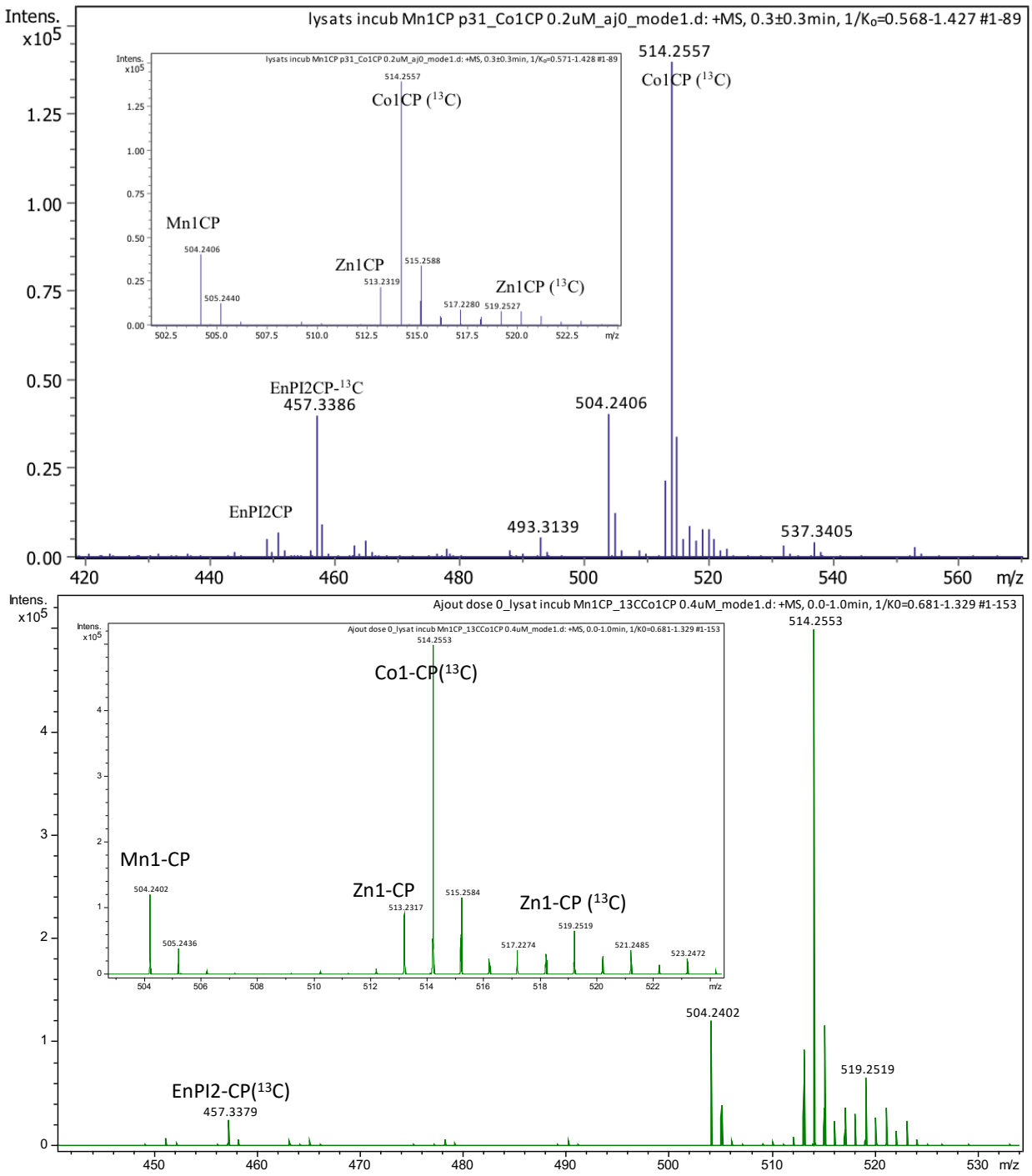
lysats incub Mn1CP p31_Co1CP 0.2uM_aj0_mode1.d: +MS, 0.3±0.3min, 1/K₀=0.568-1.427 #1-89
Intens.
x10^5
514.2557
Co1CP (13C)
Mn1CP
504.2406
Zn1CP
513.2319
515.2588
Zn1CP (13C)
517.2280
519.2527
EnPI2CP-13C
457.3386
504.2406
EnPI2CP
493.3139
537.3405
m/z
Ajout dose 0_lysat incub Mn1CP_13CCo1CP 0.4uM_mode1.d: +MS, 0.0-1.0min, 1/K0=0.681-1.329 #1-153
514.2553
Co1-CP(13C)
Mn1-CP
504.2402
Zn1-CP
513.2317
515.2584
Zn1-CP (13C)
519.2519
517.2274
521.2485
523.2472
504.2402
519.2519
EnPI2-CP(13C)
457.3379

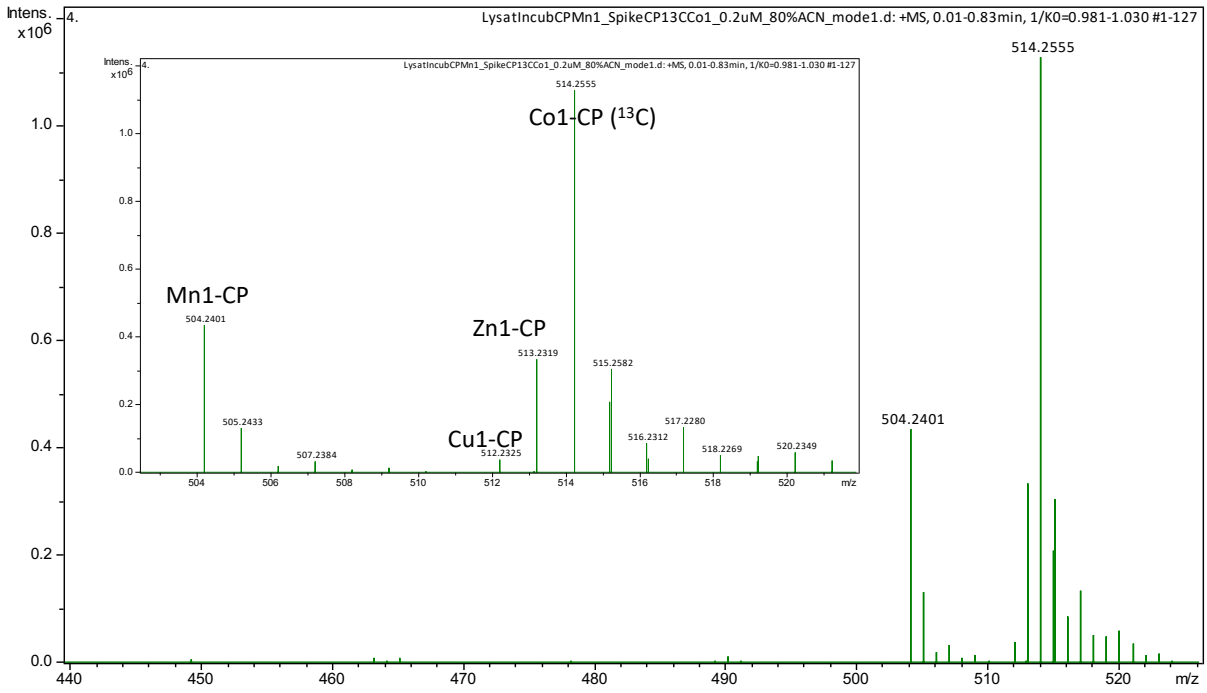

Figure S34: Examples of mass spectra of a LPS-stimulated HT29-MD2 lysates, previously incubated with the SOD mimic Mn1CP for 6 hours and ultra-centrifuged at 100,000 rpm for 20 minutes. The lysates (10-15 10^6 cells in 2 mL in NH_4CO_3 (50 mM) were diluted in 20% NH_4CO_3/ 80% ACN and spiked with the standard Co1CP (^{13}C) at 0.4 µM. The figures were zoomed onto the m/z region containing the studied complexes. The peak corresponding to Mn1CP, Co1CP (^{13}C) and their isotopic pattern are clearly visible and annotated on the spectrum. Zn1CP (^{13}C) displays peaks with relatively low intensity and was neglected for the quantification.

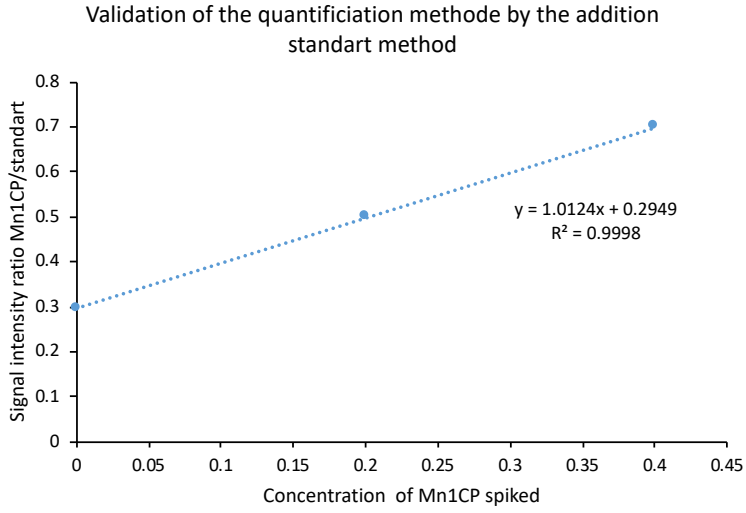

Figure S35: Quantification of Mn1CP in LPS-stimulated HT29-MD2 lysates by the method of standard additions. The lysates were beforehand ultra-centrifuged at 100,000 rpm for 20 minutes, diluted in 20% NH_4CO_3/ 80% ACN and spiked with the standard Co1CP (^{13}C) at 0.4 µM. Mn1CP was spiked at known concentration (0.2 µM and 0.4 µM) in the lysates of cells previously incubated with Mn1CP at 100 µM for 6 hours. The equation of the linear regression and the R-squared value of the regression are indicated on the graph. By taking into account the dilution done for the analysis and the number of cells in the lysate, an intracellular molar amount of $2.69.10^{-16}$ mol of Mn1CP per cells was measured using this method. This is close to the values obtained with the previous quantification. This result validates our approach based on the use of a heavy analog of Mn1CP as a standard and on the establishment of a calibration curve to quantify the SOD mimic inside cells.

VI.1.a.iv. References

[1] F. Cisnetti et al., « A New Pentadentate Ligand Forms Both a Di- and a Mononuclear MnII Complex: Electrochemical, Spectroscopic and Superoxide Dismutase Activity Studies », Eur. J. Inorg. Chem., vol. 2007, no 28, p. 4472-4480, oct. 2007, doi: 10.1002/ejic.200601236.

[2] Z.-M. Yang et L. Lu, « Synthesis of deuterated herbicidal ZJ0273, ZJ0702, ZJ0777, and SIOC0163 », J Label Compd Radiopharm, p. n/a-n/a, 2010, doi: 10.1002/jlcr.1749.

[3] Z.-M. Yang, L. Lu, Synthesis of deuterated herbicidal ZJ0273, ZJ0702, ZJ0777, and SIOC0163, J Label Compd Radiopharm. (2010) n/a-n/a. https://doi.org/10.1002/jlcr.1749.

[4] P. Thordarson, « Determining association constants from titration experiments in supramolecular chemistry », Chem. Soc. Rev., vol. 40, no 3, p. 1305-1323, 2011, doi: 10.1039/C0CS00062K.

[5] C. Policar, « Mimicking SOD, Why and How: Bio-Inspired Manganese Complexes as SOD Mimic », in Redox-Active Therapeutics, 2016, p. 125-164.

[6] S. Durot, F. Lambert, J.-P. Renault, et C. Policar, « A Pulse Radiolysis Study of Catalytic Superoxide Radical Dismutation by a Manganese(II) Complex with an N-Tripodal Ligand », Eur. J. Inorg. Chem., vol. 2005, no 14, p. 2789-2793, juill. 2005, doi: 10.1002/ejic.200400834.

VI.1.b. Supplementary materials of "Deciphering the Metal Speciation in Low-Molecular-Weight Complexes by IMS-MS: Application to the Detection of Manganese Superoxide Dismutase Mimics in Cell Lysates" publication

VI.1.b.i. Experimental Procedures

- Materials and reagents

ICP-MS: Nitric acid (HNO_3) 65% Suprapur (#1.00441.1000) and ICP multi-element standard XVI (#1.09487.0100) were from Merck. Manganese Standard for ICP (1003 mg/L ± 4 mg/L, TraceCERT #74128) was from Sigma Aldrich.

IMS-MS: Ultrapure ULC/MS–CC/SFC grade solvents were purchased from Biosolve: 2-propanol (#162641), Acetonitrile (#12041), Water (#232141). Syringes for IMS-MS direct infusion were from Agilent: Manual syringe, removable needle 22/51/LC, PTFE-tip plunger 500 µL (#5190-1526), 250 µL (#5190-1520), 100 µL (#5190-1512). PFA (metal-free) labware were purchased from AHF ANALYSENTECHNIK: Narrow Neck Bottle 100 mL (T81-100), Micro Spatulas made of CTFE (T29-578), Measuring Cylinder 50 mL (T89-050).

Protein quantitation: Bicinchoninic acid (BCA, Interchim BC assay Reagent A UP95424A), Bovine serum albumin (BSA) and Copper sulfate ($CuSO_4$, Interchim BC assay Reagent B UP95425A) were from Uptima-Interchim.

ELISA: Horseradish peroxidase (HRP)-conjugated antibodies were from Rockland. Human IL-8 detection ELISA kit (DuoSet, #DY208), containing IL-8-specific capture and detection antibodies, IL-8 standards, as well as streptavidin-HRP, was provided by R&D Systems. 3,3',5,5'-tetramethylbenzidine (TMB) substrate set was from BioLegend (#421101).

Western Blot: Acrylamide gel (Mini Protean TGX Stain-free Precast Gel, 10%), nitrocellulose membranes (Trans-Blot Turbo Transfer Packs, #1704158) and Clarity Western ECL substrate kit were from BioRad. MnSOD (SOD2) rabbit antibody was from Life Technologies SAS. Anti-rabbit (HRP donkey) secondary antibody was from Jackson Immuno research.

HT29-MD2 cell culture: Blasticidin was from InvivoGen. Dulbecco's modified eagle medium (DMEM), Dulbecco's phosphate buffered saline (DPBS, 10X), HEPES buffer solution (1 M), and Trypsin-EDTA were from Gibco. Fetal bovine serum (FBS) was from GE Healthcare Life Sciences. LPS (Escherichia coli O55:B5, purified by phenol extraction) was from Merck. Protease Inhibitors (cOmplete™ Protease Inhibitor Cocktail, #11836145001) were from Roche.

All other chemical reagents not mentioned were from Sigma-Aldrich.

- Instrumentation

HPLC Purification: Analytical HPLC was performed on an Agilent 1200 series; equipped with a quaternary pump using a Proto 200 C18 from Higgins Analytical Inc (particles size 3 µm, 100 x 4.6 mm column). Preparative HPLC was performed on an Agilent 1260 Infinity using a Nucleodur C18 HTech column from Macherey-Nagel Inc. (particles size 5 µm, 250 x 16 mm column).

NMR spectrometry: The NMR experiments were performed at 298K on a Bruker model spectrometer from the ENS chemistry department, with a proton frequency of 600 MHz equipped with a triple resonance inverse detection probe with triple axes pulsed field gradients.

UV-vis spectroscopy: UV−visible spectra (for all physicochemical characterization experiments of the Mn complexes) were recorded on a CARY 300 Bio UV−visible spectrophotometer using

a double-beam mode with media as the reference. Plastic UV-cuvettes, semi-micro (1.5 mL) were from BRAND (12.5 x 12.5 x 45 mm, #7591 50). UV−visible spectra (for all biological experiments) were recorded on a SpectraMax M5 Series Multi-Mode Microplate Reader from Molecular Devices.

Electrochemistry: Cyclic voltammograms were recorded on an Autolabμ (Metrohm). Small size electrodes were purchased from ALS (distributed by BAS Inc, Japan) on the advice of Dr. Christelle Hureau (LCC, Toulouse): Glassy carbon electrode (GCE, 6.0 x 3.0 mm, #002012), Platinum electrode (PTE, 6.0 x 3.0 mm, #002422), Calomel Reference electrode in saturated KCl (RE-2BP, #013458).

HT29-MD2 cell culture: Soniprep Ultrasonic disintegrator, with high frequency vibration by a titanium probe, was used for sonication cell lysis from MSE.

LC-MS/MS: For the analysis of the SOD mimic complexes, nano HPLC (ThermoFisher Scientific) with a ZIC-Hilic nano column (75 μm internal diameter PEEK-covered silica, Merck) and precolumn, were coupled to the nano ESI metal-free source TriVersa NanoMate (Advion) and the Orbitrap Fusion Lumos MS (ThermoFisher Scientific) in ESI (positive mode).

Direct MS infusion: Classic electrospray source from ThermoFisher Scientific was used for direct infusion MS analysis of the SOD mimic complexes, coupled to a Qq Orbitrap mass spectrometer; Q Exactive Hybrid Quadrupole-Orbitrap. Direct infusion was also performed using the nano ESI metal-free source TriVersa NanoMate (Advion) coupled to an Orbitrap Fusion Lumos MS from ThermoFisher Scientific.

ELISA: Immuno Clear Flat Bottom Transparent 96-Well Plates, with MaxiSorp™, Nunc™ fixation surface, were used for the ELISA quantitative immunoassay, from ThermoFisher Scientific (#442404). Automatic PBS Tween washings of the 96-well plates were performed with a HydroFlex™ microplate washer (ELISA washing protocol) form TECAN.

Western Blot: Gel electrophoresis was performed with the Mini-PROTEAN Tetra Vertical Electrophoresis Cell and PowerPac Power Supply, membrane transfer with the Trans-Blot Turbo Transfer System and gel imaging with the ChemiDoc XRS+ System (BioRad).

ICP-MS: A 7700 Series ICP-MS system with an ASX-500 Series autosampler from Agilent was used, with the following parameters: RF power: 1550 W; sampling depth: 10 mm; helium flow

rate: 5 mL/min measurement, replicated five times with 100 sweeps per replicate, and an integration time/mass of 1 s.

IMS-MS: A Beckman Coulter Optima Max-XP Ultracentrifuge with a TLA-110 Fixed-Angle Rotor (110 000 rpm max) was used for 100 000 rpm centrifugations and a Beckman Coulter Optima L-90K Ultracentrifuge with a SW 55 Ti Rotor (55 000 rpm max) was used for 50 000 rpm centrifugations, with OptiSeal Polypropylene Ultracentrifugation Tubes (13 x 48 mm, 4.7 mL, #361621) from Beckman Coulter Life Sciences. A timsTOF from Bruker Daltonics was used for the IMS-MS experiments. The Ion Source was an ApolloII ESI, working at room temperature (20-25°C), just pneumatically assisted (no make-up, no heater and earthed, just the transfert capillary was under potential. Less internal energy was given to the molecular ions with minimizing the possible rearrangement in the ion source (to be noted when working with non-covalent compounds, and in native conditions).

- Synthesis of $enPI_2$

$EnPI_2$ was synthesized according to the previously reported procedure.[1]

- Synthesis of $enPI_2$-$^{13}C_6$

Synthesis of 2

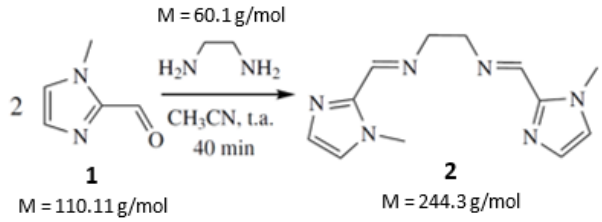

Compound 1 (1 g, 9.1 mmol) was suspended in one half equivalent of 1,2-diaminoethane (304 µL, 4.54 mmol, d=0.898 kg/L). Anhydrous acetonitrile was added until compound 2 was fully dissolved (500 µL). The reaction mixture was stirred for 40 minutes at room temperature under argon. The obtained precipitate was filtered, washed with petroleum ether, and analyzed by NMR. NMR ^1H ($CDCl_3$, 300 MHz): 8.31 (s, 2H, HC=N), 7.08 (d, 2H, CH_3-N-CH=CH), 6.90 (d, 2H, CH_3-N-CH=CH), 3.95 (s, 6H, N−CH_3), 3.91 (m, 4H, CH_2−CH_2).

Synthesis of 3

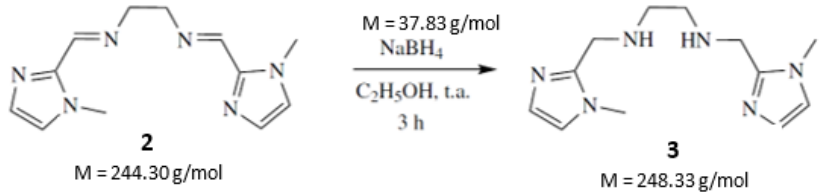

Compound 2 (1.0917 g, 4.4687 mmol) was diluted in absolute ethanol (10 mL). Sodium borohydride (473 mg, 12.5 mmol, 2.8 eq.) was added and the reaction mixture was stirred for 3 hours under argon at room temperature. Aqueous hydrochloric acid at 1 mol/L was then added to remove the excess sodium borohydride. The obtained compound 3 was extracted with dichloromethane (3 × 20 mL) after adding 10 mL of distilled water. The organic layers were collected, combined, dried over anhydrous sodium sulfate (Na_2SO_4) and filtered. Dichloromethane and ethanol were removed by rotary evaporation under vacuum to afford a yellow solid. NMR ^1H ($CDCl_3$, 300 MHz): 6.90 (d, 2H, CH_3-N-CH=CH), 6.80 (d, 2H, CH_3-N-CH=CH), 3.82 (m, 4H, NH-CH_2), 3.65 (m, 6H, N-CH_3), 2.75 (m, 4H, CH_2-CH_2).

Synthesis of 4

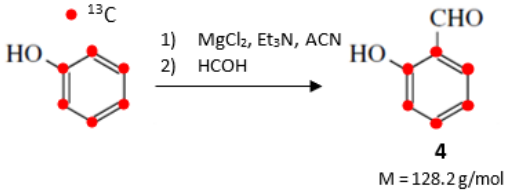

A mixture of ($^{13}C_6$)phenol (0.5434 g, 5.429 mmol), anhydrous magnesium dichloride (1.312 g, 8.119 mmol), anhydrous triethylamine (2.8 mL), and anhydrous acetonitrile (purchased from Sigma Aldrich) (4.9 mL) was stirred under argon at room temperature for 30 minutes. Paraformaldehyde (1.315 g, 43.9 mmol) was added to the mixture. The resulting mixture was refluxed for 4 hours and then cooled to room temperature. A color change from white to orange was observed. The mixture was added 10% hydrochloric acid (6.5 mL) to neutralize the triethylamine and get a pH of around 5. The obtained compound 4 was extracted with diethyl ether (3 × 20 mL), and the combined organic layers were washed with distilled water (10 mL) and saturated brine (10 mL), dried over anhydrous Na_2SO_4, and filtered. The solvent was removed by rotary evaporation under vacuum to afford a brown oil. NMR ^1H ($CDCl_3$, 300 MHz): 11.0 (m, 1H, C_{ar}-CH=O), 9.9 (m, 1H, C_{ar}-OH), 6.5-8 (m, 4H, H_{ar}). NMR ^{13}C ($CDCl_3$, 75 MHz): 161 (1C_{ar}), 137 (1C_{ar}), 134 (1C_{ar}), 121-117 (3C_{ar}).

Synthesis of 5

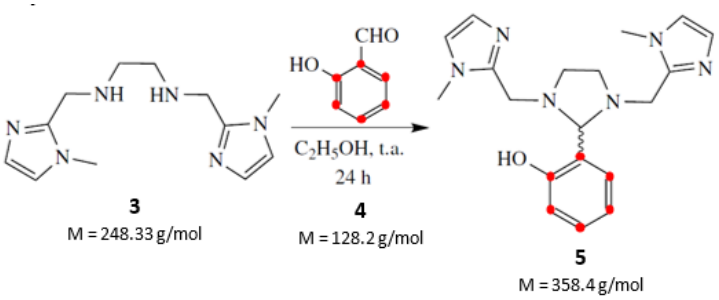

Compound 3 (0.8065 g, 3.2477 mmol) was diluted in 8 mL of absolute ethanol (1.62 mmol per flask). One equivalent of compound 4 (1.62 mmol, 174 µL, d=1.193 g/mL) was added, and the reaction mixture was stirred for 24 h under argon at room temperature. The reaction mixture was then dried over anhydrous sodium sulfate (Na_2SO_4) and filtered under vacuum. Ethanol was removed by rotary evaporation under vacuum to obtain compound 5 as a solid. NMR ^1H ($CDCl_3$, 300 MHz): 6.93-6.74 (m, Har, CH_3-N-CH=CH and CH_3-N-CH=CH), 3.84-3.53 (m, N-CH-N and N-CH_2-Imi), 3.39 (s, N-CH_3), 2.82 (m, N-CH_2-CH_2-N).

Synthesis of 6

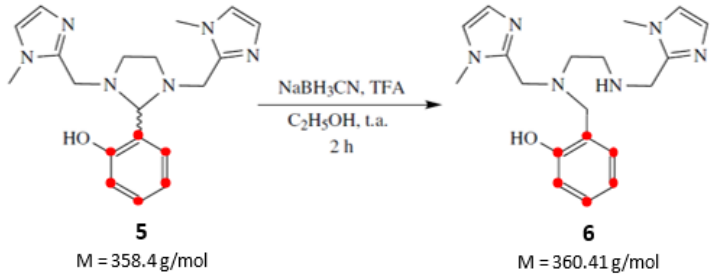

Compound 5 (1.67 mmol) was dissolved in 5 mL of absolute ethanol. One equivalent of sodium cyanoborohydride ($NaBH_3CN$, 0.105 g, 1.67 mmol, M=62.84 g/mol) and two equivalents of trifluoroacetic acid (256 µL, 3.34 mmol, M=114.02 g/mol, d=1.49 kg/L) were added, and the two reaction mixtures were stirred for 2 hours at room temperature. A color change from yellow to colorless was observed. After removing the ethanol by rotary evaporation, the mixtures were diluted with dichloromethane (20 mL) and water (20 mL). The pH of the combined aqueous layers was then adjusted to 8-8.4 by adding HCl at 1 M and sodium hydroxide at 1 M. The aqueous phase was then extracted with dichloromethane (3 x 20 mL). The extraction of the products of interest was monitored by measuring the absorbance at 254 nm by UV-Vis in a plastic cuvette (the organic phase has to absorb much more than the aqueous ones). The combined organic layers were dried over anhydrous sodium sulfate and

filtered. Dichloromethane was removed by rotary evaporation to afford compound 6 as a yellow powder. Compound 6 was purified by preparative HPLC using a C18 column (NUCLEODUR R C18 HTec particles size 5 µm, 250 × 16 mm column) on an Agilent 1260 Infinity. The elution gradient increases from 5% to 50% in ACN/TFA 0.1% in 10 minutes, with a retention time at 4.79 min. NMR ^{1}H ($CDCl_3$, 300 MHz): 7.53/7.48 (d, 2H, CH_3-N-CH=CH), 7.32/7.2 (d, 2H, CH_3-N-CH=CH), 7.38/7.05/6.85/6.52 (m, 4H, H_{ar}), 4.67/4.06 (s, 4H, N-CH_2-Imii), 3.93/3.70 (s, 6H, N-CH_3), 3.78 (m, 2H, N-CH_2-Ar), 3.49/3.06 (t, 4H, N-CH_2-CH_2-N).

- Synthesis of enPI2P

To N,N'-bis-(2-(N-methylimidazolyl)-methyl)-N(2-hydroxybenzyl)-1ethane-1,2-diamine (0.200 g, 0.564 mmol, 1 eq) in absolute ethanol (30 mL) was added propanal (0.056 g, 0.069 mL, 0.564 mol, 1 eq). After stirring for 2 hours, under argon, was added $NaBH_3CN$ (0.043 g, 0.0677 mmol, 1eq) and CFCOOH (0.038 g, 0.025 mL). After stirring for 2 hours, 1 M NaOH (10 mL) was added, and ethanol was evaporated. CH_2Cl_2 (20 mL) was added. The pH was adjusted to 9 by the addition of 1 M HCl. The organic phase was decanted, and the aqueous phase was extracted with 3x20 mL of CH_2Cl_2. The combined organic fractions were concentrated to obtain the product as a yellow oil. NMR ^{1}H ($CDCl_3$, 300 MHz): 7.53/7.23/6.87 (m, 4H, H_{ar}), 4.63/4.16, (m, 4H, N-CH_2-Imii), 3.77 (m, 4H, N-CH_2-C_{ar}), 3.86/3.64 (6H, N-CH_3), 3.30/2.97 (t, 4H, N-CH_2-CH_2-N), 1.50 (m, 2H, CH_2-CH_2-CH_3), 1.18 (t, 2H, CH_2-CH_2-CH_3), 0.80 (t, 3H, CH_2-CH_2-CH_3).

- Synthesis of enPI2P-13C6

EnpI_2P labeled with ^{13}C was synthesized following the same procedure as that used for EnPI2P except the use of ^{13}C labelled N,N'-bis-(2-(N-methylimidazolyl)-methyl)-N(2-hydroxybenzyl)-1ethane-1,2-diamine as reagent. NMR ^{1}H (MeOD, 300 MHz): 7.46/7.37 (m, 4H, H_{ar}), 7.30/7.03/6.88/6.50 (s, 4H, N-CH_2-C_{ar}), 4.18/4.11, (s, 4H, N-CH_2-Imii), 3.83/3.75 (6H, N-CH_3), 3.04/2.97 (t, 4H, N-CH_2-CH_2-N), 2.63 (t, 2H, CH_2-CH_2-CH_3), 1.50 (m, 2H, CH_2-CH_2-CH_3), 0.86 (t, 3H, CH_2-CH_2-CH_3). NMR ^{13}C (MeOD, 75 MHz): 157.8 (CPh-OH), 157.0 (C_{quat},Im), 156.1 (C_{quat},Im), 133.3 (CPh-H), 132.2 (CPh-H), 131.4 (CImH), 130.50 (CImH), 123.4 (C_{quat},Ph), 121.6 (CPh-H), 120.7 (CImH), 119.9 (CImH), 116.5 (CPh-H), 57.67 (N-CH_2-CH_2-CH_3), 55.50 (CPh-**C**H_2), 55.00 (N-CH_2-CH_2-N), 52.85 (N-CH_2-CH_2-N), 52.67 (N-**C**H_2-CIm), 50.00 (N-**C**H_2-CIm), 34.73 (N-CH_3), 34.80 (N-CH_3), 19.87 (N-CH_2-**C**H_2-CH_3), 11.66 (N-CH_2-CH_2-**C**H_3).

- Crystallization of Mn1P

$[Mn_2(EnPI_2P)_2](PF_6)_2]$ (M=1190,87 g/mol): NEt_3 (15 mg, 20 µL, 0.146 mmol, 0.5 equiv.) was added to a solution of $EnPI_2P$ (0.116 g, 0.292 mmol, 1 eq) in MeOH (2.5 mL) and argon was bubbled into the solution to remove O_2. A deoxygenated solution of $MnBr_2$ (63 mg, 0.292 mmol, 1 eq) in MeOH (1 mL) was added to this mixture, and the solution was heated at 50°C for 30 min. A deoxygenated solution of NH_4PF_6 (95 mg, 0.585 mmol, 2 eq) in methanol (1 mL) was then added, and the resulting solution was left to cool overnight. The complex started to crystallize out of solution, and 63 mg (0,053 mmol, 36% yield) of dark brown crystals were isolated by filtration.

Crystallographic Data

A crystal of Mn1P suitable for X-ray diffraction was obtained by slow evaporation of methanol at room temperature. X-ray diffraction data for the compound Mn1P were collected by using a Kappa X8 APPEX II Bruker diffractometer with graphite-monochromated Mo Kα radiation (0.71073 Å). Crystal was mounted on a CryoLoop (Hampton Research) with Paratone-N (Hampton Research) as cryoprotectant and flash-frozen in a nitrogen-gas stream at 200 K. For compound, the temperature of the crystal was maintained at the selected value using a 700 series Cryostream cooling device to within an accuracy of ± 1 K. The data were corrected for Lorentz polarization and absorption effects. The structures were solved by direct methods using SHELXS-97[2] and refined against F^2 by full-matrix least-squares techniques using SHELXL-2018[3] with anisotropic displacement parameters for all non-hydrogen atoms. Hydrogen atoms were located on a difference Fourier map and introduced into the calculations as a riding model with isotropic thermal parameters. All calculations were performed by using the Crystal Structure crystallographic software package WINGX.[4]

Table S1. Crystallographic data and structure refinement details.

Compound	Mn1P
CCDC	2112875
Empirical Formula	C44 H62 Mn2 N12 O2, 2(F6 P)
Mr	1190.87
Crystal size, mm3	0.28 x 0.11 x 0.03
Crystal system	orthorhombic
Space group	F d d 2
a, Å	26.7635(18)
b, Å	31.595(2)
c, Å	13.3689(8)
α, °	90
β, °	90
γ, °	90
Cell volume, Å3	11304.5(12)
Z ; Z’	8 ; 1/2
T, K	200(1)
Radiation type ; wavelength Å	Mo Kα ; 0.71073
F000	4912
μ, mm–1	0.589
θ range, °	1.821 - 30.558
Reflection collected	70355
Reflections unique	6585
Rint	0.0811
GOF	1.008
Refl. obs. (I>2σ(I))	3540
Parameters	337
wR2 (all data)	0.1708
R value (I>2σ(I))	0.0548

Largest diff. peak and hole (e–.Å-3)	0.542 ; -0.366

Table S2. Comparison of selected bond lengths (Å) and angles (°) for the coordination sphere of the [(L) Mn Mn (L)]. The uncertainties correspond to 2σ.

	Mn1P	Mn1 [5]
Mn(1)-N(1)	2.374(10)	2.354(8)
Mn(1)-N(4)	2.481(10)	2.205(8)
Mn(1)-O(1)	2.110(8)	2.172(6)
Mn(1)-N(2)	2.225(10)	2.226(8)
Mn(1)-N(5)	2.163(10)	2.420(8)
Mn(1)-O(1)i	2.128(8)	2.111(6)
Mn(1)-Mn(1)i	3.292(2)	3.301(2)
O(1)-Mn(1)-N(1)	85.9(4)	83.1(1)
O(1)-Mn(1)-N(4)	104.2(3)	94.2(3)
O(1)-Mn(1)-O(1)i	75.5(3)	79.2(2)
N(1)-Mn(1)-N(4)	74.1(3)	113.7(3)
O(1)-Mn(1)-N(2)	104.1(4)	109.9(3)
O(1)-Mn(1)-N(5)	166.4(4)	128.5(2)
N(1)-Mn(1)-N(2)	74.9(3)	72.8(2)
N(1)-Mn(1)-N(5)	105.1(4)	76.8(3)

i : -x, -y ,z.

- Calculation of K (Mn-L) and K (Zn-L) complexes from UV titration experiments

The association constants of the studied ligands with Mn and Zn were previously reported.[6]

- Calculation of K (Co-L) complexes: competition with the formation of MnL

The direct measure of the association constant for Co(II) complexes is not possible because the K (Co-L) value is too high. The initial concentration of the ligand (C_L) should be $<100*K_d$ to

observe an equilibrium between the uncoordinated ligand L, Co(II), and the complex in solution at the 1:1 Co:L ratio and obtain not only the stoichiometry but also the association constant.[6,7] This would impose to use a very low initial concentration of the ligand for the titration, at which the absorbance would be too small to be precisely measured by a classical spectrophotometer. Therefore, the association constants of the studied ligands with Co were determined with competition experiments between the formation of MnL, with known K (M-L) and CoL, followed by UV-vis. The protocol is detailed below.

The initial HEPES 50 mM solution at pH=7.5 was added in a 1 mL cuvette (used for the baseline subtraction), and was equilibrated in the spectrophotometer for 10 min at 25°C. Two equivalents of Mn(II) ($MnCl_2$) (80 µM) were added to a 40 µM ligand solution and stirred using a parafilm to cover the cuvette. The absorbance was measured between 200 nm and 600 nm. Afterward, 0.2 equivalent of Co(II) ($CoCl_2$) (4 mM) were added successively to the 40 µM solution of manganese complex, stirred, and the absorbance of the Co(II) complex was monitored between 200 nm and 600 nm. The addition of an excess of manganese is necessary to (1) assume that the concentration of free ligand is null (see calculation of K_{CoL} below), (2) to shift the equilibrium to the formation of the Mn(II) complex and disfavor the Co(II) complex that is more thermodynamically favored. The absorbance of the metal complex (around 255 nm for the CoL complexes) was then plotted as a function of the number of added Co(II) equivalents. The cobalt complexes' association constants were obtained by fitting the theoretical absorbance curve to the experimental one using the MATLAB curve fitting tool based on a non-linear least-square regression method. The calculation of K_{CoL} is detailed in the table below.

	$\mathbf{C_{Mn}}$	$\mathbf{C_L}$	$\mathbf{C_{MnL}}$	$\mathbf{C_{Co}}$	$\mathbf{C_{CoL}}$
Initial state	C2	C1	0	$\boldsymbol{C_1 \times n_{eq}}$	0
Equilibrium state (intermediate or for n<1)	$\boldsymbol{C_2 - C_1 \times e}$	$\boldsymbol{C_1 \times (1 - e - e')}$	$\boldsymbol{C_1 \times e}$	$\boldsymbol{C_1 \times (n_{eq} - e')}$	$\boldsymbol{C_1 \times e'}$
Equilibrium state (final or for n>>1)	C2	0	0	$\boldsymbol{(n_{eq} - 1) \times C_1}$	C1

C_1 = initial ligand concentration

C_2 = initial Mn concentration = $2 \times C_1$

e= extent of the reaction of Mn with L to form MnL

e'= extent of the reaction of Zn with L to form CoL

n_{eq} = number of added molar equivalent of Co (compared to initial L)

K_{MnL}= Association constant of ligand L with Mn

K_{CoL}= Association constant of ligand L with Co

$$K_{MnL} = \frac{[\mathrm{MnL}]}{[\mathrm{Mn}] \times [L]} \quad and \quad K_{CoL} = \frac{[\mathrm{CoL}]}{[\mathrm{Zn}] \times [L]}$$

$$\frac{K_{CoL}}{K_{MnL}} = \frac{e' \times C_1 \times (C_2 - C_1 \times e)}{e \times C_1 \times \ C_1 \times (n_{eq} - e')} = \frac{e' \times (C_2 - C_1 \times e)}{e \times \ C_1 \times (n_{eq} - e')}$$

Assumption: no free ligand in solution (high K_{CoL} and $C_1 < C_2$): $e = 1 - e'$

$$\frac{K_{CoL}}{K_{MnL}} = \frac{e' \times [C_2 - C_1 \times (1 - e')]}{(1 - e') \times (C_1 \times \ n_{eq} - e' \times C_1)} = \frac{e' \times (C_2 - C_1 + C_1 \times e')}{C_1 \times n_{eq} - C_1 \times e' - C_1 \times n_{eq} \times e' + C_1 \times e'^2}$$

$$\frac{K_{CoL}}{K_{MnL}} = \frac{C_1 \times e'^2 - (C_1 - C_2) \times e'}{C_1 \times e'^2 - \left(C_1 + C_1 \times n_{eq}\right) \times e' + C_1 \times n_{eq}}$$

$$\left(e'^2 - \left(e' \times n_{eq}\right) + n_{eq} - e'\right) \times \frac{K_{CoL}}{K_{MnL}} = e'^2 + e' \times \left(\frac{C_2}{C_1} - 1\right)$$

$$e'^2 \times \left(1 - \frac{K_{\mathrm{CoL}}}{K_{MnL}}\right) + e' \times \left(\frac{C_2}{C_1} - 1 + \frac{K_{\mathrm{CoL}}}{K_{MnL}}\left(n_{eq} + 1\right)\right) - n_{eq} \times \frac{K_{CoL}}{K_{MnL}} = 0$$

Solution of the quadratic equation:

$$e' = \frac{-\frac{C_2}{C_1} + 1 - \frac{K_{CoL}}{K_{MnL}}\left(n_{eq} + 1\right) + \sqrt{\left(\frac{C_2}{C_1} - 1 + \frac{K_{CoL}}{K_{MnL}}\left(n_{eq} + 1\right)\right)^2 + 4 \times \left(1 - \frac{K_{CoL}}{K_{MnL}}\right) \times n_{eq} \times \frac{K_{CoL}}{K_{MnL}}}}{2 \times \left(1 - \frac{K_{CoL}}{K_{MnL}}\right)}$$

$$A_{th} = \varepsilon_{MnL} C_{MnL} l + \varepsilon_{CoL} C_{CoL} l$$

A_{th} = Theoretical absorbance at a fixed wavelength

ε_{MnL} = Molar attenuation coefficient of MnL complex at the same fixed wavelength

C_{MnL} = Concentration in MnL

ε_{CoL} = Molar attenuation coefficient of CoL complex at the same fixed wavelength

C_{CoL} = Concentration in CoL

$l =$ Width of the spectrophotometer cuvette.

$A_0 = \varepsilon_{MnL} C_1 l$ and $A_f = \varepsilon_{CoL} C_1 l$

$A_0 =$ Theoretical initial absorbance of the MnL solution

$A_f =$ Theoretical final absorbance of the CoL solution

$$A_{th} = C_{MnL} \times \frac{A_0}{C_1} + C_{CoL} \times \frac{A_f}{C_1}$$

$$A_{th} = (1 - e') \times A_0 + e' \times A_f = A_0 - e' \times (A_0 - A_f)$$

With e' detailed above.

- Electrochemistry

Cyclic voltammetry experiments were performed with solutions at 200 µM (1:1 SODm complex, ligand and $MnCl_2$ (anhydrous)) in HEPES buffer (50 mM, pH 7.5), in 1 mL final volume in a small size electrochemical cell (see materials), at room temperature. The auxiliary electrode was a Pt wire and the working electrode was a glassy carbon disk (3 mm diameter) carefully polished manually with a 1 µm diamond paste, washed with water and air dried before each voltammogram. The reference electrode was a SCE saturated with KCl. Solutions were deoxygenated and mixed with a magnetic stirrer before each measure. Data acquisition was performed with the Nova 2.12 software. The following parameters of the cv staircase command were used: scan rate 0.1 or 0.2 V/s, step -0.005 (reduction), 0.005 (oxidation), number of scans 1, start potential 0 V_{OCP}, upper vertex potential 0.7 V_{REF}, lower vertex potential -0.5 V_{REF}, stop potential 0 V_{OCP}.

- Determination of intrinsic SOD activity by McCord-Fridovich Assay

The catalytic rate for superoxide dismutation of the SOD mimics has been determined using an indirect assay developed by McCord and Fridovich. Xanthine (50 µmol) was dissolved in HEPES 50 mM (250 mL) by heating at 80°C for 3 h under reflux, to obtain a solution at 200 µM. The solution was cooled to r.t. Ferricytochrome c (5 µmol) was dissolved in the xanthine solution (50 mL) to get a solution at 100 µM in Fe(III)-cytc. Then, 1.5 mL of the xanthine/Fe(III)-cytc solution was added in a microcuvette. The cuvette was left in the thermostated spectrophotometer (10 min) to reach 25°C. 4 µL of a solution of xanthine oxidase at 20 mg/mL in milli Q water (always be kept on ice to maintain its activity) was added in the microcuvette. The absorbance at 550 nm was measured over 4 min and after 1.5 min, few µL of the SOD

mimic at 100 µM were added in the cuvette. The slope of the absorbance was measured in absence of SODm (p_1) between 0 and 1.5 min and in presence of SODm (p_2) between 2 and 4 min. The volume of xanthine oxidase (20 mg/mL) was tuned (4 min) to get a slope p_1 between 0.025 et 0.030 min^{-1}, ensuring a flow of superoxide of about 1.2 µM/min.[8] This protocol was repeated for several volumes of SODm added. For each volume, the value $(p_1-p_2)/p_2$ was calculated and plotted as a function of the concentration in SODm in the microcuvette. The IC_{50} can be extrapolated from the linear regression of this curve by determining the concentration for which $(p_1-p_2)/p_2$ is equal to 1 ($p_1=2\cdot p_2$).[9] The IC_{50} value is dependent on the nature of the redox indicator and its concentration. From the measured IC_{50} values, an apparent kinetic constant value, independent of both the concentration and the nature of the detector can be calculated. At IC_{50}, the superoxide reacts with the ferricytochrome c and with the SOD mimic at the same speed. From the known kinetic constant of Fe(III)-cytc (kcyt c=2.6 10^5 $mol^{-1}Ls^{-1}$)[10] that of the SOD mimic can be determined, according to the following equation:

$$k_{ferricytochrome\ c} \cdot [O_2^{\bullet -}] \cdot [ferricytochrome\ c] = k_{SOD\ mimic} \cdot [O_2^{\bullet -}] \cdot IC_{50}$$

$$k_{SOD\ mimic} = \frac{k_{ferricytochrome\ c} \cdot [ferricytochrome\ c]}{IC_{50}}$$

The intrinsic activities of SOD mimics can be compared by using these catalytic rate values.[9]

- Mass spectrometry characterization of Mn1 and Mn1P

QqOrbitrap (Q Exactive)

Direct infusion 2-5 µL/min in ESI 4 kV source. Injection in LC coupling with nano-ESI 1.6 kV source. Full range analysis at m/z 67-1000.

Table S3. Theoretical exact mass of $enpi_2$ and $enpi_2P$ ligand in different metal forms and heavy standards.

m/z	$enPI_2$	$enPI_2{}^{13}C_6$
Molecular Formula	$[C_{19}H_{26}N_6O+H]^+$	$[C_{13}[^{13}C]_6H_{26}N_6O+H]^+$
$[L+H]^+$	355.22409	361.24421
Mn	408.14648	414.16661
$[Mn-H]^+$	407.1387	413.1600
Fe	409.14337	415.16350
$[Fe-H]^+$	408.1355	414.1569
Co	412.14163	418.16176
Ni	411.14378	417.16391
Cu	416.13803	422.15816
Zn	417.13758	423.15771
m/z	$enPI_2P$	$enPI_2{}^{13}C_6P$
Mol Formula	$[C_{22}H_{32}N_6O+H]^+$	$[C_{16}[^{13}C]_6H_{32}N_6O+H]^+$
$[LP+H]^+$	397.27104	403.29117
Mn	450.19343	456.21356
Fe	451.19032	457.21045
$[Fe+H_2O]^+$	468.19306	475.22102
Co	454.18858	460.20871
Ni	453.19073	459.21086
Cu	458.18498	464.20511
Zn	459.18453	465.20466

 Metal ion content measurement by ICP-MS

ICP-MS samples preparation

Samples (100 µL) were diluted in 2% HNO_3 to obtain a final volume of 2 mL and were filtered (0.2 µm). A calibration curve was established using the ICP multi-element standard XVI at 100 ppm (S_0) to quantify the amount of metal ions contained in each sample. From the standard S_0 solution, the S_1 solution was prepared (200 µL of S0 in a total volume of 40 mL 2% HNO_3) at

0.5 ppm or 500 ppb (part per billion, with 1 ppm = 1 000 ppb). For a given standard, the volume (in µL) of stock solution was diluted to a total volume of 2% HNO_3 solution (20 mL). The theoretical metal ion concentration is indicated in ppb. ^{55}Mn, ^{59}Co, ^{60}Ni, ^{63}Cu, and ^{66}Zn were selected as isotopes to avoid isobaric interferences. The S_1 was used to prepare the standards for the calibration curve at 0, 0.2, 2, 10, 20, 50, 100 ppb as listed in the table below.

Standards Preparation	**0 ppb**	**0.1 ppb**	**0.2 ppb**	**2 ppb**	**10 ppb**	**20 ppb**	**50 ppb**	**100 ppb**	**500 ppb**
S_1 (µl)	0	4	8	80	400	800	2000	4000	20000
2% HNO_3 (ml)	20.000	19.996	19.992	19.920	19.600	19.200	18.000	16.000	20.000
Total (ml)	20.000	20.000	20.000	20.000	20.000	20.000	20.000	20.000	20.000
Theoretical ppb									
55 Mn	0.00	0.10	0.20	2.02	10.10	20.20	50.50	101.00	505.00
59 Co	0.00	0.10	0.20	2.00	10.00	20.00	50.00	100.00	500.00
60 Ni	0.00	0.10	0.20	2.02	10.10	20.20	50.50	101.00	505.00
63 Cu	0.00	0.10	0.20	2.02	10.10	20.20	50.50	101.00	505.00
66 Zn	0.00	0.10	0.20	2.04	10.20	20.40	51.00	102.00	510.00

ICP-MS calibration

The counts per second (CPS), representing the average of three measurements, and the standard deviation (CPS RSD) are given in the table here blow. The concentration determined from the linear fit of the standard calibration curve (CPS plotted vs the theoretical ppb) is referred to as C_a (for concentration analyzed) of each meal ion. The C_a in ppb was calculated from the CPS values (NCPS) that were converted to ppb (1 ppb = 10^{-9} g (metal)/1 g (solvent), or 1 µg/L) with the slope (f_{cal}) of the standard calibration curve, following the equation:

$$C_a = \frac{N_{CPS}}{f_{cal}}\ ppb\ \left(or\ \frac{\mu g}{L}\right)$$

Measurement	0 ppb	0.1 ppb	0.2 ppb	2 ppb	10 ppb	20 ppb	50 ppb	100 ppb	500 ppb
CPS **Mn**	-95.07	3754.02	5020.79	25663.05	93433.13	184373.09	447266.41	866467.22	4119742.57
CPS RSD **Mn**	-54.40	3.62	3.36	1.12	0.20	0.30	0.50	0.35	0.45
CPS **Co**	-36.00	4139.72	8184.10	82337.12	410006.16	816324.85	1997290.61	3875804.91	19005195.36
CPS RSD **Co**	-53.56	2.61	0.38	1.11	0.73	0.72	0.44	0.38	0.81
CPS **Ni**	-11.20	1208.63	1810.27	24949.02	119829.22	242064.78	585892.63	1145111.81	5558667.71
CPS RSD **Ni**	-674.87	3.04	3.79	2.35	0.58	0.41	0.41	0.37	0.80
CPS **Cu**	175.86	47355.40	5020.12	72237.92	347080.94	686273.47	1673208.08	3239146.05	15333062.35
CPS RSD **Cu**	70.47	0.84	2.92	1.63	0.46	0.47	0.52	0.31	0.73
CPS **Zn**	-335.05	1909.36	524.72	8340.76	41154.54	82555.45	203569.10	397708.13	1918375.69
CPS RSD **Zn**	-42.24	6.20	17.03	5.65	0.59	0.33	0.47	0.33	0.50

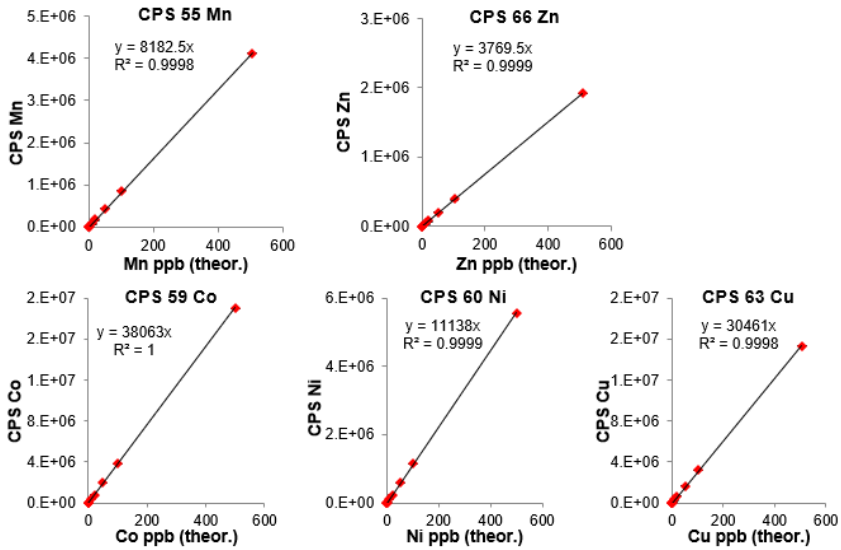

Determination of metal ions total amount

Each sample was measured in triplicate. Counts value (CPS) and standard deviation (CPS RSD) are listed in the following table. From the calibration curve, the C_a concentrations in ppb in the diluted samples were determined by using the previous equation. Using the diluted volume of each sample (or analyzed volume, V_a = 2 mL), the amount of metal ions in ng was determined. Using the molecular weight, the amount of each metal ion in nmol was determined. This corresponds to the total amount of metal ions in each sample. This amount can be converted in a concentration in µM of the initial sample, considering the initial volume

of each sample (V_0 = 0.1 mL). Overall, the calculations for the concentration C_0 in µM can be resumed in the following equation:

$$C_0 = C_a \times \frac{V_a}{MW_{metal\ ion}} \times \frac{1}{V_0}$$

CPS	55 Mn [He]	59 Co [He]	60 Ni [He]	63 Cu [He]	66 Zn [He]
H_2O pure	19519.82	1762.80	9884.86	56100.28	8030.78
ACN pure	31799.36	3885.05	27592.03	101018.65	23041.04
NH_4HCO_3 pH 7.4	24724.64	5001.38	23359.72	96494.99	14902.42
NH_4HCO_3 pH 6.5	45468.13	4656.07	28580.10	86110.68	15729.11
HEPES pH 7.5	46644.05	2299.09	10914.32	54129.78	8863.57
$enPI_2$ 100 µM	60418.66	2637.76	14437.59	59857.36	9030.05
$enPI_2$ P 100 µM	47025.48	1548.56	9751.71	54817.13	23253.65
Mn1 100 µM	2097021.74	5228.45	19616.84	63490.17	54576.84
Mn1P 100 µM	2195912.22	4150.12	10206.65	93180.02	19352.22
$MnCl_2$ 100 µM	1970301.77	5539.37	21915.89	66014.85	12140.81
CPS RSD	**55 Mn [He]**	**59 Co [He]**	**60 Ni [He]**	**63 Cu [He]**	**66 Zn [He]**
H_2O pure	1.27	4.10	2.00	0.82	1.94
ACN pure	0.95	0.67	1.20	0.82	1.90
NH_4HCO_3 pH 7.4	1.36	2.13	0.88	1.00	0.77
NH_4HCO_3 pH 6.5	0.94	2.10	1.24	0.37	0.26
HEPES pH 7.5	0.93	3.37	1.02	0.33	2.39
$enPI_2$ 100 µM	0.31	5.69	1.31	0.67	1.92
$enPI_2$ P 100 µM	0.55	4.04	2.02	0.31	0.34
Mn1 100 µM	0.34	2.09	0.72	0.21	0.56
Mn1P 100 µM	0.19	1.37	1.97	1.08	0.92
$MnCl_2$ 100 µM	0.41	1.13	1.70	0.42	1.75

- Experiments on HT29-MD2 cells

Cell culture

HT29 human colon adenocarcinoma cells obtained from the European Collection of Cell Cultures (Wiltshire, UK) and stably transfected to overexpress MD2, as previously described, were used. HT29-MD2 cells were seeded at 3E6/flask in a T-75 flask to reach 80-90% confluence in three days and cultured in DMEM (Dulbecco's Modified Eagle Medium) supplemented with 10% of heat-activated FBS and 0.1% of blasticidin (10 µg/mL) at 37°C in a

5% CO_2/air atmosphere. Cell media was changed for fresh every 2-3 days. After reaching 80%-90% of confluence, cells were washed with DPBS 1X and then detached by exposure to 0.05% trypsin-EDTA (5-10 min, 37°C). The action of trypsin was stopped by dilution with fresh media. After centrifugation, cells were suspended in fresh media (10 mL) and counted on Malassez lamella. 1E6 cells were suspended in fresh media (10 mL) and cultured until further use. Cells were grown at least for three-five passages prior to experiments.

Compounds cytotoxicity with LDH assay

Cell lysates and supernatants were added in a solution of NADH 0.18 mM and pyruvate 0.62 mM in PBS 1X and the absorbance of NADH at 340 nm was recorded. A decrease in absorbance indicates the oxidation of NADH due to the presence of lactate dehydrogenase (LDH). The concentration of LDH is proportional to the slope of the decrease in absorbance over time. For the supernatant samples, pyruvate/NADH solution (800 µL) and supernatant (200 µL) was added (for an initial total volume of 500 µL → correction factor = 5/2) in a plastic cuvette (1 mL) and the decrease in absorbance at 340 nm was recorded for 1 min. For the cell lysates, pyruvate/NADH solution (800 µL), PBS 1X (190 µL,) and cell lysate (10 µL) was added (for an initial total volume of 100 µL → correction factor = 10) in a plastic cuvette (1 mL) and the decrease in absorbance at 340 nm was recorded for 1 min. The percentage of LDH released in the supernatant was calculated as follows:

$$\%\,\mathrm{LDH}_{\text{released in supernatant}} = \frac{\mathrm{Slope}_{\text{supernatant}} \times \frac{V_{supern.(i)}}{V_{supern.(f)}}}{[\mathrm{Slope}_{\text{supernatant}} \times \frac{V_{supern.(i)}}{V_{supern.(f)}}] + [\mathrm{Slope}_{\text{lysate}} \times \frac{V_{lysate(i)}}{V_{lysate(f)}}]} =$$

$$>$$

$$\%\,\mathrm{LDH}_{\text{released in supernatant}} = \frac{\mathrm{Slope}_{\text{supernatant}} \times \frac{5}{2}}{[\mathrm{Slope}_{\text{supernatant}} \times \frac{5}{2}] + [\mathrm{Slope}_{\text{lysate}} \times 10]}$$

Cytotoxicity was considered when LDH release in supernatant exceeded 10%.

LPS cell activation with and without Mn1 or Mn1P incubation

HT29-MD2 cells were seeded in 12 well-plates at 200 000 or 250 000 cells/well to reach 80-90% confluence after 3 or 4 days. Cells were incubated with culture medium (500 µL) containing LPS 0.1 µg/mL with and without Mn1 (or Mn1P) 100 µM for 6 h. At the end of the

incubation, supernatants were collected and stored at -20°C before ELISA and LDH assay. Cells were washed with PBS 1X and lysed by Triton 1X solution (100 µL) with protease inhibitors. Cell lysates were harvested by scraping, sonicated, and stored at -20°C before cytotoxicity, protein quantitation, and Western Blot experiments.

Protein quantitation in cell lysates

The BCA (bicinchoninic acid) protein assay was used for protein quantitation. A calibration curve was established using bovine serum albumin (BSA), at a standard range from 0 mg/mL to 1 mg/mL. In 96-well plates, cell lysates (3 µL) were deposited in Milli-Q water (22 µL). Revealing solution (200 µL, from 10 mL BCA + 200 µL copper sulfate stock solution) was then added to each well. After incubation (37°C, 30 min), the absorbance at 560 nm was measured directly in the 96-well plates.

MnSOD quantitation by Western Blot

Cell lysates were incubated (95 °C, 5 min) in Laemmli buffer 5X (recipe: 4 mL Tris 1.5 M pH 6.8, 10 mL glycerol, 5 mL β-mercaptoethanol, 2 g sodium dodecyl sulfate (SDS), 1 mL bromophenol blue 1%) to denature the proteins. A protein molecular weight marker (5 µL) followed by samples of denatured proteins (20 µg) were loaded into each well of an acrylamide gel (10%). Deposited volumes of denatured proteins were calculated from the protein quantitation results in cell lysates to deposit approximately the same amount of proteins in each well. Denatured proteins were then separated by gel electrophoresis (150 V, 1 h). The electrophoresis buffer was 144 g glycine, 30 g Tris, 1 L Milli-Q water, 10 mL SDS 10% solution, 900 mL Milli-Q water. The stain-free gel was activated with UV-light in the Chemidoc imaging system (BioRad) and imaged in to detect the migrated proteins. Proteins were then transferred to a nitrocellulose membrane (1.3 A, 25 V, 7 min). The membrane was first incubated (r.t., 1 h) in a solution containing non-fat dry milk 5% and Tween-20 0.05% in PBS 0.1 M. The membrane was then incubated (overnight, 5°C) with MnSOD (rabbit) antibodies (diluted 1 250-fold) in 5% non-fat dry milk. After three washes in PBS-Tween 20 0.05%, the membrane was incubated (r.t., 2 h) with horseradish-peroxidase-conjugated secondary (rabbit) antibodies (diluted 10 000-fold) in 5% non-fat dry milk. After the addition of luminol solution (1 mL) and peroxide solution (1 mL), protein bands were visualized by

chemiluminescence (Chemidoc). Intensity bands analysis was performed by the Image Lab Software (BioRad).

IL-8 quantitation by ELISA

Quantification of IL-8 was performed using a commercial IL-8 detection ELISA kit containing IL-8-specific capture and detection antibodies, IL-8 standards, and streptavidin-HRP by following the manufacturer's instructions. The coating was accomplished by incubating capture antibodies (4 µg/mL: 100 µL/well in DPBS 1X) in an ELISA-specific 96-well plate, sealed with an adhesive strip, and incubated (overnight, 4°C). After removing the capture solution, nonspecific binding sites were blocked (1 h, light-protected) by BSA (1%, 200 µL/well in PBS 1X). Supernatants were diluted 250-fold for LPS-activated samples and 10-fold for non-activated samples in dilution buffer (BSA 0.1% with Tween 20 0.05%). A standard curve was generated by serial dilution (31.3-2,000 pg/mL) of commercial IL-8 solution. The plate was washed (x3) with 300 µL DPBS 1X containing Tween 20 0.05%, with an automatic 96-well plate washer. The plate was incubated (2 h, protected from light) with the diluted supernatants (100 µL/well) and washed with 300 µL (PBS Tween) (x3) to remove unbound IL-8. Detection solution with detection biotinylated antibodies was added (10 ng/mL: 100 µL/well in PBS 1X), and the plate was incubated (2 h, light-protected) and washed with 300 µL (PBS Tween) (x3) to remove unbound detection antibodies. A commercial solution of streptavidin-HRP (diluted 40-fold) in dilution buffer was added (100 µL/well), and the plate was incubated (20 min, light-protected). After 3 washes, revealing solution (100 µL/well, from H_2O_2 solution 5 mL + TMB solution 5 mL) was added and incubated (20 min, light-protected). H_2SO_4 1 M addition (50 µL/well) stopped the reaction and turned TMB diimine yellow. Absorbance at 450 nm was measured to quantify the IL-8 in each supernatant. IL-8 levels were normalized by the protein content determined by the BCA protein assay in the corresponding cell lysates, as described previously.

- IMS-MS experiments of Mn1 and Mn1P in cell lysates

Cell cultures and cell sample preparation

HT29-MD2 cells were seeded in 250 mL culture flasks at 5E6 cells/flasks to reach 90% confluence after 3 or 4 days. Cells were then incubated for 6 h with 10 mL of cell medium containing LPS at 0.1 µg/mL and Mn1 at 100 µM or Mn1P at 100 µM. Cells were washed with PBS 1X, and 2 mL of ammonium bicarbonate at 50 mM buffer at pH 7.4 were added to the

flasks. Cells were harvested by scraping, and the number of cells present in each cell sample was counted using a Malassez counting chamber. Cells were sonicated and stored at -20 °C. Ammonium bicarbonate (volatile and not saline) buffer has been chosen because it does not interfere with the MS analysis compared to HEPES 0.1 M (or Triton 1X). Before being injected in the timsTOF apparatus, the cell lysates were centrifuged at 50 000 or 100 000 rpm for 20 min at 4°C to remove the large proteins and cellular debris. The cell lysates were aliquoted and stored at -80 °C until further use.

Complex preparation

The Mn1 (or Mn1P) and Co1$^{13}C_6$ (or Co1P$^{13}C_6$) complexes were prepared at 100 µM from $MnCl_2$ and $CoCl_2$ stock solutions (at 10 mM in miliQ H_2O) mixed in 1 eq. with the enPI_2 (or enPI_2P) and enP$I_2{}^{13}C_6$ (or enP$I_2{}^{13}C_6$P) ligands in a total volume of 200 µL NH_4HCO_3 50 mM pH 7.4 (2 µL of ligand + 2 µL of metal + 196 µL NH_4HCO_3 50 mM).

Sample preparation for ionization and IMS-MS analysis

The complexes have then been diluted in different percentages of ACN/NH_4HCO_3 50 mM pH 7.4 to facilitate ionization in the timsTOF system. For the Mn1P quantification, the diluted cell lysates (incubated with the complex as described before) were spiked with the Co1$^{13}C_6$P internal standard at different concentrations just before the IMS direct infusion. Aliquots of cell lysates stored at -80°C were defrosted and kept on ice before analysis. Samples were prepared in 250 µL of ionization solution for IMS-MS analysis. For the ionization of a complex at 2 µM in 80% ACN, 5 µL of the complex at 100 µM were added in 45 µL NH_4HCO_3 50 mM (or cell lysate, incubated with just LPS or with LPS + Mn1P), the tube was vortexed for 5 s and 200 µL ACN were added. Cell lysate samples in ACN ionization solution were centrifuged for 5 min at 13 000 rpm at 4°C, and the supernatant was used for direct infusion. Sample injection was performed with a 250 µL syringe at 5 µL/min flow rate. Once the spray was stabilized after 1 min, the acquisition was performed over 3-5 min in lock accumulation mode (mode 2) to a mobility range (selected according to the IM of each analyzed complex). After each sample, the system was washed with 40 µL isopropanol (with a 500 µL syringe), 20 µL water (with a 100 µL syringe) and 40 µL isopropanol (with a 500 µL syringe), to avoid contaminating the following sample and capillary blockage. The flow rate was switched to 10 µL/min during the

washes. Ultrapure solvents (Biosolve) and metal-free labware were used to avoid metal contamination.

Calibration curve for the quantification of Mn1P

The calibration curve generated for the quantification of pure Mn1P at 0, 0.001, 0.002, 0.005, 0.01 µM in 80% ACN/20% NH_4HCO_3 50 mM pH 7.4, with the Co1$^{13}C_6$P internal standard spiked at 0.02 µM was performed according to the following table.

Mn1P final C	V ACN	V Mn1P	V Co1$^{13}C_6$P 1 µM	V buffer
0 µM	200 µL	-	5 µL	45 µL
0.001 µM	200 µL	2.5 µL 0.1 µM	5 µL	42.5 µL
0.002 µM	200 µL	5 µL 0.1 µM	5 µL	40 µL
0.005 µM	200 µL	1.25 µL 1 µM	5 µL	43.75 µL
0.01 µM	200 µL	2.5 µL 1 µM	5 µL	42.5 µL

The intensity values for the observed species in the spiked buffer of the calibration curve are shown in the table below.

C $[Mn1P]^+$	Intensity $[Mn1P]^+$	Intensity $[Co1^{13}C_6P]^+$	$[Mn1P]^+/[Co1^{13}C_6P]^+$
0 µM	876	1.3 x 10^6	0.000658505
0.001 µM	1.2 x 10^4	1.7 x 10^6	0.006634954
0.002 µM	1.0 x 10^4	0.9 x 10^6	0.010799934
0.005 µM	5.2 x 10^4	1.1 x 10^6	0.046644803
0.01 µM	6.3 x 10^4	0.9 x 10^6	0.06617076

Table S4. Intensity values for the observed species in the cell lysates incubated with Mn1P (at 100 µM) and spiked with Co1$^{13}C_6$P (at 0.02 µM), (45 µL cell lysate + 5 µL Co1$^{13}C_6$P 1 µM + 200 µL ACN), for the quantification experiment of Mn1P in cell lysates.

Cell sample	Intensity $[Mn1P]^+$	Intensity $[Co1^{13}C_6P]^+$	$[Mn1P]^+/[Co1^{13}C_6P]^+$	[Mn1P injected] µM	[Mn1P cell lysate] µM	[Mn1P cells] fmol/cell
Rep Bio 1 - 1	3.1 x 10^4	3.6 x 10^5	0.086269785	0.012273988	0.068188824	0.009031632
Rep Bio 1 - 2	5.9 x 10^4	3.8 x 10^5	0.154219987	0.022077939	0.122655216	0.016245724
Rep Bio 1- 3	2.8 x 10^4	3.3 x 10^5	0.08637299	0.012288879	0.068271549	0.009042589
Rep Bio 2 - 1	7.5 x 10^4	4.8 x 10^5	0.155799013	0.022305763	0.123920906	0.024784181
Rep Bio 2 - 2	4.1 x 10^4	4.1 x 10^5	0.100687274	0.014354164	0.079745355	0.015949071

Experiments were performed in two biological replicates and analyzed in technical triplicates.

VI.1.b.ii. Supplementary Figures

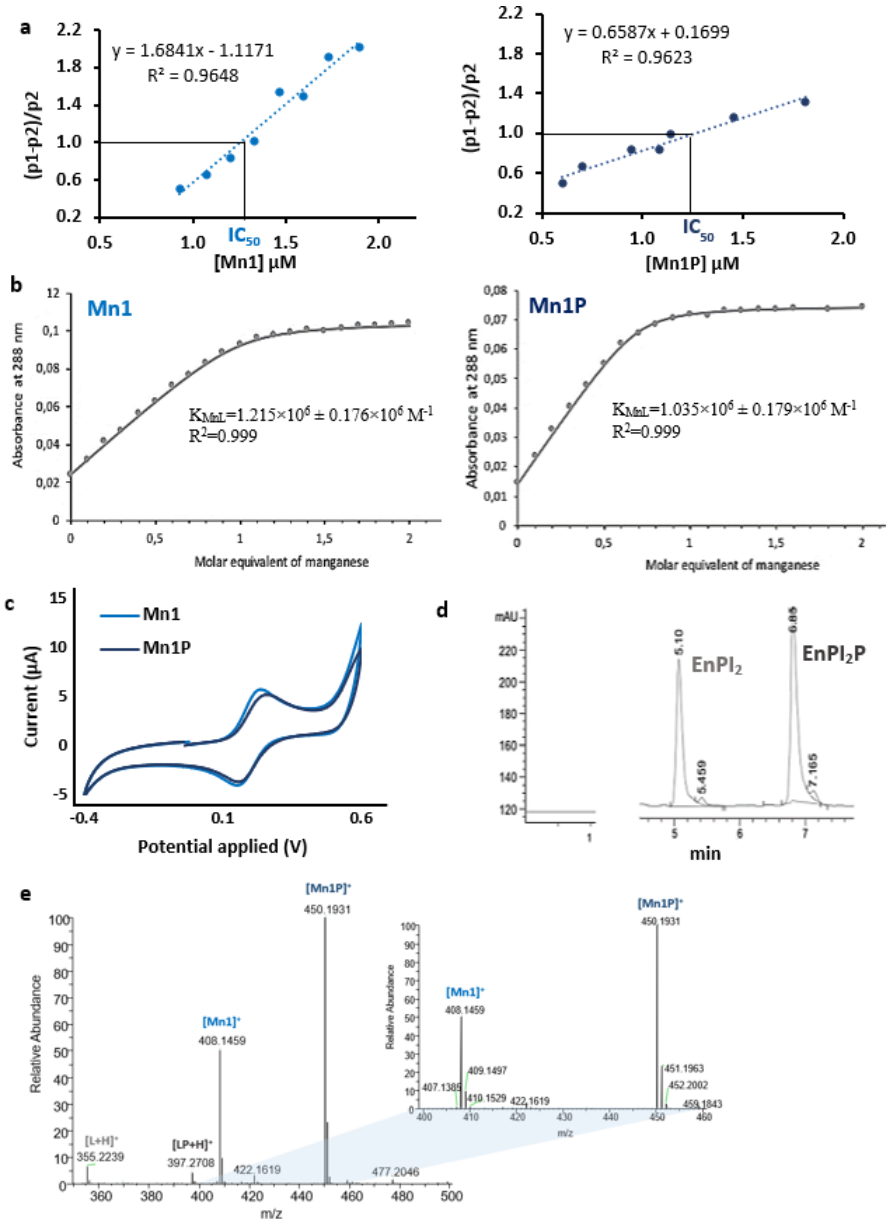

Figure S1. *a. SOD activity by McCord - Fridovich assay. A Xanthine (200 µM)/xanthine oxidase system was used to continuously produce superoxide with ferricytochrome c at 100 µM as a competitive indicator, in HEPES 50 mM at pH 7.5. b. Association constant of Mn-ligand by UV-vis titration. The absorbance of the manganese complexes was monitored at 288 nm while adding successively 0.1 equivalent of Mn (4.5 µM final concentration) to a solution of ligand at 45 µM. The absorbance was plotted as a function of the number of added Mn equivalents. The association constants of Mn-enPI₂P and Mn-enPI₂ were obtained by fitting the theoretical absorbance curve to the experimental one using a MATLAB program and based on a non-linear regression method. The calculated association constant K (M-L) and the associated R^2 are mentioned in each plot. The measures were performed in a HEPES 50 mM buffer at pH 7.5 with ionic force F=12.5 mM. c. Cyclic voltammograms by electrochemistry. Measures were taken for the HEPES buffer alone, for Mn1, Mn1P and $MnCl_2$ at 400 µM in HEPES 100 mM at pH 7.4. The electrochemical setup contained a glassy carbon working electrode (3 mm diameter), a platinum wire counter electrode, and an aqueous saturated calomel electrode (ECS) as the reference electrode (0.241 V + ECS = normal hydrogen electrode). d. Lipophilicity by liquid chromatography. HPLC analysis of the enPI₂ ligands on a C18 column using a water/ACN gradient increasing from 5% to 50% in water in 10 min and then from 50% to 100% in 2 min before going back to 5% in 1 min. The mobile phase solvent was complemented with TFA at 0.1%. The ligands were pooled at 1 mM and injected together in the chromatographic system. e. Ionization properties by ESI-MS. MS spectra for Mn1 + Mn1P analyzed in a 1 to 1 ratio. b was from* [6].

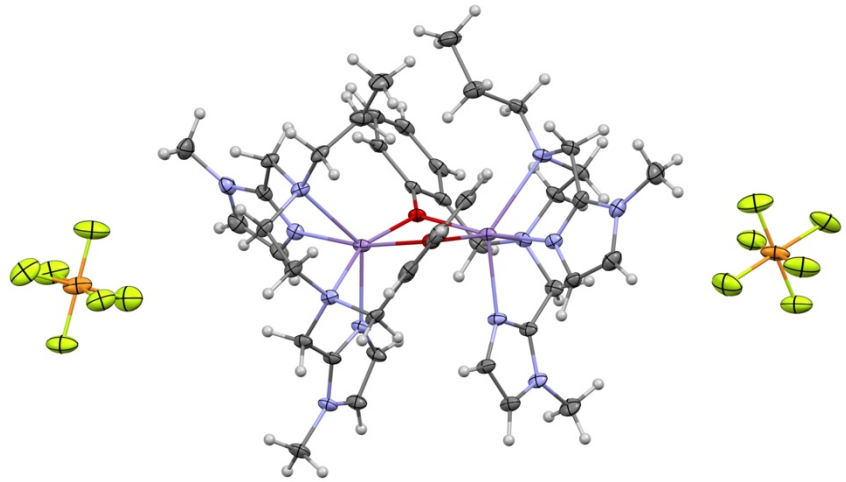

Figure S2. *Crystallographic structure of Mn1P, consisting of the [(enPI$_2$P) Mn Mn (enPI$_2$P)] (PF$_6$)$_2$ dimer. Thermal ellipsoids are shown at the 10% level. A crystallographic twofold axis is located between the two Mn atoms. The resulting binuclear complex contains a doubly bridged bimetallic core with Mn ⋯Mn distance of 3.292(1) Å. For each Mn, the atoms comprising the equatorial plane are O(1), O(1)i, N(1), N(5), and Mn is 0.024 A out of this plane. The two axial sites are occupied by N(2), N(4), respectively. The bond angle for N(2)-Mn-N(4) is 135.9(2)°. Thus, the coordination sphere of the metal atom Mn is best described as a capped distorted octahedron.*

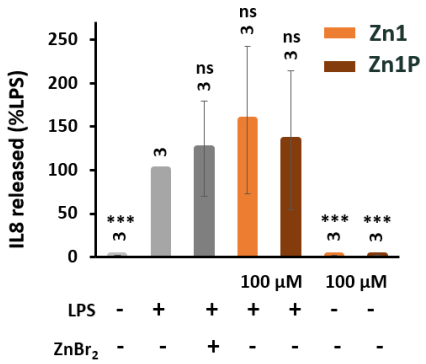

Figure S3. *Interleukin 8 quantitation of Zn analogs in the supernatants measured by ELISA. LPS-activated (0.1 µg/mL) cells were incubated in the presence of ZnBr$_2$, Zn1 or Zn1P at 100 µM for 6 h. Non-activated cells were incubated with Zn1 or Zn1P at 100 µM for 6 h. Positive and negative controls respectively consist of LPS-activated and non-activated HT29-MD2 cells. The IL-8 amount was normalized by the total protein amount present at each sample and was reported as ng/mg of proteins. Normalized IL-8 amount is presented % vs. the LPS positive control. Results represent mean ± SEM for three biological experiments in technical duplicates. The p-values were calculated using the Student's t-test. The mean rank of each column was compared to that of the LPS control, each comparison stands alone. (***) $p < 0.001$, (**) $p < 0.01$, and (*) $p < 0.05$ versus LPS control, and ns means nonsignificant.*

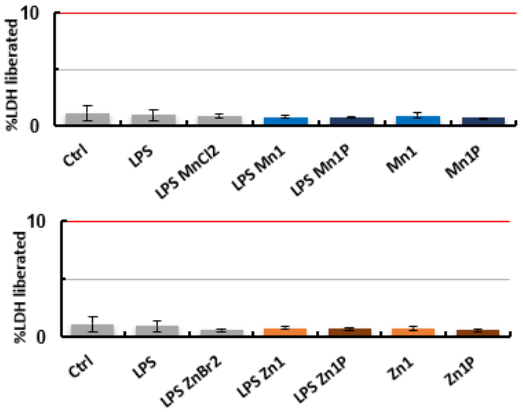

Figure S4. *Compounds cytotoxicity with the lactate dehydrogenase assay. Cells were incubated for 6-hours with just cell media, with LPS 0.1 µg/mL, with LPS + $MnCl_2$, LPS + Mn1, LPS + Mn1P, Mn1, Mn1P and LPS + $ZnBr_2$, LPS + Zn1, LPS + Zn1P, Zn1, Zn1P at 100 µM. None of the studied conditions were toxic since LDH release in the supernatant did not exceed 10%. Results represent three biological experiments in technical duplicates*

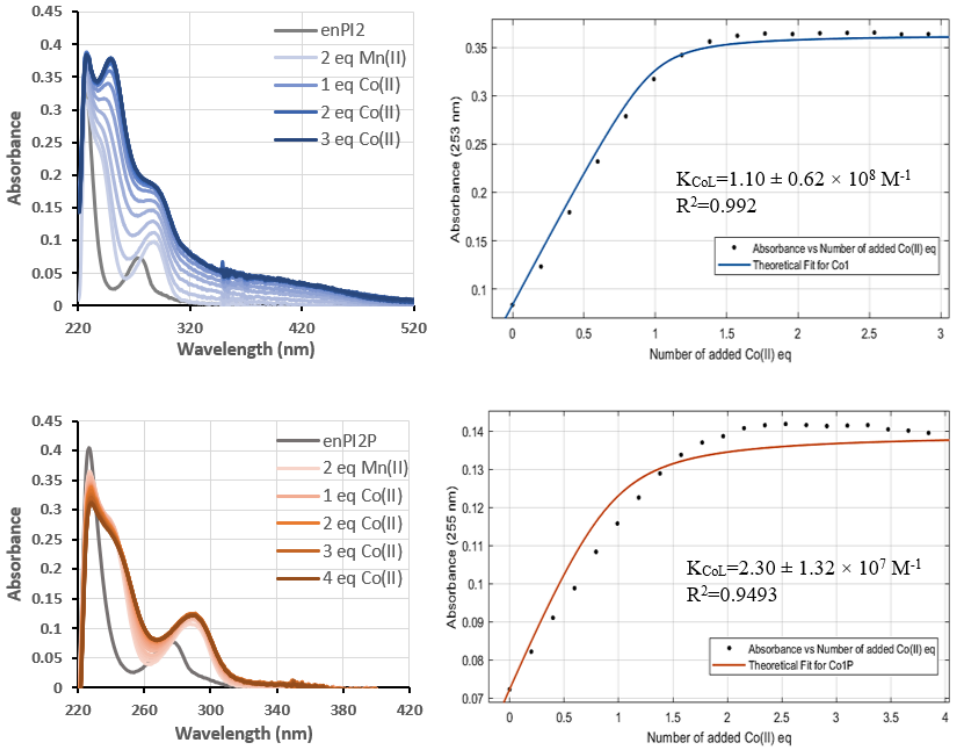

Figure S5. *Determination of the association constants of the studied ligands with Co(II) from competition experiments in HEPES 50 mM pH 7.5. The absorbance of the Co(II) complex has been monitored while adding successively 0.2 eq of Co(II) ($CoCl_2$) (4 mM) to a solution of manganese complex at 40 µM. The initial solution was prepared by adding 2 eq of Mn(II) ($MnCl_2$) (80 µM) to a solution of ligand at 40 µM. The addition of an excess of manganese is necessary to (1) assume that the concentration of ligand is null (see calculation of K_{CoL} in supplementary information), (2) to shift the equilibrium to the formation of the Mn(II) complex and disfavor the Co(II) complex that is more thermodynamically favored. The absorbance is plotted as a function of the number of added Co(II) equivalents. The association constants of the cobalt complexes were obtained by fitting the theoretical absorbance curve to the experimental one using the MATLAB curve fitting tool based on a non-linear least-square regression method (see calculation of K_{CoL} in supplementary information). Dots correspond to the experimental data and the continuous line corresponds to the fit. The calculated K (M-L) and the associated R^2 are mentioned in each plot.*

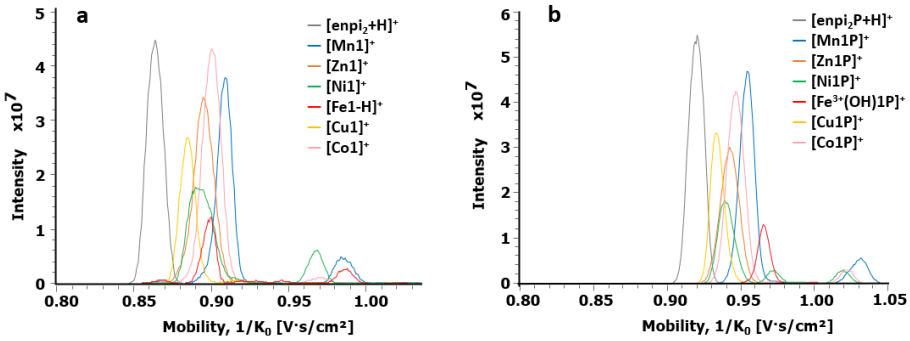

Figure S6. *a. $[enPI_2+M]^+$ species ion mobilograms. The samples were analyzed at 20 µM in 1:1 ratio in 80% ACN/20% NH_4HCO_3 50 mM pH 7.4. Ion mobilograms of $[enPI_2+H]^+$, $[Mn1]^+$, $[Zn1]^+$, $[Ni1]^+$, $[Fe1\text{-}H]^+$, $[Cu1]^+$ and $[Co1]^+$ and b. $[enPI_2P+H]^+$, $[Mn1P]^+$, $[Zn1P]^+$, $[Ni1P]^+$, $[Fe^{3+}(OH)1P]^+$, $[Cu1P]^+$ and $[Co1P]^+$ were extracted with their corresponding theoretical m/z (see Table S3) with 5 mDa precision.*

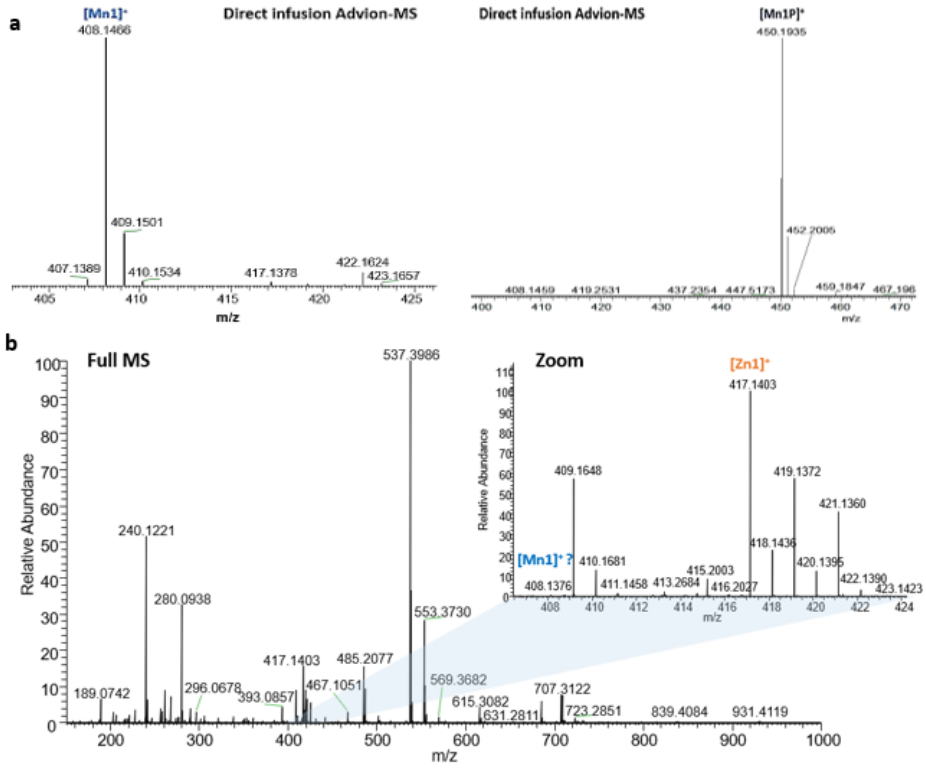

Figure S7 *MS spectra with Advion metal-free nano ESI. Nano ESI metal-free TriVersa NanoMate (Advion) source coupled to an Orbitrap Fusion Lumos MS (ThermoFisher Scientific). a. Direct infusion of pure Mn1 (MS signature at m/z 408.1465) and Mn1P (MS signature at m/z 450.1935) b. Direct infusion of cell lysate in ammonium bicarbonate buffer from cells incubated with Mn1 (at 100 µM for 6 h). Ionization at 50 µM in 85% ACN/15% ammonium formate 50 mM pH 7.35.*

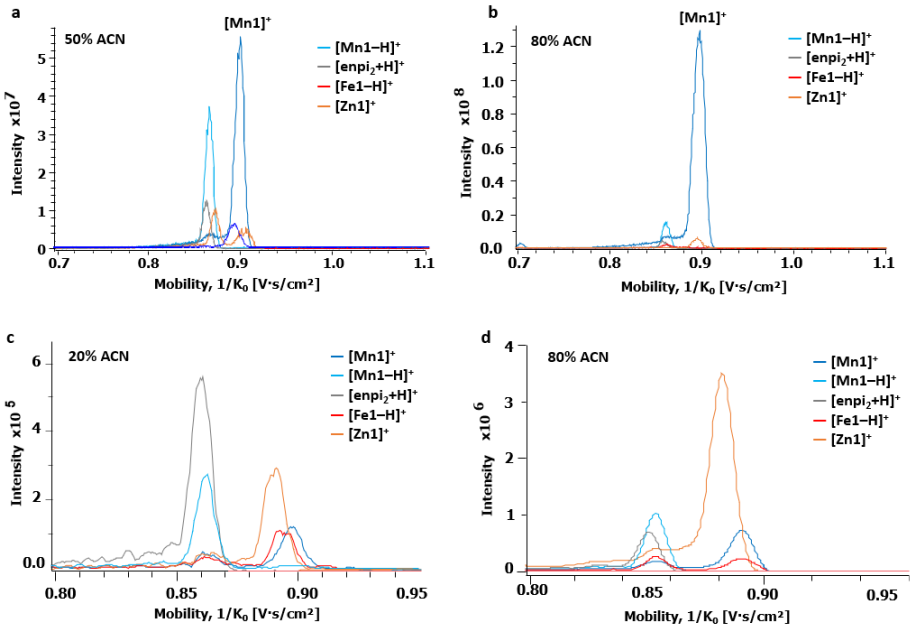

Figure S8. *IMS-MS extracted ion mobilograms. a. Mn1 ionized at 50 µM in a solution of 50% ACN/50% NH_4HCO_3 50 mM pH 7.35, b. Mn1 ionized at 50 µM in a solution of 80% ACN/20% NH_4HCO_3 50 mM pH 7.35. c. Mn1 analyzed at 0.5 µM in 20% ACN/80% NH_4HCO_3 50 mM pH 7.35, d. Mn1 analyzed at 0.4 µM in 80% ACN/20% NH_4HCO_3 50 mM at pH 7.35. IM of the species were extracted with their corresponding m/z with 5 mDa precision.*

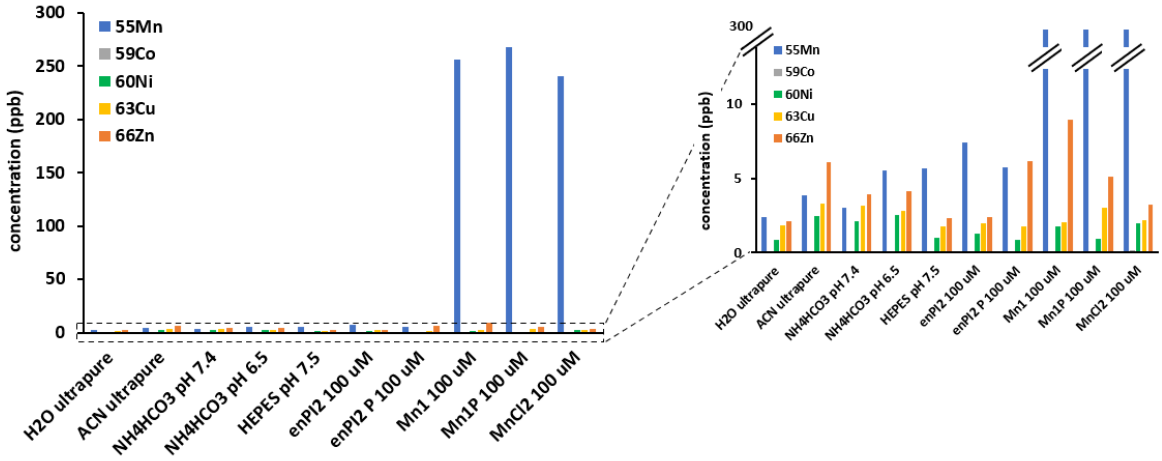

Figure S9. *Verification of metal presence in the Mn1 and Mn1P preparation step by ICP-MS. A standard solution containing ^{55}Mn, ^{59}Co, ^{60}Ni, ^{63}Cu, and ^{66}Zn at 10 ppb each was used to calculate the concentration of these metals in ppb in the analyzed samples. All samples were analyzed in 2% HNO_3. No significant quantity (<10 ppb) of metals was found in the buffers used for the Mn1 and Mn1P preparation. ^{55}Mn was the primary metal in the Mn1, Mn1P and $MnCl_2$ samples.*

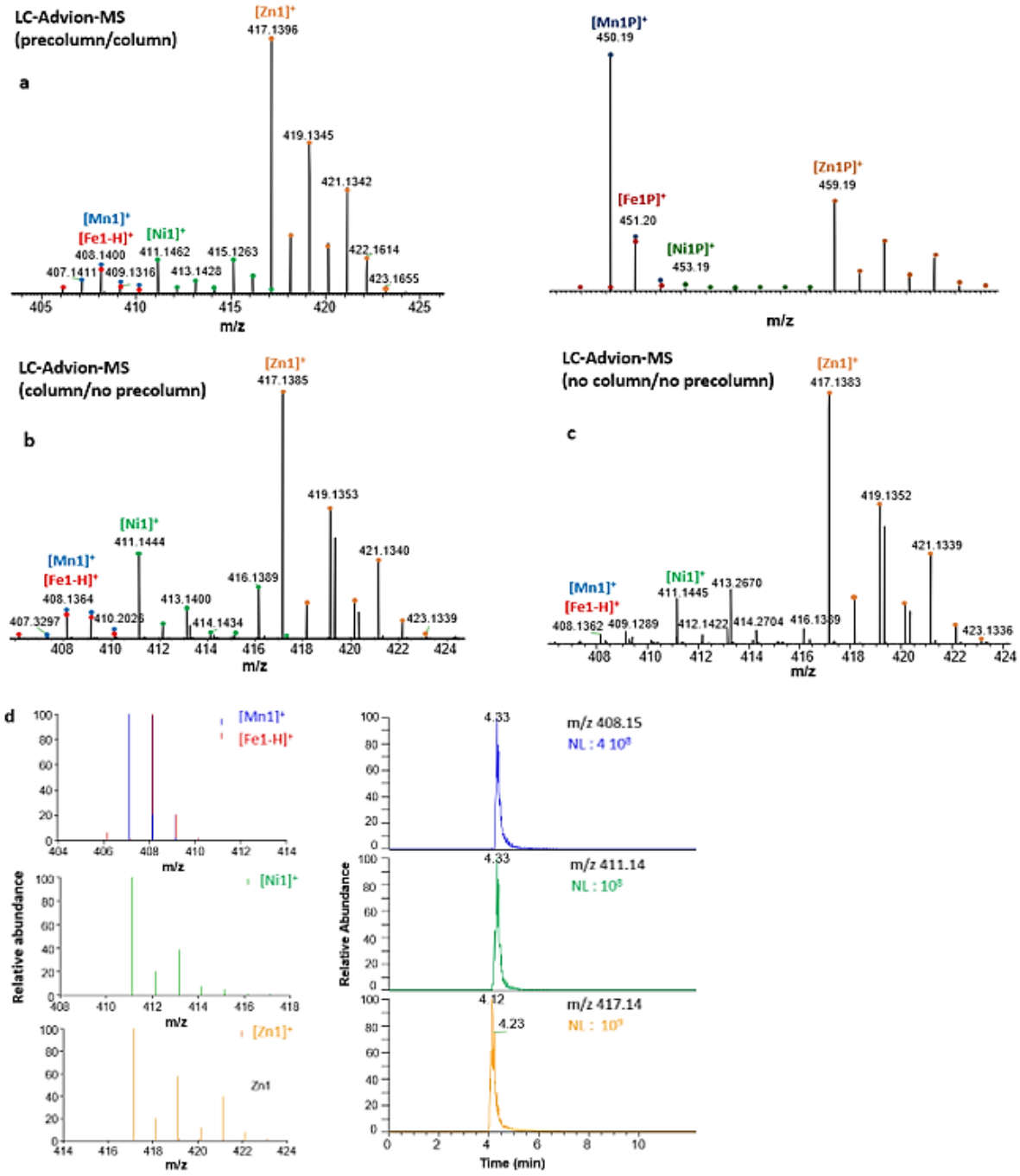

Figure S10. *LC-MS spectra with Advion metal-free nano ESI. Liquid Chromatography RSLC 3000 (ThermoFisher), coupled with the nano ESI metal-free TriVersa NanoMate (Advion) source and the Orbitrap Fusion Lumos MS (ThermoFisher Scientific). Elution in 85% ACN/15% ammonium formate 50 mM pH 7.35 gradient over 30 min. a. MS spectra obtained by injection of pure Mn1 or Mn1P at 50 µM with a Zic-HILIC nano column (75 µm internal diameter PEEK-covered silica, Merck) and precolumn, b. just with a Zic-HILIC column (no precolumn), c. with no column (and no precolumn). d. Theoretical isotope patterns for $[Mn1]^+$, $[Fe1\text{-}H]^+$, $[Zn1]^+$ and $[Ni1]^+$ formed by coordination of the enPI$_2$ ligand with Mn(II) coinciding with Fe(II) in a dehydrogenated form, as well as Zn(II) and Ni(II) and co-elution of chromatography peaks of Mn1 injected at 50 µM. The peaks were extracted at m/z 408.15, 411.14, and 417.14.*

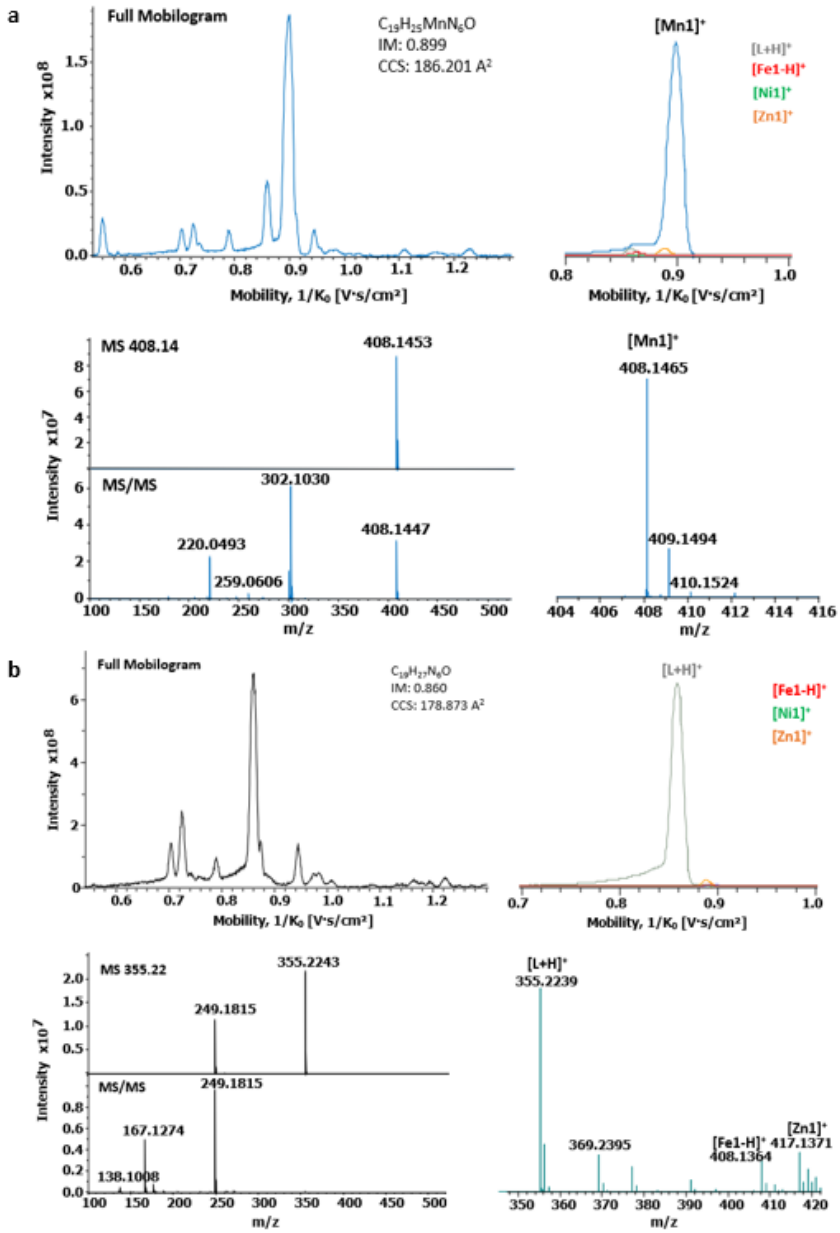

Figure S11. *a. IMS-MS analysis of Mn1. Full IM of Mn1 (IM 0.899, CCS of 186.201 A²), MS at m/z 408.1453, MS/MS at m/z 220.0493, 302.1030, IM of Mn1 was extracted with m/z 408.1465 with 5 mDa precision. The sample was injected at 50 µM in a solution of 80% ACN / 20% NH_4HCO_3 50 mM at pH 7.35. b. IMS-MS analysis of the $enPI_2$ ligand. Full IM of $enPI_2$ (IM 0.860, CCS of 178.873 A²), MS at m/z 355.2243, MS/MS at m/z 249.2815 and 162.1274, IM of $enpi_2$ was extracted with m/z 355.2239 with 5 mDa precision.The sample was ionized at 50 µM in a solution of 80% ACN / 20% NH_4HCO_3 50 mM at pH 6.5.*

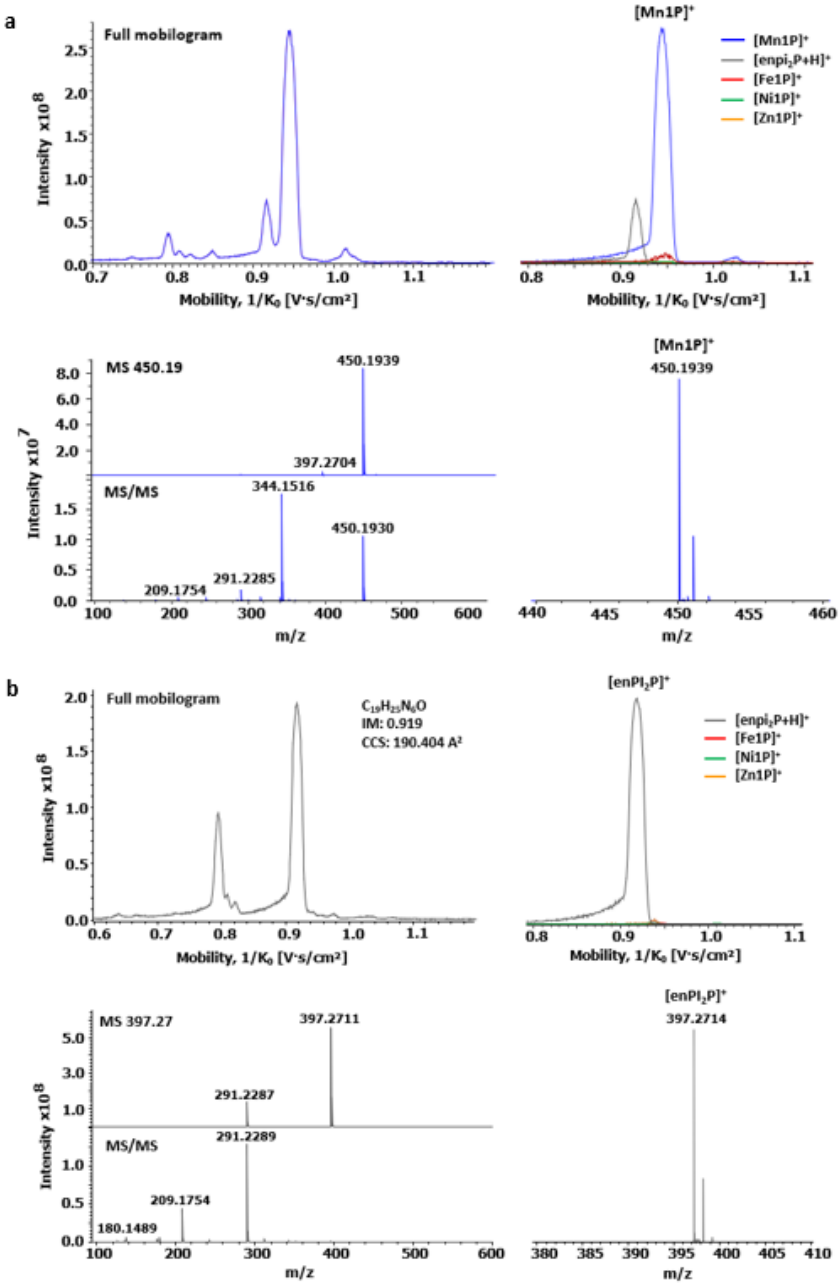

Figure S12. *a. IMS-MS analysis of the Mn1P. Full IM of Mn1P (IM 0.950), MS at m/z 450.1939, MS/MS at m/z 344.1516 and 291.2285. IM of Mn1P was extracted with m/z 450.1939 with 5 mDa precision. The sample was ionized at 50 µM in a solution of 80% ACN / 20% NH_4HCO_3 50 mM at pH 7.35. b. IMS-MS analysis of the $enPI_2P$ ligand. Full IM of $enPI_2P$ (IM 0.919, CCS of 190.404 A^2), MS at m/z 397.2714, MS/MS at m/z 291.2289 and 209.1754. IM of $enPI_2P$ was extracted with m/z 397.27104 with 5 mDa precision. The sample was ionized at 50 µM in a solution of 80% ACN/20% NH_4HCO_3 50 mM at pH 6.5.*

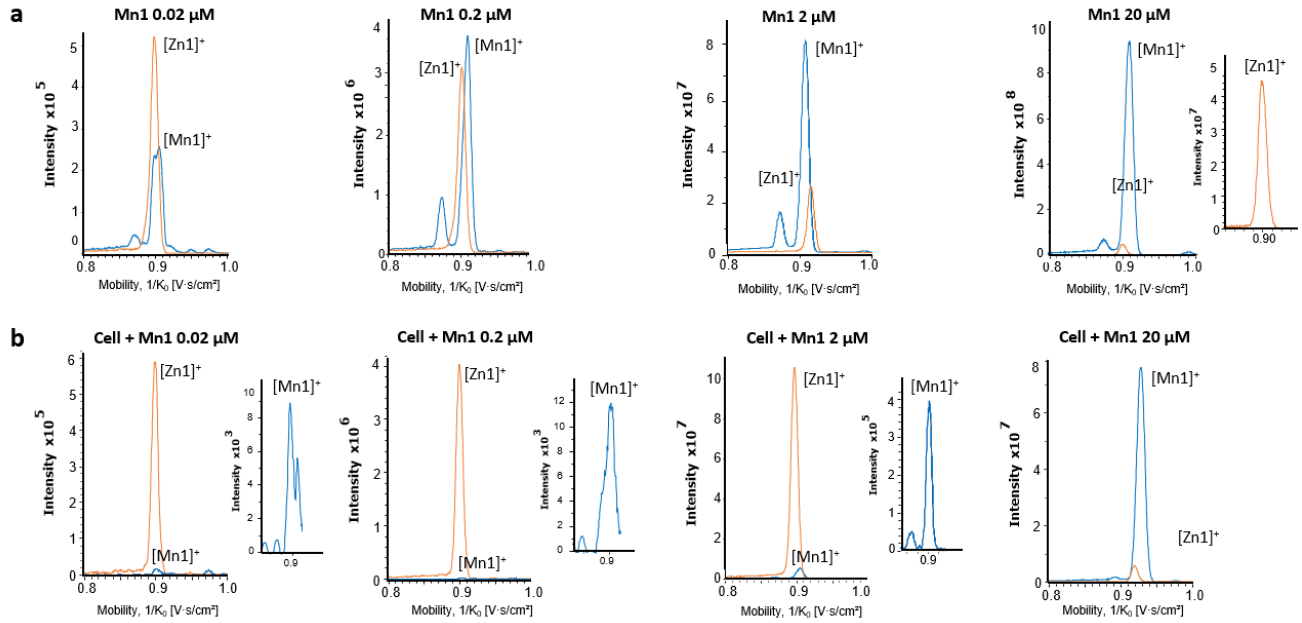

Figure S13. *IMS-MS dynamic range for Mn1 a. in a non-cell environment, b. in a cell environment. Ion mobilograms for Mn1 and Zn1 were extracted according to the respective exact masses with 5 mDa precision. LPS stimulated cell lysates were spiked with the complexes in different concentrations at 0.02, 0.2, 2 and 20 µM. The samples were analyzed in 80% ACN/20% NH_4HCO_3 50 mM at pH 7.4.*

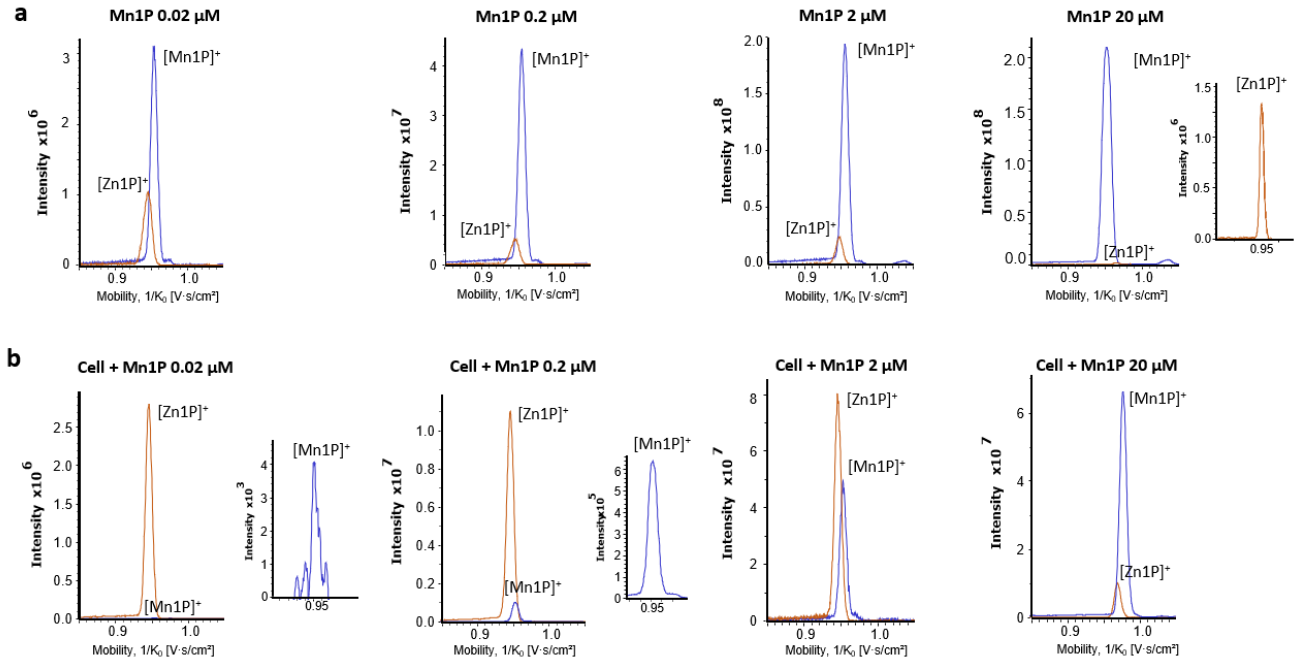

Figure S14. *IMS-MS dynamic range for Mn1P a. in a non-cell environment, b. in a cell environment. Ion mobilograms for Mn1P and Zn1P were extracted according to the respective exact masses with 5 mDa precision. LPS stimulated cell lysates were spiked with the complexes in different concentrations at 0.02, 0.2, 2 and 20 µM. The samples were analyzed in 80% ACN/20% NH_4HCO_3 50 mM at pH 7.4.*

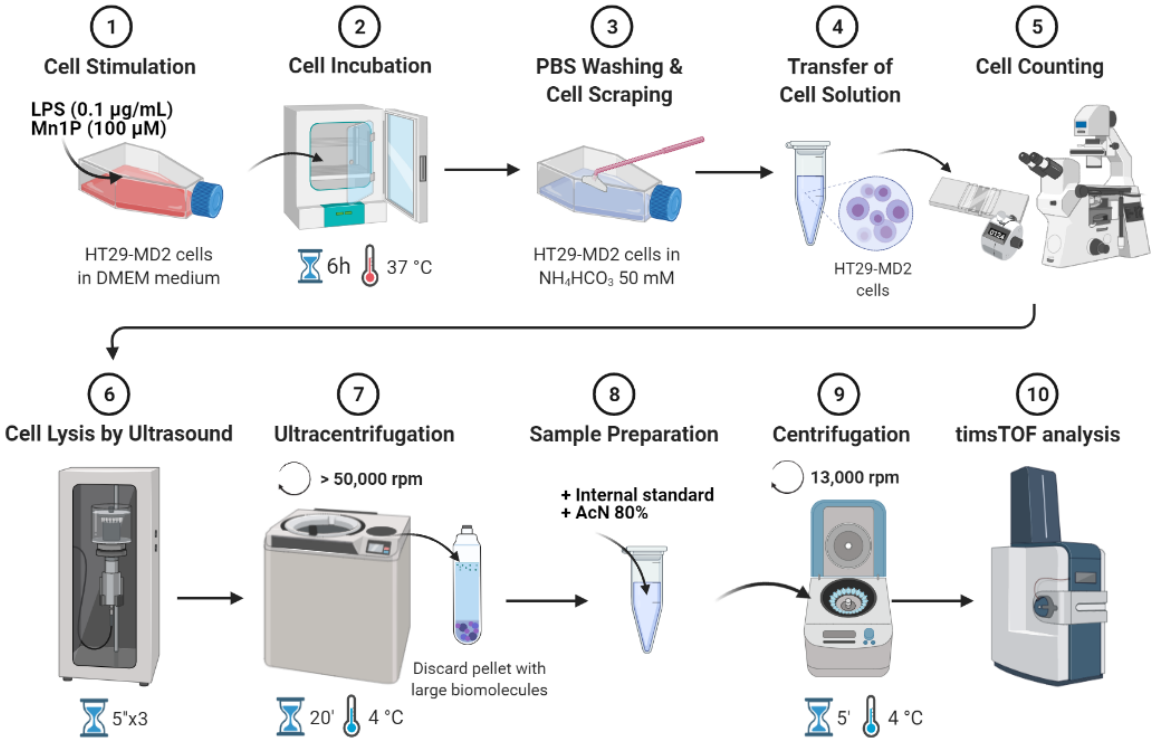

Figure S15. *Workflow of the IMS-MS strategy for MnSOD mimic detection and quantification in HT29-MD2 cells. 1. Cells were stimulated with Mn1P at 100 µM and LPS (0.1 µg/mL) in cell medium (DMEM, 20% FBS, 0.1% blasticidin). 2. Cells were incubated for 6 h at 37°C. 3. Cells were washed with PBS 1X and detached by scraping (to avoid trypsin-EDTA, as EDTA is a good Mn chelator that could shift the complexation equilibrium) in 2 mL ammonium bicarbonate 50 mM buffer at pH 7.4. 4. The cell solution was transferred to a clean tube. 5. Cells were counted on a Malassez cell counting chamber. 6. Cells were lysed by ultrasound (5 sec cycles x3). 7. Cell lysates were ultracentrifuged at 50 000 or 100 000 rpm for 20 min at 4°C to eliminate large biomolecules that would perturb the MS analysis. 8. The samples were diluted in ACN to facilitate ionization (optimal ionization solution: 80% ACN/20% NH_4HCO_3, total 250 µL). The diluted cell lysates were spiked with an internal standard ($Co1P^{13}C_6$) at a specific concentration. 9. The cell lysate samples in ACN ionization solution were then centrifuged for 5 min at 13 000 rpm at 4°C. 10. The supernatant was used for direct infusion by IMS-MS (timsTOF system).*

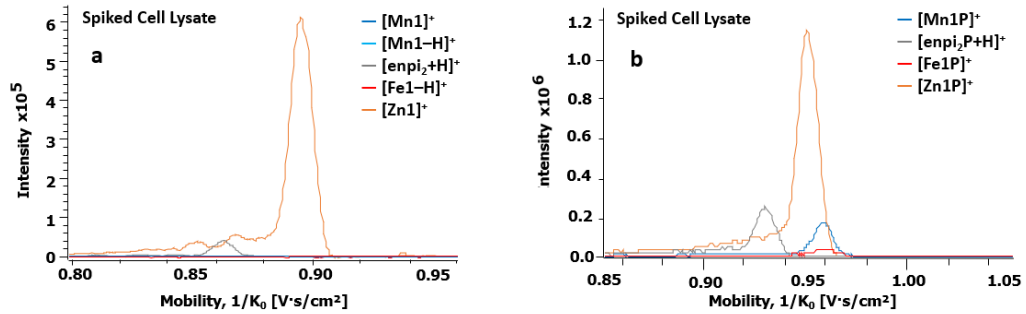

Figure S16. *IMS-MS extracted ion mobilograms. a. cell lysate spiked with Mn1 at 0.4 µM, b. cell lysate spiked with Mn1P at 0.4 µM ionized in a solution of 80% ACN/20% NH_4HCO_3 50 mM pH 7.4. IM of the species were extracted with their corresponding m/z with 5 mDa precision.*

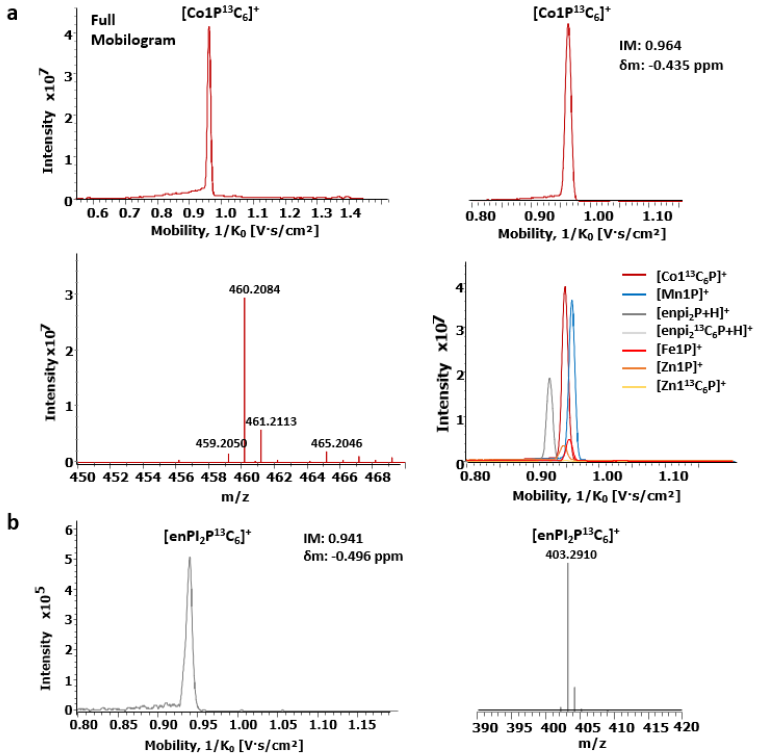

Figure S17. *IMS-MS analysis of a. the $Co1^{13}C_6P$ internal standard. Full IM of $Co1^{13}C_6P$, extracted IM (IM 0.964 V.s.cm^{-1}), MS signature at m/z 460.2084, extracted ion mobilogram of Mn1P with $Co1^{13}C_6P$ 1:1, with 5 mDa precision, b the heavy $enPI_2{}^{13}C_6P$ ligand. Extracted IM of $enPI_2{}^{13}C_6P$ (IM 0.941 V.s.cm^{-1}) with 5 mDa precision. MS signature at m/z 403.2910. The samples were ionized at 2 µM in a solution of 80% ACN/20% NH_4HCO_3 mM at pH 7.4.*

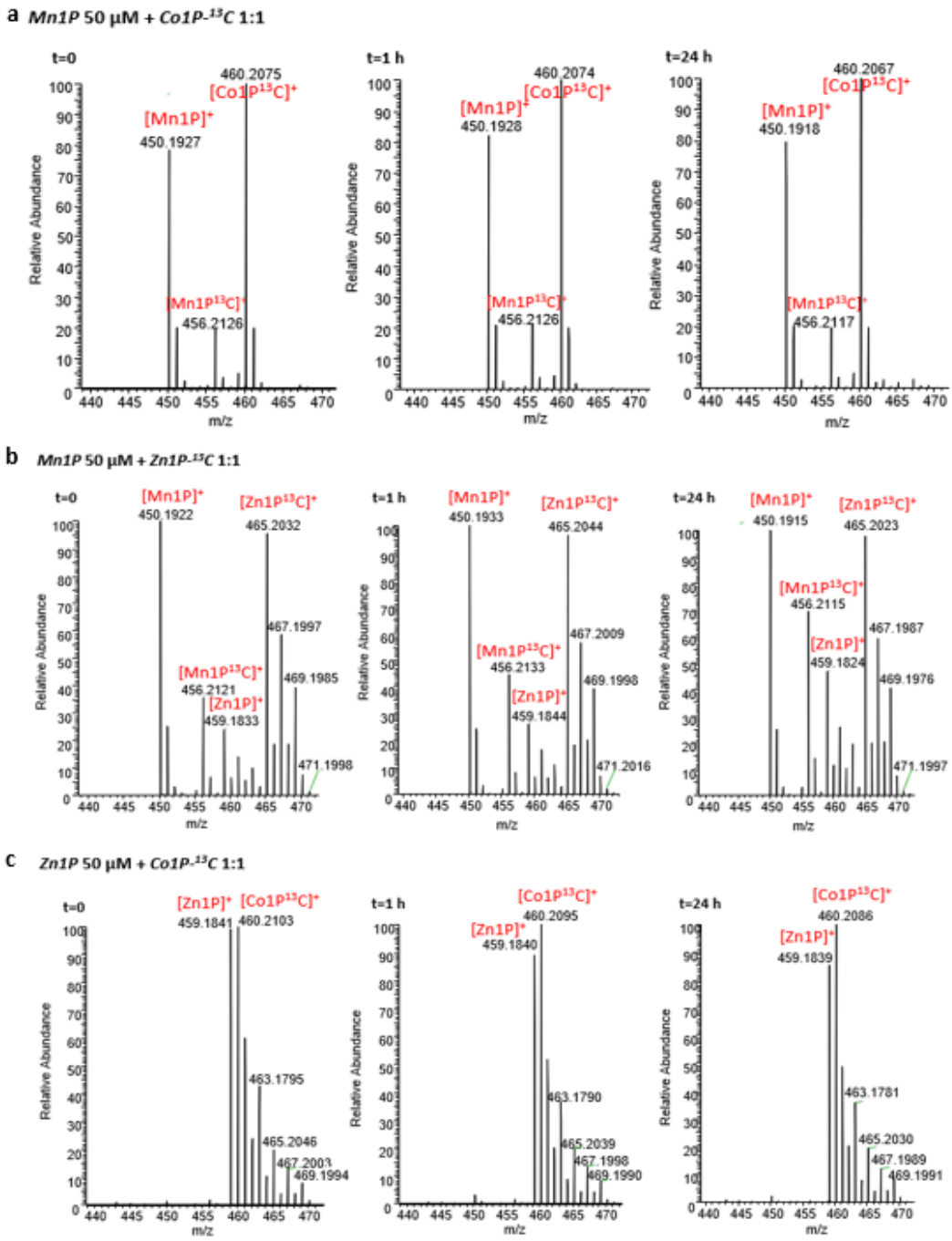

Figure S18. *ESI-MS analysis of the internal standard by direct infusion. a) Mn1P 50 µM + Co1$^{13}C_6$P 1:1, b) Zn1P 50 µM + Co1$^{13}C_6$P 1, c) Mn1P 50 µM + Zn1$^{13}C_6$P 1:1 in a solution of 80% ACN/20% NH_4HCO_3 50 mM pH 7.4.*

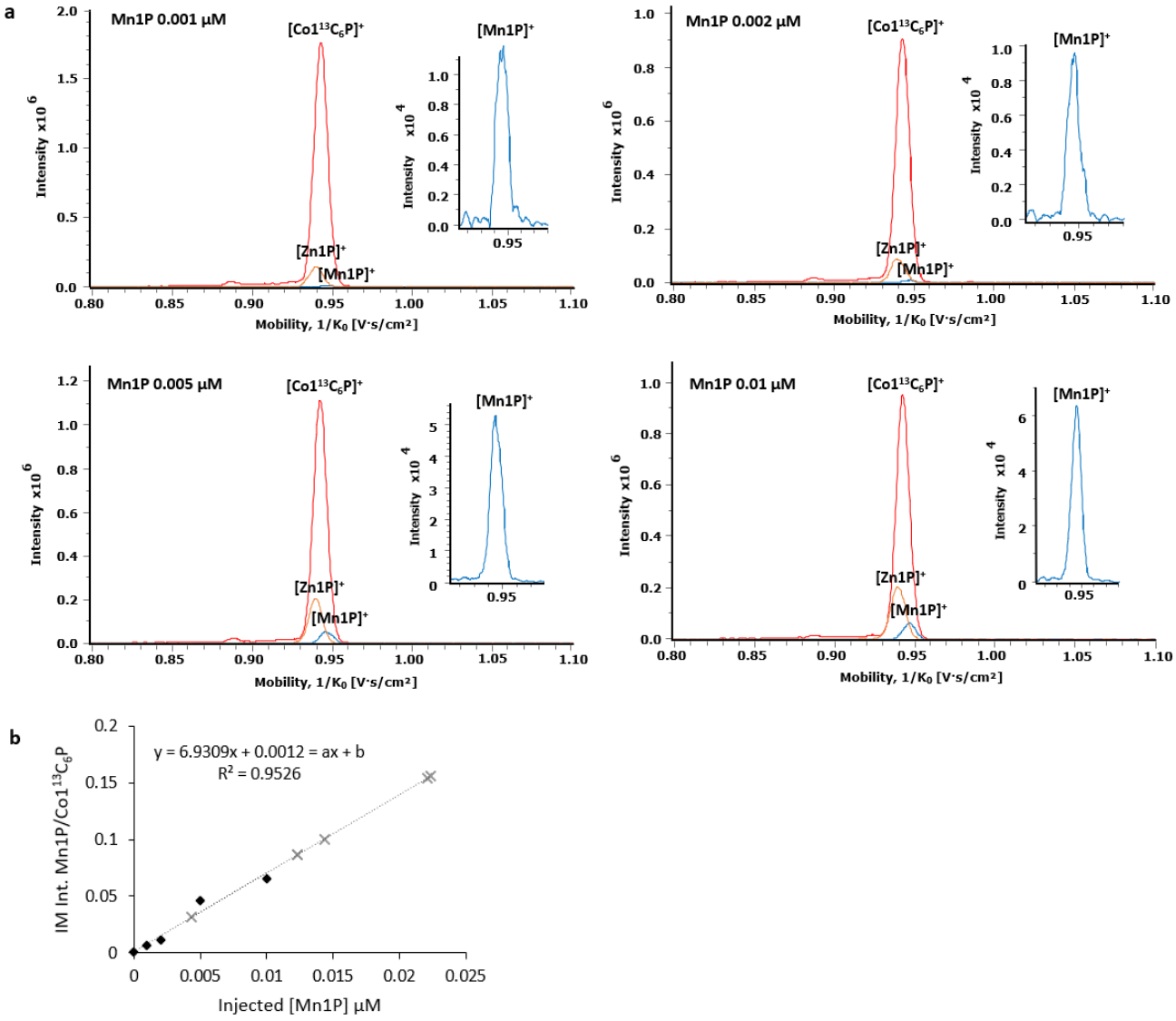

c

$$y = \frac{Intensity\ [Mn1P]^+_{calibration\ curve}}{Intensity\ [Co1P^{13}C_6]^+_{calibration\ curve}}, \qquad x = C_{Mn1P\ (injected)}\ in\ \mu M$$

$$C_{Mn1P\ (injected\ sample)} = \frac{\frac{Intensity\ [Mn1P]^+_{cell\ lysate}}{Intensity\ [Co1P^{13}C_6]^+_{cell\ lysate}} - b}{a}$$

$$C_{Mn1P\ (in\ cell\ lysate)} = C_{Mn1P\ (injected\ sample)} \cdot F_{dilution}$$

$$N_{Mn1P\ (in\ cells)} = C_{Mn1P\ (in\ cell\ lysate)} \cdot \frac{V_{cell\ lysate}}{N_{cells}}$$

Figure S19. *Calibration curve and quantification of Mn1P in cell lysates by IMS-MS. Pure internal standard at 0.02 µM and Mn1P from 0.001 to 0.01 µM in 80% ACN/20% NH_4HCO_3 50 mM at pH 7.4. a) Extracted ion mobilograms for Mn1P and Co1$^3C_6$P with 5 mDa precision. b) Linear calibration curve, with the increasing concentration of injected Mn1P in the x and intensity of Mn1/Co1$^{13}C_6$P extracted ion mobilities in the y axis. The rhombuses correspond to the calibration curve points. The crosses corresponded to the experimental points of the injected cell lysates from cells incubated with Mn1P (6 h, 100 µM) and spiked with Co1$^{13}C_6$P (see Figure S15) c. Calculation of the Mn1P intracellular concentration from the calibration's curve linear equation in mol/cell. Fdilution=250/45, Vcell lysates= 2 mL (see Table S4 Fig. S15). Typically, N_{cell} (counted in a Malassez chamber, see Fig. S15) were in the range of 10-15 E6 cells. Note that a Vcell of about 2 pL corresponds to an intracellular concentration of 7.5 ± 3.2 µM/cell.*

VI.1.b.iii. Supplementary References

[1] A.-S. Bernard, C. Giroud, H. Y. V. Ching, A. Meunier, V. Ambike, C. Amatore, M. G. Collignon, F. Lemaître, C. Policar, *Dalton Trans*. **2012**, *41*, 6399.

[2] G. M. Sheldrick, "SHELXS-97 Program for Crystal Structure Solution, **1997**.

[3] G. M. Sheldrick, *Acta Crystallogr C Struct Chem* **2015**, *71*, 3–8.

[4] L. J. Farrugia, *J Appl Crystallogr* **1999**, *32*, 837–838.

[5] F. Cisnetti, A.-S. Lefèvre, R. Guillot, F. Lambert, G. Blain, E. Anxolabéhère-Mallart, C. Policar, *Eur. J. Inorg. Chem*. **2007**, 4472–4480.

[6] G. Schanne, M. Zoumpoulaki, G. Gazzah, A. Vincent, H. Preud'homme, R. Lobinski, S. Demignot, P. Seksik, N. Delsuc, C. Policar, *Oxid. Med. Cell. Longev*., **2022**, *2022*, 1-16

[7] P. Thordarson, *Chem. Soc. Rev*., **2011**, *40*, 1305-1323

[8] P. R. Castello, D. A. Drechsel, B. J. Day, M. Patel, *J Pharmacol Exp Ther* **2008**, *324*, 970–976.

[9] C. Policar, in *Redox-Active Therapeutics*, **2016**, pp 125–164.

[10] J. Butler, W. H. Koppenol, E. Margoliash, *Journal of Biological Chemistry* **1982**, *257*, 10747–10750.

VI.1.b.iv. Author Contributions

N. Delsuc, J. Vinh, R. Lobinski and C. Policar conceived and designed the research. M. Zoumpoulaki, G. Schanne and G. Gazzah performed the synthesis; G. Schanne and G. Gazzah performed the crystallization experiment, R. Guillot acquired and analyzed the crystallographic data; M. Zoumpoulaki, G. Schanne and N. Delsuc performed the K (M-L) UV titration experiments; M. Zoumpoulaki performed the electrochemistry, determination of intrinsic SOD activity, mass spectrometry characterization and ICP-MS experiments; N. Eskenazi acquired preliminary MS and LC-MS/MS data (not shown); P. Seksik provided the HT29-MD2 cell line; E. Quévrain performed preliminary cell experiments for IMS-MS; M. Zoumpoulaki performed all cell experiments, except for the western blot experiments that were performed by G. Schanne; M. Zoumpoulaki, G. Schanne and H. Preud'homme performed the IMS-MS experiments; M. Zoumpoulaki analyzed the data and designed all figures; M. Zoumpoulaki, N. Delsuc and C. Policar co-wrote the manuscript; M. Zoumpoulaki, G. Schanne, N. Delsuc, H. Preud'homme, J. Vinh, R. Lobinski, and C. Policar corrected and edited the manuscript.

VI.1.c. Publication and supplementary materials of "Rhenium carbonyl complexes bearing methylated triphenylphosphonium cations as antibody-free mitochondria trackers for X-ray fluorescence imaging".

Rhenium carbonyl complexes bearing methylated triphenylphosphonium cations as antibody-free mitochondria trackers for X-ray fluorescence imaging

Gabrielle Schanne,[a] Lucas Henry,[a] How Chee Ong,[b] Andrea Somogyi,[c] Kadda Medjoubi,[c] Nicolas Delsuc,[a] Clotilde Policar,[a] Felipe García,[b*] Helene C. Bertrand[a,b*]

[a] Laboratoire des biomolécules, LBM, Département de chimie, Ecole normale supérieure, PSL University, Sorbonne université, CNRS, 75005 Paris, France.
E-mail: helene.bertrand@ens.psl.eu
[b] School of Physical and Mathematical Sciences, Division of Chemistry and Biological Chemistry, Nanyang Technological University, 21 Nanyang Link, 637371, Singapore
E-mail: fgarcia@ntu.edu.sg
[c] Synchrotron SOLEIL, BP 48, Saint-Aubin, 91192 Gif sur Yvette, France

Abstract

Synchrotron Radiation X-ray Fluorescence (SXRF) imaging is a powerful technique for the visualization of metal complexes in biological systems. However, due to the lack of an endogenous elemental signature for mitochondria, probes for the localization of this organelle are required for colocalization studies. In this work, we designed and synthesized rhenium pyta tricarbonyl complexes conjugated to methylated triphenylphosphonium TP*P$^+$ cations as multimodal probes for the visualization of mitochondria, suitable for fluorescence and SXRF imaging and quantification. Accumulation of the methylated triphenylphosphonium TP*P$^+$-based conjugates in cells was observed in fixed A549 cells, and the amount of mitochondrial uptake was linked to the lipophilicity of the TPP$^+$ vector. Our work highlights a convenient rhenium-based multimodal mitochondrial-targeted probe compatible with SXRF nano-imaging.

Introduction

The subcellular detection, localization, and quantification of small molecules in cellular medium and in particular of transition metal complexes are crucial in their development in biology and medicine and in the understanding of their biological mode of action. Several methods can be used to study the subcellular localization of a compound of interest: study of

pharmacological effects, chemical analysis and the most widely employed microscopic imaging studies using spectroscopic probes specific for individual organelles.[1] Among the common approaches, fluorescence microscopy using fluorescent probes is pivotal as a non-invasive imaging technique for its convenience, good sensitivity and high spatial resolution, resulting in the routine use of organelle-specific fluorophores as conventional markers in fluorescence imaging.[2-4] Despite their popularity and utility, fluorescent probes still suffer from some drawbacks such as photobleaching and limited laser penetration depths. Moreover, fluorescence imaging is dependent on environmental factors such as medium polarity, pH, binding status, *etc.*, that can modify the quantum yield and/or emission spectrum, possibly rendering apparent subcellular distribution inaccurate.[5-6] More importantly, the commonly used strategy of appending a large organic fluorophore on a non-fluorescent compound of interest to enable its detection may modify its molecular parameters and hence alter subcellular distribution.[7-8]

The developments of imaging techniques and organelle-specific probes based on complementary modalities are hence of primary importance. In the context of metal imaging, X-ray fluorescence (XRF) nano-imaging is highly promising as it allows for the specific and direct imaging of the metal centre. Hard X-ray scanning XRF spectroscopy enables the simultaneous mapping of all elements having Z>14 provided their edge energy is lower than the incident X-ray energy. Thus, information on both the chemical environment and the studied metal centre's distribution in biological environments and cells[9] is readily available. Using highly focalised synchrotron beams, resolutions as good as a few 10 nm's can be obtained. Moreover, scanning Synchrotron Radiation X-ray Fluorescence (SXRF) imaging has a high analytical sensitivity (≤ ppm). SXRF spectroscopy thus exhibits a high detection sensitivity, a high specificity and a high spatial resolution. SXRF nano-imaging in studies of metallodrugs have received increasing attention in the last decade[10-15] and provided valuable information on the fate of the metal complexes in the cellular context. XRF imaging is, hence, highly promising as a tool in the growing field of inorganic medicinal chemistry.

For co-localization studies by XRF, some endogenous elements can be indicative of a subcellular compartment – *e.g*. phosphorus and zinc reveal nucleus localization,[16] while manganese has been shown to accumulate in the Golgi apparatus in neural cells – [17] although this is not the case for all the organelles. 3D XRF nano-imaging was recently used to determine

the subcellular localization of anticancer metal complexes.[18-19] Sealed carbon nanotubes filled with heavy metals and decorated with organelle-specific peptides were described for the XRF mapping of cell membrane, nucleus and endoplasmic reticulum.[20] Mitochondria localization, up to now, has only been identified by XRF using correlative imaging with fluorescence[21] or electron microscopy[22] or using an immunolabeling technique involving a secondary antibody functionalized with gold nanoparticles.[23-24] Hence, systems of easier access such as low molecular weight XRF imaging molecular probes with specific organelle targeting in the manner of conventional fluorophores, with an additional modality such as classical fluorescence for validation, would be highly valuable tools for colocalization studies and convenient access to the accurate localization of metal complexes by XRF.

One promising system for that purpose is multimodal rhenium(I) carbonyl-based probes, that can be visualized through infrared (IR), fluorescence and XRF imaging. These biologically-stable octahedral d^6 low-spin Re(I) tricarbonyl complexes, of general formula $[Re(CO)_3(N^N)X]$ (with N^N a diimine ligand with low-energy π* orbitals), show exciting and valuable photophysical properties such as low toxicity, large Stokes shifts and long luminescent lifetimes that render them suitable for bio-imaging.[25-27] These complexes have thus been developed to target different cell compartments as luminescent organelle trackers as described in recent reviews.[28-29] $Re(CO)_3$ complexes also display IR absorptions in the range 1800-2200 cm^{-1}, a spectral region in which biological media are transparent. This combination of properties enables the use of these complexes as Single Core Multimodal Probe for Imaging (SCoMPI) in cells and tissues,[30-33] while the IR signature of the complexes enabled their quantification inside cells, [5] as demonstrated in correlative fluorescence and infrared imaging studies. Most notably, these $Re(CO)_3$ complexes can also be mapped by XRF nano-imaging, as recently demonstrated.[12, 34-35] Rhenium is highly suitable for this function as it is highly emissive in X-fluorescence (after irradiation at > 12.53 keV), and its natural abundance is very low (ultra-trace element in urine and plasma (< 1 µg/g)),[36] leading to a good signal-to-noise ratio.

Ideally, to exert their biological effect, compounds must reach their subcellular targets while reducing accumulation in non-targeted sites to reduce associated side effects. There is therefore a high interest in drug targeting strategies to direct a compound to its specific site of action.[37-38, 39] One of such targets that have recently drawn attention has been mitochondria

organelle due to its increasing association with metabolic diseases and neurodegenerative diseases *inter alia*.[40-42] To confer mitochondrial selectivity,[43-44] lipophilic cations such as mitochondrial-targeting peptides (MTPs)[45-47] or triphenylphosphonium (TPP^+)[48-49] derivatives can be conjugated to the cargo of interest, thus exploiting the mitochondrion's strong negative potential (up to 180–200 mV), allowing accumulation within the mitochondrial matrix according to the Nernst equation.[50] In this context, the triphenylphosphonium (TPP^+) moiety – which is the "gold standard" among mitochondrial delivery vectors – has been broadly used as a molecular vector for selective mitochondrial delivery owing to its high lipophilicity, cationic nature, high stability in physiological conditions and its ease of conjugation to molecular cargo.[49] The versatility of this platform is exemplified by the wide range of molecules that has been delivered into the mitochondria through TPP^+ conjugation, such as spin-traps, antioxidants, prodrugs, protonophores, fluorophores, photodynamic therapy sensitizers as well as positron emitters.[49]

Although metal-based probes – mainly Ir(III), Ir(I) and Ru(II)[51] and a handful of $Re(CO)_3$ complexes[52-55] – have been described to target mitochondria, to the best of our knowledge, none were used as molecular probes in XRF imaging. As mentioned above, the techniques used so far require the most advanced 3D XRF processes or immunolabeling techniques that could be cumbersome. Finally, there is no XRF-detectable endogenous and ubiquitous element characteristic for the mitochondria, making a mitochondria targeting XRF probe of particular interest.

In light of the need for an organelle-specific multimodal probe compatible with XRF techniques, we have designed and synthesized three triarylphosphonium-[$Re(CO)_3$(pyta)X] mitochondria-targeted probes suitable for X-fluorescence mapping and quantification. We explored methylated TPP derivatives (i.e., TP^*P^+) that were shown in recent studies to display enhanced performance as compared to the conventionally used TPP^+ moiety. For instance, TP^*P^+ species have shown a two-fold performance enhancement in *in-vitro* photodynamic therapy (PDT) studies, and have also enabled the accumulation of dicationic species previously described as unable to permeate the mitochondrial membrane.[56-57] The increase in lipophilicity by enhancement of the molecular volume and solvent accessible surface area (SASA) of the cations was proposed as key determinant to improve mitochondria accumulation.[56-57]

Here, we report the synthesis of a series of rhenium pyta tricarbonyl complexes conjugated to triarylphosphonium cations. Toxicity and imaging studies were performed in A549 cells, revealing lipophilicity-dependent toxicity associated with increasing internalization of the compounds. Mitochondria localization was assessed by colocalization studies in fluorescence imaging using a conventional mitochondria stain Mitotracker Deep Red. Subcellular XRF mapping of the compounds was successfully achieved by SXRF imaging using the Re-Lß edge of Re. We describe here the conjugate with the bis-methyl TP*P$^+$ cation **C3** as a low toxicity mitochondria-targeted metal-based multimodal probe that can be mapped and quantified inside cells using SXRF. Our study confirms the potential of methyl functionalized TPP$^+$ as mitochondrial delivery vectors with enhanced properties.

Synthesis

We synthesized conjugates **C1-3** comprising three triphenylphosphonium cation derivatives with a rhenium pyta tricarbonyl complex[58-60] based respectively on the classical TPP$^+$ cation ($R^m = R^p = H$), the modified TP*P$^+$ cation bearing a methyl group on phenyl *para* positions ($R^m = H$, $R^p = Me$) and the modified TP*P$^+$ cation bearing methyl groups on all phenyl *meta* positions ($R^m = Me$, $R^p = H$) (Scheme 1). A beta-alanine spacer was chosen to bridge the pyta ligand with the aminoethyl phosphonium cations. Increasing the alkyl chain length between the cargo and the TPP$^+$ cation vector is known to increase the cell penetration of the construct.[61-63] For practical reasons in the synthesis and consistent data interpretation, we chose to keep the spacer constant and only the nature of the phosphonium vector was changed.

Therefore, β-Alanine *tert*-butyl ester hydrochloride was first reacted with chloroacetyl chloride in the presence of diisopropylethylamine (DIEA) in dichloromethane (Scheme 1, step i). Chloride nucleophilic substitution with sodium azide followed by a copper catalyzed azide alkyne cycloaddition (CuAAC) using copper sulfate pentahydrate and sodium ascorbate with ethynyl pyridine generated the pyridine-triazole (pyta) ligand functionalized with a *tert*-butyl ester terminated linker **3** (steps ii-iii).[34] The corresponding rhenium carbonyl complex **4** was obtained by reaction with rhenium pentacarbonyl chloride in toluene under heating (step iv). Hydrolysis of the ester function was performed at this stage by treatment in a mixture of TFA in DCM, followed by treatment with concentrated HCl to afford a complex **5** with a chloride

as unique X ligand (step v). The conjugates **C1-3** were finally obtained *via* an amide coupling with aminoethylphosphonium bromide derivatives **P1-3** prepared as previously described[56] using HOBt and EDC.HCl as coupling agents in the presence of DIEA in DMF (step vi).

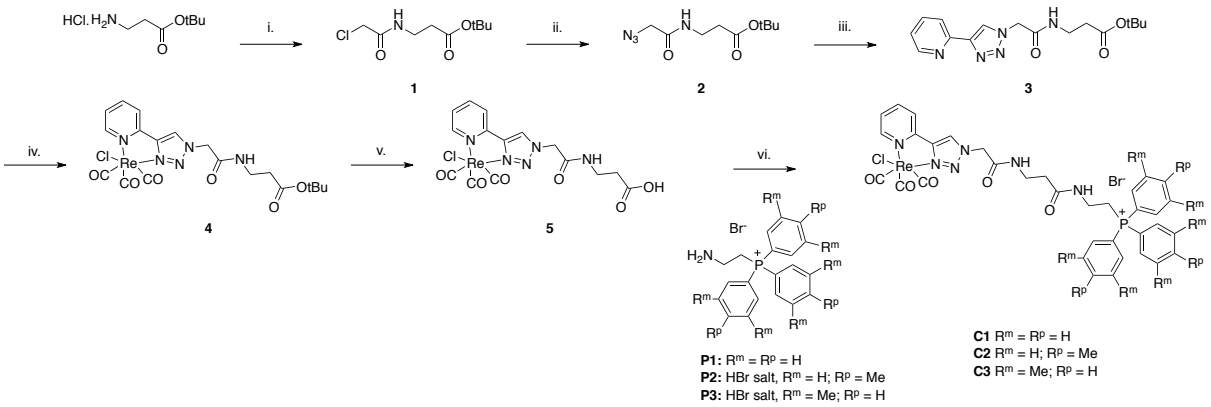

Scheme 1. *Synthesis of conjugates **C1-3**. Conditions: i. chloroacetyl chloride (1.0 eq.), DIEA (2.5 eq.), DCM, 1 h, 25 °C (quantitative); ii. NaN_3 (1.97 eq.), NaI (0.1 eq.), acetone/H_2O 3:1 v:v, 17 h, 50 °C (89 %); iii. 2-ethynylpyridine (1.2 eq.), $CuSO_4.5H_2O$ (0.26 eq.), sodium ascorbate (1.0 eq.), acetone/H_2O 2:1 v:v, 2h, 25 °C (85%); iv. $Re(CO)_5Cl$ (1.1 eq.), toluene, 5 h, 80 °C (99%); v. TFA/DCM 1:1 v:v, 1 h, 25 °C then conc. HCl, 10 min, 25 °C (86 %); vi. (2-aminoethyl)triphenylphosphonium bromide derivative **P1-3** (1.1 eq.), HOBt (1.5 eq.), EDC.HCl (1.5 eq.), DMF, 24-48 h (20-70 %).*

Photophysical properties

The photophysical properties of the conjugates **C1-3** were characterized in acetonitrile and are summarized in Table 1 and Figure S1. The three conjugates show typical absorptions of rhenium carbonyl complexes with a MLCT band centered at 330 nm in acetonitrile (Figure S1).[5, 58, 60] Excitation at 330 nm led to a broad emission band centered at 530 nm. **C1-3** showed similar low quantum yields around 0.25-0.27%, consistent with rhenium carbonyl complexes with substitutions of comparable features.[58, 64]

Table 1. *Photophysical properties of conjugates **C1-3** in acetonitrile and IC_{50} from MTT assay.*

Complex	Excitation (nm)	Emission (nm)	Range (nm)	Quantum yield[a] (%)	IC_{50} (μM)	Hydrophobicity as per rt in RP-HPLC (min)
C1	330	530	450 - 620	0.27	413 ± 65	6.40
C2	330	530	450 - 620	0.27	100 ± 26	7.93
C3	330	530	450 - 620	0.25	46 ± 10	8.52

[a] Quinine sulfate in 0.1 N sulfuric acid was used as a standard with a known quantum yield of 54.6% (λ_{exc} 320 nm).

Toxicity

The toxicity of the conjugates was evaluated in A549 non-small cell lung cancer cell line using a classical 3-(4, 5-dimethylthiazol-2-yl)-2, 5-diphenyl tetrazolium bromide (MTT) assay. The cells were incubated with a range of concentrations (1-1000 μM) for 4 h. The conjugates showed differential toxicity with IC_{50} comprised between 46 ± 10 μM for **C3** and 413 ± 65 μM for **C1** (Table 1, Figure S2-S3). The higher toxicity with increasing methyl functionalization of the phenyl rings of the phosphonium targeting moieties (**C1** to **C3**, with **C3** 10 times more cytotoxic than **C1**) is consistent with an increased hydrophobicity, as supported by the increased retention time in reverse phase analytical HPLC (6.40, 7.93, 8.52 min for **C1**, **C2**, and **C3**, respectively). This may be, in turn, consistent with a greater cell penetration. The viability at 10 μM and 20 μM, concentrations used for the subsequent imaging experiments, were > 80% for the three conjugates, and the slight toxicity observed at these concentrations did not preclude the imaging studies. Consequently, imaging studies using fluorescence and X-ray fluorescence spectroscopy were then performed to investigate the conjugates' sub-cellular localisation and quantify their accumulation in A549 cells.

Fluorescence imaging

A549 cells were incubated with 10 μM or 20 μM of the conjugates **C1-C3** for 4 h, fixed with 4% PFA and imaged by single photon excitation at 350 nm (Figure 1 and Figures S4-S7). For all the conjugates, a significant fluorescence signal was detected and localized around the nucleus. Mitochondrial labeling was then investigated using co-incubation with a conventional mitochondrial marker, MitoTracker Deep Red, characterized by an excitation maximum at 644 nm and an emission in the 650-750 nm range. The use of Mitotracker green (excitation 490 nm, emission 516 nm) as alternative mitochondria stain was not compatible with the $Re(CO)_3$ conjugates. During the imaging studies, a loss in intensity of the luminescence signal detected for the three conjugates **C1-C3** was observed when coincubated with MitoTracker Deep Red. Further studies in solution (see SI, Figure S8) showed that, although there is no overlap in the excitation spectra of the conjugates and the Mitotracker, there is a partial overlay between the emission of the conjugates (450-650 nm, centered at 530 nm in water) and the excitation of the organic fluorophore. An enhancement of Mitotracker fluorescence signal, along with a loss in luminescence signal of **C3** (λ_{exc} 320 nm) was consistently observed with an increasing

concentration of Mitotracker. (SI Figure S9-S11). This suggests the existence of a fluorescence resonance energy transfer (FRET) between the two compounds, implying in turn, that the conjugates and the Mitotracker are in close proximity in cells, since FRET is distance-dependent. Despite this intensity loss, the luminescence of the conjugates could still be detected without parasite signal (the signal emitted by the Mitotracker upon excitation at the λ_{exc} of the conjugates (Figure S10) is filtered out with a filter cut-off above 600 nm). Moreover, the FRET phenomenon is expected to occur to the same extent for complexes of similar photophysical properties, which allows us to qualitatively compare the cellular luminescence images in all three cases. Co-localization results were analyzed using the Van Steensel curve and Pearson value methods between the labeling of **C1-C3** and Mitotracker Deep Red in cells.

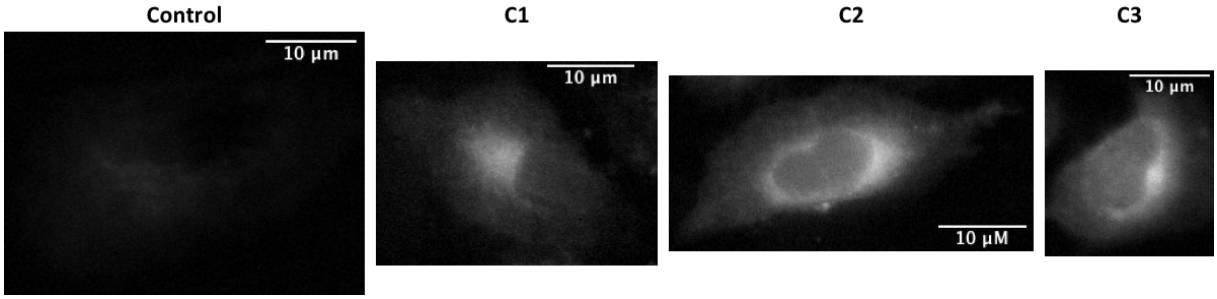

Figure 1. *Fluorescence imaging of A549 control cells (control) and cells incubated with conjugates **C1-C3** (at 20 µM for 4 h) (λ_{exc} 350 nm). The signal-to-noise ratio were equal to 23.5 dB, 32.0 dB, 34.5 dB and 36.0 dB for control cells, cells incubated with **C1**, **C2** and **C3**, respectively. Fixed fluorescence intensity scale (0-7500 a.u.). Scale bar: 10 µm (fixed at 3.1 cm).*

In cells incubated with the conjugate **C1** with a classical TPP vector, the luminescence signal observed appeared less clearly than that of **C2** and **C3**. This may be explained by a poor internalization in these conditions. In contrast, a clear luminescence signal could be detected in the case of the conjugate **C2** compared to control cells. Gaussian maxima shifted from the zero position of dx (red line) were obtained in the Van Steensel method and a mean Pearson coefficient of 0.83 ± 0.04 was calculated, both suggesting a partial overlay of **C2** labeling with the mitochondrial marker. The conjugate **C3** gave a luminescence signal qualitatively stronger than **C2**, with a comparable sub-cellular distribution as shown by the similar results in colocalization methods (mean Pearson coefficient 0.68 ± 0.06, Figure 2 and Figures S12-S16).

The fluorescence studies are consistent with toxicity studies suggesting a cell penetration increasing in the order **C1**<**C2**<**C3**. They show a partial overlay of the labeling of the conjugates

with that of the MitoTracker Deep Red, pointing to a partial preferential localization at the mitochondria, particularly for **C2** and **C3** (Figure 3).

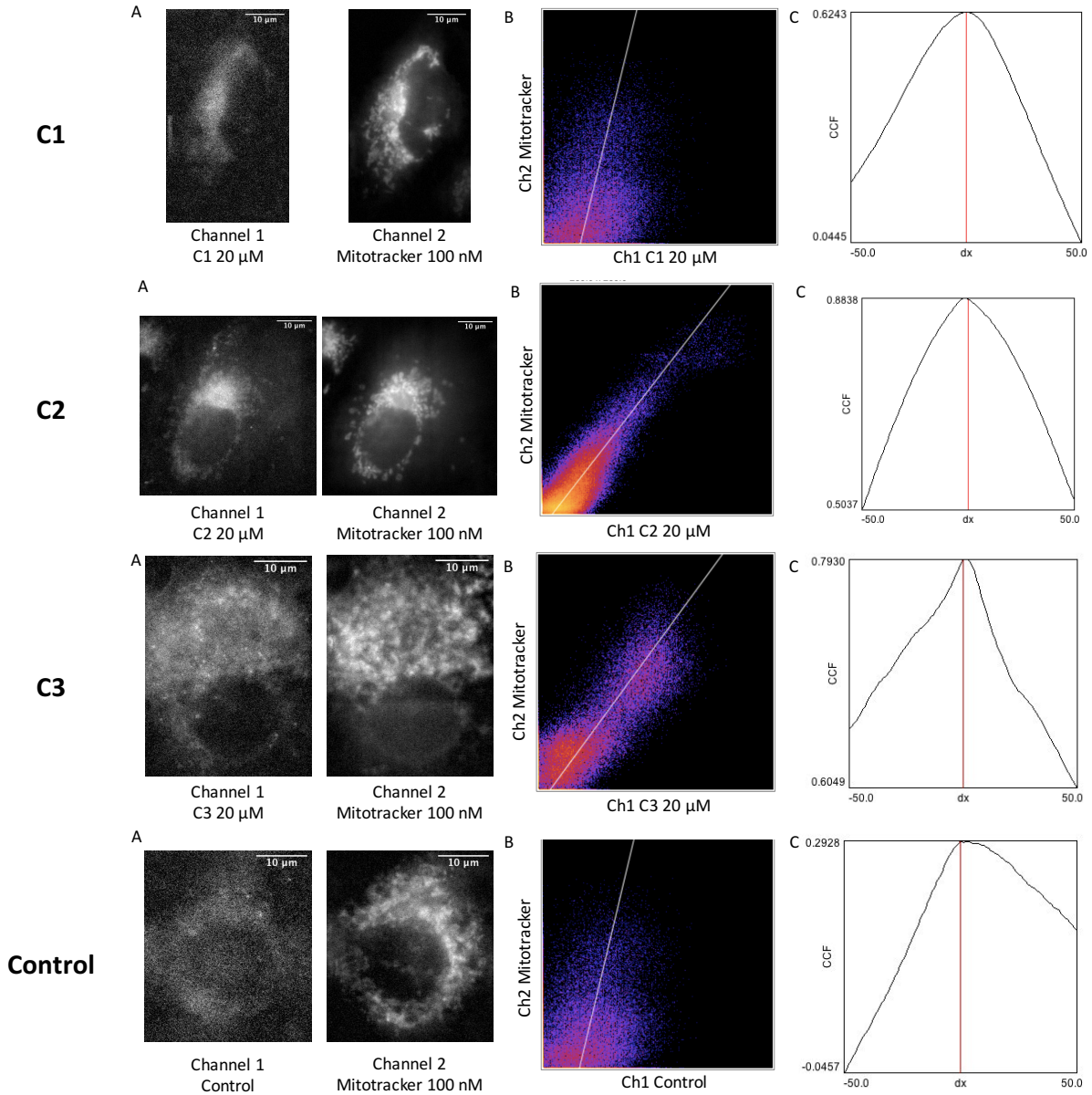

Figure 2. *Colocalization analyses with the fluorescence signal of Mitotracker Deep Red. A549 cells were incubated with **C1-C3** probes at 20 µM for 4 hours or without incubation (control). (A) Left: channel 1 - fluorescence image with excitation at λ_{exc} 350 nm, obtained with a gain of 0 over an exposure time of 3s. The signal-to-noise ratio is equal to 17 dB for **C1**, 22 dB for **C2**, 20 dB for **C3** and 12 dB for control cells; Right: channel 2 - fluorescence image of the mitotracker Deep Red (λ_{exc} 644 nm) obtained with a gain of 0 over an exposure time of 5s. (B) Scatter plot or 2D-histogram with a linear regression representing the signal intensity relationship of the two fluorescence images. (C) Van Steensel curve (see SI for details). The cross correlation function is maximal for a shift dx equal to 0, 2, 2 and 1 pixels for **C1**, **C2**, **C3** and control cells, respectively. The Pearson coefficient is equal to 0.62 for **C1**, 0.88 for **C2**, 0.79 for **C3** and 0.30 for control cells.*

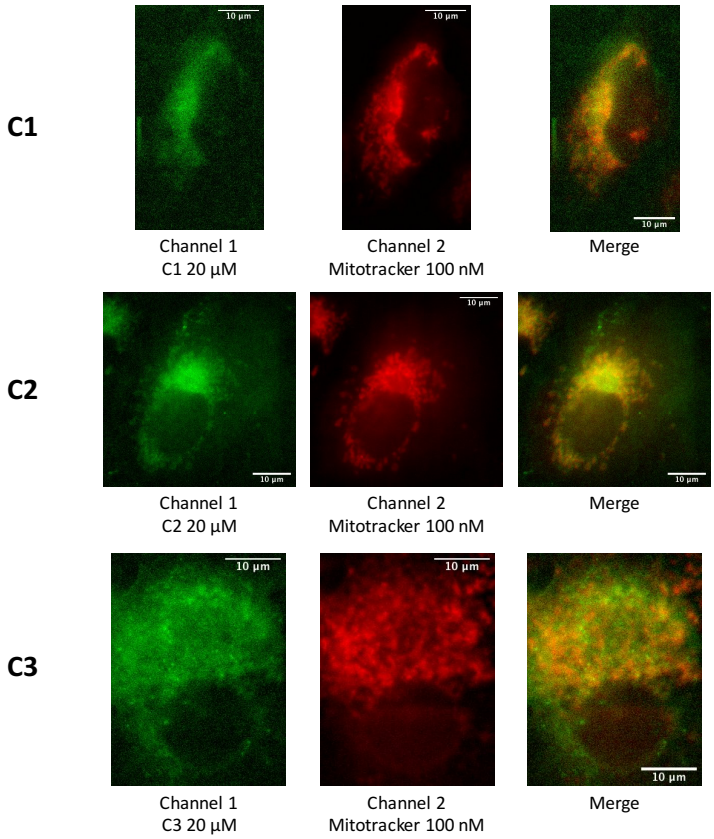

Figure 3. *A549 cells were incubated with* ***C1-C3*** *probes (20 µM, 4 h). Left: fluorescence signal of the conjugate (λ_{exc} 350 nm); middle: fluorescence signal of Mitotracker Deep Red (λ_{exc} 644 nm); right: merge of conjugate (green) and Mitotracker Deep Red (red) with their overlay in yellow.*

Synchrotron radiation scanning X-ray fluorescence nano-imaging (SXRF)

SXRF was used to study the intracellular distribution of rhenium in A549 cells incubated with the probes (20 µM for 4 hours). The cells were seeded on Si_3N_4 silicon nitride membranes, fixed with 4% paraformaldehyde and air-dried (see SI). Chemical fixation and air drying could be used here, the focus of the study not being endogenous metals that can diffuse upon this treatment.[34, 65] Figure 4 shows the elemental distributions of calcium, phosphorus, zinc and rhenium in a single incubated A549 cell (see SI Figure S16-S26 for the mapping of other incubated cells and control cells). In order to avoid spectral overlapping between the Zn-Kα and Re-Lα (~8.6 keV) XRF lines, we use the Zn-Kβ (~9.6 keV) and Re Lß (~10.15 and 10.28 keV) spectral lines to produce the Re and the Zn distribution maps[34] (see SI). The localization of the nucleus is indicated by the phosphorus and zinc mapping. As rhenium is an ultratrace element in biological samples,[36] the rhenium signal can therefore be attributed to the conjugates **C1-C3**.

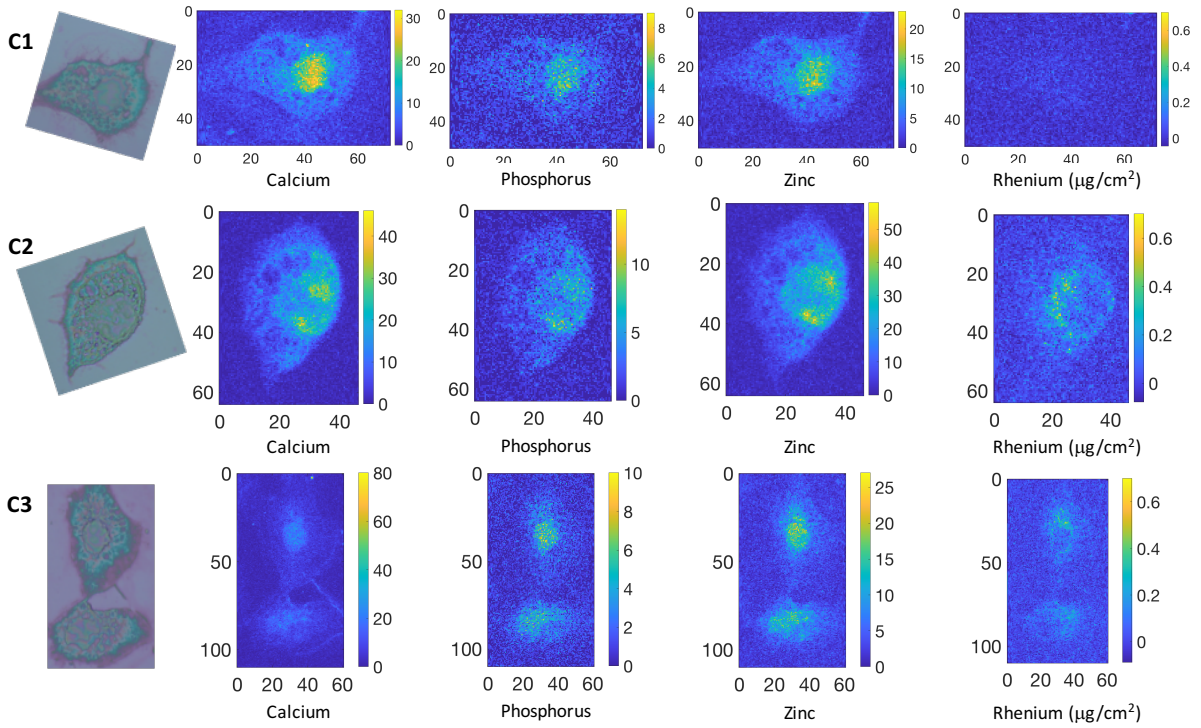

Figure 4. *Transmission optical microscope images (left) and elemental distributions of Ca, P, Re, and Zn in A459 cells incubated with* ***C1-C3*** *(with color coded map (intensity) (right)). The phosphorus (P), and zinc (Zn) maps, are used to identify the nucleus area. Re was mapped using the Lß lines. A459 cells were incubated for 4 hours with* ***C1-C3*** *(20 μM) before fixation and air-drying (excitation at 14 keV; integration time, 300 ms per pixel; pixel size, 500 nm). Scale axis in μm.*

Rhenium could not be significantly detected in cells incubated with **C1** (Figures 4 and S16-S18 in comparison to control cells (Figures S24-S26). By contrast, the probes **C2** and **C3** can be unambiguously detected in incubated cells. They show a perinuclear and punctuate distribution that qualitatively matches that observed by fluorescence imaging.

Finally, the amount of rhenium in cells incubated with the three conjugates **C1-C3** was quantified by XRF using a rhenium standard (see SI). The average concentrations expressed in μg per cell are shown in Figure 5. A differential accumulation of the probes in cells in the order **C1** < **C2** < **C3** was confirmed, supporting a reduced internalization of **C1**. The amount of **C1** was not significant compared to control cells. The average amount of rhenium in cells incubated with **C2** and **C3** was 4.00 10^{-7} μg per cell and 1.01 10^{-6} μg per cell, respectively, indicating a more than 2-fold increase in cellular accumulation for the **C3** conjugate.

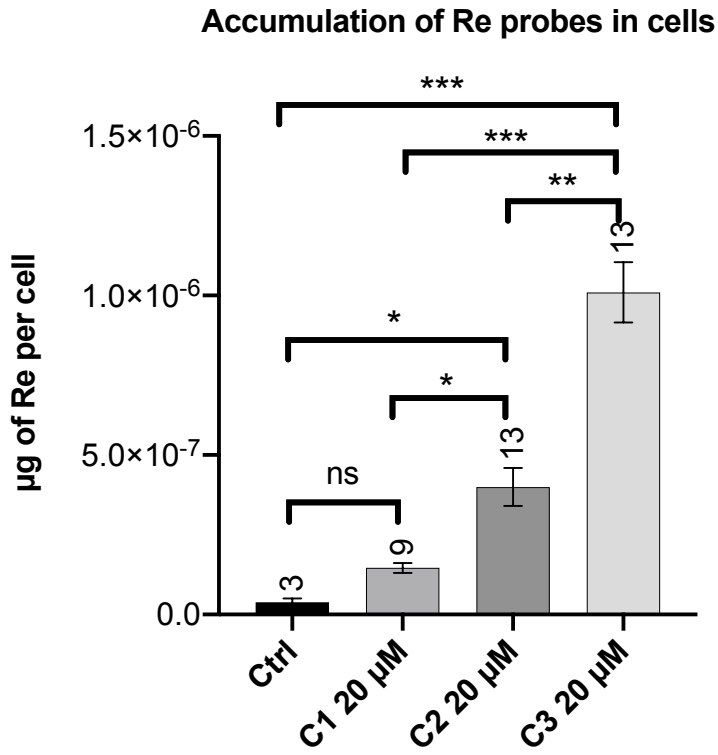

Figure 5. Quantification of rhenium accumulation in cells by X-ray fluorescence. *A549 cells were incubated in presence of the rhenium probes **C1-C3** at 20 µM for 4 h. Data represent mean ± SEM. The number of measurements is indicated above each column. The p-values were calculated from the Kruskal-Wallis test (non-parametric ANOVA test) using Prism software. Each comparison stands alone. (***) p < 0.001, (**) p < 0.002 and (*) p < 0.033 and ns means non-significant.*

Conclusions

We designed and synthesized rhenium pyta tricarbonyl complexes with triphenylphosphonium cation derivatives as mitochondria targeting probes. The classical TPP^+ was evaluated along with two poly-methylated derivatives TP^*P^+ that were proposed as valuable alternative for mitochondria accumulation.[56-57] The appendage of the non-polar methyl groups enhances the cation's lipophilicity while increasing its solvent accessible surface area and molecular volume, suggested as a key parameter to predict targeting ability. The conjugates displayed typical photophysical properties of rhenium carbonyl complexes with a MLCT absorption band centered at 330 nm and an emission at 530 nm with low quantum yields below 1% in acetonitrile. An increasing toxicity on A549 cells was observed with the lipophilicity of the conjugates, the **C3** complex with a bis-methyl TP^*P^+ being the more toxic with an IC_{50} of 46 µM, still suitable for bioimaging. Fluorescence imaging studies in fixed A549 cells and colocalization studies showed a partial localization at the mitochondria for TP^*P^+ conjugates **C2** and **C3** while no significant signal was observed for TPP^+ complex **C1**

when co-incubated with a Mitotracker. The conjugates were finally mapped in fixed dried cells and quantified using XRF spectroscopy. Compared to **C1**, TP*P$^+$ conjugates **C2** and **C3** were unambiguously detected in incubated single cells with a perinuclear accumulation of punctuate appearance consistent with a partial mitochondrial localization. A higher penetration and accumulation in cells was confirmed with the use of TP*P$^+$ cations, with twice as much bis-methyl cation **C3** compared to mono methyl cation **C2**. Our study expands the use of this alternative family of mitochondria targeting agents and further supports its potential for enhanced mitochondrial therapies. Besides, we identify two Re tricarbonyl complexes as multimodal imaging probes targeting mitochondria as observed by fluorescence and X-ray fluorescence spectroscopies. These probes are a very convenient alternative to immunolabeling involving gold-modified secondary antibodies and compatible with chemical fixation and air drying easily applied for SXRF. Further studies are underway to further demonstrate mitochondrial localization in live cells and in cryofixed samples. Finally, this paves the way towards the development and applications of organelle specific XRF molecular probes that would undoubtedly bring invaluable insights in medicinal inorganic chemistry approaches.

Acknowledgments

We thank IPV doctoral program (Sorbonne Université) for GS's PhD fellowship and École Normale Supérieure for LH's PhD fellowship. CNRS is acknowledged for HB delegation to Singapore. We thank the Fondation pour la Recherche Médicale for financial support (contract DIE20151234413, call « Pionniers de la recherche, Etudes physico-chimiques innovantes pour la biologie et la médecine). We thank Institut Curie (UMR9187, F. Poyer and F. Mahuteau-Betzer) for providing A549 cells. We thank Z. Gueroui (ENS chemistry department) for useful discussions and help with fluorescence microscopy. F.G. would like to thank A*STAR AME IRG A1783c0003, NTU for a start-up grant (M4080552) and MOE Tier 1 grants (RG 11/15 and RG 113/16) for financial support. H.C. would like to thank NTU for NPGS scholarship.

References

1. Zheng, N.; Tsai, H. N.; Zhang, X.; Rosania, G. R., The Subcellular Distribution of Small Molecules: From Pharmacokinetics to Synthetic Biology. *Mol. Pharmaceutics* **2011,** *8* (5), 1619-1628.

2. Haughland, R. P., The Molecular Probes Handbook: A Guide to Fluorescent Probes and Labeling Technologies. Carlsbad, CA, 2010.
3. Ueno, T.; Nagano, T., Fluorescent probes for sensing and imaging. *Nature Methods* **2011,** *8*, 642-645.
4. Zhu, H.; Fan, J.; Du, J.; Peng, X., Fluorescent Probes for Sensing and Imaging within Specific Cellular Organelles. *Acc. Chem. Res.* **2016,** *49* (10), 2115-2126.
5. Clède, S.; Lambert, F.; Saint-Fort, R.; Plamont, M.-A.; Bertrand, H.; Vessières, A.; Policar, C., Influence of the Side-Chain Length on the Cellular Uptake and the Cytotoxicity of Rhenium Triscarbonyl Derivatives: A Bimodal Infrared and Luminescence Quantitative Study. *Chem. A Eur. J.* **2014,** *20* (28), 8714-8722.
6. Yang, Z.; Cao, J.; He, Y.; Yang, J. H.; Kim, T.; Peng, X.; Kim, J. S., Macro-/micro-environment-sensitive chemosensing and biological imaging. *Chem. Soc. Rev.* **2014,** *43* (13), 4563-4601.
7. Horobin, R. W.; Rashid-Doubell, F.; Pediani, J. D.; Milligan, G., Predicting small molecule fluorescent probe localization in living cells using QSAR modeling. 1. Overview and models for probes of structure, properties and function in single cells. *Biotech. Histochem.* **2013,** *88* (8), 440-460.
8. Králová, J.; Jurášek, M.; Mikšátková, L.; Marešová, A.; Fähnrich, J.; Cihlářová, P.; Dražar, P.; Bartůněk, P.; Král, V., Influence of fluorophore and linker length on the localization and trafficking of fluorescent sterol probes. *Sci. Rep.* **2020,** *10* (1), 22053.
9. McRae, R.; Bagchi, P.; Sumalekshmy, S.; Fahrni, C. J., In Situ Imaging of Metals in Cells and Tissues. *Chem. Rev.* **2009,** *109* (10), 4780-4827.
10. Antony, S.; Aitken, J. B.; Vogt, S.; Lai, B.; Brown, T.; Spiccia, L.; Harris, H. H., X-ray fluorescence imaging of single human cancer cells reveals that the N-heterocyclic ligands of iodinated analogues of ruthenium anticancer drugs remain coordinated after cellular uptake. *J. Biol. Inorg. Chem.* **2013,** *18* (7), 845-853.
11. Hall, M. D.; Dillon, C. T.; Zhang, M.; Beale, P.; Cai, Z.; Lai, B.; Stampfl, A. P. J.; Hambley, T. W., The cellular distribution and oxidation state of platinum(II) and platinum(IV) antitumour complexes in cancer cells. *J. Biol. Inorg. Chem.* **2003,** *8* (7), 726-732.
12. Mathieu, E.; Bernard, A.-S.; Quévrain, E.; Zoumpoulaki, M.; Iriart, S.; Lung-Soong, C.; Lai, B.; Medjoubi, K.; Henry, L.; Nagarajan, S.; Poyer, F.; Scheitler, A.; Ivanović-Burmazović, I.; Marco, S.; Somogyi, A.; Seksik, P.; Delsuc, N.; Policar, C., Intracellular location matters: rationalization of the anti-inflammatory activity of a manganese(ii) superoxide dismutase mimic complex. *Chem. Commun.* **2020,** *56* (57), 7885-7888.
13. Morrison, D. E.; Aitken, J. B.; de Jonge, M. D.; Ioppolo, J. A.; Harris, H. H.; Rendina, L. M., High mitochondrial accumulation of new gadolinium(iii) agents within tumour cells. *Chem. Commun.* **2014,** *50* (18), 2252-2254.
14. Sanchez-Cano, C.; Gianolio D Fau - Romero-Canelon, I.; Romero-Canelon I Fau - Tucoulou, R.; Tucoulou R Fau - Sadler, P. J.; Sadler, P. J., Nanofocused synchrotron X-ray absorption studies of the intracellular redox state of an organometallic complex in cancer cells. *Chem. Commun.* **2019,** *55*, 7065-7068.
15. Sanchez-Cano, C.; Romero-Canelón, I.; Yang, Y.; Hands-Portman, I. J.; Bohic, S.; Cloetens, P.; Sadler, P. J., Synchrotron X-Ray Fluorescence Nanoprobe Reveals Target Sites for Organo-Osmium Complex in Human Ovarian Cancer Cells. *Chem. Eur. J.* **2017,** *23* (11), 2512-2516.
16. McRae, R.; Lai, B.; Fahrni, C. J., Subcellular redistribution and mitotic inheritance of transition metals in proliferating mouse fibroblast cells. *Metallomics* **2013,** *5* (1), 52-61.

17. Carmona, A.; Devès, G.; Roudeau, S.; Cloetens, P.; Bohic, S.; Ortega, R., Manganese Accumulates within Golgi Apparatus in Dopaminergic Cells as Revealed by Synchrotron X-ray Fluorescence Nanoimaging. *ACS Chem. Neurosci.* **2010,** *1* (3), 194-203.
18. Conesa, J. J.; Carrasco, A. C.; Rodríguez-Fanjul, V.; Yang, Y.; Carrascosa, J. L.; Cloetens, P.; Pereiro, E.; Pizarro, A. M., Unambiguous Intracellular Localization and Quantification of a Potent Iridium Anticancer Compound by Correlative 3D Cryo X-Ray Imaging. *Angew. Chem. Int. Ed.* **2020,** *59* (3), 1270-1278.
19. Fus, F.; Yang, Y.; Lee, H. Z. S.; Top, S.; Carriere, M.; Bouron, A.; Pacureanu, A.; da Silva, J. C.; Salmain, M.; Vessières, A.; Cloetens, P.; Jaouen, G.; Bohic, S., Intracellular Localization of an Osmocenyl-Tamoxifen Derivative in Breast Cancer Cells Revealed by Synchrotron Radiation X-ray Fluorescence Nanoimaging. *Angew. Chem. Int. Ed.* **2019,** *58* (11), 3461-3465.
20. Serpell, C. J.; Rutte, R. N.; Geraki, K.; Pach, E.; Martincic, M.; Kierkowicz, M.; De Munari, S.; Wals, K.; Raj, R.; Ballesteros, B.; Tobias, G.; Anthony, D. C.; Davis, B. G., Carbon nanotubes allow capture of krypton, barium and lead for multichannel biological X-ray fluorescence imaging. *Nat. Commun.* **2016,** *7* (1), 13118.
21. Roudeau, S.; Carmona, A.; Perrin, L.; Ortega, R., Correlative organelle fluorescence microscopy and synchrotron X-ray chemical element imaging in single cells. *Anal. Bioanal. Chem.* **2014,** *406* (27), 6979-6991.
22. Suárez, V. T.; Gallet, B.; Chevallet, M.; Jouneau, P.-H.; Tucoulou, R.; Veronesi, G.; Deniaud, A., Correlative transmission electron microscopy and high-resolution hard X-ray fluorescence microscopy of cell sections to measure trace elements concentrations at the organelle level. *bioRxiv* 2020.11.21.392738.
23. Matsuyama, S.; Shimura, M.; Mimura, H.; Fujii, M.; Yumoto, H.; Sano, Y.; Yabashi, M.; Nishino, Y.; Tamasaku, K.; Ishikawa, T.; Yamauchi, K., Trace element mapping of a single cell using a hard x-ray nanobeam focused by a Kirkpatrick-Baez mirror system. *X-Ray Spectrom.* **2009,** *38* (2), 89-94.
24. McRae, R.; Lai, B.; Vogt, S.; Fahrni, C. J., Correlative microXRF and optical immunofluorescence microscopy of adherent cells labeled with ultrasmall gold particles. *J. Struct. Biol.* **2006,** *155* (1), 22-29.
25. Clède, S.; Policar, C., Metal–Carbonyl Units for Vibrational and Luminescence Imaging: Towards Multimodality. *Chem. Eur. J.* **2015,** *21* (3), 942-958.
26. Coogan, M. P.; Fernández-Moreira, V., Progress with, and prospects for, metal complexes in cell imaging. *Chem. Commun.* **2014,** *50* (4), 384-399.
27. Lo, K. K.-W., Molecular Design of Bioorthogonal Probes and Imaging Reagents Derived from Photofunctional Transition Metal Complexes. *Acc. Chem. Res.* **2020,** *53* (1), 32-44.
28. Gillam, T. A.; Sweetman, M. J.; Bader, C. A.; Morrison, J. L.; Hayball, J. D.; Brooks, D. A.; Plush, S. E., Bright lights down under: Metal ion complexes turning the spotlight on metabolic processes at the cellular level. *Coord. Chem. Rev.* **2018,** *375*, 234-255.
29. Hostachy, S.; Policar, C.; Delsuc, N., Re(I) carbonyl complexes: Multimodal platforms for inorganic chemical biology. *Coord. Chem. Rev.* **2017,** *351*, 172-188.
30. Clède, S.; Delsuc, N.; Laugel, C.; Lambert, F.; Sandt, C.; Baillet-Guffroy, A.; Policar, C., An easy-to-detect nona-arginine peptide for epidermal targeting. *Chem. Commun.* **2015,** *51* (13), 2687-2689.
31. Clède, S.; Lambert, F.; Sandt, C.; Gueroui, Z.; Réfrégiers, M.; Plamont, M.-A.; Dumas, P.; Vessières, A.; Policar, C., A rhenium tris-carbonyl derivative as a single core multimodal probe for imaging (SCoMPI) combining infrared and luminescent properties. *Chem. Commun.* **2012,** *48* (62), 7729-7731.

32. Clède, S.; Lambert, F.; Sandt, C.; Kascakova, S.; Unger, M.; Harté, E.; Plamont, M.-A.; Saint-Fort, R.; Deniset-Besseau, A.; Gueroui, Z.; Hirschmugl, C.; Lecomte, S.; Dazzi, A.; Vessières, A.; Policar, C., Detection of an estrogen derivative in two breast cancer cell lines using a single core multimodal probe for imaging (SCoMPI) imaged by a panel of luminescent and vibrational techniques. *Analyst* **2013,** *138* (19), 5627-5638.
33. Henry, L.; Delsuc, N.; Laugel, C.; Lambert, F.; Sandt, C.; Hostachy, S.; Bernard, A.-S.; Bertrand, H. C.; Grimaud, L.; Baillet-Guffroy, A.; Policar, C., Labeling of Hyaluronic Acids with a Rhenium-tricarbonyl Tag and Percutaneous Penetration Studied by Multimodal Imaging. *Bioconj. Chem.* **2018,** *29* (4), 987-991.
34. Hostachy, S.; Masuda, M.; Miki, T.; Hamachi, I.; Sagan, S.; Lequin, O.; Medjoubi, K.; Somogyi, A.; Delsuc, N.; Policar, C., Graftable SCoMPIs enable the labeling and X-ray fluorescence imaging of proteins. *Chem. Sci.* **2018,** *9* (19), 4483-4487.
35. Wedding, J. L.; Harris, H. H.; Bader, C. A.; Plush, S. E.; Mak, R.; Massi, M.; Brooks, D. A.; Lai, B.; Vogt, S.; Werrett, M. V.; Simpson, P. V.; Skelton, B. W.; Stagni, S., Intracellular distribution and stability of a luminescent rhenium(i) tricarbonyl tetrazolato complex using epifluorescence microscopy in conjunction with X-ray fluorescence imaging. *Metallomics* **2017,** *9* (4), 382-390.
36. Rodushkin, I.; Engström, E.; Stenberg, A.; Baxter, D. C., Determination of low-abundance elements at ultra-trace levels in urine and serum by inductively coupled plasma–sector field mass spectrometry. *Anal. Bioanal. Chem.* **2004,** *380* (2), 247-257.
37. Rajendran, L.; Hj, K.; Simons, K., Subcellular targeting strategies for drug design and delivery. *Nat. Rev. Drug Discov.* **2010,** *9*, 29-42.
38. Sakhrani, N. M.; Padh, H., Organelle targeting: third level of drug targeting. *Drug Des Devel Ther* **2013,** *7*, 585-599.
39. Xu, Z.; Xu, L., Fluorescent probes for the selective detection of chemical species inside mitochondria. *Chem. Commun.* **2016,** *52* (6), 1094-1119.
40. Di Lisa, F.; Kaludercic, N.; Carpi, A.; Menabò, R.; Giorgio, M., Mitochondria and vascular pathology. *Pharmacol. Rep.* **2009,** *61* (1), 123-130.
41. Frantz, M.-C.; Wipf, P., Mitochondria as a target in treatment. *Environ. Mol. Mutagen.* **2010,** *51* (5), 462-475.
42. Haelterman, N. A.; Yoon, W. H.; Sandoval, H.; Jaiswal, M.; Shulman, J. M.; Bellen, H. J., A Mitocentric View of Parkinson's Disease. *Ann. Rev. Neurosci.* **2014,** *37* (1), 137-159.
43. Smith, R. A.; Hartley, R. C.; Murphy, M. P., Mitochondria-targeted small molecule therapeutics and probes. *Antioxid Redox Signal* **2011,** *15* (12), 3021-3038.
44. Yousif, L. F.; Stewart, K. M.; Kelley, S. O., Targeting Mitochondria with Organelle-Specific Compounds: Strategies and Applications. *ChemBioChem* **2009,** *10* (12), 1939-1950.
45. Horton, K. L.; Stewart, K. M.; Fonseca, S. B.; Guo, Q.; Kelley, S. O., Mitochondria-penetrating peptides. *Chem Biol* **2008,** *15* (4), 375-382.
46. Kim, S.; Nam, H. Y.; Lee, J.; Seo, J., Mitochondrion-Targeting Peptides and Peptidomimetics: Recent Progress and Design Principles. *Biochemistry* **2020,** *59* (3), 270-284.
47. Zhao, K.; Zhao, G.-M.; Wu, D.; Soong, Y.; Birk, A. V.; Schiller, P. S.; Szeto, H. H., Cell-permeable peptide antioxidants targeted to inner mitochondrial membrane inhibit mitochondrial swelling, oxidative cell death, and reperfusion injury. *J. Biol. Chem.* **2004,** *279* (33), 34682-34690.
48. Smith, R. A. J.; Porteous, C. M.; Gane, A. M.; Murphy, M. P., Delivery of bioactive molecules to mitochondria *in vivo*. *Proc. Nat. Acad. Sci.* **2003,** *100* (9), 5407.

49. Zielonka, J.; Joseph, J.; Sikora, A.; Hardy, M.; Ouari, O.; Vasquez-Vivar, J.; Cheng, G.; Lopez, M.; Kalyanaraman, B., Mitochondria-Targeted Triphenylphosphonium-Based Compounds: Syntheses, Mechanisms of Action, and Therapeutic and Diagnostic Applications. *Chem. Rev.* **2017,** *117* (15), 10043-10120.
50. Murphy, M. P., Slip and leak in mitochondrial oxidative phosphorylation. *Biochim. Biophys. Acta - Bioenergetics* **1989,** *977* (2), 123-141.
51. Qiu, K.; Chen, Y.; Rees, T. W.; Ji, L.; Chao, H., Organelle-targeting metal complexes: From molecular design to bio-applications. *Coord. Chem. Rev.* **2019,** *378*, 66-86.
52. Amoroso, A. J.; Arthur, R. J.; Coogan, M. P.; Court, J. B.; Fernández-Moreira, V.; Hayes, A. J.; Lloyd, D.; Millet, C.; Pope, S. J. A., 3-Chloromethylpyridyl bipyridine fac-tricarbonyl rhenium: a thiol-reactive luminophore for fluorescence microscopy accumulates in mitochondria. *New J. Chem.* **2008,** *32* (7), 1097-1102.
53. Louie, M.-W.; Liu, H.-W.; Lam, M. H.-C.; Lam, Y.-W.; Lo, K. K.-W., Luminescent Rhenium(I) Polypyridine Complexes Appended with an α-D-Glucose Moiety as Novel Biomolecular and Cellular Probes. *Chem. Eur. J.* **2011,** *17* (30), 8304-8308.
54. Skiba, J.; Bernaś, T.; Trzybiński, D.; Woźniak, K.; Ferraro, G.; Marasco, D.; Merlino, A.; Shafikov, M. Z.; Czerwieniec, R.; Kowalski, K., Mitochondria Targeting with Luminescent Rhenium(I) Complexes. . *Molecules* **2017,** *22* (5), 809.
55. Ye, R.-R.; Tan, C.-P.; Chen, M.-H.; Hao, L.; Ji, L.-N.; Mao, Z.-W., Mono- and Dinuclear Phosphorescent Rhenium(I) Complexes: Impact of Subcellular Localization on Anticancer Mechanisms. *Chem. Eur. J.* **2016,** *22* (23), 7800-7809.
56. Hu, Z.; Sim, Y.; Kon, O. L.; Ng, W. H.; Ribeiro, A. J. M.; Ramos, M. J.; Fernandes, P. A.; Ganguly, R.; Xing, B.; García, F.; Yeow, E. K. L., Unique Triphenylphosphonium Derivatives for Enhanced Mitochondrial Uptake and Photodynamic Therapy. *Bioconj. Chem.* **2017,** *28* (2), 590-599.
57. Ong, H. C.; Hu, Z.; Coimbra, J. T. S.; Ramos, M. J.; Kon, O. L.; Xing, B.; Yeow, E. K. L.; Fernandes, P. A.; García, F., Enabling Mitochondrial Uptake of Lipophilic Dications Using Methylated Triphenylphosphonium Moieties. *Inorg. Chem.* **2019,** *58* (13), 8293-8299.
58. Bertrand, H. C.; Clède, S.; Guillot, R.; Lambert, F.; Policar, C., Luminescence modulations of rhenium tricarbonyl complexes induced by structural variations. *Inorg. Chem.* **2014,** *53* (12), 6204-6223.
59. Ching, H. Y. V.; Wang, X.; He, M.; Perujo Holland, N.; Guillot, R.; Slim, C.; Griveau, S.; Bertrand, H. C.; Policar, C.; Bedioui, F.; Fontecave, M., Rhenium Complexes Based on 2-Pyridyl-1,2,3-triazole Ligands: A New Class of CO2 Reduction Catalysts. *Inorg. Chem.* **2017,** *56* (5), 2966-2976.
60. He, M.; Ching, H. Y. V.; Policar, C.; Bertrand, H. C., Rhenium tricarbonyl complexes with arenethiolate axial ligands. *New J. Chem.* **2018,** *42* (14), 11312-11323.
61. Antonenko, Y. N.; Denisov, S. S.; Silachev, D. N.; Khailova, L. S.; Jankauskas, S. S.; Rokitskaya, T. I.; Danilina, T. I.; Kotova, E. A.; Korshunova, G. A.; Plotnikov, E. Y.; Zorov, D. B., A long-linker conjugate of fluorescein and triphenylphosphonium as mitochondria-targeted uncoupler and fluorescent neuro- and nephroprotector. *Biochim. Biophys. Acta - General Subjects* **2016,** *1860* (11, Part A), 2463-2473.
62. Asin-Cayuela, J.; Manas, A.-R. B.; James, A. M.; Smith, R. A. J.; Murphy, M. P., Fine-tuning the hydrophobicity of a mitochondria-targeted antioxidant. *FEBS Lett.* **2004,** *571* (1-3), 9-16.
63. Rokitskaya, T. I.; Murphy, M. P.; Skulachev, V. P.; Antonenko, Y. N., Ubiquinol and plastoquinol triphenylphosphonium conjugates can carry electrons through phospholipid membranes. *Bioelectrochemistry* **2016,** *111*, 23-30.

64. Coogan, M. P.; Fernández-Moreira, V.; Hess, J. B.; Pope, S. J. A.; Williams, C., Rhenium fac-tricarbonyl bisimine complexes: luminescence modulation by hydrophobically driven intramolecular interactions. *New J. Chem.* **2009,** *33* (5), 1094-1099.
65. Jin, Q.; Paunesku, T.; Lai, B.; Gleber, S. C.; Chen, S. I.; Finney, L.; Vine, D.; Vogt, S.; Woloschak, G.; Jacobsen, C., Preserving elemental content in adherent mammalian cells for analysis by synchrotron-based x-ray fluorescence microscopy. *J. Microsc.* **2017,** *265* (1), 81-93.

Supporting Information

- Experimental part

Synthesis

General considerations

^{1}H and ^{13}C NMR spectra were recorded on a Bruker DRX 300 using solvent residuals as internal references. The following abbreviations are used: singlet (s), doublet (d), doubled doublet (dd), triplet (t), doubled triplet (td), quadruplet (q) and multiplet (m). High resolution mass spectrometry (HRMS) was performed on a Bruker hybride APEX spectrometer (electrospray) at the ICMMO (Institut de chimie et des matériaux d'Orsay). The following abbreviations are used: electrospray (ESI), time of flight (TOF). TLC analysis was carried out on silica gel (Merck 60F-254) with visualization at 254 and 366 nm. Preparative flash chromatography was carried out with Merck silica gel (Si 60, 40-63 µm). Reagents and chemicals were purchased from Merck, Acros, Alfa Aesar, TCI or Strem Chemicals. Dry solvents (dichloromethane (CH_2Cl_2 or DCM), toluene, tetrahydrofuran (THF) and dimethylformamide (DMF)) and reagents (diisopropylethylamine (DIEA)) were purchased from Merck and used without further purification. Analytical HPLC was performed on an Agilent 1200 series equipped with a quaternary pump using a Proto 200 C18 from Higgins Analytical Inc (particles size 3 µm, 100 × 4.6 mm column). Preparative HLC was performed on an Agilent 1260 Infinity using a Nucleodur C18 HTech column from Macherey-Nagel Inc. (particles size 5 µm, 250 × 16 mm column). UV-visible absorption spectra were recorded on a Varian Cary 300 Bio spectrophotometer, luminescence emission spectra on a Jasco FP-8300 spectrofluorimeter. Infrared spectra were recorded on a Perkin Elmer Spectrum 100 in ATR mode (background on air) and analyzed using the Omnic software. The following abbreviations are used: weak (w), strong (S), broad (br).

TP*P (2-aminoethyl)triphenylphosphonium bromide derivatives were synthesized according to published procedures.[1]

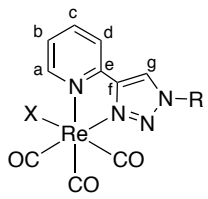

Numbering used in the NMR attributions.

β-Alanine(*N*-2-chloroacetyl) *tert*-butyl ester 1: β-alanine tert-butyl ester hydrochloride (1.50 g, 8.26 mmol, 1.2 eq.) was suspended in dry DCM (15 mL) under argon. Dry DIEA (2.9 mL, 17.2 mmol, 2.5 eq.) was added and the suspension was cooled down in an ice bath. Chloroacetyl chloride (0.6 mL, 6.9 mmol, 1.0 eq.) was added dropwise and the reaction mixture was stirred for 1 h at room temperature (ca. 25 °C). The reaction mixture was then diluted with DCM (15 mL) and washed with a 0.1 M HCl aqueous solution (30 mL), a 10 % $NaHCO_3$ aqueous solution (30 mL) and brine (30 mL). The organic phase was dried over $MgSO_4$, filtered and evaporated to afford β-alanine(*N*-2-chloroacetyl) *tert*-butyl ester **1** as a pale-yellow oil (1.61 g, quantitative yield).

Rf(SiO_2**,** cyclohexane/ethyl acetate 70:30 v:v) = 0.28); ^{1}H NMR (300 MHz, $CDCl_3$): δ (ppm) 7.16 (broad s, 1H, N*H*), 3.92 (s, 2H, Cl-CH_2), 3.41 (q, 2H, *J* = 6.1 Hz, CONH-CH_2), 2.36 (t, 2H, *J* = 6.1 Hz, CH_2-COOtBu), 1.34 (s, 9H, -C(CH_3)$_3$); ^{13}C NMR (75 MHz, $CDCl_3$): δ (ppm) 172.1 (*C*OOtBu), 165.8 (*C*ONH), 81.1 (-*C*(CH_3)$_3$), 42.5 (Cl-*C*H_2), 35.3 (NH-*C*H_2), 34.8 (NH-CH_2-*C*H_2), 27.9 (-C(*C*H_3)$_3$); HRMS (ESI+): m/z calculated for $C_9H_{16}ClNNaO_3$ $[M + Na]^+$: 244.0711, found: 244.0722.

***tert*-Butyl 3-(2-azidoacetamido)propanoate 2:** β-alanine(*N*-2-chloroacetyl)*tert*-butyl ester **1** (1.02 g, 4.58 mmol, 1.0 eq.) was dissolved in a 3:1 v:v mixture of acetone (15 mL) and water (5 mL). NaN_3 (587.1 mg, 9.16 mmol, 1.97 eq.) and NaI (69.1 mg, 461 µmol, 0.1 eq.) were added and the reaction mixture was stirred for 17 h at 50 °C. NaI (0.1 eq.) was added again and the reaction stirred for one additional hour. Acetone was evaporated and the mixture was diluted with DCM (15 mL) and water (5 mL). The aqueous phase was extracted with DCM (3 × 10 mL); the combined organic phases were dried over $MgSO_4$, filtered and evaporated to afford *tert*-butyl 3-(2-azidoacetamido)propanoate **2** as a pale-yellow oil (0.93 g, 89% yield).

Rf(SiO_2**,** cyclohexane/ethyl acetate 70:30 v:v) = 0.22); ^{1}H NMR (300 MHz, $CDCl_3$): δ (ppm) 7.00 (broad s, 1H, N*H*), 3.79 (s, 2H, N_3-CH_2), 3.35 (q, 2H, *J* = 6.2 Hz, NH-CH_2), 2.32 (t, 2H, *J* = 6.2 Hz,

NH-CH_2-CH_2), 1.30 (s, 9H, -C(CH_3)$_3$); ^{13}C NMR (75 MHz, $CDCl_3$): δ (ppm) 171.1 (*C*OOtBu), 166.6 (*C*ONH), 80.9 (-*C*(CH_3)$_3$), 52.2 (N_3-*C*H_2), 34.8 (NH-*C*H_2), 34.7 (NH-CH_2-*C*H_2), 27.7 (-C(*C*H_3)$_3$); IR: 3304 (br, NH), 2980 (w, CH), 2102 (S, N_3), 1723, 1659 (S, C−O). HRMS (ESI+): m/z calculated for $C_9H_{16}N_4NaO_3$ $[M + Na]^+$: 251.1115, found: 251.1118.

***tert*-Butyl 3-(2-(4-(pyridin-2-yl)-1*H*-1,2,3-triazol-1-yl)acetamido)propanoate 3:** *tert*-butyl 3-(2-azidoacetamido)propanoate **2** (485.0 mg, 2.12 mmol, 1.0 eq.) was dissolved in a 2:1 v:v mixture of acetone (20 mL) and water (10 mL). 2-Ethynylpyridine (264.0 mg, 2.56 mmol, 1.2 eq.), copper sulfate pentahydrate (87.7 mg, 549 µmol, 0.26 eq.) and sodium ascorbate (434 mg, 2.19 mmol, 1.03 eq.) were then added and the suspension was sonicated for a few minutes, during which a light brownish precipitate formed. The reaction mixture was then stirred for 2 h at room temperature (ca. 25 °C). Acetone was evaporated, the mixture was diluted with DCM (30 mL), and the resulting solution was poured into an aqueous 28 % ammonia solution (30 mL) and extracted with DCM (3 × 10 mL). The organic phases were combined, dried over Na_2SO_4, filtered and concentrated. The resulting brown solid was purified by column chromatography on silica gel (ethyl acetate/cyclohexane 60:40 to 100:0 v:v) to afford *tert*-butyl 3-(2-(4-(pyridin-2-yl)-1*H*-1,2,3-triazol-1-yl)acetamido)propanoate **3** as a white solid (598.4 mg, 85% yield).

Rf(SiO_2, ethyl acetate) = 0.23); ^{1}H NMR (300 MHz, $CDCl_3$): δ (ppm) 8.59 (d, 1H, *J* = 5.0 Hz, H^a pyta), 8.37 (s, 1H,H^g pyta), 8.19 (d, 1H, *J* = 7.9 Hz, H^d pyta), 7.82 (td, 1H, *J* = 7.9, 1.8 Hz, H^c pyta), 7.33-7.27 (m, 1H, H^b pyta), 6.60 (broad s, 1H, N*H*), 5.11 (s, 2H, pyta-CH_2), 3.50 (q, 2H, *J* = 6.2 Hz, CONH-CH_2), 2.43 (t, 2H, *J* = 6.2 Hz, CH_2-COOtBu), 1.38 (s, 9H, -C-(CH_3)$_3$); ^{13}C NMR (75 MHz, $CDCl_3$): δ (ppm) 171.5 (*C*OOtBu), 164.9 (*C*ONH), 149.4 (C^e pyta), 148.9 (C^a pyta), 148.3 (C^f pyta), 137.8 (C^c pyta), 124.1 (C^g pyta), 123.4 (C^b pyta), 120.7 (C^d pyta), 81.6 (-*C*(CH_3)$_3$), 53.3 (pyta-*C*H_2), 35.5 (NH-*C*H_2), 34.9 (NH- CH_2-*C*H_2), 28.1 (-C(*C*H_3)$_3$); IR: 3357 (S, CH aromatic), 2985 (w, CH aliphatic), 1712, 1681 (S, C−O); HRMS (ESI+): m/z calculated for $C_{16}H_{21}N_5NaO_3$ $[M + Na]^+$: 354.1537, found: 354.1529.

$Re(CO)_3Cl$(*tert*-butyl 3-(2-(4-(pyridin-2-yl)-1*H*-1,2,3-triazol-1-yl)acetamido)propanoate) 4: *tert*-butyl 3-(2-(4-(pyridin-2-yl)-1*H*-1,2,3-triazol-1-yl)acetamido)propanoate **3** (399.8 mg, 1.21 mmol, 1.0 eq.) was dissolved in hot toluene (60 °C, 20 mL), $Re(CO)_5Cl$ (484.1 mg, 1.34 mmol, 1.1 eq.) was added and the reaction mixture was refluxed for 5 h. The reaction mixture was

cooled down to room temperature, the precipitated solid was filtered, washed with cold toluene (0 °C, 10 mL) and dried under vacuum to afford $Re(CO)_3Cl$(*tert*-butyl 3-(2-(4-(pyridin-2-yl)-1*H*-1,2,3-triazol-1-yl)acetamido)propanoate) **4** as a yellow solid (880.0 mg, 99% yield).

Rf(SiO_2, ethyl acetate) = 0.34; ^{1}H NMR (300 MHz, $CDCl_3$): δ (ppm) 9.02 (ddd, 1H, *J* = 5.6, 1.5, 0.8 Hz, H^a pyta), 8.54 (s, 1H, H^g pyta), 8.06 (td, 1H, *J* =7.8, 1.5 Hz, H^c pyta), 7.91 (dt, *J* = 7.8, 1.2 Hz, 1H, H^d pyta), 7.47 (ddd, 1H, *J* = 7.8, 5.6, 1.2 Hz, H^b pyta), 7.19 (t, 1H, *J* = 5.8 Hz, N*H*), 5.22-4.89 (m, 2H, pyta-C*H*$_2$), 3.52 (qd, 2H, *J* = 6.6, 2.2 Hz, NH-C*H*$_2$), 2.48 (t, 2H, *J* = 6.6 Hz, C*H*$_2$-COOtBu), 1.46 (s, 9H, -C(C*H*$_3$)$_3$); ^{13}C NMR (75 MHz, CD_3OD): δ (ppm) 172.6 (*C*OOtBu), 166.5 (*C*ONH), 154.3 (C^f pyta), 150.8 (C^e pyta), 150.2 (C^a pyta), 141.4 (C^c pyta), 127.9 (C^g pyta), 127.3 (C^b pyta), 123.6 (C^d pyta), 82.1 (-*C*$(CH_3)_3$), 54.3 (pyta-*C*H_2), 36.9 (NH-*C*H_2), 35.9 (NH-CH_2-*C*H_2), 28.4 (-C(*C*$H_3)_3$); IR: 3288 (br, NH), 2980 (w, CH), 2021 (s, CO A_1), 1883 (s, CO E), 1681 (s, C=O), 1153 (S, C-O); HRMS (ESI+): m/z calculated for $C_{19}H_{21}ClN_5NaO_6Re$ $[M + Na]^+$: 635.9657, found: 635.9355.

$Re(CO)_3Cl$(3-(2-(4-(pyridin-2-yl)-1*H*-1,2,3-triazol-1-yl)acetamido)propanoic acid) 5: $Re(CO)_3Cl$(*tert*-butyl 3-(2-(4-(pyridin-2-yl)-1*H*-1,2,3-triazol-1-yl)acetamido)propanoate) **4** (880.0 mg, 1.38 mmol, 1 eq.) was dissolved in DCM (4 mL) and trifluoroacetic acid (4 mL, 52 mmol, 35 eq.) was added slowly. The reaction mixture was stirred at room temperature for 1 h. The solvents were evaporated and concentrated HCl (37%, 4 mL) was added. The reaction mixture was stirred for 10 min at room temperature, HCl was evaporated and the residue dried under vacuum to afford $Re(CO)_3Cl$(3-(2-(4-(pyridin-2-yl)-1*H*-1,2,3-triazol-1-yl)acetamido)propanoic acid) **5** as a whitish solid (650.0 mg, 86% yield).

Rf(SiO_2, DCM/EtOH 75:25 v:v + 1% v CH_3COOH) = 0.61; ^{1}H NMR (300 MHz, $CDCl_3$/CD_3OD): δ (ppm) 8.97 (dt, 1H, *J* = 5.5, 1.2 Hz, H^a pyta), 8.93 (s, 1H, H^g pyta), 8.18-8.08 (m, 2H, Hc & H^d pyta), 7.54 (td, 1H, *J* = 5.5, 4.0 Hz, H^b pyta), 5.45-5.25 (m, 2H, pyta-C*H*$_2$), 3.52 (t, 2H, *J* = 6.6 Hz, NH-C*H*$_2$), 2.57 (t, 2H, *J* = 6.6 Hz, C*H*$_2$-COOH); ^{13}C NMR (75 MHz, $CDCl_3$/CD_3OD): δ (ppm) 173.6 (*C*OOH), 164.4 (*C*ONH), 152.7 (C^f pyta), 149.1 (C^e pyta), 148.6 (C^a pyta), 139.6 (C^c pyta), 128.5 (C^g pyta), 127.7 (C^b pyta), 125.6 (C^d pyta), 122.0, 52.8 (pyta-*C*H_2), 35.4 (NH-*C*H_2), 33.0 (NH-CH_2-*C*H_2); IR: 3353, (br, OH), 3129 (w, CH), 2015 (s, CO A_1), 1897.6 (s, CO E), 1719 (s, C=O); HRMS (ESI+): m/z calculated for $C_{15}H_{13}ClN_5NaO_6Re$ $[M + Na]^+$: 603.9995, found: 603.9991.

(2-Aminoethyl)triphenylphosphonium bromide:[1] (2-bromoethyl) amine hydrobromide (7.81 g, 38.1 mmol, 1.0 eq.) was dissolved in acetonitrile (50 mL). Triphenylphosphine (10.0 g, 38.1 mmol, 1.0 eq.) was added and the solution was refluxed overnight (82 °C). The precipitate was filtered, dissolved in water and treated with a saturated aqueous solution of K_2CO_3 until pH > 11. The product was extracted with DCM (3 × 10mL); the organic phases were combined, dried over $MgSO_4$ and evaporated to afford (2-aminoethyl)triphenylphosphonium bromide as a white solid (4.47 g, 30% yield).

Rf(SiO_2, DCM/EtOH 70:30 v:v) = 0.39 ; ^{1}H NMR (300 MHz, $CDCl_3$): δ (ppm) 7.75 (m, 15 H, PPh_3), 4.06 (m, 2H, *J* = 1.1 Hz, H_2N-C*H*$_2$), 3.15 (m, 2H, *J* = 1.1 Hz, C*H*$_2$-PPh_3); IR: 3316 (w, NH), 2903 (w, CH), 1743 (C=C); HRMS (ESI+): m/z calculated for $[C_{20}H_{21}NP]^+$: 306.139502, found: 306.140613. NMR Data in agreement with literature.

(2-ammonioethyl)tri(p-tolyl)phosphonium bromide: (2-bromoethyl) amine hydrobromide (0.410 g, 2 mmol, 1.0 eq.) was dissolved in acetonitrile (5 mL). Tri(p-tolyl)phosphine (0.898 g, 2.95 mmol, 1.475 eq.) was added and the solution was refluxed overnight (82 °C). The solution was allowed to cool to room temperature and the product was precipitated by the addition of diethyl ether. The solid was filtered and recrystallized in ACN/Et_2O to afford (2-ammonioethyl)tri(p-tolyl)phosphonium bromide as a white solid (0.405 g, 40% yield).

^{1}H NMR (500 MHz, $CDCl_3$): δ (ppm) 8.94 (s, 3 H, -N*H*$_3$), 7.73 – 7.36 (m, 12 H, Ar-*H*), 4.35 (m, 2 H, H_3N-C*H*$_2$), 3.33 (s, 2 H, C*H*$_2$-PAr_3), 2.51 (s, 9 H, Ar-*Me*); ^{31}P{^{1}H} NMR (121 MHz, $CDCl_3$): δ (ppm) 21.58.

(2-ammonioethyl)tris(3,5-dimethylphenyl)phosphonium bromide: (2-bromoethyl) amine hydrobromide (0.246 g, 1.2 mmol, 1.0 eq.) was dissolved in acetonitrile (3 mL). Tris(3,5-dimethylphenyl)phosphine (0.555 g, 1.60 mmol, 1.33 eq.) was added and the solution was refluxed overnight (82 °C). The solution was allowed to cool to room temperature and the product was precipitated by the addition of diethyl ether. The solid was filtered and recrystallized in ACN/Et_2O to afford (2-ammonioethyl)tris(3,5-dimethylphenyl)phosphonium bromide as a white solid (0.425 g, 64% yield).[1]

^{1}H NMR (500 MHz, $CDCl_3$): δ (ppm) 8.76 (s, 3 H, -NH_3), 7.42 (s, 3 H, o-Ph), 7.31 (d, $J_{P\text{-}H}$ = 14.1 Hz, 6 H), 4.39 – 4.17 (m, 2 H, H_2N-C*H*$_2$), 3.31 (s, 2 H, C*H*$_2$-PAr_3), 2.43 (s, 18 H, Ar-*Me*); ^{31}P{^{1}H} NMR (121 MHz, $CDCl_3$): δ (ppm) 21.34.

General procedure for conjugates 1-3:

$Re(CO)_3Cl$(3-(2-(4-(pyridin-2-yl)-1*H*-1,2,3-triazol-1-yl)acetamido)propanoic acid) **5** (1.0 eq.), N-ethyl-N'-(3-dimethylaminopropyl)carbodiimide hydrochloride (EDC·HCl, 1.5 eq.) and hydroxybenzotriazole (HOBt, 1.5 eq.) were dissolved in DMF (2.8 mL / 100 mg). After 5 min of stirring, (2-aminoethyl)triphenylphosphonium bromide derivative **P1-3** (1.1 eq.) and DIEA (3.3 eq.) were added and the reaction mixture was stirred at room temperature (ca. 25 °C) for 24 or 48 h. After evaporation of the solvent, the resulting solid was dissolved in DCM (15 mL) and a saturated aqueous $NaHCO_3$ solution (15 mL) was added. The aqueous phase was extracted with DCM (10 mL); the combined organic phases were dried over Na_2SO_4, filtered and evaporated. The crude product was purified by column chromatography on aluminum oxide with a DCM/EtOH gradient from 100:0 to 80:20 v:v as eluent.

[$Re(CO)_3Cl$(triphenyl(2-(3-(2-(4-(pyridin-2-yl)-1H-1,2,3-triazol-1-yl)acetamido)propanamido)ethyl)phosphonium bromide)] C1: was obtained following general procedure from $Re(CO)_3Cl$(3-(2-(4-(pyridin-2-yl)-1*H*-1,2,3-triazol-1-yl)acetamido)propanoic acid) **5** (100.7 mg, 173.3 µmol, 1.0 eq.) and (2-aminoethyl)triphenylphosphonium bromide **P1** (90.3 mg, 193 µmol, 1.1 eq.) in 48 h after purification by column chromatography on aluminum oxide, DCM/EtOH gradient from 100:0 to 80:20 v:v: as a yellow sticky solid (74.7 mg, 70 % yield).

^{1}H NMR (300 MHz, $CDCl_3$): δ (ppm) 9.23 (s, 1H, H^g pyta), 8.99 (t, 1H, *J* = 5.4 Hz, N*H*), 8.88 (dd, 1H, *J* = 5.6, 1.3 Hz, H^a pyta), 8.56 (t, 1H, *J* = 5.1, N*H*), 8.03 (d, 1H, *J* = 7.6 Hz, H^d pyta), 7.94 (td, 1H, *J* = 7.6, 1.3 Hz, H^c pyta), 7.82-7.73 (m, 9H, PPh_3), 7.67 (m, 6H, PPh_3), 7.34 (dd, *J* = 7.6, 5.6 Hz, 1H, H^b pyta), 5.45 (s, 2H, pyta-CH_2), 3.80 (m, 2H, CONH-CH_2), 3.59-3.40 (m, 4H, 2 × CH_2), 2.32 (t, 2H, *J* = 5.7 Hz, CH_2); ^{13}C NMR (75 MHz, $CDCl_3$): δ (ppm) 172.5 (*C*ONH), 164.7 (*C*ONH), 152.8 (C^a pyta), 149.6 (C^f pyta), 148.7 (C^e pyta), 139.9 (C^c pyta), 135.5 (PPh_3 C_{para}), 135.4 (C^b pyta), 133.8, 133.7 (PPh_3 C_{ortho}), 130.8, 130.6 (PPh_3 C_{meta}), 125.7 (C^d pyta), 122.9 (C^g pyta), 118.6, 117.4 (Ph_3P-*C*), 60.3 (pyta-*C*H_2), 36.8 (NH-*C*H_2), 36.3 (NH-*C*H_2), 27.6 (NH-CH_2-*C*H_2); ^{31}P NMR (121 MHz, $CDCl_3$): δ (ppm) 21.06; IR: 3207 (br, NH), 3059 (w, CH aromatic), 2927 (w, CH aliphatic), 2020 (S, CO A_1), 1911 (S, CO E), 1885 (S, CO E), 1684 (C=O amide); HRMS (ESI+): m/z calculated for $[C_{35}H_{32}ClN_6O_5PRe]^+$: 869.1413 found: 869.1390; HPLC (5 to 100 % of acetonitrile in 10 min): t_r = 6.4 min, purity > 85%.

[$Re(CO)_3Cl$((2-(3-(2-(4-(pyridin-2-yl)-1*H*-1,2,3-triazol-1-yl)acetamido)propanamido)ethyl)tri-*p*-tolylphosphonium bromide)] C2: was obtained following general procedure from $Re(CO)_3Cl$(3-(2-(4-(pyridin-2-yl)-1*H*-1,2,3-triazol-1-yl)acetamido)propanoic acid) **5** (100.1 mg, 172 µmol, 1.1 eq) and (2-aminoethyl)tri-p-tolylphosphonium bromide **P2** (79.1 mg, 155 µmol, 1.0 eq.) in 24 h after purification by column chromatography on aluminum oxide, DCM/EtOH gradient from 100:0 to 80:20 v:v: as a yellow solid (30.0 mg, 20 % yield).

^{1}H NMR (300 MHz, $CDCl_3$): δ (ppm) 9.20 (s, 1H, H^g pyta), 8.94-8.87 (m, 2H, H^a pyta & N*H*), 8.53 (t, 1H, *J* = 5.6 Hz, N*H*), 8.03 (m, 1H, H^d pyta), 7.94 (td, 1H, *J* = 7.6, 1.5 Hz, H^c pyta), 7.64-7.55 (m, 6H, PPh_3), 7.45 (dd, 6H, *J* = 8.2, 3.3 Hz, 6H, PPh_3), 7.34 (ddd, 1H, *J* = 7.6, 5.5, 1.5 Hz, H^b pyta), 5.43 (s, 2H, pyta-C*H*$_2$), 3.69-3.56 (m, 2H, CONH-C*H*$_2$), 3.50 (m, 2 × C*H*$_2$), 2.45 (s, 9H, 3 × C*H*$_3$), 2.36 (t, 2H, *J* = 5.9 Hz, 2H, C*H*$_2$); ^{13}C NMR (75 MHz, $CDCl_3$): δ (ppm) 172.4 (*C*ONH), 164.6 (*C*ONH), 149.6 (C^f pyta), 148.7 (C^e pyta), 146.7, 146.6 (PPh_3 C_{para}), 139.5 (C^a pyta), 133.6, 133.5 (PPh_3 C_{ortho}), 133.5 (C^c pyta), 131.4, 131.2 (PPh_3 C_{meta}), 125.7 (C^b pyta), 123.2 (C^d pyta), 122.7 (C^g pyta), 115.3, 114.2 (PPh_3-C), 54.0 (pyta-*C*H_2), 33.7 (NH-CH_2-*C*H_2); ^{31}P NMR (121 MHz, $CDCl_3$): δ (ppm) 19.94; IR: 3225 (br, NH), 3048 (w, CH aromatic), 2924 (w, CH aliphatic), 2020 (S, CO A_1), 1910 (S, CO E), 1882 (S, CO E), 1665 (C=O amide); HRMS (ESI+): m/z calculated for $[C_{38}H_{38}ClN_6O_5PRe]^+$: 911.1875 found: 911.1858; HPLC (5 to 100 % of acetonitrile in 10 min): t_r = 7.93 min, purity > 85 %.

[$Re(CO)_3Cl$(tris(3,5-dimethylphenyl)(2-(3-(2-(4-(pyridin-2-yl)-1H-1,2,3-triazol-1-yl)acetamido)propanamido)ethyl)phosphonium bromide)] C3: was obtained following general procedure from $Re(CO)_3Cl$(3-(2-(4-(pyridin-2-yl)-1*H*-1,2,3-triazol-1-yl)acetamido)propanoic acid) 5 (99.8 mg, 172 µmol, 1.1 eq) and (2-aminoethyl)tris(3,5-dimethylphenyl)phosphonium bromide P3 (85.8 mg, 156 µmol, 1.0 eq.) in 24 h after purification by column chromatography on aluminium oxide, DCM/EtOH gradient from 100:0 to 80:20 v:v: as a yellow sticky solid (62.9 mg, 39 %yield).

^{1}H NMR (300 MHz, $CDCl_3$): δ (ppm) 9.18 (s, 1H, H^g pyta), 9.14 (t, 1H, *J* = 5.4 Hz, N*H*), 8.92-8.89 (dt, 1H, *J* = 5.4, 1.2 Hz, H^a pyta), 8.56 (m, 1H, N*H*), 7.95-7.93 (m, 2H, $H^{d\&c}$ pyta), 7.37 (s, 3H, PPh_3), 7.36-7.32 (m, 4H, H^b pyta + PPh_3), 7.27 (s, 3H, PPh_3), 5.40 (m, 2H, C*H*$_2$), 5.29 (s, 2H, pyta-C*H*$_2$), 3.59-3.46 (m, 6H, 3 x C*H*$_2$), 2.40 (s, 18H, 6 x C*H*$_3$); ^{13}C NMR (75 MHz, $CDCl_3$): δ (ppm) 172.3 (*C*ONH), 164.5 (*C*ONH), 152.9 (C^a pyta), 149.6 (C^f pyta) 148.7 (C^e pyta), 140.9, 140.7 (PPh_3

C_{meta}), 139.7 (C^c pyta), 137.11, 137.07 (PPh_3 C_{para}), 130.9, 130.8 (PPh_3 C_{ortho}), 125.7 (C^d pyta), 122.6 (C^g pyta), 118.5, 117.4 (PPh_3), 54.0 (pyta-CH_2), 37.0 (NH-CH_2), 36.4 (NH-CH_2), 33.8 (NH-CH_2-CH_2), 21.6 (CH_3); ^{31}P NMR (121 MHz, $CDCl_3$): δ (ppm) 19.82; IR: 3224 (br, NH), 3037 (w, CH aromatic), 2922 (w, CH aliphatic), 2020 (S, CO A_1), 1910 (S, CO E), 1883 (S, CO E), 1670 (C=O amide); HRMS (ESI+): m/z calculated for $[C_{41}H_{44}ClN_6O_5PRe]^+$: 953.2344 found: 953.2312; HPLC (5 to 100 % of acetonitrile in 10 min): t_r = 8.52 min, purity > 85%.

Spectroscopy.

Fluorescence emission studies were performed on a Jasco spectrofluorometer FP-8300 in acetonitrile or MilliQ water (with 10% DMSO).

For luminescence quantum yields determination, fluorescence and absorbance spectra were recorded in acetonitrile (with 10% DMSO) at different concentrations for the three conjugates and in 0.1 N sulfuric acid solution for the reference quinine sulfate. For fluorescence spectra, the excitation was set at 330 nm and emission light was detected between 350 nm and 600 nm. Quinine sulfate in 0.1 N sulfuric acid was used as a standard with a known quantum yield of 54.6% (exc 320 nm).

The quantum yields were determined with the following equation:

$\phi_s = \phi_r\left(\frac{A_r}{A_s}\right)\left(\frac{F_s}{F_r}\right)\left(\frac{n^2{}_s}{n^2{}_r}\right)$ where the subscripts s and r refer to the sample and the standard reference solution respectively; *n* is the refractive index of the solvents (the refractive index of 10% DMSO in acetonitrile was considered equal to that of acetonitrile); *F* is the integrated emission intensity; *A* is the absorbance at the excitation wavelength (A < 0.1) and ϕ is the luminescence quantum yield. The ratio F/A is given by the linear regressions.

Cell Culture.

A549 epithelial human lung carcinoma cells were cultured at 37 °C in a 5% CO_2 in air atmosphere. They were grown in high glucose DMEM with pyruvate sodium supplemented with 10% heat-inactivated FBS and 1% penicillin/streptomycin.

Fluorescence Microscopy.

A549 cells were grown on glass coverslip to reach around 50% confluency and were then incubated for 4 hours in presence of the probes at 10 or 20 µM (final volume of DMSO ≤ 0,2%).

At the end of the incubation, the medium was removed and a solution of fluorescent mitochondria tracker Mitotracker Deep Red (provided by Invitrogen) at 100 nM in complete media were added. After 30 minutes of incubation at 37 °C, the mitochondria staining solution were removed and the cells were washed twice with phosphate buffer. The cells were fixed with 4% para-formaldehyde for 8 min at room temperature and washed twice with PBS and once with milliQ water. Slides were air-dried and laid on a microscope slide with mounting media Vectashield (from Vector Laboratories) in between to minimize photobleaching and thus increase the sensitivity.

Fluorescence imaging was performed using an Olympus X71 microscope equipped with a C9100-02 camera (Hamamatsu Corporation, Sewickley, PA), a X60 oil-objective, a Lumencor Spectra X light source and a Hg lamp (100 W) attenuated by a neutral density filter. Microscopic slides were illuminated with the Hg lamp and luminescence signal of **C1**, **C2** and **C3** probes were detected using the following filter set: excitation D350/50x; beam splitter 400DCLP; emission HQ560/80m; Chroma Technology. For imaging, the glass coverslip (thinner part) was in contact with the oil. Microscopic slides were illuminated with the red source of Lumencor Spectra X and luminescence signal of the mitochondria tracker were detected using the appropriate filter set provided by Semrock (dichroic mirror: FF409/493/573/652-Di01-25x36 and emission filter: FF01-432/515/595/730-25). Image analysis was performed using Fiji software. The image background was subtracted using the “rolling ball” algorithm provided by Fiji.

The colocalization analysis were performed using the plugin coloc2 and JacoP implemented on Fiji software. The statistical confidence of the colocalization analysis results (Pearson value, Van-Steensel curve, scatter plot) were validated by the Costes’ method. This method consists in randomizing the first image channel 200 times and to check that the Pearson coefficient is below that of the unrandomized image in 100% of cases.

The Van Steensel crosscorrelation function (CCF)[2] is a technique that shifts an image A on the x-axis pixel per pixel relative to another image B and calculate the respective Pearson Coefficient. A cross correlation function is obtained by plotting the Pearson coefficient as a function of the pixel shift dx. Complete colocalization shows a bell-shaped curve with maximum at dx = 0; partial colocalization shows a peak shifted from dx = 0. The CCF obtained

for our conjugates show a partial overlay of the conjugates' labeling with that of the MitoTracker Deep Red.

Synchrotron Radiation X-ray Fluorescence (SXRF) Nano-imaging.

The intracellular distribution of rhenium in control cells and cells incubated with the probes was determined using SXRF nano-imaging. A549 cells were seeded on Si_3N_4 silicon nitride membranes (purchased from Silson Ltd, membrane size: 1.5 mm x 1.5 mm; membrane thickness: 500 nm) to reach around 50% confluency and treated with the probes at 20 µM (final volume of DMSO $\leq$ 0,2%) for 4 hours at 37 °C under 5% CO_2. After incubation, they were washed twice with PBS, fixed with 4% paraformaldehyde, washed again twice with PBS and once with milliQ water and eventually air-dried.

The samples were examined on the hard X-ray nano-probe beamline, NANOSCOPIUM of the French national synchrotron facility, SOLEIL, Paris, France. Maps were recorded using a 14 keV incident beam energy. A549 cells were imaged by using a continuous scanning mode with a pixel size of 0.5 µm and with an accumulation time per pixel equal to 100, 200 or mostly 300 ms/pixel. Rapid scans were obtained beforehand at lower resolution (1 µm) and shorter dwell time (50 ms) to select the desired cells, previously located using phase- contrast optical microscopy. A total of 13 cells incubated with **C2** and **C3** probes and 9 cells incubated with **C1** were mapped. The full XRF spectra were collected in each pixel by two Si-drift detectors (Ketek) in order to increase the solid angle of detection.

The elemental calcium, phosphorus, rhenium and zinc distribution maps were extracted from the full XRF spectra using a MATLAB program developed by the NANOSCOPIUM team. For rhenium, the background was subtracted and for all elements, the maps were normalized to the dwell time per pixel allowing direct comparison across samples. The XRF sum-spectra extracted from the maps were processed by PyMCA.

The Cu-Kβ, Zn-Kα and Re-Lα lines at ~8.6 keV are 100 % overlapping. However, the good energy resolution of the XRF detectors of the Nanoscopium beamline ensures the unambiguous deconvolution of the Zn-Kβ (9.6 keV) and the Re-Lβ lines (~10.15 and 10.28 keV). As such, in order to avoid the eventual overlapping of Zn and Re signal in the Re images, we used only the Re-Lβ lines to create the X-ray intensity maps. The detailed description of the data treatment of the XRF data-set can be found in Hostachi *et al.*[3]

Quantification of rhenium accumulation in cells

The amount of Re accumulated in the cells were calculated by comparing the rhenium signal summed within a mask of the mapped cells to the rhenium signal of a rhenium external standard. Masks of the cells were determined from the calcium map or the phosphorus spectra map. The Re standard was prepared by depositing 0.3 µL of a 10 µM solution of $Re(CO)_5Cl$ in MeOH (3.0×10^{-12} mol) on a silicon nitride SiN_3 membrane. The membrane was air-dried and the imaging of this rhenium standard (pixel size = 1 µm and integration time = 10 ms, Figure S27) allows us to identify the whole area of the Re droplet and to calculate precisely the total Re intensity, 2.32×10^7 I_{fluo}/s corresponding to the deposited rhenium molar quantity (3.0×10^{-12} mol) within the droplet by fitting the Re spectrum by PyMCA. This permits to calculate the conversion factor between the measured Re XRF intensity and molar concentrations, which is: 1.29×10^{-19} $mol.s/I_{fluo}$.

Cytotoxicity Assay

The probes cytotoxicity was assessed by using the MTT (3-(4,5-dimethylthiazol-2-yl)-2,5-diphenyltetrazolium bromide) assay based on the mitochondrial-dependent reduction of MTT to formazan. A549 cells were grown in 96-well plate to reach around 90% confluency and were then incubated for 4 hours at 37 °C in the presence of the probes at concentrations varying between 1 µM and 1 mM. The medium was then removed; the cells were washed with PBS and were incubated with a solution of MTT at 0.5 mg/mL for two hours at 37 °C. At the end of the incubation, formazan crystals were visible under the microscope. Three quarters of the MTT solution were removed in each well and were replaced by DMSO. The plate was incubated for 30 minutes at 37 °C to solubilize the formazan crystals. After complete solubilization of the formazan crystals, the extent of reduction of MTT to formazan by the cells was quantified by the measurement of the absorbance at 570 nm. A blank without cells were included in order to subtract the background corresponding to the culture medium from all samples. The percentage of cell viability compared to the untreated control were then calculated and were plotted as a function of the probe concentration. IC50 were calculated by fitting this curve with a four-parameter logistic curve using the Matlab L4P regression function. The MTT assay was performed for two biological replicates. For each biological replicate, the compounds' cytotoxicity was screened at each concentration in triplicate.

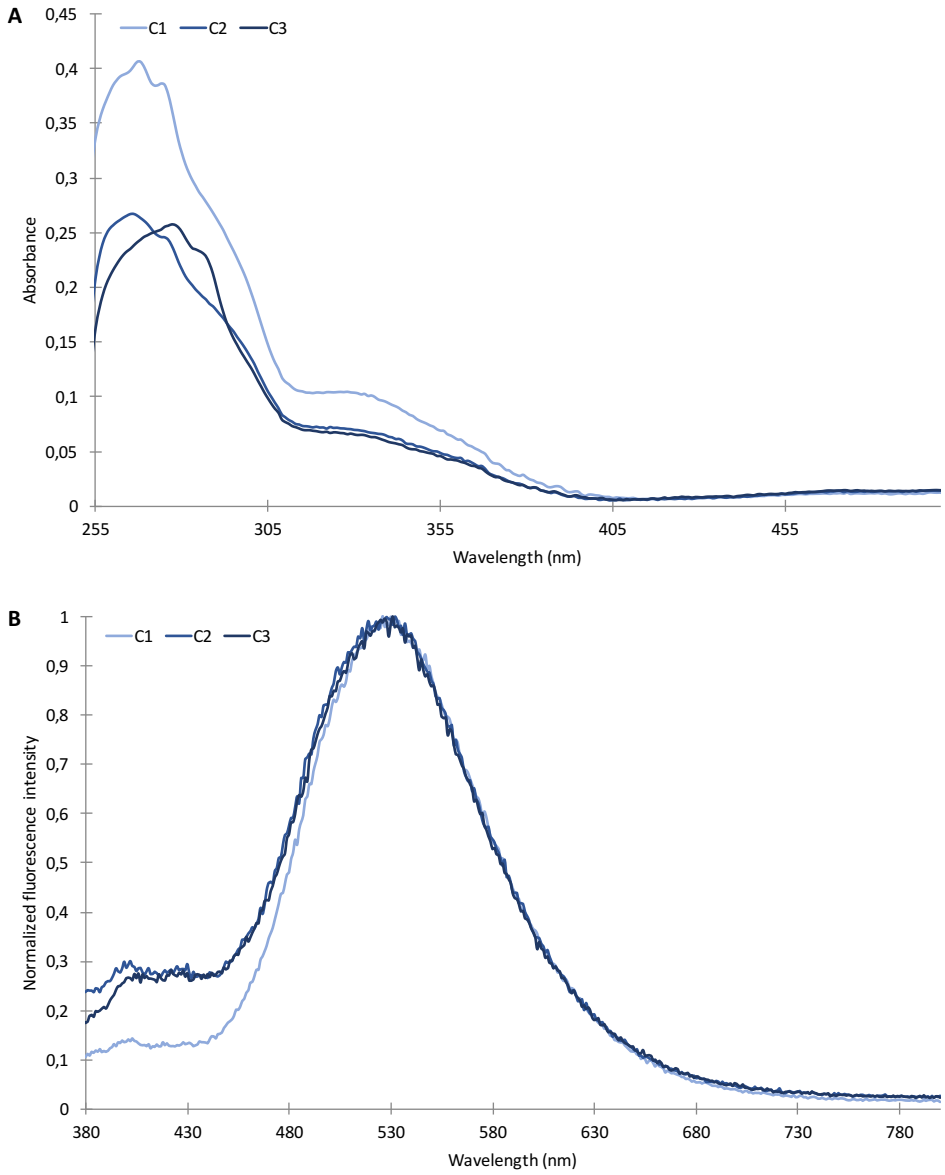

Figure S1. A. *UV-vis absorption spectra of complexes* ***C1-C3*** *in acetonitrile (with 10% DMSO, 20 µM);* ***B.*** *Normalized luminescence emission spectra of complexes* ***C1-C3*** *(20 µM) in acetonitrile (with 10% DMSO) (λexc 330 nm).*

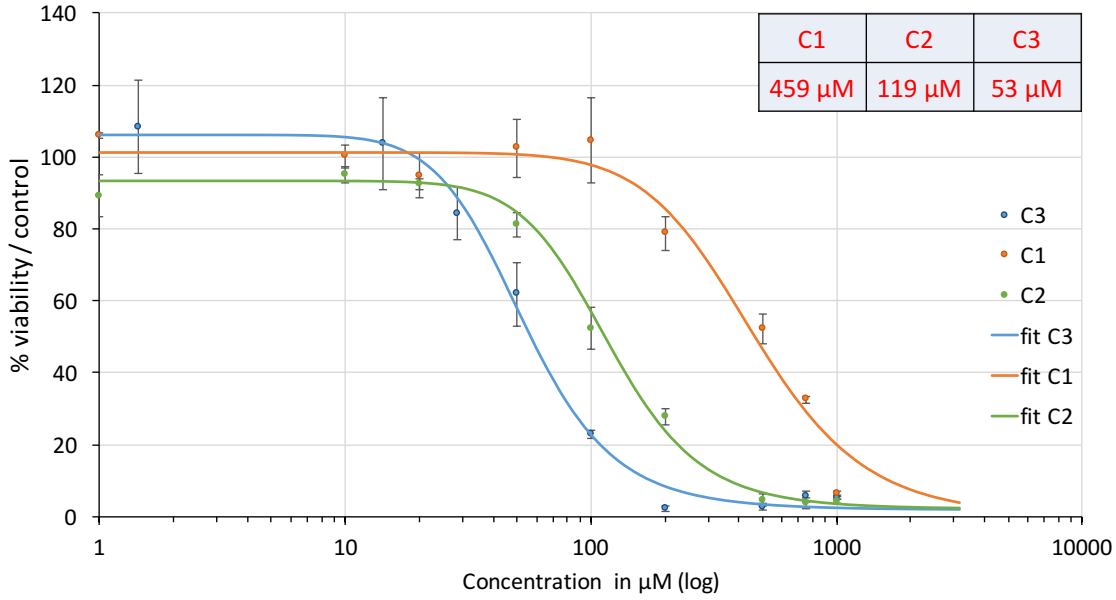

Fig. S2. Example of determination of IC50. *The cytotoxicity of the three probes were assessed from the MTT assay at concentrations varying between 1 µM and 1 mM. IC50 were calculated by fitting the plot of cell survival (%) versus probe concentration (µM) with a four-parameter logistic curve. The curves represented here correspond to one biological replicate and each dot to the mean of technical triplicates.*

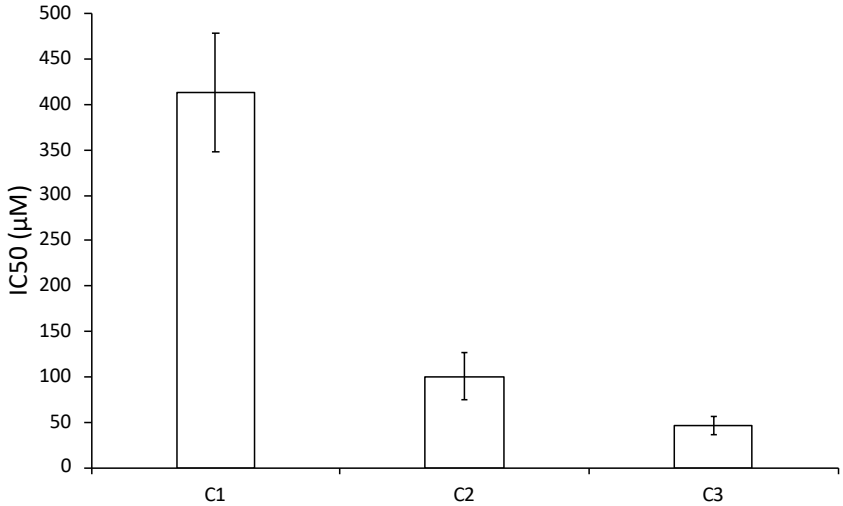

	IC50 (µM)
C1	413 ± 65
C2	100 ± 26
C3	46 ± 10

Figure S3. *Probe concentrations that produce 50 % cell growth inhibition (IC50). IC50 were calculated from curves constructed by plotting cell survival (%) versus probe concentration (µM). The percentage of cell survival was calculated at each concentration using the MTT viability assay. The MTT assay was performed for two biological replicates. For each biological replicate, the compounds cytotoxicity was screened at each concentration in triplicate.*

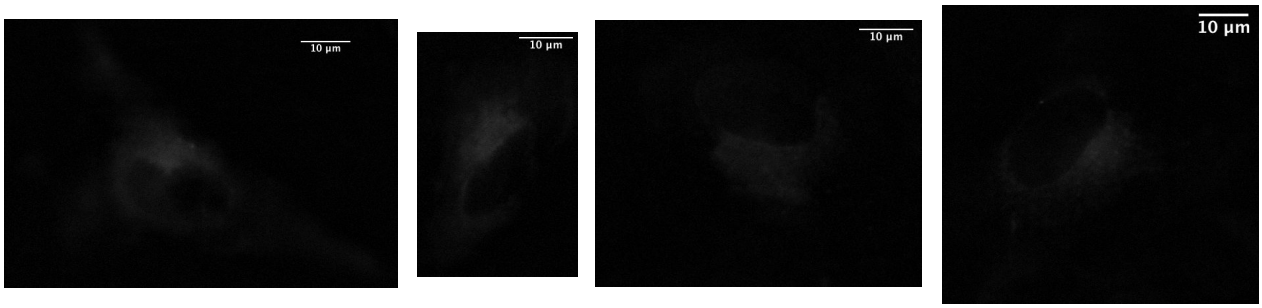

Figure S4. *Fluorescence imaging of A549 control cells (excitation 350 nm). The signal-to-noise ratio were equal to 23.5 dB, 22.9 dB, 22.0 dB and 22.3 dB respectively. Fixed fluorescence intensity scale (0-7500 u.a). Scale bar: 10 µm (fixed at 1.55 cm).*

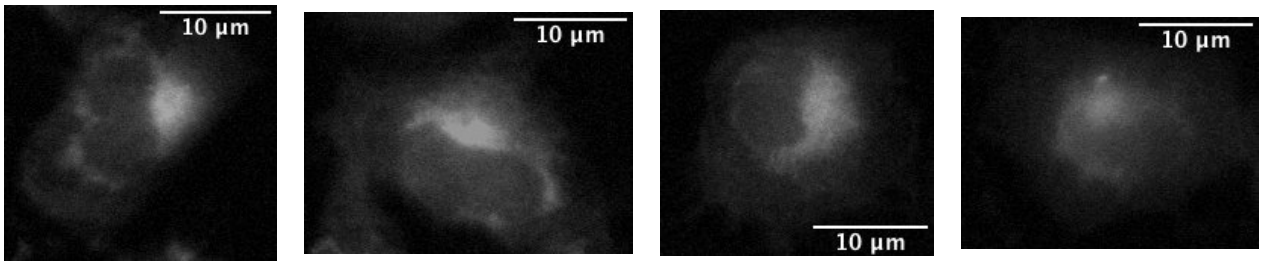

Figure S5. *Fluorescence imaging of A549 cells incubated with conjugate **C1** (at 20 µM for 4 h) (excitation 350 nm). The signal-to-noise ratio were equal to 32.9 dB, 32.5 dB, 33.3 dB and 30.9 dB respectively. Fixed fluorescence intensity scale (0-7500 u.a). Scale bar: 10 µm (fixed at 3.1 cm).*

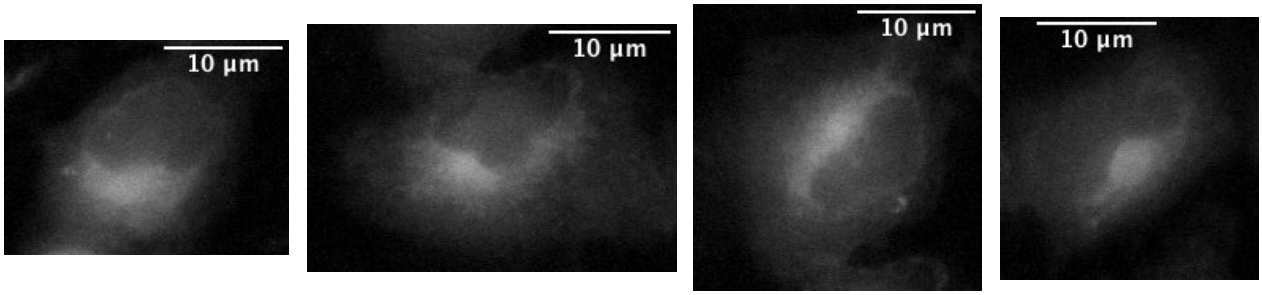

Figure S6. *Fluorescence imaging of A549 cells incubated with conjugate **C2** (at 20 µM for 4 h) (excitation 350 nm). The signal-to-noise ratio were equal to 32.5 dB, 33.1 dB, 35.0 dB and 33.4 dB respectively. Fixed fluorescence intensity scale (0-7500 u.a). Scale bar: 10 µm (fixed at 3.1 cm).*

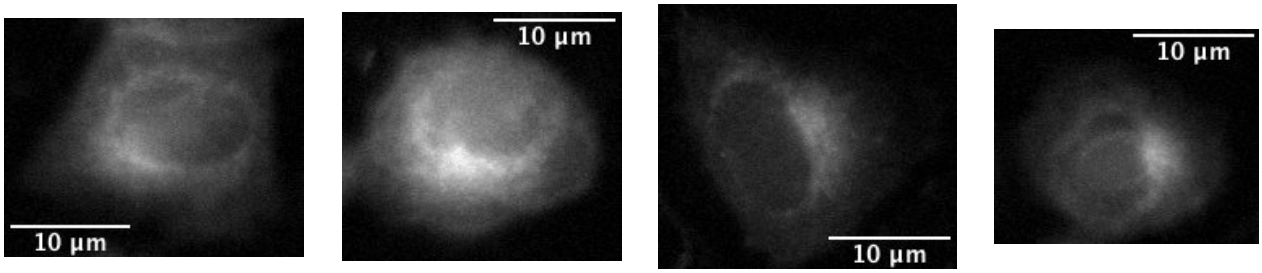

Figure S7. *Fluorescence imaging of A549 cells incubated with conjugate **C3** (at 20 µM for 4 h) (excitation 350 nm). The signal-to-noise ratio were equal to 34.5 dB, 35.4 dB, 33.4 dB and 36.5 dB respectively. Fixed fluorescence intensity scale (0-7500 u.a). Scale bar: 10 µm (fixed at 3.1 cm).*

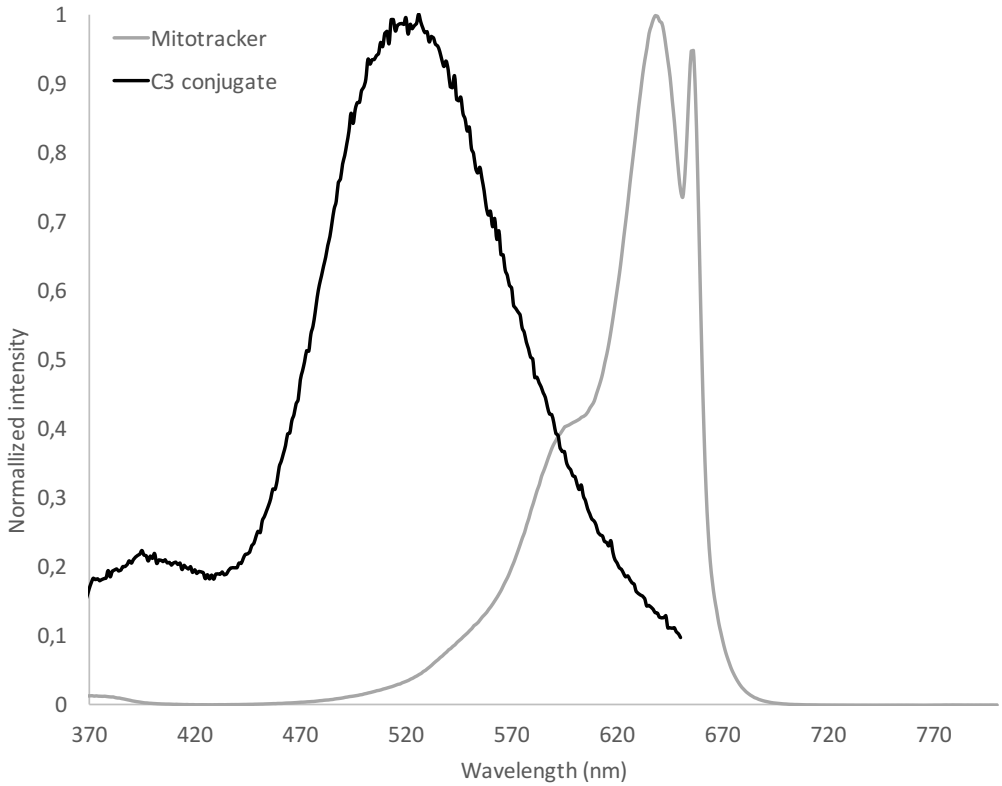

Figure S8. *Normalized luminescence emission spectrum of **C3** conjugate (50 µM, in H_2O/DMSO 90/10 v/v, black curve) (λexc 320 nm) and excitation spectrum of Mitotracker Deep Red (100 nM in H_2O) (λem 657 nm).*

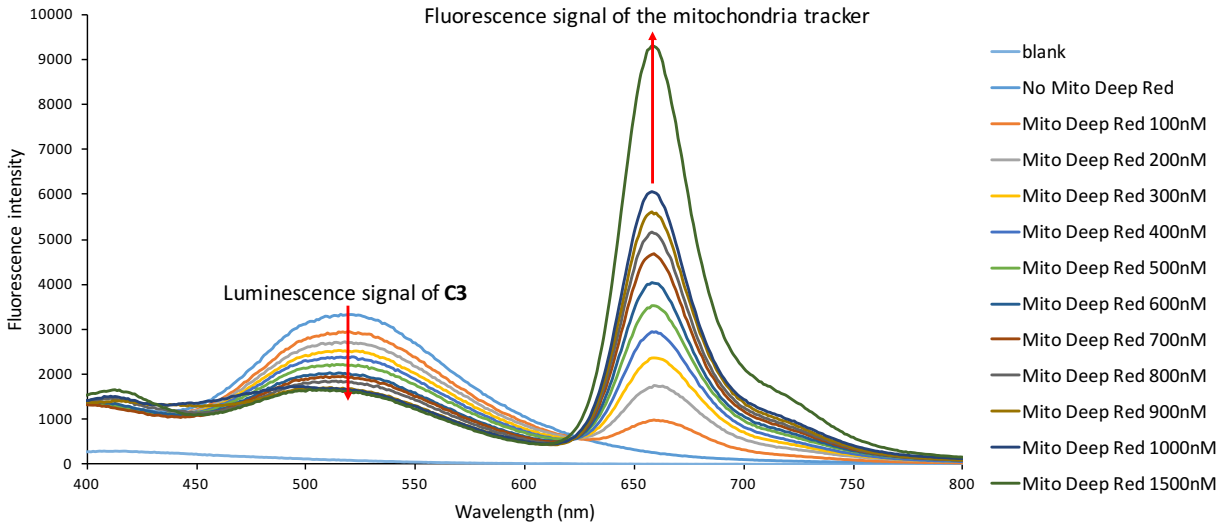

Fig S9. *Effect of mitochondria tracker co-incubation on the luminescence signal of the C3 probe. The **C3** probe was prepared at 50 µM in MilliQ water (with 10% DMSO). The mitochondria tracker Mitotracker Deep Red was added to the **C3** solution at concentrations varying between 100 nM and 1500 nM. Fluorescence spectra were recorded by exciting at 320 nm and detecting emission light between 400 nm and 800 nm.*

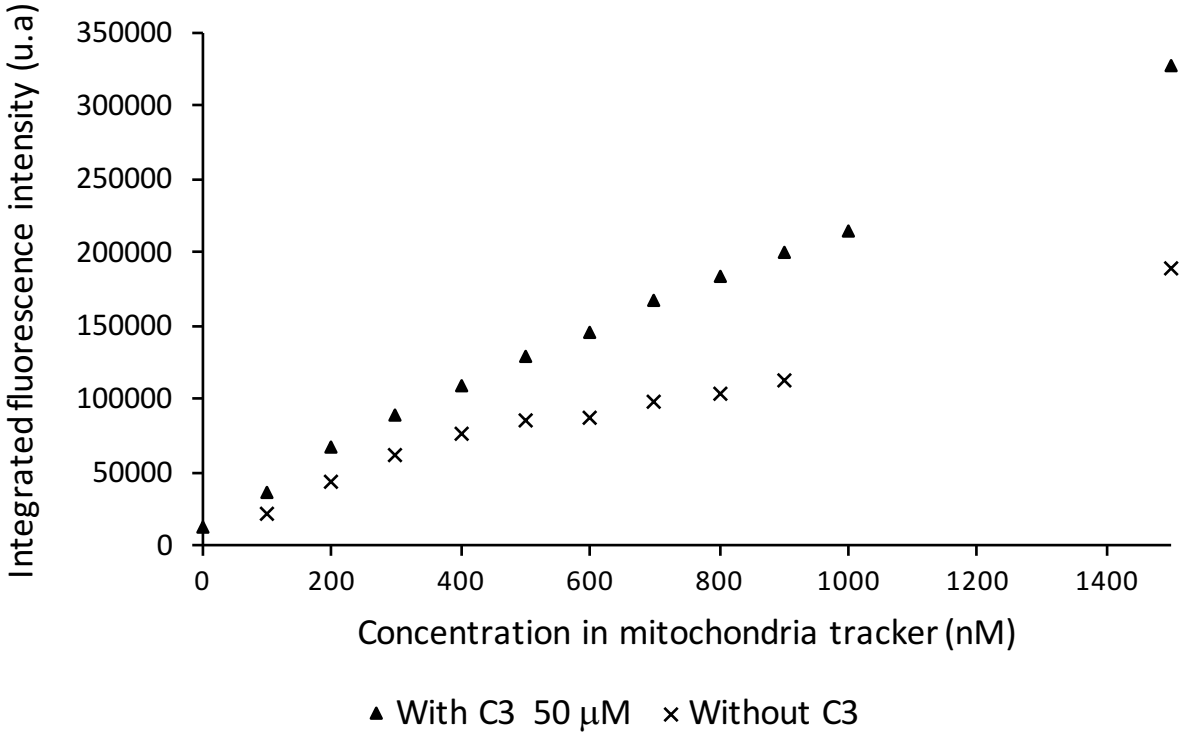

Fig. S10. *Integrated fluorescence intensity (635 to 685 nm) of a solution of the mitochondria tracker in presence or not of* ***C3*** *at 50 µM, upon excitation at 320 nm. The fluorescence intensity of the mitochondria tracker is higher when co-incubated with* ***C3****. This result suggests the existence of fluorescence resonance energy transfer between the two compounds.*

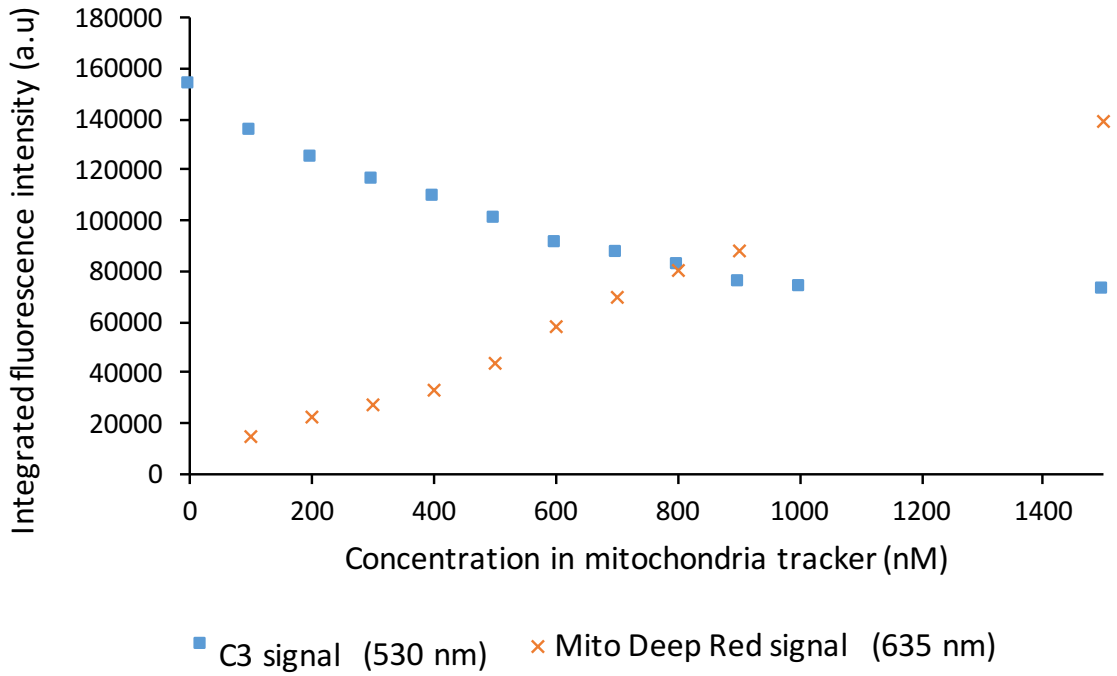

Fig S11. *Effect of the co-incubation of* ***C3*** *with the mitochondria tracker on their respective fluorescence intensity.* ***C3*** *integrated luminescence intensity (500 - 550 nm) (50 µM in MilliQ water, λexc 320 nm) was plotted as a function of the concentration of mitochondria tracker. The integrated fluorescence intensity of the mitochondria tracker co-incubated with* ***C3*** *was subtracted by that of the mitochondria tracker at the same concentration without* ***C3*** *and plotted as a function of the mitochondria tracker concentration.*

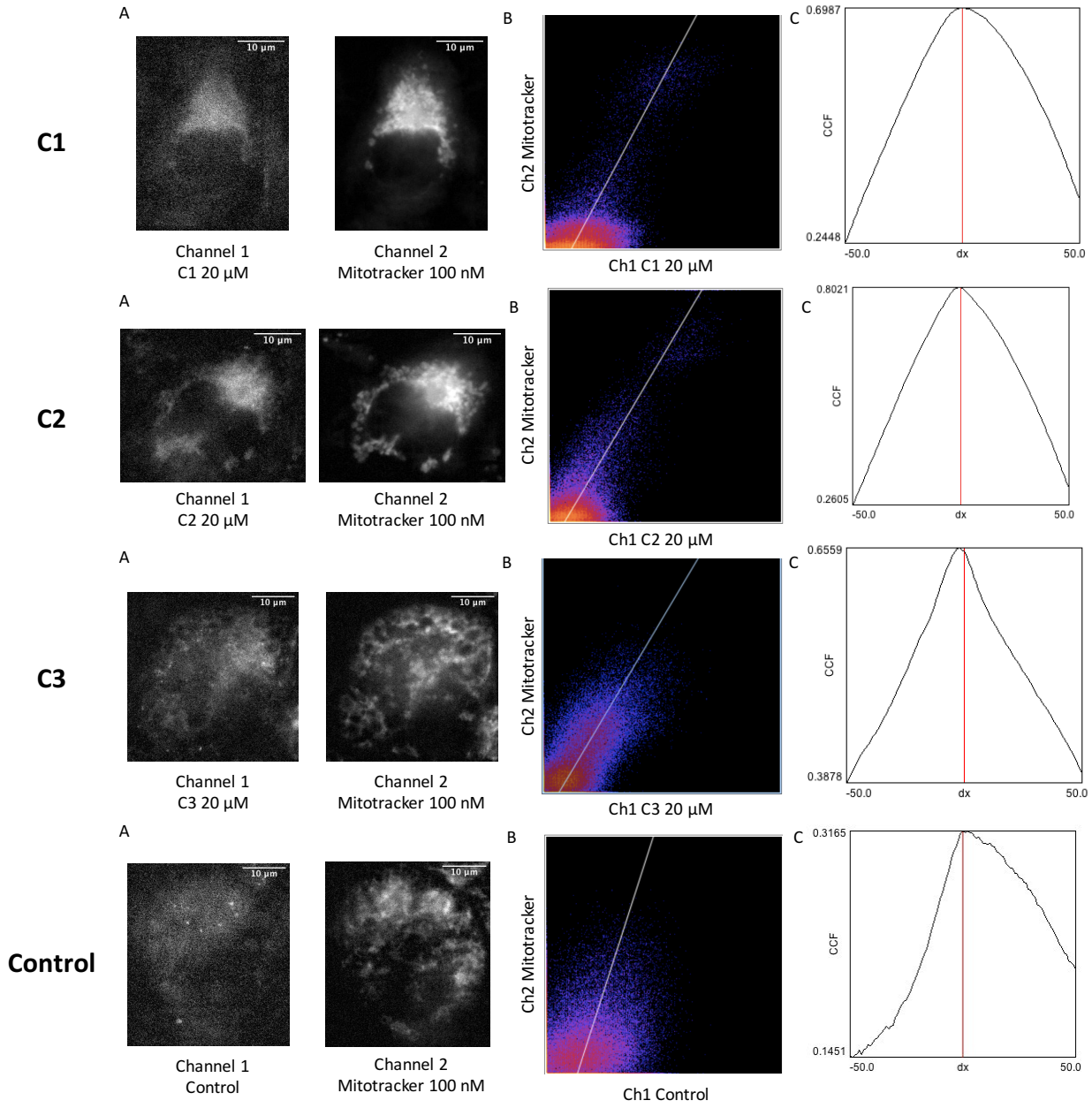

Figure S12. *Colocalization analyses with the fluorescence signal of Mitotracker Deep Red. A549 cells were incubated with* ***C1-C3*** *probes at 20 µM for 4 hours or without incubation (control). (A) Left: channel 1 – fluorescence image with excitation at λexc 350 nm, obtained with a gain of 0 over an exposure time of 3s. The signal-to-noise ratio is equal to 17dB for* ***C1****, 24 dB for* ***C2****, 23 dB for* ***C3*** *and 10 dB for control cells; Right: channel 2 – fluorescence image of the Mitotracker Deep Red (λexc 644 nm) obtained with a gain of 0 over an exposure time of 5s. (B) Scatter plot or 2D-histogram with a linear regression representing the signal intensity relationship of the two fluorescence images. (C) Van Steensel curve. The cross correlation function is maximal for a shift dx equal to 0, 1, 2 and 0 pixels for* ***C1****,* ***C2****,* ***C3*** *and control cells, respectively. The Pearson coefficient is equal to 0.70 for* ***C1****, 0.80 for* ***C2****, 0.66 for* ***C3*** *and 0.32 for control cells.*

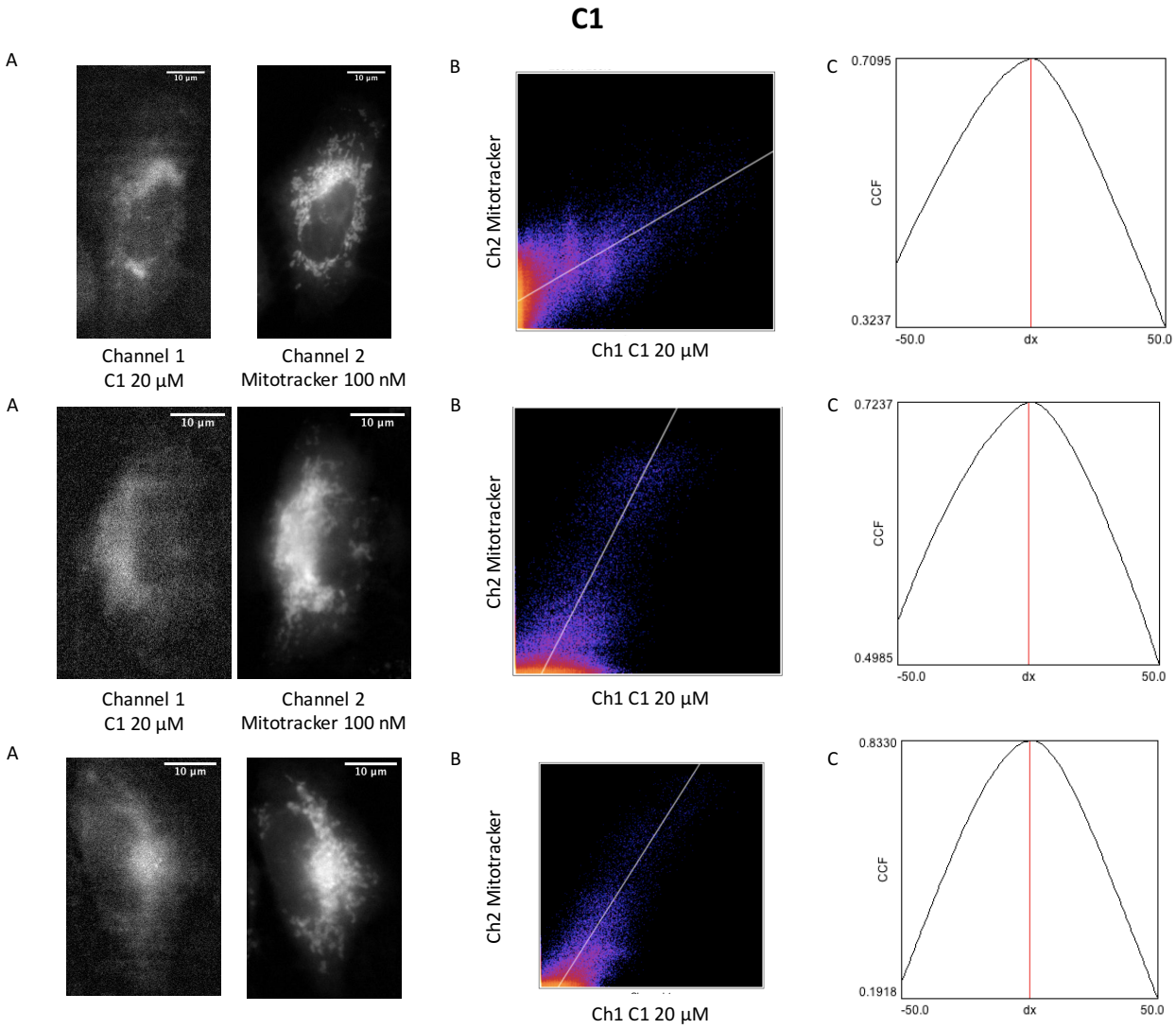

Figure S13. *Colocalization analyses with the fluorescence signal of Mitotracker Deep Red. A549 cells were incubated with* ***C1*** *probe at 20 µM for 4 hours. (A) Left: channel 1 – fluorescence image with excitation at λexc 350 nm, obtained with a gain of 0 over an exposure time of 3s. The signal-to-noise ratio is equal to 16.9 dB; Right: channel 2 – fluorescence image of the Mitotracker Deep Red (λexc 644 nm) obtained with a gain of 0 over an exposure time of 5s. (B) Scatter plot or 2D-histogram with a linear regression representing the signal intensity relationship of the two fluorescence images. (C) Van Steensel curve. The cross correlation function is maximal for a shift dx equal to 1, 2 and 2 pixels, respectively. The Pearson coefficient is equal to 0.71, 0.72, 0.83 respectively.*

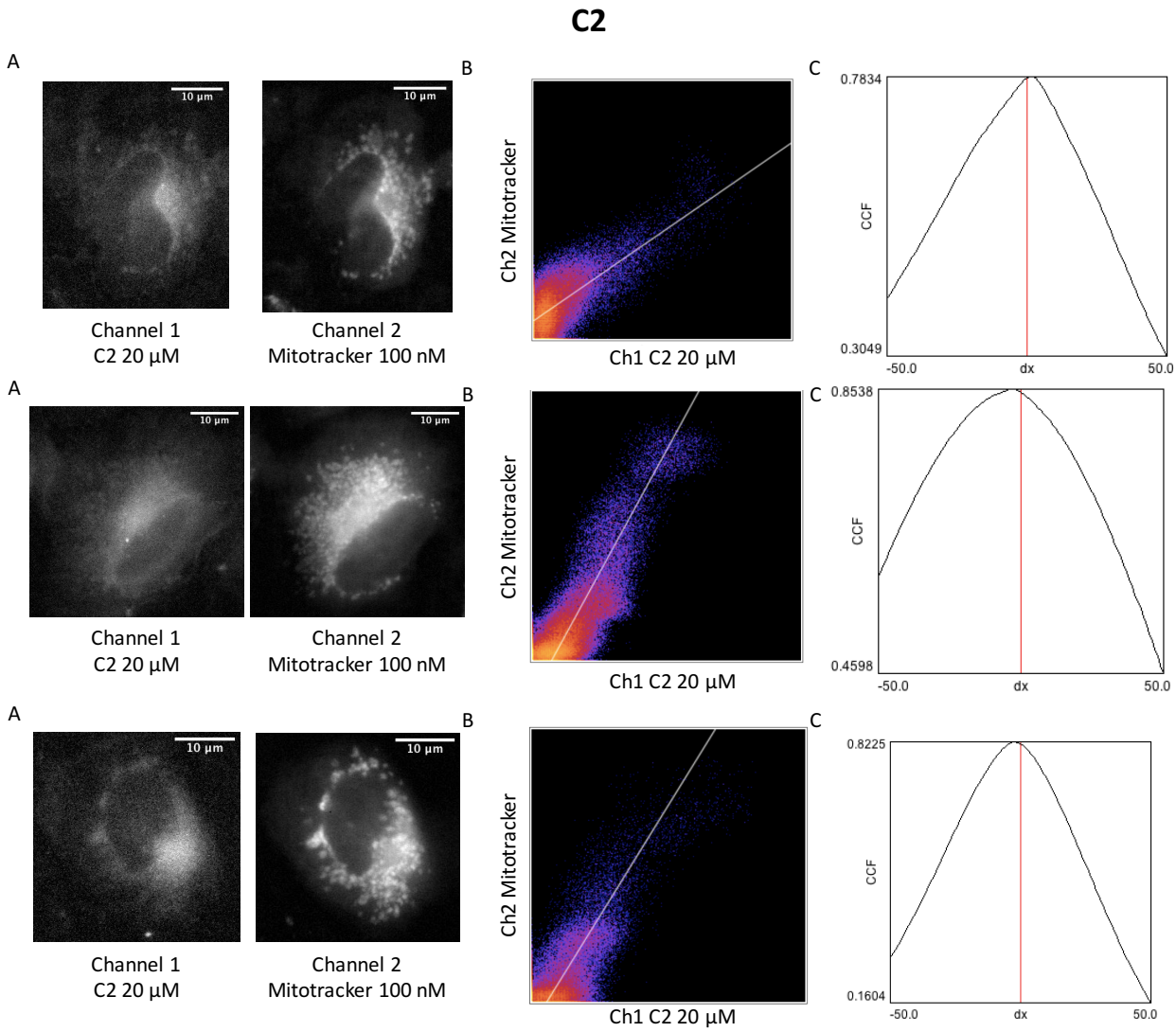

Figure S14. *Colocalization analyses with the fluorescence signal of Mitotracker Deep Red. A549 cells were incubated with* ***C2*** *probe at 20 µM for 4 hours. (A) Left: channel 1 – fluorescence image with excitation at λexc 350 nm, obtained with a gain of 0 over an exposure time of 3s. The signal-to-noise ratio is equal to 19 dB and 20 dB respectively; Right: channel 2 – fluorescence image of the Mitotracker Deep Red (λexc 644 nm) obtained with a gain of 0 over an exposure time of 5s. (B) Scatter plot or 2D-histogram with a linear regression representing the signal intensity relationship of the two fluorescence images. (C) Van Steensel curve. The cross correlation function is maximal for a shift dx equal to 2, 3 and 3 pixels, respectively. The Pearson coefficient is equal to 0.78, 0.85, 0.82 respectively.*

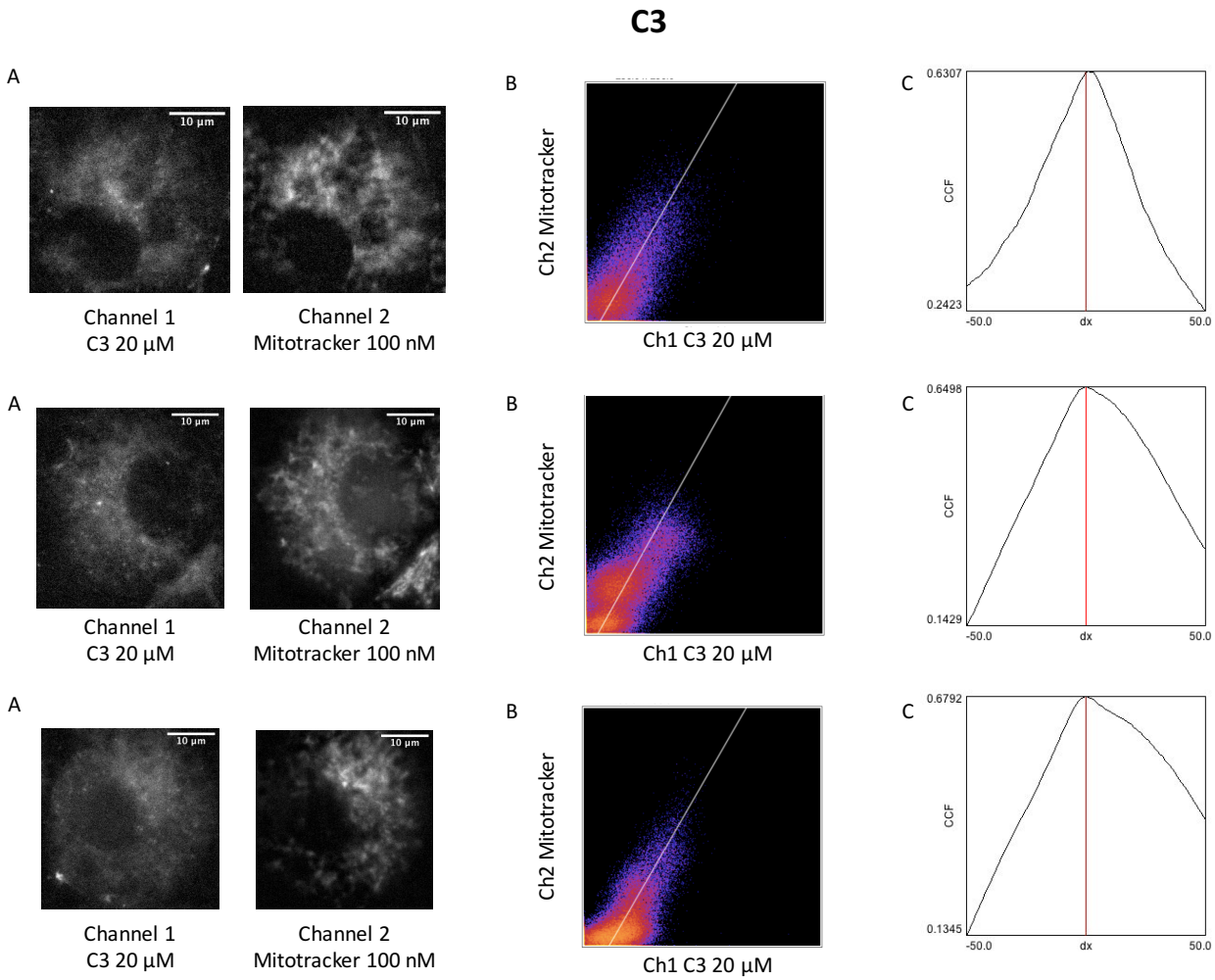

Figure S15. *Colocalization analyses with the fluorescence signal of Mitotracker Deep Red. A549 cells were incubated with* ***C3*** *probe at 20 µM for 4 hours. (A) Left: channel 1 – fluorescence image with excitation at λexc 350 nm, obtained with a gain of 0 over an exposure time of 3s. The signal-to-noise ratio is equal to 19.2 dB; Right: channel 2 – fluorescence image of the Mitotracker Deep Red (λexc 644 nm) obtained with a gain of 0 over an exposure time of 5s. (B) Scatter plot or 2D-histogram with a linear regression representing the signal intensity relationship of the two fluorescence images. (C) Van Steensel curve. The cross correlation function is maximal for a shift dx equal to 2, 0 and 0 pixels, respectively. The Pearson coefficient is equal to 0.63, 0.65, 0.68 respectively.*

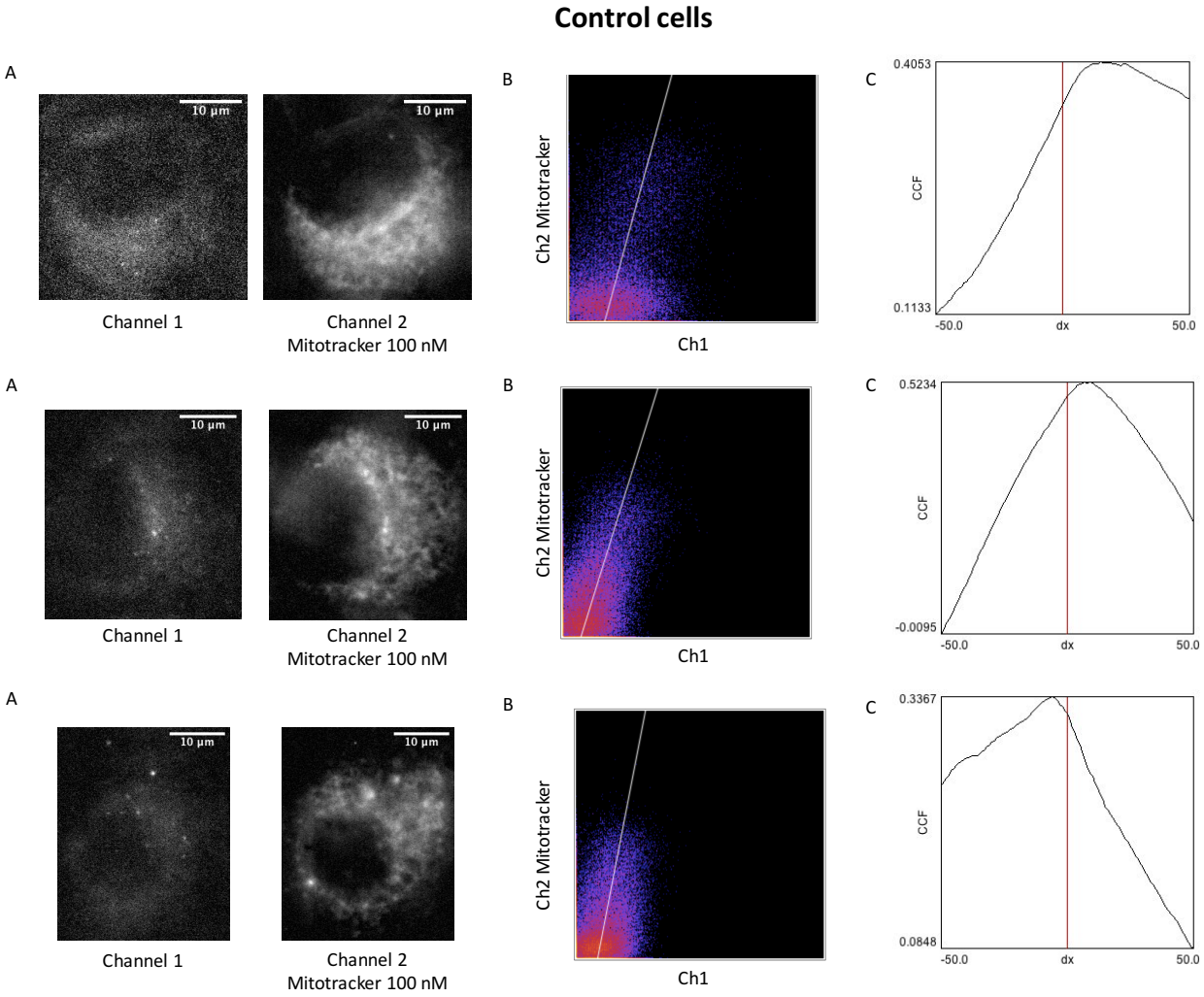

Figure S15. *A549 control cells in colocalization analyses with the fluorescence signal of Mitotracker Deep Red. (A) Left: channel 1 - fluorescence image with excitation at λexc 350 nm, obtained with a gain of 0 over an exposure time of 3s. The signal-to-noise ratio is equal to 12.9 dB; Right: channel 2 – fluorescence image of the Mitotracker Deep Red (λexc 644 nm) obtained with a gain of 0 over an exposure time of 5s. (B) Scatter plot or 2D-histogram with a linear regression representing the signal intensity relationship of the two fluorescence images. (C) Van Steensel curve. The cross correlation function is maximal for a shift dx equal to 17, 8 and 6 pixels, respectively. The Pearson coefficient is equal to 0.36, 0.50, 0.32 respectively.*

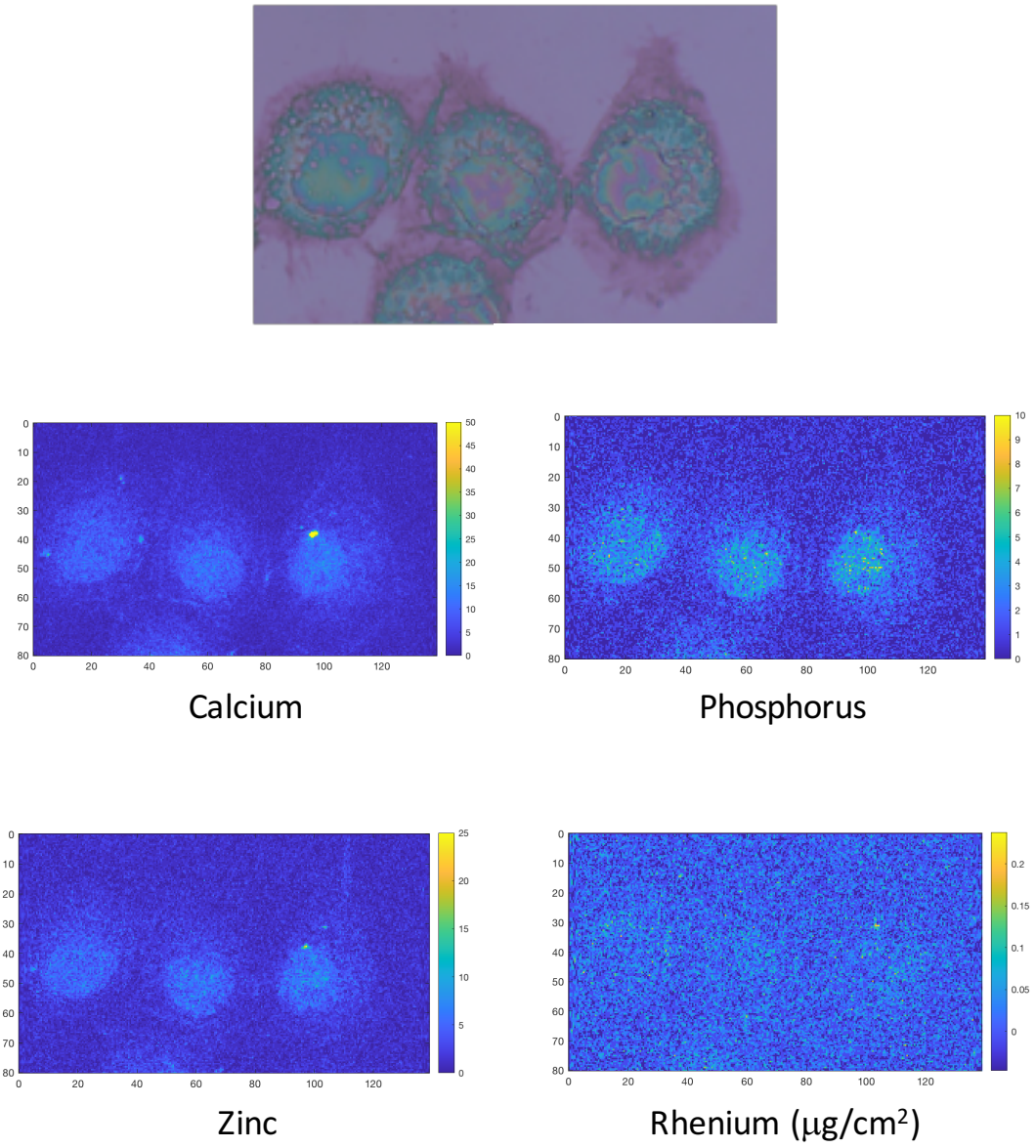

Figure S16. *Elemental distributions of Ca, P, Re, and Zn in A549 cells incubated with* ***C1*** *(with color map (intensity) (right) and corresponding transmission optical microscope image (top). The phosphorus (P), and zinc (Zn, Kβ-lines) maps are used to identify the nucleus area. Re was mapped using the Lß lines (~10.15 and 10.28 keV). A549 cells were incubated for 4 hours with* ***C1*** *(20 μM) before fixation and air-drying (excitation at 14 keV; integration time, 300 ms per pixel; pixel size, 500 nm). Scale axis in μm.*

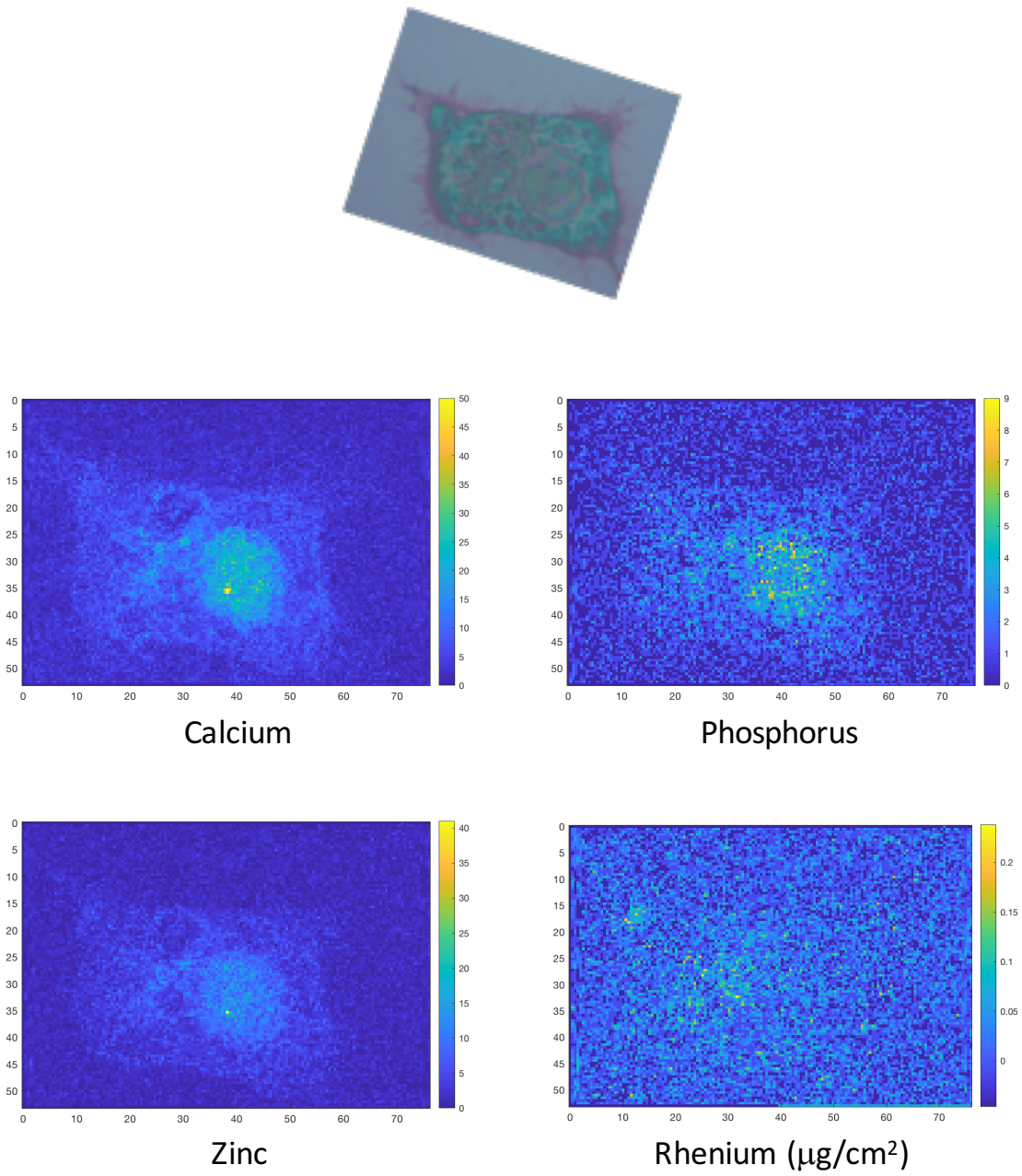

Figure S17. *Elemental distributions of Ca, P, Re, and Zn in A549 cells incubated with* ***C1*** *(with color map (intensity) (right) and corresponding transmission optical microscope image (top). The phosphorus (P), and zinc (Zn, Kβ-lines) maps are used to identify the nucleus area. Re was mapped using the Lß lines (~10.15 and 10.28 keV). A549 cells were incubated for 4 hours with* ***C1*** *(20 μM) before fixation and air-drying (excitation at 14 keV; integration time, 300 ms per pixel; pixel size, 500 nm). Scale axis in μm.*

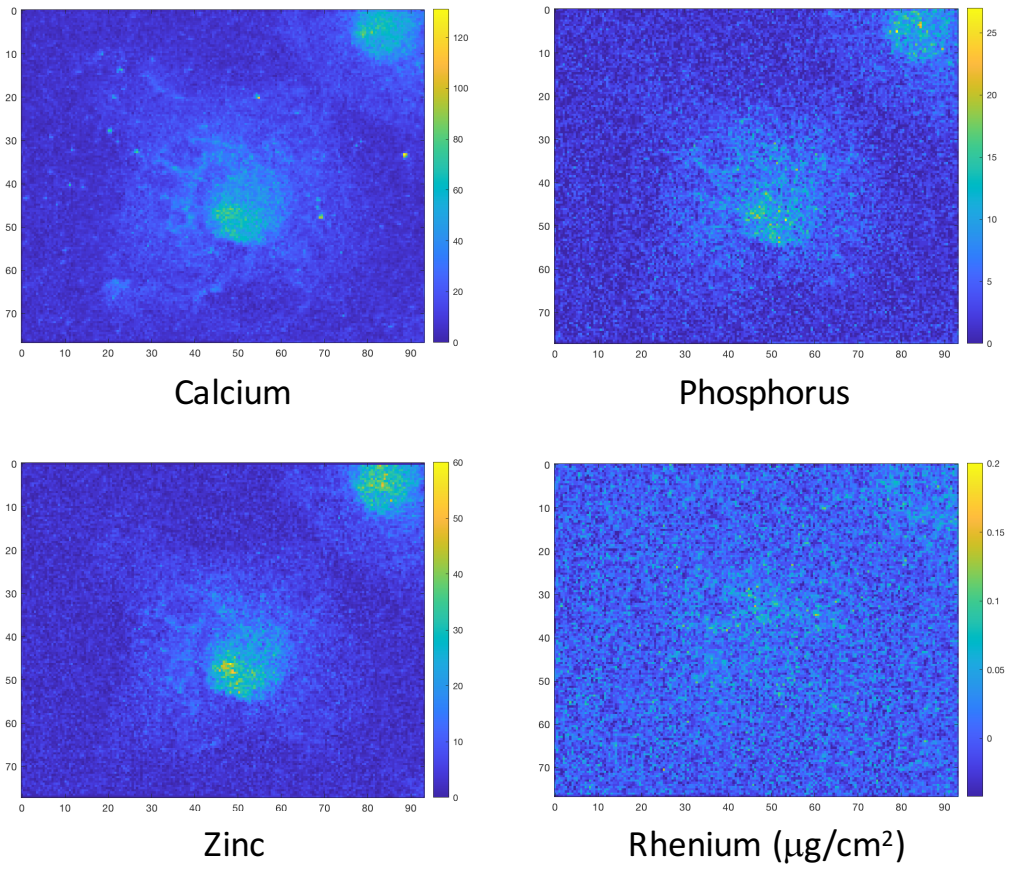

Figure S18. *Elemental distributions of Ca, P, Re, and Zn in A549 cells incubated with* ***C1*** *(with color map (intensity) (right). The phosphorus (P), and zinc (Zn, Kβ-lines) maps are used to identify the nucleus area. Re was mapped using the Lß lines (~10.15 and 10.28 keV). A549 cells were incubated for 4 hours with* ***C1*** *(20 μM) before fixation and air-drying (excitation at 14 keV; integration time, 300 ms per pixel; pixel size, 500 nm). Scale axis in μm.*

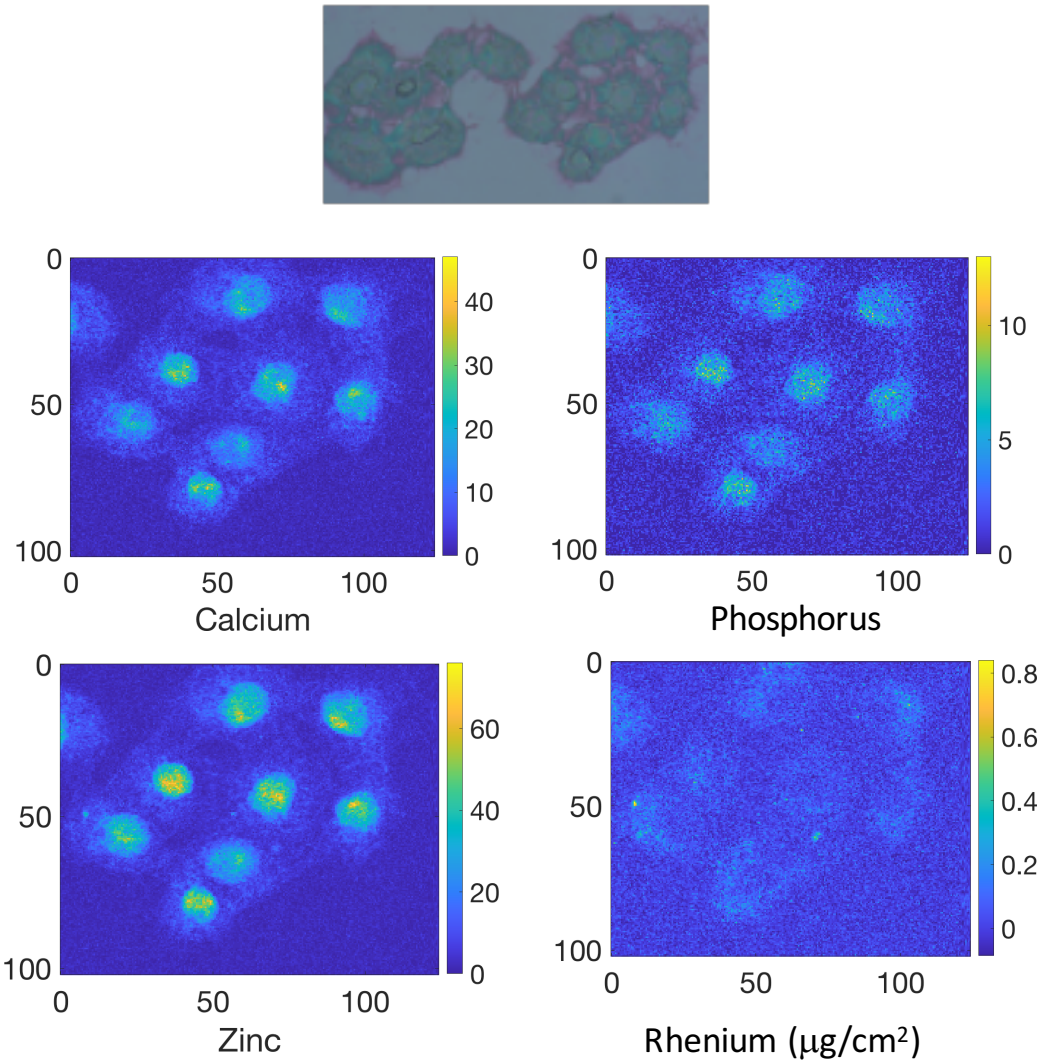

Figure S19. *Elemental distributions of Ca, P, Re, and Zn in A549 cells incubated with* ***C2*** *(with color map (intensity) (right) and corresponding transmission optical microscope image (top). The phosphorus (P), and zinc (Zn, Kβ-lines) maps are used to identify the nucleus area. Re was mapped using the Lß lines (~10.15 and 10.28 keV). A549 cells were incubated for 4 hours with* ***C2*** *(20 μM) before fixation and air-drying (excitation at 14 keV; integration time, 300 ms per pixel; pixel size, 500 nm). Scale axis in μm.*

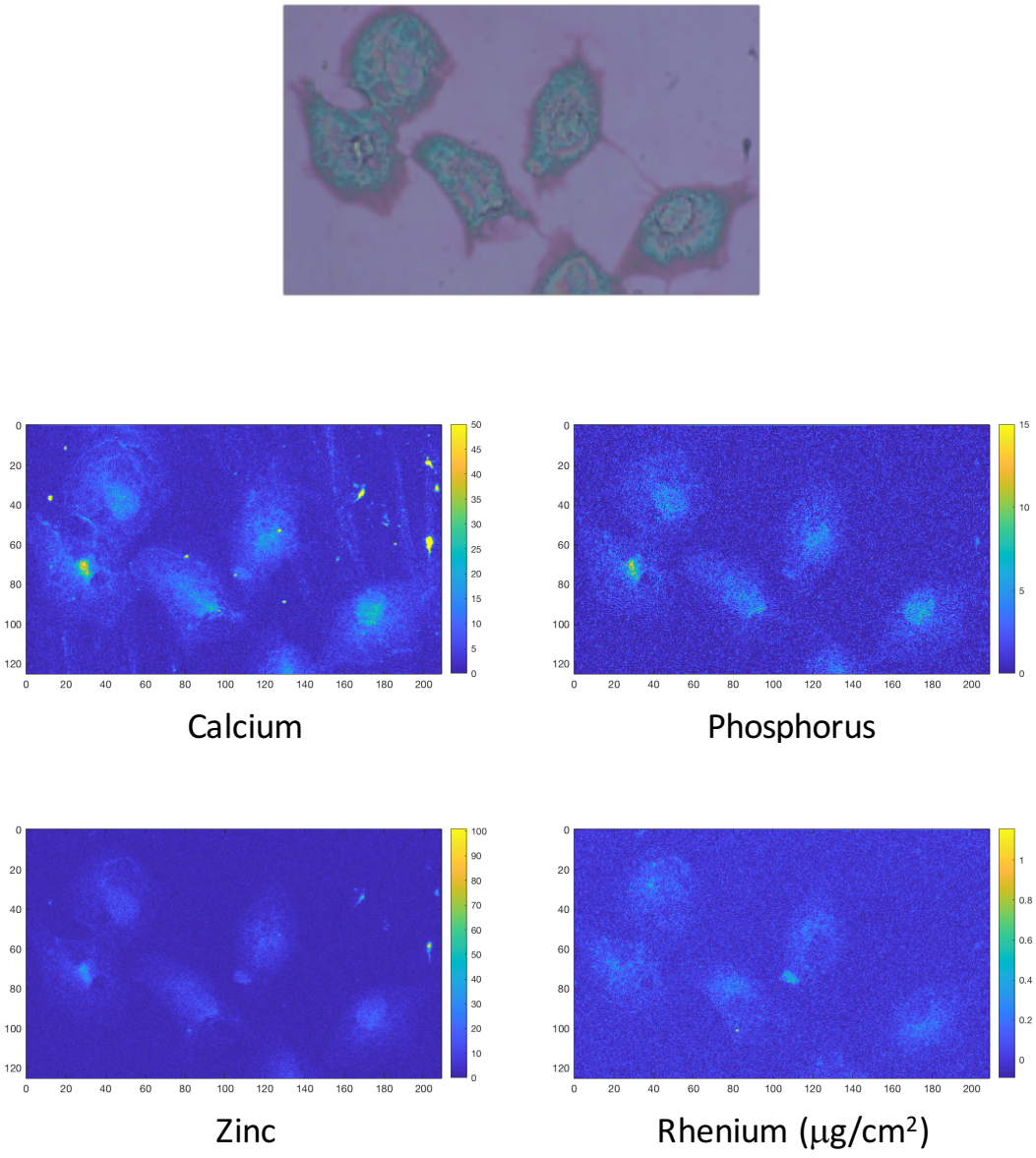

Figure S20. *Elemental distributions of Ca, P, Re, and Zn in A549 cells incubated with* ***C3*** *(with color map (intensity) (right) and corresponding transmission optical microscope image (top). The phosphorus (P), and zinc (Zn, Kβ-lines) maps are used to identify the nucleus area. Re was mapped using the Lß lines (~10.15 and 10.28 keV). A549 cells were incubated for 4 hours with* ***C3*** *(20 μM) before fixation and air-drying (excitation at 14 keV; integration time, 300 ms per pixel; pixel size, 500 nm). Scale axis in μm.*

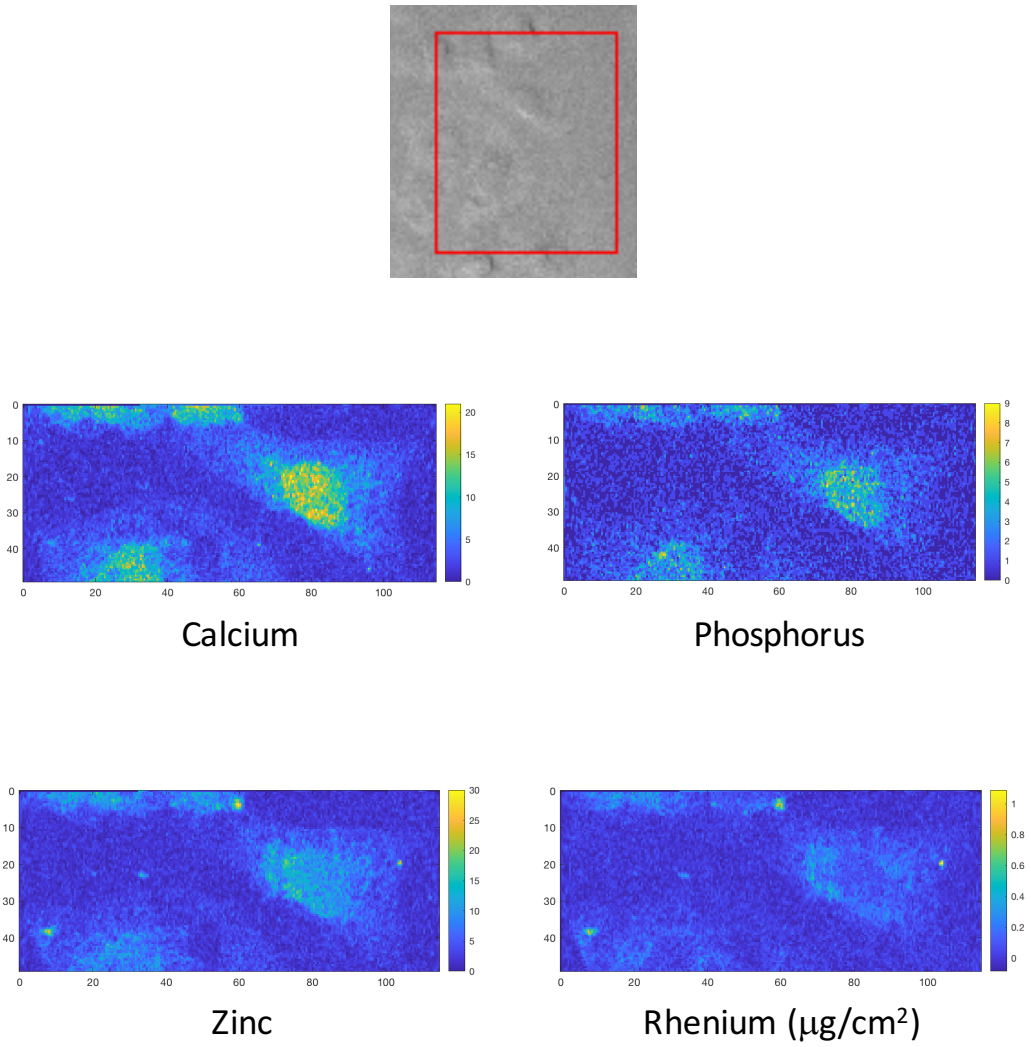

Figure S21. *Elemental distributions of Ca, P, Re, and Zn in A549 cells incubated with* ***C3*** *(with color map (intensity) (right) and corresponding transmission optical microscope image (top). The phosphorus (P), and zinc (Zn, Kβ-lines) maps are used to identify the nucleus area. Re was mapped using the Lß lines (~10.15 and 10.28 keV). A549 cells were incubated for 4 hours with* ***C3*** *(20 μM) before fixation and air-drying (excitation at 14 keV; integration time, 300 ms per pixel; pixel size, 500 nm). Scale axis in μm.*

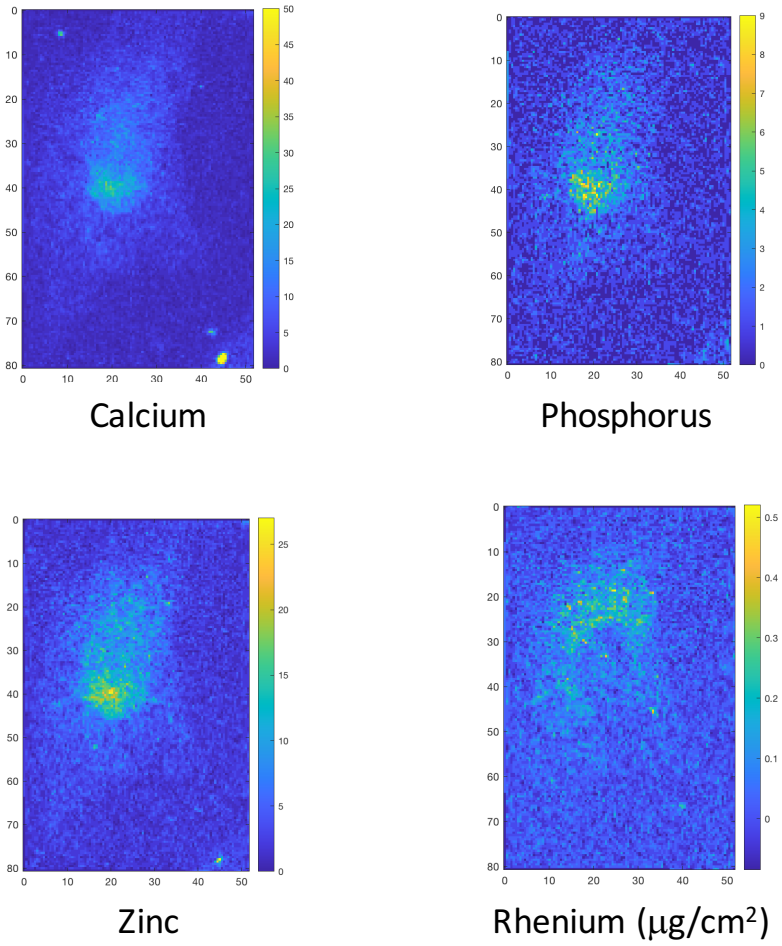

Figure S22. *Elemental distributions of Ca, P, Re, and Zn in A549 cells incubated with* ***C3*** *(with color map (intensity) (right). The phosphorus (P), and zinc (Zn, Kβ-lines) maps are used to identify the nucleus area. Re was mapped using the Lß lines (~10.15 and 10.28 keV). A549 cells were incubated for 4 hours with* ***C3*** *(20 μM) before fixation and air-drying (excitation at 14 keV; integration time, 300 ms per pixel; pixel size, 500 nm). Scale axis in μm.*

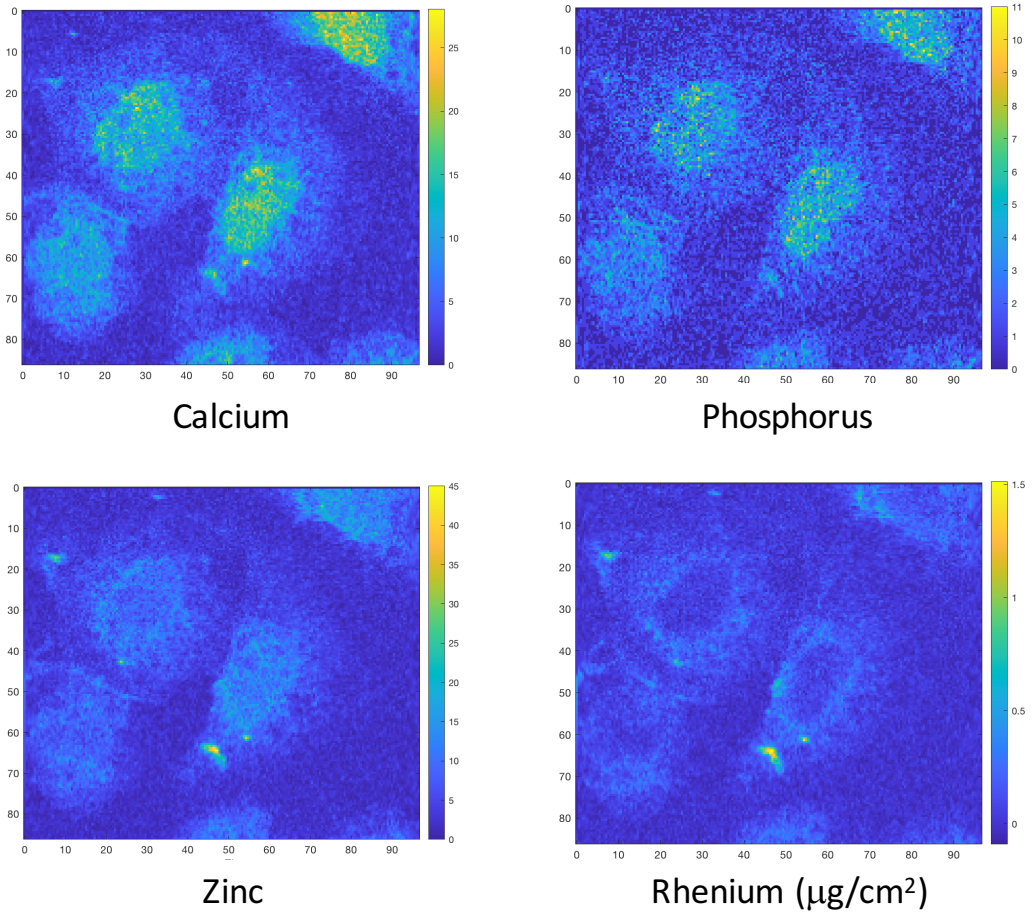

Figure S23. *Elemental distributions of Ca, P, Re, and Zn in A549 cells incubated with* ***C3*** *(with color map (intensity) (right). The phosphorus (P), and zinc (Zn, Kβ-lines) maps are used to identify the nucleus area. Re was mapped using the Lß lines (~10.15 and 10.28 keV). A549 cells were incubated for 4 hours with* ***C3*** *(20 μM) before fixation and air-drying (excitation at 14 keV; integration time, 300 ms per pixel; pixel size, 500 nm). Scale axis in μm.*

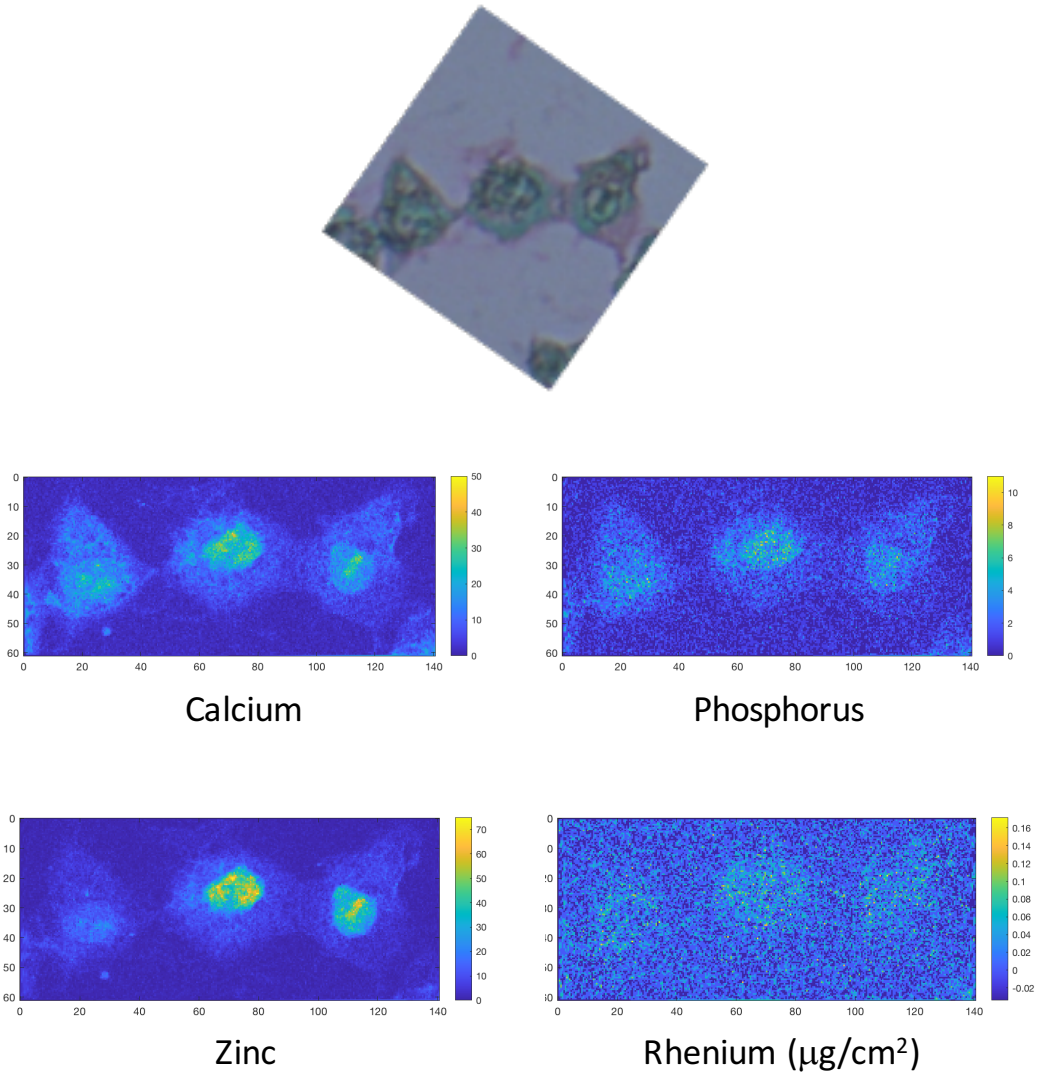

Figure S24. *Elemental distributions of Ca, P, Re, and Zn in control A549 cells (with color map (intensity) (right) and corresponding transmission optical microscope image (top). The phosphorus (P), and zinc (Zn, Kβ-lines) maps are used to identify the nucleus area. Re was mapped using the Lß lines (~10.15 and 10.28 keV). A549 cells were fixed and air-dried (excitation at 14 keV; integration time, 300 ms per pixel; pixel size, 500 nm). Scale axis in μm.*

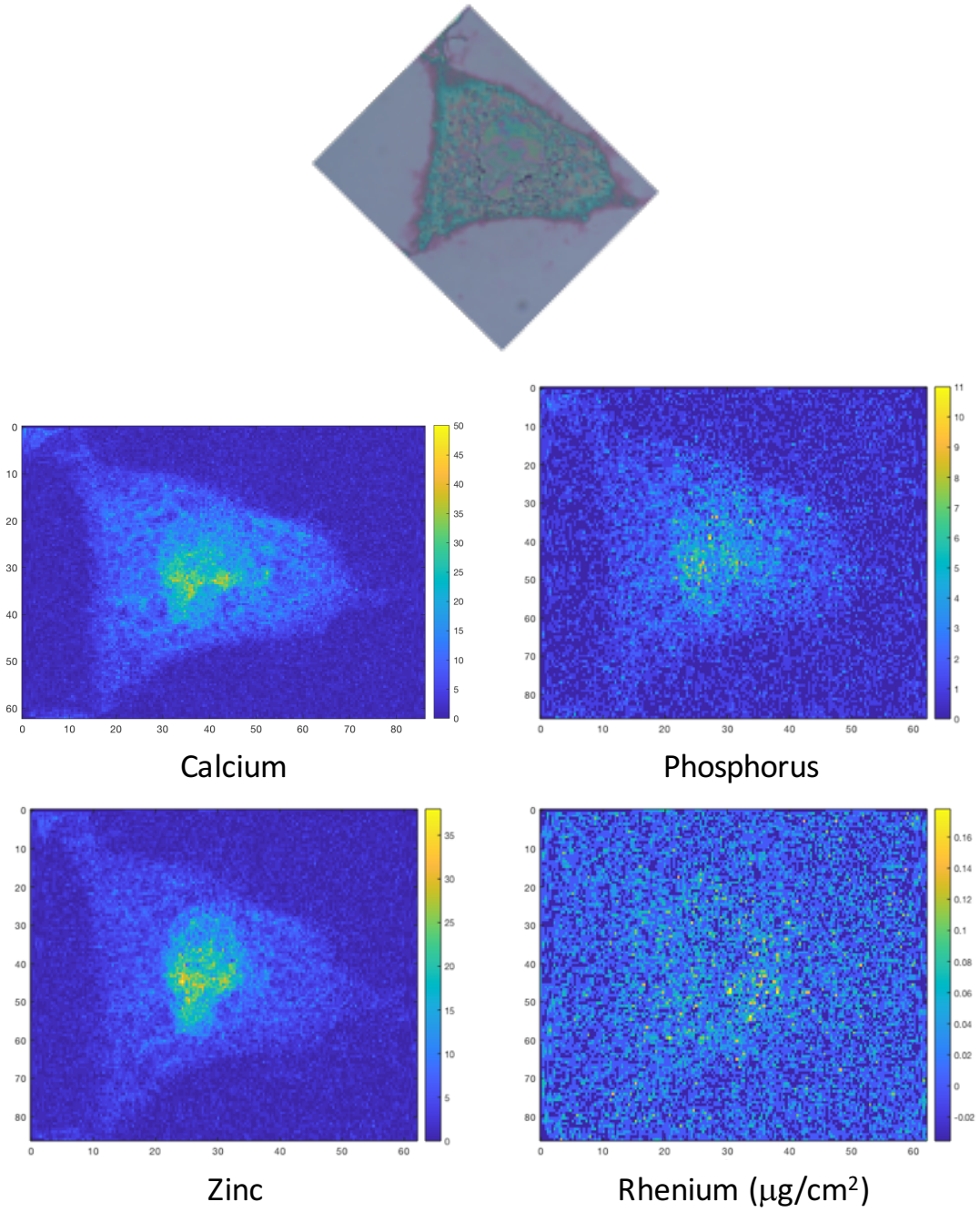

Figure S25. *Elemental distributions of Ca, P, Re, and Zn in control A549 cells (with color map (intensity) (right) and corresponding transmission optical microscope image (top). The phosphorus (P), and zinc (Zn, Kβ-lines) maps are used to identify the nucleus area. Re was mapped using the Lß lines (~10.15 and 10.28 keV). A549 cells were fixed and air-dried (excitation at 14 keV; integration time, 300 ms per pixel; pixel size, 500 nm). Scale axis in μm.*

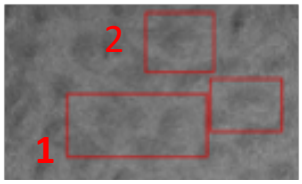

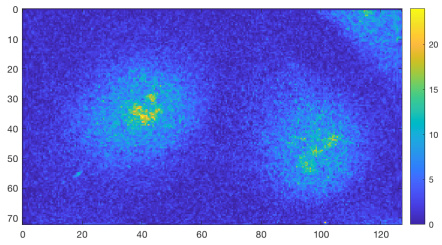

Calcium

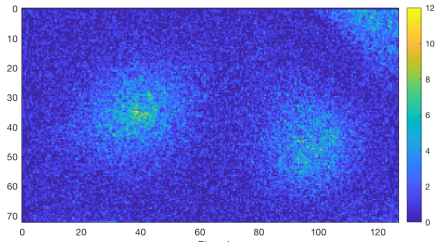

Phosphorus

Area 1

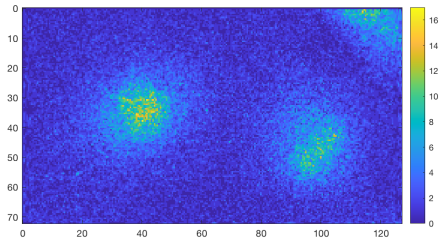

Zinc

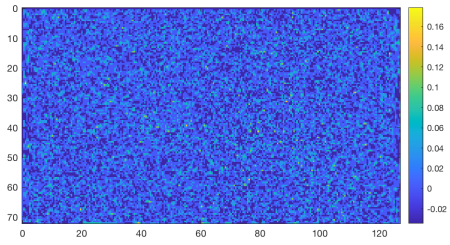

Rhenium (μg/cm^2)

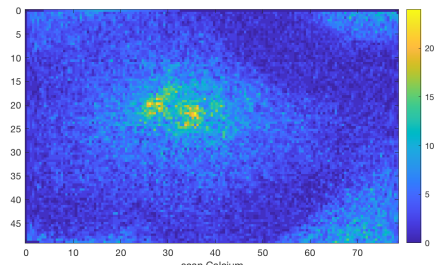

Calcium

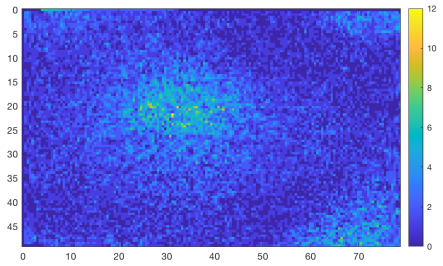

Phosphorus

Area 2

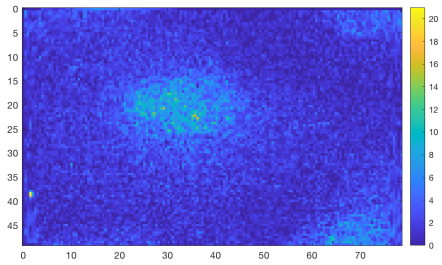

Zinc

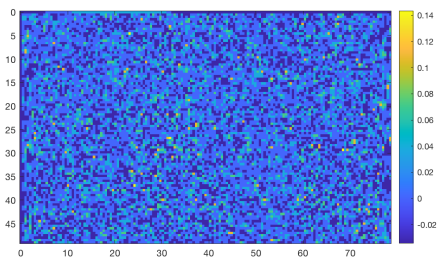

Rhenium (μg/cm^2)

Figure S26. *Elemental distributions of Ca, P, Re, and Zn in control A549 cells (with color map (intensity) (right) and corresponding transmission optical microscope image (top). The phosphorus (P), and zinc (Zn, Kβ-lines) maps are used to identify the nucleus area. Re was mapped using the Lß lines (~10.15 and 10.28 keV). A549 cells were fixed and air-dried (excitation at 14 keV; integration time, 300 ms per pixel; pixel size, 500 nm). Scale axis in μm.*

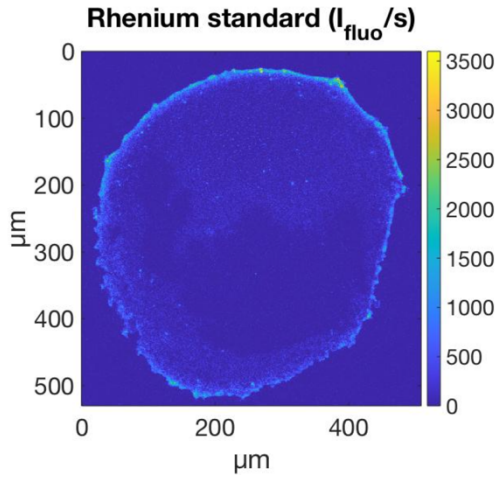

Figure S27. *X-ray fluorescence imaging of a rhenium external standard (0.3 µL of a 10 µM rhenium solution) on a SiN_3 membrane (excitation at 14 keV; integration time, 10 ms per pixel; pixel size, 1 µm; I_{fluo} = 2.32 x 10^7/s).*

References

1. Maryanoff, B.E.; Reitz, A.B.; and Duhl-Emswiler, B.A., Stereochemistry of the Wittig reaction. Effect of nucleophilic groups in the phosphonium ylide, *J.Am.Chem.Soc.* **1985**, *107* (1), 217–226.

2. Bolte S., Cordelières F. P., A guided tour into subcellular colocalization analysis in light microscopy, *J. Microsc.,* **2006**, *224*, 213–232.

3. Hostachy, S.; Masuda, M.; Miki, T.; Hamachi, I.; Sagan, S.; Lequin, O.; Medjoubi, K.; Somogyi, A.; Delsuc, N.; Policar, C., Graftable SCoMPIs enable the labeling and X-ray fluorescence imaging of proteins. *Chem. Sci.* **2018,** *9* (19), 4483-4487.

VI.2. Chapter III

VI.2.a. Supplementary tables

SOD-Cu gene	CCAATGCATCAGGTGGTGGTGGTTCAGGTGGTGGTGGTTCAGGTGGTGGTGGTTCAC CAGATCACAAACACCACCTTCACGGTGGTGGTGGTTCAGGTGGTGGTGGTTCAGGTG GTGGTGGTTCACCAGATCACAAACACCACCTTCACGGTGGTGGTGGTTCAGGTGGTGG TGGTTCAGGTGGTGGTGGTTCACCAGATCACAAACACCACCTTCACGATTACAAAGAT GATGATGATAAATAAGGGAATTCCC
CAT-Cu gene	CCAATGCATCAGGTGGTGGTGGTTCAGGTGGTGGTGGTTCAGGTGGTGGTGGTTCAC CACACTACAAACACCGTCTTCACGGTGGTGGTGGTTCAGGTGGTGGTGGTTCAGGTGG TGGTGGTTCACCACACTACAAACACCGTCTTCACGGTGGTGGTGGTTCAGGTGGTGGT GGTTCAGGTGGTGGTGGTTCACCACACTACAAACACCGTCTTCACGATTACAAAGATG ATGATGATAAATAAGGGAATTCCC
SOD-Mn gene	CCAATGCATCAGGTGGTGGTGGTTCAGGTGGTGGTGGTTCAGGTGGTGGTGGTTCAA AAGCAGAAGATTACGAAGATCCAGGTGATGAATACGATGAAGCAAAAGGAGGAGGA GGATCTGGAGGAGGAGGATCTGGAGGAGGAGGATCTAAGGCTGAGGACTATGAGGA CCCTGGCGACGAGTATGACGAGGCTAAGGGCGGCGGCGGCTCCGGCGGCGGCGGCT CCGGCGGCGGCGGCTCGAAAGCCGAGGACTACGAGGACCCCGGAGATGAGTATGAC GAAGCCAAGGATTACAAAGATGATGATGATAAATAAGGGAATTCCC

Table S3. 1: Genes encoding for SOD-Cu, CAT-Cu and SOD-Mn peptides (except the signal peptide part that is included in the plasmid vector). The genes were ordered to Genecust company.

SP_SOD-Cu	MKKINLALLTLATLMGVSSTAVVFADDASGGGGSGGGGSGGGGSPDHKHHLHGG GGSGGGGSGGGGSPDHKHHLHGGGGSGGGGSGGGGSPDHKHHLHDYKDDDDK MKKKIISAILMSTVILSAAAPLSGVYASGGGGSGGGGSGGGGSPDHKHHLHGGGG SGGGGSGGGGSPDHKHHLHGGGGSGGGGSGGGGSPDHKHHLHDYKDDDDK
SP_CAT-Cu	MKKINLALLTLATLMGVSSTAVVFADDASGGGGSGGGGSGGGGSPHYKHRLHGG GGSGGGGSGGGGSPHYKHRLHGGGGSGGGGSGGGGSPHYKHRLHDYKDDDDK MKKKIISAILMSTVILSAAAPLSGVYASGGGGSGGGGSGGGGSPHYKHRLHGGGGS GGGGSGGGGSPHYKHRLHGGGGSGGGGSGGGGSPHYKHRLHDYKDDDDK
SP_CAT-Mn	MKKINLALLTLATLMGVSSTAVVFADDASGGGGSGGGGSGGGGSKAEDYEDPGD EYDEAKGGGGSGGGGSGGGGSKAEDYEDPGDEYDEAKGGGGSGGGGSGGGGSK AEDYEDPGDEYDEAKDYKDDDDK

Table S3. 2: The sequence of the signal peptides are detailed. In red is the signal peptide of Exp4 protein found in pSICE plasmid. In underlined black is the signal peptide of Usp45 protein found in pNICE plasmid. The peptides with SOD-activity upon copper or manganese complexation are in green and blue respectively. The peptides with CAT-activity upon copper complexation are in orange. They are separated by flexible linker made of glycine and serine (in black). The purple part corresponds to the FLAG-tag.

VI.2.b. Supplementary figures

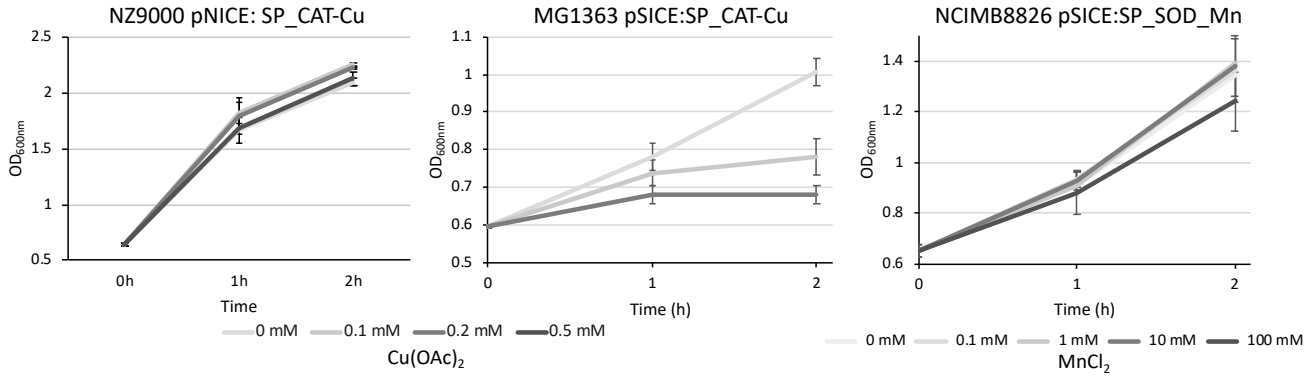

Figure S3. 1: Monitoring of the optical density at 600 nm of MG1363 pSICE:SP_CAT-Cu, NZ9000 pNICE:SP_CAT-Cu and NCIMB8826 pSICE:SP_SOD-Mn cultures. The bacteria were incubated with different concentrations of metal salts ($Cu(OAc)_2$ for MG1363 and NZ9000 strains and $MnCl_2$ for NCIMB8826 strain).

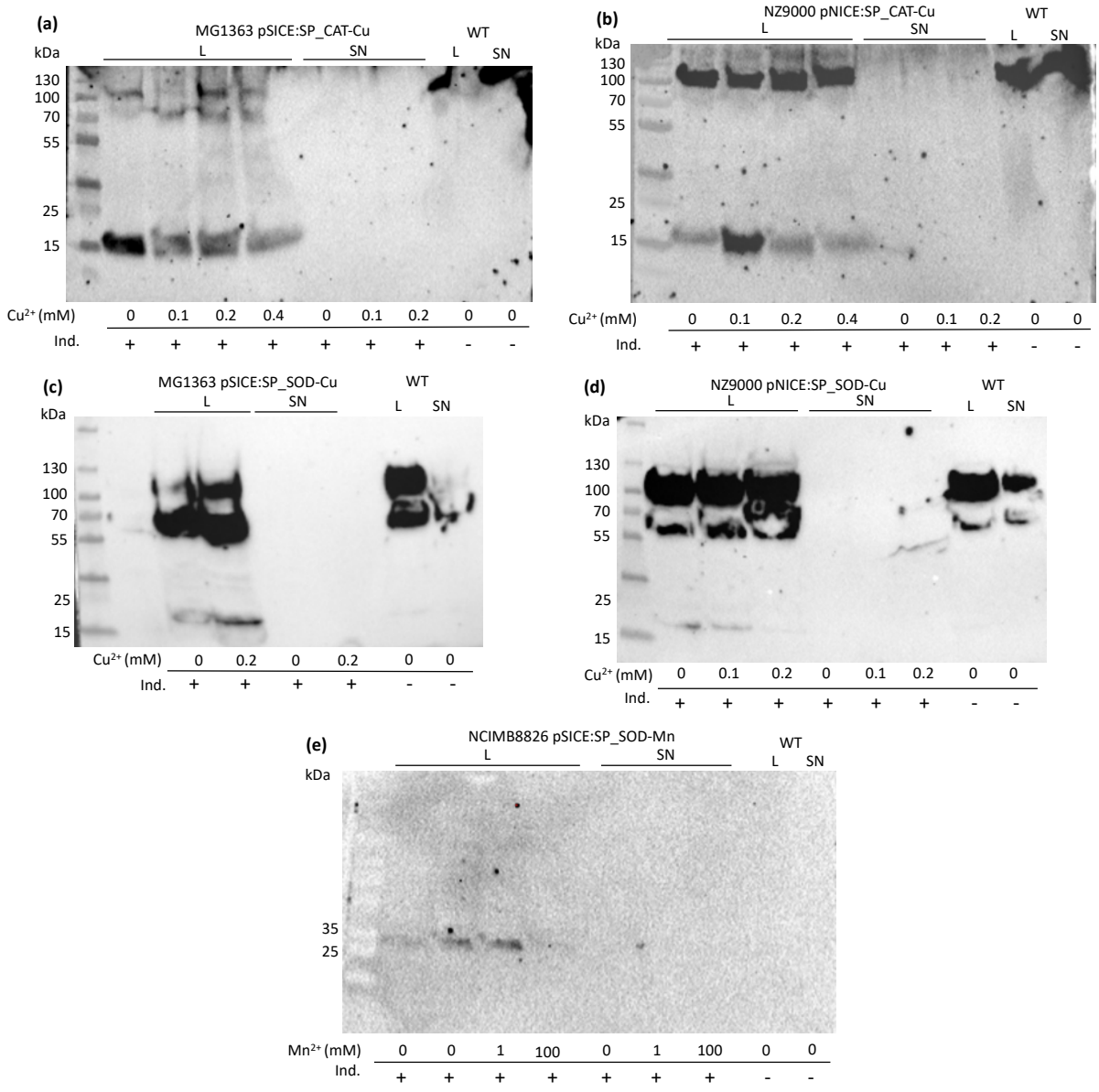

Figure S3. 2: Western Blot analysis to investigate the production and secretion of the peptidyl ligand (SP_SOD-Cu, SP_CAT-Cu and SP_SOD-Mn) by the recombinant bacteria a) MG1363 pSICE:SP_CAT-Cu, b) NZ9000 pNICE:SP_CAT-Cu, c) MG1363 pSICE:SP_SOD-Cu, d) NZ9000 pNICE:SP_SOD-Cu and e) NCIMB8826 pSICE:SP_SOD-Mn. The expression of the peptides was induced using the appropriate inductor that is NaCl 3% for MG1363 and NCIMB8826 strains and nisin at 10 ng/µL for NZ9000 strains. The recombinant bacteria were incubated with various concentrations of the metal required for SOD/CAT activity (Cu^{2+} or Mn^{2+}). After 2 hours of metal incubation and induction, the bacterial cultures were centrifuged, the pellet and the supernatant were then separated. The pellets were homogenized giving bacteria lysates (L) and the proteins from supernatant (SN) were extracted by TCA precipitation. The presence of the expressed peptides in L and SN samples was checked by Western Blot using anti-FLAG tag primary antibody. Unspecific bands are visible between 55 kDa and 130 kDa in the lysates of wild-type and recombinant MG1363 and NZ9000 strains.

1)  2) 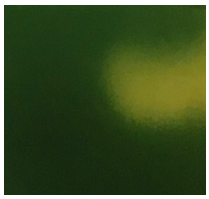

Figure S3. 3: Colored image of protein gels loaded with commercial bovine 1) SOD and 2) CAT and submitted to the in-gel enzymatic assay described by C. Weydert and J. Cullen for 1) SOD activity detection and 2) CAT activity detection. The achromatic bands are related to the respective SOD and CAT activity of the commercial enzymes.

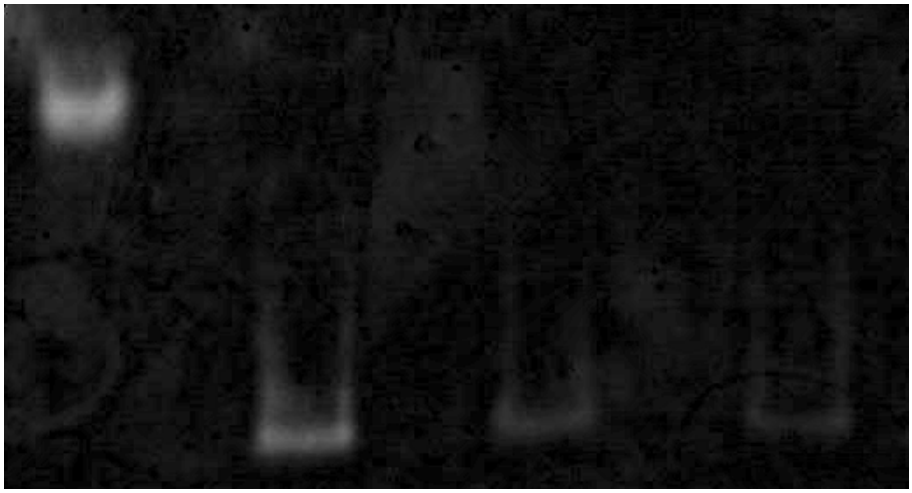

Figure S3. 4: Example of protein gel stained for SOD activity by following C. Weydert and J. Cullen protocol. Gel loading from left to right : commercial bovine SOD 1U, MG1363 pSICE:SP_SOD-Cu + NaCl 3% lysate, MG1363 pSICE:SP_SOD-Cu + NaCl 3% + Cu2+ 0.2mM lysate and MG1363 WT lysate.

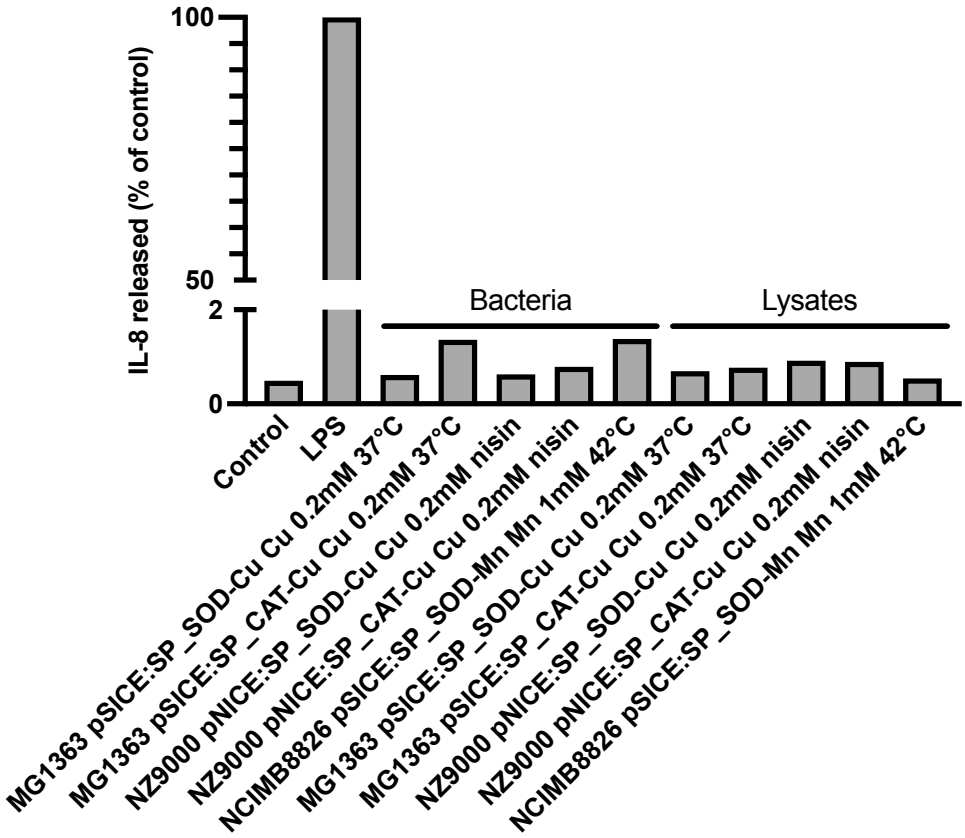

Figure S3. 5: Quantification of IL-8 secretion in controls without LPS. IL-8 secretion was measured by ELISA in supernatant of non-activated HT29–MD2 cells incubated for 5.5 hours with the bacteria or lysates of recombinant LAB. The IL-8 amount measured for activated cells is set at 100 %. Data represent one experiment.